Journal of Experimental and Theoretical Physics, Vol. 101, No. 4, 2005, pp. 577–583.
From Zhurnal Éksperimental'noĭ i Teoreticheskoĭ Fiziki, Vol. 128, No. 4, 2005, pp. 675–681.

ATOMS, MOLECULES, OPTICS

The Non-Markovian Stochastic Liouville Equation and Anomalous Quantum Relaxation Kinetics¶

A. I. Shushin
Institute of Chemical Physics, Russian Academy of Sciences, Moscow, 117977 Russia
e-mail: shushin@chph.ras.ru
Received January 25, 2005

Abstract—We analyze within the continuous-time random walk approach, the kinetics of phase and population relaxation in quantum systems induced by noise with the anomalously slowly decaying correlation function $P(t) \propto (wt)^{-\alpha}$, where $0 < \alpha < 1$. The relaxation kinetics is shown to be anomalously slow. Moreover, for $\alpha < 1$, in the limit of a short characteristic time of fluctuations w^{-1}, the kinetics is independent of w. As $\alpha \longrightarrow 1$, the relaxation regime changes from the static limit to narrowing of fluctuation. Simple analytical expressions are obtained that describe the specific features of the kinetics. © *2005 Pleiades Publishing, Inc.*

1. INTRODUCTION

The noise-induced relaxation in quantum systems is a very important process observed in magnetic resonance [1], quantum optics, nonlinear spectroscopy [2], etc. These processes are often analyzed assuming conventional stochastic properties of the noise: fast decay of correlation functions and a short correlation time τ_c [1]. In the absence of memory, the relaxation is described by very popular Bloch-type equations. The memory effects are also discussed (within the Zwanzig projection operator approach [3]), but either in the lowest orders in the fluctuating interaction V that induces the relaxation or by approximate summation of terms of different orders in V [4].

Recently, much attention was drawn to the processes governed by noises with anomalously slowly decaying correlation functions $P(t) \propto t^{-\alpha}$ with $\alpha < 1$. They are discussed in relation to spectroscopic studies of quantum dots (see [5, 6] and references therein). Similar problems are analyzed in the theory of stochastic resonances [7].

Such anomalous processes cannot be properly described by methods based on expansion in powers of V. The goal of this paper is to analyze the corresponding anomalous relaxation within the continuous-time random walk approach (CTRWA) [8] with the use of the recently derived non-Markovian stochastic Liouville equation (SLE) [9], which enables one to describe relaxation kinetics without the above-mentioned approximations (expansions in V), although it assumes the classical nature of the noise. In some physically reasonable models, it allows description of the phase and population relaxation kinetics in the analytical form even for multilevel systems. In particular, the kinetics is shown to be strongly nonexponential.

2. GENERAL FORMULATION

We consider noise-induced relaxation in a quantum system whose dynamical evolution is governed by the Hamiltonian

$$H(t) = H_s + V(t), \tag{1}$$

where H_s is a term independent of time and $V(t)$ is fluctuating interaction, which models the effects of the noise. The evolution is described by the density matrix $\rho(t)$ satisfying the Liouville equation ($\hbar = 1$)

$$\begin{aligned} \dot{\rho} &= -i\hat{H}(t)\rho, \\ \hat{H}\rho &= [H, \rho] = [H\rho - \rho H]. \end{aligned} \tag{2}$$

$V(t)$-fluctuations are assumed to be symmetric ($\langle V \rangle = 0$) and to result from stochastic jumps between the states $|x_\nu\rangle$ in the (discrete or continuum) space $\{x_\nu\} \equiv \{x\}$ with different $V = V_\nu$ and $H = H_\nu$ (i.e., different $\hat{V} = \hat{V}_\nu \equiv [V_\nu, \ldots]$ and $\hat{H} = \hat{H}_\nu$):

$$\begin{aligned} \hat{\mathcal{V}} &= \sum_\nu |x_\nu\rangle \hat{V}_\nu \langle x_\nu|, \\ \hat{\mathcal{H}} &= \sum_\nu |x_\nu\rangle \hat{H}_\nu \langle x_\nu|. \end{aligned} \tag{3}$$

We use the bracket notation $|k\rangle$ and $|kk'\rangle \equiv |k\rangle\langle k'|$ for eigenstates of H (in the original space) and $\hat{H}$ (in the Liouville space), respectively, and the notation $|x\rangle$ for states in the $\{x\}$-space.

¶ The text was submitted by the author in English.

The macroscopic evolution of the system under study is determined by the evolution operator $\hat{\mathcal{R}}(t)$ in the Liouville space averaged over $V(t)$ fluctuations,

$$\rho(t) = \hat{\mathcal{R}}(t)\rho_i,$$
$$\hat{\mathcal{R}}(t) = \sum_{x, x_i} \hat{\mathcal{G}}(x, x_i|t)P_e(x_i), \tag{4}$$

where $\hat{\mathcal{G}}(x, x'|t)$ is the averaged evolution operator and $P_e(x)$ is the equilibrium distribution in the $\{x\}$ space.

Non-Markovian $V(t)$ fluctuations are described with the use of the CTRWA (which leads to the non-Markovian SLE [9] for $\hat{\mathcal{G}}(t)$). It treats fluctuations as a sequence of sudden changes of $\hat{V}$. The onset of any particular change labeled by j is described by the matrix $\hat{P}_{j-1}$ (in the $\{x\}$ space) of the probabilities not to have any change during time t and its derivative

$$\hat{W}_{j-1}(t) = -\frac{d\hat{P}_{j-1}(t)}{dt}.$$

These matrices are diagonal and independent of j:

$$\hat{P}_{j-1}(t) = \hat{P}(t),\ \hat{W}_{j-1}(t) = \hat{W}(t) = -\frac{d\hat{P}(t)}{dt},\ j > 1,$$

except for

$$\hat{P}_0(t) \equiv \hat{P}_i(t),\ \hat{W}_0(t) \equiv \hat{W}_i(t) = -\frac{d\hat{P}_i(t)}{dt},$$

depending on the problem considered. For nonstationary (n) and stationary (s) fluctuations [8],

$$\hat{W}_i(t) = \hat{W}_n(t) = \hat{W}(t),$$
$$\hat{W}_i(t) = \hat{W}_s(t) = \hat{t}_w^{-1}\int_t^\infty d\tau \hat{W}(\tau),$$

respectively, where

$$\hat{t}_w = \int_0^\infty d\tau\tau\hat{W}(\tau)$$

is the matrix of average times of waiting for the change [8].

In what follows, we operate mainly with Laplace transforms, denoted as

$$\tilde{Z}(\epsilon) = \int_0^\infty dt Z(t)e^{-\epsilon t}$$

for any function $Z(t)$. In particular, noteworthy is the relation

$$\hat{\tilde{P}}_j(\epsilon) = \frac{1 - \hat{\tilde{W}}_j(\epsilon)}{\epsilon}$$

and suitable representations

$$\hat{\tilde{W}}(\epsilon) = [1 + \hat{\Phi}(\epsilon)]^{-1},$$
$$\hat{\tilde{P}}(\epsilon) = [\epsilon + \epsilon/\hat{\Phi}(\epsilon)]^{-1} \tag{5}$$

in terms of a diagonal matrix $\hat{\Phi}(\epsilon)$ with

$$\hat{\Phi}(\epsilon) \overset{\epsilon \to 0}{\approx} (\epsilon/\hat{w})^\alpha,$$

where $\hat{w}$ is a constant matrix and $\alpha \le 1$ (see below).

Evolution in the $\{x\}$-space is governed by the jump operator

$$\hat{\mathcal{L}} = 1 - \hat{\mathcal{P}},$$

where $\hat{\mathcal{P}}$ is the nondiagonal matrix of jump probabilities. This evolution results in relaxation to the equilibrium state $|e_x\rangle$, satisfying the equation

$$\hat{\mathcal{L}}\hat{w}^\alpha|e_x\rangle = 0$$

and is represented as

$$|e_x\rangle = \sum_x P_e(x)|x\rangle,$$
$$\langle e_x| = \sum_x \langle x|$$

(see [9]). We note that (see Eq. (4))

$$\hat{\mathcal{R}}(t) = \langle e_x|\hat{\mathcal{G}}|e_x\rangle \equiv \langle\hat{\mathcal{G}}\rangle. \tag{6}$$

The CTRWA leads to the non-Markovian SLE for $\hat{\mathcal{G}}(x, x_i|t)$ [9]. Solving this SLE yields [9]

$$\hat{\tilde{\mathcal{G}}} = \hat{\tilde{P}}_i(\hat{\Omega}) + \hat{\Omega}^{-1}\hat{\Phi}(\hat{\Omega})[\hat{\Phi}(\hat{\Omega}) + \hat{\mathcal{L}}]^{-1}\hat{\mathcal{P}}\hat{\tilde{W}}_i(\hat{\Omega}), \tag{7}$$

where

$$\hat{\mathcal{L}} = 1 - \hat{\mathcal{P}},$$
$$\hat{\Omega} = \epsilon + i\hat{\mathcal{H}}. \tag{8}$$

In particular, in the case of n fluctuations ($\hat{W}_i = \hat{W}$)

$$\hat{\tilde{\mathcal{G}}} = \hat{\tilde{\mathcal{G}}}_n = \hat{\Omega}^{-1}\hat{\Phi}(\hat{\Phi} + \hat{\mathcal{L}})^{-1}. \tag{9}$$

For s fluctuations ($\hat{W}_i = \hat{W}_s$),

$$\hat{\tilde{\mathcal{G}}} = \hat{\Omega}^{-1} - \hat{\tilde{\mathcal{G}}}_n\hat{\mathcal{L}}(\hat{\Omega}\hat{t}_w)^{-1}.$$

Hereafter, for brevity, we omit the argument $\hat{\Omega}$ of all Laplace transforms unless is results in confusion.

3. USEFUL MODELS AND APPROACHES

3.1. Sudden Relaxation Model

The sudden relaxation model (SRM) [9] assumes sudden equilibration in the $\{x\}$ space described by the operator

$$\hat{\mathcal{L}} = (1 - |e_0\rangle\langle e_0|)\hat{Q}^{-1},$$
$$\hat{Q} = 1 - \sum_x P_0(x)|x\rangle\langle x|, \tag{10}$$

where

$$|e_0\rangle = \sum_x P_0(x)|x\rangle, \quad \langle e_0| = \sum_x \langle x|.$$

For this $\hat{\mathcal{L}}$,

$$|e_x\rangle = \hat{q}|e_0\rangle,$$
$$\hat{q} = \frac{\hat{Q}\hat{w}^{-\alpha}}{\langle e_0|\hat{Q}\hat{w}^{-\alpha}|e_0\rangle} \tag{11}$$

and

$$\langle e_x| = \langle e_0|.$$

In model (10), we obtain

$$\hat{\tilde{\mathcal{R}}}_i = \langle \hat{\tilde{P}}_{Q_i}\rangle + \langle \hat{q}^{-1}\tilde{P}_Q\rangle[1 - \langle \hat{q}^{-1}\hat{\tilde{W}}_Q\rangle]^{-1}\langle \hat{\tilde{W}}_{Q_i}\rangle \tag{12}$$

for any $\hat{\tilde{W}}_i$, where

$$\hat{\tilde{P}}_{Q_i} = \frac{1 - \hat{\tilde{W}}_{Q_i}}{\hat{\Omega}}, \quad \hat{\tilde{W}}_Q = (1 + \hat{\Phi}\hat{Q})^{-1} \tag{13}$$

and

$$\hat{\tilde{W}}_{Q_i} = \hat{\tilde{W}}_i(\hat{\tilde{W}}_Q/\hat{\tilde{W}}).$$

3.2. Short Correlation Time Limit

In practical applications, of special importance is the short correlation time limit (SCTL) for $V(t)$ fluctuations, in which Eq. (12) can be markedly simplified. It corresponds to large characteristic rates w_c of the dependence $\hat{\Phi}(\hat{\Omega}) \equiv \hat{\Phi}(\hat{\Omega}/w_c)$:

$$w_c \gg \|V\|.$$

In this limit, the relaxation kinetics is described by the first terms of the expansion of $\hat{\Phi}(\hat{\Omega}/w_c)$ in small $\hat{\Omega}/w_c$, because $\hat{\Phi}(\epsilon)$ is an increasing function of ϵ with

$$\hat{\Phi}(\epsilon) \xrightarrow{\epsilon \to 0} 0.$$

Some important general conclusions, however, can be made independently of the form of $\hat{\Phi}(\Omega)$ (see below).

3.3. Models for Quantum Evolution and Fluctuations

The obtained general results are conveniently illustrated with the quantum two-level model and the stochastic two-state SRM for $V(t)$-fluctuations.

Quantum evolution of the two-level system is governed by the Hamiltonian (assumed to be a real matrix)

$$H_s = \frac{\omega_s}{2}\begin{bmatrix} 1 & 0 \\ 0 & -1 \end{bmatrix},$$
$$\mathcal{V} = \begin{bmatrix} \mathcal{V}_d & \mathcal{V}_n \\ \mathcal{V}_n & -\mathcal{V}_d \end{bmatrix} \begin{matrix} |+\rangle \\ |-\rangle \end{matrix}. \tag{14}$$

The two-state SRM suggests that fluctuations result from jumps between two states (in the $\{x\}$ space), for example, $|x_+\rangle$ and $|x_-\rangle$, whose kinetics is described by

$$\hat{\mathcal{L}} = 2(1 - |e_x\rangle\langle e_x|),$$
$$|e_x\rangle = \frac{1}{2}\||x_+\rangle + |x_-\rangle\rangle. \tag{15}$$

Below, we consider two examples of these models.

1. Diagonal noise [10]:

$$\omega_s = 0, \quad \mathcal{V}_n = 0,$$
$$\mathcal{V}_d = \omega_0(|x_+\rangle\langle x_+| - |x_-\rangle\langle x_-|),$$

and

$$H_{\nu = \pm} = \pm\frac{1}{2}\omega_0(|+\rangle\langle +| - |-\rangle\langle -|). \tag{16}$$

2. Nondiagonal noise:

$$\mathcal{V}_d = 0, \quad \mathcal{V}_n = \nu(|x_+\rangle\langle x_+| - |x_-\rangle\langle x_-|),$$

and, hence,

$$H_{\nu = \pm} = H_s \pm \nu(|+\rangle\langle -| + |-\rangle\langle +|). \tag{17}$$

The first model describes dephasing, and the second is useful for studying population relaxation.

In model (14), dephasing and population relaxation are characterized by two functions.

1. The spectrum $I(\omega)$, which is taken in a form corresponding to Fourier-transformed free-induction-decay (FTFID) experiments [11]:

$$I(\omega) = \frac{1}{\pi}\mathrm{Re}\langle s|\hat{\tilde{\mathcal{R}}}(i\omega)|s\rangle. \tag{18}$$

2. The difference of level populations:

$$N(t) = \langle n|\hat{\mathcal{R}}(t)|n\rangle. \tag{19}$$

In these two functions,

$$|s\rangle = \frac{1}{\sqrt{2}}\||+-\rangle + |-+\rangle\rangle,$$
$$|n\rangle = \frac{1}{\sqrt{2}}\||++\rangle - |--\rangle\rangle. \quad (20)$$

4. GENERAL RESULTS IN THE SCTL

Within the SCTL ($\|V\|/w_c \ll 1$), particularly simple results are obtained for $\|H_s\|/w_c \ll 1$. In the lowest order in $\|\hat{\Phi}(\hat{\Omega}/w_c)\| \ll 1$,

$$\hat{\tilde{\mathcal{R}}} \approx \hat{\tilde{\mathcal{R}}}_n \approx \frac{\langle \hat{q}^{-1}\hat{Q}\hat{\Omega}^{-1}\hat{\Phi}(\hat{\Omega})\rangle}{\langle \hat{q}^{-1}\hat{Q}\hat{\Phi}(\hat{\Omega})\rangle} \quad (21)$$

$$= \frac{\langle \hat{w}^{\alpha}\hat{\Omega}^{-1}\hat{\Phi}(\hat{\Omega})\rangle}{\langle \hat{w}^{\alpha}\hat{\Phi}(\hat{\Omega})\rangle}. \quad (22)$$

This formula holds for any initial matrix $\hat{\tilde{W}}_i$ and, in particular, for *s* fluctuations if

$$\|\hat{t}_w\| \sim \frac{1}{w_c} \ll \frac{1}{\|\hat{\Omega}\|}.$$

The more complicated SCTL case

$$\|H_s\|/w_c \approx 1$$

can be analyzed by expanding $\hat{\tilde{\mathcal{G}}}$ in powers of the parameter

$$\xi = \|V\|/\|H_s\| \ll 1.$$

In particular, within the general two-level model (Eq. (14)) with $V_d = 0$, in the second order in ξ, the diagonal and nondiagonal elements of $\rho(t)$ are decoupled and the corresponding elements of $\hat{\mathcal{R}}(t)$ are expressed in terms of the universal function

$$R_k(t) = \frac{1}{2\pi i}\int_{-i\infty}^{i\infty} d\epsilon \frac{e^{i\epsilon t}}{\epsilon + k\epsilon/\langle\hat{\Phi}(\epsilon)\rangle}, \quad (23)$$

$$\langle\mu|\hat{\mathcal{R}}(t)|\mu\rangle = \exp(-i\omega_\mu t)R_{k_\mu}(t)$$
$$(\mu = n, +-, -+), \quad (24)$$

where

$$\omega_\mu = \langle\mu|\hat{H}_s|\mu\rangle, \quad k_n = 2\mathrm{Re}(k_{+-}),$$
$$k_{+-} = k_{-+}^* = \frac{1}{2}\omega_s^{-2}\langle\mathcal{V}_n\hat{q}^{-1}[1-\hat{\tilde{W}}_Q(2i\omega_s)]\mathcal{V}_n\rangle. \quad (25)$$

5. ANOMALOUS FLUCTUATIONS

The simplest model for anomalous fluctuations can be written as [12]

$$\hat{\Phi}(\epsilon) = (\epsilon/\hat{w})^{\alpha}, \quad 0 < \alpha < 1, \quad (26)$$

where $\hat{w}$ is the matrix of fluctuation rates, diagonal in the $|x\rangle$-basis. For simplicity, $\hat{w}$ is assumed to be independent of *x*, i.e., $\hat{w} \equiv w$ (this parameter can be associated with w_c mentioned above). Model (26) describes the anomalously slow decay of the matrix

$$\hat{W}(t) \propto 1/t^{1+\alpha}$$

(very long memory effects in the system [12]), for which only the case of *n* fluctuations is physically sensible.

In SCTL (22), model (26) yields the expression

$$\hat{\tilde{\mathcal{R}}}_n(\epsilon) = \langle\hat{\Omega}^{\alpha-1}(\epsilon)\rangle\langle\hat{\Omega}^{\alpha}(\epsilon)\rangle^{-1},$$
$$\hat{\Omega}(\epsilon) = \epsilon + i\hat{\mathcal{H}}, \quad (27)$$

which shows that $\hat{\tilde{\mathcal{R}}}_n(\epsilon)$ (and $\hat{\mathcal{R}}_n(t)$) is independent of the characteristic rate *w*. For $\alpha = 0$ and $\alpha = 1$, Eq. (27) reproduces the static and fluctuation narrowing limits [1]:

$$\hat{\tilde{\mathcal{R}}}_n(\epsilon) = \langle\hat{\Omega}^{-1}(\epsilon)\rangle$$

and

$$\hat{\tilde{\mathcal{R}}}_n(\epsilon) = \frac{1}{\langle\hat{\Omega}(\epsilon)\rangle},$$

respectively.

Of certain interest is the limit as $\alpha \longrightarrow 1$, in which formula (27) predicts the Bloch-type exponential relaxation

$$\hat{\tilde{\mathcal{R}}}_n(\epsilon) \approx [\epsilon + i\hat{H}_s + (\alpha-1)\langle\hat{\Omega}\ln(\hat{\Omega})\rangle_{\epsilon\to 0}]^{-1}, \quad (28)$$

controlled by the relaxation rate matrix

$$\hat{W}_r = (\alpha-1)\mathrm{Re}\langle\hat{\Omega}\ln(\hat{\Omega})\rangle_{\epsilon\to 0}$$

and accompanied by frequency shifts represented by

$$\hat{h} = i(\alpha-1)\mathrm{Im}\langle\hat{\Omega}\ln(\hat{\Omega})\rangle_{\epsilon\to 0}.$$

However, the matrices $\hat{W}_r$ and $\hat{h}$ (unlike those in the conventional Bloch equation) are independent of the characteristic rate *w* of $V(t)$ fluctuations.

5.1. Dephasing for Diagonal Noise

In model (16), the spectrum $I(\omega)$ can be obtained in the general SRM (10),

$$I(\omega) = n_\alpha \frac{\psi_-^{\alpha}\psi_+^{\alpha-1} + \psi_-^{\alpha-1}\psi_+^{\alpha}}{(\psi_-^{\alpha})^2 + (\psi_+^{\alpha})^2 + 2\psi_-^{\alpha}\psi_+^{\alpha}\cos(\pi\alpha)}, \quad (29)$$

where

$$\psi_{\pm}^{\beta}(\omega) = \langle|\omega - 2V_d|^{\beta}\theta[\pm(\omega - 2V_d)]\rangle,$$

where $\theta(z)$ is the Heaviside step function and

$$n_{\alpha} = \sin(\pi\alpha)/\pi.$$

In the two-state SRM (16),

$$I(\omega) = \frac{n_{\alpha}}{2\omega_0}\theta(y)\frac{y + y^{-1} + 2}{y^{\alpha} + y^{-\alpha} + 2\cos(\pi\alpha)}, \qquad (30)$$

where

$$y = \frac{\omega_0 + \omega}{\omega_0 - \omega}$$

(see also [6]). According to this formula, the anomalous dephasing (unlike conventional dephasing [1]) leads to broadening of $I(\omega)$ only in the region $|\omega| < \omega_0$ and singular behavior of $I(\omega)$ at $\omega \longrightarrow \pm\omega_0$:

$$I(\omega) \sim \frac{1}{(\omega \pm \omega_0)^{1-\alpha}}.$$

For $\alpha > \alpha_c \approx 0.59$ (α_c satisfies the relation $\alpha_c = \cos(\pi\alpha_c/2)$), the two-state-SRM formula also predicts the occurrence of the central peak (at $\omega = 0$) [6] of the Lorenzian shape and width

$$w_L \approx \frac{\omega_0\cos(\pi\alpha/2)}{\sqrt{\alpha^2 - \cos^2(\pi\alpha/2)}},$$

$$I(\omega) \approx \frac{1}{2\pi}\frac{\tan(\pi\alpha/2)\omega_0^{-1}}{1 + (\omega/w_L)^2},$$

whose intensity increases with increasing $\alpha - \alpha_c$ (Fig. 1). At $\alpha \sim 1$, the parameters of this peak are reproduced by Eq. (28), in which

$$\langle\hat{\Omega}\ln\hat{\Omega}\rangle_{\epsilon} = -\frac{\pi}{2}\omega_0.$$

The origin of the peak indicates the transition from static broadening at $\alpha \ll 1$ to narrowing at $\alpha \sim 1$ (see Eq. (27)). For systems with complex spectra, this transition can, of course, be strongly smoothed. The behavior of $I(\omega)$ is illustrated in Fig. 1 for different values of the parameters of the model.

5.2. Dephasing for Nondiagonal Noise

The model in Eq. (17) makes it possible to reveal certain additional specific features of dephasing. We restrict ourselves to analysis of the case where $\|H_s\| \sim w_s \gtrsim w$ and the most interesting part of the spectrum at $|\omega| \sim \omega_s$. Equations (23) and (24) show that the elements $\langle\mu|\mathcal{R}(t)|\mu\rangle$ ($\mu = +-, -+$), which describe phase relaxation, are then given by

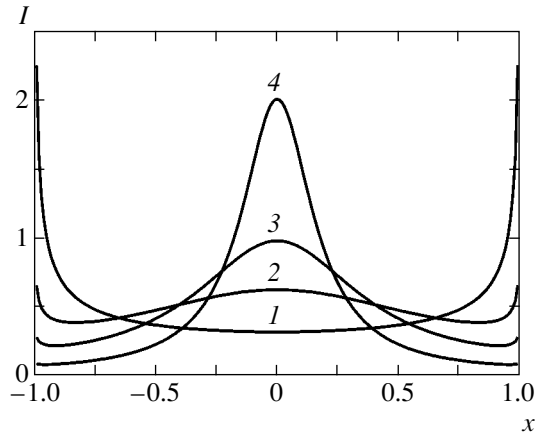

Fig. 1. Spectrum $I(x) = I(\omega)\omega_0$, where $x = \omega/\omega_0$, calculated in model (16) (using Eq. (29)) for different values of α = 5 (*1*), 7 (*2*), 8 (*3*), and 9 (*4*).

$$\langle\mu|\mathcal{R}(t)|\mu\rangle = \exp(-i\omega_{\mu}t)E_{\alpha}[-k_{\mu}(wt)^{\alpha}], \qquad (31)$$

where

$$E_{\alpha}(-z) = (2\pi i)^{-1}\int_{-i\infty}^{i\infty}\frac{dye^{y}}{y + zy^{1-\alpha}}$$

is the Mittag–Leffler function [12]. Therefore, for $|\omega| \sim \omega_s$,

$$I(\omega) = I_0(\omega_s + \omega) + I_0(\omega_s - \omega), \qquad (32)$$

where

$$I_0(\omega) = n_0\sin\phi_x(|x|^{1+\alpha} + |x|^{1-\alpha} + 2|x|\cos\phi_x)^{-1}, \qquad (33)$$

with

$$x = \frac{\omega}{|k_{+-}|^{1/\alpha_{\omega}}}, \quad n_0 = (\pi|k_{+-}|^{1/\alpha_{\omega}})^{-1},$$

$$\phi_x = \frac{\pi\alpha}{2} + \operatorname{sgn}x\arctan\left[\frac{\sin(\pi\alpha/2)}{\cos(\pi\alpha/2) + 2^{-\alpha^{-1}}\omega_s/w}\right]. \qquad (34)$$

Formula (32) predicts singular behavior of $I(\omega)$ at $\omega \sim \pm\omega_s$,

$$I(\omega) \sim \frac{1}{|\omega \pm \omega_s|^{1-\alpha}},$$

and slow decrease of $I(\omega)$ with the increase of $|\omega \pm \omega_s|$,

$$I(\omega) \sim \frac{1}{|\omega \pm \omega_s|^{1+\alpha}}.$$

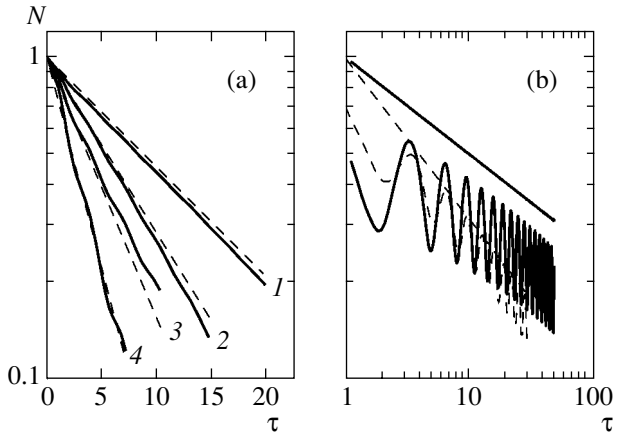

Fig. 2. Population relaxation kinetics $N(\tau)$, where $\tau = E_0 t$, calculated with Eq. (36) (a) for large α and different $r = 2\nu/\omega_s$: $\alpha = 0.95$, $r = 1.0$ (*1*); $\alpha = 0.95$, $r = 2.0$ (*2*); $\alpha = 0.88$, $r = 1.0$ (*3*); $\alpha = 0.88$, $r = 2.0$ (*4*); and (b) for small $\alpha = 0.3$ (solid line) and $\alpha = 0.5$ (dashed line) ($r = 0.7$). Straight lines in (a) and (b) represent exponential (Eq. (35)) and $t^{-\alpha}$ dependences, respectively (in (a), they are shown by dashed lines).

In the limit $\omega_s/w \ll 1$, we have

$$\phi_x \approx \pi\alpha\theta(x)$$

and, hence,

$$I_0(\omega) \sim \theta(\omega).$$

This implies that, for $\omega_s/w \ll 1$, the spectrum $I(\omega)$ is localized in the region $|\omega| < \omega_s$ and looks similar to $I(\omega)$ for diagonal dephasing at $\alpha < \alpha_c$. For $\omega_s/w \gtrsim 1$, however, $I(\omega)$ is nonzero outside this region; moreover, in the limit $\omega_s/w \gg 1$, the spectrum $I_0(\omega)$ becomes symmetric, $I_0(\omega) = I_0(-\omega)$, similarly to conventional spectra.

It is worth noting that, for $\omega_s/w \ll 1$, the functions $\langle\mu|\mathcal{R}(t)|\mu\rangle$ and $I(\omega)$ are independent of w (in agreement with Eq. (22)), because $k_\mu \propto (\omega_s/w)^\alpha$ and $k_\mu(wt)^\alpha \propto (\omega_s t)^\alpha$. In the opposite limit, however, $k_\mu \sim w^0$ and, therefore, the characteristic relaxation time behaves as w^{-1}.

5.3. Population Relaxation

Specific features of the anomalous population relaxation can be analyzed with the model of nondiagonal noise (17).

In particular, in the respective limits $\|H_s\| \sim \omega_s \gtrsim w$ and $1 - \alpha \ll 1$, Eqs. (23), (24), and (28) imply that

$$N(t) = E_\alpha[-k_n(wt)^\alpha], \quad N(t) = \exp(-w_\alpha t), \quad (35)$$

where $E_\alpha(-x)$ is the Mittag–Leffler function defined above and

$$w_\alpha \approx k_n(\alpha \longrightarrow 1)w \sim 1 - \alpha.$$

The first of these formulas predicts a very slow population relaxation at

$$t > \tau_r = w^{-1}(k_n/w)^{1/\alpha},$$

namely,

$$N(t) \propto 1/t^\alpha.$$

Similarly to $I(\omega)$, the function $N(t)$ is in fact independent of w in the limit $\omega_s/w \ll 1$, because $k_n \propto (\omega_s/w)^\alpha$ in this case. In the opposite limit $\omega_s/w > 1$, the characteristic time population relaxation behaves as w^{-1}, because k_n is independent of w (as in the case of phase relaxation).

In the limit $\|H_s\|, \|V\| \ll w$, we obtain

$$N(t) = \frac{1}{2\pi i}\int_{-i\infty}^{i\infty} d\epsilon e^{\epsilon t}\frac{\omega_s^2\epsilon^{\alpha-1} + 4\nu^2\Omega_{\alpha-1}(\epsilon)}{\omega_s^2\epsilon^\alpha + 4\nu^2\Omega_\alpha(\epsilon)}, \quad (36)$$

where

$$\Omega_\beta(\epsilon) = [(\epsilon + 2iE_0)^\beta + (\epsilon - 2iE_0)^\beta]/2 \quad (37)$$

and

$$E_0 = \sqrt{\nu^2 + \omega_s^2/4}.$$

Naturally, in the corresponding limits, expression (36) reproduces formulas (35) with

$$k_n \approx 2^{\alpha-1}\cos(\pi\alpha/2)(E_0/w)^\alpha$$

and

$$w_\alpha \approx \pi(1-\alpha)\nu^2/E_0$$

(see Fig. 2). Outside these limits, $N(t)$ can be evaluated numerically (some results are shown in Fig. 2). In general, $N(t)$ is the oscillating function (of frequency $\sim E_0$) with slowly decreasing average value and oscillation amplitude: for $E_0 t \gg 1$,

$$N(t) \sim 1/t^\alpha$$

(except in the limit as $\alpha \longrightarrow 1$).

6. CONCLUSIONS

The above analysis of relaxation kinetics in quantum systems induced by anomalous noise demonstrates a number of specific features of this kinetics. They are analyzed with the use of the two-level quantum model, as an example, although the observed anomalous effects can manifest themselves in more complicated multilevel quantum systems. The proposed theoretical method is quite suitable for analyzing these systems, a study currently in progress.

Noteworthy is the fact that in some limits, the theory predicts relaxation kinetics described by the Mittag–Leffler function $E_\alpha[-(wt)^\alpha]$. Following a number of recent works (see [12]), this kinetics can be considered

a result of the anomalous Bloch equation with a fractional time derivative. For brevity, we have not discussed the corresponding representations.

It is also interesting to note that, with increasing α, the effects of the anomaly of fluctuations decrease but still persist. To clarify them, we briefly consider the model

$$\Phi(\epsilon) = (\epsilon/w) + \zeta(\epsilon/w)^{1+\alpha},$$

in which $0 < \alpha < 1$, and w and ζ are constants with $\zeta \ll 1$ (a small value of ζ ensures that $W(t) > 0$). Possible effects can be analyzed within the SCTL with the use of Eqs. (22)–(24). For example, in the limit $||H||/w \ll 1$, we obtain the formula

$$\tilde{\mathcal{R}} \approx [\epsilon + i\hat{H}_s + \zeta w^{-\alpha}\langle(i\hat{\mathcal{H}})^{1+\alpha} - (i\hat{H}_s)^{1+\alpha}\rangle]^{-1},$$

predicting the Bloch-type relaxation of both phase and population, but with the rate

$$\hat{W}_r = \zeta w^{-\alpha}\mathrm{Re}\langle(i\hat{\mathcal{H}})^{1+\alpha} - (i\hat{H}_s)^{1+\alpha}\rangle,$$

which depends on w as $w^{-\alpha}$ and is, therefore, slower than in the conventional Bloch equation ($\hat{W}_r \sim 1/w$ [1]). Analysis also shows that, in the expression for $\tilde{\mathcal{R}}$, terms proportional to $w(\epsilon/w)^{1+\alpha}$ occur as well. They lead to the inverse power-type asymptotic behavior of

$$\langle\mu|\hat{R}(t)|\mu\rangle \propto 1/t^{2+\alpha},$$

observed, however, only at very long times $t \gg w^{-1}$.

In our brief analysis, we neglected the effect of a possible natural width of lines corresponding to additional slow exponential relaxation in the system. It is clear that the developed method allows taking these effects into account straightforwardly whenever needed.

ACKNOWLEDGMENTS

This paper was supported in part by the Russian Foundation for Basic Research (project no. 03-03-32253).

REFERENCES

1. A. Abragam, *The Principles of Nuclear Magnetism* (Clarendon, Oxford, 1961; Inostrannaya Literatura, Moscow, 1963).
2. S. Mukamel, *Principles of Nonlinear Optical Spectroscopy* (Oxford Univ. Press, Oxford, 1995).
3. D. Forster, *Hydrodynamic Fluctuations, Broken Symmetry, and Correlation Functions* (Benjamin, Reading, MA, 1975; Atomizdat, Moscow, 1980).
4. P. N. Argyres and P. L. Kelley, Phys. Rev. A **134**, 98 (1964).
5. K. Shimizu, R. G. Neuhauser, C. A. Leatherdale, *et al.*, Phys. Rev. B **63**, 205316 (2001).
6. Y. Jung, E. Barkai, and R. J. Silbey, Adv. Chem. Phys. **123**, 199 (2002).
7. I. Goychuk and P. Hänggi, Phys. Rev. E **69**, 021104 (2004).
8. J. W. Haus and K. W. Kehr, Phys. Rep. **150**, 263 (1987).
9. A. I. Shushin, Phys. Rev. E **64**, 051108 (2001); Phys. Rev. E **67**, 061 107 (2003).
10. P. W. Anderson, J. Phys. Soc. Jpn. **9**, 316 (1954).
11. H. van Willigen, P. R. Levstein, and M. H. Ebersole, Chem. Rev. **93**, 173 (1993).
12. R. Metzler and J. Klafter, Phys. Rep. **339**, 1 (2000).

Journal of Experimental and Theoretical Physics, Vol. 101, No. 4, 2005, pp. 584–596.
Translated from Zhurnal Éksperimental'noĭ i Teoreticheskoĭ Fiziki, Vol. 128, No. 4, 2005, pp. 682–697.

ATOMS, MOLECULES, OPTICS

Steady-State Light-Induced Forces in Atomic Nanolithography

A. V. Bezverbnyi[a,*], O. N. Prudnikov[b], A. V. Taichenachev[b], A. M. Tumaikin[c], and V. I. Yudin[c,]**

[a] *Admiral Nevelskiĭ Maritime State University, Vladivostok, 690059 Russia*

[b] *Novosibirsk State University, Novosibirsk, 630090 Russia*

[c] *Institute of Laser Physics, Siberian Division, Russian Academy of Sciences, Novosibirsk, 630090 Russia*

*e-mail: *alexb@mail.vntc.ru, alexb@msun.ru; **llf@laser.nsc.ru*

Received February 24, 2005

Abstract—An analysis of general characteristics of light-induced forces is presented for arbitrary monochromatic masks in which optical pumping of atoms and spontaneous emission play an important role. Dependence of regions of localization on detuning and ellipticity is determined for cyclic transitions of two types: $J \longrightarrow J$ with half-integer J and $J \longrightarrow J + 1$ with arbitrary J. Numerical simulations of atomic beam focusing with one- and two-dimensional light masks show that spatial atom distributions with narrow features and high contrast can be formed in dissipative masks. In particular, spherical aberration is substantially reduced when the pumping field is tuned to a $J \longrightarrow J + 1$ transition with large J in lin⊥lin configuration as compared to nondissipative masks. © *2005 Pleiades Publishing, Inc.*

1. INTRODUCTION

Direct-deposition atom lithography is an effective nanofabrication method using light-induced forces in which a combination of coplanar light beams is used as a mask for a well-collimated atomic beam impinging on a substrate to create a film with modulated thickness (see Fig. 1). The state of the art and potential applications of nanostructures created by this method were discussed in recent reviews [1, 2]. In the first successful implementation of this technology, high spatial resolution (finer than 20 nm) was attained by focusing chromium atoms in a standing wave, and effective application was made of the resulting nanostructures [3]. Subsequently, noncollinear two- and three-beam masks were used to create periodic two-dimensional nanostructures [4, 5]. It was demonstrated that gradients of light intensity [3–5] and polarization [6] play a key role in a light mask.

Two regimes of interaction between a light mask and atoms should be distinguished. In the regime characterized by coherent interaction between atoms and far-off-resonant field [1, 2], the atomic beam is focused by the adiabatic potential generated as a result of spatially modulated shift of magnetic sublevels, whereas spontaneous emission is negligible if the atom–field interaction time is relatively short. The other (dissipative) regime in atom lithography, proposed in [7, 8], combines focusing and cooling of atoms. In principle, this combination can be used to fabricate smaller nanostructures with enhanced contrast. In the latter regime, the light-induced force is the resultant of conservative, dissipative, and random components associated with the optical potential, optical friction, and diffusion in the momentum space, respectively. It should be mentioned here that a detailed analysis of cooling and local-

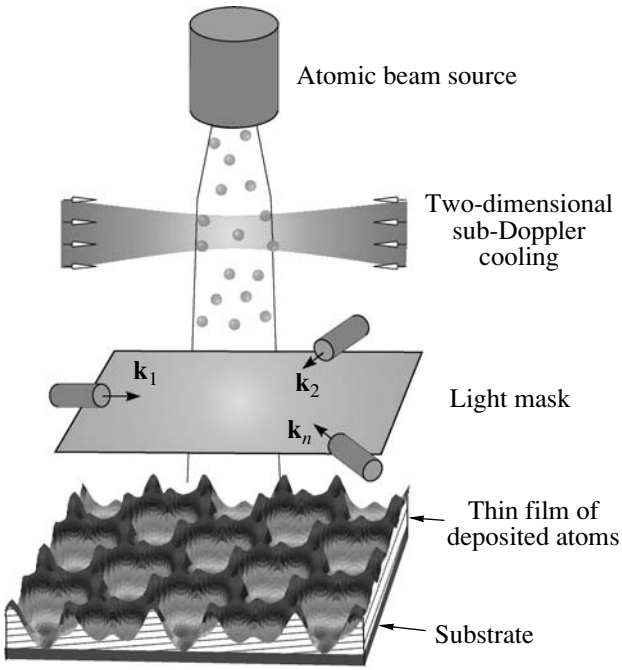

Fig. 1. Generic setup for direct-deposition atom lithography.

ization of atoms in nondegenerate states in standing waves was presented in [9].

This paper deals with the effect of spontaneous decay and optical pumping on the spatial distribution of the light-induced force $\mathbf{F}_0(\mathbf{r})$ acting on an atom at rest. The present analysis is motivated by the following considerations. First, since the atom–field interaction time (on the order of 100 ns) exceeds the decay time of the excited atomic state (on the order of 10 ns) in typical experiments [1, 2], neither spontaneous emission nor optical pumping can be ignored. Second, optical pumping of atoms must be taken into account in calculating the fluctuating force in the dissipative regime [7, 8]. An analysis shows that the incoherent contribution to atom-field interaction can substantially modify the optical potential. Assuming that the interaction time is much longer than the optical-pumping time, we obtain compact analytical expressions for the steady-state force $\mathbf{F}_0(\mathbf{r})$ in several configurations of monochromatic field for a wide range of the transition saturation parameter. We examine the spatial distribution of $\mathbf{F}_0(\mathbf{r})$ and its dependence on field invariants in one- and two-dimensional configurations. Generally, the results obtained in this study can be applied in both conservative and dissipative regimes. In particular, we show that spherical aberration is substantially reduced when the pumping field is tuned to a $J \longrightarrow J + 1$ transition with large J in the lin⊥lin configuration. Numerical simulations of atomic beam focusing based on a semiclassical (Langevin-equation) approach reveal that spatial atom distributions with narrow features and high contrast can be formed by using certain one- and two-dimensional field patterns.

2. MODEL

Consider a beam of atoms with angular momenta J_0 and J_1 in the ground and excited states, respectively. The $J_0 \longrightarrow J_1$ atomic transition is driven by the field of s resonant monochromatic light beams with wavevectors $\mathbf{k}_n$ lying in a plane orthogonal to the atomic beam:

$$\begin{aligned} \mathbf{E}(\mathbf{r}, t) &= \exp(-i\omega t)\mathbf{E}(\mathbf{r}) + \text{c.c.}, \\ \mathbf{E}(\mathbf{r}) &= \sum_{n=1}^{s} \exp(i\mathbf{k}_n \cdot \mathbf{r})\mathbf{E}_n = \exp(i\Phi)\mathscr{E}\mathbf{e}, \end{aligned} \tag{1}$$

where the unit polarization vector $\mathbf{e}$ ($\mathbf{e}^* \cdot \mathbf{e} = 1$, $\mathrm{Im}(\mathbf{e} \cdot \mathbf{e}) = 0$), the overall phase Φ, and the real amplitude $\mathscr{E}$ of the overall field are functions of the position vector $\mathbf{r}$. The analysis that follows makes use of the scalar field invariants

$$\mathscr{E}^2 = \mathbf{E} \cdot \mathbf{E}^*, \quad \mathscr{I} = \mathbf{E} \cdot \mathbf{E} = \exp(2i\Phi)(\mathbf{e} \cdot \mathbf{e})\mathscr{E}^2.$$

The former is proportional to the local intensity of the field, and the latter carries information about its local phase and polarization. In particular, the degree of linear polarization can be represented as

$$l = \mathbf{e} \cdot \mathbf{e} = \frac{\sqrt{\mathscr{I} \cdot \mathscr{I}^*}}{\mathscr{E}^2}.$$

The kinetics of atomic ensembles interacting with resonant electromagnetic field are governed by quantum master equations describing energy, momentum, and angular-momentum transfer between atoms and field. Momentum transfer is due to recoil effects in mechanical atom–field interactions, which are generally weak since the photon momentum $\hbar k$ is small as compared to the atomic momentum spread Δp. Therefore, the evolution of an atomic ensemble can follow at least two essentially different regimes [10, 11]. In one of these, the characteristic rate of relaxation of optically pumped atoms to equilibrium with respect to internal degrees of freedom can be estimated as

$$\Gamma_{\text{op}} = \gamma\pi_1,$$

where γ is the rate of spontaneous decay of the excited state and π_1 is the normalized excited-state population. Translational relaxation is much slower process, and the corresponding rate is on the order of $(\hbar k/\Delta p)\Gamma_{\text{scatt}}$, where Γ_{scatt} is the total rate of spontaneous and stimulated photon scattering by atoms. Accordingly, the kinetics of the translational degrees of freedom can be adequately described in the semiclassical approximation, which leads to the concept of light-induced force acting on atoms [10, 11]. To calculate the average force, the atomic density matrix must be determined in the zeroth-order approximation with respect to the recoil parameter by solving exactly the generalized optical Bloch equations. The required general solution is not known for an atom moving with an arbitrary velocity in an arbitrary field. However, an atom cooled to the Doppler limit or a sub-Doppler temperature in transverse directions can be treated as a slowly moving one [10]; i.e., it can be assumed that its displacement parallel to the field within the optical pumping time is much smaller than the period of spatial oscillation of the field:

$$v(\Gamma_{\text{op}})^{-1} \ll \lambda.$$

In this approximation, the light-induced force can be represented as a series

$$\mathbf{F}(\mathbf{r}, \mathbf{v}) = \mathbf{F}_0(\mathbf{r}) + \hat{\mathscr{X}}(\mathbf{r}) \cdot \mathbf{v} + \ldots, \tag{2}$$

where $\mathbf{F}_0(\mathbf{r})$ is the force on an atom at rest at a point $\mathbf{r}$ that controls the focusing and localization of atoms. The symmetric part of the tensor $\hat{\mathscr{X}}$ is responsible for momentum dissipation (optical friction). Note that

both $\mathbf{F}_0$ and $\hat{\mathscr{X}}$ can be expanded in terms of field gradients [11]:

$$\mathbf{F}_0 = \hbar\gamma\sum_{\kappa=1}^{4} F_\kappa \mathbf{g}_\kappa,$$
$$\hat{\mathscr{X}} = \hbar\left[\sum_{\kappa,\kappa'=1}^{4} X_{\kappa\kappa'}\mathbf{g}_\kappa \otimes \mathbf{g}_{\kappa'} + \sum_{\kappa,\kappa'=5}^{6} X_{\kappa\kappa'}\mathbf{g}_\kappa \otimes \mathbf{g}_{\kappa'}\right], \quad (3)$$

where $\mathbf{g}_\kappa \otimes \mathbf{g}_{\kappa'}$ denotes the tensor direct product. The field gradients are defined by the expressions

$$\mathbf{g}_1 = \partial_\mathbf{r}\ln\mathscr{E}, \quad \mathbf{g}_2 = \partial_\mathbf{r}\Phi, \quad \mathbf{g}_3 = \partial_\mathbf{r} l,$$
$$\mathbf{g}_4 = \partial_\mathbf{r}\phi, \quad \mathbf{g}_5 = \partial_\mathbf{r}\alpha, \quad \mathbf{g}_6 = \partial_\mathbf{r}\beta. \quad (4)$$

Here, $\mathbf{g}_1$, $\mathbf{g}_2$, and $\mathbf{g}_3$ are the gradients of intensity, overall phase, and ellipticity, respectively, and the angle gradients $\mathbf{g}_4$, $\mathbf{g}_5$, and $\mathbf{g}_6$ define the orientation of the polarization ellipse relative to a reference coordinate system. In particular, the angle ϕ defines the orientation of the polarization ellipse relative to the axis perpendicular to the polarization-ellipse plane. General properties of these vectors in the regions of circular and linear polarization of the overall field and in the neighborhoods of its intensity peaks were analyzed in [12].

To find analytical expressions for the coefficients F_κ, one must calculate the atomic density matrix in the zeroth-order approximation with respect to the recoil parameter and atom velocity, which can be done approximately in certain special cases. In this study, we analyze the steady-state regime in which the atom–field interaction time τ is much longer than the optical pumping time:

$$\Gamma_{op}\tau \gg 1. \quad (5)$$

Compact analytical expressions for the density matrix corresponding to arbitrary closed $J_0 \longrightarrow J_1$ dipole transitions were found in [13]. These solutions are used below to derive formulas for F_κ.

3. LIGHT-INDUCED FORCE ON AN ATOM AT REST

According to [13], the steady-state optical coherences between magnetic sublevels of the ground and excited states vanish for $J \longrightarrow J-1$ transitions with arbitrary J and for $J \longrightarrow J$ transitions with arbitrary J because of coherent population trapping. Therefore, the steady-state light-induced force on atoms also vanishes for transitions of these types. For the remaining $J \longrightarrow J+1$ transitions with arbitrary J and $J \longrightarrow J$ with half-integer J,

$$F_1 = -2\tilde{\delta}\pi_1, \quad F_2 = \pi_1,$$
$$F_3 = -\frac{\tilde{\delta}\pi_1(1 - A/\alpha_1)}{l}, \quad (6)$$
$$F_4 = -\pi_1\frac{A}{\alpha_1}\sqrt{1-l^2}, \quad \pi_1 = \frac{S\alpha_1}{\alpha_0 + 2S\alpha_1},$$

where π_1 is the total excited-state population, $\tilde{\delta} = \delta/\gamma$ is the normalized detuning, and the local saturation parameter

$$S = \frac{1}{2 + 8\tilde{\delta}^2}\frac{I}{I_{sat}}$$

is defined so that its value is 1/2 when $\delta = 0$ and I is equal to the saturation intensity[1]

$$I_{sat} = \frac{2\pi^2\hbar\gamma c}{3\lambda^3}.$$

The parameters α_0, α_1, and A depend only on the local ellipticity. Making use of results reported in [15], we obtain the following expressions.

For $J \longrightarrow J+1$ transitions,

$$\alpha_0 = \frac{1}{(2J+1)(4J+1)!l}\sum_{\substack{l=\nu \\ \nu+2,\ldots}}^{2J} C_l P_l(l^{-1}),$$
$$\alpha_1 = P_{2J+1}(l^{-1}), \quad A = \frac{P'_{2J+1}(l^{-1})}{(2J+1)l},$$
$$C_l = (2l+1)(2J-l)!(2J+l+1)!,$$

where $P_n(x)$ denotes Legendre polynomials, $\nu = 0$ for integer J, and $\nu = 1$ for half-integer J.

For $J \longrightarrow J$ transitions with half-integer J,

$$\alpha_0 = \frac{4J(J+1)}{l}\sum_{l=1,3,\ldots}^{2J} C_l P_l(l^{-1}),$$
$$\alpha_1 = 2J+1, \quad A = 0,$$
$$C_l = (2l+1)\left[\frac{(l-1)!!}{l!!}\right]^2\frac{(2J+l)!!}{(2J-l)!!}\frac{(2J-l-1)!!}{(2J+l+1)!!}.$$

[1] We use the standard definition of saturation parameter (e.g., see [14]).

The force $\mathbf{F}_0$ is the resultant of the scattering force (also called radiation pressure force)

$$\mathbf{F}_{\text{scatt}} = \hbar\gamma(\mathrm{F}_2\mathbf{g}_2 + \mathrm{F}_4\mathbf{g}_4)$$

and the dipole (or gradient) force

$$\mathbf{F}_{\text{dip}} = \hbar\gamma(\mathrm{F}_1\mathbf{g}_1 + \mathrm{F}_3\mathbf{g}_3).$$

The scattering force arises from stimulated absorption of a photon by an atom followed by spontaneous emission and is an even function of detuning. The dipole force arises from stimulated coherent emission and is an odd function of detuning. When $|\tilde{\delta}| \geq 10$, the latter contribution to $\mathbf{F}_0$ plays a dominant role; i.e., it is of primary interest for atom lithography. However, effects due to the scattering force are also considered below.

4. DIPOLE FORCE

Expressions (6) for the coefficients in the expansion of $\mathbf{F}_0$ in terms of field gradients can be used to represent the dipole force as the product of the excited-state population $\pi_1(\mathbf{r})$ with the gradient of a dimensionless scalar function $\Psi(\mathbf{r})$:

$$\mathbf{F}_{\text{dip}} = -\hbar\delta\pi_1(\mathbf{r})\partial_{\mathbf{r}}\Psi(\mathbf{r}). \quad (7)$$

Even though the dipole force is not conservative in the general case, the function Ψ is analogous to potential in many respects. For example, every point where $\mathbf{F}_{\text{dip}} = 0$ is either minimum or maximum point of Ψ. The zeros of $\pi_1(\mathbf{r})$ are not associated with any additional zeros of the dipole force. This can be shown by using formulas (8) and (10) for Ψ given below. In blue- and red-detuned light fields, the dipole force drives atoms toward the minimum and maximum points of Ψ, respectively. When $S\alpha_1/\alpha_0 \gg 1$ ($\pi_1 \approx 1/2$), the dipole force behaves as a conservative one, and the corresponding potential is proportional to Ψ.

4.1. $J \longrightarrow J$ Transitions with Half-Integer J

For these transitions, the function $\Psi(\mathbf{r})$ can be represented as

$$\Psi = \ln|\mathcal{J}|. \quad (8)$$

The corresponding dipole force never saturates in the regions where the light field is circularly polarized ($\ell = 0$) even if the light intensity is high. In these regions,

$$\mathbf{F}_{\text{dip}} \approx -\partial_{\mathbf{r}}V_{\text{eff}},$$

where the effective potential is [16]

$$V_{\text{eff},1} = \hbar\delta S\frac{1}{2J(2J+2)}\left[\frac{(2J)!!}{(2J-1)!!}\right]^2\ell^{2J+1}. \quad (9)$$

The physical explanation for the low saturation at the points of circular polarization of the total field (e.g., σ_+) lies in the fact that all atoms are pumped into a dark state $|J_0, m = J_0\rangle$. Accordingly, the light-induced force $\mathbf{F}_0$ vanishes at these points (the potential $V_{\text{eff},1}$ reaches a minimum) in any configuration of blue-detuned light field.

When $\ell \neq 0$, the dipole force $\mathbf{F}_{\text{dip}}$ is characterized as follows. When $S\alpha_1/\alpha_0 \gg 1$, it is associated with the optical potential

$$V_{\text{eff},2} = \frac{\hbar\delta}{2}\ln|\mathcal{J}|.$$

When $S \lesssim 1$, the dipole force is not conservative, and the points where $\mathbf{F}_{\text{dip}} = 0$ are determined to a lesser degree by the spatial distribution of I, being mainly associated with the extrema of the invariant

$$|\mathcal{J}| = |\mathbf{E}\cdot\mathbf{E}|.$$

Moreover, the atoms interacting with a blue-detuned mask are localized around the field nodes, where $\mathbf{E} = 0$. Therefore, the setup for atom lithography with $\delta > 0$ can be designed so that the atoms interacting with an arbitrary light mask are mainly attracted to the points of circular polarization and field nodes. Even though additional regions of localization may appear around the minimum points of $|\mathcal{J}|$, numerical simulations of specific field configurations have demonstrated that these regions play an insignificant role in forming the spatial distribution of deposited atoms. The distribution of atoms interacting with a red-detuned mask on the substrate is completely determined by the maxima of $|\mathcal{J}|$. In the general case, the regions of their localization do not coincide with those of linear polarization or maximum intensity, even though coincidence of this kind is characteristic of some field configurations used in current experiments [12].

4.2. $J \longrightarrow J+1$ Transitions

In this case, the function Ψ in (7) is

$$\Psi = \frac{1}{2J+1}\ln[(\mathscr{E}^2\ell)^{2J+1}P_{2J+1}(\ell^{-1})], \quad (10)$$

where $\ell^{2J+1}P_{2J+1}(\ell^{-1})$ is an even function of ℓ that reaches a maximum when the field is circularly polarized ($\ell = 0$) and monotonically decreases as $|\ell| \longrightarrow 1$. When $S \gg 1$, the potential associated with the dipole force $\mathbf{F}_{\text{dip}}$ is

$$V_{\text{eff},3} = \frac{\hbar\delta}{2}\Psi.$$

In the general case, the dipole force has both potential and solenoidal components. However, computations show that the latter has a negligible effect on the localization of atoms interacting with a light mask.

For a $J \longrightarrow J + 1$ transition, the regions of localization are determined by the combination of the distributions of I and $|\mathcal{J}|$. Generally, these regions are distinct both from those of circular (or linear) polarization and from the nodes (or antinodes) of light intensity and can be found only by analyzing the functions $\mathcal{E}(\mathbf{r})$, $\ell(\mathbf{r})$, and $\Psi(\mathbf{r})$ simultaneously.

5. RADIATION PRESSURE FORCE

The radiation pressure force $\mathbf{F}_{\text{scatt}}$ plays an important role in light masks, even though it is weaker by a factor of $\gamma/|\delta|$ as compared to $\mathbf{F}_{\text{dip}}$ in far-off-resonant fields, because the spatial distributions of these components of $\mathbf{F}_0$ are essentially different in D-dimensional fields configuration with $D > 1$. For example, $\mathbf{F}_{\text{scatt}}$ vanishes at every point where the field is circularly polarized; i.e., it varies as $\mathbf{C} \times \delta\mathbf{r}$ with the distance $\delta\mathbf{r}$ from the point ($\delta r \longrightarrow 0$), where $\mathbf{C}$ is a constant vector [12]. The characteristics of this force are discussed here for transitions of the two types considered above.

5.1. $J \longrightarrow J$ Transitions with Half-Integer J

In this case, the radiation pressure force is

$$\mathbf{F}_{\text{scatt}} = \frac{\hbar\gamma\pi_1\mathbf{H}}{4(2J+1)\mathcal{E}^4\ell^2}, \qquad \mathbf{H} = i(\mathcal{J}\partial_{\mathbf{r}}\mathcal{J}^* - \mathcal{J}^*\partial_{\mathbf{r}}\mathcal{J}). \tag{11}$$

In the neighborhood of some point $\mathbf{r}_0$, the invariant $\mathcal{J}$ at a point $\mathbf{r}$ can be represented as a decomposition in terms $\delta\mathbf{r} = \mathbf{r} - \mathbf{r}_0$ up to second-order terms:

$$\mathcal{J} \approx \mathcal{J}_0 + \mathbf{C}\cdot\delta\mathbf{r} + \delta\mathbf{r}\cdot\hat{\mathcal{D}}\cdot\delta\mathbf{r},$$

where $\mathcal{J}_0 \equiv \mathcal{J}(\mathbf{r}_0)$ and $\hat{\mathcal{D}}$ is a symmetric tensor. Accordingly,

$$\mathbf{H} = 2\text{Im}(\mathcal{J}_0\mathbf{C}^* + 2\mathcal{J}_0\hat{\mathcal{D}}^*\cdot\delta\mathbf{r}) + i\delta\mathbf{r}\times[\mathbf{C}\times\mathbf{C}^*],$$

where the first and second terms are potential and solenoidal vectors, respectively. The difference between the conservative contributions of $\mathbf{F}^{\text{pot}}_{\text{scatt}}$ and $\mathbf{F}^{\text{pot}}_{\text{dip}}$ manifests itself in the difference of their respective effects on the atom averaged over an arbitrary trajectory of length l,

$$\langle\mathbf{F}\rangle_l = l^{-1}\int\mathbf{F}\,d\mathbf{l}.$$

Generally, the averaged dipole force $\langle\mathbf{F}_{\text{dip}}\rangle_l$ vanishes in periodic and quasiperiodic symmetric field configurations in the limit of $l \gg \lambda$. Conversely, the effect of the mean radiation pressure force tends to increase with l, as in masks with unbalanced intensities of light beams (the simplest one-dimensional example is a traveling plane wave). This nonvanishing force drives atoms out of the region of atom–field interaction. The solenoidal component of $\mathbf{F}^{\text{pot}}_{\text{scatt}}$ also gives rise to drift on length scales $l \gg \lambda$. It should also be noted that the dipole force can be "rectified" ($\langle\mathbf{F}_{\text{dip}}\rangle_l \neq 0$) in certain configurations, which are generally not used as light masks. An example of one-dimensional field configuration of this kind was given in [15].

5.2. $J \longrightarrow J + 1$ Transitions

For these transitions, the radiation pressure force is

$$\mathbf{F}_{\text{scatt}} = \left(-\frac{\hbar\gamma\pi_1}{\alpha_1\mathcal{E}^2}\right)\left(A\mathbf{G} + \frac{P'_{2J}(l^{-1})\mathbf{H}}{4(2J+1)(\mathcal{E}l)^2}\right), \qquad (\mathbf{G})_i = \text{Im}\sum_j(\mathbf{E})_j\partial_{r_i}(\mathbf{E}^*)_j. \tag{12}$$

Here, $\mathbf{G}$ is a solenoidal vector:

$$\partial_{\mathbf{r}}\cdot\mathbf{G} = 0.$$

This additional contribution to the solenoidal component of $\mathbf{F}_{\text{scatt}}$ is significant in the regions of circular field polarization.

6. ONE-DIMENSIONAL FIELD CONFIGURATIONS

Symmetric one-dimensional field configurations giving rise to light-induced forces with periodic potentials are of special interest for atom lithography. Every such configuration is a combination of two light beams of equal amplitude $\mathcal{E}_s$ counterpropagating along the z axis. They can be parameterized by the angle θ between the semimajor axes of the polarization ellipses of the beams and their respective ellipticity angles ε_1 and ε_2. By definition of the ellipticity angle, $|\tan\varepsilon|$ is the ratio of semiminor to semimajor axis of the polarization ellipse and the sign of ε is determined by the helicity of the wave. Thus, the configurations considered in this section are characterized by certain specific relations between ε_1, θ, and ε_2. They constitute a broad class of one-dimensional potentials depending on the light beam polarizations and the type of atomic transition. These configurations have common features: first, localization regions correspond to maximum or minimum points of the function Ψ considered above; second, in far-off-resonant fields with $\delta > 0$ and $\delta < 0$, atoms are attracted to minimum and maximum points of the pseudopotential Ψ, respectively.

6.1. Simple One-Dimensional Configurations

6.1.1. Elliptically polarized standing wave. In this case, both overall phase and polarization are spa-

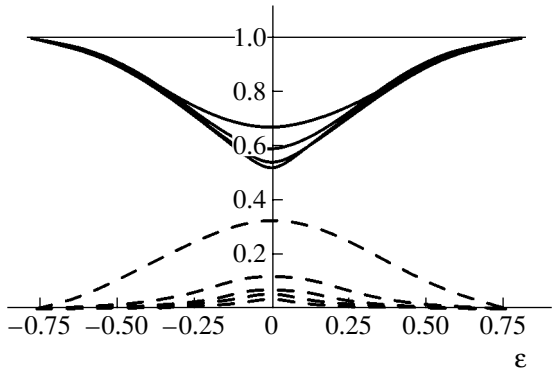

Fig. 2. Effective saturation parameter (in arbitrary units) vs. ellipticity angle in a standing wave for $J \longrightarrow J+1$ transitions with $J = 0$, 1, 2, 3, and 4 (solid curves, top to bottom) and for $J \longrightarrow J$ transitions with $J = 1/2$, 3/2, …, 9/2 (dashed curves, top to bottom).

tially uniform, and

$$S(z) = 2S_0[1 + \cos(2kz)],$$

where S_0 is the saturation parameter for an individual light beam. The radiation pressure force is

$$F(z) = -\partial_z U(z),$$
$$U(z) = \frac{\hbar\delta}{2}\ln\left[1 + \frac{2\alpha_1}{\alpha_0}S(z)\right]. \quad (13)$$

The corresponding expression for optical potential is characteristic of a two-level atom in a nondegenerate state interacting with a standing wave [9]. However, the effective saturation parameter $S_{\text{eff}} = S\alpha_1/\alpha_0$ depends both on the type of transition and on the field polarization (see Fig. 2). The focusing effect of a standing wave is well known. In blue- and red-detuned fields, atoms are attracted to intensity nodes and antinodes, respectively.

6.1.2. lin⊥lin configuration. This configuration is the superposition of counterpropagating linearly polarized traveling waves with mutually orthogonal polarizations. Both phase and intensity gradients vanish, the orientations of the major axes of the polarization ellipse remain invariant, ellipticity varies as $\ell = \cos(2kz)$, and the dipole force is

$$F(z) = -\partial_z V(\cos 2kz),$$
$$V(\ell) = \hbar\delta\int\frac{\pi_1(1 - A/\alpha_1)}{\ell}d\ell. \quad (14)$$

The results shown in Fig. 3 for several atomic transitions demonstrate qualitative difference in spatial distribution of the dipole force calculated by using (14) between transitions of two types. First, the forces calculated for $J \longrightarrow J+1$ transitions and $J \longrightarrow J$ transitions with half-integer J have opposite signs. Furthermore, the force is anharmonic in the neighborhoods of the points of circular polarization (where $\ell = \cos 2\varepsilon \longrightarrow 0$) for $J \longrightarrow J$ transitions with half-integer J, except for $J = 1/2$, because the force scales with $\propto \ell^{2J}$ according to (9). For $J \longrightarrow J+1$ transitions, the spatial distribution of the force tends to have a triangular shape; i.e., the domains of linear (harmonic) behavior of the force around the points where $\ell = 0$ become wider. This tendency is particularly pronounced when $S \gg 1$, in which case $\pi_1 \approx 1/2$ and the corresponding optical potential can be approximately expressed as

$$V(\ell) \approx \frac{\hbar\delta}{2(2J+1)}\ln[\ell^{2J+1}P_{2J+1}(\ell^{-1})].$$

Spherical aberration should be substantially weaker for $J \longrightarrow J+1$ transitions with large J, when atoms are localized around points of circular polarization in masks with $\delta < 0$, as compared to transitions with small J or standing-wave optical potentials. When $S \gg 1$, the difference between the two types of transitions also manifests itself in the potential depth, which approaches a limit that does not exceed $\hbar\delta\ln 2/2$ for $J \longrightarrow J+1$ transitions and increases as $\ln S$ for $J \longrightarrow J$

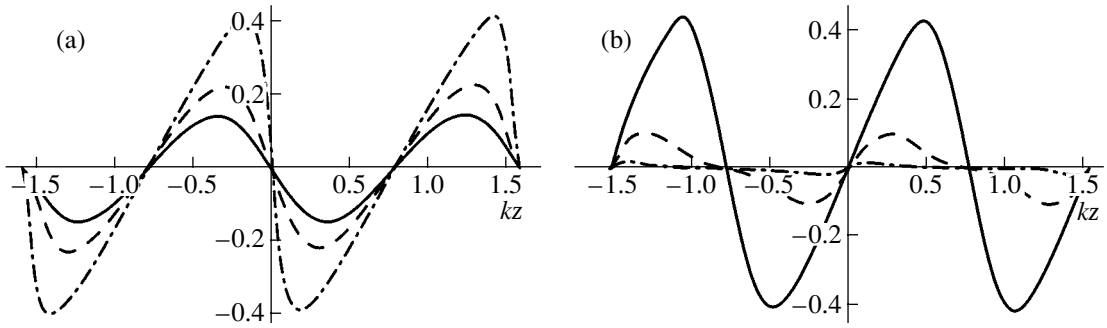

Fig. 3. Dipole force (in units of $\hbar k\delta$) vs. kz in lin⊥lin configuration: (a) $J \longrightarrow J+1$ transitions with $J = 1/2$ (solid curve), 1 (dashed curve), and 4 (dash–dot curve); (b) $J \longrightarrow J$ transitions with $J = 1/2$ (solid curve), 3/2 (dashed curve), and 9/2 (dash–dot curve). Saturation parameter is $S_0 = 1$ for an individual light beam.

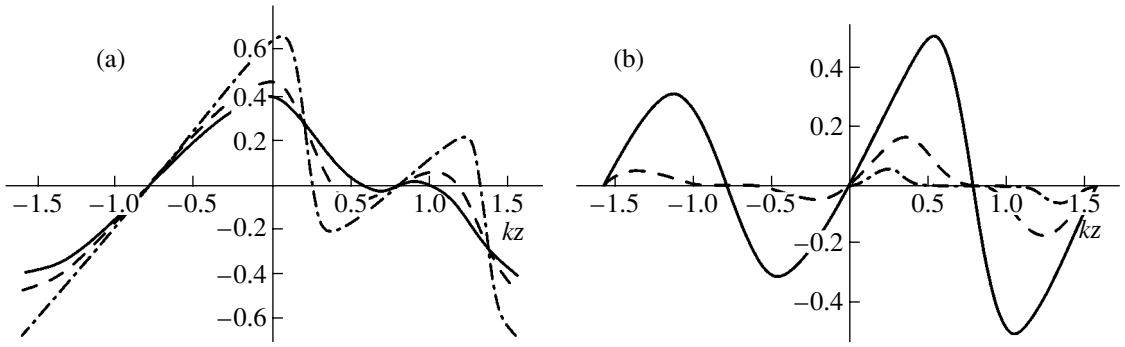

Fig. 4. Dipole force (in units of $\hbar k\delta$) vs. kz in $\varepsilon \perp \varepsilon$ configuration: (a) $J \longrightarrow J + 1$ transitions with $J = 1/2$ (solid curve), 1 (dashed curve), and 4 (dash–dot curve); (b) $J \longrightarrow J$ transitions with $J = 1/2$ (solid curve), 3/2 (dashed curve), and 9/2 (dash–dot curve). Saturation parameter is $S_0 = 1$ for an individual light beam, and ellipticity angle is $\varepsilon = \pi/16$.

transitions (in particular, its value is $\hbar\delta\ln(1 + 3S/2)/4$ for the $1/2 \longrightarrow 1/2$ transition).

6.2. One-Dimensional Configurations of Elliptically Polarized Waves

Next, we consider field distributions characterized by either two or four nonzero gradients $\mathbf{g}_i$. We single out three classes of symmetric periodic optical potentials parameterized by ε_1, θ, and ε_2 for which the light-induced force averaged over λ vanishes.

Two of these classes correspond to $\varepsilon_1 = -\varepsilon_2 = \varepsilon$ and the combination of $\varepsilon_1 = \varepsilon_2 = \varepsilon$ with $\theta = \pi/2$. Hereinafter, they are referred to as the ε–θ–$\bar{\varepsilon}$ and $\varepsilon \perp \varepsilon$ configurations, respectively. The third one is the class of elliptically polarized standing waves, for which $\varepsilon_1 = \varepsilon_2 = \varepsilon$ and $\theta = 0$.

6.2.1. $\varepsilon \perp \varepsilon$ configuration. In this case, the scalar field invariants are

$$\mathscr{E}^2 = 2\mathscr{E}_s^2[1 - \sin 2\varepsilon \sin 2kz], \qquad \mathscr{I} = 2\mathscr{E}_s^2 \cos 2\varepsilon \cos 2kz. \tag{15}$$

Since the gradients of phase and angle ϕ vanish, so therefore does the radiation pressure force. The intensity and ellipticity of the overall field are nonuniform if $\varepsilon \neq 0$. According to Eq. (15), the intensity extremum points, where $I \sim \mathscr{E}^2$, correlate with the points of circular polarization, where

$$l = \cos 2\varepsilon \cos 2kz/[1 - \sin 2\varepsilon \sin 2kz] = 0.$$

At these points, it holds that $2kz = \pi/2(2n + 1)$ and the function Ψ reaches its maxima and minima for $J \longrightarrow J + 1$ and $J \longrightarrow J$ transitions, respectively. The spatial distributions of the corresponding dipole forces illustrated by Fig. 4 have minima of two types. The potential distributions arising in the low-intensity regions when blue-detuned waves are used to pump a $J \longrightarrow J + 1$ transition are analogous to those in the high-intensity regions of a red-detuned mask in the case of a $J \longrightarrow J$ transition.

6.2.2. ε–θ–$\bar{\varepsilon}$ configuration. In this case, the field invariants are

$$\mathscr{E}^2 = 2\mathscr{E}_s^2[1 + \cos\theta \cos 2\varepsilon \cos 2kz], \qquad \mathscr{I} = 4\mathscr{E}_s^2[\cos\theta + \cos 2\varepsilon \cos 2kz + i\sin\theta \sin 2\varepsilon]. \tag{16}$$

Accordingly, all of the four gradients $\mathbf{g}_\kappa$ ($\kappa = 1, \ldots, 4$) do not vanish in the general case. The extremum points of intensity correlate with the points of linear polarization, where $\ell = 1$. The function Ψ reaches its maxima at these points for $J \longrightarrow J$ transitions, while its minima are reached at the intensity minimum points for $J \longrightarrow J + 1$ transitions. However, Ψ reaches either minima or maxima at the maximum points of I, depending on the angular momentum, θ, and ε. When the ellipticity angle is small and $\theta \approx \pi/2$, the potential distribution has minima of two types (see Fig. 5) located at the intensity maximum points for $J \longrightarrow J + 1$ when $\delta < 0$ and at the intensity minimum points for $J \longrightarrow J$ when $\delta > 0$. Since the gradients of phase and angle ϕ do not vanish in the general case ($\varepsilon \neq 0, \pm\pi/4$ and $\theta \neq 0$), radiation pressure contributes to the optical potential, vanishing at the points of linear polarization. This contribution substantially modifies the resulting optical potential when detuning is relatively small ($|\delta| \approx \gamma$).

6.3. Numerical Results

We present the numerical results obtained in simulations of atomic beam focusing in lin⊥lin configuration by the semiclassical Monte Carlo method introduced into the theory of laser cooling in [17]. As noted above, the spatial distribution of the dipole force $\mathbf{F}_0$ acting on an atom at rest via $J \longrightarrow J + 1$ transitions is well approximated by a triangle (Fig. 3a). Thus, the interval where the optical potential has a parabolic profile widens with increasing J. This tendency should lead to a substantial reduction of spherical aberration.

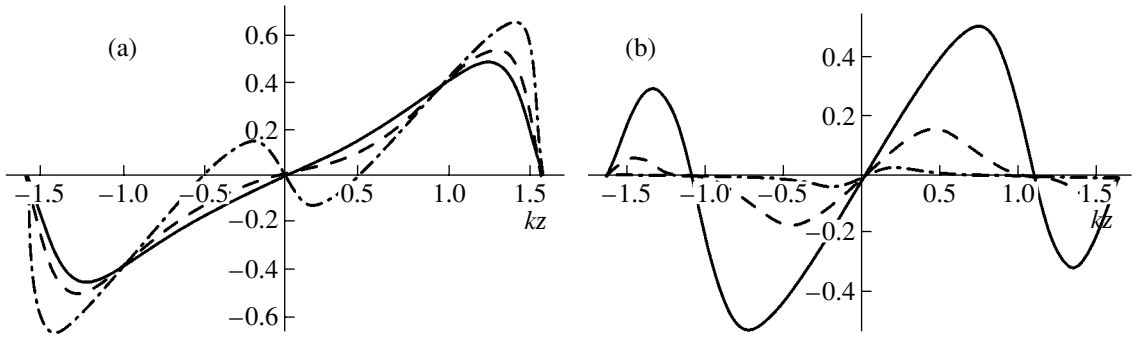

Fig. 5. Dipole force (in units of $\hbar k\delta$) vs. kz in ε–θ–$\bar{\varepsilon}$ configuration: (a) $J \longrightarrow J+1$ transitions with $J = 1/2$ (solid curve), 1 (dashed curve), and 4 (dash–dot curve); (b) $J \longrightarrow J$ transitions with $J = 1/2$ (solid curve), 3/2 (dashed curve), and 9/2 (dash–dot curve). Saturation parameter is $S_0 = 1$ for an individual light beam, $\theta = \pi/3$, and $\varepsilon = \pi/32$.

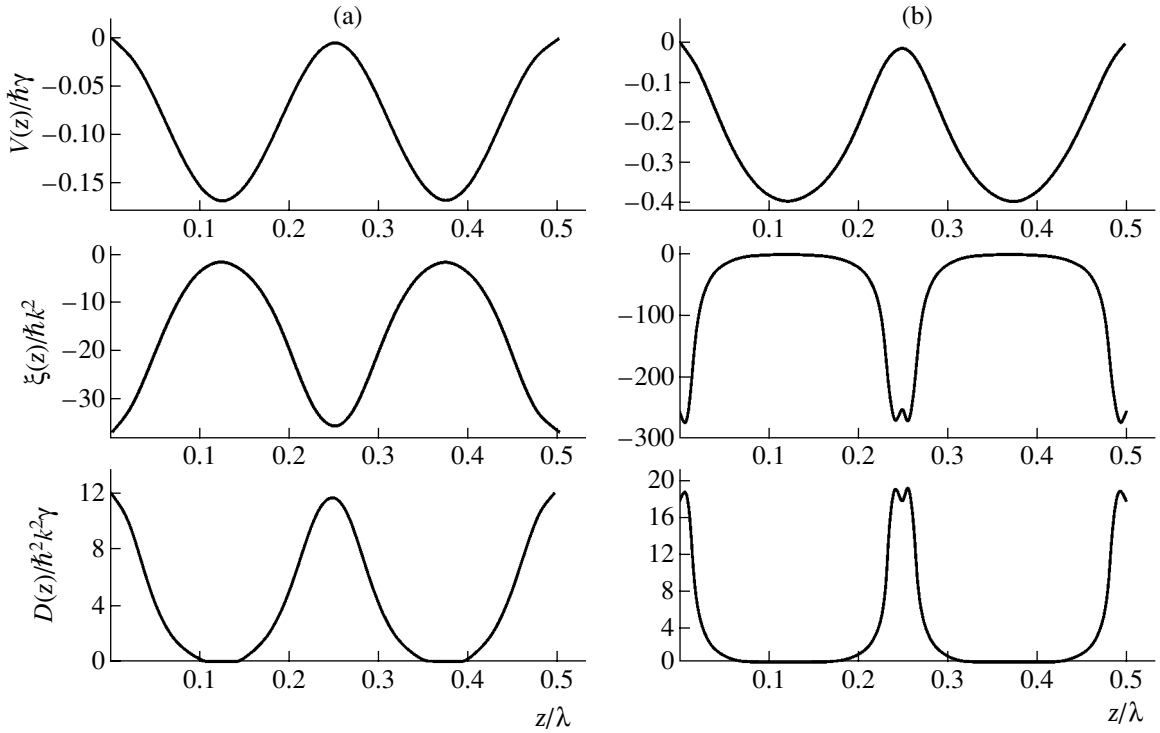

Fig. 6. Spatial distributions of optical potential $V(z)$, friction coefficient $\xi(z)$, and diffusion coefficient $D(z)$ in lin⊥lin configuration: (a) $1/2 \longrightarrow 3/2$ transitions; (b) $4 \longrightarrow 5$ transitions. Saturation parameter is $S_0 = 0.158$ for an individual light beam, and detuning is $\delta = -5\gamma$.

In addition to $\mathbf{F}_0$, we take into account optical friction (as a correction of first order in velocity) and diffusion in momentum space. It is important that the relative effects of these dissipative and random forces as compared to $\mathbf{F}_0$ depend on control parameters (detuning, intensity, atom–field interaction time, incident atomic-beam divergence, etc.), field configuration, and type of atomic transition. The results of numerical simulations show that these effects are negligible.

Let us discuss the focusing effect on a beam of cesium atoms caused by fields tuned to the $1/2 \longrightarrow 3/2$ and $4 \longrightarrow 5$ transitions. Figure 6 shows the distributions of the optical potential $V(z)$, the friction coefficient $\xi(z)$, and the diffusion coefficient $D(z)$. Steep gradients of $\xi(z)$ and $D(z)$ are observed when the angular momentum is large ($4 \longrightarrow 5$ transition). Note that these coefficients are small in the neighborhoods of potential minima, where atoms are focused. Accordingly, their effect on the spatial distribution of atoms in these neighborhoods is weak.

The atomic beams used in our simulations were assumed to have a Gaussian initial momentum distribution with $\Delta p_\perp = 10\hbar k$. Figure 7 shows the spatial distribution of atoms after their interaction with the mask.

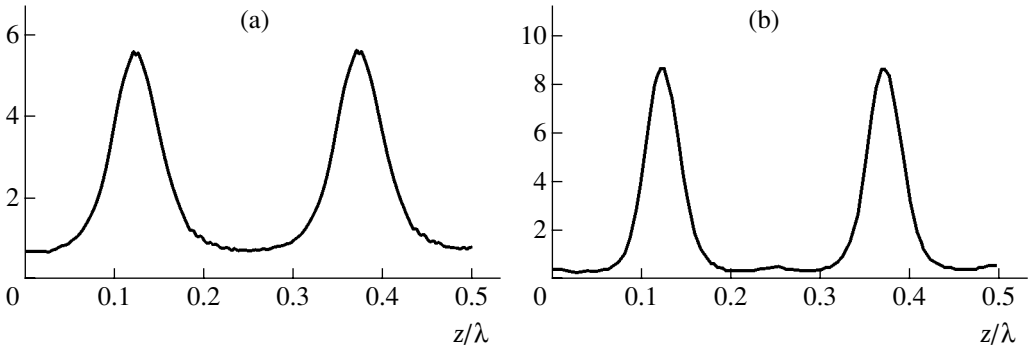

Fig. 7. Profiles of atomic beams focused onto a substrate in lin⊥lin configuration: (a) 1/2 ⟶ 3/2 transitions; (b) 4 ⟶ 5 transitions. Saturation parameter is $S_0 = 0.158$ for an individual light beam, and detuning is $\delta = -5\gamma$. Interaction time corresponds to a quarter of the optical-potential oscillation period.

Note that the observed narrow peaks, with half-width at half-maximum $\Delta x = 0.051\lambda$ in Fig. 7a and $\Delta x = 0.038\lambda$ in Fig. 7b, are characteristic of the thick-lens regime. The interaction time was set equal to a quarter of the oscillation period at a minimum point of $V(z)$: $t_{\text{int}} = 49.16\gamma^{-1}$ and $41.37\gamma^{-1}$ for the 1/2 ⟶ 3/2 and 4 ⟶ 5 transitions, respectively. The difference in Δx is primarily explained by difference between the spatial distributions of the dissipative and random forces corresponding to transitions of different types (Fig. 6). Figure 7 demonstrates that the pedestal normalized to its initial value for the 4 ⟶ 5 transition, $\mathcal{R} = 0.19$, is substantially lower than that for the 1/2 ⟶ 3/2 transition, $\mathcal{R} = 0.35$, in agreement with the expected substantial reduction of spherical aberration for the 4 ⟶ 5 transition.

7. TWO-DIMENSIONAL FIELD CONFIGURATIONS

We have also examined certain two-dimensional field configurations formed by combining three or four light beams. In the general case, a wide diversity of relations between the spatial distributions of I, ℓ, and Ψ is observed. Therefore, to predict possible distributions of deposited atoms, detailed preliminary analysis is required of the fringe patterns of $I(\mathbf{r})$ and $\ell(\mathbf{r})$ for $J \longrightarrow J$ transitions (with half-integer J) and of the more complicated function $\Psi(\mathbf{r})$ for $J \longrightarrow J+1$ transitions. As an example, we consider the symmetric combination of three light beams with $\varepsilon_1 = \varepsilon_2 = \varepsilon_3 = \varepsilon$ and equal amplitudes $\mathcal{E}_s$ [12] (see Fig. 8).

In this case,

$$\mathcal{E}^2 = \mathcal{E}_s^2[3 + C(Z^*Z - 3)], \quad Z = \sum_{n=1}^{3} \exp(i\mathbf{k}_n \cdot r),$$

$$\mathcal{I} = \mathcal{E}_s^2[(1+2C)(Z^2 - 2Z^*) - 2D(Z^2 - 3Z^*)],$$

$$C = (\mathbf{e}_i \cdot \mathbf{e}_j^*)_{i \neq j}, \quad D = (\mathbf{e}_i \cdot \mathbf{e}_j)_{i \neq j},$$

where

$$\mathbf{e}_i = \frac{\mathbf{e}_z + \epsilon \mathbf{k}_i \times \boldsymbol{\epsilon}_z}{\sqrt{1 + |\epsilon|^2}}$$

is the polarization vector of the ith beam, and

$$\epsilon = \frac{\tan\theta + i\tan\varepsilon}{1 - i\tan\theta\tan\varepsilon}.$$

Note that the condition

$$\tan^2\varepsilon_0 = \frac{3\cos 2\theta_0 + 1}{3\cos 2\theta_0 - 1}$$

implies that $C = 0$ and the overall field intensity is uniform. Therefore, when the configuration parameters are close to ε_0 and θ_0, the distributions of $\Psi(\mathbf{r})$ and $I(\mathbf{r})$ are substantially different, and $\Psi(\mathbf{r})$ and $\ell(\mathbf{r})$ are strongly correlated. Conversely, as $\varepsilon \longrightarrow 0$ and $\theta \longrightarrow 0$, strong correlation between I and Ψ is predicted. However, distinct distributions of I, ℓ, and Ψ extremum points are observed for intermediate values of these parameters.

Figures 9a–9c show, respectively, the distributions of I, ℓ, and Ψ obtained for $\tan\varepsilon = 2$ and $\tan\theta = 1/\sqrt{2}$ in the case when Ψ is calculated for the 1 ⟶ 2 transi-

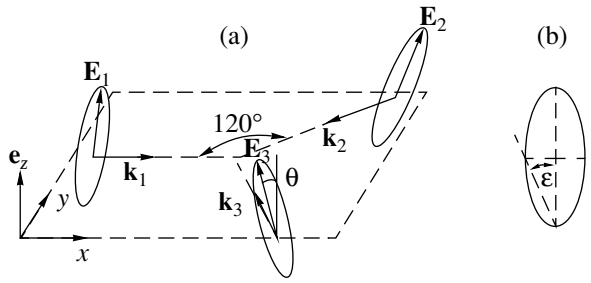

Fig. 8. (a) Three-beam configuration. (b) Polarization ellipse of an individual beam (ε is ellipticity angle).

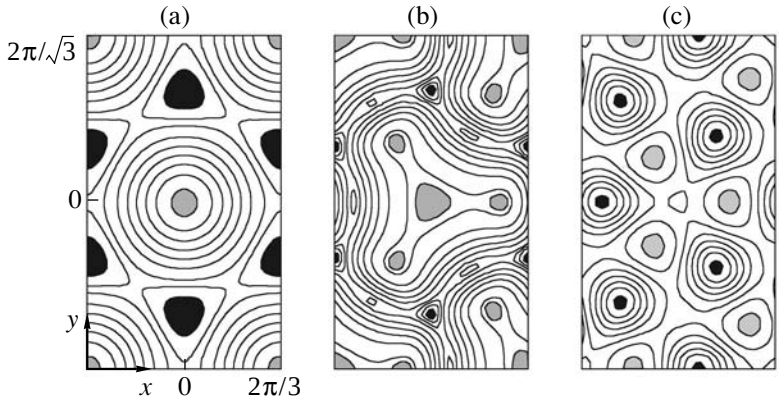

Fig. 9. Contour plots of (a) intensity $I(\mathbf{r})$, (b) ellipticity $l(\mathbf{r})$, and (c) pseudopotential $\Psi(\mathbf{r})$. Gray and black areas correspond to peaks and troughs, respectively.

tion. Note that this distribution weakly depends on J. The contour plots are restricted to the region

$$|kx| \le 2\pi/3, \quad |ky| \le 2\pi/\sqrt{3},$$

which corresponds to an elementary cell of this field configuration. Figure 9 demonstrates that the maxima of Ψ lie between extremum points of I and ℓ, whereas the minimum points of Ψ correlate with the maximum points of ℓ.

7.1. Numerical Results

We present the numerical results obtained by simulating the formation of periodic fine structures on the substrate in the three-beam configuration considered above. As in our one-dimensional simulations, we use the semiclassical Monte Carlo method proposed in [17], taking into account the corrections to the force $\mathbf{F}_0$ acting on an atom at rest due to optical friction,

$$\mathbf{F}_{\text{diss}} = \hat{\mathscr{K}}(\mathbf{r}) \cdot \mathbf{v},$$

and the random force $\mathbf{F}_{\text{rand}}$ responsible for diffusion in momentum space. Thus, we have the dimensionless Langevin equation

$$\frac{d\mathbf{P}}{d\tau} = \mathbf{f}_0 + \mathbf{f}_{\text{diss}} + \mathbf{f}_{\text{rand}}, \qquad (17)$$

where the dimensionless time $\tau = t/t_{\text{trans}}$, momentum $\mathbf{P} = \mathbf{p}/p_0$, force $\mathbf{f}_0 = \mathbf{F}_0 t_{\text{trans}}/p_0$, and other variables are defined by using $p_0 = \sqrt{\hbar\gamma m}$ and $t_{\text{trans}} = 1/\sqrt{2\omega_{\text{rec}}\gamma}$ as momentum and time scales, respectively. Since the recoil energy is

$$\hbar\omega_{\text{rec}} = \frac{(\hbar k)^2}{2m},$$

we have $t_{\text{trans}} \gg 1/\gamma$; i.e., the translational relaxation time determines the time scale of evolution of an atomic ensemble.

To compare the field distribution illustrated by Fig. 9 (with $\tan\varepsilon = 2$ and $\tan\theta = 1/\sqrt{2}$ for the $1 \longrightarrow 2$ transition) with the corresponding distributions of atoms, we assume that the incident atomic beam is uniform within the elementary cell mentioned above. Other parameters are as follows: $S_0 = 0.25$ for each light beam; $\tilde{\delta} = -10$ or 10; and the spread of the transverse-velocity distribution in the atomic beam is

$$\langle (\Delta v_\perp)^2 \rangle = 0.1\hbar\gamma/m,$$

which implies sub-Doppler cooling of the beam before its interaction with the mask. The ratio of the mean longitudinal velocity $\langle v_z \rangle$ in the atomic beam to the effective radius r_0 of an individual light beam, $t_{\text{int}} = r_0/\langle v_z \rangle$, determines the mean transit time through the mask, which plays an important role in simulations. We also used a Maxwellian longitudinal-velocity distribution. The mean transit time was $t_{\text{int}} = 0.6t_{\text{trans}}$. Note that this t_{int} can be implemented in experiments, and the corresponding force $\mathbf{F}_0$ will have a significant effect on the transverse distribution of atoms in a beam. Simulations show that its effect is insignificant when $t_{\text{int}} \sim 0.1t_{\text{trans}}$, and the cross-sectional distribution of atoms in the beam remains almost uniform after its interaction with the mask. In the opposite limit of $t_{\text{int}} \gg t_{\text{trans}}$, the transverse distribution of atoms in the beam evolves into a quasi-steady state and a dissipative optical lattice is thus created [18]. The effect of $\mathbf{F}_{\text{diss}}$ and $\mathbf{F}_{\text{rand}}$ on this process is substantial, and the contribution of these forces must be taken into account.

Figures 10 and 11 show the results of numerical simulations of thin films of atoms deposited on a substrate obtained for $\tilde{\delta} = -10$ and 10, respectively.

The contour plots show atom distributions on the substrate in the domain of $|kx| \le 1.5 \times 2\pi/3$ and $|ky| \le 1.5 \times 2\pi/\sqrt{3}$ (larger than the elementary cell). These distributions result from the interaction between the

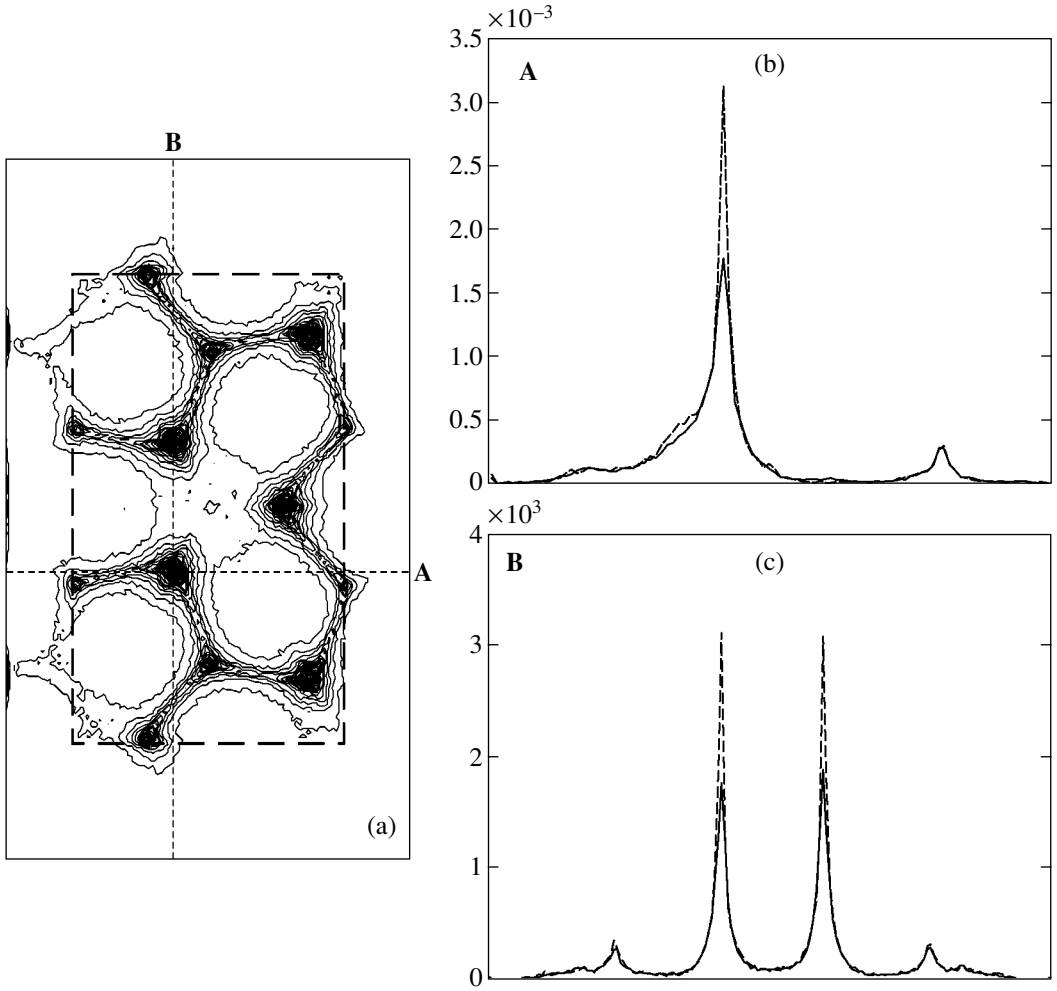

Fig. 10. Distribution of atoms on the substrate for the 1 ⟶ 2 transition: (a) contour plot; (b) normalized profile in cross section **A**; (c) normalized profile in cross section **B**. Saturation parameter is $S_0 = 0.25$, mean interaction time is $t_{int} = 0.6t_{trans}$, and detuning is $\delta = -10\gamma$.

light mask and atoms uniformly distributed within an elementary cell (rectangles with dashed boundaries in Figs. 10 and 11) before the interaction. The larger rectangular domain was partitioned into a 100×173 grid, and the resulting atom distributions were obtained by counting the atoms in each grid cell at the final stage of the interaction. The total number of atoms was 10^6 and 10^5 in the simulations illustrated by Figs. 10 and 11, respectively. Figures 10 and 11 also show the cross-sectional distributions of atoms along the mutually perpendicular lines **A** and **B**. Solid and dashed profiles represent, respectively, the results obtained by taking into account the forces $\mathbf{f}_{diss}$ and $\mathbf{f}_{rand}$ and by simulating only the effect of $\mathbf{f}_0$ (Fig. 10). It is clear that the contributions of the dissipative and random forces to the formation of the resulting overall patterns are negligible within the atom–field interaction times used in these simulations. However, the effects of these forces on certain features are quite obvious: $\mathbf{f}_{rand}$ reduces the peak heights, whereas both peak widths and pedestals remain unchanged. The light-induced force $\mathbf{f}_0$ plays a dominant role in redistributing atoms in the neighborhoods of maximum and minimum points of Ψ when $\tilde{\delta} < 0$ (Fig. 10) and $\tilde{\delta} > 0$ (Fig. 11), respectively.

We also varied both the field configuration parameters $\tilde{\delta}$, S_0, and t_0 and the parameters $\mathscr{E}_{s,i}$ and $\tilde{\varepsilon}_i$ of individual light beams. The atom distributions obtained by simulating atom–field interactions for $|\tilde{\delta}| < 1$ do not exhibit any spatial pattern. This important observation implies that the radiation pressure force cannot be used to create patterned nanostructures in two-dimensional masks. However, this force (as well as the rectified dipole force) manifests itself in violations of symmetry in field configurations. For example, a lateral shift of the atomic ensemble as a whole is observed after its interaction with a mask characterized by unbalanced $\tilde{\mathscr{E}}_i$ or $\tilde{\varepsilon}_i$. Variation of S or $t_0 > 0.5t_0$ does not result in

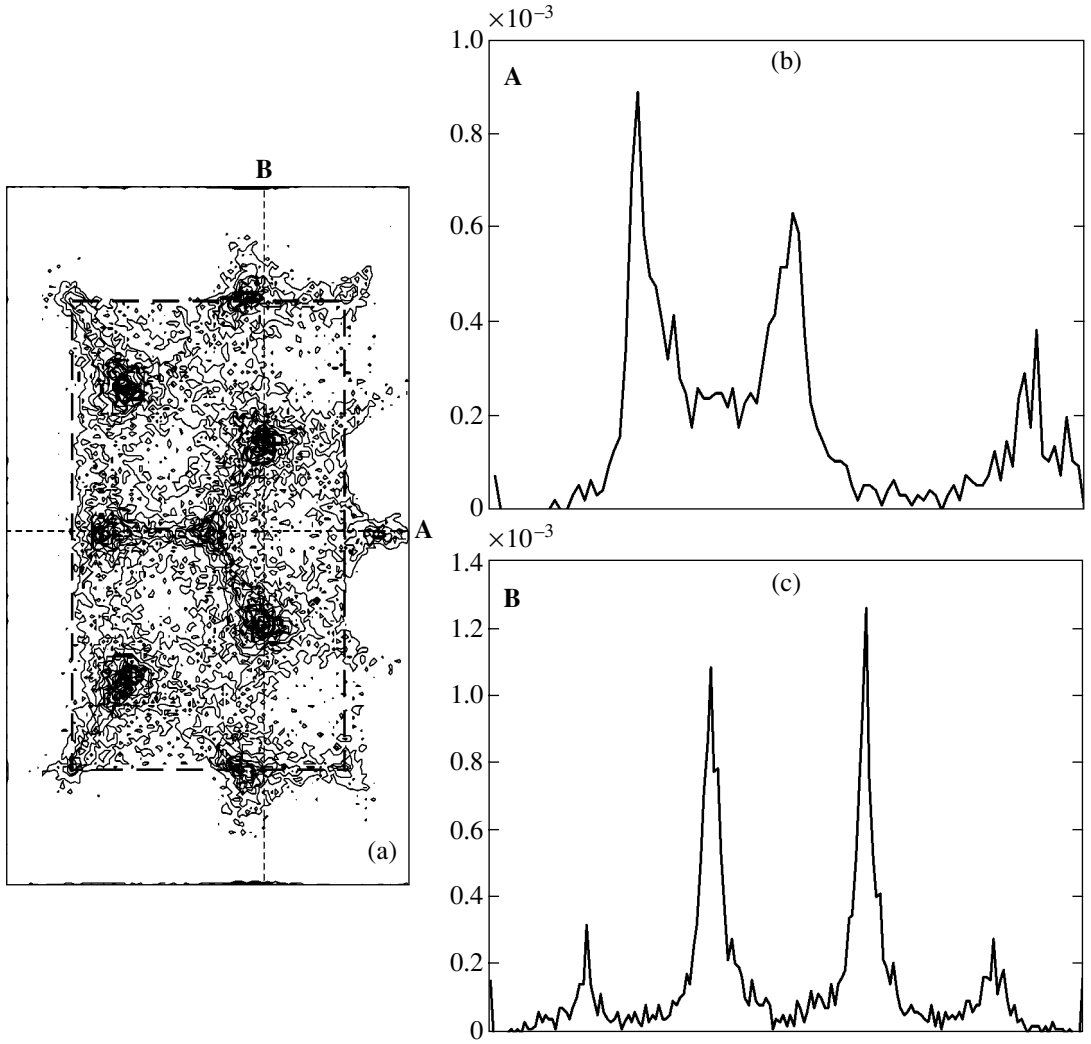

Fig. 11. Distribution of atoms on the substrate for the 1 ⟶ 2 transition: (a) contour plot; (b) normalized profile in cross section **A**; (c) normalized profile in cross section **B**. Saturation parameter is $S_0 = 0.25$, mean interaction time is $t_{int} = 0.6t_{trans}$, and detuning is $\delta = 10\gamma$.

the appearance or disappearance of any regions of localization, but can substantially modify the atom concentrations in the regions described above.

8. CONCLUSIONS

We have derived and analyzed expressions for the light-induced force acting on an atom at rest in a monochromatic light mask under steady-state conditions of optical pumping. The analysis presented in this study can be applied to determine the regions where atoms concentrate on the substrate after their interaction with a mask with arbitrary configuration and intensities of the constituent light beams.

The results obtained apply to closed cyclic transitions with arbitrary J in a wide range of mask parameters (detuning δ, saturation parameter S, lateral size r_0, and others). These results can also be applied to three-dimensional field configurations [19].

ACKNOWLEDGMENTS

This work was supported, in part, by the Russian Foundation for Basic Research, project nos. 04-02-16488 and 05-02-17086; by INTAS, grant 01-0855; and under the State Program for Support of Leading Science Schools, grant 1743.2003.2.

REFERENCES

1. M. K. Oberthaler and T. Pfau, J. Phys.: Condens. Matter **15**, R233 (2003).
2. D. Meschede and H. Metcalf, J. Phys. D: Appl. Phys. **36**, R17 (2003).

3. J. J. McClelland, R. E. Scholten, E. C. Palm, and R. Celotta, Science **262**, 87 (1993).
4. R. Gupta, J. J. McClelland, Z. J. Jabbour, and R. Celotta, Appl. Phys. Lett. **67**, 1378 (1995).
5. U. Drodofsky, J. Stuhler, T. Schulze, *et al.*, Appl. Phys. B **65**, 755 (1997).
6. B. Brezger, Th. Schulze, P. O. Schmidt, *et al.*, Europhys. Lett. **46**, 148 (1999).
7. R. Stützle, D. Jürgens, A. Habenicht, and M. K. Oberthaler, J. Opt. B: Quantum Semiclassic. Opt. **5**, S164 (2003).
8. O. N. Prudnikov and E. Arimondo, J. Opt. B: Quantum Semiclassic. Opt. **6**, 336 (2004).
9. A. P. Kazantsev, G. I. Surdutovich, and V. P. Yakovlev, *The Mechanical Action of Light on Atoms* (Nauka, Moscow, 1991) [in Russian].
10. A. P. Kazantsev, Usp. Fiz. Nauk **124**, 113 (1978) [Sov. Phys. Usp. **21**, 58 (1978)]; R. J. Cook, Phys. Rev. A **22**, 1078 (1980); V. G. Minogin, Zh. Éksp. Teor. Fiz. **79**, 2044 (1980) [Sov. Phys. JETP **52**, 1032 (1980)]; J. P. Gordon and A. Ashkin, Phys. Rev. A **21**, 1606 (1980); J. Dalibard and C. Cohen-Tannoudji, J. Phys. B **18**, 1661 (1985); J. Opt. Soc. Am. B **6**, 2023 (1989); Y. Castin and K. Mølmer, J. Phys. B **23**, 4101 (1990); G. Nienhuis, P. van der Straten, and S.-Q. Shang, Phys. Rev. A **44**, 462 (1991); J. Javanainen, Phys. Rev. A **44**, 5857 (1991).
11. A. V. Bezverbnyĭ, O. N. Prudnikov, A. V. Taĭchenachev, *et al.*, Zh. Éksp. Teor. Fiz. **123**, 437 (2003) [JETP **96**, 383 (2003)].
12. A. V. Bezverbnyĭ, Zh. Éksp. Teor. Fiz. **124**, 981 (2003) [JETP **97**, 875 (2003)].
13. A. V. Taichenachev, A. M. Tumaikin, V. I. Yudin, and G. Nienhuis, Phys. Rev. A **69**, 033410 (2004).
14. C. S. Adams and E. Riis, Prog. Quantum Electron. **21**, 1 (1997).
15. O. N. Prudnikov, A. V. Taĭchenachev, A. M. Tumaĭkin, and V. I. Yudin, Zh. Éksp. Teor. Fiz. **120**, 76 (2001) [JETP **93**, 63 (2001)].
16. A. V. Bezverbny, G. Nienhuis, and A. M. Tumaikin, Opt. Commun. **148**, 151 (1998).
17. J. Javanainen, Phys. Rev. A **46**, 5819 (1992).
18. G. Grynberg and C. Mennerat-Robilliard, Phys. Rep. **355**, 335 (2001).
19. Th. Schulze, T. Müther, D. Jürgens, *et al.*, Appl. Phys. Lett. **78**, 1781 (2001).

Translated by A. Betev

Journal of Experimental and Theoretical Physics, Vol. 101, No. 4, 2005, pp. 597–610.
Translated from Zhurnal Éksperimental'noĭ i Teoreticheskoĭ Fiziki, Vol. 128, No. 4, 2005, pp. 698–713.

ATOMS, MOLECULES, OPTICS

Many-Particle Effects in Resonant Inelastic Scattering of an X-ray Photon by an Atom

A. N. Hopersky, A. M. Nadolinsky, and V. A. Yavna

Rostov State University of Transport Communication, Rostov-on-Don, 344038 Russia

e-mail: hopersky_vm_1@rgups.ru

Received March 4, 2005

Abstract—The influence of many-particle effects on the shape and values of the double differential cross section for the resonant inelastic scattering of a linearly polarized X-ray photon by a free atom near the K and KL_{23} ionization thresholds has been theoretically analyzed for the neon atom. The calculations have been performed using the nonrelativistic Hartree–Fock approximation for single-electron wavefunctions and the dipole approximation for the anomalous dispersion component of the cross section. The analytical structure of the contact part of the scattering cross section has been obtained beyond the dipole approximation. The effects of the radial relaxation of electron shells, spin–orbit and multiplet splitting, and configuration interaction in the doubly excited atomic states, as well as the Auger and radiative decays of the produced vacancies, are taken into account. The nature and role of the effect of correlation amplitudes, which is responsible for the appearance of the nonzero amplitudes of nonradiative transitions between intermediate and final single-electron states of the same symmetry that are obtained in different Hartree–Fock fields, have been analyzed also. The calculations are predictive and, for an incident-photon energy of 5.41 keV, agree well with experimental results for the $K\alpha$ X-ray emission spectrum of the neon atom. © *2005 Pleiades Publishing, Inc.*

1. INTRODUCTION

Fast development of the technique for obtaining X-ray synchrotron radiation [1] makes it possible to study experimentally and theoretically the double differential cross section for the inelastic scattering of a photon by a free atom in the close vicinity (~±10 eV) of the ionization thresholds of its deep shells. The double differential cross section is a highly informative three-dimensional (cross section, incident-photon energy, and scattered-photon energy) quantum-mechanical observable for this fundamental process in microcosm. This process is almost one order of magnitude less intense than the elastic (Rayleigh) photon–atom scattering that occurs on atomic electrons [2, 3]. However, as compared to Rayleigh scattering, the resonant inelastic photon–atom scattering (Landsberg and Mandelstam [4], Raman [5], and Compton [6]) carries much more information on the many-electron system under study including that on the nature and role of many-particle effects and their quantum interference.

In theoretical analysis in the single available investigation for a free atom [7] (measurement and calculation of three-dimensional $L\alpha$, β X-ray emission spectra of the xenon atom), as well as in pioneering theoretical works by Åberg and Tulkki (the resonant inelastic scattering of an X-ray photon near the K-shell ionization threshold of neon, argon, and manganese, see review [8]), a wide hierarchy of many-particle effects was ignored, in particular, the radial relaxation of electron shells in the fields of formed core vacancies and the multiple excitation/ionization of the atomic ground state, which accompany and substantially determine the photon–atom interaction process [9].

Moreover, in addition to the problem of the inclusion of many-particle effects, a number of other analytical aspects of the quantum theory of the process require additional investigations. In particular, it is necessary to reveal the analytical structure of the contact part of the double differential cross section for inelastic scattering beyond the dipole approximation for describing the process even in the X-ray energy ranges of the incident and scattered photons.

In this work, considering the neon atom as an example (with nuclear charge number $Z = 10$ and ground-state electron configuration $[0] \equiv 1s^2 2s^2 2p^6 ({}^1S_0)$), we theoretically analyze for the first time the influence of many-particle effects on the values and shape of the double differential cross section for the resonant inelastic scattering of an X-ray photon ($\hbar\omega$ from 600 eV to 1.5 MeV) near the ionization threshold of a deep shell of the free atom. In this analysis, we ignore the inelastic scattering of the photon by the atomic nucleus, nuclear nucleons, and electron–positron pairs produced in the Coulomb field of the nucleus. Their effect on the inelastic scattering cross section is insignificant in the X-ray range of incident-photon energies [10]. In addition, we attempt to determine the analytical structure of the contact part of the double differential cross section for the inelastic photon–atom scattering beyond the dipole approximation.

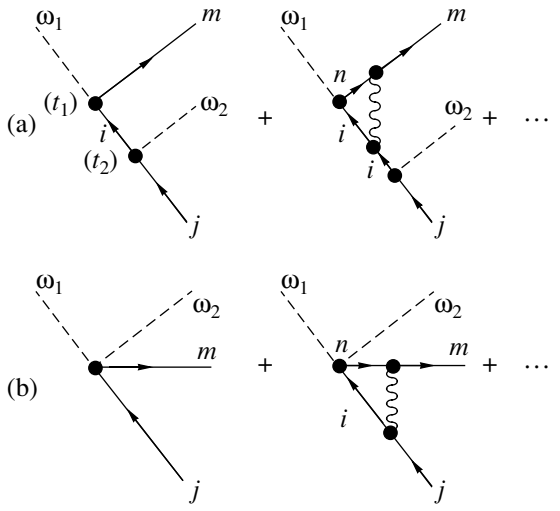

Fig. 1. Goldstone–Hubbard–Feynman diagrams for the (a) anomalous dispersion and (b) contact amplitudes of the inelastic scattering of an X-ray photon by a neon atom near the ionization threshold of the 1*s* shell. For notation, see Section 2.1. An ellipsis stands for an infinite series of diagrams.

Such investigations are important for modern physics, in particular, in view of the creation of an X-ray laser with a neon-like plasma as an active medium [11] and the acquisition of spectral data (e.g., X-ray emission spectra of neon-like elements) for astrophysics [12].

2. THEORETICAL FOUNDATIONS OF THE METHOD

2.1. Anomalous Dispersion Component of the Cross Section

We specify the analytical structure of the anomalous dispersion component of the double differential cross section for the resonant inelastic scattering of a linearly polarized photon near the ionization threshold of the 1*s* shell of the neon atom as (hereinafter, completely filled electron shells are omitted in the notation of a configuration)

$$\hbar\omega_1 + [0] \longrightarrow 1snp(^1P_1) \longrightarrow 2p^5mp(^1S_0, {}^1D_2) + \hbar\omega_2$$

for the proposed experimental scheme $\mathbf{e}_{1,2} \perp P$. The $2snp$ and $2p^5n(s, d)$ intermediate states are ignored, because the ionization thresholds of the 2*s* and 2*p* shells are far from the ionization threshold of the 1*s* shell (e.g., $I_{1s} - I_{2s} \approx 822$ eV). Here, $\hbar\omega_1$ and $\hbar\omega_2$ are the energies of the incident and scattered photons, respectively; $\mathbf{e}_1$ and $\mathbf{e}_2$ are the polarization vectors of the incident and scattered photons, respectively; and P is the scattering plane containing the wavevectors $\mathbf{k}_1$ and $\mathbf{k}_2$ of the incident and scattered photons, respectively.

In this case, $(\mathbf{e}_1 \cdot \mathbf{e}_2)^2 = 1$ and the known general analytical expression for the anomalous dispersion component of the double differential cross section for the resonant inelastic photon–atom scattering in the second order of quantum-mechanical perturbation theory (Kramers–Heisenberg–Waller formula) [8, 10] after the summation/integration over the *np* intermediate and *mp* final states of the discrete/continuous spectrum and summation over the $^1S_0$ and $^1D_2$ terms has the form

$$\frac{d^2\sigma_\perp}{d\omega_2 d\Omega} = r_0^2\frac{\omega_2}{\omega_1}\rho\sum_{i=1,2}\zeta_i Q_i, \tag{1}$$

$$Q_i = \sum_{m>f}^{\infty}(R_m^2 + I_m^2)L_{mi} + (R_i^2 + I_i^2)\Psi_i, \tag{2}$$

$$R_m = \frac{\pi}{\gamma_{1s}}\sum_{n>f}(\omega_1 - \Delta_n)A_{nm}L_n - R_m^{(e)}, \tag{3}$$

$$I_m = \pi\sum_{n>f}A_{nm}L_n. \tag{4}$$

A physical interpretation of the origin and analytical structure of the scattering amplitude $R_m\sqrt{\rho}$ can be given in terms of Goldstone–Hubbard–Feynman diagrams [13] of nonrelativistic quantum many-body theory. Figure 1a (Fig. 1b, see Section 2.2) shows some first (leading) terms of a series of diagrams for the amplitude $R_m\sqrt{\rho}$ of the inelastic scattering of the X-ray photon by the neon atom near the ionization threshold of the 1*s* shell. In this figure, $\omega_1(\omega_2)$ is the incident (scattered) photon; $i(j) = 1s(2p)$ is the vacancy; $m = mp$ and $n = np$ are the final and intermediate photoelectrons, respectively; the arrow directed to the right (left) means that the state is produced above (below) the f Fermi level (the set of the quantum numbers of the atomic valence shell); the wavy line means Coulomb interaction; and time flows from left to right ($t_1 < t_2$). In particular, the first diagram in Fig. 1a describes the amplitude of the following process. At time t_1, the deep 1*s* atomic shell absorbs the ω_1 photon. As a result of the $1s \longrightarrow mp$ radiative transition (with the amplitude $\sim\langle 1s|\hat{r}|mp\rangle$), an $i(1s)$ vacancy and an $m(mp)$ photoelectron appear. At time $t_2 > t_1$, the ω_2 photon is emitted in the $1s \longrightarrow 2p$ radiative decay of the 1*s* vacancy (with the amplitude $\sim\langle 1s|\hat{r}|2p\rangle$). As a result, the $i(1s)$ vacancy captures the $2p$ electron and a $j(2p)$ valence vacancy is formed.

The amplitude A_{nm} in Eqs. (3) and (4) has the form

$$A_{nm} = (\omega_2 - \omega_1 + \Delta_n)\Delta_n\langle 1s_0|\hat{r}|np_c\rangle\langle np_+|mp\rangle,$$

where

$$\langle 1s_0|\hat{r}|np_c\rangle = \int_0^\infty P_{1s_0}(r)P_{np_c}(r)rdr, \quad (5)$$

$$\langle np_+|mp\rangle = \int_0^\infty P_{np_+}(r)P_{mp}(r)dr.$$

Here, $P_{np_+}(r)$ is the radial wavefunction of the np_+ electron, etc. Amplitude (5) describes the absorption part of the total scattering amplitude and is defined in terms of the radiative transition amplitude from the initial state to the intermediate state described by the correlation wavefunction

$$|np_c\rangle = |np_+\rangle - |2p_+\rangle\frac{\langle 2p_0|np_+\rangle}{\langle 2p_0|2p_+\rangle}.$$

In turn, the structure of the correlation wavefunction is determined by the methods of nonorthogonal-orbital theory [9] and is expressed in terms of the nonrelativistic wavefunctions of single-electron states obtained in various Hartree–Fock fields.

Owing to the appearance of a deep *nl* vacancy in the atomic core, outer atomic residual shells first respond to the destruction of the nl^{4l+2} screen between them and the atomic nucleus such that their average radii decrease. The shift of the electron density of the atomic residual shells toward the nucleus is accompanied by the additional delocalization of the wavefunction of the photoelectron. This delocalization results in a decrease in the photoabsorption amplitude. The described effect is known as the radial relaxation of the single-electron wavefunctions that accompanies the formation of core vacancies [3, 9].

In the problem under consideration, the radial relaxation effect is taken into account as follows. The wavefunctions of $(n, 2)p_+$ electrons are obtained in the field of a 1*s* deep vacancy by solving nonlinear integrodifferential equations for the self-consistent Hartree–Fock field for the 1*snp* configuration of the intermediate state. The wavefunctions of *mp* electrons are calculated in the field of a 2*p* valence vacancy by solving Hartree–Fock equations for the $2p^5mp$ configuration of the final state. The wavefunctions of the $1s_0$ and $2p_0$ core electrons are determined by solving Hartree–Fock equations for the initial state configuration [0].

Note that $|np_c\rangle \longrightarrow |np_0\rangle$ and $\langle np_+|mp\rangle \longrightarrow \delta_{nm}$ (Kronecker–Weierstrass symbol) if the radial relaxation is ignored. Here, the wavefunction of the np_0 electron is obtained by solving the Hartree–Fock equation for the $1s_0np_0$ configuration. As a result, amplitude (5) assumes the form

$$A_{nm} \longrightarrow (\omega_2 - \omega_1 + \Delta_n)\Delta_n\langle 1s_0|\hat{r}|np_0\rangle\delta_{nm}$$

and the summation/integration in Eqs. (3) and (4) disappears, which significantly simplifies the analytical structure of cross section (1).

In Eqs. (1)–(3), the spectral functions have the form

$$L_{mi} = \frac{\gamma_b}{\pi}\frac{1}{(\omega_1 - \omega_2 - \Delta_{mi})^2 + \gamma_b^2},$$

$$L_n = \frac{\gamma_{1s}}{\pi}\frac{1}{(\omega_1 - \Delta_n)^2 + \gamma_{1s}^2},$$

$$\Psi_i = \frac{1}{2} + \frac{1}{\pi}\arctan\frac{\omega_1 - \omega_2 - \Delta_i}{\gamma_b};$$

atomic units are used ($e = \hbar = m_e = 1$); r_0 is the classical electron radius; Ω is the solid angle of the emission of the scattered photon; $\gamma_{1s}(2p) = \Gamma_{1s(2p)}/2$, where $\Gamma_{1s(2p)}$ is the total (Auger plus radiative components) width of the decay of the $1s(2p)$ vacancy;

$$\Delta_n = E(1snp) - E(0),$$

$$\Delta_{mi} = E(2p_{3/2}^5 mp) - E(0) + \delta_i,$$

$$\Delta_i = E(2p_{3/2}^5) - E(0) + \delta_i,$$

$$\delta_i = \{0, i = 1; \delta_{SO}, i = 2\}, \quad \zeta_i = \{2, i = 1; 1, i = 2\};$$

δ_{SO} is the spin–orbit splitting constant of the 2*p* atomic core shell; *E* are the total Hartree–Fock energies of the corresponding configurations; $\sum_{n>f}$ stands for the summation/integration over the discrete/continuous intermediate states; and

$$\sqrt{\rho} = \langle 1s|\hat{r}|2p_+\rangle K_{1s}K_{1s2p}.$$

Here, *K* is the product of the overlap integrals of the radial wavefunctions of the electrons that are not involved in the radiative transition, have identical symmetries, and exist in the ground-state atomic configuration and configurations with the 1*s* vacancy K_{1s}, as well as in the configurations with the 1*s* and 2*p* vacancies K_{1s2p}. The amplitude $\sqrt{\rho}$ describes the emission part of the total scattering amplitude and is defined in terms of the amplitude of the radiative transition from the intermediate state to the final state; i.e., $\sqrt{\rho} \approx \langle 1s|\hat{r}|2p_+\rangle$.

The quantity $\gamma_b = \Gamma_{beam}/2$ appears in the spectral functions L_{mi} and Ψ_i due to the integration of cross section (1) with the experimentally determined distribution function φ_b over the energy of X-ray radiation incident on the atom [8]:

$$\frac{d^2\sigma_\perp(\omega_1)}{d\omega_2 d\Omega} = \int_0^\infty \frac{d^2\sigma_\perp(\omega)}{d\omega_2 d\Omega}\varphi_b(\omega_1, \omega)d\omega. \quad (6)$$

In this work, the Cauchy–Lorentz spectral function is

used for the function φ_b:

$$\varphi_b(\omega_1, \omega) = \frac{\gamma_b}{\pi}\frac{1}{(\omega_1 - \omega)^2 + \gamma_b^2}.$$

The partial scattering amplitudes R_i and I_i are obtained from Eqs. (3) and (4) by replacing the wavefunction of a discrete final state by the wavefunction of a continuous state. In this case, the energy of the continuous-spectrum electron is determined as $\varepsilon_i = \omega_1 - \omega_2 - \Delta_i$, $\varepsilon_i \geq 0$, due to the energy conservation law in the inelastic photon–atom scattering.

When integrating over the εp_+ continuous intermediate states, the many-particle effect of the final-state interaction is ignored in the R_i and I_i amplitudes. This effect consists changing of the radial wavefunction of a continuous-spectrum photoelectron due to the $2p \longrightarrow 1s$ radiative transition and electrostatic interaction of the photoelectron with the εd continuous-spectrum electron arising in the $1s \longrightarrow 2p^4\varepsilon d$ Auger decay of the $1s$ vacancy. As was shown in [14], the inclusion of this effect in the theoretical spectra of the absorption of an X-ray photon by a deep shell of a light atom ($Z \leq 20$) almost does not change the single-electron approximation results.

However, since the total scattering amplitude enters into cross section (1) along with the absorption and emission components, the role of the final state interaction in the spectra of resonant inelastic scattering is an open problem and will be analyzed in future investigations.

Thus, we set

$$\langle \varepsilon p_+ | \varepsilon_i p \rangle \longrightarrow \delta(\varepsilon - \varepsilon_i),$$

where δ is the Dirac delta function.

The amplitude $R_m^{(e)}$ in Eq. (3) has the form

$$R_m^{(e)} = \sum_{n > f} (\omega_2 + I_n)^{-1} A_{nm}$$

and describes photon-exchange inelastic scattering processes (the atom is excited and emits the scattered ω_2 photon earlier than it absorbs the incident ω_1 photon).

Our calculation for the neon atom shows that the contribution of the amplitude $R_m^{(e)}$ does not exceed 1% of the contribution of the first terms of the amplitude R_m in Eq. (3). It is worth noting that the role of such exchange amplitudes increases considerably for the elastic (Rayleigh) photon–atom scattering. In particular, the exclusion of them for the case of the neon atom results in almost 40% error in the calculation of the differential cross section for elastic scattering near the *K*-shell ionization threshold [3]. The contribution of exchange processes to amplitude I_m given by Eq. (4) is on the order of $\gamma_{1s}(\omega_2 + I_n)^{-2} \ll 1$ and is neglected. Note that exchange contributions are absent in the contact part (see Section 2.2) of the total amplitude of inelastic scattering.

The partial amplitudes A_{nm} given by Eq. (5) are calculated in the dipole approximation for the Fourier components of the electromagnetic field operator:

$$\mathbf{k} \cdot \mathbf{r}_j \longrightarrow 0 \Rightarrow \exp\{i(\mathbf{k} \cdot \mathbf{r}_j)\} \longrightarrow 1,$$

where $\mathbf{k}$ is the wavevector of the incident (scattered) photon and $\mathbf{r}_j$ is the radius vector of the *j*th electron of the atom. As is known [10], the dipole approximation is applicable under the condition $\lambda \gg r_{nl}$, where λ is the photon wavelength and r_{nl} is the average radius of the *nl* shell of the atom, which determines the radial integral of the radiative transition. For the X-ray energy range studied in this work, this inequality is certainly satisfied. Indeed, for incident-photon energies from 860 eV to 5.42 keV, the wavelength λ ranges from 14.43 to 2.29 Å and, therefore, $\lambda \gg r_{1s}(\mathrm{Ne}) = 0.08$ Å.

Higher multipole orders of the amplitudes of the radiative transition are disregarded in the calculation of the amplitudes A_{nm}. However, we emphasize the following. A decrease in the ratio λ/r_{nl} and an increase in the scattering angle can lead to the necessity of going beyond the dipole approximation even in the X-ray energy ranges of the incident and scattered photons. In particular, as was shown in [15], the inclusion of higher multipole orders in the calculation of the differential cross section for the elastic scattering of the 22.1-keV photon ($\lambda = 0.561$ Å) by the $1s$ shell of the aluminum atom ($r_{1s}(\mathrm{Al}) = 0.063$ Å) for a scattering angle of $\theta = 150°$ changes the dipole-approximation result by a factor of about 2.

The calculation of all radial integrals of the radiative transition is performed in the length form for the transition operator. Our analysis shows that the use of the velocity form for the calculation of the integrals for transitions involving the deep $1s$ shell in atoms with a nuclear charge number $Z \geq 10$ changes the absolute values of such integrals by no more than 1%. Thus, the many-particle effect of correlations of the random phase approximation with exchange [16] (for the case of the neon atom, mixing of the $1snp$ configuration with the $2smp$ and $2p^5md$ configurations as a result of intershell correlations) turns out to be negligibly small and is ignored in this work.

2.2. Contact Part of the Cross Section

A certain number of final states of the inelastic photon–atom scattering are not included in the anomalous dispersion component of the total scattering amplitude, but they are final states of so-called contact (Thompson) scattering. In this case, in Goldstone–Hubbard–Feynman diagrams for the scattering amplitude, four

lines intersect at the interaction vertex (Fig. 1b): two photon lines (ω_1 and ω_2), electron line (ml, $m(l \pm 1)$), and vacancy line (jl). In the case of the neon atom, these are the (1*s*, 2*s*)*ms*, (1*s*, 2*s*)*mp*, and $2p^5m(s, d)$ final states.

Let us determine the analytical structure of the double differential cross section for the inelastic contact scattering of the linearly polarized photon by the atom beyond the dipole approximation, which is traditionally used for the X-ray range [8, 10]. We represent the known general analytical expression for the double differential cross section for the inelastic photon–atom scattering in the second order of quantum-mechanical perturbation theory [8, 10] in the form

$$\frac{d^2\sigma}{d\omega_2 d\Omega} = r_0^2(\mathbf{e}_1 \cdot \mathbf{e}_2)^2 \frac{\omega_2}{\omega_1} \sum_{n_1 l_1 \le f} \mathop{\mathrm{S}}_{n_2 l_2 > f} M_{12}^T L_{12}, \quad (7)$$

where

$$M_{12}^T = [J]^{-1} \sum_{T'} \sum_{MM'} \left| A_{TT'}^{MM'}(n_1, n_2) \right|^2, \quad (8)$$

$$\begin{aligned} A_{TT'}^{MM'}(n_1, n_2) &= \langle s_1, TM | \sum_{k=1}^{N} \exp\{i(\mathbf{q} \cdot \mathbf{r}_k)\} | s_{12}, T'M' \rangle, \\ L_{12} &= \frac{\gamma_1}{\pi} \frac{1}{(\omega_1 - \omega_2 - \Delta_{12})^2 + \gamma_1^2}, \\ T &\equiv LSJ, \quad \gamma_1 = \frac{\Gamma_1}{2}, \quad [x] \equiv 2x + 1. \end{aligned} \quad (9)$$

In Eq. (8), the summation is performed over the terms T' of the fixed final state $s_{12} \equiv n_1 l_1^{N_1 - 1} n_2 l_2$, as well as over the projections M' of the total angular momentum J' in the s_{12} final state, and the averaging is performed over the projections M of the total angular momentum J in the initial state $s_1 \equiv n_1 l_1^{N_1}$.

In Eq. (7), the atomic units are used, Γ_1 is the total decay width of the $n_1 l_1$ vacancy in the atomic core, N_1 is the occupation number of the $n_1 l_1$ shell of the atomic ground state, N is the number of electrons in the atom, and $\mathbf{q}$ is the scattering vector (momentum transferred to the atom) whose absolute value for the case of inelastic scattering is given by the expression

$$q = |\mathbf{k}_1 - \mathbf{k}_2| = \frac{\omega_1}{c}\sqrt{1 + \beta^2 - 2\beta\cos\theta}, \quad \beta = \frac{\omega_2}{\omega_1}. \quad (10)$$

Here, θ is the scattering angle (the angle between the wavevectors of the incident and scattered photons), c is the speed of light, $\mathbf{r}_k$ is the radius-vector of the kth electron of the atom, and $\Delta_{12} = E(s_{12}) - E(s_1)$.

Let us transform expression (8) using the theory of irreducible tensor operators [17]. We represent the exponential in Eq. (9) in the form of the functional series in the spherical functions $C^{(t)}$ and the tth order spherical Bessel functions j_t of the first kind. Taking into account the Wigner–Eckart theorem for the matrix element of the many-electron irreducible tensor transition operator,

$$Q_p^{(t)} = \sum_{k=1}^{N} C_p^{(t)}(\mathbf{r}_k) j_t(qr_k);$$

orthogonality property of Wigner symbols; and the theorem of the summation of spherical functions, we reduce Eq. (8) to the form

$$M_{12}^T = [J]^{-1} \sum_{T'} \sum_{t=0}^{\infty} \left| (s_1, T \,\|\, Q^{(t)} \,\|\, s_{1,2}, T') \right|^2. \quad (11)$$

Here, the reduced matrix element of the transition operator $Q^{(t)}$ in the LS coupling scheme is expressed as

$$\begin{aligned} &(s_1, T \| Q^{(t)} \| s_{12} L_1 S_1, T') \\ &= (-1)^{l_2 + L_1 - S - J'} \delta(S, S') \\ &\times \sqrt{N_1 [L, L', J, J']} (l_1^{N_1} LS \,\|\, l_1^{N_1 - 1} (L_1 S_1) l_1) \\ &\times \begin{Bmatrix} l_1 & L & L_1 \\ L' & l_2 & t \end{Bmatrix} \begin{Bmatrix} L & J & S \\ J' & L' & t \end{Bmatrix} \\ &\times (l_1 \,\|\, C^{(t)} \,\|\, l_2) W_t(n_1 l_1, n_2 l_2), \end{aligned} \quad (12)$$

where

$$W_t(n_1 l_1, n_2 l_2) = \langle n_1 l_1 | j_t(qr) | n_2 l_2 \rangle$$

and $L_1 S_1$ is the term of the $n_1 l_1^{N_1 - 1}$ atomic residual shell.

Expression (7), together with Eqs. (11) and (12), provides the desired analytical representation for the double differential cross section for the inelastic contact photon–atom scattering beyond the dipole approximation ($qr \longrightarrow 0$). In this case, in order to include the effects of the spin–orbit splitting of the $n_1 l_1$ atomic core shells ($l_1 \ge 1$), it is necessary to make the change

$$M_{12}^T L_{12} \longrightarrow \sum_{i=1,2} \zeta_i (M_{12}^T L_{12})_i,$$

and in order to take into account the distribution over the energy of X-ray radiation incident on the atom, it is necessary to perform integration (6).

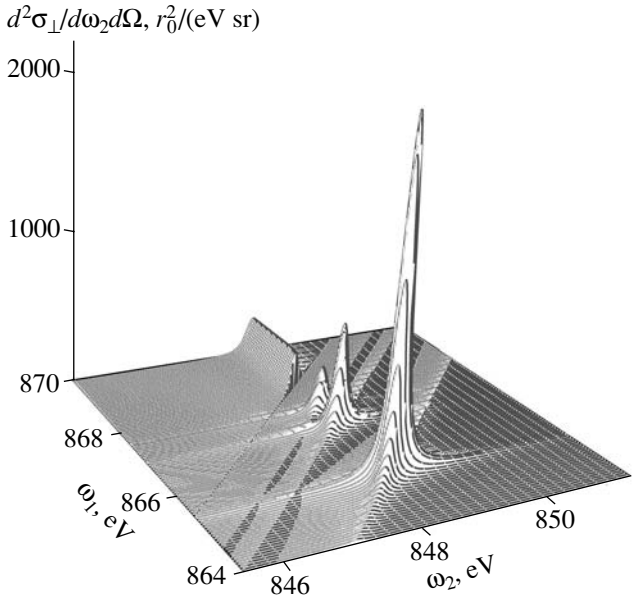

Fig. 2. Double differential cross section for the resonant inelastic scattering of a linearly polarized (perpendicularly to the scattering plane) X-ray photon by a neon atom near the *K*-shell ionization threshold I_{1s} = 868.399 eV. Here, ω_1 (ω_2) is the energy of the incident (scattered) photon, Ω is the solid angle of the emission of the scattered photon, $r_0^2 \equiv 7.941 \times 10^{-26}$ cm^2, Γ_{beam} = 0.20 eV, Γ_{1s} = 0.23 eV, $\Gamma_{2p} = 3.95 \times 10^{-8}$ eV, and δ_{SO} = 0.094 eV.

Moreover, the amplitudes of contact scattering that interfere with the anomalous dispersion amplitude should be included in addition to Eq. (7). For the case of the neon atom in the proposed experimental scheme ($\mathbf{e}_{1,2} \perp P$), in order to take into account the interference between the contact and anomalous dispersion components of the total amplitude of transition to the $2p^5mp$ final states, the following change is necessary in amplitude (3):

$$R_m \longrightarrow R_m + K_{1s}K_{2p}\rho^{-1/2}W_0(2p, mp). \qquad (13)$$

We have not analyzed in detail the shape and values of the cross section for contact scattering given by Eq. (7) in wide X-ray and gamma ranges of the incident-photon energies. Such an analysis is a subject for future investigations. However, to estimate the contribution of the contact part of cross section to the total scattering cross section near the *K* and KL_{23} ionization thresholds, we analyze the shape and values of the modification of cross section (7) for the neon atom:

$$\frac{d^2\sigma_\perp}{d\omega_2 d\Omega} = r_0^2\frac{\omega_2}{\omega_1}\sum_{nl \le f}(4l+2)K_{nl}^2\Psi_{nl}\Phi_{nl}. \qquad (14)$$

Here,

$$\Phi_{nl} = W_0^2(nl, \varepsilon_n l) + lW_1^2(nl, \varepsilon_n(l-1)) + (l+1)W_1^2(nl, \varepsilon_n(l+1)),$$
$$\Psi_{nl} = \frac{1}{2} + \frac{1}{\pi}\arctan\frac{\omega_1 - \omega_2 - I_{nl}}{\gamma_{nl}}, \qquad (15)$$

where

$$\varepsilon_n = \omega_1 - \omega_2 - I_{nl}, \quad \gamma_{nl} = \frac{\Gamma_{nl}}{2},$$

I_{nl} is the ionization threshold of the *nl* shell of the atomic ground state, and Γ_{nl} is the total decay width of the *nl* atomic residual vacancy. Formula (14) follows from Eq. (7) with allowance for interference (13) and the following simplifications:

(i) only transitions to the $\varepsilon_n(l, l, \pm 1)$ continuous final states are taken into account;

(ii) the effects of the spin–orbit splitting of the *nl* atomic core shells ($l \ge 1$) are disregarded.

In the dipole approximation for the contact transition operator in amplitude (9), the spherical Bessel functions satisfy the relations $j_0(qr) \longrightarrow 1$ and $j_1(qr) \longrightarrow 0$ and Eq. (15) is reduced to

$$\Phi_{nl} \longrightarrow \langle nl|\varepsilon_n l\rangle^2. \qquad (16)$$

We emphasize that the scattering-angle dependence of the contact-scattering cross section given by Eq. (7) disappears in the dipole approximation for the given scheme of the proposed experiment.

Then, taking into account the relaxation of the electron shells of the atomic residual in the field of an *nl* vacancy, we compare result (15) with result (16), which is formally extended to the range $0 < qr < 1$, and find that they are noticeably different for nonzero scattering angles even in the X-ray energy ranges of the incident and scattered photons.

In this work, we do not compare result (14) with results obtained in other approximations that have been widely used in available papers to analyze Compton scattering (the final state of inelastic scattering is a continuous state) [10, 18]. In particular, we do not consider the so-called impulse approximation, because the main condition of the applicability of this approximation, $qa_0 \gg 1$ [19, 20], is not satisfied. Indeed, for the energies of the incident ($\omega_1^{\max} \sim 5500$ eV) and scattered ($\omega_2^{\max} \sim 880$ eV) photons under investigation and using

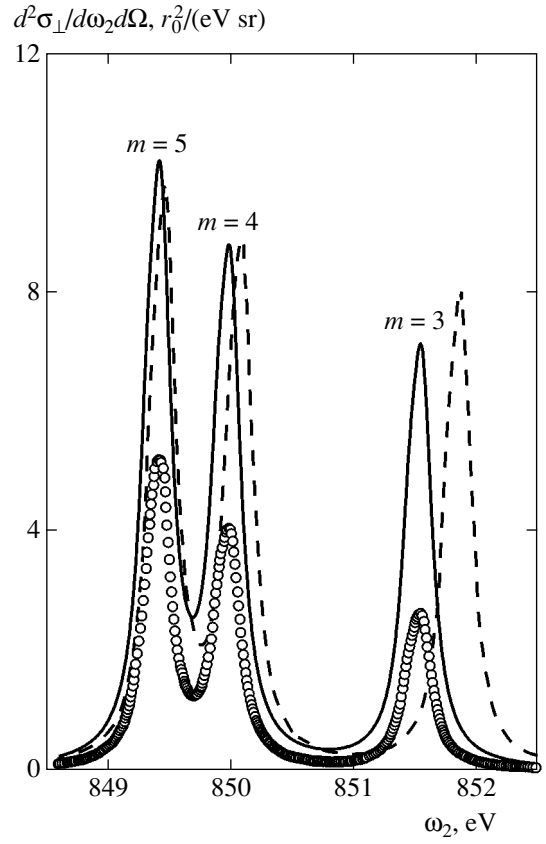

Fig. 3. Role of the R_m^C and I_m^C correlation transition amplitudes given by Eq. (17) for the principal quantum numbers m = 3, 4, and 5 of the discrete final state. The dashed line and circles are obtained without and with the inclusion of the radial relaxation of electron shells, respectively, and the solid line is calculated with allowance for radial relaxation and correlation amplitudes. The incident-photon energy is ω_1 = 868.5 eV. The widths, parameter δ_{SO}, and notation are the same as in Fig. 2.

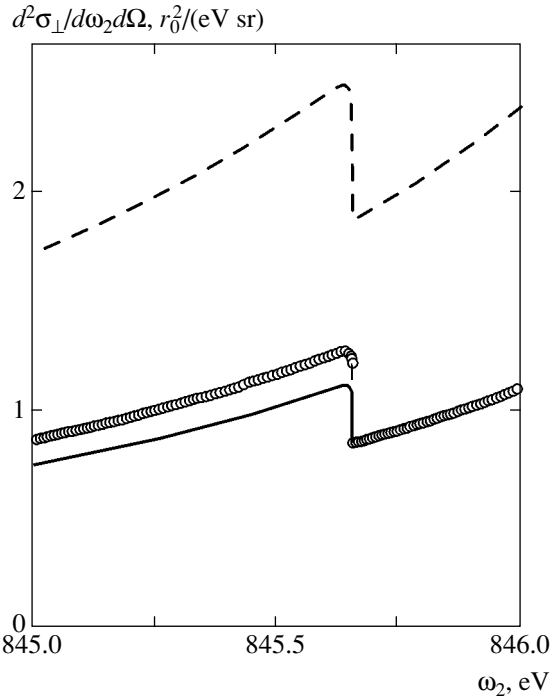

Fig. 4. Role of the R_i^C and I_i^C correlation transition amplitudes given by Eq. (20) in the region in which appears the leading $1s_0 \longrightarrow 3p_+$ resonance of the intermediate state. The incident-photon energy is ω_1 = 865.6 eV. The widths, parameter δ_{SO}, and notation are the same as in Figs. 2 and 3.

Eq. (10) for the scattering angle, e.g., $\theta = 90°$, we obtain $qa_0 \approx 1.5$, where a_0 is the Bohr radius.

3. CALCULATION RESULTS AND DISCUSSION

We consider a free neon atom as the object of investigation. Figures 2–7 and Tables 1 and 2 present the scattering cross sections calculated by Eqs. (1) and (14) for the X-ray energy ranges of the incident (ω_1 = 860–5500 eV) and scattered (ω_2 = 760–880 eV) photons.

The values Γ_{1s} = 0.23 eV (measured by X-ray photoelectron spectroscopy and taken from [21]) and $\Gamma_{2p} = 3.95 \times 10^{-8}$ eV (theoretical result taken from [22]) are used for the total decay widths of the 1*s* and 2*p* vacancies, respectively. The value Γ_{beam} = 0.20 eV is taken for the width parameter in the function φ_b in Eq. (6). Thus, we assume that the spectral resolutions of the experiment in the energies of the incident (Γ_{beam}) and scattered ($\sim\Gamma_{1s}$) photons are almost identical. The theoretical value δ_{SO} = 0.094 eV of the spin–orbit splitting constant for the 2*p* shell is taken from [23].

3.1. Energy Range of the K-Shell Ionization Threshold

Figure 2 shows cross section (1) in a close vicinity of the *K* ionization threshold of the 1*s* shell I_{1s} = 868.399 eV (nonrelativistic calculation performed in this work). The wavefunctions and energies of the initial, intermediate, and final states are obtained in the nonrelativistic single-configuration Hartree–Fock approximation. States with n, m = 3, 4, and 5 are taken as the np_+ intermediate and mp final discrete states. The amplitudes A_{nm} with the principal quantum numbers $n = m$ determine the leading shape resonances in the cross section: $A_{33} > A_{44} > A_{55}$ for the photon energies (in electronvolts) (ω_1, ω_2) = (865.420, 848.470), (867.030, 848.515), and (867.612, 848.530).

An example of the analytical solution to the problem of taking into account the completeness of the set of discrete states (n, m = 3, …, ∞) was recently given in [24] for the case of the constructing the differential cross section for resonant elastic (Rayleigh) scattering of the X-ray photon near the *K*-shell ionization thresh-

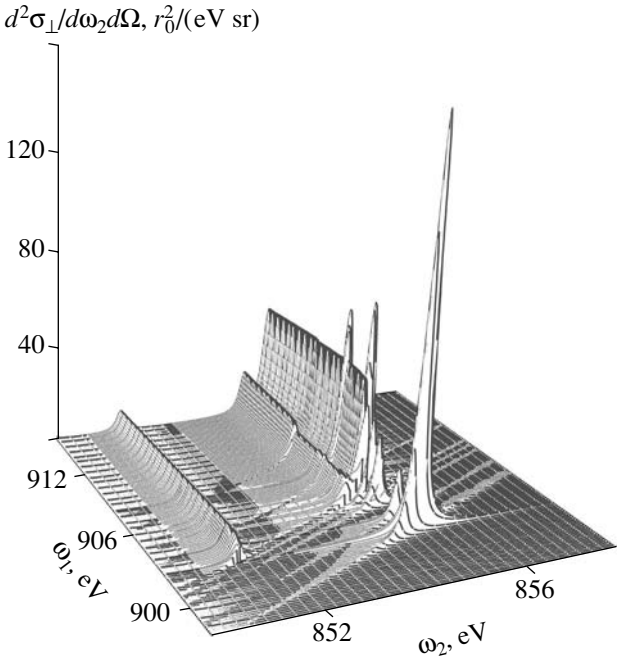

Fig. 5. Double differential cross section for the resonant inelastic scattering of a linearly polarized X-ray photon by a neon atom near the KL_{23} ionization threshold I_{1s2p} = 914.637 eV. The widths, parameter δ_{SO}, and notation are the same as in Fig. 2. The spectral characteristics of the scattering resonances are given in Table 1 and the cross sections, in Table 2.

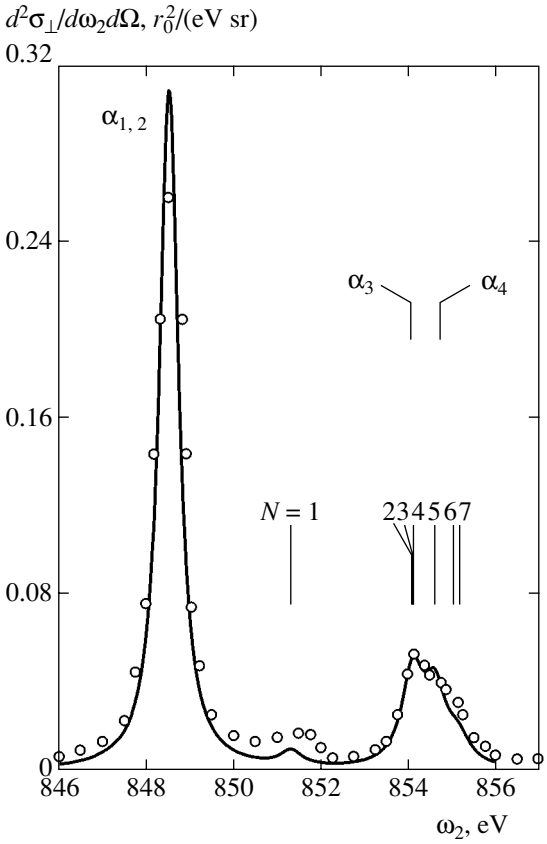

Fig. 6. $K\alpha$ X-ray emission spectrum of the neon atom. The circles are experimental data from [25] (obtained in arbitrary units for the energy ω_1 = 5410.17 eV of the X-ray exciting photon corresponding to the $K\alpha$ radiation of the chromium atom). The solid line is theoretically calculated in this work with Γ_{1s} = ($K\alpha_{1,2}$) 0.50 and ($K\alpha_{3,4}$) 0.60 eV. The parameters of the resonances of the theoretical $K\alpha_{3,4}$ structures of the spectrum that are marked by the digits are presented in Table 2. The widths Γ_{beam} and Γ_{2p}, parameter δ_{SO}, and notation are the same as in Fig. 2.

old of the neon atom. The analytical solution to this problem for the case of resonant inelastic scattering is much more difficult because of the presence of two (absorption and emission) components in the total scattering amplitude and is a subject for future investigations.

The continuous spectrum channel of the $2p^5\varepsilon_i p$ final state opens at $\omega_1 = I_{1s}$ and ω_2 = 848.555 eV. For $\omega_1 > I_{1s}$, cross section (1) has the spatially extended form of the $K\alpha_{1,2}$ X-ray emission spectrum of the neon atom (excited by the photon) [25].

Allowance for the radial relaxation of the electron shells of states in the fields of the 1*s* and 2*p* vacancies almost halves cross section (1). Cross section (1) calculated disregarding the relaxation effect coincides in shape with the result obtained with the inclusion of this effect and is not shown in order to avoid overloading Fig. 2.

The "ribbed" structures that diverge at an angle of 45° on the (ω_1, ω_2) plane on both sides of each resonance, as well as the threshold of the arising $K\alpha_{1,2}$ structure of the scattering spectrum, appear because expression (1) for the cross section contains the spectral functions L_{mi} (the denominator is minimal on the straight lines specified by the equation $\omega_1 = \omega_2 + \Delta_{mi}$) and the minimum energy ($\varepsilon_i = 0$) of the continuous-spectrum electron (radiative-transition amplitude $\langle 1s_0|\hat{r}|\varepsilon_i p_+\rangle$ is maximal on the straight line specified by the equation $\omega_1 = \omega_2 + \Delta_i$).

The $j + 1/2$ and $j - 1/2$ components of the spin–orbit doublet of the 2*p* shell ($j = 1$) are virtually not resolved in Fig. 2 (as well as in next figures), because the value δ_{SO} = 0.094 eV is small compared to the width Γ_{1s} = 0.23 eV for the neon atom.

The radial relaxation of electron shells results in the appearance of not only the correlation wavefunction $|np_c\rangle$ in the transition from the initial state to the intermediate state, but also nonzero $\langle np_+|\varepsilon p\rangle$ and $\langle xp_+|mp\rangle$ amplitudes of nonradiative transitions between excited states with the same symmetry that are obtained in different Hartree–Fock fields. These amplitudes are not manifested in absorption and elastic scattering [3], but are manifested in the resonant inelastic photon–atom scattering as follows.

(i) In the expressions for the R_m and I_m amplitudes of scattering to discrete states, the following components appear:

$$R_m^C = \langle mp|C_R^+\rangle, \quad I_m^C = \gamma_{1s}\langle mp|C_I^+\rangle. \tag{17}$$

Here, the correlation wavefunctions have the form

$$|C_R^+\rangle = \int_0^\infty (\omega_1 - x_{1s})|D(x)\rangle dx, \tag{18}$$

$$|C_I^+\rangle = \int_0^\infty |D(x)\rangle dx,$$

$$|D(x)\rangle = x_{1s}(x_{1s} + \omega_2 - \omega_1)\frac{\langle 1s_0|\hat{r}|xp_c\rangle}{(\omega_1 - x_{1s})^2 + \gamma_{1s}^2}|xp_+\rangle, \tag{19}$$

where

$$x_{1s} = x + I_{1s}.$$

(ii) In the expressions for the R_i and I_i amplitudes of scattering to continuous states, the following components appear:

$$R_i^C = \langle \varepsilon_i p|S_R^+\rangle, \quad I_i^C = \gamma_{1s}\langle \varepsilon_i p|S_I^+\rangle. \tag{20}$$

Here, the correlation wavefunctions have the form

$$|S_R^+\rangle = \sum_{n>f}^\infty (\omega_1 - I_{1snp})|B_n\rangle, \tag{21}$$

$$|S_I^+\rangle = \sum_{n>f}^\infty |B_n\rangle, \tag{22}$$

where

$$|B_n\rangle = I_{1snp}(I_{1snp} + \omega_2 - \omega_1) \times \frac{\langle 1s_0|\hat{r}|np_c\rangle}{(\omega_1 - I_{1snp})^2 + \gamma_{1s}^2}|np_+\rangle,$$

$$I_{1snp} = E(1snp) - E(0).$$

We refer to the appearance of amplitudes (17) and (20) with correlation functions (18), (19) and (21), (22), respectively, as the effect of the correlation amplitudes in the resonant inelastic scattering of the photon by the free atom.

Amplitudes (17) describe the transition of the xp_+ continuous intermediate state to the mp discrete final states. This process almost doubles the scattering probability calculated disregarding this effect. Figure 3 shows the corresponding calculation of cross section (1).

Amplitudes (20) describe the transition of the $\varepsilon_i p$ continuous final state to the infinite Rydberg series of the np_+ intermediate states. As a result, a part of the continuous spectrum $\varepsilon_i p$ falls in the "shadow" region and is not realized as final states. Therefore, the scattering probability decreases compared to the value calculated disregarding this process. The corresponding calculations of cross section (1) are shown in Fig. 4 and indicate that the above process noticeably affects the values and shape of the scattering cross section.

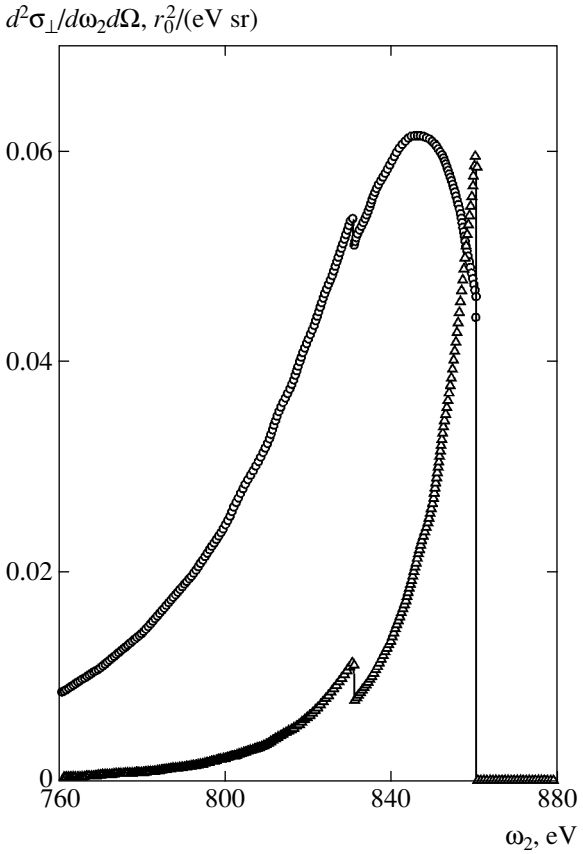

Fig. 7. Contact part of the double differential cross section for the resonant inelastic scattering of a linearly polarized (perpendicularly to the scattering plane) X-ray photon by a neon atom near the *K*-shell ionization threshold. The circles are calculated by Eq. (14) with the function Φ_{nl} given by Eq. (15), the triangles are obtained in the dipole approximation by Eq. (14) with the function Φ_{nl} given by Eq. (16). The scattering angle is $\theta = 90°$. The incident-photon energy is $\omega_1 = 880$ eV.

Thus, the simultaneous inclusion of amplitudes (17) and (20) results in the redistribution of the scattering probability from the long-wavelength region of the energies of the incident and scattered X-ray photons to the short-wavelength region.

3.2. Energy Range of the KL_{23} Ionization Threshold

It is reasonable to assume that allowance for the multiple excitation/ionization of the ground state of the neon atom results in the appearance of the nearest fine

Table 1. Double differential cross section for the resonant inelastic scattering $\omega_1 + [0] \longrightarrow |n\rangle \longrightarrow |2p^4 n_1 p n_2 p\rangle + \omega_2$ of a linearly polarized (perpendicularly to the scattering plane) X-ray photon by a neon atom near the KL_{23} ionization threshold (see Fig. 5)

n	n_1, n_2	ω_1, eV	$\frac{d^2\sigma_\perp}{d\omega_2 d\Omega}, \frac{r_0^2}{\text{eV sr}}$
1	3, 3	902.42	156.57
2	3, 3	903.62	20.37
3	3, 4	904.92	29.16
4	3, 4	905.52	34.27
5	3, 3	906.02	45.59
6	3, 4	908.02	29.28

Note: ω_1 is the incident-photon energy, $|n\rangle$ are intermediate states [see Eqs. (24)] and $|2p^4 n_1 p n_2 p\rangle$ are final states. For all n, n_1, and n_2 values, the emitted-photon energy is $\omega_2 = 854.80$ eV (see Eq. (26)).

structure of the double differential cross section for resonant inelastic scattering calculated in Section 3.1.

Near the KL_{23} ionization threshold ($I_{1s2p} = 914.637$ eV, nonrelativistic calculation performed in this work), we consider only the processes of double excitation/ionization that make the main contribution to the total intensity of the multiple excitation/ionization of the ground state of the neon atom. The leading role of the channels of double excitation/ionization is corroborated, in particular, by the calculation [26] and measurements [27, 28] near the I_{1s2p} ionization threshold, as well as by calculation and measurement [29] near the KL_1 ionization threshold in the absorption spectrum of the X-ray photon by the neon atom.

At the first stage of the construction of the amplitude A_{nm} in Eqs. (3) and (4), double excitation processes are considered for intermediate and final states. The wavefunctions and energies of the intermediate states are obtained in the *LS* coupling scheme and in the nonrelativistic multiconfiguration Hartree–Fock approximation by diagonalizing the secular-equation matrix constructed on the basis of the wavefunctions

$$|n\rangle = \sum_{LS} \sum_{n_{1,2} > f} \sum_{l_{1,2}} a_{12}^{LS} |\zeta n_1 l_1 n_2 l_2 (LS);\, {}^1P\rangle, \qquad (23)$$

where

$$\zeta \equiv 1s2s^2 2p^5 ({}^{2S+1}P),$$

$$n_1 l_1 n_2 l_2 = 3pmp,\ 3sm(s,d),\ 3dmd,\ m = 3, 4, 5,$$

a_{12}^{LS} are the configuration mixing coefficients and *LS* is the term of a pair of the $n_1 l_1$ and $n_2 l_2$ excited electrons.

The wavefunctions of the $n_1 l_1$ and $n_2 l_2$ excited electrons are determined by solving Hartree–Fock equations averaged over the ${}^{1,3}P$ and *LS* terms of the $\zeta n_1 l_1 n_2 l_2$ configuration. The wavefunctions of the 1*s*, 2*s*, and 2*p* atomic residual electrons are obtained by solving Hartree–Fock equations averaged over the ${}^{1,3}P$ terms of the ζ configuration.

Table 2. Wavefunctions of the $1s2p^5(L_1S_1)np(L_2S_2)\varepsilon' p$ intermediate and $2p^4(L_3S_3)np(L_4S_4)\varepsilon' p$ final states of the resonant inelastic scattering of a linearly polarized (perpendicularly to the scattering plane) X-ray photon by a neon atom near the KL_{23} ionization threshold and the energy at which the corresponding spatially extended structures arise in double differential cross section (1) (see Fig. 5)

n	L_1S_1	L_2S_2	L_3S_3	L_4S_4	ω_1, eV	ω_2, eV	N	$\frac{d^2\sigma_\perp}{d\omega_2 d\Omega}, \frac{r_0^2}{\text{eV sr}}$
3	$\psi({}^1P)$		$\phi({}^1S)$		902.40	851.32	1	0.0074
	$\psi({}^3P)$		$\phi({}^3P)$		905.20	854.12	4	0.0221
	$\psi({}^1P)$		$\phi({}^1D)$		905.70	854.61	5	0.0280
4	${}^3P$	${}^2S$	${}^3P$	${}^2P$	910.20	854.08	2	0.0074
	${}^1P$	${}^2S$	${}^1D$	${}^2P$	911.15	855.03	6	0.0040
ε	${}^3P$	${}^2S$	${}^3P$	${}^2P$	914.60	854.11	3	0.0120
	${}^1P$	${}^2S$	${}^1D$	${}^2P$	915.68	855.19	7	0.0068

Note: ω_1 is the incident-photon energy [see Eqs. (30) and (31)], ω_2 is the emitted-photon energy [see Eq. (32)], $\psi(LS)$ is given by Eqs. (28), $\phi(LS)$ is given by Eqs. (29), N is the ordinal number of a resonance, and $d^2\sigma_\perp/d\omega_2 d\Omega$ is theoretical cross section (1) for $\omega_1 = 5410.17$ eV at the Nth resonance maximum in Fig. 6 for the $K\alpha_{3,4}$ X-ray emission spectrum of the neon atom.

Wavefunctions (23) of states that make the main contribution to the intensity of double excitation have the form (components with $|a_{12}^{LS}| \geq 0.40$ are retained)

$$\begin{aligned}
|1\rangle &= 0.97|\zeta 3p^2(^3P)\rangle,\\
|2\rangle &= 0.47|\zeta 3p^2(^1D)\rangle - 0.88|\zeta 3s3d(^1D)\rangle,\\
|3\rangle &= |\xi 3p4p[0.70(^3P) + 0.70(^3D)]\rangle,\\
|4\rangle &= |\zeta 3p4p[0.70(^3P) - 0.60(^3D)]\rangle,\\
|5\rangle &= |\zeta 3p^2[0.70(^1D) + 0.60(^1S)]\rangle\\
&\quad + 0.43|\zeta 3s3d(^1D)]\rangle,\\
|6\rangle &= 0.90|\zeta 3p4p(^1D)]\rangle.
\end{aligned} \tag{24}$$

The structures of the wavefunctions $|2\rangle$ and $|5\rangle$ indicate that the $3p^2$–$3s3d$ electrostatic interaction plays a considerable role in the formation of intermediate states of inelastic scattering of the X-ray photon by the neon atom.

The resonance energies of the incident photon (ω_{1n}) as the energies of radiative transitions from the ground state to states (23) are calculated by the formula

$$\omega_{1n} = E_n - E(0), \tag{25}$$

where E_n is the energy of state (23). Note that Eq. (25) does not include a correlation energy of about 1–3 eV for each electron [30]. This disregarded correlation energy provides an estimate of the calculation accuracy for radiative-transition energies (25).

The wavefunctions and energies of the final states are obtained in the nonrelativistic single-configuration Hartree–Fock approximation. The $2p^43p^2$ configuration is taken as the final state configuration for the transition from the intermediate states $|1\rangle$, $|2\rangle$, and $|5\rangle$. The $2p^43p4p$ configuration is taken as the final state configuration for the transition from the intermediate states $|3\rangle$, $|4\rangle$, and $|6\rangle$.

It is assumed that the emitted-photon energy for all radiative transitions to final states that involve states (24) is given by the expression

$$\omega_2 = \omega_{11} - E(2p^43p^2) + E(0), \tag{26}$$

where ω_{11} = 902.42 eV (see Table 1). Going beyond approximation (26) is necessary primarily for the inclusion of the configuration interactions in final states and is a subject for future investigations.

The radial relaxation of electron shells in the fields of the 1*s* and 2*p* vacancies in the structure of the amplitudes of radiative transitions from the ground state to states (24) and from states (24) to the $2p^4(3p^2, 3p4p)$ final states is taken into account by the nonorthogonal orbital method [9, 26]. In particular, for the $1s2p \longrightarrow 3p^2$ excitation, the expression for the radial part (R) of the amplitude of the radiative transition in the length form is written as ($\hat{D}$ is the many-electron radiative-transition operator):

$$\langle 0|\hat{D}|\zeta 3p^2\rangle_{\mathrm{R}} = M\langle 1s_0|\hat{r}|\phi_1\rangle\langle 2p_0|\phi_2\rangle, \tag{27}$$

where

$$M = \langle 1s_0|1s\rangle\langle 2s_0|2s\rangle^2\langle 2p_0|2p\rangle^5,$$

$$|\phi_1\rangle = |3p\rangle - |2p\rangle\frac{\langle 2p_0|3p\rangle}{\langle 2p_0|2p\rangle},$$

$$|\phi_2\rangle = (1-\eta^2)^{-1/2}(|3p\rangle - \eta|2p_+\rangle), \quad \eta = \langle 2p_+|3p\rangle.$$

Amplitude (27) was constructed using the Gram–Schmidt orthogonalization method [31] and the general quantum-mechanical requirement [32] that the wavefunction of the $1s2p \longrightarrow 3p^2$ excited state be orthogonal to the wavefunctions of lower-lying $1s \longrightarrow 3p$ and $2s2p \longrightarrow 3p^2$ excited states. The wavefunctions of the $1s_0$ (as well as $2s_0$), $2p_0$, 1*s*, 2*s*, 2*p*, 3*p*, and $2p_+$ electrons are obtained by solving Hartree–Fock equations for the $1s^22s^22p^6$, $\zeta 3p^2$, and $1s3p$ configurations, respectively.

It is worth noting that the ζn_1dn_2d and $\zeta n_1sn_2(s, d)$ components of states (24) are manifested in the scattering cross section only via their electrostatic mixing with the ζn_1pn_2p components, because they do not contribute to the matrix element of the radiative transition operator in the dipole approximation. Indeed, transitions to the ζn_1dn_2d states are forbidden by the selection rule in the orbital quantum number *l*, and transitions to the $\zeta n_1sn_2(s, d)$ states are virtually forbidden under the above requirement that the wavefunctions of these states be orthogonal to the wavefunctions of low-lying states with the same symmetry.

The calculation results for cross section (1) including doubly excited states for the energy range near the KL_{23} ionization threshold of the neon atom are given in Table 1 and Fig. 5.

At the second stage of the construction of the amplitude A_{nm} in Eqs. (3) and (4), the excitation/ionization processes (*n* = 3 and 4):

$$\omega_1 + [0] \longrightarrow \zeta np\varepsilon p \longrightarrow 2p^4np\varepsilon p + \omega_2,$$

and the double ionization

$$\omega_1 + [0] \longrightarrow \zeta\varepsilon p\varepsilon' p \longrightarrow 2p^4\varepsilon p\varepsilon' p + \omega_2,$$

are considered for intermediate and final states. Single-electron wavefunctions of the intermediate and final states are obtained by solving Hartree–Fock equations averaged over the terms of the ζnp and $2p^4np$ configurations (*n* = 3, 4, ε), respectively.

The total wavefunctions and energies of the intermediate and final states are determined in the *LS* coupling scheme in the nonrelativistic single-configuration Hartree–Fock approximation with allowance for the multiplet splitting by diagonalizing the secular-equation matrices constructed on the basis of the $|\zeta np\rangle$ and $|2p^4np\rangle$ wavefunctions, respectively. Calculating the energy structure of the $\zeta\varepsilon p\varepsilon' p$ and $2p^4\varepsilon p\varepsilon' p$ states with the εp and $\varepsilon' p$ continuous-spectrum electrons, we neglect the $1s$–εp and $2p$–εp electrostatic interactions and set $F_2(2p\varepsilon p) = G_{0,2}(2p\varepsilon p) = G_1(1s\varepsilon p) = 0$ in the secular-equation matrices for Slater integrals.

After the diagonalization of the secular-equation matrices, we arrive at the following conclusions.

(i) Among the components of the ζnp multiplet of intermediate states, only the $(^{1,3}P)^2S$ terms of the $\zeta 3p$ configuration are really mixed:

$$\begin{aligned}\Psi(^1P) &= 0.96|^1P, {}^2S\rangle - 0.28|^3P, {}^2S\rangle,\\ \Psi(^3P) &= 0.28|^1P, {}^2S\rangle + 0.96|^3P, {}^2S\rangle,\end{aligned} \tag{28}$$

where $|^{1,3}P, {}^2S\rangle = |1s2p^5(^{1,3}P)3p(^2S)$.

(ii) Among the components of the $2p^4np$ multiplet of final states, only the $(^1S, {}^1D, {}^3P)^2P$ terms of the $2p^43p$ configuration are actually mixed:

$$\begin{aligned}\phi(^1S) &= 0.998|^1S, {}^2P\rangle + 0.057|^3P, {}^2P\rangle,\\ \phi(^1D) &= 0.935|^1D, {}^2P\rangle + 0.353|^3P, {}^2P\rangle,\\ \phi(^3P) &= 0.934|^3P, {}^2P\rangle - 0.353|^1D, {}^2P\rangle - 0.052|^1S, {}^2P\rangle,\end{aligned} \tag{29}$$

where $|LS, {}^2P\rangle = |2p^4(LS)3p(^2P)\rangle$.

The incident-photon threshold energies for the formation of the extended structures of cross section (1) that are associated with transitions to the intermediate states corresponding to excitation/ionization and double ionization are calculated by the formulas

$$\omega_1 = E(^{1,3}P) - E(0), \quad n = 3, \tag{30}$$

$$\omega_1 = E(LS, L'S') - E(0), \quad n = 4, \varepsilon. \tag{31}$$

Here, $E(^{1,3}P)$ are the energies of states (28) and $E(LS, L'S')$ are the energies of the terms of the $\zeta(LS)np(L'S')$ multiplet. The corresponding energies of emitted photons are calculated by the formula

$$\omega_2 = E(k_{1n}) - E(k_{2n}) + E_T(k_{1n}) - E_T(k_{2n}), \tag{32}$$

where $E(k_{1n})$ and $E_{k_{2n}}$ are the total Hartree–Fock energies of the $k_{1n} = \zeta np$ and $k_{2n} = 2p^4np$ states and E_T are the energies of the terms (for $n = 3$, energies of states (28) and (29)) of the corresponding multiplets with respect to their centroids.

The calculation results for cross section (1) including the states of excitation/ionization and double ionization near the KL_{23} ionization threshold of the neon atom are presented in Table 2 and Fig. 5.

3.3. Comparison of Theory with Experiment

As the incident-photon energy increases, the spatially extended structures of cross section (1) that are presented in Figs. 2 and 5 evolve to the main $K\alpha_{1,2}$ and satellite $K\alpha_{3,4}$ X-ray emission spectra of the neon atom, respectively. Since the $K\alpha$ X-ray emission spectrum of the neon atom was measured in experiment [25] carried out at the incident-photon energy $\omega_1 = 5410.17$ eV, the theory and calculation methods developed in this work can be tested. The calculation results of this work are compared with experiment in Fig. 6.

The experimental $K\alpha$ emission spectrum of the neon atom was obtained in arbitrary units. For this reason, we normalize it to the theoretical value of cross section (1) near the α_3 structure of the emission spectrum (see $N = 4$ in Table 2). In this case, the theoretical spectrum near the $\alpha_{1,2}$ and $\alpha_{3,4}$ structures of the emission spectra was calculated with the total widths $\Gamma_{1s} = 0.50$ and 0.60 eV, respectively, of the decay of the $1s$ vacancy, which are taken from [27] (synchrotron experiment on measuring the spectrum of the photon absorption by the neon atom near the K and KL_{23} ionization threshold).

The contribution of the contact part of the cross section for $\omega_1 = 5410.17$ eV is equal to a negligibly small value of about $10^{-6}r_0^2$/eV sr and is ignored.

The theoretical calculation of this work agrees well with the experimental data. The cause of the remaining discrepancies of about 16% near the $K\alpha_{1,2}$ resonance of the emission spectrum is not understood and is a subject for future investigations.

Discussing the features of the evolution of the spatially extended structures of cross section (1) (see Fig. 5) to the emission-spectrum structure (see Fig. 6), we mention that the role of the radial relaxation of electron shells in the fields of $1s$ and $2p$ vacancies decreases as the incident-photon energy increases. Indeed, when ω_1 increases, in the amplitude of the radiative transition to the intermediate state

$$M_n(LS) \equiv \langle 0|\hat{D}|\zeta(LS)np\varepsilon' p\rangle = \alpha_{LS}a_n + \beta_{LS}b_n,$$

where $n = 3$ and 4 and α_{LS} and β_{LS} are the angular coefficients, the component

$$a_n = \langle 1s_0|\hat{r}|np_c\rangle\langle 2p_0|\varepsilon' p_+\rangle$$

becomes negligibly small compared to the component

$$b_n = \langle 1s_0|\hat{r}|\varepsilon' p_c\rangle\langle 2p_0|np_+\rangle$$

and the contribution of the additional term to the radial integral $\langle 1s_0|\hat{r}|\varepsilon' p_c\rangle$ decreases strongly. As a result, the

ratio $M_n(^3P)/M_n(^1P)$ increases and the scattering probability is redistributed from the $K\alpha_4$ region of the emission spectrum to the $K\alpha_3$ region.

3.4. Calculation of the Contact Part of the Cross Section

Figure 7 shows the contact part of cross section (14) calculated near the *K*-shell ionization threshold of the neon atom with the function Φ_{nl} obtained in this work (see Eq. (15)) and in the dipole approximation (see Eq. (16)), which is formally extended to the range $0 < qr < 1$. The wavefunctions of the $\varepsilon_n(l, l \pm 1)$ continuous-spectrum electrons in the final states are obtained by solving Hartree–Fock equations for a configuration containing an *nl* vacancy. The wavefunctions of *nl* electrons in the initial states are determined by solving Hartree–Fock equations for the ground state configuration. In calculating spectral functions Ψ_{nl} in (14), we used the total decay widths $\Gamma_{1s} = 0.23$ eV and $\Gamma_{2s} = 0.05$ eV (measured from the experimental spectrum of the absorption of the photon by the 2*s* shell of the neon atom [33]), as well as the width $\Gamma_{2p} = 3.95 \times 10^{-8}$ eV and ionization thresholds $I_{1s} = 868.399$ eV, $I_{2s} = 49.314$ eV, and $I_{2p} = 19.845$ eV (nonrelativistic calculation performed in this work).

The jumps in the scattering cross section in Fig. 7 at the emitted-photon energies 830.866 and 860.155 eV correspond to the condition of zero energy of the continuous-spectrum electron, $\omega_2 = \omega_1 - I_{2s}$ and $\omega_2 = \omega_1 - I_{2p}$, for the $2s_0 \longrightarrow \varepsilon(s, p)$ and $2p_0 \longrightarrow \varepsilon(s, p, d)$ transitions, respectively. As follows from the results presented in Fig. 7, the contribution of the contact part of the cross section to the total cross section of the process is negligibly small [$\sim 0.07 r_0^2$/eV sr] compared to the contribution of the anomalous dispersion component [$\sim 250 r_0^2$/eV sr] in the region of the formation of the $K\alpha_{1,2}$ structure in the scattering spectrum.

However, even in the X-ray energy ranges for the incident and scattered photons and for nonzero scattering angles, the dipole approximation, in principle, significantly changes not only the values but also the shape of the contact part of the cross section compared to those calculated beyond its framework. Moreover, when the radial relaxation of electron shells in the field of an *nl* atomic-residual vacancy is ignored, $\Phi_{nl} = 0$ in the dipole approximation, whereas $\Phi_{nl} \neq 0$ beyond the framework of the dipole approximation (for $qr > 0$).

The inclusion of the configuration interaction and multiple excitation/ionization in the initial and final states of inelastic contact scattering, as well as the additional terms in the functions $W_t(n_1l_1, n_2l_2)$ in Eq. (12), when the radial relaxation of electron shells in the field of the core vacancies (e.g., allowance for the change of $\langle 1s_0|j_1(qr)|\varepsilon p_+\rangle$ by $\langle 1s_0|j_1(qr)|\varepsilon p_c\rangle$ in Eq. (15)) is taken into account, is a subject for future investigations.

4. CONCLUSIONS

The basic results of this work are as follows.

The radial relaxation of the electron shells of the intermediate and final states in the Hartree–Fock fields of the deep 1*s* and valence 2*p* vacancies almost halves the value (but does not change the shape of the surface) of the double differential cross section for the resonant inelastic scattering of the X-ray photon near the *K*-shell ionization threshold of the neon atom.

In addition to the effects of the configuration interaction and multiplet splitting in the intermediate and final states, the radial relaxation significantly determines the value, structure, and shape of the resonance and the spatially extended thin structure in the double differential cross section for inelastic scattering near the KL_{23} ionization threshold of the neon atom.

When the incident-photon energy increases, the contribution of the radial relaxation to the value and shape of the double differential cross section for inelastic scattering decreases, which determines the features of the evolution of the spatially extended structures of the cross section to the $K\alpha$ X-ray emission spectrum of the neon atom.

The radial relaxation is responsible for a new type of many-particle effect—the effect of correlation amplitudes in the resonant inelastic scattering of the X-ray photon by the free atom. In turn, this effect significantly determines the value and shape of the double differential cross section for scattering near the *K*-shell ionization threshold of the neon atom.

The analytical structure of the contact part of the double differential cross section for the inelastic scattering of the photon by the free atom has been determined using the irreducible tensor operator method. It has been shown that the transition from the found structure to, e.g., the dipole approximation for the theoretical description of the contact part of the cross section strongly changes not only the values but also the shape of the scattering cross section even in the X-ray energy ranges of the incident and scattered photons.

REFERENCES

1. C.-C. Kao, K. Hamalainen, M. Krisch, *et al.*, Rev. Sci. Instrum. **66**, 1699 (1995).
2. P. P. Kane, L. Kissel, R. H. Pratt, and S. C. Roy, Phys. Rep. **140**, 75 (1986).
3. A. N. Khoperskiĭ and V. A. Yavna, *Photon Scattering by a Multielectron System* (Énergoatomizdat, Moscow, 2004) [in Russian].
4. G. S. Landsberg and L. I. Mandelstam, Z. Phys. **50**, 769 (1928).
5. C. V. Raman, Indian J. Phys. **2**, 387 (1928).
6. A. H. Compton, Phys. Rev. **21**, 483 (1923).
7. M. A. MacDonald, S. H. Southworth, J. C. Levin, *et al.*, Phys. Rev. A **51**, 3598 (1995).

8. T. Åberg and J. Tulkki, in *Atomic Inner-Shell Physics*, Ed. by B. Crasemann (Plenum, New York, 1985), Chap. 10.
9. V. Schmidt, Rep. Prog. Phys. **55**, 1483 (1992).
10. P. P. Kane, Phys. Rep. **218**, 67 (1992).
11. H. Daido, Rep. Prog. Phys. **65**, 1513 (2002).
12. K. Moribayashi, T. Kagawa, and D. E. Kim, Nucl. Instrum. Methods Phys. Res. B **205**, 334 (2003).
13. N. H. March, W. H. Young, and S. Sampanthar, *The Many-Body Problem in Quantum Mechanics* (Cambridge Univ. Press, Cambridge, 1967; Mir, Moscow, 1969).
14. A. N. Hopersky and V. V. Chuvenkov, J. Phys. B: At. Mol. Opt. Phys. **36**, 2987 (2003).
15. A. Costescu, P. M. Bergstrom, Jr., C. Dinu, and R. H. Pratt, Phys. Rev. A **50**, 1390 (1994).
16. M. Ya. Amusia and N. A. Cherepkov, Case Stud. At. Phys. **5**, 47 (1975).
17. R. Karaziya, *Introduction to the Theory of X-ray and Electron Spectra of Free Atoms* (Mokslas, Vilnius, 1987) [in Russian].
18. J. H. Hubbell, Radiat. Phys. Chem. **50**, 113 (1997).
19. P. Eisenberger and P. M. Platzmann, Phys. Rev. A **2**, 415 (1970).
20. D. A. Owen, Phys. Rev. A **16**, 1594 (1977).
21. J. L. Campbell and T. Papp, At. Data Nucl. Data Tables **77**, 1 (2001).
22. A. Hibbert, M. Le Dourneuf, and M. Mohan, At. Data Nucl. Data Tables **53**, 23 (1993).
23. K.-N. Huang, M. Aoyagi, M. H. Chen, *et al.*, At. Data Nucl. Data Tables **18**, 243 (1976).
24. A. N. Hopersky, V. A. Yavna, A. M. Nadolinsky, and D. V. Dzuba, J. Phys. B: At. Mol. Opt. Phys. **37**, 2511 (2004).
25. O. Keski-Rahkonen, Phys. Scr. **4**, 173 (1973).
26. V. L. Sukhorukov, A. N. Hopersky, I. D. Petrov, *et al.*, J. Phys. (Paris) **48**, 45 (1987).
27. J. M. Esteva, B. Gauthe, P. Dhez, and R. C. Karnatak, J. Phys. B: At. Mol. Phys. **16**, L263 (1983).
28. L. Avaldi, R. Camilloni, G. Stefani, *et al.*, J. Phys. B: At. Mol. Opt. Phys. **29**, L737 (1996).
29. M. Oura, H. Yamaoka, Y. Senba, *et al.*, Phys. Rev. A **70**, 062502 (2004).
30. R. K. Nesbet, Phys. Rev. **155**, 56 (1967).
31. M. C. Reed and B. Simon, *Methods of Modern Mathematical Physics* (Academic, New York, 1972; Mir, Moscow, 1977), Vol. 1.
32. A. Messiah, *Quantum Mechanics* (Interscience, New York, 1961; Nauka, Moscow, 1978), Vol. 1.
33. O. Wilhelmi, G. Mentzel, B. Zimmermann, *et al.*, J. Electron Spectrosc. Relat. Phenom. **101**–**103**, 155 (1999).

Translated by R. Tyapaev

Journal of Experimental and Theoretical Physics, Vol. 101, No. 4, 2005, pp. 611–627.
From Zhurnal Éksperimental'noĭ i Teoreticheskoĭ Fiziki, Vol. 128, No. 4, 2005, pp. 714–731.

ATOMS, MOLECULES, OPTICS

Electron Terms and Resonant Charge Exchange Involving Oxygen Atoms and Ions¶

A. V. Kosarim and B. M. Smirnov

Institute for High Temperatures, Russian Academy of Sciences, Moscow, 127412 Russia
e-mail: kosarim@mail.ru

Received May 17, 2005

Abstract—The electron terms are constructed for oxygen dimer ions at large ion–atom distances taking into account a certain scheme of summation of electron momenta on the basis of a hierarchy of various ion–atom interactions. Because the number of interaction types exceeds that in the Hund scheme, a realistic hierarchy of interactions and corresponding quantum numbers of the diatomic ion are outside the Hund coupling scheme. Electron terms are evaluated for the oxygen dimer ion in the case where the ground and first excited states of an atom and an ion belong to the respective valence electron shells p^4 and p^3 and correspond to the range of separations that determine the cross sections of resonant charge exchange in plasma. These electron terms allow us to calculate the partial and average cross sections for resonant charge exchange involving an oxygen ion and atom in the ground and first excited states in the range of collision energies of interest for oxygen plasmas. The specific features of electron terms of the oxygen ion dimer and the cross section of electron transfer are analyzed. © *2005 Pleiades Publishing, Inc.*

1. INTRODUCTION

In slow collision processes, electrons follow changes of atomic fields and therefore the cross section of a slow collision process is determined by the behavior of electron terms for a quasimolecule consisting of the colliding atomic particles. Below, we consider the resonant charge-exchange processes

$$\begin{aligned} &O^+(2p^3)(^4S, ^2D, ^2P) + O(2p^4)(^3P, ^1D, ^1S) \\ &\longrightarrow O(2p^4)(^3P, ^1D, ^1S) + O^+(2p^3)(^4S, ^2D, ^2P) \end{aligned} \quad (1)$$

at low collision velocities compared to those of valence electrons. Because the cross section of resonant charge exchange is large in comparison with a typical atomic cross section, i.e., the electron transfer proceeds at large distances between colliding particles, analysis of electron terms is required at large ion–atom distances, where various types of interactions may be separated.

The character of coupling of electron momenta may be constructed on the basis of the Hund coupling scheme [1–3], which consists in analyzing the hierarchy of interactions in the quasimolecule, which also allows one to determine the quasimolecule quantum numbers. Because the potentials of different interactions depend on distances between atomic particles, the coupling scheme and quantum numbers of the quasimolecule can vary with changing distances between atomic particles. Therefore, for analysis of collision processes, the relative trajectory of particle motion can be conveniently divided into several parts such that a certain type of coupling of electron momenta is realized in each part [4–7]. The transition between different coupling schemes leads to a change of quantum numbers of colliding particles.

The processes under consideration are of importance for a nonequilibrium dissociating oxygen plasma, in particular, for atmospheric plasma at altitudes above 100 km. Indeed, oxygen is partially atomic at these altitudes, due to oxygen dissociation under the action of solar radiation. Because the cross section of resonant charge exchange significantly exceeds the cross sections of other processes, including elastic collisions of atoms and molecules, the resonant charge-exchange process determines the mobility of ions in this plasma and the parameters of other transport processes involving ions. Oxygen atoms and ions are in the ground and lowest-excited electron states, and the cross sections of resonant charge exchange depend on these states. Because the distribution over these states at a given point of space depends on external conditions, measurement of the mobility for oxygen ions in different electron states at this point allows us to determine the atom distribution over the lowest electron states at a specified point. Hence, determination of the cross sections of resonant electron transfer for oxygen atoms and ions in different states has an applied interest.

The first stage of determining the cross sections is the construction of electron terms of the quasimolecule, which can be done on the basis of the standard Mulliken scheme of momentum summation [1]. This scheme includes three types of interactions in the quasimolecule: V_e, the electrostatic interaction responsible

¶ The text was submitted by the authors in English.

for energy splitting at different angular momentum projections on the molecule axis; δ_f, which corresponds to the spin–orbit interaction and other relativistic interactions; and V_{curl}, the rotational energy or Coriolis interaction, which accounts for the interaction between the orbital and spin electron momenta with the rotation of the molecular axis. Depending on the ratio between these interaction energies, one can construct six cases of Hund coupling [1–3], each of which corresponds to a certain scheme of momentum summation and is characterized by certain quantum numbers of the diatomic molecule. These cases can be used as model ones for analyzing certain transitions in atomic collisions [6–8].

This general scheme may be used for analyzing the resonant charge-exchange process involving an ion and an atom with nonfilled electron shells when different schemes are possible for coupling of electron momenta and, correspondingly, when the resonant charge-exchange process is entangled with other processes (rotation of electron momenta, transitions between fine structure states) in different ways. Nevertheless, electron exchange and other transition processes usually correspond to different trajectory segments, which makes it possible to separate the exchange process from other processes. It is therefore necessary to use the correct scheme of angular momentum coupling in the quasimolecule, which consists of the colliding ion and atom. Analysis of the resonant charge exchange for halogens [9, 10] shows that the real character of angular momentum coupling corresponds to none of the Hund cases, because the number of different interactions is greater than that used in the standard scheme. Nevertheless, the general concept of constructing electron terms of a quasimolecule on the basis of the interaction hierarchy remains valid and underlies the analysis.

Thus, the goal of this paper is to find the character of coupling for the oxygen diatomic ion O_2^+ at large distances between the nuclei on the basis of constructing an interaction hierarchy in this quasimolecule. This allows us to evaluate the partial and average cross sections of resonant charge exchange in the case of oxygen for the lowest state of electron shells. Solution of this problem also gives a general scheme for determining the cross section of resonant charge exchange for ion and atom with nonfilled electron shells.

2. HIERARCHY OF ION–ATOM INTERACTIONS FOR OXYGEN

We determine the cross sections of processes (1) on the basis of the asymptotic theory [11–13], i.e., as a result of expansion of the cross section with respect to the small parameter, the ratio of the typical atomic size to the typical distance of electron transfer. This theory uses a large electron transfer cross section compared to the typical atomic cross section at low velocities, and its first stage is evaluation of the electron terms for the quasimolecule consisting of colliding particles. We find the hierarchy of interactions at large distances between $O^+(2p^3)$ and $O(2p^4)$ and then the electron terms of this system and quantum numbers for the description of the molecular ion states.

Based on the experience for the case of halogen [9, 10], as the basis ion–atom interactions at large distances R we use the fine spin–orbit interaction for $O^+(2p^3)$ and $O(2p^4)$ and the quadrupole interaction of the ion charge with the atom quadrupole moment. In this approximation, the Hamiltonian of the molecular ion at large distances between nuclei is given by

$$\hat{H} = -a\hat{\mathbf{L}}\cdot\hat{\mathbf{S}} - b\hat{\mathbf{I}}\cdot\hat{\mathbf{s}} - \frac{e\hat{Q}}{R^3}. \tag{2}$$

This is valid for light atoms in the case of the *LS* coupling scheme for atoms and ions; here, $\hat{\mathbf{L}}$ is the operator of the angular atom momentum, $\hat{\mathbf{S}}$ is the atom spin operator, $\hat{\mathbf{I}}$ is the operator of the angular ion momentum, $\hat{\mathbf{s}}$ is the ion spin operator, and $\hat{Q}$ is the quadrupole momentum operator for the atom, and we take the interaction of a positively charged ion with the quadrupole moment of valence electrons into account.

The parameters of the spin–orbit interaction of an oxygen atom and its ion are given by $a = 77 \pm 2$ cm^{-1} for the atom state ^3P, $b = 8.4$ cm^{-1} for the oxygen ion state ^2D, and $b = 0.7$ cm^{-1} for the ion state ^2P [14, 15]. Because the typical value of the ion–atom exchange interaction potential is several cm^{-1}, we can ignore the fine splitting of levels in the last case. Correspondingly, the matrix elements for the spin–orbit interaction are [3, 16, 17]

$$\begin{aligned}
&\langle M_L, M_S|\hat{\mathbf{L}}\cdot\hat{\mathbf{S}}|M_L, M_S\rangle = M_L M_S,\\
&\langle M_L, M_S|\hat{\mathbf{L}}\cdot\hat{\mathbf{S}}|M_L+1, M_S-1\rangle\\
&= \langle M_L+1, M_S-1|\hat{\mathbf{L}}\cdot\hat{\mathbf{S}}|M_L, M_S\rangle\\
&= \frac{1}{2}\sqrt{(L+|M_L|+1)(L-|M_L|)(S+|M_S|)(S-|M_S|+1)},\\
&\langle M_L, M_S|\hat{\mathbf{L}}\cdot\hat{\mathbf{S}}|M_L-1, M_S+1\rangle\\
&= \langle M_L-1, M_S+1|\hat{\mathbf{L}}\cdot\hat{\mathbf{S}}|M_L, M_S\rangle\\
&= \sqrt{(L+|M_L|)(L-|M_L|+1)(S+|M_S|+1)(S-|M_S|)},
\end{aligned} \tag{3}$$

where L and M_L are the atom orbital momentum and its projection onto the molecular axis, S and M_S are the atom spin and its projection on the molecular axis. For the matrix elements of the ion spin–orbit interaction, we have identical expressions.

Table 1. Diagonal matrix elements of the quadrupole moment Q_{MM} expressed in ea_0^2 for an oxygen atom with the electron shell $2p^4$

State	^3P, $M = 0$	^3P, $M = \pm 1$	^1D, $M = 0$	^1D, $M = \pm 1$	^1D, $M = \pm 2$
Q_{MM}	1.6	−0.8	−1.87	−0.93	1.87

We consider the quadrupole interaction between an ion and an oxygen atom, which, in this case, corresponds to the second expansion term of the ion charge–valence electron interaction:

$$\frac{e^2}{R} - \left\langle \frac{e^2}{|\mathbf{R} - \mathbf{r}|} \right\rangle$$

in the small parameter r/R, where $\mathbf{r}$ is the valence electron coordinate in its atom, $\mathbf{R}$ is the distance between the ion of charge e and the atom nucleus, and the average is taken over the wavefunction of the valence electron. The quadrupole moment of an individual electron is then given by [18]

$$q = 2\langle r^2 P_2 \cos\theta \rangle = 2\frac{l_e(l_e+1) - 3m^2}{(2l_e - 1)(2l_e + 3)}\overline{r^2}, \quad (4)$$

where r, θ are spherical coordinates of the valence electron and l_e and m are the orbital momentum of this electron and its projection on the molecular axis.

For oxygen, it is more convenient to consider a valence electron shell as two p-holes in addition to a completed p-electron shell. The hole quadrupole moment differs from that of the electron by sign only. The total wavefunction of these holes that corresponds to the total orbital momentum of holes L and its projection M onto a given direction is given by

$$\Psi_{LM} = \sum_m \begin{bmatrix} 1 & 1 & L \\ m & M-m & M \end{bmatrix} \psi_{1m}(1)\psi_{1,M-m}(2), \quad (5)$$

where $\psi_{1m}(i)$ is the wavefunction of the ith p-hole with the momentum projection m and the Clebsch–Gordan coefficient

$$\begin{bmatrix} 1 & 1 & L \\ m & M-m & M \end{bmatrix}$$

is responsible for summation of the momenta of individual holes into the momentum of the entire system. Correspondingly, the electron shell is characterized by quantum numbers L, $-M$ in this case, and because its atomic quadrupole moment is conserved under $M \longrightarrow -M$, we ignore the difference between a hole and an electron below.

We use the fact that the sum of quadrupole moments of an electron shell and a hole shell is zero, and therefore, expressing the quadrupole moment of an electron shell through the quadrupole moments of a hole shell, it is necessary to change the sign of the quadrupole moment. In another way, the sign of the electron quadrupole moment is reciprocal to that of a hole and therefore, constructing the quadrupole moment of an electron shell through those of individual holes, we must change sign. Hence, the quadrupole moment of an oxygen atom is given by

$$\langle M|\hat{Q}|M'\rangle = -\delta_{MM'}\sum_m \begin{bmatrix} 1 & 1 & L \\ m & M-m & M \end{bmatrix}^2 (q_m + q_{M-m}), \quad (6)$$

where q_m is the quadrupole moment of an individual electron with the momentum projection m on the molecular axis, and, according to formula (3), we have

$$q_0 = \frac{4e\overline{r^2}}{5}, \quad q_1 = q_{-1} = -\frac{2e\overline{r^2}}{5}, \quad (7)$$

where $\overline{r^2}$ is the mean square of a valence electron orbit. For an oxygen atom in the ground state, we have $\overline{r^2} \approx 2a_0^2$ [15], where a_0 is the Bohr radius. For excited oxygen atom states, we take

$$\overline{r^2} \sim 1/\gamma^2, \quad \gamma^2 = J/J_H,$$

where J is the ionization potential for this state and J_H is the ionization potential for a hydrogen atom in the ground state. In particular, it follows that $\overline{r^2} = 2.33a_0^2$ for the ^1D-state of an oxygen atom. Table 1 contains values of the quadrupole moments for an oxygen atom, and we use these values for determination of electron terms of a diatomic oxygen ion.

In addition, Table 2 contains the values of γ for oxygen atom and ion states. The atom ionization potential with transition to a given ion state is

$$J = J^0 - \Delta E_a + \Delta E_i, \quad (8)$$

where J^0 is the oxygen ionization potential with the electron transition from the ground atom state to the ion ground state, ΔE_a is the atom excitation energy, and ΔE_i is the ion excitation energy. Because a given ion state results from a one-electron transition from an indicated atom state, we ignore the cases of ion–atom interactions if a given ion state cannot be formed from the indicated atom state as a result of a one-electron transition.

Table 2. The parameter $\gamma = \sqrt{J/J_H}$ for various atom and ion oxygen states

Atom state / Ion state	^3P	^1D	^1S
^4S	1.000	–	–
^2D	1.116	1.049	–
^2P	1.170	1.107	1.030

In considering the electron terms of the quasimolecule O_2^+, we start from large distances R between the nuclei, where the electron energy is equal to

$$\varepsilon = \varepsilon_0 + \Delta E_a + \Delta E_i + \frac{aJ(J+1)}{2} - \frac{aJ_0(J_0+1)}{2} + \frac{bj(j+1)}{2} - \frac{bj_0(j_0+1)}{2}, \quad (9)$$

where ε_0 corresponds to the atom and ion ground state, such that ΔE_a and ΔE_i account for electron excitation of the quasimolecule; J_0 and j_0 are the total electron moments of the atom and ion in the ground fine state, and the last terms in formula (9) take fine states of the atom and ion into account. Therefore, in evaluating the quasimolecule electron terms, we measure the quasimolecule energy from the value $\varepsilon_0 + \Delta E_a + \Delta E_i$ at large separations, adding it to Hamiltonian (2) at finite separations. Because the ion and atom parts of this Hamiltonian commute, we can add the ion and atom parts to the electron energy independently. Quantum numbers due to the ion part—the total ion angular momentum j and its projection on the molecular axis m_j—are conserved at any ion–atom distances, whereas the atom quantum numbers J and M_J are valid at large separations, or quantum numbers M_L and M_S are accurate quantum numbers only if we neglect spin–orbit interaction. Therefore, finding electron terms accurately, we use the notation M_L, M_S or J, M_J for them only to label the quasimolecule states.

In addition, because the quadrupole interaction is symmetric during the transformation $M_L \longrightarrow -M_L$ and the spin–orbit interaction is symmetric during the transformation $M_L + M_S \longrightarrow -M_L - M_S$, we find that the electron terms of a quasimolecule described by Hamiltonian (2) are degenerate with respect to the simultaneous transformations

$$M_L, M_S \longrightarrow -M_L, -M_S. \quad (10)$$

We can therefore restrict ourselves to a part of electron terms for the diatomic ion O_2^+ at large separations with

$$|M_L + M_S| \geq 0.$$

In particular, if the oxygen atom is found in the ground state $O(^3P)$, the number of nondegenerate electron terms is six with respect to atom states.

In constructing the electron terms for the atom part, we construct the Hamiltonian matrix elements

$$\langle M_L, M_S|\hat{H}|M_L', M_S'\rangle.$$

Next, by diagonalization of this matrix, we find the energy positions at a fixed distance R between the nuclei by solving the secular equation for the Hamiltonian matrix elements [3]. This is given by the vanishing condition for the determinant,

$$\left|E\delta_{M_L M_L'}\delta_{M_S M_S'} - \langle M_L, M_S|\hat{H}|M_L', M_S'\rangle\right| = 0. \quad (11)$$

Solutions $E(R)$ of Eq. (10) give the positions of the electron terms at a given separation R.

Table 3 gives the Hamiltonian matrix $\hat{H}_{ik}$ for the interaction of $O^+(^4S) + O(^3P)$ as an example. We here use Hamiltonian (2), and the electron energies of an oxygen diatomic ion at a given separation follow from solution of Eq. (10). We can see that this matrix can be divided into five independent blocks, such that one block contains three diagonal elements, two identical blocks contain two diagonal elements, and two identical blocks contain one diagonal element. These identical matrix blocks can be converted into each other by transformations (10), and we include only one of the two identical matrices in Table 2.

In Figs. 1–3, we give the electron terms of the oxygen diatomic ion for the respective atom and ion states

$$O(^3P) + O^+(^3S),$$
$$O(^3P) + O^+(^2D),$$

and

$$O(^1D) + O^+(^2D)$$

with the interactions in Hamiltonian (2) taken into account. The range of separations is such that it makes the main contribution to the cross section of resonant charge exchange at thermal and eV-energies of collision. We characterize the atom state by the quantum numbers J and M_J, the total atom momentum and its projection on the molecular axis, which are precise atomic numbers at very large separations and are used as notation at smaller separations where the ion–quadrupole interaction becomes important. Correspondingly, the electron terms of the oxygen diatomic ion are described by the quantum numbers J, $|M_J|$, j, where j is the total ion angular momentum.

3. ION–ATOM EXCHANGE INTERACTION POTENTIAL

The next step of our program is to determine the ion–atom exchange interaction potential. It is small

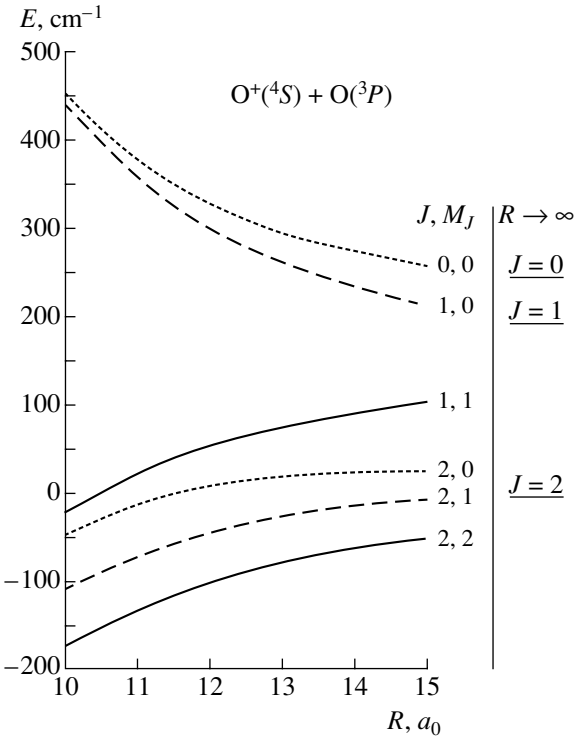

Fig. 1.

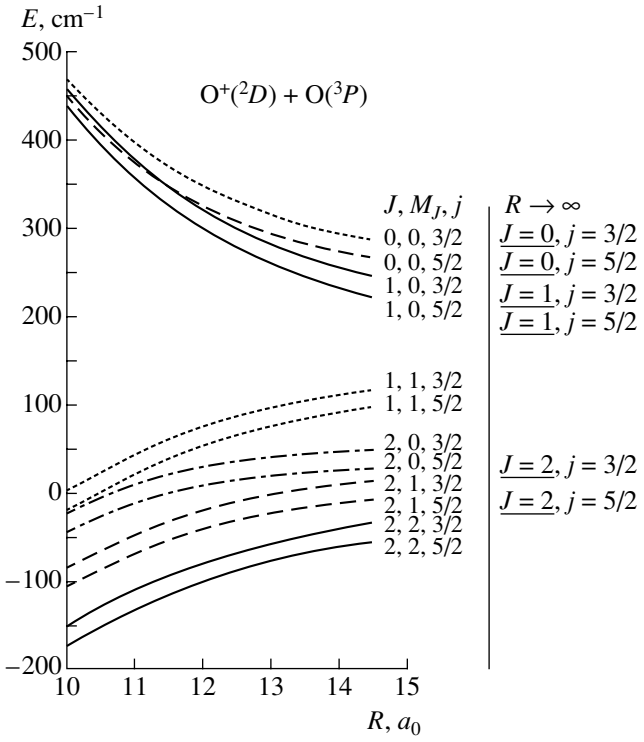

Fig. 2.

compared to the interactions in Hamiltonian (2), and, therefore, each electron term splits into levels with different parities. The ion–atom exchange interaction removes the degeneration with respect to different m_j, the ion momentum projection on the molecular axis. The exchange ion–atom interaction allows us to evaluate the partial cross section of resonant charge exchange that proceeds inside a given electron term.

Table 3. The Hamiltonian matrix $\hat{H}_{ik}$ for the quasimolecule $O^+(^4S_{3/2}) + O(^3P)$ if the exchange ion–atom interaction is neglected; the Hamiltonian is given by formula (2); $a = 77 \pm 2$ cm^{-1}

M_L, M_S	1, 1	1, 0	0, 1	1, –1	0, 0	–1, 1
1, 1	$-a - \frac{0.8e^2a_0^2}{R^3}$	0	0	0	0	0
1, 0	0	$-\frac{0.8e^2a_0^2}{R^3}$	$-a$	0	0	0
0, 1	0	$-a$	$\frac{1.6e^2a_0^2}{R^3}$	0	0	0
1, –1	0	0	0	$a - \frac{0.8e^2a_0^2}{R^3}$	$-a$	0
0, 0	0	0	0	$-a$	$\frac{1.6e^2a_0^2}{R^3}$	$-a$
–1, 1	0	0	0	0	$-a$	$a - \frac{0.8e^2a_0^2}{R^3}$

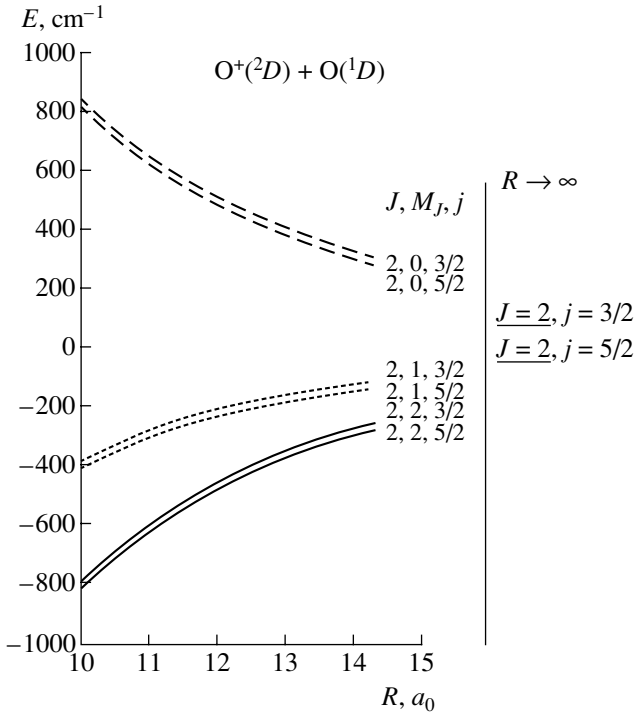

Fig. 3.

The exchange ion–atom interaction results from the transition of a valence electron from one atomic rest to another one. This interaction divides the quasimolecule states into even (g) and odd (u) according to the property of the corresponding molecular wavefunction to preserve or change sign as a result of reflection of all the electrons with respect to the symmetry plane perpendicular to the molecular axis. If a valence electron with an orbital momentum l_e and its projection μ on the molecular axis is located in the field of two structureless cores, the exchange interaction potential $\Delta_{l_e\mu}$ is given by the formula [5, 7, 13, 19]

$$\Delta_{l_e\mu}(R) = A^2 R^{\frac{2}{\gamma}-1-|\mu|} e^{-R\gamma-\frac{1}{\gamma}} \frac{(2l+1)(l_e+|\mu|)!}{(l_e-|\mu|)!|\mu|!(\gamma)^{|\mu|}}, \quad (12)$$

where R is the distance between the nuclei and γ and A are the parameters of the asymptotic wavefunction of the valence electron; the radial wavefunction of this electron in the atom at large distances r from its center is given by

$$\psi(r) = Ar^{\frac{1}{\gamma}-1} e^{-r\gamma}, \quad r\gamma \gg 1.$$

Formula (12) contains the first term of the asymptotic expansion with respect to the small parameter $1/\gamma R$ for the ion–atom exchange interaction potential at large distances between nuclei. For a valence p-electron, formula (12) becomes

$$\Delta_{10}(R) = 3A^2 R^{\frac{2}{\gamma}-1} e^{-R\gamma-\frac{1}{\gamma}},$$
$$\Delta_{1,\pm1}(R) = \frac{2}{R\gamma}\Delta_{10}(R). \quad (13)$$

This one-electron interaction is the basis of the exchange interaction potential in the case where the interacting atom and ion have nonfilled electron shells and the coupling of electron momenta for a transferring electron and the atomic rest is of importance. We use the LS coupling scheme, which suitable for light atoms. Then, the wavefunction of an atom with n valence electrons of momentum l_e is given by [16, 17, 20]

$$\Phi_{LSM_LM_S}(1, 2, \ldots, n) = \frac{1}{\sqrt{n}}\hat{P}$$
$$\times \sum_{l, m, s, m_s, \mu, \sigma} G_{ls}^{LS}(l_e, n) \begin{bmatrix} l_e & l & L \\ \mu & m & M_L \end{bmatrix} \begin{bmatrix} \frac{1}{2} & s & S \\ \sigma & m_s & M_S \end{bmatrix} \quad (14)$$
$$\times \varphi_{l_e \frac{1}{2}\mu\sigma}(1)\psi_{lsmm_s}(2, \ldots, n).$$

Here, Φ, ψ, and φ are the respective wavefunctions of the atom, ion, and valence electron with the indicated quantum numbers, μ and σ are the projections of the angular momentum and spin of the valence electron, the argument of the wavefunction indicates electrons involved in each atomic particle, the operator $\hat{P}$ permutes these electrons, and the parentage coefficient $G_{ls}^{LS}(l_e, n)$ is responsible for addition of a valence electron to the ion for the construction of an atom for given quantum numbers of these atomic particles.

The exchange interaction potential is given by the formula [7, 13]

$$\Delta(R) = 2\langle\Psi_1|\hat{H}|\Psi_2\rangle - 2\langle\Psi_1|\hat{H}|\Psi_1\rangle\langle\Psi_1|1|\Psi_2\rangle, \quad (15)$$

where Ψ_1 is the wavefunction of the quasimolecule in the case where a valence electron is located near the first core (the electron is connected with the first nucleus), Ψ_2 corresponds to the electron location near the second nucleus, and $\hat{H}$ is the Hamiltonian of the electrons. We note that an accurate evaluation of this interaction requires using the accurate wavefunctions of the quasimolecule such that the interaction of a valence electron located between the cores with both cores is taken into account simultaneously. We assume this to be fulfilled within the framework of the asymptotic theory. Using a general method of calculation of the exchange interaction potential $\Delta(R)$ by analogy with

that for case (a) of the Hund coupling [13, 21–23] and using the properties of Clebsch–Gordan coefficients, we obtain

$$\Delta_{LSM_LM_Slsmm_s}(R) = n(G_{ls}^{LS})^2 \times \sum_{\mu,\sigma,\sigma'} \begin{bmatrix} l_e & l & L \\ \mu & M_L-\mu & M_L \end{bmatrix} \begin{bmatrix} \frac{1}{2} & s & S \\ \sigma & M_S-\sigma & M_S \end{bmatrix} \begin{bmatrix} l_e & l & L \\ \mu & m & m+\mu \end{bmatrix} \times \begin{bmatrix} \frac{1}{2} & s & S \\ \sigma' & m_s & m_s+\sigma' \end{bmatrix} \Delta_{l_e\mu}(R). \quad (16)$$

Here, we take into account the character of the coupling of electron momenta in the quasimolecule, such that, the quantum numbers of an atomic core ls, $M_L - \mu$, $M_S - \sigma$ and the atomic quantum numbers of a valence electron $l_e\mu\frac{1}{2}\sigma$ are first summed into the atomic quantum numbers LSM_LM_S, and after the electron transition to another atomic rest, the other quantum numbers of the atomic core $lsmm_s$ and electron quantum numbers $l_e\mu\frac{1}{2}\sigma'$ are summed into the atom quantum numbers LS, $m + \mu$, $m_s + \sigma'$. We note that the electron spin projections are identical, $\sigma = \sigma'$ in the fields of both cores because of normalization of the electron spin wavefunctions. If we use the atom basis M_LM_S and the ion quantum numbers are $lsjm_j$, formula (16) becomes

$$\Delta_{LSM_LM_Slsjm_j}(R) = n(G_{ls}^{LS})^2 \times \sum_{\mu,\sigma\, m,\, m_s} \begin{bmatrix} l_e & l & L \\ \mu & M_{L-\mu} & M_L \end{bmatrix} \times \begin{bmatrix} l_e & l & L \\ \mu & m & m+\mu \end{bmatrix} \begin{bmatrix} \frac{1}{2} & s & S \\ \sigma & M_S-\sigma & M_S \end{bmatrix} \times \begin{bmatrix} \frac{1}{2} & s & S \\ \sigma & m_s & m_s+\sigma \end{bmatrix} \begin{bmatrix} l & s & j \\ m & m_s & m_j \end{bmatrix} \times \begin{bmatrix} l & s & j \\ M_L-\mu & M_S-\sigma & M_L-\mu+M_S-\sigma \end{bmatrix} \Delta_{l_e\mu}. \quad (17)$$

In reality, due to the properties of the Clebsch–Gordan coefficients, this formula is simplified. In particular, the exchange interaction potential is conserved under the transformations

$$M_L, M_S, m_j \longrightarrow -M_L, -M_S, -m_j. \quad (18)$$

4. ION–ATOM EXCHANGE INTERACTION FOR THE DIATOMIC OXYGEN ION

Formula (17) gives the ion–atom exchange interaction potential that determines the cross section of resonant charge exchange at given quantum numbers. This is considered below for different states of an oxygen atom and an ion. We start from the ground state of the atom and ion, with the ion–atom exchange interaction potential given by formula (18). The analysis of this case in [9, 10] was based on the limiting coupling cases where the quasimolecule is characterized by the quantum numbers J, M_J or J, M_L depending on the relation between spin–orbit and quadrupole interactions. We now consider the general case numerically by the Hamiltonian diagonalization for an arbitrary relation between these values.

Formula (17) gives the ion–atom exchange interaction potential at large separations for the ion ground state $O^+(^4S_{3/2})$ ($l = 0$, $m = 0$, $s = j = 3/2$). We then have $M_L = \mu$, $m_j = m_s$, and formula (17) is reduced to the form ($l_e = 1$, $n = 4$, $G_{ls}^{LS} = -1/\sqrt{3}$)

$$\Delta_{LSM_LM_Slsm_s}(R) = \frac{4}{3}\Delta_{1M_L}(R) \times \sum_{\sigma} \begin{bmatrix} \frac{1}{2} & s & S \\ \sigma & M_S-\sigma & M_S \end{bmatrix} \begin{bmatrix} \frac{1}{2} & s & S \\ \sigma & m_s & m_s+\sigma \end{bmatrix}. \quad (19)$$

Table 4 contains the values of the ion–atom interaction potential obtained on the basis of formula (19). We account for symmetry (18), and the one-electron exchange interaction potentials are given by formulas (13).

We next use the same operation for determining the exchange interaction potential for excited ion and atom states at large separations. Table 5 contains the exchange interaction potential for the quasimolecule $O^+(^2D) + O(^3P)$, and Table 6 contains the exchange interaction potentials for the quasimolecule $O^+(^2D) + O(^1D)$ for the basis M_L, M_S, j, m_j. Because $\Delta_{11}(R) \ll \Delta_{10}(R)$ at large separations, we ignore $\Delta_{11}(R)$ wherever possible. We also take the symmetry of the exchange interaction potential in (18) into account, and in the M_L, M_S atom basis used, the identical values of the exchange interaction potential correspond to quantum numbers in parentheses.

The electron terms of the quasimolecule with the ion–atom exchange interaction potential taken into account can be found by diagonalization of the corresponding Hamiltonian matrix. Because the splitting of

Table 4. The exchange interaction potential $\Delta_{LSM_LM_Ssm_s}$ for the ground state of the quasimolecule $O^+(^4S) + O(^3P)$ at given quantum numbers M_L, M_S of an atom and quantum numbers s, m_s of an ion on the basis of formula (18)

M_L, M_S / s, m_s	1, 1	1, 0	0, 1	1, –1	–1, 1	0, 0
$\frac{3}{2}, \frac{3}{2}$	Δ_{11}	$\sqrt{\frac{2}{3}}\Delta_{11}$	Δ_{10}	$\frac{1}{\sqrt{3}}\Delta_{11}$	Δ_{11}	$\sqrt{\frac{2}{3}}\Delta_{10}$
$\frac{3}{2}, \frac{1}{2}$	$\frac{1+\sqrt{6}}{3}\Delta_{11}$	$\frac{2+\sqrt{2}}{3}\Delta_{11}$	$\frac{1+\sqrt{6}}{3}\Delta_{10}$	$\frac{\sqrt{3}+\sqrt{2}}{3}\Delta_{11}$	$\frac{1+\sqrt{6}}{3}\Delta_{11}$	$\frac{2+\sqrt{2}}{3}\Delta_{10}$
$\frac{3}{2}, -\frac{1}{2}$	$\frac{\sqrt{3}+\sqrt{2}}{3}\Delta_{11}$	$\frac{2+\sqrt{2}}{3}\Delta_{11}$	$\frac{\sqrt{2}+\sqrt{3}}{3}\Delta_{10}$	$\frac{1+\sqrt{6}}{3}\Delta_{11}$	$\frac{\sqrt{2}+\sqrt{3}}{3}\Delta_{11}$	$\frac{2+\sqrt{2}}{3}\Delta_{10}$
$\frac{3}{2}, -\frac{3}{2}$	$\frac{1}{\sqrt{3}}\Delta_{11}$	$\sqrt{\frac{2}{3}}\Delta_{11}$	$\frac{1}{\sqrt{3}}\Delta_{10}$	Δ_{11}	$\frac{1}{\sqrt{3}}\Delta_{11}$	$\sqrt{\frac{2}{3}}\Delta_{10}$

Table 5. The exchange interaction potential for the quasimolecule $O^+(^2D) + O(^3P)$ at given quantum numbers M_L, M_S of an atom and quantum numbers j, m_j of an ion

M_L, M_S / j, m_j	1, 1	1, 0	0, 1	1, –1	0, 0	–1, 1
$\frac{5}{2}, \frac{5}{2}$	Δ_{11}	$\frac{\sqrt{10}+2}{2\sqrt{10}}\Delta_{11}$	$\frac{\sqrt{2}}{\sqrt{5}}\Delta_{11}$	$\frac{1}{\sqrt{10}}\Delta_{11}$	$\frac{\sqrt{2}}{\sqrt{5}}\Delta_{11}$	$\frac{1}{\sqrt{10}}\Delta_{11}$
$\frac{5}{2}, \frac{3}{2}$	$\frac{2}{5}\Delta_{10}$	$\frac{2}{5}\Delta_{10}$	$\frac{2}{5}\Delta_{10}$	$\frac{1}{5}\Delta_{10}$	$\frac{\sqrt{2}+1}{5}\Delta_{10}$	$\frac{\sqrt{2}}{5}\Delta_{10}$
$\frac{5}{2}, \frac{1}{2}$	$\frac{3}{5}\Delta_{10}$	$\frac{7}{10}\Delta_{10}$	$\frac{3}{5}\Delta_{10}$	$\frac{2}{5}\Delta_{10}$	$\frac{1}{5}\left(2+\frac{3}{\sqrt{2}}\right)\Delta_{10}$	$\frac{3\sqrt{2}}{10}\Delta_{10}$
$\frac{5}{2}, -\frac{1}{2}$	$\frac{2\sqrt{2}}{5}\Delta_{10}$	$\frac{\sqrt{2}}{2}\Delta_{10}$	$\frac{2\sqrt{2}}{5}\Delta_{10}$	$\frac{3\sqrt{2}}{10}\Delta_{10}$	$\frac{1}{5}\left(2+\frac{3}{\sqrt{2}}\right)\Delta_{10}$	$\frac{2}{5}\Delta_{10}$
$\frac{5}{2}, -\frac{3}{2}$	$\frac{\sqrt{2}}{5}\Delta_{10}$	$\frac{3\sqrt{2}}{10}\Delta_{10}$	$\frac{\sqrt{2}}{5}\Delta_{10}$	$\frac{\sqrt{2}}{5}\Delta_{10}$	$\frac{\sqrt{2}+1}{5}\Delta_{10}$	$\frac{1}{5}\Delta_{10}$
$\frac{5}{2}, -\frac{5}{2}$	$\frac{1}{2\sqrt{5}}\Delta_{11}$	$\frac{10+2\sqrt{5}}{\sqrt{20}}\Delta_{11}$	$\frac{1}{\sqrt{10}}\Delta_{11}$	$\frac{1}{\sqrt{10}}\Delta_{11}$	$\frac{\sqrt{2}}{\sqrt{5}}\Delta_{11}$	$\frac{1}{\sqrt{10}}\Delta_{11}$
$\frac{3}{2}, \frac{3}{2}$	$\frac{1}{10}\Delta_{10}$	$\frac{-\sqrt{6}+1}{20}\Delta_{10}$	$\frac{\sqrt{6}}{15}\Delta_{10}$	$\frac{-\sqrt{6}}{20}\Delta_{10}$	$\frac{\sqrt{6}-2\sqrt{3}}{30}\Delta_{10}$	$\frac{\sqrt{3}}{10}\Delta_{10}$
$\frac{3}{2}, \frac{1}{2}$	$\frac{\sqrt{6}}{60}\Delta_{10}$	$\frac{-3-\sqrt{6}}{60}\Delta_{10}$	$\frac{1}{15}\Delta_{10}$	$\frac{1}{10}\Delta_{10}$	$\frac{-\sqrt{2}-2}{30}\Delta_{10}$	$\frac{\sqrt{2}}{20}\Delta_{10}$
$\frac{3}{2}, -\frac{1}{2}$	$\frac{-\sqrt{3}}{30}\Delta_{10}$	$\frac{-3\sqrt{2}-\sqrt{3}}{60}\Delta_{10}$	$\frac{\sqrt{2}}{15}\Delta_{10}$	$\frac{\sqrt{2}}{20}\Delta_{10}$	$\frac{-\sqrt{2}-2}{30}\Delta_{10}$	$\frac{1}{10}\Delta_{10}$
$\frac{3}{2}, -\frac{3}{2}$	$\frac{-1}{10\sqrt{2}}\Delta_{10}$	$\frac{-\sqrt{3}-\sqrt{2}}{20}\Delta_{10}$	$\frac{-1}{5\sqrt{3}}\Delta_{10}$	$\frac{\sqrt{3}}{10}\Delta_{10}$	$\frac{\sqrt{6}-2\sqrt{3}}{30}\Delta_{10}$	$\frac{-\sqrt{6}}{20}\Delta_{10}$

electron terms due to the exchange interaction depends on a fine ion state, the number of electron levels in this case increases in comparison with the case of Hamiltonian (2). Performing this diagonalization for each fine ion state at a distance of $12a_0$ between the nuclei (this distance determines the resonant charge-exchange cross section in thermal collisions), we assume that the renormalization of the exchange interaction potential in comparison with the basis M_L, M_S, j, m_j is the same in a neighboring range of distances. This allows us to determine the exchange interaction potentials given in Table 5 for the quasimolecule and in Table 7 for the quasimolecule $O^+(^2P) + O(^3P)$. As the quantum numbers of the quasimolecule, we now take the total atom momentum J and its projection M_J on the molecular axis. Although these are accurate quantum numbers only at very large separations, where the ion–atom quadrupole interaction can be ignored, they can be used for labeling electron states of the quasimolecule.

5. MIXING OF EXCHANGE INTERACTIONS FOR COUPLED ELECTRON TERMS

Above, we have determined the ion–atom exchange interaction potential in the basis M_L, M_S, j, m_j, which are not quantum numbers of the quasimolecule, and the Hamiltonian matrix H_{ik} is not diagonal in this basis. The electron terms of the quasimolecule follow from diagonalization of the Hamiltonian matrix, and the electron levels $E(R)$ at a given separation are solutions of the secular equation

$$|E\delta_{ik} - H_{ik}| = 0.$$

Above (see Figs. 1–3), we solved this equation for Hamiltonian (2) with the ion–atom exchange interaction ignored. We now solve this equation including the ion–atom exchange interaction potential into consideration and determine the exchange interaction potential for eigenstates of the quasimolecule.

Table 6. The exchange interaction potential $\Delta_{LSM_LM_Slsjm_j}(R)$ for quasimolecule $O^+(^2D) + O(^1D)$ at given quantum numbers M_L, M_S of an atom and quantum numbers j, m_j of an ion

M_L, M_S / j, m_j	2, 0 (–2, 0)	1, 0 (–1, 0)	0, 0
$\frac{5}{2}, \frac{5}{2}$	Δ_{10}	$\frac{1}{\sqrt{5}}\Delta_{10}$	$\frac{\sqrt{3}}{\sqrt{10}}\Delta_{11}$
$\frac{5}{2}, \frac{3}{2}$	$\left(\frac{1}{\sqrt{5}} + \frac{1}{5}\right)\Delta_{10}$	$\frac{2+\sqrt{2}}{10}\Delta_{10}$	$\frac{3(2+\sqrt{3})}{10}\Delta_{11}$
$\frac{5}{2}, \frac{1}{2}$	$\frac{1}{5\sqrt{2}}\Delta_{10}$	$\frac{1}{10}\Delta_{10}$	$\left(\frac{3}{10} + \frac{3}{10\sqrt{2}} + \frac{\sqrt{3}}{2}\right)\Delta_{11}$
$\frac{5}{2}, -\frac{1}{2}$	$-\frac{1}{\sqrt{10}}\Delta_{10}$	$\frac{-1}{5\sqrt{2}}\Delta_{10}$	$\left(\frac{3}{10} + \frac{3}{10\sqrt{2}} + \frac{\sqrt{3}}{2}\right)\Delta_{11}$
$\frac{5}{2}, -\frac{3}{2}$	$\frac{-\sqrt{5}-1}{\sqrt{5}}\Delta_{10}$	$\frac{-\sqrt{2}-1}{5\sqrt{2}}\Delta_{10}$	$\frac{3(2+\sqrt{3})}{10}\Delta_{11}$
$\frac{5}{2}, -\frac{5}{2}$	$\frac{-1}{\sqrt{5}}\Delta_{10}$	$-\frac{1}{\sqrt{10}}\Delta_{10}$	$\frac{\sqrt{3}}{\sqrt{10}}\Delta_{11}$
$\frac{3}{2}, \frac{3}{2}$	$\frac{4}{5}\Delta_{10}$	$\frac{1+4\sqrt{3}}{20}\Delta_{10}$	$\left(\frac{3}{20} + \frac{9}{10\sqrt{2}}\right)\Delta_{11}$
$\frac{3}{2}, \frac{1}{2}$	$\frac{\sqrt{3}}{5}\Delta_{10}$	$\frac{3}{20}\Delta_{10}$	$\left(\frac{9}{20} + \frac{3}{10\sqrt{2}} + \frac{3}{5\sqrt{2}}\right)\Delta_{11}$
$\frac{3}{2}, -\frac{1}{2}$	$\frac{6+3\sqrt{2}}{20}\Delta_{11}$	$\frac{-\sqrt{3}}{20}\Delta_{10}$	$\left(\frac{9}{20} + \frac{3}{10\sqrt{2}} + \frac{3}{5\sqrt{2}}\right)\Delta_{11}$
$\frac{3}{2}, -\frac{3}{2}$	$-\frac{1}{5}\Delta_{10}$	$\frac{-\sqrt{3}-4}{20}\Delta_{10}$	$\left(\frac{3}{20} + \frac{9}{10\sqrt{2}}\right)\Delta_{11}$

Table 7. The exchange interaction potential for the quasimolecule $O^+(^2P) + O(^3P)$ at given quantum numbers j, m_j of an ion obtained in the basis M_L, M_S

M_L, M_S / j, m_j	1, 1	1, 0	0, 1	1, –1	0, 0	–1, 1
$\frac{3}{2}, \frac{3}{2}$	$\frac{1}{2}\Delta_{10}$	$\frac{3+\sqrt{6}}{12}\Delta_{10}$	$\frac{1}{2}\Delta_{11}$	$\frac{1}{2\sqrt{6}}\Delta_{10}$	$\frac{3+\sqrt{6}}{12}\Delta_{11}$	$\frac{-1}{2\sqrt{3}}\Delta_{10}$
$\frac{3}{2}, \frac{1}{2}$	$\frac{1}{2\sqrt{6}}\Delta_{10}$	$\frac{1+\sqrt{6}}{12}\Delta_{10}$	$\frac{3\sqrt{6}+2\sqrt{3}}{12}\Delta_{11}$	$\frac{1}{6}\Delta_{10}$	$\frac{3+\sqrt{2}+2\sqrt{3}+3\sqrt{6}}{12}\Delta_{11}$	$\frac{-1}{6\sqrt{2}}\Delta_{10}$
$\frac{3}{2}, -\frac{1}{2}$	$-\frac{1}{2\sqrt{3}}\Delta_{10}$	$\frac{-\sqrt{3}-\sqrt{2}}{12}\Delta_{10}$	$\frac{2+\sqrt{3}}{6}\Delta_{11}$	$-\frac{1}{6\sqrt{2}}\Delta_{10}$	$\frac{3+\sqrt{2}+2\sqrt{3}+3\sqrt{6}}{12}\Delta_{11}$	$\frac{1}{6}\Delta_{10}$
$\frac{3}{2}, -\frac{3}{2}$	$-\frac{1}{2\sqrt{2}}\Delta_{10}$	$\frac{-3\sqrt{2}-\sqrt{3}}{12}\Delta_{10}$	$\frac{1}{2\sqrt{6}}\Delta_{11}$	$-\frac{1}{2\sqrt{3}}\Delta_{10}$	$\frac{3+\sqrt{6}}{12}\Delta_{11}$	$\frac{1}{2\sqrt{6}}\Delta_{10}$
$\frac{1}{2}, \frac{1}{2}$	$\frac{1}{6}\Delta_{11}$	$\frac{1}{6}\Delta_{10}$	$\frac{1}{3\sqrt{2}}\Delta_{11}$	$\frac{1}{3}\Delta_{10}$	$\frac{1}{6\sqrt{2}}\Delta_{11}$	$\frac{1}{3\sqrt{2}}\Delta_{10}$
$\frac{1}{2}, -\frac{1}{2}$	$-\frac{1}{6\sqrt{2}}\Delta_{11}$	$\frac{1}{3\sqrt{2}}\Delta_{10}$	$-\frac{1}{6}\Delta_{11}$	$\frac{1}{3\sqrt{2}}\Delta_{10}$	$\frac{1}{6\sqrt{2}}\Delta_{11}$	$\frac{1}{3}\Delta_{10}$

We demonstrate this operation for the interaction of the oxygen ion and atom in the ground states $O^+(^3P) + O^+(^4S)$. Table 3 then gives the Hamiltonian matrix without the exchange interaction, and the matrix of the ion–atom exchange interaction potential is diagonal in the M_L, M_S, j, m_j basis. We note that the matrix H_{ik} in Table 3 is divided into three blocks consisting of matrices with one, two, and three diagonal elements. For a block with one element, where $M_L = 1$, $M_S = 1$, the exchange interaction potential is $\Delta_{11}(R)$. For the two other blocks, the exchange interaction follows from diagonalization of the Hamiltonian matrix for the gerade and ungerade states of the quasimolecule, and the exchange interaction potential is the difference of the electron energies for the gerade and ungerade quasimolecule states taking into account the smallness of the exchange interaction potential in comparison with a typical potential of electrostatic interaction.

We perform this operation analytically for a block consisting of two diagonal terms. Diagonalization of the Hamiltonian matrix gives the energy of two levels as [3]

$$E_{I,II} = \frac{H_{11}+H_{22}}{2} \pm \sqrt{\frac{(H_{11}-H_{22})^2}{4} + |H_{12}|^2},$$

where the indices 1 and 2 relate to the first and second states in the basis M_L, M_S. We next construct the energy matrix for the interaction of an oxygen ion and an atom with taking into account the exchange interaction in addition to Hamiltonian (2). For the states under consideration, according to the data in Table 3, we have

$$H_{11} = -0.8\frac{e^2a_0^2}{R^3} \pm \frac{\Delta_1}{2},$$
$$H_{22} = 1.6\frac{e^2a_0^2}{R^3} \pm \frac{\Delta_2}{2}, \qquad (20a)$$
$$H_{12} = a, \quad \Delta H = H_{11} - H_{22} = 2.4\frac{e^2a_0^2}{R^3},$$

where the plus sign corresponds to the gerade state and the minus sign corresponds to the ungerade state. From this, we have the energy levels of eigenstates given by

$$E_I = E_0 - \varepsilon \pm \frac{1}{2}\Delta_I, \quad E_{II} = E_0 + \varepsilon \pm \frac{1}{2}\Delta_{II},$$
$$E_0 = 0.4\frac{e^2a_0^2}{R^3}, \quad \varepsilon = \sqrt{\left(1.2\frac{e^2a_0^2}{R^3}\right)^2 + a^2}. \qquad (20b)$$

Correspondingly, the exchange interaction potential for each state is

$$\Delta_I = \frac{\Delta_1 + \Delta_2}{2} + \frac{\Delta H}{4\varepsilon}(\Delta_1 - \Delta_2),$$
$$\Delta_{II} = \frac{\Delta_1 + \Delta_2}{2} - \frac{\Delta H}{4\varepsilon}(\Delta_1 - \Delta_2). \quad (21)$$

As can be seen, if $a = 0$ and, hence, the Hamiltonian matrix is diagonal in the M_L, M_S basis, we have $\Delta_I = \Delta_1$ and $\Delta_{II} = \Delta_2$ in accordance with the expression for the Hamiltonian diagonal elements.

We use the expressions in Table 8 for the exchange interaction potential at a distance of $12a_0$ between nuclei for different electron terms; this distance determines the cross section of resonant charge-exchange process in thermal collisions involving the $O(^3P)$ atom and $O^+(^4S_{3/2})$ ion in the ground states. We note that, according to formula (13), at this distance, $\Delta_{10} = 6\Delta_{11}$, which is used in Table 8. In Table 8, we give the values of the coefficient

$$\kappa = \frac{\Delta}{\Delta_{M_L M_S}},$$

where $\Delta_{M_L M_S}$ is the exchange interaction potential for the basis $M_L M_S m_s$ according to formula (19), and Δ is its value after diagonalization of the Hamiltonian matrix. As follows from the data in Table 8, the value κ is close to one; below, because of the logarithmic dependence of the cross section on this value, we ignore the variation of the exchange interaction potential due to diagonalization of the Hamiltonian. This simplifies the problem.

6. RESONANT CHARGE-EXCHANGE PROCESS FOR OXYGEN

The above values of the ion–atom exchange interaction potentials allow us to determine the partial cross sections of resonant charge exchange on the basis of the asymptotic theory [11, 12]. The asymptotic theory of resonant charge exchange is based on the assumption that the main contribution to the cross section of this process is given by large impact parameters of collisions in comparison with the typical atomic size. Then, the inverse value is a small parameter of the asymptotic theory, and the cross section is represented as an expansion over this small parameter. Hence, determination of the exchange ion–atom interaction potential at large separations allows us to determine the cross section of resonant charge exchange. If electron terms are nondegenerate, the relation between the probability and cross section of this process and the exchange interaction potential in the two-level approximation can be used [24]. In particular, this approximation is valid for the transition of an *s*-electron between two structureless cores (for example, for the processes H^+–H, He^+–He), and, then, the cross section σ_{ex} of the resonant charge-exchange process is given by [11, 12, 24]

Table 8. The values of κ resulting from diagonalization of the Hamiltonian matrix

M_L, M_S / s, m_s	1, 1	1, 0	0, 1	1, –1	–1, 1	0, 0
$\frac{3}{2}, \frac{3}{2}$	1	1.35	0.95	1.4	1.36	0.87
$\frac{3}{2}, \frac{1}{2}$	1	1.27	0.96	1.05	1.65	0.88
$\frac{3}{2}, -\frac{1}{2}$	1	1.25	0.96	1.65	1.05	0.88
$\frac{3}{2}, -\frac{3}{2}$	1	1.18	0.95	1.37	1.37	0.88

$$\sigma_{ex} = \frac{\pi R_0^2}{2}, \quad (22)$$

where

$$\frac{1}{v}\sqrt{\frac{\pi R_0}{2\gamma}}\Delta(R_0) = 0.28.$$

This formula can be used in the cases under consideration for the structureless oxygen ion $O^+(^4S)$ or if the fine ion splitting is small compared to the exchange interaction potential, as for $O^+(^2P)$. We take quantum numbers J, M_J to characterize the atom state at the beginning. Of course, this is valid only at very large distances between the nuclei when the ion–quadrupole interaction can be neglected. Therefore, we use these quantum numbers for labeling the electron terms only. In addition, the cross section of processes

$$\begin{pmatrix} O^+(^4S) + O(^1D) \longrightarrow O(^1D) + O^+(^4S) \\ O^+(^4S) + O(^1S) \longrightarrow O(^1S) + O^+(^4S) \\ O^+(^2D) + O(^1S) \longrightarrow O(^1S) + O^+(^2D) \end{pmatrix} \quad (23)$$

is zero for the one-electron atom scheme under consideration, because the transition of a *p*-electron cannot lead to these processes.

In Tables 9–13, we give the partial cross sections of other electron transfer processes involving the electron shells $2p^3$ and $2p^4$ for the oxygen ion and atom at energies of interest for plasma. The indicated quantum numbers J, M_J of the atom and j, m_j of the ion are accu-

Table 9. The cross section of resonant charge exchange σ_{ex} (in 10^{-16} cm^2) for the process $O^+(^4S) + O(^3P) \longrightarrow O(^3P) + O^+(^4S)$ at the collision energies 0.1 and 1 eV (in parentheses) in the laboratory frame of reference

J, M_J / j, m_j	2, 2	2, 1	2, 0	1, 1	1, 0	0, 0
$\frac{3}{2}, \frac{3}{2}$	60(48)	57(46)	54(43)	82(67)	60(48)	79(64)
$\frac{3}{2}, \frac{1}{2}$	61(49)	61(49)	60(48)	84(69)	61(49)	83(68)
$\frac{3}{2}, -\frac{1}{2}$	60(48)	61(49)	61(49)	82(67)	60(48)	83(68)
$\frac{3}{2}, -\frac{3}{2}$	54(43)	57(46)	60(48)	74(60)	54(43)	79(64)
Average	59(47)	59(47)	59(47)	81(66)	59(47)	81(66)

Table 10. The cross section of resonant charge exchange σ_{ex} (in 10^{-16} cm^2) for the process $O^+(^2D) + O(^3P) \longrightarrow O(^3P) + O^+(^2D)$ at the collision energies 0.1 and 1 eV in the laboratory frame of reference

J, M_J / j, m_j	2, 2	2, 1	2, 0	1, 1	1, 0	0, 0
$\frac{5}{2}, \frac{5}{2}$	43(34)	41(33)	39(31)	34(26)	34(26)	39(31)
$\frac{5}{2}, \frac{3}{2}$	50(40)	50(40)	50(40)	44(34)	47(37)	52(41)
$\frac{5}{2}, \frac{1}{2}$	54(43)	55(45)	54(43)	50(40)	51(40)	57(46)
$\frac{5}{2}, -\frac{1}{2}$	53(43)	56(45)	53(43)	51(40)	50(40)	57(46)
$\frac{5}{2}, -\frac{3}{2}$	47(37)	51(40)	47(37)	47(37)	44(34)	52(41)
$\frac{5}{2}, -\frac{5}{2}$	32(25)	36(28)	34(26)	34(26)	34(26)	39(31)
$\frac{3}{2}, \frac{3}{2}$	38(29)	35(26)	42(32)	39(30)	42(33)	29(21)
$\frac{3}{2}, \frac{1}{2}$	31(22)	37(28)	34(26)	38(29)	35(26)	39(30)
$\frac{3}{2}, -\frac{1}{2}$	33(25)	38(29)	37(28)	35(26)	38(29)	39(30)
$\frac{3}{2}, -\frac{3}{2}$	35(26)	24(16)	39(30)	42(33)	39(30)	29(21)
Average	42(32)	42(33)	41(32)	43(34)	41(32)	43(34)

rate only at large separations and are used for labeling the electron states at intermediate separations when the ion–atom quadrupole interaction is important. We also note that the small parameter of the asymptotic theory is now

$$\frac{1}{\gamma R_0} \ll 1. \tag{24}$$

In evaluating the cross section of electron transfer, we use the values of the parameter γ in accordance with the data in Table 2. Expanding with respect to this small parameter, we keep two expansion terms in formula (22). For the cases in Tables 8 and 9, the values of γR_0 are between 10 and 14. This means that the accuracy of the asymptotic theory is about 1%. Of course, the real accuracy is worse because of additional factors [26] that affect the accuracy of the cross sections. Nevertheless, we estimate this accuracy at several percent.

Table 11. The cross section of resonant charge exchange σ_{ex} (in 10^{-16} cm^2) for the process $O^+(^2D) + O(^1D) \longrightarrow O(^1D) + O^+(^2D)$ at the collision energies 0.1 and 1 eV in the laboratory frame of reference

J, M_J / j, m_j	2	1	0
$\frac{5}{2}, \frac{5}{2}$	71(58)	62(49)	46(36)
$\frac{5}{2}, \frac{3}{2}$	66(53)	59(47)	53(42)
$\frac{5}{2}, \frac{1}{2}$	49(38)	46(35)	47(37)
$\frac{5}{2}, -\frac{1}{2}$	58(46)	49(38)	47(37)
$\frac{5}{2}, -\frac{3}{2}$	75(62)	59(47)	53(42)
$\frac{5}{2}, -\frac{5}{2}$	62(49)	58(46)	46(36)
$\frac{3}{2}, \frac{3}{2}$	68(55)	60(48)	49(39)
$\frac{3}{2}, \frac{1}{2}$	59(47)	50(39)	54(43)
$\frac{3}{2}, -\frac{1}{2}$	45(36)	44(34)	54(43)
$\frac{3}{2}, -\frac{3}{2}$	53(41)	57(45)	49(39)
Average	61(48)	54(43)	50(40)

If an electron term is degenerate for the quasimolecule consisting of a colliding ion and an atom, and if the ion–atom exchange interaction removes this degeneracy, the charge-exchange process in the course of ion–atom collisions is entangled with other transition processes. In the case under consideration, this degeneracy relates to the projection of the ion total momentum on the molecular axis, and, hence, the exchange process is entangled with rotation of the ion total momentum. However, because the ion–atom exchange interaction potential decreases exponentially as the separation increases, the region of the exchange process is narrow, and, hence, the rotation angle of the molecular axis is relatively small [5]. This allows us to separate the process of resonant charge exchange from the processes of moment rotation, i.e., to consider the resonant charge process for each angular momentum direction of the ion independently. Therefore, we evaluate the cross section of resonant charge exchange for each ion moment projection on the basis of formula (22).

On the basis of the partial cross sections of resonant charge exchange in Tables 9–13, we can find the average cross sections (see Table 14) that are convenient for applications. In averaging a cross section, we assume that the population of electron levels of a given group is proportional to the statistical weights of individual states, which is valid at high temperatures. As a result, in Table 12, we give the average cross sections of resonant charge exchange for a given orbital momentum and spin of the colliding ion and atom.

We note that the difference in the cross section for ions in different states is determined mostly by different ionization potentials of the oxygen atom in a given state with ion formation in these states.

The cross sections obtained allow us to determine the mobilities of an oxygen ion in atomic oxygen. In particular, if the atoms are the ground electron and the fine state $O(^3P_2)$, the respective mobilities of the oxygen ions $O^+(^4S)$, $O^+(^2D)$, and $O^+(^2P)$ in atomic oxygen are 2.6, 4.1, and 4.6 $cm^2/(V\,s)$; for the mixture of atoms in the electron states $O(^3P_2)$ and $O(^1D_2)$ with equal populations of these states at room temperature, the respective mobilities are 2.6, 3.8, and 4.3 $cm^2/(V\,s)$ at room temperature. These values may be of interest for plasmas of Earth's upper atmosphere and for a nonequilibrium gas-discharge oxygen plasma. We see that measurement of the mobilities of ions in different states makes it possible to analyze the atomic distribution over excited states.

Thus, due to high symmetry of atoms and ions with nonfilled electron shells, we obtain a large number of electron terms within the framework of the *LS* coupling scheme for a diatomic ion when the ion and the atom have nonfilled electron shells. Because the exchange interaction is shared between these states, the cross sections of resonant charge exchange are lower. This can be demonstrated by comparing the cross sections of resonant charge exchange for the *LS* and *j–j* types of electron coupling in the oxygen atom and ion. In the case of *j–j* coupling, we have a lower symmetry and, therefore, a simpler character for this process.

Table 12. The cross section of resonant charge exchange σ_{ex} (in 10^{-16} cm^2) for the process $O^+(^2P) + O(^3P) \longrightarrow O(^3P) + O^+(^2P)$ at given quantum numbers J, M_J of an atom and j, m_j of an ion at the collision energies 0.1 and 1 eV in the laboratory frame of reference

J, M_J / j, m_j	2, 2	2, 1	2, 0	1, 1	1, 0	0, 0
$\frac{3}{2}, \frac{3}{2}$	45(36)	45(35)	33(25)	38(29)	29(22)	45(35)
$\frac{3}{2}, \frac{1}{2}$	38(29)	41(32)	37(29)	36(28)	34(26)	39(31)
$\frac{3}{2}, -\frac{1}{2}$	41(32)	40(31)	34(27)	34(26)	34(28)	39(31)
$\frac{3}{2}, -\frac{3}{2}$	42(33)	45(36)	27(20)	41(32)	36(29)	45(35)
$\frac{1}{2}, \frac{1}{2}$	26(19)	36(28)	28(21)	42(33)	38(30)	24(18)
$\frac{1}{2}, -\frac{1}{2}$	24(18)	39(30)	26(19)	39(30)	39(33)	24(18)
Average	36(28)	41(32)	31(24)	38(30)	36(28)	36(28)

Table 13. The cross section of resonant charge exchange σ_{ex} (in 10^{-16} cm^2) for the processes $O^+(^2D) + O(^1D) \longrightarrow O(^1D) + O^+(^2D)$ and $O^+(^2P) + O(^1S) \longrightarrow O(^1S) + O^+(^2P)$ (the last column) at the collision energies 0.1 and 1 eV in the laboratory frame of reference

L, M / j, m_j	$^1D, M_L = 2$	$^1D, M_L = 1$	$^1D, M_L = 0$	$^1S, M_L = 0$
$\frac{3}{2}, \frac{3}{2}$	38(30)	47(37)	46(36)	50(40)
$\frac{3}{2}, \frac{1}{2}$	38(29)	49(39)	50(40)	65(52)
$\frac{3}{2}, -\frac{1}{2}$	34(25)	48(38)	50(40)	65(52)
$\frac{3}{2}, -\frac{3}{2}$	28(21)	42(32)	46(36)	50(40)
$\frac{1}{2}, \frac{1}{2}$	35(27)	43(33)	47(37)	57(45)
$\frac{1}{2}, -\frac{1}{2}$	30(23)	41(31)	47(37)	57(45)
Average	34(26)	45(35)	47(38)	58(46)

Table 14. The average cross sections of resonant charge exchange σ_{ex} (in 10^{-16} cm^2) at the collision energies 0.1, 1, and 10 eV (in brackets) in the laboratory frame of reference

Atom state / Ion state	$O(^3P)$	$O(^1D)$	$O(^1S)$
$O^+(^4S)$	66(53)[44]	0(0)[0]	0(0)[0]
$O^+(^2D)$	42(33)[25]	56(44)[34]	0(0)[0]
$O^+(^2P)$	34(29)[22]	41(32)[24]	58(46)[35]

The accuracy of the cross sections of resonant charge exchange is mostly determined by the accuracy of determination of the asymptotic coefficient A and, according to the analysis in [23, 26], is several percent. Comparing the ground state of a colliding ion and an atom shows [8, 10] that the average cross section differs by about 10% from that evaluated within the framework of the Hund coupling. As regards the two-level approximation for electron terms of O_2^+, any coincidence may be random, because this scheme of electron term splitting does not take into account the important special features of this interaction.

7. COMPARISON WITH OTHER SCHEMES OF ELECTRON COUPLING

We have constructed the lowest electron terms of O_2^+ at large separations which determine the cross sections of resonant charge exchange. Of course, the character of coupling in this range of distances between the nuclei differs from those at low separations [25]. We next use the *LS* type of electron coupling in the atom and ion, and the accuracy of using this coupling scheme is about 2%, which is determined by the coincidence with formula (9) of the level positions for fine states of an oxygen atom located in the ground electron state.

Nevertheless, we use the *j–j* coupling scheme in the case under consideration in order to understand the dependence of the resonant charge-exchange cross sections on the coupling type. We consider the collision of an oxygen ion and an atom in the ground electron states, with the resonant charge-exchange process occurring according to the scheme

$$\begin{aligned} &O^+\left[\left(\frac{1}{2}\right)^2\left(\frac{3}{2}\right)\right]_{\frac{3}{2}} + O\left[\left(\frac{1}{2}\right)^2\left(\frac{3}{2}\right)^2\right]_2 \\ &\longrightarrow O\left[\left(\frac{1}{2}\right)^2\left(\frac{3}{2}\right)^2\right]_2 + O^+\left[\left(\frac{1}{2}\right)^2\left(\frac{3}{2}\right)\right]_{\frac{3}{2}} \end{aligned} \qquad (25)$$

instead of the process

$$O^+\left(^4S_{\frac{3}{2}}\right) + O(^3P_2) \longrightarrow O(^3P_2) + O^+\left(^4S_{\frac{3}{2}}\right), \qquad (26)$$

that occurs in the case of the *LS* coupling scheme. As follows from process (25), within the framework of the *j–j* coupling scheme, the ion–atom exchange interaction and the resonant charge-exchange process are determined by the transition of a valence electron with $j = 3/2$ from the field of one core to the other one.

Based on the *j–j* coupling scheme for valence electrons in the atom and ion for the electron terms of the ion dimer at large separations [23], we note that, in this case, the character of the exchange splitting is simpler than in the case of the *LS* coupling scheme. Indeed, we represent the wavefunction of two valence electrons from a nonfilled electron shell $j = 3/2$ of an oxygen atom as

$$\begin{aligned} \Phi_{JM_J}(1,2) &= \frac{1}{\sqrt{2}}\hat{P}\sum_{m_1,m_2}\begin{bmatrix} 3/2 & 3/2 & J \\ m_1 & m_2 & M_J \end{bmatrix} \\ &\times \psi_{\frac{3}{2}m_1}(1)\psi_{\frac{3}{2}m_2}(2). \end{aligned} \qquad (27)$$

This wavefunction is simpler than formula (14) for the *LS* coupling in an atom. From Eq. (15), we obtain the ion–atom exchange interaction potential:

$$\begin{aligned} \Delta_{JM_Jjm_j}(R) &= \sum_m \begin{bmatrix} \frac{3}{2} & \frac{3}{2} & J \\ M_J - m & m & M_J \end{bmatrix} \\ &\times \begin{bmatrix} \frac{3}{2} & \frac{3}{2} & J \\ m_j & m & m_j + m \end{bmatrix} \Delta_{\frac{3}{2}m}(R), \end{aligned} \qquad (28)$$

which is simpler than formula (17) for the *LS* coupling in an atom and an ion. The one-electron exchange interaction potentials for case "c" of the Hund coupling, which are used in this formula, are given by [22, 26]

$$\begin{aligned} \Delta_{\frac{3}{2}\frac{3}{2}}(R) &= \Delta_{11}(R), \\ \Delta_{\frac{3}{2}\frac{1}{2}}(R) &= \frac{2}{3}\Delta_{10}(R) + \frac{1}{3}\Delta_{11}(R), \end{aligned} \qquad (29)$$

where the one-electron exchange interaction potentials $\Delta_{10}(R)$ and $\Delta_{11}(R)$ for case "a" of the Hund coupling are given by formula (13). Below, we neglect Δ_{11} compared to Δ_{10}.

We note that, according to formula (28), the ion–atom exchange interaction potential $\Delta_{JM_Jjm_j}(R)$ for the

j–j coupling in the atom and ion is unchanged under the transformations

$$M_J, m_j \longrightarrow -M_J, -m_j. \quad (30)$$

Table 15 contains the exchange interaction potentials in the case of oxygen and the *j–j* coupling scheme. Evidently, this scheme may be valid for heavy atoms of the fourth group of the periodical table of elements.

Table 16 contains the partial cross sections for resonant charge exchange. We see that they are in a restricted range of values. The average cross sections of the resonant charge-exchange process (25) at collision energies of 0.1, 1, and 10 eV in the laboratory frame of reference are 10^{-16} cm^2. As follows from Table 16, although the partial cross sections are different, the average cross sections for a given total atom momentum practically coincide.

Above, we have rigorously found the partial cross sections of resonant charge exchange in slow collisions for oxygen. We take into account various factors that influence the positions of electron terms of the O_2^+ quasimolecule at large separations within the framework of the *LS* coupling scheme for valence electrons. This allows us to evaluate the partial cross sections. At the next step, we can find the average cross sections of resonant charge exchange by averaging over states using a real distribution over excited states of the quasimolecule. Although this operation is accurate, it is quite cumbersome, and it is therefore interesting to compare accurate cross sections with those obtained in simplified schemes. We do not consider the two-level approximation [24] suitable for transition of an *s*-electron between two structureless cores. This approximation was also used for oxygen (see, e.g., [27, 28]); it may lead to a relatively large error, because it is restricted by one transferring electron, while each valence electron can in fact transfer to the ion core. In the case of oxygen, this gives a factor of 7/3 [22, 26] for the exchange interaction potential for case "a" of the Hund coupling. For an ion and an atom in the ground electron state, this leads to an error of approximately 20% [9] for the cross section of resonant charge exchange and for the range 0.1–10 eV of the collision energies. Rejecting the model of a transferring *s*-electron and a structureless core, we restrict ourselves to cases "a" and "c" of the Hund coupling for a valence *p*-electron and assume the ion–atom exchange interaction potential to be independent of the fine ion state.

Reducing the problem of the ion–atom exchange interaction to the standard Hund coupling scheme for the interaction of ion and atom valence electrons, we can take this into consideration for the Hamiltonian if we ignore the spin–orbit interaction for the atom (Hund case "a") or the ion–quadrupole interaction (Hund case "c"). Therefore, averaging the exchange interaction potential in (16) over ion and atom spins, we obtain the ion–atom exchange interaction potential for case "a" of the Hund coupling [5, 8, 13]:

$$\Delta_{LSM_L lsm}(R) = n(G_{ls}^{LS})^2 \times \sum_{\mu} \begin{bmatrix} l_e & l & L \\ \mu & M_L-\mu & M_L \end{bmatrix} \begin{bmatrix} l_e & l & L \\ \mu & m & m+\mu \end{bmatrix} \Delta_{l_e\mu}(R). \quad (31)$$

In the same manner, in case "a" of the Hund coupling, if we sum the atom orbital *L* and spin *S* momenta into the total electron momentum *J* and average over ion

Table 15. The ion–atom exchange interaction potential $\Delta_{JM_J jm_j}(R)$ for the *j–j* coupling scheme for oxygen

M_J / m_j	0	1	2
$\frac{3}{2}$	$\frac{\sqrt{2}}{3}\Delta_{10}$	$\frac{1}{3}\Delta_{10}$	$\frac{1}{3}\Delta_{10}$
$\frac{1}{2}$	$\frac{1}{6}\Delta_{10}$	$\frac{1}{3\sqrt{2}}\Delta_{10}$	$\frac{1}{2}\Delta_{11}$
$-\frac{1}{2}$	$\frac{1}{6}\Delta_{10}$	$\frac{1}{2}\Delta_{11}$	$\frac{1}{3\sqrt{2}}\Delta_{10}$
$-\frac{3}{2}$	$\frac{\sqrt{2}}{3}\Delta_{10}$	$\frac{1}{3}\Delta_{10}$	$\frac{1}{3}\Delta_{10}$

Table 16. The partial cross sections σ_{ex} (in 10^{-16} cm^2) of resonant charge-exchange process (25) at the collision energies 0.1, 1, and 10 eV in the laboratory frame of reference

M_J / m_j	0	1	2
$\frac{3}{2}$	72(58)[45]	67(54)[42]	67(54)[42]
$\frac{1}{2}$	59(46)[35]	63(50)[38]	52(41)[32]
$-\frac{1}{2}$	59(46)[35]	52(41)[32]	63(50)[38]
$-\frac{3}{2}$	72(58)[45]	67(54)[42]	67(54)[42]
Average	65(52)[40]	63(50)[38]	63(50)[38]

Table 17. The cross section of resonant charge exchange σ_{ex} (in 10^{-16} cm^2) for the process $O^+(^4S) + O(^3P)$ at given quantum numbers J, M_J of an atom and j, m_j of an ion at the collision energies 0.1 and 1 eV in the laboratory frame of reference. The indicated quantum numbers are accurate only at large separations and are used for labeling the electron states at intermediate separations where the ion–atom quadrupole interaction is important

Quantum numbers M_L, M_s	1, 1	1, 0	1, –1	0, 0	–1, 1	0, 0
Quantum numbers J, M_J	2, 2	2, 1	2, 0	1, 1	1, 0	0, 0
Case a	69(56)	84(68)	63(51)	77(62)	51(41)	63(50)
Case c	63(51)	77(62)	81(66)	77(62)	56(44)	72(57)
Average for the accurate scheme	59(47)	59(47)	59(47)	81(66)	59(47)	81(66)

fine states according to formulas (14) and (17), we obtain

$$\begin{aligned}\Delta_{LSJM_J ls_j}(R) &= n(G_{ls}^{LS})^2 \\ &\times \sum_{\mu,\sigma} \sum_{m, m_s, m_j, M_L, M_S} \begin{bmatrix} l_e & l & L \\ \mu & M_L-\mu & M_L \end{bmatrix} \\ &\times \begin{bmatrix} l_e & l & L \\ \mu & m & m+\mu \end{bmatrix} \begin{bmatrix} \frac{1}{2} & s & S \\ \sigma & M_S-\sigma & M_S \end{bmatrix} \\ &\times \begin{bmatrix} \frac{1}{2} & s & S \\ \sigma & m_s & m_s+\sigma \end{bmatrix} \begin{bmatrix} l & s & j \\ m & m_s & m_j \end{bmatrix} \\ &\times \begin{bmatrix} l & s & j \\ M_L-\mu & M_S-\sigma & M_L-\mu+M_S-\sigma \end{bmatrix} \\ &\times \begin{bmatrix} L & S & J \\ M_L & M_S & M_J \end{bmatrix} \begin{bmatrix} L & S & J \\ m+\mu & m_s+\sigma & m+\mu+m_s+\sigma \end{bmatrix} \Delta_{l_e\mu}.\end{aligned} \tag{32}$$

In Table 17, cases "a" and "c" of the Hund coupling are compared with a rigorous evaluation for the quasimolecule under consideration. The general conclusion from this and previous comparisons is that the average cross sections for the precise and approximate methods are close if we take into account the transition of any electron from the atom valence electron shell. If we reduce the problem to electron transfer between two structureless cores, the difference in average cross sections may reach 20%.

8. CONCLUSIONS

We have constructed the electron terms for the oxygen ion dimer at large separations by an asymptotically accurate method, with various interactions in this system taken into account within the framework of the *LS* coupling scheme for the oxygen atom and ion. The hierarchy of interactions in this quasimolecule is such that the exchange electrostatic interaction is stronger for lowest nonfilled electron shells p^3 and p^4 for the ion and atom. As a result, the atom orbital momentum L, its spin S, the ion orbital momentum l, and its spin s are the quasimolecule quantum numbers. The spin–orbit interaction for an atom and an ion and the interaction of the ion charge and the atom quadrupole moment are weaker interactions. Because these interactions are comparable, one can find the electron terms at large separations with these interactions taken into account by diagonalization of the Hamiltonian matrix. The quasimolecule eigenstates are characterized by the total ion angular momentum j and its projection m_j on the molecular axis; atom momenta and their projections are mixed in eigenstates of the quasimolecule. The electron term positions for the quasimolecule are determined for each electron term of the diatomic oxygen ion; the exchange interaction potentials for each electron term and for each ion state are also evaluated at large separations. Although this is done for the quasimolecule O_2^+, we thus obtain a general scheme for determining the electron term energies and exchange interaction potentials at large separations for an atom and its ion with unfilled electron shells within the *LS* scheme of electron coupling.

We note that a general scheme developed for evaluating electron terms and the cross sections of resonant charge exchange is asymptotically accurate, but it is at the same time quite cumbersome. Indeed, in the case of $O^+(^4S) + O(^3P)$ interaction, we have nine electron terms that are partially degenerate if we neglect the ion–atom exchange interaction; taking into account the ion–atom exchange interaction, we obtain 36 partially degenerate electron terms. In the case of $O^+(^2D) + O(^3P)$ interaction, we have 18 partially degenerate electron terms with the ion–atom exchange interaction ignored and 90 electron terms with the ion–atom exchange interaction taken into account. Because this method is cumbersome, it may be simplified with partial loss of rigor but with small loss in accuracy. Nevertheless, at least one

accurate evaluation is needed in the asymptotically accurate scheme in order to know the accuracy of various approximate methods. This procedure is fulfilled in this paper in the case of oxygen.

ACKNOWLEDGMENTS

This paper was supported in part by the Russian Foundation for Basic Research (project no. 04-03-32736) and grant LSS-1953.2003.2.

REFERENCES

1. R. S. Mulliken, Rev. Mod. Phys. **2**, 60 (1930).
2. F. Hund, Z. Phys. **36**, 637 (1936).
3. L. D. Landau and E. M. Lifshitz, *Course of Theoretical Physics*, Vol. 3: *Quantum Mechanics: Non-Relativistic Theory*, 4th ed. (Nauka, Moscow, 1989; Pergamon, London, 1980).
4. E. E. Nikitin, Opt. Spektrosk. **22**, 379 (1966).
5. E. E. Nikitin and B. M. Smirnov, Usp. Fiz. Nauk **124**, 201 (1978) [Sov. Phys. Usp. **21**, 95 (1978)].
6. E. E. Nikitin and S. Ya. Umanskiĭ, *Theory of Slow Atomic Collisions* (Atomizdat, Moscow, 1979; Springer, Berlin, 1984).
7. E. E. Nikitin and B. M. Smirnov, *Atomic and Molecular Processes* (Nauka, Moscow, 1988) [in Russian].
8. B. M. Smirnov, *Physics of Atoms and Ions* (Springer, New York, 2003).
9. B. M. Smirnov, Zh. Éksp. Teor. Fiz. **124**, 545 (2003) [JETP **97**, 493 (2003)].
10. B. M. Smirnov, in *Theory of Chemical Reaction Dynamics*, Ed. by A. Lagana and G. Lendvay (Kluwer Academic, Amsterdam, 2004), p. 29.
11. B. M. Smirnov, Zh. Éksp. Teor. Fiz. **46**, 1017 (1964) [Sov. Phys. JETP **19**, 692 (1964)].
12. B. M. Smirnov, Zh. Éksp. Teor. Fiz. **47**, 518 (1964) [Sov. Phys. JETP **20**, 345 (1965)].
13. B. M. Smirnov, *Asymptotic Methods in Theory of Atomic Collisions* (Atomizdat, Moscow, 1972) [in Russian].
14. S. Bashkin and J. Stoner, *Atomic Energy Levels and Grotrian Diagrams* (North-Holland, Amsterdam, 1978, 1981, 1982), Vols. 1, 2, 3, 4.
15. A. A. Radtsig and B. M. Smirnov, *Reference Data on Atoms, Molecules, and Ions* (Atomizdat, Moscow, 1980; Springer, Berlin, 1985).
16. E. U. Condon and G. H. Shortley, *Theory of Atomic Spectra*, 2nd ed. (Cambridge Univ. Press, Cambridge, 1949; Inostrannaya Literatura, Moscow, 1949).
17. I. I. Sobel'man, *Atomic Spectra and Radiative Transitions* (Nauka, Moscow, 1977; Springer, Berlin, 1979).
18. W. Heitler and F. London, Phys. Z. **44**, 445 (1927).
19. B. M. Smirnov, Teplofiz. Vys. Temp. **4**, 429 (1966).
20. G. Racah, Phys. Rev. **61**, 186 (1942); Phys. Rev. **62**, 438 (1942).
21. E. L. Duman and B. M. Smirnov, Zh. Tekh. Fiz. **40**, 91 (1970) [Sov. Phys. Tech. Phys. **15**, 61 (1970)].
22. B. M. Smirnov, Usp. Fiz. Nauk **171**, 233 (2001) [Phys. Usp. **44**, 221 (2001)].
23. B. M. Smirnov, Zh. Éksp. Teor. Fiz. **119**, 1099 (2001) [JETP **92**, 951 (2001)].
24. O. B. Firsov, Zh. Éksp. Teor. Fiz. **21**, 1001 (1951).
25. E. R. Gilmore, J. Quant. Spectrosc. Radiat. Transf. **5**, 369 (1965).
26. B. M. Smirnov, Phys. Scr. **61**, 595 (2000).
27. F. B. M. Copeland and D. S. F. Crothers, At. Data Nucl. Data Tables **65**, 273 (1997).
28. A. V. Eletskii, M. Capitelli, R. Celiberto, and A. Laricchiuta, Phys. Rev. A **69**, 042718 (2004).

Journal of Experimental and Theoretical Physics, Vol. 101, No. 4, 2005, pp. 628–634.
Translated from Zhurnal Éksperimental'noĭ i Teoreticheskoĭ Fiziki, Vol. 128, No. 4, 2005, pp. 732–739.

ATOMS, MOLECULES, OPTICS

Femtosecond Laser Photoemission Microscopy of Capillary Nanotips with Ultrahigh Spatial Resolution

B. N. Mironov, S. A. Aseev*, S. V. Chekalin, and V. S. Letokhov

Institute of Spectroscopy, Russian Academy of Sciences, Troitsk, Moscow oblast, 142190 Russia

**e-mail: isanfemto@yandex.ru*

Received May 19, 2005

Abstract—A nanolocalized electron beam emitted from silicon nanotubes has been used to image the aperture of a quartz capillary with a channel diameter of 100 nm. An analogous nickel-coated capillary was used as a tip for imaging deposited organic nanostructures by means of femtosecond laser photoelectron projection microscopy (LPPM). Organic nanocomplexes deposited onto the tip surface change the dependence of the photoelectron response signal on the energy density of probing femtosecond laser pulses. An analysis of the LPPM images of capillary nanotips shows that the spatial resolution achieved in these experiments is on a level of 5 nm. © *2005 Pleiades Publishing, Inc.*

I. INTRODUCTION

The development of optical methods not limited by diffraction is of considerable importance for the investigation of nanostructural composite materials. In this context, reaching a spatial resolution on the level of several nanometers is among the most urgent tasks in nanooptics [1]. The method of scanning near-field optical microscopy (SNOM) in the standard realization is based on the illumination of an object through a subwavelength aperture [2] and the detection of light scattered from the object. The SNOM image of a nanostructure is obtained by placing it on a scanned substrate at a distance of several nanometers from the aperture. The spatial resolution reached using this method in most cases falls within 30–100 nm. Methods employing apertureless near-field microscopy are also under development.

Ultrahigh spatial resolution in nanooptics can be reached using a combination of the emission projection microscopy with selective laser-induced photoemission techniques [3]. In this geometry, the surface of a sharp tip with the surface curvature radius much smaller than the laser wavelength λ is projected onto a position-sensitive detector by charged particles, which are emitted from the point surface under the action of laser radiation (for photoelectrons, the escape depth is typically within several nanometers [4]) and move in the radial electric field. As a result, a photoelectron projection image of the nanodimensional tip surface magnified to a macroscopic size (up to several centimeters) is obtained in the detector plane. The use of laser pulses of femtosecond duration is important for providing effective laser-induced photoemission without significant heating of the tip.

Capillary nanotips offer certain advantages as compared to the classical tips of simpler topography. First, the image of the aperture (hole) of a capillary can provide a convenient reference signal. Second, sharp tips with a hole in the central part are also of considerable interest as nanowells for accommodating organic nanoclusters. A proper nanowell, whose characteristic size can be controlled by deposition of a thin film of variable thickness, will naturally hinder the motion of the irradiated nanocluster over the tip surface. Third, the aperture can be used for supplying additional electrons to the sample, which is important for the investigation of weakly conducting nanostructures in the regime of laser photoelectron projection microscopy (LPPM). It should be noted that a nanolocalized electron beam obtained at the capillary exit using an internal field-emission cathode can be used for imaging the aperture of the capillary.

This study was aimed at obtaining images of a dielectric aperture and an organic nanostructure at the tip of a 100-nm quartz capillary. Section 2 describes the experimental setup, procedures, and methods used to prepare nanodimensional tips for LPPM. Section 3 presents the results obtained for a quartz capillary nanotip by LPPM using femtosecond laser radiation and a nanolocalized electron beam. The concluding Section 4 summarizes the obtained results.

2. EXPERIMENTAL SETUP AND TECHNIQUES

Figure 1 shows a scheme of the laser projection microscope. The setup is based on a vacuum chamber in which a magnetic discharge pump of the Nord type (Russia) provides an oilless vacuum on a level of 10^{-7} Torr. The main elements of such a microscope are a sharp tip and a position-sensitive detector of charged particles. We used a position-sensitive detector (Hamamatsu Photonics K.K., Japan) comprising a pair of

microchannel plates with a diameter of 28 mm and a luminescent screen. The image formed on the screen was monitored by a CCD camera, transmitted to a computer, and processed by an Argus-50 processor.

The tips were manufactured using commercially available quartz capillaries with a channel diameter of 100 nm (μTIP™, WPI, Israel) and glass capillaries with a 1-μm channel (Pushchino, Russia). The tip of a capillary could be coated with a nickel film of definite thickness (determined by the deposition time) in an auxiliary vacuum chamber (not depicted in Fig. 1). In order to obtain organic nanostructures on the tip surface, a nickel-coated capillary was dipped into a solution of the organic dye Coumarin 153 (C153) in ethyl alcohol (we used a solution concentration of $n_{C153} \approx 2.4 \times 10^{19}$ cm^{-3}) and then dried. It should be noted that this organic dye belongs to a group of promising chromophores for biological macromolecules [5].

A capillary nanotip was fixed with a metal ring in a sample holder, which was mounted on a special movable feedthrough of the vacuum chamber. A bundle of silicon nanotubes inserted into the capillary from the rear end served as an internal cold electron emitter. The tip and the emitter were provided with separate electric leads. The assembly comprising the capillary nanotip with the internal cold electron emitter was oriented so that the tip was facing the position-sensitive detector. The movable feedthrough allowed the tip to be adjusted in the vertical direction and the tip axis to be rotated within ±10° in the horizontal plane (Fig. 1). In most experiments, a distance from the tip to the detector surface was about $L = 7$ cm.

The LPPM measurements were performed using femtosecond pulses of laser radiation with a wavelength of $\lambda \approx 400$ nm, a pulse duration of $\tau_p \approx 100$ fs, and a pulse repetition rate of ≈76 MHz. Note that 400-nm light is effectively absorbed by C153 molecules [6]. The pulses of 400-nm probing laser radiation were obtained by focusing 800-nm fundamental radiation of a femtosecond generator (Avesta Co., Russia) pumped by a cw Millennia laser (Spectra Physics, United States) onto a nonlinear BBO crystal. The second harmonic pulses with an energy of 0.3 nJ generated in this crystal were additionally attenuated using a neutral metal filter. The output laser beam was focused by an external quartz lens with a focal distance of $f_L \approx 12$ cm and introduced into the vacuum chamber via a special window.

3. EXPERIMENTAL RESULTS

In the first stage of experiments, we studied the surface of an uncoated 100-nm quartz capillary. For this purpose, a negative potential $U_{Si} = -1.6$ kV was applied to the internal cold emitter, while the dielectric tip was not biased ($U_T = 0$, Fig. 1). In this case, the position-sensitive detector monitored a beam of electrons emitted from silicon nanotubes and transmitted through the capillary aperture. Figure 2 shows the electron density distributions observed for two orientations of the tip relative to the detector.

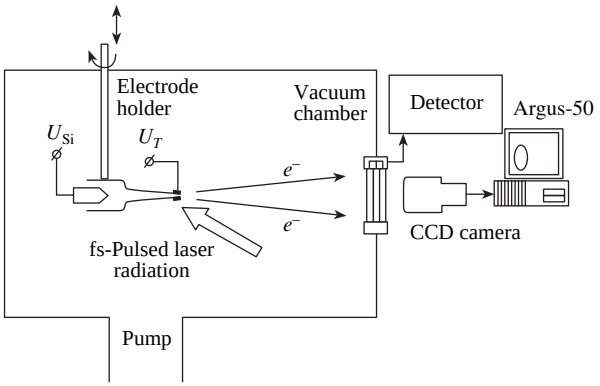

Fig. 1. Schematic diagram of the experimental setup.

A circular distribution of the emission current density in Fig. 2a can be explained using the following qualitative considerations. For simplicity, let us consider a conical cylinder with a large aspect ratio instead of the capillary (Fig. 3). We may naturally suggest that the internal nanotube cathode emits electrons within a broad solid angle (about 1 sr). The fraction of electrons ejected from the capillary without collisions with walls (Fig. 3a) is apparently small, being proportional to d^2 (where d is the aperture diameter). The main part of emitted electrons strike the capillary walls in the immediate vicinity of the emitter (Fig. 3b). We believe that, in the case of a 100-nm capillary, the main contribution to the detected signal is due to electrons ejected upon inelastic reflection and secondary electron emission along the capillary walls [7, 8] without subsequent collisions with these walls. As can be see from Fig. 3b, the electron density distribution in this case should have a ring shape, in agreement with experiment. It should be noted that a decrease in the kinetic energy of electrons upon multiple inelastic collisions with walls leads to a significant decrease in the efficiency of detection for such electrons and, hence, their contribution in the first approximation can be ignored.

The coefficient of magnification in these measurements, which could be readily determined from the experimental data, amounted to $M_E \approx 3 \times 10^5$. An analysis of the electron density distribution in Fig. 2b also allows the spatial resolution of LPPM images to be evaluated. Indeed, the smearing of the inner part of the ring in Fig. 2a is approximately $v \approx 1.5$ mm, from which the spatial resolution can be estimated as $v/M_E \approx 5$ nm.

When the electron beam was passed through a 1-μm glass capillary, the electron density distribution (Fig. 4) was different from that observed for the 100-nm capillary. According to the above model (Fig. 3b), the signal related to collisionless ejection of electrons for a 1-μm

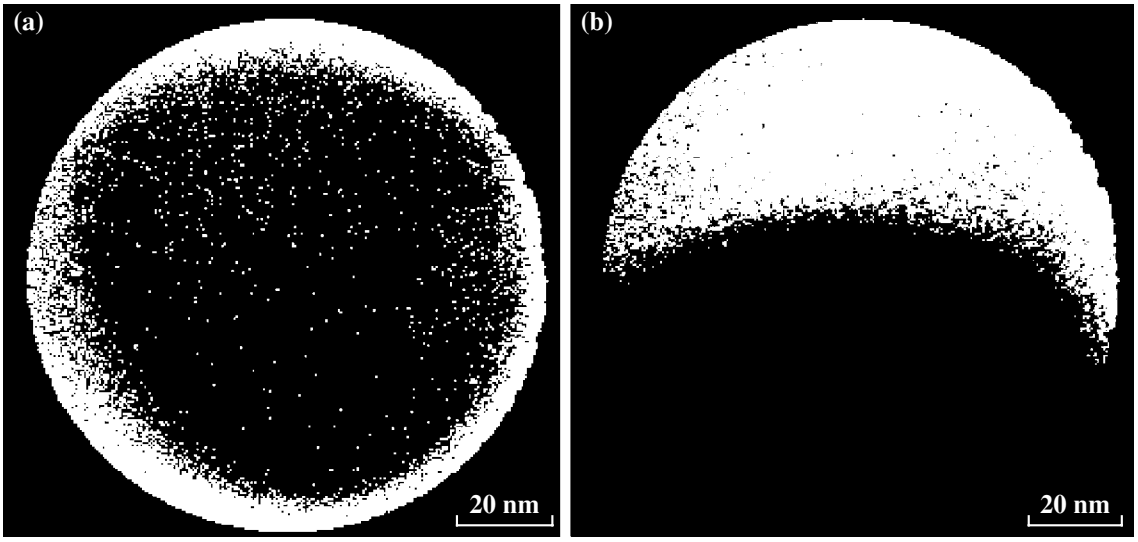

Fig. 2. Aperture of a 100-nm quartz capillary imaged using a nanolocalized internal electron beam at (a) the normal and (b) altered orientation of the tip.

aperture must be two orders of magnitude as large as that for a 100-nm hole. The absence of a bright ring in Fig. 4 is explained by the fact that these electrons do not strike the detector, since the diameter of this ring exceeds that of the microchannel plate size. The low quality of the obtained image can be related to poor spatial resolution (at the 100-nm level) and to inhomogeneity of the cross section of the ejected electron beam. Assuming that the spot in Fig. 4 is a projection image of the 1-μm aperture, we can estimate the corresponding coefficient of magnification as $M_{EG} \approx 5 \times 10^3$.

It should be noted that the electron beam obtained in this case has a quite satisfactory divergence, which can be estimated as approximately $\alpha \approx 4 \times 10^{-2}$ rad.

A nanolocalized electron beam obtained at the output of a 100-nm capillary tip can be used for the shadow imaging of nanostructures near the tip. We should like to point out that it is also possible to generate an ultrashort bunch of electrons by irradiating the internal emitter with femtosecond laser radiation pulses (it is expedient to use a single sharp point, such as an internal cold cathode). This will ensure electron-microscopic

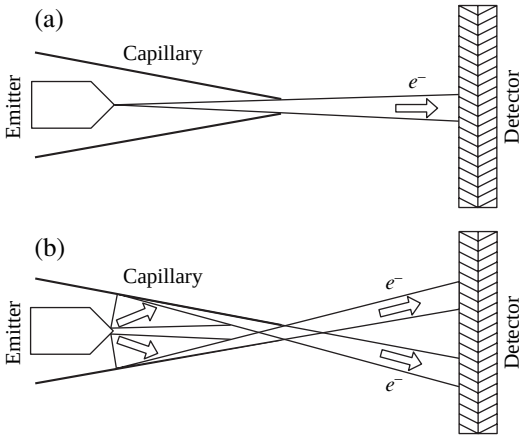

Fig. 3. Schematic diagram of the nanolocalized electron beam formation at the output of a capillary in the case of ejection of electrons (a) without collisions and (b) upon inelastic collisions with capillary walls.

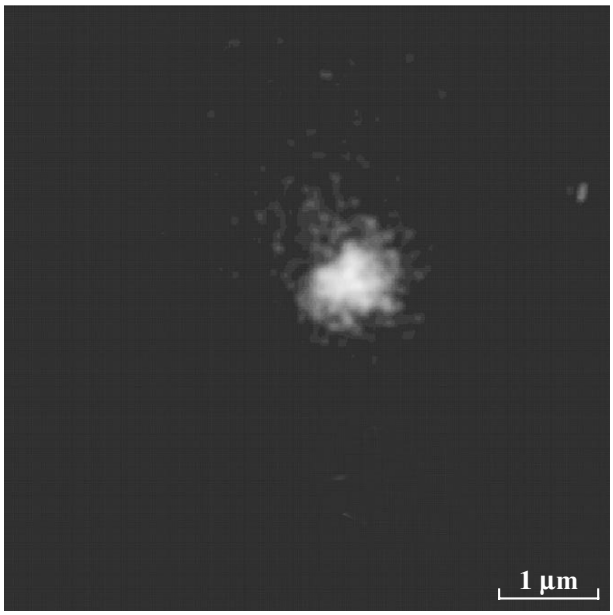

Fig. 4. Aperture of a 1-μm glass capillary imaged using electrons emitted from the internal nanotube cathode.

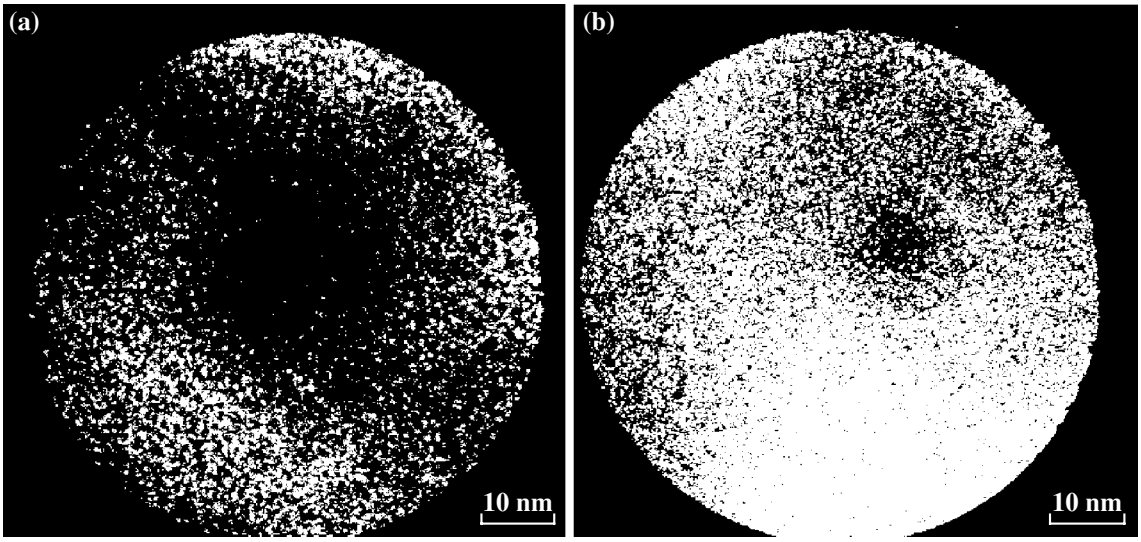

Fig. 5. LPPM images of the aperture of a quartz capillary with a 100-nm channel covered with a (a) 25- and (b) 40-nm-thick layer of nickel (for an observation time of 1.5 and 3 min, respectively).

imaging of nanostructures at a high temporal resolution. In particular, such nanolocalized beams can be used for combined femtosecond electron and laser excitation of a sample.

In the second stage of this study, we obtained LPPM images of two 100-nm quartz capillaries covered with nickel layers of different thicknesses (Fig. 5). The thickness of a deposited nickel layer was 25 nm (Fig. 5a) and 40 nm (Fig. 5b). Therefore, the difference between the capillary channel diameters in the two cases must be $\Delta d \approx 30 \pm 5$ nm (this fact will be checked in the subsequent analysis). In these experiments, the internal cathode was not biased ($U_{Si} = 0$), while the tip was at a small negative potential ($U_T = -300$ V), which was necessary for the effective detection of electrons emitted from the capillary. Note that the photoelectron response signal is linearly dependent on the laser radiation energy density (Fig. 6a). This is related to the fact that the applied static field ($F \sim U_T/3d \approx 1$ V/nm) decreases the work function $e\varphi_{WF}$ (for nickel, $e\varphi_{WF} \approx$ 4.6 eV [7]) and thus provides for a single-photon-induced electron emission from the metal surface irradiated by light quanta with $\lambda = 400$ nm.

In order to interpret the images, we have to evaluate the magnification coefficient M_L. This coefficient can be calculated using an expression for the classical electron projector [9]:

$$M_L \approx \frac{L}{\eta r \theta}, \qquad (1)$$

where r is the tip radius, $\theta \approx 1.5$ [9], and η is a factor taking into account a difference of the field distribution at the capillary end from the radial configuration. This

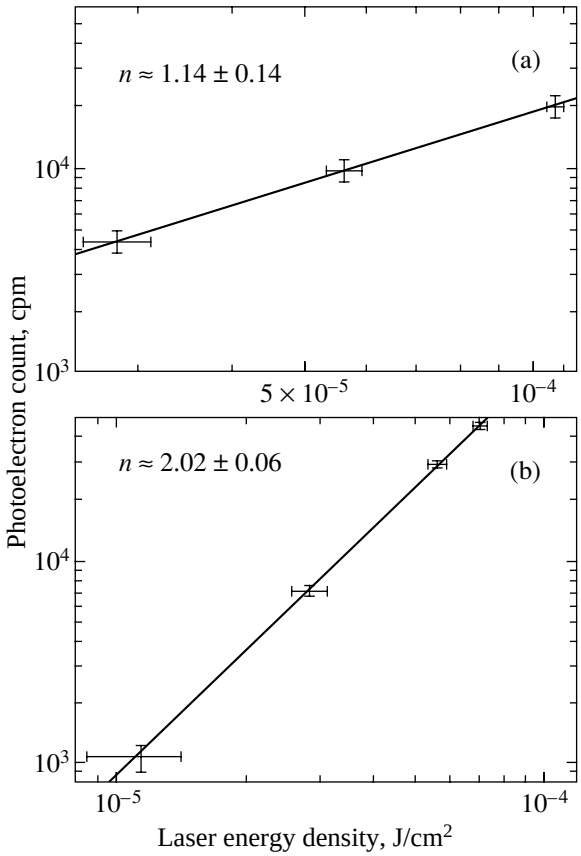

Fig. 6. Plots of the photoelectron current versus laser pulse energy density for (a) a capillary covered with a 40-nm-thick layer of nickel and (b) the same metallized capillary with deposited Coumarin 153 dye molecules. Points present the experimental data with error bars; solid lines correspond to the (a) linear and (b) quadratic dependences of photocurrent on the laser pulse energy density.

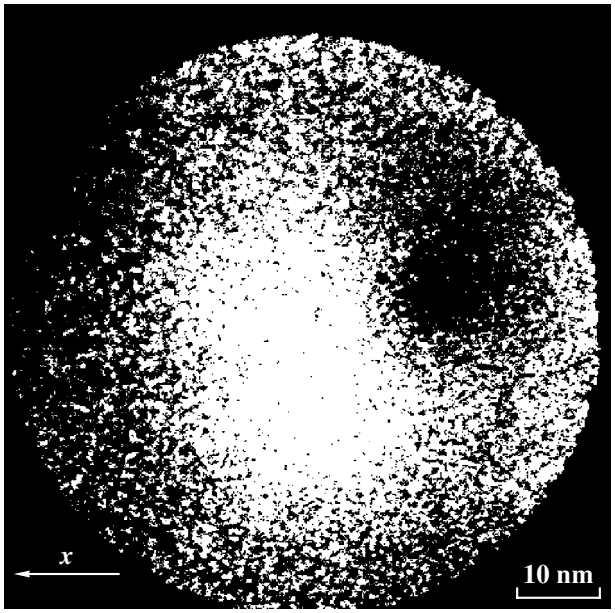

Fig. 7. LPPM image of the quartz capillary with a deposited organic nanostructure.

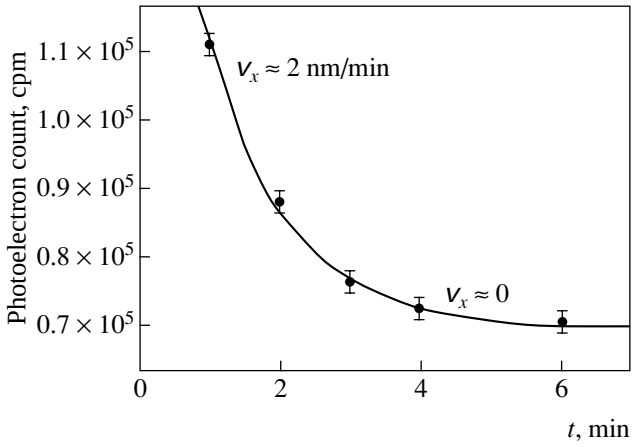

Fig. 8. Plot of the photoelectron current versus time of irradiation of the sample at a laser pulse energy of 0.28 nJ. Points represent the experimental data with error bars (data acquisition time, 30 s); solid curve shows the results of interpolation $y = 102000e^{-t/1.16} + 69000$; v_x is the projection of the velocity of nanocomplex on the x axis (depicted in Fig. 7).

factor reflects a contraction of the image of the central region of the capillary end due to converging field lines. Assuming that $\eta \approx 2$, we can estimate the magnification coefficient as $M_L \approx 4.7 \times 10^5$. This estimate will be checked below.

The spatial resolution in LPPM is limited by a nonzero initial transverse velocity component of emitted photoelectrons relative to the static electric field direction. Indeed, an electron possessing a nonzero energy $E_0 = mv^2/2$ is detected by a position-sensitive detector with a spatial uncertainty of

$$\delta \approx 2L(E_0/eU_T)^{1/2}. \quad (2)$$

For $E_0 \le 0.1$ eV, the error of determination of the electron position is approximately $\Delta \approx \delta/M_L \le 5$ nm. This allows the proposed method to be used for the investigation of nanostructures with characteristic dimensions as small as ~5–10 nm, which is sufficient for LPPM imaging of small clusters.

Let us analyze the LPPM images presented in Fig. 5 in terms of formula (1). According to this, the diameters of channels in the capillaries coated with 25- and 40-nm-thick nickel films are $d_{25} \approx 35 \pm 5$ nm (Fig. 5a) and $d_{40} \approx 11 \pm 5$ nm (Fig. 5b), respectively. The difference $\Delta d \approx 24 \pm 7$ nm agrees (to within the experimental uncertainty) with the estimate obtained above using the relation between the hole size and the deposited layer thickness. This agreement confirms the validity of the assumptions made above.

Figure 7 shows the LPPM image of a nickel-coated nanocapillary tip with a deposited organic nanostructure. The probability of photoinduced decomposition of molecules on a metal-coated substrate significantly decreases because the metal produces rapid quenching of the excited molecular electronic states [10, 11]. Irradiation of such samples with femtosecond pulses of 400-nm laser radiation showed a quadratic dependence of the photoelectron current on the laser energy density (Fig. 6b). According to published data [12], the ionization potential of an organic dye molecule is higher than 7 eV. Therefore, the photodetachment of one electron from such a molecule requires several light quanta with $\lambda = 400$ nm. It should be recalled that the dependence of the photoelectron current on the laser energy density measured before the application of dye molecules on the tip surface was linear (Fig. 6a).

The characteristic size of the organic nanocomplex imaged in Fig. 7 amounts to several tens of nanometers. This nanostructure was imaged using femtosecond laser pulses with an energy of $E = 0.16$ nJ. When the laser pulse energy was increased to 0.28 nJ, the nanocomplex exhibited motions over the tip surface. This was accompanied by a decrease in the photoelectron current, which was well described by an exponential function of the laser irradiation time (Fig. 8). We believe that this behavior is caused by heating of the sample, which leads to photoinduced decomposition or desorption of fragments of the organic nanostructure.

Using the vacuum feedthrough (Fig. 1), it was possible to adjust the orientation of the capillary nanotip relative to the detector and thus shift the image of the capillary aperture to the center of the detector area. Figure 9 shows the measured photoemission intensity distribution (the contrast used to obtain these data did not allow the image of the aperture to be observed simulta-

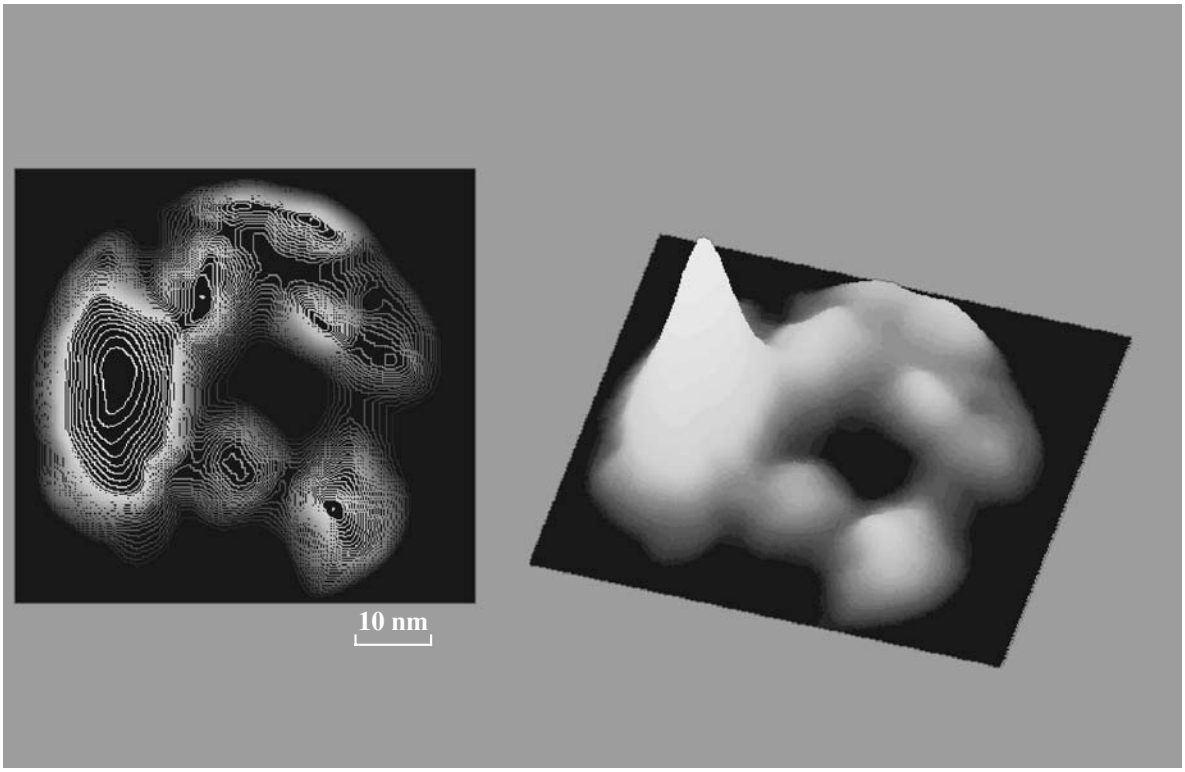

Fig. 9. The LPPM image of an adjusted nanocapillary with organic nanocomplexes at the tip (the contrast used to obtain this image does not allow the image of the aperture in the central part of the detector area to be simultaneously observed). For better illustration, the right-hand panel shows a three-dimensional pattern in which the height and brightness are proportional to the photoelectron response magnitude.

neously). Note that the nanoclusters with characteristic dimensions about 5–10 nm are imaged less brightly than the main structure (representing approximately 20-nm organic cluster). This fact can be related to manifestation of the limited ($\Delta \approx 5$ nm) spatial resolution of the system. Indeed, when the size of a nanoobject decreases below Δ, the characteristic size of the image is unchanged but the number of emitted electrons decreases.

4. CONCLUSIONS

We have successfully imaged an organic nanocomplex and a dielectric aperture at the tip of a 100-nm quartz capillary. Using femtosecond LPPM, an approximately 20-nm organic structure composed of Coumarin-153 molecules was imaged by LPPM with a magnification coefficient of $M_L \approx 4.7 \times 10^5$. An increase in the laser pulse energy above a certain level leads to the motion of the nanocomplex over the tip surface and is accompanied by a decrease in the photoemission current, which is well described by an exponential function of the laser irradiation time with a decay time constant of about 1 min. LPPM imaging of a metal-coated capillary tip with a 10-nm aperture is evidence of the high spatial resolution (on a level of $\Delta \approx 5$ nm) achieved in our experiments.

Using the internal cold cathode in the form of a bundle of silicon nanotubes, it is possible to obtain a nanolocalized electron beam at the output of a 100-nm capillary tip. Such a beam was successfully used for imaging the aperture of the quartz capillary with a magnification coefficient of about $M_E \approx 3 \times 10^5$ (note that the magnification coefficients and the values of spatial resolution determined by two methods were very close). The electron beam obtained at the output of a 100-nm capillary tip can be used for the shadow imaging of nanostructures near the tip aperture. By irradiating the internal emitter with femtosecond laser radiation pulses, it is also possible to generate nanolocalized ultrashort bunches of electrons.

ACKNOWLEDGMENTS

The authors are grateful to S.K. Sekatskiĭ for kindly providing 100-nm quartz capillaries for experiments.

This study was supported by the Russian Foundation for Basic Research, project no. 05-02-16900a.

REFERENCES

1. *Nano-Optics*, Ed. by S. Kawata, M. Ohtsu, and M. Irie (Springer, Berlin, 2002).

2. M. A. Paesler and P. J. Moyer, *Near-Field Optics: Theory, Instrumentation, and Application* (Wiley, New York, 1996).

3. V. S. Letokhov and S. K. Sekatskiĭ, in *Advances in Laser Physics*, Ed. by V. S. Letokhov and P. Meystre (Harwood Academic, Australia, 2000), p. 85.

4. O. H. Griffith and G. F. Rempfer, Adv. Opt. Electron. Microsc. **10**, 269 (1987).

5. P. K. Chowdhury, M. Halder, L. Sanders, *et al.*, Photochem. Photobiol. **79**, 440 (2004).

6. *Lambdachrome Laser-grade Dyes Data Sheets, First Edition*, Ed. by U. Brackmann (Lambda Physik GmbH, Göttingen, 1986).

7. *Physical Values: Handbook*, Ed. by I. S. Grigor'ev and E. Z. Meĭlikhov (Énergoatomizdat, Moscow, 1991) [in Russian].

8. I. M. Bronshteĭn and B. S. Fraĭman, *Secondary Electron Emission* (Nauka, Moscow, 1969) [in Russian].

9. E. W. Muller and T. T. Tsong, *Field Ion Microscopy, Field Ionization, and Field Evaporation* (Pergamon, Oxford, 1973).

10. Sh. Nie and St. R. Emory, Science **275**, 1102 (1997).

11. K. H. Drexhage, J. Lumin. **1**, 693 (1970).

12. I. V. Sokolova, N. Yu. Vasil'eva, Ya. O. Vylegzhanina, and G. V. Maier, Opt. Spektrosk. **79**, 460 (1995) [Opt. Spectrosc. **79**, 426 (1995)].

Translated by P. Pozdeev

Journal of Experimental and Theoretical Physics, Vol. 101, No. 4, 2005, pp. 635–645.
Translated from Zhurnal Éksperimental'noĭ i Teoreticheskoĭ Fiziki, Vol. 128, No. 4, 2005, pp. 740–751.

NUCLEI, PARTICLES, FIELDS, GRAVITATION, AND ASTROPHYSICS

Influence of Strongly Magnetized Plasma on Photon Splitting

D. A. Rumyantsev* and M. V. Chistyakov**
Yaroslavl State University, Sovetskaya ul. 14, Yaroslavl, 150000 Russia
**e-mail: rda@uniyar.ac.ru*
***e-mail: mch@uniyar.ac.ru*
Received February 3, 2005

Abstract—The photon splitting $\gamma \longrightarrow \gamma\gamma$ in a strongly magnetized medium of arbitrary temperature and chemical potential is considered. In comparison with the case of a pure magnetic field, a new photon splitting channel is shown to be possible below the electron–positron pair production threshold. The partial splitting amplitudes and probabilities are calculated by taking into account the photon dispersion in a strong magnetic field and a charge-symmetric plasma. An enhancement of the photon splitting probability compared to the case of a magnetic field without plasma has been found to be possible under certain conditions. © *2005 Pleiades Publishing, Inc.*

1. INTRODUCTION

The photon splitting into two photons, which is forbidden in a vacuum by the Farry theorem, but is possible in the presence of an electromagnetic field and/or a plasma, is a shining example of the influence of an active external medium on the reactions involving elementary particles. Remarkably, this exotic (at first glance) process can play a significant role in astrophysical phenomena. In particular, it is suggested that this process could explain spectral features in some of the radio pulsars [1] and the absence of radio emission in recently discovered X-ray and gamma-ray sources, the so-called anomalous X-ray pulsars (AXP) and soft gamma repeaters (SGR) [2]. Such astrophysical objects can possess a strong magnetic field that significantly exceeds a critical value of $B_e = m^2/e \approx 4.41 \times 10^{13}$ G[1] and that reaches ~10^{14}–10^{16} G [3]. In addition, analysis of the spectra for some of these objects points to the existence of a relatively hot and dense electron–positron plasma in their neighborhood [3].

The theoretical study of the photon splitting $\gamma \longrightarrow \gamma\gamma$ in an active external medium has a rather long history. In a magnetic field, this process has been considered by a number of authors (see, e.g., [4] where a detailed list of previous papers can be found); among the relatively recent papers are [5–12]. In particular, the case of a strong magnetic field was considered in [6–9]. In an electron–positron plasma without any influence of an external field, the propagation of photons was studied both in the case of a medium at rest [13] and in the case where the plasma moves with an arbitrary velocity [14]. In [14], the most general expression for the photon splitting amplitude in a relativistic plasma was derived by the method of temperature Green functions. The effects of both components of the active medium on the dispersive properties of photons and their kinematics in a weakly magnetized, cold plasma were simultaneously taken into account by Adler [15]. In [16], the Heisenberg–Euler Lagrangian for the effective six-photon interaction was used to derive an expression for the photon splitting probability in a magnetized plasma by taking into account the photon dispersion in the plasma. The influence of a weak magnetic field and a medium of arbitrary temperature on the modification of the photon splitting amplitude was considered in [17–19]. The influence of the plasma in this case was shown to be negligible. However, the situation can change significantly in the strong-field limit, which has not been considered previously. It should also be noted that no joint analysis of the influence of a magnetized plasma on the dispersive properties of photons and on the modification of the photon splitting amplitude was performed in the above papers.

In this paper, we consider the photon splitting $\gamma \longrightarrow \gamma\gamma$ in the case of a strongly magnetized plasma where $\sqrt{eB}$ is believed to be much larger than the characteristic parameters of the medium: the temperature T, the chemical potential μ, and the photon energy. In Section 2, the amplitude of the process in a strong magnetic field is calculated by taking into account the photon scattering by real electrons and positrons of the medium. We show that the result obtained can be used to calculate the amplitudes of the processes involving neutrinos ($\gamma\gamma \longrightarrow \nu\bar{\nu}$) and axions ($a \longrightarrow \gamma\gamma$). In Section 3, we analyze the photon splitting kinematics in a strongly magnetized charge-symmetric ($\mu = 0$) plasma

[1] We use the natural system of units in which $c = \hbar = k = 1$, where m is the electron mass. Throughout this paper, $e > 0$ is the elementary charge.

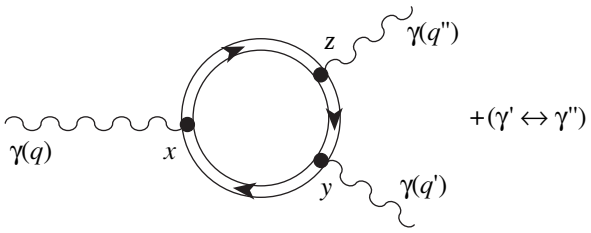

Fig. 1. Feynman diagrams for the photon splitting in a magnetic field.

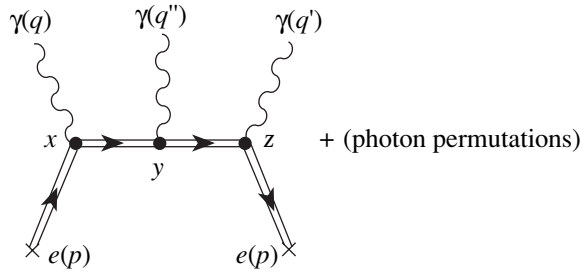

Fig. 2. Additional photon scattering by electrons of the medium with the emission of two photons in a magnetic field in the presence of a plasma. The diagrams with the substitution $p \longrightarrow -p$ will correspond to the scattering by positrons.

with allowance made for the photon dispersion. We point out that the renormalization of the photon wavefunctions near the cyclotron resonance should be taken into account. In Section 4, the splitting probabilities of real photons are calculated by taking into account the dispersion laws and the renormalization of the wavefunctions. We discuss our results and present our conclusions in Section 5.

2. CALCULATING THE AMPLITUDE

In this section, we calculate the amplitude of the process $\gamma \longrightarrow \gamma\gamma$ in a strongly magnetized medium. It can be represented as the sum of two terms:

$$\mathcal{M} = \mathcal{M}_B + \mathcal{M}_{\rm pl}, \tag{1}$$

where $\mathcal{M}_B$ is the amplitude of the process $\gamma \longrightarrow \gamma\gamma$ that corresponds to a purely field contribution ($\mu = T = 0$). It is described by two Feynman diagrams (Fig. 1) and can be taken from [8, 9, 20].

The second term on the right-hand side of Eq. (1) corresponds to coherent photon scattering by real electrons and positrons of the medium without any change in their state (forward scattering) with the emission of two photons. Graphically, such scatterings, for example, by plasma electrons can be represented by the six diagrams in Fig. 2. The cross at the end of the electron line means that the particle belongs to the medium. Such coherent scattering will give an additional contribution to the amplitude of the process $\gamma \longrightarrow \gamma\gamma$. Let us define the $\mathcal{S}$-matrix element of the plasma contribution as the sum over all states including the corresponding distribution functions:

$$\mathcal{S}_{\rm pl} = \sum_{n,s}\int dn_p[\mathcal{S}_- f_-(p) + \mathcal{S}_+ f_+(p)]. \tag{2}$$

Here, dn_p is a phase volume element,

$$dn_p = \frac{dp_3 dp_2 L_3 L_2}{(2\pi)^2},$$

where L_3 and L_2 are the parameters that define the quantization volume, $V = L_1L_2L_3$. The $\mathcal{S}$-matrix elements $\mathcal{S}_\mp$ describe the forward photon scattering with the emission of two photons, respectively, by electrons and positrons; $f_\mp(p)$ are the corresponding distribution functions. In thermodynamic equilibrium and in the rest frame of the plasma, the latter are

$$f_\mp(p) = \frac{1}{\exp\dfrac{p_0 \mp \mu}{T} + 1}.$$

The summation in Eq. (2) is over the spins and Landau levels of the plasma electrons and positrons.

In the strong-field limit, the plasma electrons and positrons are at the ground Landau level, $n = 0$. The well-known solutions of the Dirac equation in a magnetic field should be used to determine the matrix elements $\mathcal{S}_\mp$ in this limit. For the ground Landau level, these solutions are known (see, e.g., [21]) to be representable as (the vector potential was chosen to be $\mathbf{A} = (0, Bx_1, 0)$

$$\begin{aligned}\psi_{p\epsilon} &= \frac{\beta^{1/4}}{(2\sqrt{\pi}E_p L_2 L_3)^{1/2}} \\ &\times \exp[-i\epsilon(E_p x_0 - p_2 x_2 - p_3 x_3)] \\ &\times \exp\left(-\frac{\xi_\epsilon^2}{2}\right) u_\epsilon(p_\parallel),\end{aligned} \tag{3}$$

where

$$E_p = \sqrt{p_3^2 + m^2}, \quad \xi_\epsilon = \sqrt{\beta}\left(x_1 + \epsilon\frac{p_2}{\beta}\right),$$

$$\beta = eB,$$

and $\epsilon = \pm 1$ denote the solutions for an electron with positive and negative energies, respectively. The bispinor

amplitudes are

$$u_\epsilon(p_\parallel) = \frac{1}{\sqrt{E_p + \epsilon m}}\begin{pmatrix} (E_p + \epsilon m)\Psi \\ -p_3\Psi \end{pmatrix}, \quad (4)$$

where

$$\Psi = \begin{pmatrix} 0 \\ 1 \end{pmatrix}$$

describes the state with the spin directed against the field.

Using these solutions, we obtain the following expression for the $\mathcal{S}$-matrix element that corresponds to the diagrams in Fig. 2:

$$\mathcal{S}_{\rm pl} = \int \frac{dp_3 dp_2}{(2\pi)^2}\sum_{i=1}^{6}[\mathcal{S}_-^{(i)} f_-(p) + \mathcal{S}_+^{(i)} f_+(p)], \quad (5)$$

where $\mathcal{S}_\mp^{(i)}$ denotes the matrix element of the scattering by electrons (positrons) for the ith diagram. For example,

$$\mathcal{S}_-^{(1)} = -\frac{ie^3\sqrt{\beta/\pi}}{2E\sqrt{2\omega V 2\omega' V 2\omega'' V}}\int d^4x d^4y d^4z$$

$$\times \mathrm{Sp}\{[(p\gamma)_\parallel + m]\Pi_-(\varepsilon'\gamma)S(z,y)(\varepsilon''\gamma)S(y,x)(\varepsilon\gamma)\}$$
$$\times \exp[-i(qx - g'z - q''y)]$$
$$\times \exp[i(p(z-x))_\parallel]\exp[-i(p(z-x))_2] \quad (6)$$

$$\times \exp\left\{-\frac{\beta}{2}\left[\left(z_1 + \frac{p_2}{\beta}\right)^2 + \left(x_1 + \frac{p_2}{\beta}\right)^2\right]\right\}.$$

Here, $S(x, y)$ is the fermion propagator in a magnetic field, which can be represented as [22]

$$S(x,y) = \exp(i\Phi(x,y))\hat{S}(x-y), \quad (7)$$

$$\Phi(x,y) = -e\int_x^y d\xi_\mu\left[A_\mu(\xi) + \frac{1}{2}F_{\mu\nu}(\xi - y)_\nu\right], \quad (8)$$

where A_μ is the 4-potential, $F_{\mu\nu}$ is the tensor of the external constant uniform magnetic field. The translation-invariant part of the propagator $\hat{S}(x-y)$ has several representations. For our purposes, it is convenient to write it as a partial Fourier integral expansion:

$$\hat{S}(X) = -\frac{i}{4\pi}\int_0^\infty \frac{d\tau}{\tanh\tau}$$

$$\times \int \frac{d^2p}{(2\pi)^2}\left\{[(p\gamma)_\parallel + m]\Pi_-(1 + \tanh\tau)\right.$$

$$+ [(p\gamma)_\parallel + m]\Pi_+(1 - \tanh\tau)$$

$$\left. - (X\gamma)_\perp \frac{i\beta}{2\tanh\tau}(1 - \tanh^2\tau)\right\} \quad (9)$$

$$\times \exp\left(-\frac{\beta X_\perp^2}{4\tanh\tau} - \frac{\tau(m^2 - p_\parallel^2)}{\beta} - i(pX)_\parallel\right),$$

$$d^2p = dp_0 dp_3, \quad \Pi_\pm = \frac{1}{2}(1 \pm i\gamma_1\gamma_2),$$

$$\Pi_\pm^2 = \Pi_\pm, \quad [\Pi_\pm, (a\gamma)_\parallel] = 0.$$

Here, γ_α are the Dirac matrices in the standard representation; the 4-vectors with the subscripts $\perp$ and $\parallel$ refer, respectively, to the Euclidean {1, 2} and Minkowski {0, 3} subspaces, when the field **B** is directed along the third axis. For the arbitrary vectors a_α and b_α, we have

$$a_{\perp\alpha} = (0, a_1, a_2, 0), \quad a_{\parallel\alpha} = (a_0, 0, 0, a_3),$$
$$(ab)_\perp = (a\Lambda b) = a_1b_1 + a_2b_2, \quad (10)$$
$$(ab)_\parallel = (a\tilde{\Lambda}b) = a_0b_0 - a_3b_3,$$

where we introduced the matrices $\Lambda_{\alpha\beta} = (\varphi\varphi)_{\alpha\beta}$ and $\tilde{\Lambda}_{\alpha\beta} = (\tilde{\varphi}\tilde{\varphi})_{\alpha\beta}$ related by $\tilde{\Lambda}_{\alpha\beta} - \Lambda_{\alpha\beta} = g_{\alpha\beta} = \mathrm{diag}(1, -1, -1, -1)$, $\varphi_{\alpha\beta} = F_{\alpha\beta}/B$ is the tensor of the external magnetic field reduced to dimensionless form, $\tilde{\varphi}_{\alpha\beta} = \varepsilon_{\alpha\beta\mu\nu}\varphi_{\mu\nu}/2$ is the dual tensor; the tensor indices in the 4-vectors and the tensors in parentheses are assumed to be folded sequentially: for example, $(a\Lambda b) = a_\alpha\Lambda_{\alpha\beta}b_\beta$.

Changing the variables $Y = z - y$ and $Z = y - x$ in Eq. (6) and integrating over x yields the following

expression for $\mathcal{S}_-^{(1)}$:

$$\mathcal{S}_-^{(1)} = -\frac{ie^3(2\pi)^3}{2E\sqrt{2\omega V 2\omega' V 2\omega'' V}}\delta(\omega-\omega'-\omega'')$$
$$\times\delta(q_2-q_2'-q_2'')\delta(q_3-q_3'-q_3'')\int d^4Y d^4Z$$
$$\times \mathrm{Sp}\{[(p\gamma)_\parallel + m]\Pi_-(\varepsilon'\gamma)S(Y)(\varepsilon''\gamma)S(Z)(\varepsilon\gamma)\}$$
$$\times\exp[i((q'+q'')Z+q'Y)] \quad (11)$$
$$\times\exp\frac{ip_2(q_1-q_1'-q_1'')}{\beta}\exp[i(p(Y+Z))_\parallel]$$
$$\times\exp\left\{-\frac{\beta}{4}[Y_\perp^2+Z_\perp^2+2(YZ)_\perp+2i(Y\varphi Z)]\right\}.$$

The remaining elements $\mathcal{S}_-^{(i)}$ that correspond to the diagrams with photon permutations can now be easily obtained from Eq. (11). The substitution $p \longrightarrow -p$ allows the matrix elements $\mathcal{S}_+^{(i)}$ of the scattering by positrons to be determined. In general, the $\mathcal{S}$-matrix element for arbitrary particle momenta and magnetic fields is rather difficult to calculate. Substituting the propagator $S(X)$ in Eq. (11) leads to an overly cumbersome expression in the form of a double integral over the proper time. Deducing the strong-field limit from this expression is a fairly laborious task. In calculations, it proves to be more convenient to use the expansion of the electron propagator in terms of the inverse magnetic field strength. For this purpose, let us represent the translation-invariant part of the electron propagator $\hat{S}(X)$ as [23]

$$\hat{S}(X) = \hat{S}_-(X) + \hat{S}_+(X) + \hat{S}_\perp(X), \quad (12)$$

$$\hat{S}_-(X) \approx \frac{i\beta}{2\pi}\exp\left(-\frac{\beta X_\perp^2}{4}\right)$$
$$\times\int\frac{d^2p_\parallel}{(2\pi)^2}\frac{(p\gamma)_\parallel+m}{p_\parallel^2-m^2}\Pi_-\exp[-i(pX)_\parallel], \quad (13)$$

$$\hat{S}_+(X) \approx -\frac{i}{4\pi}\left[-i\left(\gamma\frac{\partial}{\partial X}\right)_\parallel + m\right]\delta_\parallel^2(X)\Pi_+$$
$$\times\exp\frac{\beta X_\perp^2}{4}\,\Gamma\left(0,\frac{\beta X_\perp^2}{2}\right), \quad (14)$$

$$\hat{S}_\perp(X) \approx -\frac{1}{2\pi}\delta_\parallel^2(X)\frac{(X\gamma)_\perp}{X_\perp^2}\exp\left(-\frac{\beta X_\perp^2}{4}\right), \quad (15)$$

where $\delta_\parallel^2(X) = \delta(X_0)\delta(X_3)$, $\Gamma(a, z)$ is the incomplete gamma function,

$$\Gamma(a,z) = \int_z^\infty t^{a-1}e^{-t}dt.$$

Only the combinations $\hat{S}_-\hat{S}_-$, $\hat{S}_-\hat{S}_+$, $\hat{S}_-\hat{S}_\perp$, and $\hat{S}_\perp\hat{S}_\perp$ will contribute to the first two terms of the expansion of the $\mathcal{S}$-matrix element in terms of the inverse magnetic field strength.

Our analysis shows (for details, see the Appendix) that the matrix elements $\mathcal{S}_-^{(i)}$ in the strong-field limit ($\beta \gg q_\perp^2, q_\parallel^2$) can be transformed to $\mathcal{S}_+^{(i)}$ in such a way that all of the even and odd (in external field, i.e., in φ and $\tilde{\varphi}$) terms will enter into the $\mathcal{S}$-matrix element (5) in the form of odd and even (in μ) functions, respectively. This assertion is consistent with the generalization of the Farry theorem to the case of a magnetized medium considered in [24].

Since the scattering $\gamma e^\pm \longrightarrow \gamma\gamma e^\pm$ takes place without any transfer of the 4-momentum to the plasma, this process physically manifests itself as the photon splitting with the corresponding conservation of all four energy–momentum components. Equation (6), which describes the scattering by a single electron, contains only three δ functions. However, the $\mathcal{S}$-matrix element (5), which includes the scattering by all plasma electrons and positrons, contains an integral over the generalized momentum p_2, which gives the missing δ function. The amplitude corresponding to the plasma contribution can then be defined in the standard way,

$$\mathcal{S}_{\mathrm{pl}} = \frac{i(2\pi)^4\delta^4(q-q'-q'')}{\sqrt{2\omega V 2\omega' V 2\omega'' V}}\mathcal{M}_{\mathrm{pl}}. \quad (16)$$

Given Eq. (16), amplitude (1) can be represented as

$$\mathcal{M} = \varepsilon_\mu(q)\varepsilon_\nu^*(q'')\varepsilon_\rho^*(q')(\beta\Pi_{\mu\nu\rho}^{(0)} + \Pi_{\mu\nu\rho}^{(1)}), \quad (17)$$

where

$$\Pi_{\mu\nu\rho}^{(0)} = 2\pi\left(\frac{\alpha}{\pi}\right)^{3/2}\frac{(\tilde{\varphi}q)_\mu(\tilde{\varphi}q'')_\nu(\tilde{\varphi}q')_\rho}{(q'\tilde{\varphi}q'')}$$
$$\times[\mathcal{T}_\perp^{(-)}(q_\parallel, q_\parallel') - \mathcal{T}_\perp^{(-)}(-q_\parallel', -q_\parallel)$$
$$-\mathcal{T}_\perp^{(-)}(-q_\parallel'', q_\parallel') - (q' \longleftrightarrow q'')], \quad (18)$$

$$\Pi_{\mu\nu\rho}^{(1)} = -i4\pi\left(\frac{\alpha}{\pi}\right)^{3/2}$$
$$\times\{(q'\varphi q'')(\pi_{\mu\nu\rho} + \nu_{\mu\nu\rho}) + (q'^{\mathcal{G}(q'')})_\nu\varphi_{\rho\mu}$$

$$+\frac{1}{2}((q''-q')\mathcal{G}(q))_\mu\varphi_{\nu\rho}+(q''\mathcal{G}(q'))_\rho\varphi_{\nu\mu}$$
$$-\mathcal{G}_{\nu\rho}(q'')(q'\varphi)_\mu+\mathcal{G}_{\mu\nu}(q'')(q\varphi)_\rho$$
$$+\mathcal{G}_{\mu\rho}(q')(q\varphi)_\nu-\mathcal{G}_{\nu\rho}(q')(q''\varphi)_\mu \quad (19)$$
$$-\mathcal{G}_{\mu\nu}(q)(q''\varphi)_\rho-\mathcal{G}_{\mu\rho}(q)(q'\varphi)_\nu$$
$$-\frac{i(\tilde\varphi q)_\mu(\tilde\varphi q'')_\nu(\tilde\varphi q')_\rho}{4(q'\tilde\varphi q'')}$$
$$\times[q_\perp'^2+q_\perp''^2+(q'q'')_\perp][\mathcal{T}_\perp^{(-)}(q_\parallel,q_\parallel')-\mathcal{T}_\perp^{(-)}(-q_\parallel',-q_\parallel)$$
$$-\mathcal{T}_\perp^{(-)}(-q_\parallel'',q_\parallel')-(q'\longleftrightarrow q'')]\}.$$

Here,

$$\mathcal{G}_{\mu\nu}(q)=\left(\tilde\Lambda_{\mu\nu}-\frac{q_{\parallel\mu}q_{\parallel\nu}}{q_\parallel^2}\right)\left[H\left(\frac{4m^2}{q_\parallel^2}\right)+\mathcal{T}^{(+)}(q_\parallel)\right], \quad (20)$$
$$\mathcal{T}^{(\pm)}(q_\parallel)=2q_\parallel^2m^2\int\frac{dp_3}{E_p}\frac{f_-(E_p)\pm f_+(E_p)}{q_\parallel^4-4(pq)_\parallel^2},$$

$$\mathcal{T}_\perp^{(\pm)}(q_\parallel,q_\parallel')$$
$$=2m^2\int\frac{dp_3}{E_p}\frac{f_-(E_p)\pm f_+(E_p)}{[q_\parallel^2+2(pq)_\parallel][q_\parallel'^2+2(pq')_\parallel]}. \quad (21)$$

The function $H(z)$ is defined as

$$H(z)=\frac{z}{\sqrt{z-1}}\arctan\frac{1}{\sqrt{z-1}}-1,\quad z\ge1,$$
$$H(z)=\frac{1}{2}\left(\frac{z}{\sqrt{1-z}}\ln\left|\frac{\sqrt{1-z}-1}{\sqrt{1-z}+1}\right|-2+i\pi\frac{z}{\sqrt{1-z}}\right),\quad z<1. \quad (22)$$

The expression for $\pi_{\mu\nu\rho}$ can be represented as

$$\pi_{\mu\nu\rho}=\frac{1}{q_\parallel^2q_\parallel'^2q_\parallel''^2}[(q'\tilde\varphi q''))\{(\tilde\varphi q)_\mu(\tilde\varphi q'')_\nu(\tilde\varphi q')_\rho\pi_\perp$$
$$+(\tilde\varphi q)_\mu(\tilde\Lambda q'')_\nu(\tilde\Lambda q')_\rho H$$
$$-(\tilde\Lambda q)_\mu(\tilde\varphi q'')_\nu(\tilde\Lambda q')_\rho H''-(\tilde\Lambda q)_\mu(\tilde\Lambda q'')_\nu(\tilde\varphi q')_\rho H'\} \quad (23)$$
$$+(q'q'')_\parallel(\tilde\Lambda q)_\mu(\tilde\varphi q'')_\nu(\tilde\varphi q')_\rho(H'-H'')$$
$$+(qq'')_\parallel(\tilde\varphi q)_\mu(\tilde\varphi q'')_\nu(\tilde\Lambda q')_\rho(H-H'')$$
$$+(qq')_\parallel(\tilde\varphi q)_\mu(\tilde\Lambda q'')_\nu(\tilde\varphi q')_\rho(H'-H)],$$

$$\pi_\perp=H+H'+H''+2\{q_\parallel^2q_\parallel'^2q_\parallel''^2$$
$$-2m^2[q_\parallel^2(q'q'')_\parallel H-q_\parallel'^2(qq'')_\parallel H'-q_\parallel''^2(qq')_\parallel H'']\} \quad (24)$$
$$\times\{q_\parallel^2q_\parallel'^2q_\parallel''^2-4m^2[q_\parallel'^2q_\parallel''^2-(q'q'')_\parallel^2]\}^{-1},$$

where

$$H\equiv H\left(\frac{4m^2}{q_\parallel^2}\right),\quad H'\equiv H\left(\frac{4m^2}{q_\parallel'^2}\right),\quad H''\equiv H\left(\frac{4m^2}{q_\parallel''^2}\right).$$

The expression for $V_{\mu\nu\rho}$ is

$$V_{\mu\nu\rho}=\pi_{\mu\nu\rho}[\pi_\perp\longrightarrow V_\perp,H\longrightarrow\mathcal{T}^{(+)}(q_\parallel),$$
$$H'\longrightarrow\mathcal{T}^{(+)}(q_\parallel'),H''\longrightarrow\mathcal{T}^{(+)}(q_\parallel'')],$$

$$V_\perp=\frac{1}{(q'\tilde\varphi q'')^2}\{(qq')_\parallel(qq'')_\parallel\mathcal{T}^{(+)}(q_\parallel)$$
$$-(qq')_\parallel(q'q'')_\parallel\mathcal{T}^{(+)}(q_\parallel') \quad (25)$$
$$-(qq'')_\parallel(q'q'')_\parallel\mathcal{T}^{(+)}(q_\parallel'')$$
$$+\frac{q_\parallel^2q_\parallel'^2q_\parallel''^2}{4}[\mathcal{T}_\perp^{(+)}(q_\parallel,q_\parallel')$$
$$+\mathcal{T}_\perp^{(+)}(-q_\parallel',-q_\parallel)+\mathcal{T}_\perp^{(+)}(-q_\parallel'',q_\parallel')+(q'\longleftrightarrow q'')]\}.$$

The derived expression for the amplitude is clearly gauge-invariant, since

$$q_\mu\Pi_{\mu\nu\rho}^{(0,1)}=q_\nu''\Pi_{\mu\nu\rho}^{(0,1)}=q_\rho'\Pi_{\mu\nu\rho}^{(0,1)}=0, \quad (26)$$

has the property of being real in the kinematic region $q_\parallel^2\le4m^2$,

$$\mathcal{M}(q,q',q'')=[\mathcal{M}(-q,-q',-q'')]^*, \quad (27)$$

and agrees with the previously derived expression for the vector part of the amplitude of the process $\gamma\gamma\longrightarrow\nu\bar\nu$ in a pure magnetic field in the case where $T=\mu=0$ [23].

Note that Eq. (17) for the amplitude was derived in the rest frame of the plasma. However, it can also be generalized to the case where the plasma moves as a whole along the magnetic field. For this purpose, it will suffice to make the following substitution in the electron and positron distribution functions appearing in integrals (20) and (21): $f_\pm(E_p)\longrightarrow f_\pm(up)$, where u_μ is the 4-vector of the medium ($u^2=1$). The condition for the absence of an electric field in this frame can be written in relativistically covariant form: $u_\mu\varphi_{\mu\nu}=0$. Note also that in contrast to the case of an electron–positron plasma without any magnetic field, where introducing the 4-velocity vector of the medium is required to write the two- or three-photon vertex in covariant form [24], in the presence of a magnetic field, as can be seen from our result, the three-photon vertex can be represented in covariant form without using the vector u_μ. This is

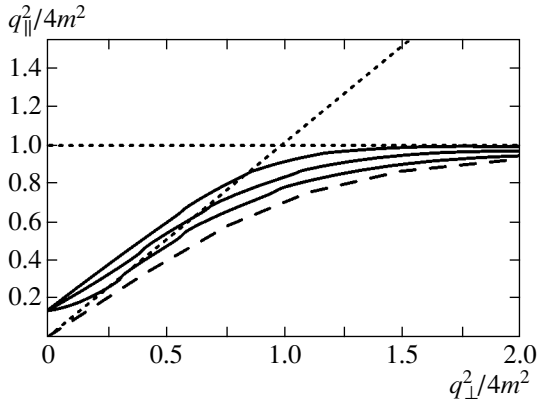

Fig. 3. Photon dispersion in a strong magnetic field (B/B_e = 200) and a charge-symmetric plasma (T = 1 MeV, μ = 0) at various angles between the photon momentum and the magnetic field direction: $\theta = \pi/2$ (upper solid curve), $\pi/6$ (middle solid curve), and $\pi/12$ (lower solid curve). The dashed curve represents the dispersion in the absence of a plasma.

because an orthogonal basic can be constructed from the field tensor and the 4-momentum vector:

$$b_\mu^{(1)} = \frac{(\varphi q)_\mu}{\sqrt{q_\perp^2}}, \quad b_\mu^{(2)} = \frac{(\tilde{\varphi} q)_\mu}{\sqrt{q_\parallel^2}},$$

$$b_\mu^{(3)} = \frac{q_\parallel^2(\Lambda q)_\mu - q_\perp^2(\tilde{\Lambda} q)_\mu}{\sqrt{q^2 q_\parallel^2 q_\perp^2}}, \quad b_\mu^{(4)} = \frac{q_\mu}{\sqrt{q^2}},$$

using which any tensor can be represented in covariant form.

To conclude this section, note that using result (17) with the substitution

$$\varepsilon_\mu \longrightarrow j_\mu \frac{G_F}{\sqrt{2}e}, \qquad \Pi_{\mu\nu\rho}^{(0,1)} \longrightarrow C_V \Pi_{\mu\nu\rho}^{(0,1)} + C_A \tilde{\varphi}_{\mu\sigma} \Pi_{\sigma\nu\rho}^{(0,1)} \tag{28}$$

we can easily determine the amplitude of the process $\gamma\gamma \longrightarrow \nu\bar{\nu}$ in a strongly magnetized plasma, and with the substitution

$$\varepsilon_\mu \longrightarrow q_\mu \frac{i q_{ae}}{2me}, \quad \Pi_{\mu\nu\rho}^{(0,1)} \longrightarrow \tilde{\varphi}_{\mu\sigma} \Pi_{\sigma\nu\rho}^{(0,1)}, \tag{29}$$

we can determine the contribution of the axion–photon interaction $a \longrightarrow \gamma\gamma$ induced by the plasma in a magnetic field to the amplitude. Here, C_V and C_A are the vector and axial constants of the effective $\nu\nu ee$ Lagrangian of the standard model,

$$C_V = \pm 1/2 + 2\sin^2\theta_W, \quad C_A = \pm\frac{1}{2},$$

θ_W is the Weinberg angle, the upper sign pertains to an electron neutrino, the lower sign corresponds to muon and tau neutrinos, j_μ is the Fourier transform of the neutrino current, and g_{ae} is the dimensionless axion–electron coupling constant.

It is interesting to note the following. The amplitudes of the processes $\gamma\gamma \longrightarrow \nu\bar{\nu}$ and $a \longrightarrow \gamma\gamma$ in a strong magnetic field are known to be independent of the field strength [23, 25]. In contrast, as can be seen from (17) and (18), the presence of a charge-asymmetric ($\mu \neq 0$) plasma leads to a linear increase in the amplitudes of these processes with magnetic field strength. This may prove to be important when considering the various applications of these processes in astrophysics.

3. THE PHOTON SPLITTING KINEMATICS

The kinematics of the process under consideration is determined by both the vacuum polarization and the photon scattering by plasma electrons and positrons. The eigenvalues of the polarization operator for a charge-symmetric plasma (μ = 0) can be taken from [26] and be represented as

$$\mathcal{P}^{(1)}(q) \approx -\frac{\alpha}{3\pi} q_\perp^2 - q^2 \Lambda(B), \tag{30}$$

$$\mathcal{P}^{(2)}(q) \approx -\frac{2\beta\alpha}{\pi}\left[H\left(\frac{4m^2}{q_\parallel^2}\right) + \mathcal{T}^{(+)}(q_\parallel)\right] - q^2\Lambda(B), \tag{31}$$

$$\mathcal{P}^{(3)}(q) \approx -q^2\Lambda(B), \tag{32}$$

where

$$\Lambda(B) = \frac{\alpha}{3\pi}\left(1.792 - \ln\frac{B}{B_e}\right).$$

It follows from our analysis of the solutions to the dispersion equations,

$$q^2 - \mathcal{P}^{(\lambda)}(q) = 0, \quad \lambda = 1, 2, 3, \tag{33}$$

that the modes with λ = 1, 2 and with the polarization vectors

$$\varepsilon_\alpha^{(1)}(q) = \frac{(q\varphi)_\alpha}{\sqrt{q_\perp^2}}, \quad \varepsilon_\alpha^{(2)}(q) = \frac{(q\tilde{\varphi})_\alpha}{\sqrt{q_\parallel^2}} \tag{34}$$

are physical in the charge-symmetric case, just as in the case of a pure magnetic field. However, it should be emphasized that the coincidence of the polarization vectors in the plasma is approximate, to within $O(1/\beta)$. At the same time, there are a number of differences between the plasma and the magnetic field. The first significant difference from the case of a pure magnetic field is that for a mode-2 photon (Fig. 3), the situation where this photon can have a positive value of q^2 in the kinematic region $q_\parallel^2 \leq 4m^2$ is possible. This is attributable to the appearance of eigenmodes in the plasma

with the frequency ω_p that can be determined from the equation

$$\omega_p^2 - \mathcal{P}^{(2)}(\omega_p, \mathbf{k} = 0) = 0. \quad (35)$$

In this region, a new channel, $\gamma_2 \longrightarrow \gamma_1\gamma_1$, which is forbidden in a magnetic field in the absence of a plasma, becomes possible. At the same time, the splitting channels $\gamma_1 \longrightarrow \gamma_2\gamma_2$ and $\gamma_1 \longrightarrow \gamma_1\gamma_2$, which are permitted in a magnetic field [15], are kinematically closed in this region. Another important difference is an essentially different dependence of the dispersion law in variables $q_\parallel^2$ and $q_\perp^2$ on the angle between the photon momentum and the magnetic field direction (see Fig. 3).

It follows from Eq. (31) that the eigenvalue of the polarization operator $\mathcal{P}^{(2)}(q)$ is large near the electron–positron pair production threshold. This suggests that the renormalization of the wavefunction for a photon of this polarization should be taken into account:

$$\varepsilon_\alpha^{(2)} \longrightarrow \varepsilon_\alpha^{(2)}\sqrt{Z_2}, \quad Z_2^{-1} = 1 - \frac{\partial \mathcal{P}^{(2)}(q)}{\partial \omega^2}. \quad (36)$$

The amplitudes for the permitted channels $\gamma_1 \longrightarrow \gamma_2\gamma_2$, $\gamma_1 \longrightarrow \gamma_1\gamma_2$, and $\gamma_2 \longrightarrow \gamma_1\gamma_1$ can be determined from (17) and be represented as

$$\mathcal{M}_{112} = i4\pi\left(\frac{\alpha}{\pi}\right)^{3/2}\frac{(q'\varphi q'')(q'\tilde{\varphi}q'')}{[q_\perp'^2 q_\parallel''^2 q_\perp^2]^{1/2}} \times\left[H\left(\frac{4m^2}{q_\parallel''^2}\right) + \mathcal{T}^{(+)}(q_\parallel'')\right], \quad (37)$$

$$\mathcal{M}_{122} = i4\pi\left(\frac{\alpha}{\pi}\right)^{3/2}\frac{(q'\tilde{\Lambda}q'')}{[q_\perp'^2 q_\parallel''^2 q_\perp^2]^{1/2}} \times\left\{(q\Lambda q'')\left[H\left(\frac{4m^2}{q_\parallel'^2}\right) + \mathcal{T}^{(+)}(q_\parallel')\right] + (q\Lambda q') \times\left[H\left(\frac{4m^2}{q_\parallel''^2}\right) + \mathcal{T}^{(+)}(q_\parallel'')\right]\right\}, \quad (38)$$

$$\mathcal{M}_{211} = \mathcal{M}_{112}(q \longleftrightarrow q''). \quad (39)$$

Analysis shows that the function $\mathcal{T}^{(+)} < 0$ almost in the entire domain of parameters T, ω, and q_z, while the function $H > 0$ in this domain. Thus, the functions H and $\mathcal{T}^{(+)}$, which define the dependences of the amplitude on the magnetic field and the plasma, respectively, appear in the derived expressions (37) and (38) with opposite signs. Consequently, in contrast to the case of a magnetic field, a plasma will suppress the amplitudes of the channels $\gamma_1 \longrightarrow \gamma_2\gamma_2$ and $\gamma_1 \longrightarrow \gamma_1\gamma_2$. At the same time, as we show below, the probabilities of these processes can be enhanced through the induced emission of photons in the case of a cold charge-symmetric plasma.

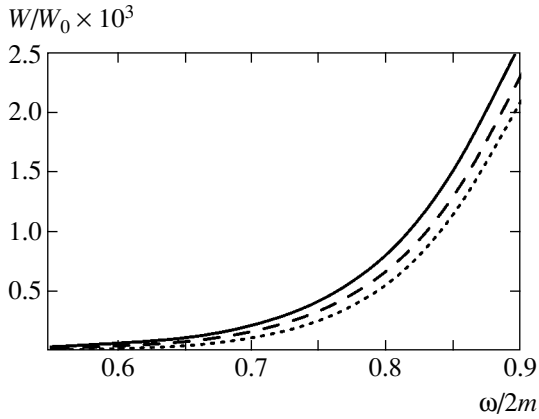

Fig. 4. Relative probability of the channel $\gamma_1 \longrightarrow \gamma_1\gamma_2$ in a strong magnetic field ($B/B_e = 100$) and a charge-symmetric plasma ($\mu = 0$) at temperatures of 50 keV (solid line) and 250 keV (dotted line), $W_0 = (\alpha/\pi)^3 m$. The dashed curve represents the probability in a pure magnetic field ($T = \mu = 0$) [8].

4. THE PHOTON SPLITTING PROBABILITY IN A STRONGLY MAGNETIZED MEDIUM

The general expression for the photon splitting probability can be written as

$$W_{\lambda\to\lambda'\lambda''} = \frac{g_{\lambda'\lambda''}}{32\pi^2\omega}\int|\mathcal{M}_{\lambda\lambda'\lambda''}|^2 Z_\lambda Z_{\lambda'} Z_{\lambda''} \times(1 + f_{\omega'})(1 + f_{\omega''}) \times\delta(\omega_\lambda(\mathbf{k}) - \omega_{\lambda'}(\mathbf{k} - \mathbf{k}'') - \omega_{\lambda''}(\mathbf{k}''))\frac{d^3k''}{\omega_{\lambda'}\omega_{\lambda''}}, \quad (40)$$

where

$$f_\omega = \left(\exp\frac{\omega}{T} - 1\right)^{-1}$$

is the photon distribution function, and the factor $g_{\lambda'\lambda''} = 1 - \delta_{\lambda'\lambda''}/2$ was introduced to allow for the possible identity of the photons in the final state.

In general, as can be seen from Eq. (40), calculating the probability is a fairly complex mathematical problem. Analysis shows that a photon splits through all the permitted channels with the highest probability when it propagates perpendicularly to the magnetic field direction. For plasma parameters typical of astrophysical objects (T = 50 keV, 250 keV, 1 MeV, $\mu = 0$) and magnetic field strengths $B = 100B_e$ and $200B_e$, we numeri-

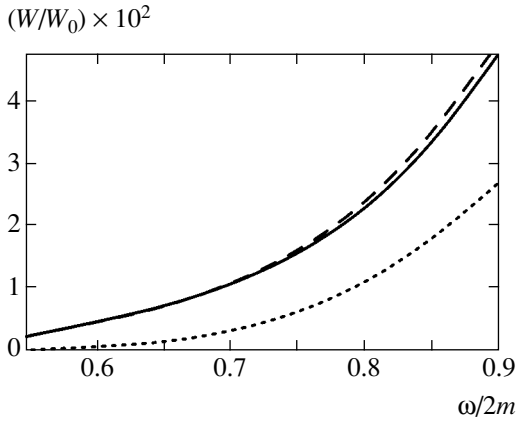

Fig. 5. Relative probability of the channel $\gamma_1 \longrightarrow \gamma_2\gamma_2$ for the same parameters and notation as those in Fig. 4.

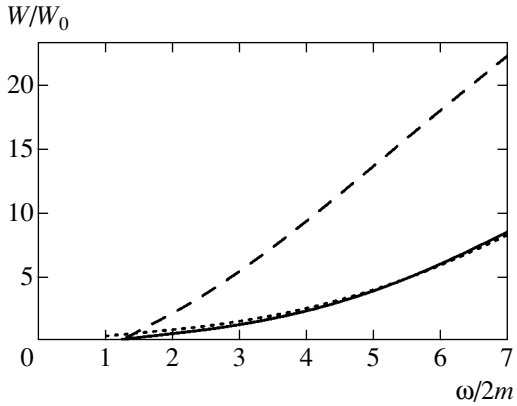

Fig. 6. Relative probability (solid line) of the channel $\gamma_1 \longrightarrow \gamma_1\gamma_2$ in a strong magnetic field ($B/B_e = 200$) and a hot plasma ($T = 1$ MeV, $\mu = 0$). The dashed line represents the probability in a pure magnetic field ($T = \mu = 0$) [8]; the dotted line represents the asymptotic limit (43).

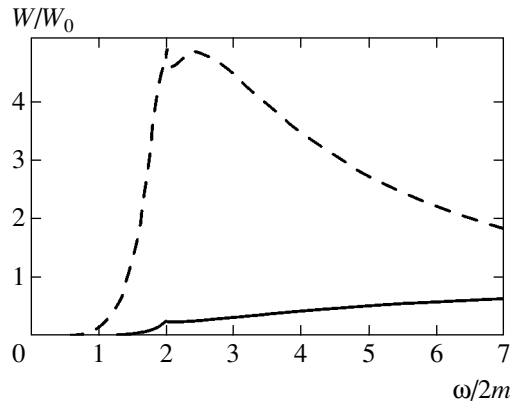

Fig. 7. Relative probability of the channel $\gamma_1 \longrightarrow \gamma_2\gamma_2$ for the same parameters as those in Fig. 6 (solid line). The dashed line represents the probability in a pure magnetic field ($T = \mu = 0$) [8].

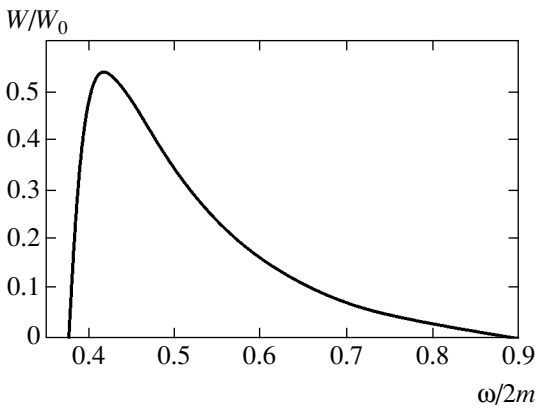

Fig. 8. Relative probability of the channel $\gamma_2 \longrightarrow \gamma_1\gamma_1$ in a strong magnetic field ($B/B_e = 200$) and a hot plasma ($T = 1$ MeV, $\mu = 0$).

cally calculated the photon splitting probabilities for the channels $\gamma_1 \longrightarrow \gamma_1\gamma_2$, $\gamma_1 \longrightarrow \gamma_2\gamma_2$, and $\gamma_2 \longrightarrow \gamma_1\gamma_1$. The results of our calculations are shown in Figs. 4–8. We see from Figs. 4 and 5 that the photon splitting probability can be higher than that in a pure magnetic field. This is because allowance for the influence of a plasma on the photon splitting in the low-temperature limit, $T \ll m$, is reduced only to allowance for the photon distribution functions and, as a result, leads to an increase in the phase volume of the reaction. Indeed, at temperatures $T \lesssim 0.1m$ and fields $B \approx 100B_e$, the following estimate holds for the plasma frequency: $\omega_p^2 \lesssim 10^{-5}m^2$. It follows from this estimate that the plasma frequency is low compared to the characteristic ($\sim T$) momenta on which integral (40) gains its value. This allows $\mathcal{P}^{(2)}(q)$ to be represented as

$$\mathcal{P}^{(2)}(q) \approx -\xi q_\parallel^2, \tag{41}$$

where, for convenience, we introduced the parameter

$$\xi = \frac{\alpha}{3\pi}\frac{B}{B_e},$$

that characterizes the degree of influence of the magnetic field. It thus follows that the dispersion law and the renormalization of the wavefunctions for a photon of the second mode can be written as

$$\omega^2 = \frac{q_\perp^2}{1+\xi} + q_3^2, \quad Z_2 \approx \frac{1}{1+\xi}. \tag{42}$$

In addition, for typical fields in astrophysical objects, $\xi \le 0.1$. In this case, the limit of collinear kinematics can be used. As we see from Eqs. (37) and (38), the channel $\gamma_1 \longrightarrow \gamma_1\gamma_2$ in this limit will be suppressed compared to the channel $\gamma_1 \longrightarrow \gamma_2\gamma_2$, as follows from

Figs. 4 and 5. On the other hand, as we see from Figs. 6 and 7, the influence of a hot plasma leads to the suppression of the probabilities of the channels $\gamma_1 \longrightarrow \gamma_1\gamma_2$ and $\gamma_1 \longrightarrow \gamma_2\gamma_2$ compared to the case of a pure magnetic field.

In the asymptotic limit $m^2 \le \omega^2\sin^2\theta \le eB$, we were able to derive simple expressions for the probabilities of the channels $\gamma_1 \longrightarrow \gamma_1\gamma_2$ and $\gamma_1 \longrightarrow \gamma_2\gamma_2$:

$$W_{1\to 12} \approx \frac{\alpha^3 T^2}{4\omega\sin^2\theta} \times\left[(1-u)^2 F\left(\frac{\omega(1+u)}{2T}\right) + (u \longrightarrow -u)\right], \tag{43}$$

$$W_{1\to 22} \approx \frac{\alpha^3 m^2}{4\omega} \times \frac{1}{1-\exp\left[-\frac{\omega}{T}(1-u)\right]}\frac{1}{1-\exp\left[-\frac{\omega}{T}(1+u)\right]} \times\left\{\tanh^2\left[\frac{\omega}{8T}(1-u)\right] + (u \longrightarrow -u)\right\}, \tag{44}$$

where $u = \cos\theta$, θ is the angle between the momentum vector of the decaying photon **k** and the magnetic field vector **B**,

$$F(z) = \int_0^z \frac{x\tanh^2(x/4)dx}{[1-\exp(-x)]\left[1-\exp\left(x-\frac{\omega}{T}\right)\right]}.$$

An analytical expression for the probability of the channel $\gamma_2 \longrightarrow \gamma_1\gamma_1$ can be derived in the case of a rare photon gas ($f_{\omega'} = f_{\omega''} = 0$) and be represented as

$$W_{2\to 11} \approx \frac{\alpha^3}{8\pi^2} Z_2\left[H\left(\frac{4m^2}{q_\parallel^2}\right) + \mathcal{T}^{(+)}(q_\parallel)\right]^2 \frac{q_\perp^2}{\omega} \times\left(\ln\frac{q_\parallel^2}{q_\perp^2} - 1 + \frac{q^2}{q_\parallel^2}\right)\theta(q^2). \tag{45}$$

In the limit $T = 0$, the asymptotic formula (43) transforms to the well-known expression in a strong magnetic field [8, 9, 20].

5. CONCLUSIONS

We have calculated the amplitude of the photon splitting process $\gamma \longrightarrow \gamma\gamma$, analyzed its kinematics, and found the polarization selection rules. For the permitted splitting channels, we calculated the corresponding probabilities by taking into account the photon dispersion and the renormalization of the photon wavefunctions. Our results show that the presence of a plasma, on the one hand, significantly changes the polarization selection rules compared to the case of a pure magnetic field. In particular, a new splitting channel, $\gamma_2 \longrightarrow \gamma_1\gamma_1$, which is forbidden in the absence of a plasma, becomes possible. On the other hand, we see from our numerical calculations (Figs. 7 and 8) and the asymptotic formulas (43) and (44) that a hot plasma has an overwhelming effect on the channels $\gamma_1 \longrightarrow \gamma_1\gamma_2$ and $\gamma_1 \longrightarrow \gamma_2\gamma_2$. Nevertheless, as can be seen from Figs. 4 and 5, a cold charge-symmetric plasma in combination with a strong magnetic field is capable of enhancing the splitting probability through these channels compared to the case of a pure magnetic field.

Analysis of the case of a charge-asymmetric plasma ($\mu \neq 0$) is a natural continuation of this work. For astrophysical applications, it makes sense to compare the calculated splitting probabilities through each channel with the probability of the Compton photon scattering. It is well known that in a weakly magnetized plasma, the process $\gamma \longrightarrow \gamma\gamma$ can dominate over the Compton scattering at certain parameters of the medium [17]. Therefore, exploring the possibility of such an effect in a strongly magnetized plasma is of considerable interest.

The results obtained can play an important role in shaping the spectra of such astrophysical objects as soft gamma repeaters (SGR).

ACKNOWLEDGMENTS

We thank N.V. Mikheev, V.B. Semikoz, A.V. Kuznetsov, A.A. Gvozdev, and A.Ya. Parkhomenko for helpful discussions and valuable remarks. This work was done as part of the subject plan of research at Yaroslavl State University on the instructions of Russian Education under partial financial support of the Council for Grants from the President of Russia for Support of Young Russian Scientists and Leading Scientific Schools of Russia (grant no. NSh-1916.2003.2) and the Russian Foundation for Basic Research (project no. 04-02-16253). M.V. Chistyakov thanks the Dynasty Foundation for Noncommercial Programs with assistance of the International Center for Fundamental Physics for financial support.

APPENDIX

TRANSFORMATION OF THE $\mathcal{S}$-MATRIX ELEMENTS

The calculation of the amplitude can be simplified significantly if the $\mathcal{S}$-matrix elements corresponding to the electron contributions are transformed to the $\mathcal{S}$-matrix elements corresponding to the positron contributions. For example, let us transform the $\mathcal{S}_-^{(1)}$-

matrix element corresponding to the first diagram in Fig. 2 to the $\mathcal{S}_+^{(6)}$-matrix element of the scattering by positrons corresponding to the same diagram, but with the photon permutation $\varepsilon_\alpha(q) \longleftrightarrow \varepsilon_\alpha^*(q')$ and the substitution $p \longrightarrow -p$. For this purpose, let us integrate (11) over d^4Y and d^4Z with allowance made for the asymptotic form of propagator (12). In the limit $\beta \gg q_\perp^2, q_\parallel^2$, we obtain the following expression for $\mathcal{S}_-^{(1)}$:

$$\mathcal{S}_-^{(1)} = -\frac{ie^3\beta(2\pi)^3}{4E\sqrt{2\omega V 2\omega' V 2\omega'' V}} \times \delta(\omega-\omega'-\omega'')\delta(q_2-q_2'-q_2'')\delta(q_3-q_3'-q_3'') \times \exp\left[\frac{ip_2}{\beta}(q_1-q_1'-q_1'')\right]\mathrm{Sp}\hat{\mathcal{A}}^{(1)}. \quad \text{(A.1)}$$

Here,

$$\hat{\mathcal{A}}^{(1)} = \hat{\mathcal{A}}_{--}^{(1)} + \hat{\mathcal{A}}_{-+}^{(1)} + \hat{\mathcal{A}}_{+-}^{(1)} + \hat{\mathcal{A}}_{-\perp}^{(1)} + \hat{\mathcal{A}}_{\perp-}^{(1)} + \hat{\mathcal{A}}_{\perp\perp}^{(1)}, \quad \text{(A.2)}$$

$$\hat{\mathcal{A}}_{--}^{(1)} = [2\beta-(q_\perp)^2-(q_\perp')^2+(q'\Lambda q)+i(q'\varphi q)] \times [(p\gamma)_\parallel+m](\varepsilon'\gamma)_\parallel\frac{(p\gamma)_\parallel+(q'\gamma)_\parallel+m}{(q')_\parallel^2+2(pq')_\parallel} \times (\varepsilon''\gamma)_\parallel\frac{(p\gamma)_\parallel+(q\gamma)_\parallel+m}{q_\parallel^2+2(pq)_\parallel}(\varepsilon\gamma)_\parallel\Pi_-, \quad \text{(A.3)}$$

$$\hat{\mathcal{A}}_{-+}^{(1)} = -[(p\gamma)_\parallel+m](\varepsilon'\gamma)_\parallel\frac{(p\gamma)_\parallel+(q'\gamma)_\parallel+m}{(q')_\parallel^2+2(pq')_\parallel} \times (\varepsilon''\gamma)_\perp[(p\gamma)_\parallel+(q\gamma)_\parallel+m](\varepsilon\gamma)_\perp\Pi_-, \quad \text{(A.4)}$$

$$\hat{\mathcal{A}}_{+-}^{(1)} = -[(p\gamma)_\parallel+m](\varepsilon'\gamma)_\perp[(p\gamma)_\parallel+(q'\gamma)_\parallel+m] \times (\varepsilon''\gamma)_\perp\frac{(p\gamma)_\parallel+(q\gamma)_\parallel+m}{q_\parallel^2+2(pq)_\parallel}(\varepsilon\gamma)_\parallel\Pi_-, \quad \text{(A.5)}$$

$$\hat{\mathcal{A}}_{-\perp}^{(1)} = -[(p\gamma)_\parallel+m](\varepsilon'\gamma)_\parallel\frac{(p\gamma)_\parallel+(q'\gamma)_\parallel+m}{(q')_\parallel^2+2(pq')_\parallel} \times\left\{(\varepsilon''\gamma)_\perp\left[(q\gamma)_\perp-\frac{(q'\gamma)_\perp+i(q'\varphi\gamma)}{2}\right](\varepsilon\gamma)_\parallel + (\varepsilon''\gamma)_\parallel\left[(q\gamma)_\perp-\frac{(q'\gamma)_\perp+i(q'\varphi\gamma)}{2}\right](\varepsilon\gamma)_\perp\right\}\Pi_-, \quad \text{(A.6)}$$

$$\hat{\mathcal{A}}_{\perp-}^{(1)} = -[(p\gamma)_\parallel+m] \times\left\{(\varepsilon'\gamma)_\perp\left[(q'\gamma)_\perp-\frac{(q\gamma)_\perp-i(q\varphi\gamma)}{2}\right](\varepsilon''\gamma)_\parallel + (\varepsilon'\gamma)_\parallel\left[(q'\gamma)_\perp-\frac{(q\gamma)_\perp-i(q\varphi\gamma)}{2}\right](\varepsilon''\gamma)_\perp\right\} \times\frac{(p\gamma)_\parallel+(q\gamma)_\parallel+m}{q_\parallel^2+2(pq)_\parallel}(\varepsilon\gamma)_\parallel\Pi_-, \quad \text{(A.7)}$$

$$\hat{\mathcal{A}}_{\perp\perp}^{(1)} = \frac{1}{4}[(p\gamma)_\parallel+m](\varepsilon'\gamma) \times[(\Lambda\gamma)_\beta+i(\gamma\varphi)_\beta](\varepsilon''\gamma)\gamma_\beta(\varepsilon\gamma)\Pi_-. \quad \text{(A.8)}$$

Here, the subscripts –, +, or ⊥ show which of the combinations of propagators, $\hat{S}_-\hat{S}_-$, $\hat{S}_-\hat{S}_+$, $\hat{S}_-\hat{S}_\perp$, or $\hat{S}_\perp\hat{S}_\perp$, contributes to the corresponding part of the spur.

The $\mathcal{S}_+^{(6)}$-matrix element of the scattering by positrons can be calculated in a similar way:

$$\mathcal{S}_+^{(6)} = -\frac{ie^3\beta(2\pi)^3}{4E\sqrt{2\omega V 2\omega' V 2\omega'' V}}\delta(\omega-\omega'-\omega'') \times\delta(q_2-q_2'-q_2'')\delta(q_3-q_3'-q_3'') \times\exp\left[\frac{ip_2}{\beta}(q_1-q_1'-q_1'')\right]\mathrm{Sp}\hat{\mathcal{B}}^{(6)}, \quad \text{(A.9)}$$

where $\hat{\mathcal{B}}^{(6)}$ is defined similarly to (A.2), with

$$\hat{\mathcal{B}}_{--}^{(6)} = -[2\beta-(q_\perp)^2-(q_\perp')^2+(q'\Lambda q)-i(q'\varphi q)] \times[(p\gamma)_\parallel-m](\varepsilon\gamma)_\parallel\frac{(p\gamma)_\parallel+(q\gamma)_\parallel-m}{q_\parallel^2+2(pq)_\parallel} \times(\varepsilon''\gamma)_\parallel\frac{(p\gamma)_\parallel+(q'\gamma)_\parallel-m}{(q')_\parallel^2+2(pq')_\parallel}(\varepsilon'\gamma)_\parallel\Pi_-, \quad \text{(A.10)}$$

$$\hat{\mathcal{B}}_{-+}^{(6)} = [(p\gamma)_\parallel-m](\varepsilon\gamma)_\parallel[(p\gamma)_\parallel+(q\gamma)_\parallel-m] \times(\varepsilon''\gamma)_\perp\frac{(p\gamma)_\parallel+(q'\gamma)_\parallel-m}{(q')_\parallel^2+2(pq')_\parallel}(\varepsilon'\gamma)_\perp\Pi_-, \quad \text{(A.11)}$$

$$\hat{\mathcal{B}}_{+-}^{(6)} = [(p\gamma)_\parallel-m](\varepsilon\gamma)_\perp\frac{(p\gamma)_\parallel+(q\gamma)_\parallel-m}{q_\parallel^2+2(pq)_\parallel} \times(\varepsilon''\gamma)_\perp[(p\gamma)_\parallel+(q\gamma)_\parallel-m](\varepsilon'\gamma)_\parallel\Pi_-, \quad \text{(A.12)}$$

$$\hat{\mathcal{B}}^{(6)}_{-\perp} = [(p\gamma)_\parallel - m]$$
$$\times\left\{(\varepsilon\gamma)_\perp\left[(q'\gamma)_\perp - \frac{(q\gamma)_\perp + i(q'\varphi\gamma)}{2}\right](\varepsilon''\gamma)_\parallel\right.$$
$$\left. + (\varepsilon\gamma)_\parallel\left[(q'\gamma)_\perp - \frac{(q\gamma)_\perp + i(q'\varphi\gamma)}{2}\right](\varepsilon''\gamma)_\perp\right\} \quad \text{(A.13)}$$
$$\times\frac{(p\gamma)_\parallel + (q'\gamma)_\parallel - m}{(q')^2_\parallel + 2(pq')_\parallel}(\varepsilon'\gamma)_\parallel\Pi_-,$$

$$\hat{\mathcal{B}}^{(6)}_{\perp-} = [(p\gamma)_\parallel - m](\varepsilon\gamma)_\parallel\frac{(p\gamma)_\parallel + (q\gamma)_\parallel - m}{q^2_\parallel + 2(pq)_\parallel}$$
$$\times\left\{(\varepsilon''\gamma)_\perp\left[(q'\gamma)_\perp - \frac{(q\gamma)_\perp - i(q\varphi\gamma)}{2}\right](\varepsilon'\gamma)_\parallel\right. \quad \text{(A.14)}$$
$$\left. + (\varepsilon''\gamma)_\parallel\left[(q'\gamma)_\perp - \frac{(q\gamma)_\perp - i(q\varphi\gamma)}{2}\right](\varepsilon'\gamma)_\perp\right\}\Pi_-,$$

$$\hat{\mathcal{B}}^{(6)}_{\perp\perp} = -\frac{1}{4}[(p\gamma)_\parallel - m](\varepsilon\gamma)\gamma_\beta(\varepsilon''\gamma)$$
$$\times[(\Lambda\gamma)_\beta + i(\gamma\varphi)_\beta](\varepsilon'\gamma)\Pi_-. \quad \text{(A.15)}$$

Performing the charge conjugation operation on all γ matrices under the spur sign in (A.9) and using the properties of the operators $\Pi_\pm$,

$$\mathrm{Sp}[\gamma_\mu\gamma_\nu\ldots\Pi_+] = \mathrm{Sp}[\gamma_\mu\gamma_\nu\ldots\Pi_-],$$
$$\Pi_\pm\gamma_{\perp\mu}\gamma_{\perp\nu}\Pi_\pm = (-\Lambda_{\mu\nu} \pm i\varphi_{\mu\nu})\Pi_\pm,$$

we find that the spur of the matrices $\hat{\mathcal{A}}^{(1)}$ can be transformed to the spur of the matrices $\hat{\mathcal{B}}^{(6)}$ in such a way that

$$\mathrm{Sp}\hat{\mathcal{A}}^{(1)} = -\mathrm{Sp}\hat{\mathcal{B}}^{(6)*}. \quad \text{(A.16)}$$

The remaining $\mathcal{S}$-matrix elements that define the plasma contribution to the photon splitting can be calculated by photon permutation. Using now relation (A.16) and Eq. (5), we can easily show that all of the even and odd (in external field) terms will contain the difference and sum of the electron and positron distribution functions, respectively.

REFERENCES

1. A. C. Harding, M. G. Baring, and P. L. Gonthier, Astrophys. J. **476**, 246 (1997).
2. M. G. Baring and A. C. Harding, Astrophys. J. Lett. **507**, L55 (1998).
3. R. C. Duncan and C. Thompson, Astrophys. J. **392**, L9 (1992).
4. V. O. Papanyan and V. I. Ritus, Tr. Fiz. Inst. im. P. N. Lebedeva, Akad. Nauk SSSR **168**, 120 (1986).
5. S. L. Adler and C. Schubert, Phys. Rev. Lett. **77**, 1695 (1996).
6. V. N. Baier, A. I. Milstein, and R. Zh. Shaisultanov, Phys. Rev. Lett. **77**, 1691 (1996).
7. V. N. Baĭer, A. I. Mil'shteĭn, and R. Zh. Shaĭsultanov, Zh. Éksp. Teor. Fiz. **111**, 52 (1997) [JETP **84**, 29 (1997)].
8. M. V. Chistyakov, A. V. Kuznetsov, and N. V. Mikheev, Phys. Lett. B **434**, 67 (1998).
9. A. V. Kuznetsov, N. V. Mikheev, and M. V. Chistyakov, Yad. Fiz. **62**, 1638 (1999) [Phys. At. Nucl. **62**, 1535 (1999)].
10. M. G. Baring, Phys. Rev. D **62**, 016003 (2000).
11. J. I. Weise, M. G. Baring, and D. B. Melrose, Phys. Rev. D **57**, 5526 (1998).
12. C. Wilke and G. Wunner, Phys. Rev. D **55**, 997 (1997).
13. D. B. Melrose, Plasma Phys. **16**, 845 (1974).
14. V. de la Incera, E. Ferrer, and A. E. Shabad, Tr. Fiz. Inst. im. P. N. Lebedeva, Akad. Nauk SSSR **169**, 183 (1986).
15. S. L. Adler, Ann. Phys. (New York) **67**, 599 (1971).
16. T. Bulik, Acta Astron. **48**, 695 (1998).
17. P. Elmfors and B. Skagerstam, Phys. Lett. B **427**, 197 (1998).
18. H. Gies, Phys. Rev. D **61**, 085021 (2000).
19. J. M. Martinez Resco and M. A. Valle Basagoiti, Phys. Rev. D **64**, 016006 (2001).
20. A. V. Kuznetsov and N. V. Mikheev, *Electroweak Processes in External Electromagnetic Fields* (Springer, New York, 2003).
21. A. I. Akhiezer and V. B. Berestetskiĭ, *Quantum Electrodynamics*, 4th ed. (Nauka, Moscow, 1981; Wiley, New York, 1965).
22. J. Schwinger, Phys. Rev. **82**, 664 (1951).
23. M. V. Chistyakov and N. V. Mikheev, Mod. Phys. Lett. A **17**, 2553 (2002).
24. E. S. Fradkin, Tr. Fiz. Inst. im. P. N. Lebedeva, Akad. Nauk SSSR **29**, 7 (1965).
25. N. V. Mikheev, A. Ya. Parkhomenko, and L. A. Vasilevskaya, Yad. Fiz. **63**, 1122 (2000) [Phys. At. Nucl. **63**, 1046 (2000)].
26. A. E. Shabad, Tr. Fiz. Inst. im. P. N. Lebedeva, Akad. Nauk SSSR **192**, 5 (1988).

Translated by V. Astakhov

Journal of Experimental and Theoretical Physics, Vol. 101, No. 4, 2005, pp. 646–652.
Translated from Zhurnal Éksperimental'noĭ i Teoreticheskoĭ Fiziki, Vol. 128, No. 4, 2005, pp. 752–759.

NUCLEI, PARTICLES, FIELDS, GRAVITATION, AND ASTROPHYSICS

Analysis of Small-Scale Wave Structures in the Saturnian A Ring Based on Data from the Cassini Interplanetary Spacecraft

E. B. Postnikov[a] and A. Yu. Loskutov[b]

[a] *Kursk State University, ul. Radishcheva 33, Kursk, 305000 Russia*
[b] *Moscow State University, Vorob'evy gory, Moscow, 119992 Russia*
e-mail: loskutov@chaos.phys.msu.ru
Received April 19, 2005

Abstract—The images obtained during the second half of 2004 by the Cassini interplanetary spacecraft are analyzed. The method of analysis is based on the original algorithm of a continuous wavelet transform with a complex Morlet wavelet that reduces the integral transform to solving a Cauchy problem for a system of partial differential equations. This method is shown to be a fairly efficient tool for analyzing the instant variable periodicity of the spatial particle inhomogeneity in the radial structure of Saturn's rings. © *2005 Pleiades Publishing, Inc.*

1. INTRODUCTION

The structure of planetary rings generally and Saturn's rings specifically arouses constant scientific interest in studying them as a dynamical system of many particles (see, e.g., [1] for an overview of the status of the problem as of 2002 and references). A characteristic feature of Saturn's main rings (A, B, C) is their small-scale structure detected by the Voyagers. Its preliminary analysis (see [2–4]) led to a model for the formation of thin spiral density waves through the resonant interaction of ring particles with Saturnian satellites.

Subsequently, a window Fourier transform was used to analyze the Voyager data on the A ring [5]. This analysis revealed and identified about 40 resonance structures attributed to the influence of various Saturnian satellites. At the same time, the authors of [5] pointed out a number of resonance regions in which the achieved resolution and the capabilities of the processing algorithm did not allow any features in the ring matter distribution to be detected.

Over the last year, the data obtained by the Cassini spacecraft, including high-resolution photographs (see [6] for a preliminary report of the Cassini task group), have opened up new opportunities for studies in this field. The wavelet transform, a method of analysis that has been actively developed in the past two decades, can be used to process them. An important advantage of this technique over other approaches (see, e.g., [7]) is a high degree of localization of the basis function in both the spatial and frequency domains. This allows nonstationary signals to be effectively studied based on the concept of an instant frequency (or period). The interrelationship between the window width and the instant period (the window contracts for high-frequency signals and expands for low-frequency signals; as a result, the effective number of oscillations of the basis sine wave in the window is conserved) favorably distinguishes the wavelet transform from the window Fourier transform.

As applied to celestial mechanics, the wavelet analysis method has shown its efficiency in processing the solution functions generated by Hamiltonian systems, in particular, in the three-body problem [8] and in studying the variations in the revolution periods of asteroids in near-resonance regions [9]. As applied to the Saturnian system, the wavelet transform was suggested to be used to study the structure of the Encke gap based on Voyager-2 data [10]. Since the main objective of the authors of the cited paper was to identify structures of various scales in a noisy image, only real wavelets were used. However, determining the pattern of local periodicity in Saturn's ring structure requires using a transform with a complex wavelet. The possible efficiency of such an approach to this problem was demonstrated with specific examples in [6, 11].

The main goal of this paper is to study the small-scale structure of Saturn's A ring using a new approach to calculating the complex integral transform with a Morlet wavelet based on the representation of the wavelet transform as the solution to a system of partial differential equations.

2. DESCRIPTION OF THE METHOD

The most suitable method for solving the problem of distinguishing the instant period in a signal is the com-

plex continuous wavelet transform

$$w(a, b) = \int_{-\infty}^{\infty} f(t)\psi^*\left(\frac{t-b}{a}\right)\frac{dt}{a} \quad (1)$$

(the asterisk denotes complex conjugate) in the amplitude normalization

$$\int_{-\infty}^{\infty}\left|\psi\left(\frac{t-b}{a}\right)\right|\frac{dt}{a} = \text{const} \quad (2)$$

with the Morlet basis. In the exact form that satisfies the admissibility condition

$$\int_{-\infty}^{\infty}\psi(\xi)d\xi = 0,$$

it is

$$\psi(\xi) = \frac{1}{\sqrt{2\pi}} \times\left[\exp(-i\omega_0\xi) - \exp\left(-\frac{\omega_0^2}{2}\right)\right]\exp\left(-\frac{\xi^2}{2}\right). \quad (3)$$

The corresponding wavelet transform $w(a, b)$ acts as a local spectral distribution in periods a of the harmonics that constitute the signal in the neighborhood of point b.

However, in most practical applications, the second term in Eq. (3) is disregarded if the basis frequency is fairly high (in general, $\omega_0 \geq 5$), and the following simplified definition is used:

$$\psi(\xi) = \frac{1}{\sqrt{2\pi}}\exp(-i\omega_0\xi)\exp\left(-\frac{\xi^2}{2}\right). \quad (4)$$

It corresponds to normalization (2) with const = $\exp(\omega_0^2/2)$. A significant advantage of this approximation is the simple relationship between the instant period of the wavelet transform and the period of the harmonic oscillation with frequency ω. In other words, the two-dimensional plot of the distribution of the modulus of the wavelet transform for a complex monochromatic function has a line of maximum that corresponds to the period $a = \pm\omega_0/\omega$. The factor, which is a Gaussian function, performs a smoothing that automatically suppresses the signal noise. The relationship also remains valid for a real function.

Varying the basis frequency allows the frequency resolution to be changed: the higher the frequency ω_0, the more oscillations the basis wavelet function executes on the characteristic window width and the closer the modulus of the wavelet transform to the locally smoothed Fourier spectrum. At low ω_0, it reveals an individual spike.

It should be noted that, despite such advantages as the simplicity of the algorithm and the high speed of calculations, the standard method for calculating the continuous wavelet transform associated with the intermediate passage to the frequency domain and with the use of the fast Fourier transform algorithm has a number of shortcomings. The latter follow from peculiarities of the fast Fourier transform: the initial data must be represented by a sample of 2^N equidistant nodes. Departures from this condition lead to a significant complication of the calculations and/or loss of accuracy.

Therefore, in this paper, we introduce an alternative algorithm based on the observation that the transform obtained by the convolution with the Morlet wavelet satisfies the differential equation

$$\left(a\frac{\partial^2}{\partial b^2} - \frac{\partial}{\partial a} - i\omega_0\frac{\partial}{\partial b}\right)w(a, b) = 0. \quad (5)$$

The latter was derived in [12], but it was used only to demonstrate the local properties of the a priori known wavelet transform.

Let us represent the result of the wavelet transform as a sum of the real and imaginary parts:

$$w(a, b) = u(a, b) + iv(a, b),$$

for which Eq. (5) can be written as the system

$$\frac{\partial u}{\partial a} = a\frac{\partial^2 u}{\partial b^2} + \omega_0\frac{\partial v}{\partial b}, \quad (6)$$

$$\frac{\partial v}{\partial a} = a\frac{\partial^2 v}{\partial b^2} - \omega_0\frac{\partial u}{\partial b}. \quad (7)$$

To find the corresponding initial conditions, let us write the integral transform (1) with kernel (4) as

$$w(a, b) = \int_{-\infty}^{\infty} f(t)\frac{\exp\left[-\frac{1}{2}\left(\frac{t-b}{a} - i\omega_0\right)^2\right]}{\sqrt{2\pi a^2}}dt.$$

This integral is known to be independent of the imaginary subtrahend in the exponent, and the kernel of the transform in the limit $a \longrightarrow 0$ is a delta function. Consequently, $w(0, b) = f(b)$. The initial conditions for the system of differential equations (6) and (7) follow from the latter equality:

$$u(0, b) = \text{Re}(f(b)),$$

$$v(0, b) = \text{Im}(f(b)).$$

The modulus of the wavelet transform required for our

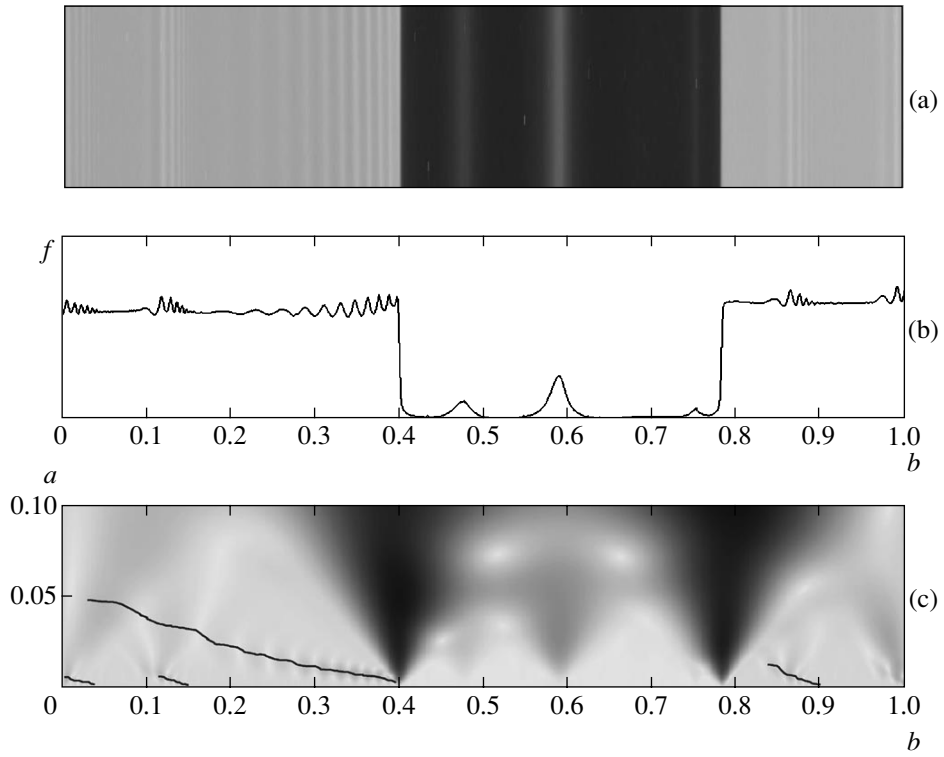

Fig. 1. The Encke gap. The coordinate origin almost coincides with the position of the 11 : 10 resonance with Pandora. The next wave structure is generated by the 15 : 14 resonance with Prometheus. The first wave train after the gap is generated by the 12 : 11 resonance with Pandora.

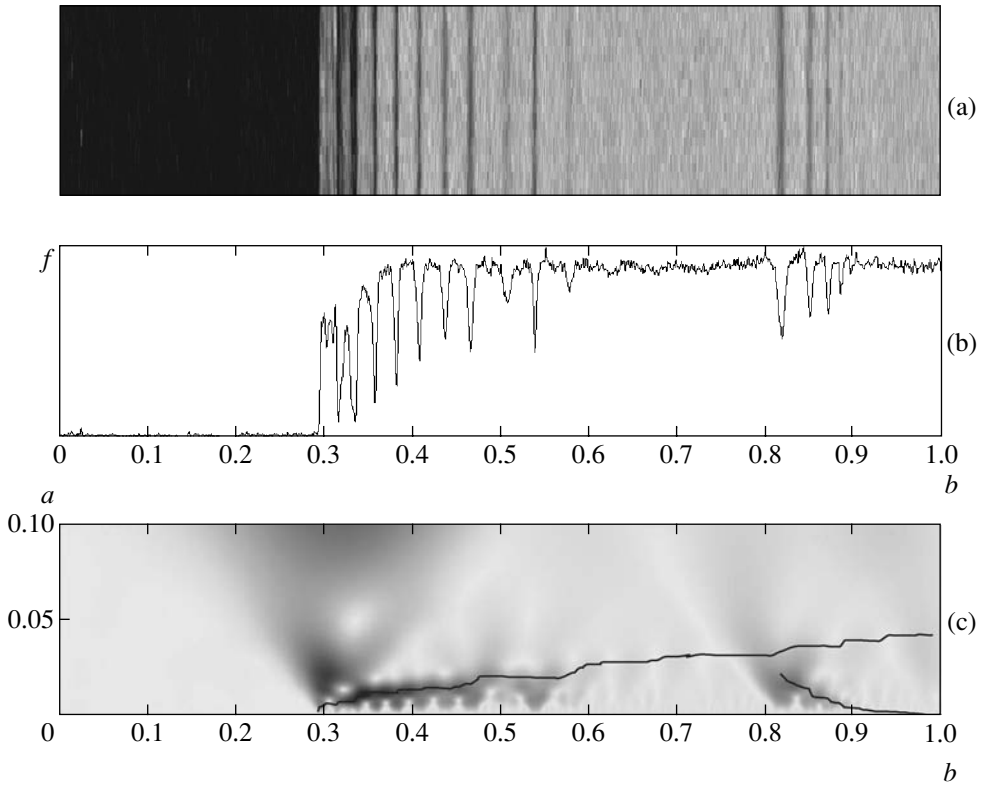

Fig. 2. The far (from Saturn) edge of the Encke gap.

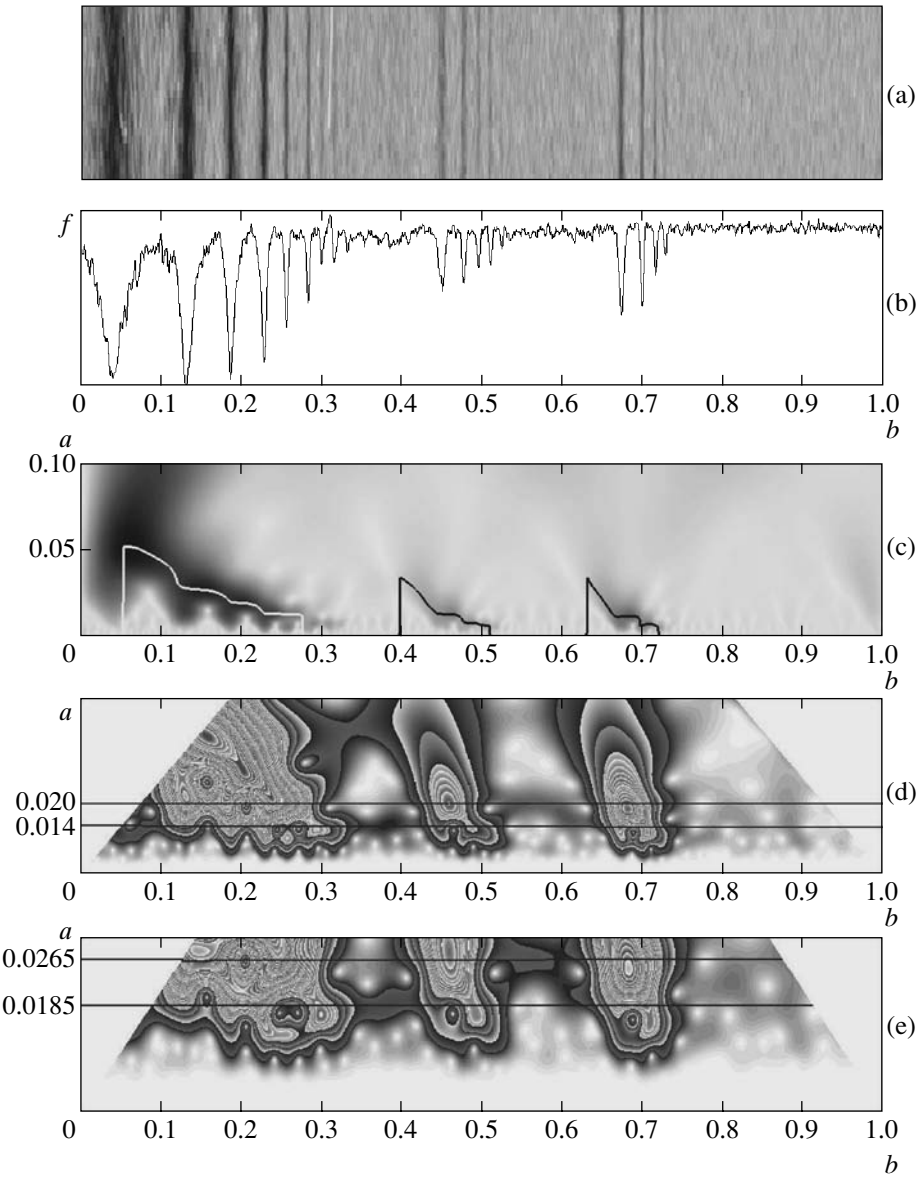

Fig. 3. The outer part of the A ring containing the 4 : 3, 6 : 5, and 7 : 6 resonance with Janus, Pandora, and Prometheus, respectively.

analysis can be easily calculated:

$$|w(a, b)| = \sqrt{u^2(a, b) + v^2(a, b)}.$$

3. IMAGE PROCESSING RESULTS FOR SEGMENTS OF THE A RING

We use the algorithm described above to analyze the radial matter density distribution at the center of Saturn's A ring based on photographic data from the Cassini spacecraft (July 2004). For our analysis, we chose images from the NASA/JPL/Space Science Institute collection. A narrow stripe was separated from each image in the radial direction: PIA06099 (1022 × 20 pixels, Fig. 1a), PIA06094 (891 × 23 pixels, Fig. 2a), PIA06095 (902 × 23 pixels, Fig. 3a), and PIA06093 (855 × 20 pixels, Fig. 4a). It is easy to verify that the curvature of the structures constituting the ring within each sample may be disregarded. For clarity, all images were significantly stretched in the transverse direction.

We used the pair of initial conditions $u(0, b) = f(b)$ and $v(0, b) = 0$, where the function $f(b)$ is obtained by averaging over the sample (Figs. 1b–4b). Since the signal length is finite, the Cauchy problem for Eqs. (6) and (7) must be replaced with a boundary-value problem. We used boundary conditions of the first kind: respectively, the initial signal value at these points and zero for the real and imaginary parts of the wavelet transform.

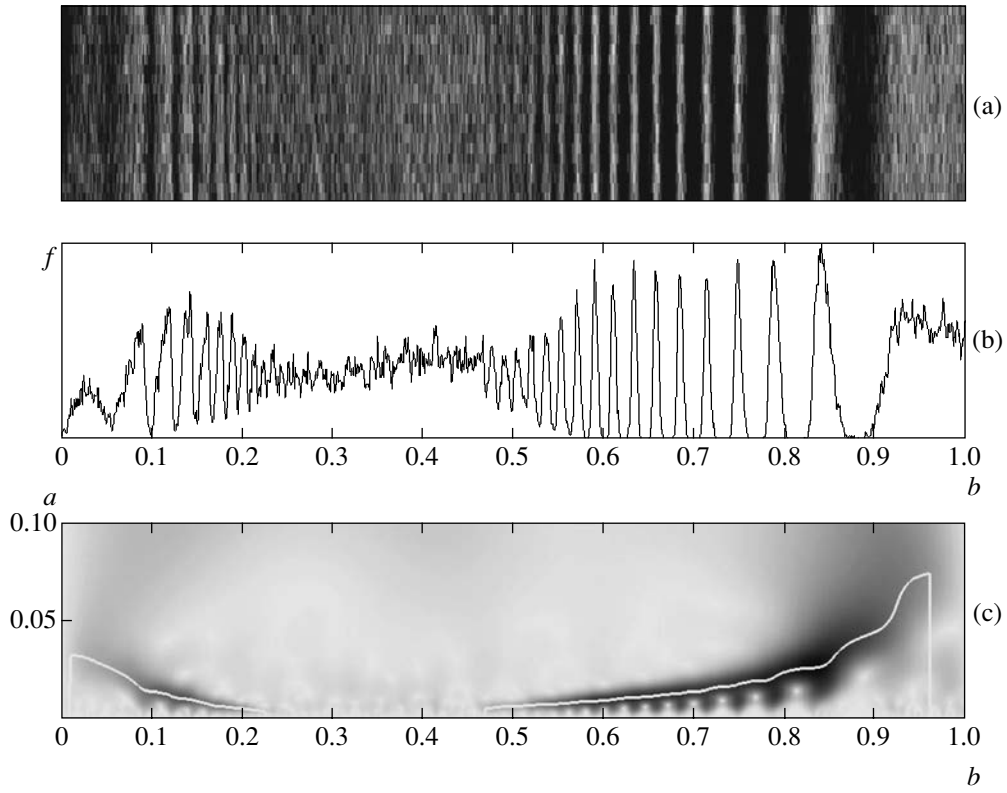

Fig. 4. The density waves generated by the 12 : 11 and 5 : 3 resonances with Prometheus and Mimas, respectively.

Values that are sufficiently high and convenient for interpreting the results should be chosen for the basis frequency. The frequencies $\omega_0 = \pi$ (Figs. 1c–4c), 1.5π (Figs. 3d and 5b), and 2π (Fig. 3c and 5c) in dimensionless units of the sample length satisfy these conditions. At the last two basis frequencies, the regions distorted by the edge effect were removed from the figures. A quantitative criterion for this in the (b, a) plane is the condition

$$\exp\left(-\frac{(b-b_0)^2}{2a^2}\right) \geq 10^{-5},$$

where $b_0 = 0$ or 1.

The image being processed (Fig. 1a) represents the neighborhood of the Encke gap. A characteristic feature that is not revealed by the window Fourier transform is the possibility of tracing the distribution of the instant spatial period of the wave structure of the Encke gap edge. In the plot of the modulus of the wavelet transform (Fig. 1c), the lines of maxima are painted black. Note that the large-scale development of a spiral density wave, which is accompanied by an increase in its instant period, admits of a continuous passage to the line of maximum corresponding to the large-scale spikes. As follows from Fig. 1c, the characteristic size on such scales is on the order of the extent of the train of resonant waves generated by the 11 : 10 and 15 : 14 resonances with the satellites Pandora and Prometheus, respectively. There is a clear overlap between the lines of maxima of various resonances (Fig. 1c). A similar structure (but without a detailed analysis) has also been revealed recently [6]. However, only one line of maximum may be preserved in our approach, which allows relatively low ω_0 to be used. We also found a similar overlap between the lines of maximum of the instant period for the small-scale and large-scale (formed by Pan) resonant wave structures in the outer part of the Encke gap (Fig. 2).

Another type of inhomogeneity that the suggested wavelet analysis method can reveal consists in the presence of a small-scale periodicity in the interresonance intervals. The high (up to 270 m per pixel) resolution of the Cassini images and the algorithm described above, which admits (in view of the peculiarities of the numerical solution of differential equations) of a small step in scale variable, makes such a study possible.

To analyze in detail the small-scale structure in the interresonance region, let us consider the density waves generated by the resonances of Janus, Pandora, and Prometheus. The characteristic ladder form of their instant spatial period is shown in Fig. 3c. To achieve a higher spatial resolution, let us increase the basis frequency to $\omega_0 = 1.5\pi$ (Fig. 3d) and 2π (Fig. 3e). To increase the sensitivity to the modulus of a low amplitude, we will use various shades of gray for high values. This leads to a smearing of the resonance lines, allow-

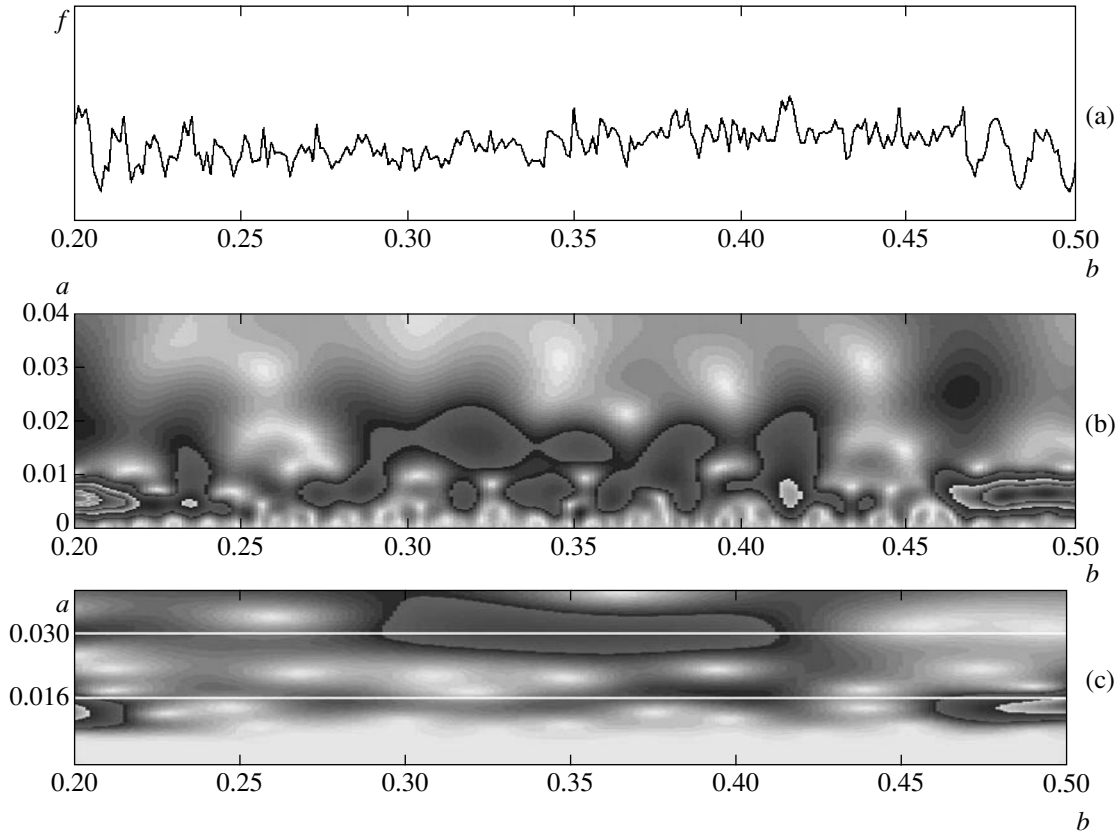

Fig. 5. The region between the 12 : 11 and 5 : 3 resonances with Prometheus and Mimas, respectively.

ing an almost stably periodic signal on the segment [0.35, 0.45] connecting the first two resonant wave trains to be highlighted by brightness lines. A short-wavelength signal is also detected on the segment [0.52, 0.67] between the second and third resonances. However, it has an unstable spatial frequency varying within the range 75π–107π (in units of the sample length). The second frequency is equal to the frequency of the wave between the resonances of Janus (4 : 3) and Pandora (6 : 5). Its refinement using the basis frequency $\omega_0 = 2\pi$ yields $108(\pm1)\pi$ and confirms the stability of the monochromaticity.

The spiral density waves in Fig. 4 generated by the resonances of Prometheus (12 : 11) and Mimas (5 : 3) are among the most distinct in Saturn's ring structure. For this reason, they were studied in detail and modeled using Voyager data (see the earlier papers [2–4] and [5]). Let us analyze the interresonance region by the wavelet method using a recent Cassini photograph. Analysis of the images obtained by a transform with a high frequency resolution (Figs. 5b, 5c) reveals no stable periodicity in this region. However, the existence of an unstable signal with a spatial frequency of 125π (see Fig. 5c, where the lines of maxima are painted white) can be easily seen. In fact, it is close to the highest frequency of the resonant trains. In addition, a short region of more intense periodicity with a frequency of 67π occupying the segment [0.30, 0.41] of the signal under study is revealed. Examining the feature of the instant period on the segment [0.36, 0.38] with a shape similar to the resonance inclined line of the instant period, we can assume that the frequency of 67π is related to the longest-wavelength resonant perturbations.

4. CONCLUSIONS

Thus, the continuous wavelet transform with a complex Morlet wavelet is an efficient tool for studying the spatial radial structure of Saturn's rings. It enables the evolution of the instant period to be traced in detail on various scales. A detailed analysis of the wave processes in Saturn's ring matter should include the interaction of the long-wavelength perturbation segments with the small-scale wave trains generated by the resonant interaction with other satellites and the formation mechanisms of nearly monochromatic waves in the regions connecting the high-frequency ends of the resonant zones.

The main results that allow a wavelet analysis of high-resolution Cassini images to be performed are the following. There are overlaps between the lines of the instant period of the resonant waves generated by Pan and the smaller-scale wave trains generated by other satellites near both boundaries of the Encke gap. In

addition, nearly monochromatic waves of various extents, up to the joining of the resonant trains, can be present in the interresonance regions.

It should be noted that our analysis is preliminary one and is in further elaboration with allowance made for the image adjustment depending on the inclination at which the photographs were taken and the absolute distances to the region of the rings under study.

REFERENCES

1. L. W. Esposito, Rep. Prog. Phys. **65**, 1741 (2002).
2. F. H. Shu, J. N. Cuzzi, and J. J. Lissauer, Icarus **53**, 185 (1983).
3. F. H. Shu, C. Yuan, and J. J. Lissauer, Astrophys. J. **291**, 356 (1985).
4. F. H. Shu, C. Yuan, and J. J. Lissauer, Astrophys. J. **299**, 542 (1985).
5. L. J. Spilker, S. Pilorz, L. A. Lane, *et al.*, Icarus **171**, 373 (2004).
6. C. C. Porco, E. Baker, J. Barbara, *et al.*, Science **307**, 1226 (2005).
7. *The Transforms and Applications Handbook*, Ed. by A. Poularikas (IEEE Press, New York, 2000).
8. L. V. Vela-Arevalo, PhD Thesis (Caltech, 2002).
9. T. A. Michtchenko and D. Nesvorný, Astron. Astrophys. **313**, 674 (1996).
10. Ph. Bendjoya, J.-M. Petit, and F. Spahn, Icarus **105**, 385 (1993).
11. E. B. Postnikov and A. Loskutov, astro-ph/0502375.
12. M. Haase, in *Paradigms of Complexity*, Ed. by M. M. Novak (World Sci., Singapore, 2000), p. 287.

Translated by V. Astakhov

Journal of Experimental and Theoretical Physics, Vol. 101, No. 4, 2005, pp. 653–660.
Translated from Zhurnal Éksperimental'noĭ i Teoreticheskoĭ Fiziki, Vol. 128, No. 4, 2005, pp. 760–767.

ORDER, DISORDER, AND PHASE TRANSITIONS IN CONDENSED SYSTEMS

Effective Demagnetization Factor of Quasi-Single-Crystal and Granular $YBa_2Cu_3O_{7-x}$ Thin Disks

Kh. R. Rostami

Institute of Radio Engineering and Electronics, Russian Academy of Sciences, Fryazino, Moscow oblast, 141190 Russia

e-mail: rost18@yandex.ru

Received February 25, 2005

Abstract—The effective demagnetization factor n_{eff} of quasi-single-crystal and granular $YBa_2Cu_3O_{7-x}$ thin disks with different values of the edge barrier height, bulk pinning, and demagnetization is measured by a Hall probe with the use of a trapped magnetic flux as a test field. As the trapped magnetic flux increases, n_{eff} reaches a maximum as a function of the external field; the qualitative behavior of this maximum is independent of the morphology of a sample. It is shown that, when the densities of intragranular and intergranular critical currents differ by about one and a half orders of magnitude, the demagnetization factor n_{eff} is mainly determined by the geometry of a sample rather than by the energy of Josephson coupling between grains. The experimental results are in agreement with the results of calculations performed within the proposed model of isolated crystallites (grains). © *2005 Pleiades Publishing, Inc.*

1. INTRODUCTION

Recently, nonlocal phenomena, demagnetization phenomena, and the phenomena of bulk and edge pinning of a magnetic flux in high-temperature superconductors (HTSCs) have been intensively studied for constructing a generalized model of the critical state of type-II semiconductors (see, for example, [1–6]). It has been found that, due to these phenomena, the distribution of the magnetic-flux and current-density profiles in HTSC plates and films deviates from that described by the Bean model [7]. Therefore, the following topics are of considerable interest: (a) the transformation of the demagnetization factor of a sample under an increasing external magnetic field H_0 [8, 9]: after the penetration of the field into the sample, the effective demagnetization factor n_{eff}, which represents an integral demagnetization factor of individual crystallites (grains), becomes a unified macroscopic demagnetization factor n of the sample; and (b) the influence of the n_{eff} of a sample on

(1) the processes of penetration (exit), distribution, and trapping of a magnetic flux;

(2) the redistribution of the current density in a sample;

(3) the transition [10] from the domain of fields in which the critical state is established in a Josephson medium [11, 12] to the domain of fields in which the critical state is established in individual crystallites [10, 13];

(4) the manifestation of the above-listed phenomena; and

(5) the formation of macroscopic parameters of HTSC samples.

The dependence of demagnetization fields on the prehistory of a sample and on the configuration of a trapped magnetic flux [14, 15], as well as the demagnetization factor of a sample with the trapped magnetic flux [2], have also been poorly studied.

To avoid difficulties associated with consideration of the demagnetization factor of crystallites in analyzing the processes that occur in a Josephson medium, one usually assumes that all grains in HTSC samples are of the same size and have the shape of either infinitely long cylinders [13, 16] or infinitely thin plates [17] in a longitudinal field.

In the present paper, we propose and demonstrate a method for the experimental measurement of n_{eff}. In dense, nearly sintered HTSC samples, n_{eff} is mainly determined by the total demagnetization factor of crystallites. It is well-known [18] that the critical current in HTSC ceramics and polycrystals at 77.4 K decrease by more than two orders of magnitude under the application of a field of up to 100 Oe. When the local scattering fields of Abrikosov vortices trapped into crystallites are greater than the characteristic field H_{0m} that suppresses the intercrystallite (intergranular) critical current J_{cJ},[1] weak bonds are broken. As a magnetic flux is trapped by a sample and as this trapping becomes stronger, one can observe the dynamics of the formation of isolated conglomerates of crystallites, which represent either noninteracting [13, 19] identically magnetized crystallites [10] or their combinations. The magnetization $\mathbf{I} = V^{-1}\Sigma\mathbf{M}_{\text{g}}$ of a sample is determined by the screening

[1] For $YBa_2Cu_3O_{7-x}$ at a temperature of 77.4 K, $H_{0m} \approx 22.5$ Oe, while the first critical magnetic field of grains is $H_{\text{c1g}} \approx 40$ Oe [18].

supercurrents $\mathbf{J}_{cg} = \mathbf{c}\,\mathrm{curl}\,\mathbf{M}_g$ that are formed within individual crystallites, where V is the sample volume, $\mathbf{M}_g$ is the magnetic moment, and $\mathbf{c}$ is the velocity of light) [20].

As is known, the internal field in a sample is given by [21]:

$$H_i = H_0 - H_D. \quad (1)$$

The greater the magnetization $4\pi n\mathbf{I}$ of the sample, the stronger the demagnetization field H_D. To determine the n_{eff} as a function of the density of the trapped magnetic flux B_{tr} and H_0 in two close regimes ZFC_1 and ZFC_2 (see the explanation below), we magnetize a sample so that $B_{\mathrm{tr}}^{\mathrm{ZFC}_2} > B_{\mathrm{tr}}^{\mathrm{ZFC}_1}$. The field magnitudes are given by

$$H_{i2} = H_0 - 4\pi n_{\mathrm{eff}} B_{\mathrm{tr}}^{\mathrm{ZFC}_2}, \quad (2)$$

$$H_{i1} = H_0 - 4\pi n_{\mathrm{eff}} B_{\mathrm{tr}}^{\mathrm{ZFC}_1}. \quad (3)$$

Let us subtract Eq. (2) from Eq. (3) to obtain

$$n_{\mathrm{eff}} = \frac{H_{i1} - H_{i2}}{4\pi(B_{\mathrm{tr}}^{\mathrm{ZFC}_2} - B_{\mathrm{tr}}^{\mathrm{ZFC}_1})}. \quad (4)$$

According to (4), the quantity $H_{i1} - H_{i2}$ increases with $B_{\mathrm{tr}}^{\mathrm{ZFC}_2} - B_{\mathrm{tr}}^{\mathrm{ZFC}_1}$. Since a decrease in the sample volume due to the suppression of weak bonds occurs faster than the magnetization of crystallites, the quantity $H_{i1} - H_{i2}$ grows faster than $B_{\mathrm{tr}}^{\mathrm{ZFC}_2} - B_{\mathrm{tr}}^{\mathrm{ZFC}_1}$, although it follows the same variation law. In Section 4, we present an algorithm for calculating (for given H_0 and B_{tr}) the values of n_{eff} from the experimental functions of H_0:

$$n_{\mathrm{eff}}(B_{\mathrm{tr}}) \equiv B_{\mathrm{tr}}^{\mathrm{ZFC}_2} - B_{\mathrm{tr}}^{\mathrm{ZFC}_1}. \quad (5)$$

The goal of the present paper is to develop a method for measuring n_{eff}, to investigate the effect of H_0 and B_{tr} and the sample morphology on n_{eff}, and to determine the role of the demagnetization factor of crystallites in the macroscopic distribution of the magnetic fields in the vicinity of a sample and of the currents in a sample.

2. SAMPLES AND EXPERIMENTAL TECHNIQUE

Since the ranges and the manifestations of the demagnetization phenomena and of the edge and bulk pinnings of a magnetic flux largely overlap, we carried out the following procedures to investigate the function $n_{\mathrm{eff}}(H_0)$ and the effect of the sample morphology on these phenomena:

(1) bulk scanning of samples by an external field [10, 15];

(2) simultaneous measurement of the above-mentioned parameters in the ZC, ZFC_1, and ZFC_2 regimes (see below);

(3) measurement of the thickness of samples;

(4) study of the evolution of the spatial distribution of a trapped magnetic flux [10, 15].

A comparative analysis was carried out on $YBa_2Cu_3O_{7-x}$ samples with different structures, heights of the edge barrier, bulk pinning, and demagnetization. Quasi-single-crystal (nongranular) and ceramic samples in the shape of a disk with a diameter of 9 mm and different thicknesses were cut out of a cylindrical ingot. Textured quasi-single-crystal sintered samples (with the axis **c** parallel to the cylinder axis) were synthesized by a seed crystal placed on the top of the cylinder at a high temperature [22]. The examination of a mechanically well-polished surface of a sample along its perimeter through a microscope revealed 0.11-cm^2 bright (single-crystal) blocks separated by narrow green inclusions. This fact was confirmed by mapping a trapped magnetic flux with a Hall probe. Ceramic samples were synthesized by the standard solid-phase technology and had a relative density of ~95% (the theoretical density was chosen as 6.38 g cm^{-3}) with the average size of grains of about 1 μm [10]. To eliminate the inhomogeneity in the distribution of oxygen at the butt ends with respect to the bulk of samples, the end surfaces of the samples were cut out by a diamond cutter. The temperature of the superconducting transition (T_c, ΔT_c) was measured by the inductive method; for polycrystalline and ceramic samples, we obtained $T_c \approx 91.5$ K and $\Delta T_c \approx 0.8$ and 3.5 K, respectively. The measurements were carried out at liquid nitrogen temperature in a constant magnetic field of up to 1 kOe by a Hall probe with the working area equal to 50×50 $\mu\mathrm{m}^2$ and the sensitivity of about 20 μV G^{-1}. The equipment enabled us to detect a signal from the Hall probe with an accuracy of at least 2.5×10^{-6} G and to move the probe along the z axis from the center to the periphery of a sample. At the center of a sample, at a minimal distance of about 200 μm from its surface, we measured the magnetic induction $B(0)$ and $B_{\mathrm{tr}}(0)$ (the choice of the reference point of the coordinate z at z = 200 μm was associated with the thickness of the current and Hall contacts on the surface of the Hall probe) as a function of H_0 and the normalized axial distributions $B_{\mathrm{tr}}(z)/B_{\mathrm{tr}}^{\max}(0)$ versus the coordinate z; $B_{\mathrm{tr}}(z)$ is the axial dependence of B_{tr} measured for different values of the external field, and $B_{\mathrm{tr}}^{\max}(0)$ is the maximal density of the trapped magnetic flux at the center of a sample on its surface. The dependence of $B_{\mathrm{tr}}(0)$ on H_0 (further, $B_{\mathrm{tr}}(H_0)$) was measured in the following regimes:

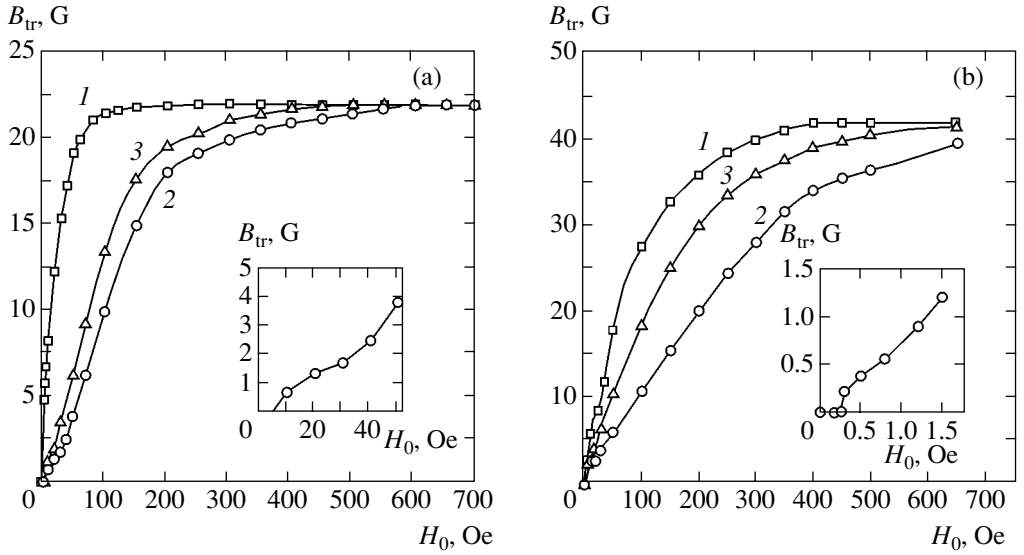

Fig. 1. Typical magnetic-field dependences of the trapped magnetic flux density $B_{tr}(H_0)$ for polycrystalline (a) and ceramic (b) $YBa_2Cu_3O_{7-x}$ samples with a diameter $D = 9$ mm and thickness $d = 1$ mm. Curves *1*, *2*, and *3*, correspond to the FC, ZFC_1, and ZFC_2 regimes, respectively. The temperature is 77.4 K.

(1) The FC regime. A sample in a given field is cooled to the temperature of liquid nitrogen. Then, the external field is switched off and, after 10 min (a period sufficient for the relaxation of component B_{tr} associated with a viscous flow of the flux and the development of a rigidly fixed vortex lattice), B_{tr} is measured at the center of the sample on its surface. After that, the sample is heated to a temperature above T_c and the experiment is repeated at another value of H_0.

(2) The ZFC_1 regime. A sample is cooled to the temperature of liquid nitrogen in zero magnetic field. Then, an impulse of an external magnetic field is applied to the sample, and, after 10 min, B_{tr} is measured at the center of the sample on its surface. After that, the sample is heated to a temperature above T_c and the experiment is repeated at another value of H_0.

(3) The ZFC_2 regime. This regime differs from ZFC_1 in that, after the initial trapping without changing the magnitude of the trapped B_{tr} and without heating a sample, an impulse of H_0 of the next step is applied to the sample and the total B_{tr} is measured after 10 min, etc. In this case, the amplitudes of the field steps are gradually increased step by step by equal values. Such an approach was applied to break, stage by stage, the weak bonds by the scattering fields of the vortices trapped by a sample and to guarantee the interaction of the external field with individual crystallites. The impulse of the external magnetic field of length $\tau \geq 1$ min was applied perpendicular to the plane of the samples. To eliminate the influence of spikes near the fronts that arise when switching on the power supply of a solenoid with inductance >10 H and to transform a rectangular impulse into a trapezoidal one, the solenoid was shunted by a 50-μF capacitor. The length τ was specified depending on the supply voltage. These measures were taken to eliminate the effect of the entry and exit velocities of a magnetic field on the magnetization of samples [23]. The component H_z of the Earth's magnetic field was compensated by a coil, coaxial with the solenoid, that produced an external magnetic field. The experimental technique and the equipment have been described in detail in [15, 24].

3. EXPERIMENTAL RESULTS

Figure 1 represents the typical magnetic-field dependence $B_{tr}(H_0)$ for polycrystalline (Fig. 1a) and ceramic (Fig. 1b) samples with a diameter of $D = 9$ mm and a thickness of $d = 1$ mm at a temperature of 77.4 K in three measurement regimes. Curves *2* and the insets to Fig. 1 show that the values of the first critical magnetic field for polycrystalline and ceramic samples are $H_{c1} = H_0/(1-n) \approx 14$ Oe and $H_{c1} \approx 0.5$ Oe, respectively. The function $B_{tr}(H_0)$ for a polycrystalline sample reaches a saturation at lower fields (at $H_0 \approx 600$ Oe) compared with that for a ceramic sample ($H_0 > 650$ Oe). For a polycrystalline sample, $B_{tr}^{max}(0) \approx 22$ G, whereas, for a ceramic sample, $B_{tr}^{max}(0) \approx 42$ G. The characteristics show that a polycrystalline sample has a narrower energy spectrum of the distribution of pinning centers and has a high edge barrier and low bulk pinning compared with a ceramic sample [25].

In the FC regime (curves *1* in Fig. 1), small magnetic fields penetrate into a sample and are trapped after switching off the field. Such a situation is analogous to the case of an infinite film with the demagnetization factor $n = 1$ in a perpendicular magnetic field. In the

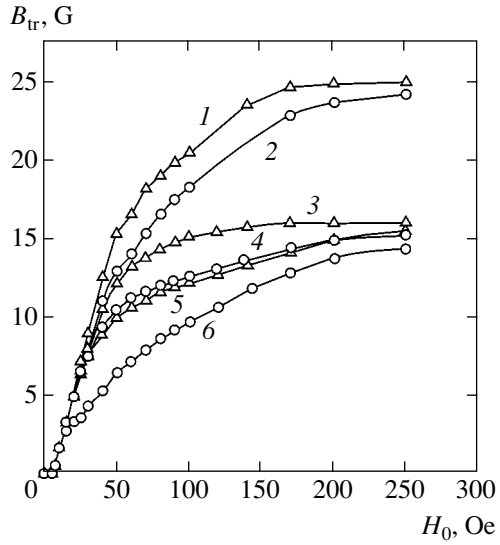

Fig. 2. Functions $B_{tr}(H_0)$ for polycrystalline samples with diameter D = 9 mm and different thicknesses d; d = 5.7 mm (curves *1* and *2*), d = 2.2 mm (curves *3* and *4*), and d = 0.7 mm (curves *5* and *6*). Curves *1*, *3*, and *5* are recorded in the ZFC_2 regime, and curves *2*, *4*, and *6*, in the ZFC_1regime. The temperature is 77.4 K.

ZFC_1 regime (curves *2* in Fig. 1), the trapping of a magnetic field does not influence n. In the ZFC_2 regime (curves *3* in Fig. 1), before applying the next step of a magnetic field, the trapped magnetic flux of the preceding step is stored. For the ZFC_1 and ZFC_2 regimes, one may assume that the influence of the edge and bulk pinnings on n is roughly identical; therefore, an increase in n_{eff} (the shift of curves *3* toward curves *1* in Fig. 1) is attributed to the increase of the trapped magnetic flux. Figure 1 shows that a high value of a trapped field produces a stronger effect on n_{eff} (the gap between curves *1* and *3* for a ceramic sample is less than that for a polycrystalline sample).

To find out the dependence of n_{eff} on the structure of the trapped magnetic flux, we will analyze B_{tr} and $B_{tr}(z)/B_{tr}^{max}(0)$ as a function of thickness d for a series of samples measured in three regimes.

Figure 2 presents the function $B_{tr}(H_0)$ for polycrystalline samples of diameter D = 9 mm with different thicknesses d. Curves *1* and *2* correspond to d = 5.7 mm, curves *3* and *4* correspond to d = 2.2 mm, and curves *5* and *6* correspond to d = 0.7 mm. Curves *1*, *3*, and *5* are recorded in the ZFC_2 regime, while curves *2*, *4*, and *6*, in the ZFC_1 regime. Figure 2 shows that, as d decreases, the effect of the trapped magnetic flux on n_{eff} becomes stronger in spite of the decrease in B_{tr}. This fact is clearly illustrated in Fig. 3a, which represents the dependence of $n_{eff}(B_{tr}) \equiv B_{tr}^{ZFC_2} - B_{tr}^{ZFC_1}$ on H_0, obtained from Fig. 2 by subtracting curves *2* from *1* (curve *1*), *4* from *3* (curve *2*), and *6* from *5* (curve *3*). Figure 3b demonstrates the dependence of $n_{eff}(B_{tr}) \equiv B_{tr}^{ZFC_2} - B_{tr}^{ZFC_1}$ on H_0, which is obtained from Fig. 2 by subtracting curves *2* from *3*, Fig. 1. Curve *1* corresponds to polycrystalline samples, and curve *2*, to ceramic samples.

Figure 4 demonstrates the normalized axial distribution $B_{tr}(z)/B_{tr}^{max}(0)$ for polycrystalline samples with

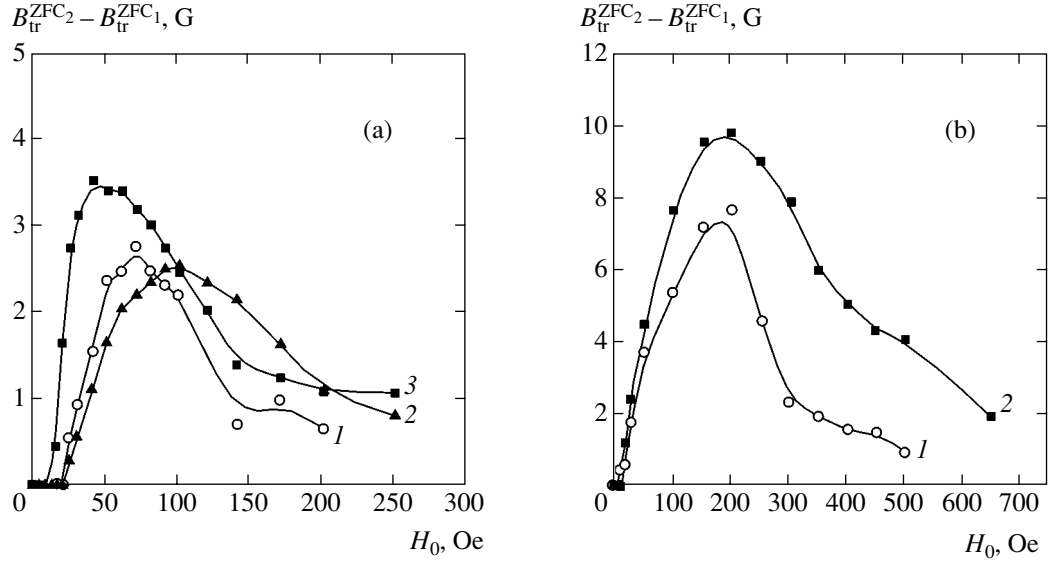

Fig. 3. $B_{tr}^{ZFC_2} - B_{tr}^{ZFC_1}$ as a function of H_0. (a) Curve *1* represents the difference between curves *3* and *2* in Fig. 2, curve *2* represents the difference between curves *3* and *4* in Fig. 2, and curve *3* represents the difference between curves *5* and *6* in Fig. 2. (b) Curve *1* is the difference of curves *3* and *2* in Fig. 1a and curve *2* is the difference of curves *3* and *2* in Fig. 1b. The temperature is 77.4 K.

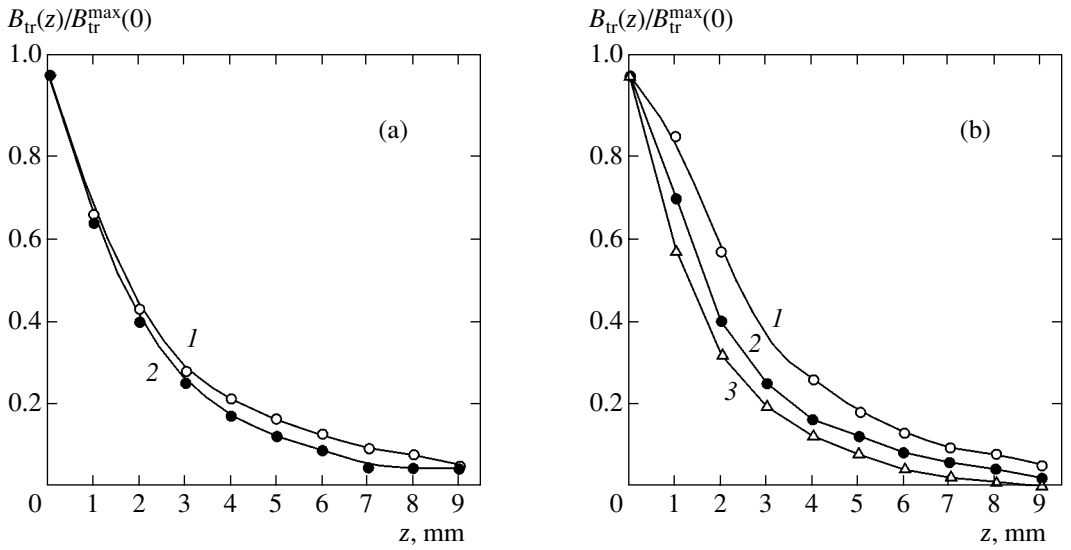

Fig. 4. Normalized axial distribution $B_{tr}(z)/B_{tr}^{max}(0)$ for polycrystalline samples of diameter D = 9 mm. (a) d = 1 mm; curve *1* is recorded in the FC regime and curve *2*, in the ZFC_2 regime. (b) Measurements in the ZFC_2 regime for samples of different thicknesses: d = 8 mm (curve *1*), d = 4 mm (curve *2*), and d = 1 mm (curve *3*). The temperature is equal to 77.4 K.

diameter D = 9 mm. In the FC regime, the distribution of a trapped magnetic flux is more uniform than that in the ZFC_2 regime, because an originally uniform external field is trapped more uniformly after its switching off. Figure 4a shows that, in the case of a uniform magnetization, the function $B_{tr}(z)/B_{tr}^{max}(0)$ decreases slower (curve *1*) than that in the case of a nonuniform magnetization (curve *2*). According to Fig. 4b (see also Fig. 3a), as the sample thickness decreases, its morphology is changed, and the distribution of the trapped magnetic flux becomes more nonuniform. Thus, a nonuniform spatial distribution of the trapped magnetic flux in a sample stronger deforms the field around this sample. The variations in the amplitude of n_{eff} and the area under the curve of $n_{eff}(H_0)$, as well as the displacement of the maximum of this curve along the axis H_0 as the sample thickness is changed (Fig. 3a), are attributed to the variation in the relative number of crystallites with different sizes, shapes, and orientations with respect to the external magnetic field, as well as with the change in the arrangement of these crystallites.

Note that similar dependences were obtained for ceramic samples.

4. DISCUSSION OF THE RESULTS

To interpret the dependence $n_{eff}(H_0)$ and demonstrate the enhancement of the demagnetization of a sample or of individual crystallites by a trapped magnetic flux and the distribution of a field around a sample, we will use the scheme shown in Fig. 5. When the magnetic induction B_0 is less than or equal to $B_0 \le B_{tr}$, the external magnetic field around a sample is either compensated or removed from its edges (see the solid field lines ($B_{tr} \neq 0$) and the dashed lines ($B_{tr} = 0$) in Fig. 5). First, the difference between the effective diameter and the thickness of a sample increases due to the enhanced interaction between the increasing scattering fields B_{tr} and the field B_0. When $B_0 \ge B_{tr}$, the external field suppresses the scattering field of the trapped magnetic flux, and the solid field lines approach the edges of the sample and merge with the dashed lines.

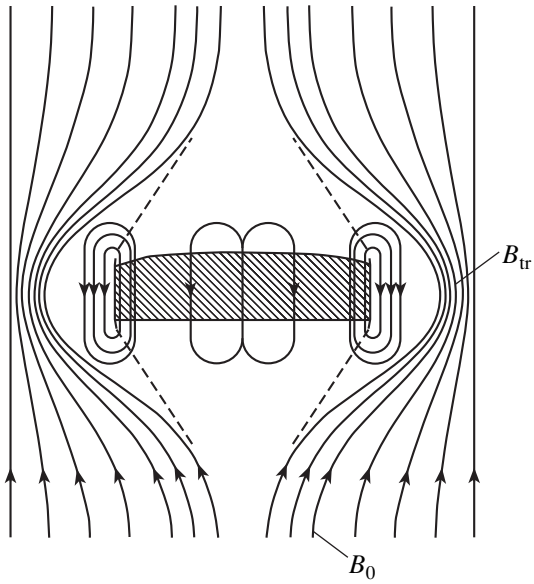

Fig. 5. Distribution of the field lines of the trapped magnetic flux density B_{tr} and the magnetic induction B_0 around a sample.

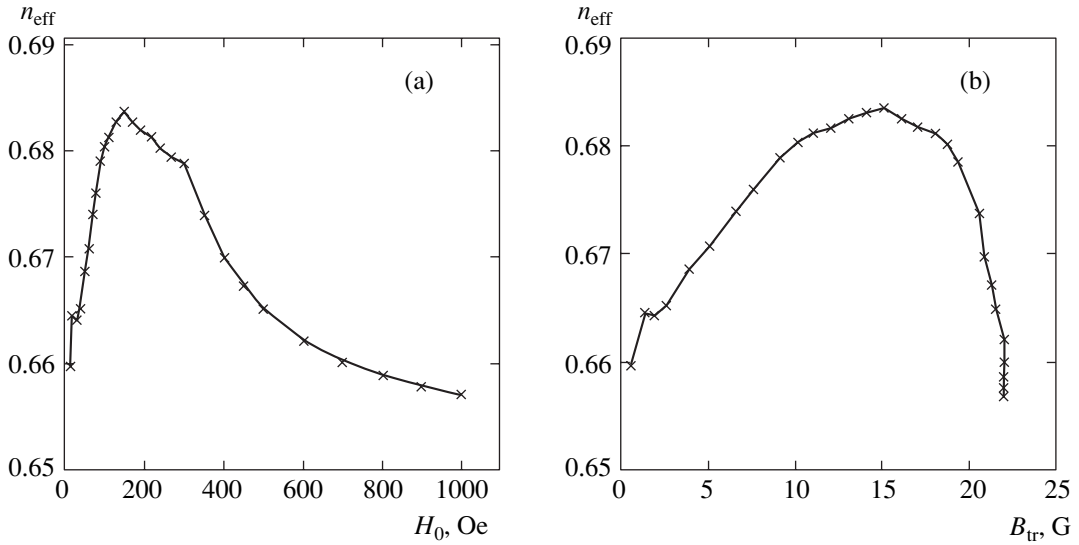

Fig. 6. Calculated magnetic-field dependence of the effective demagnetization factor n_{eff} of a sample: (a) $n_{eff}(H_0)$ and (b) $n_{eff}(B_{tr})$ for the same sample as in Fig. 1a. The temperature is equal to 77.4 K.

As a result, the function $n_{eff}(H_0)$ passes through its maximum.

The results cannot be explained within the interacting loops model in a more general case. According to [26], the size of a loop with a trapped magnetic flux in a field of 50 Oe reaches a value of 30–40 μm and decreases as the field increases. Therefore, the maximum of the function $n_{eff}(H_0)$, which is observed in a field of about 200 Oe, can be explained with the use of much smaller loops. Since the area of crystallites in a polycrystalline sample is about 0.11 cm^2 and the formation of a loop requires two to three crystallites, the loop size must be very large, which contradicts the arguments presented above.

The results can be explained based on the following ideas. It is well known [27] that, for a sample in the form of an oblate ellipsoid of rotation with the minor axis d and diameter $D \gg d$ in an external uniform magnetic field directed along the minor axis, the thermodynamic, or intrinsic, field H_i and magnetic induction B are related to the external field H_0 by the formula

$$(1-n)H_i = H_0 - nB, \tag{6}$$

where $n = 1 - \pi d/D$ is the demagnetization factor in the direction of the field. In a mixed state, to apply formula (6), it is necessary that the sample should consist of uniformly distributed identical magnetic moments—dipoles [10]. Such a situation may occur in HTSC samples near the saturation point of the trapped magnetic flux when the Bean model (J_{cg} = const) is valid within the crystallites considered [13]. In this case [28], the thermodynamic field H_i depends not only on the external field H_0 but also on the coordinate y, and the induction B additionally depends on B_{tr}. A solution to Eq. (6) is obtained by analyzing the dependence of B_1 (y, H_0) and B_2 (y, B_{tr}, H_0) on H_0 measured in the ZFC_1 and ZFC_2 regimes. For the ZFC_1 regime, formula (6) is rewritten as

$$H_i(y, H_0) = \frac{H_0 - nB_1(y, H_0)}{1-n}. \tag{7}$$

In (7), the quantity n specifies the onset of penetration of a magnetic field into a sample, and the variation of n during the penetration of a field into a sample is determined by the dependence of H_i and B_1 on H_0 and the coordinate y. To determine n_{eff} in the ZFC_2 regime, we rewrite formula (7) as

$$n_{eff} = \frac{H_i(y, H_0) - H_0}{H_i(y, H_0) - B_2(y, B_{tr}, H_0)}. \tag{8}$$

Figure 6 shows the functions $n_{eff}(H_0)$ and $n_{eff}(B_{tr})$ calculated by formula (8) for a sample described in Fig. 1a. Figures 3b (curve *1*) and 6a show that the calculated curves are in agreement with the experimental ones. The values of $n_{eff} \approx 0.66$ (for $B_{tr} = 0$) and $n_{eff} \approx 0.65$ (in the range of fields where n_{eff} is independent of B_{tr}) coincide with a value of $n \approx 0.65$ determined from the geometrical size of a sample in the Meissner state. This fact confirms the results of the present study and agrees with the earlier experimental results stating that dense, nearly sintered HTSC samples predominantly consist of crystallites. According to Fig. 1 (curves *2*), the density of the critical current J_{cJ} in a polycrystalline sample is about 28 times greater than J_{cJ} in a ceramic sample. The values of the fields H_p at which the fronts of these fields reach the axes of polycrystalline and

ceramic samples are of the same order of magnitude; this fact strongly differs from the estimates made by the formula [7],

$$H_p = \frac{2\pi}{c} J_{cJ} D. \quad (9)$$

Hence, the fact that the value $H_0 \approx 200$ Oe of the field at which the maxima of $n_{eff}(H_0)$ coincide (Fig. 3b) is associated with the value of J_{cg}, which specifies approximately equal magnetization currents ($J = cId$) [10, 20] in polycrystalline and ceramic samples.

The analysis carried out shows that, when J_{cg} differs from J_{cJ} by about 28 times, the demagnetization factor is mainly determined by the geometry of a sample, rather than by the energy of Josephson coupling between crystallites.

The results obtained in the present study are interpreted according to the conditions under which HTSC samples with relatively low values of J_{cJ} and high values of a magnetic flux trapped in crystallites were chosen. For higher quality samples [30, 31], the degree of such trapping is insufficient for suppressing J_{cJ}. Since $J_{cg} \geq 10J_{cJ}$ even in high-quality HTSC samples, in the range of strong fields, the suppression of J_{cJ} and the decomposition of a sample into individual crystallites will occur due to the amplification of H_0 and the associated concentration of the field around the crystallites.

Thus, the character of $n_{eff}(H_0)$ is not changed as the morphology (Fig. 3a) and the parameters of the samples change, which have different initial structures and critical parameters (Fig. 3b). Taking into account that HTSC films and single crystals are multiconnected Josephson media, we can assume that a similar dependence $n_{eff}(H_0)$ will also be observed in conventional spatially inhomogeneous type-II semiconductors [32].

5. CONCLUSIONS

Thus, the study of the interaction between a magnetic flux trapped by a sample and an external field has revealed that the dynamics of the effective demagnetization factor can be investigated by an example of quasi-single-crystal and granular $YBa_2Cu_3O_{7-x}$ thin disks. The effect of the external field and the magnitude and the topology of the trapping of a magnetic flux on n_{eff} has been analyzed. For given B_{tr} and H_0, the profile of the thermodynamic magnetic field has been measured. As the trapped magnetic flux increases, the function $n_{eff}(H_0)$ shows a maximum whose qualitative behavior is not changed under substantial variations of the sample morphology. It has been shown that, when $J_{cg} \geq 28J_{cJ}$, the demagnetization factor is mainly determined by the geometry of a sample, rather than by the energy of Josephson coupling between crystallites.

The results obtained and the planned cycle of investigations contribute to the correct determination of fundamental quantities such as the first and second critical magnetic fields and the practically important quantity J_c, as well as to the improvement of the existing models of the critical state of type-II semiconductors.

ACKNOWLEDGMENTS

I am grateful to V.N. Gubankov for his interest in this work, useful discussions, and valuable remarks.

REFERENCES

1. V. S. Gorbachev and S. E. Savel'ev, Zh. Éksp. Teor. Fiz. **109**, 1387 (1996) [JETP **82**, 748 (1996)].
2. A. A. Elistratov and I. L. Maksimov, Fiz. Tverd. Tela (St. Petersburg) **42**, 196 (2000) [Phys. Solid State **42**, 201 (2000)].
3. M. Benkraouda and J. R. Clem, Phys. Rev. B **53**, 5716 (1996).
4. E. Zeldov, A. Larkin, V. Geshkenbein, *et al.*, Phys. Rev. Lett. **73**, 1428 (1994).
5. E. Zeldov, J. R. Clem, M. Mcelfresh, *et al.*, Phys. Rev. B **49**, 9802 (1994).
6. D. Yu. Vodolazov, Pis'ma Zh. Tekh. Fiz. **25** (20), 84 (1999) [Tech. Phys. Lett. **25**, 838 (1999)].
7. C. P. Bean, Rev. Mod. Phys. **36**, 31 (1964).
8. Kh. R. Rostami, in *Proceedings of International Conference on the Physics of Electronic Materials* (Kaluga, Russia, 2002), p. 402.
9. Kh. R. Rostami, in *Program and Abstracts of the 23rd International Conference on Low Temperature Physics LT 23* (Hiroshima, Japan, 2002), p. 312.
10. Kh. R. Rostami, V. V. Mantorov, and V. I. Omel'chenko, Fiz. Nizk. Temp. **22**, 736 (1996) [Low Temp. Phys. **22**, 565 (1996)].
11. É. B. Sonin, Pis'ma Zh. Éksp. Teor. Fiz. **47**, 415 (1988) [JETP Lett. **47**, 496 (1988)].
12. N. D. Kuzmichev, Pis'ma Zh. Éksp. Teor. Fiz. **74**, 291 (2001) [JETP Lett. **74**, 262 (2001)].
13. E. E. Kokorina and M. V. Medvedev, Sverkhprovodimost: Fiz. Khim. Tekh. **7**, 1127 (1994); Sverkhprovodimost: Fiz. Khim. Tekh. **7**, 1136 (1994); Sverkhprovodimost: Fiz. Khim. Tekh. **8**, 533 (1995); Sverkhprovodimost: Fiz. Khim. Tekh. **8**, 551 (1995).
14. M. P. Petrov, M. V. Krasin'kova, Yu. I. Kuz'min, *et al.*, Fiz. Tverd. Tela (St. Petersburg) **32**, 379 (1990) [Sov. Phys. Solid State **32**, 217 (1990)].
15. Kh. R. Rostami, Fiz. Nizk. Temp. **27**, 103 (2001) [Low Temp. Phys. **27**, 79 (2001)].
16. J. R. Clem, Physica C (Amsterdam) **153–155**, 50 (1988).
17. V. A. Kashurnikov, I. A. Rudnev, and M. V. Zyubin, Zh. Éksp. Teor. Fiz. **121**, 442 (2002) [JETP **94**, 377 (2002)].
18. H. Dersch and G. Blatter, Phys. Rev. B **38**, 11391 (1988).
19. D. D. Stancil, T. E. Schlesinger, A. K. Stamper, *et al.*, J. Appl. Phys. **64**, 5899 (1988).
20. I. E. Tamm, *The Principles of Electricity Theory,* 10th ed. (Nauka, Moscow, 1989).

21. E. A. Lynton, *Superconductivity*, 4th ed. (Chapman and Hall, London, 1971; Mir, Moscow, 1974).

22. I. F. Voloshin, A. V. Kalinov, L. M. Fisher, *et al.*, Zh. Éksp. Teor. Fiz. **120**, 1273 (2001) [JETP **93**, 1105 (2001)].

23. S. A. Ivanov, V. I. Kulakov, R. K. Nikolaev, *et al.*, Fiz. Tverd. Tela (Leningrad) **33**, 1387 (1991) [Sov. Phys. Solid State **33**, 782 (1991)].

24. Kh. R. Rostami, Prib. Tekh. Éksp., No. 6, 95 (2004).

25. V. N. Gubankov and Kh. R. Rostami, Fiz. Tverd. Tela (St. Petersburg) **43**, 1168 (2001) [Phys. Solid State **43**, 1210 (2001)].

26. Kh. R. Rostami, A. A. Sukhanov, and V. V. Mantorov, Supercond. Sci. Technol. **9**, 736 (1996).

27. A. A. Abrikosov, *Fundamentals of the Theory of Metals* (Nauka, Moscow, 1987; North-Holland, Amsterdam, 1988), p. 384.

28. V. G. Antonov, L. M. Petrov, and A. P. Shchelkin, *Means for Measurements of Magnetic Parameters of Materials* (Énergoatomizdat, Leningrad, 1986), p. 76 [in Russian].

29. V. M. Krasnov, V. A. Larkin, and V. V. Ryazanov, Physica C (Amsterdam) **174**, 440 (1991).

30. A. S. Mel'nikov, Yu. N. Nozdrin, I. D. Tokman, *et al.*, Phys. Rev. B **58**, 11 672 (1998).

31. S. A. Pozigun, V. M. Pan, V. A. Alekseev, *et al.*, UFM **5**, 167 (2004).

32. L. B. Ioffe and A. I. Larkin, Zh. Éksp. Teor. Fiz. **81**, 707 (1981) [Sov. Phys. JETP **54**, 378 (1981)].

Translated by I. Nikitin

Journal of Experimental and Theoretical Physics, Vol. 101, No. 4, 2005, pp. 661–675.
Translated from Zhurnal Éksperimental'noĭ i Teoreticheskoĭ Fiziki, Vol. 128, No. 4, 2005, pp. 768–784.

ORDER, DISORDER, AND PHASE TRANSITIONS IN CONDENSED SYSTEMS

Analytical Realization of Finite-Size Scaling for Anderson Localization: Is There a Transition in the 2D Case?¶

I. M. Suslov

Kapitza Institute for Physical Problems, Russian Academy of Sciences, Moscow, 117337 Russia
e-mail: suslov@kapitza.ras.ru

Received May 18, 2005

Abstract—Roughly half the numerical investigations of the Anderson transition are based on consideration of an associated quasi-1D system and postulation of one-parameter scaling for the minimal Lyapunov exponent. If this algorithm is taken seriously, it leads to unambiguous prediction of the 2D phase transition. The transition is of the Kosterlitz–Thouless type and occurs between exponential and power law localization (Pichard and Sarma, 1981). This conclusion does not contradict numerical results if raw data are considered. As for interpretation of these data in terms of one-parameter scaling, this is inadmissible: the minimal Lyapunov exponent does not obey any scaling. A scaling relation is valid not for a minimal, but for some effective Lyapunov exponent whose dependence on the parameters is determined by the scaling itself. If finite-sizedd scaling is based on the effective Lyapunov exponent, the existence of the 2D transition becomes indefinite, but still rather probable. Interpretation of the results in terms of the Gell-Mann–Low equation is also given. © *2005 Pleiades Publishing, Inc*.

1. INTRODUCTION

The one-parameter scaling hypothesis [1] leads to a conclusion that there is no Anderson transition in two dimensions. This statement has produced a breakthrough in the physics of disordered systems and led to development of the concept of weak localization with numerous experimental manifestations [2]. The recent discovery of the 2D metal-insulator transition [3–6] threatens to undermine the basic concepts of the theory. It is still unclear whether this transition can exist for a purely potential scattering or should it be related to different complications, such as interaction, spin-orbit effects, etc. It will be shown below that the first possibility is rather probable and does not suggest substantial revision in the weak localization region [1].

Initially, the present investigation was motivated by analysis of the methodical aspects of finite-sizedd scaling [7], which is a basic concept of all recent numerical studies of the Anderson transition [8–23]. There is the problem that numerical results have a tendency to contradict all other information on the critical behavior [24]. Practically all theoretical and experimental investigations agree with the result of the Vollhardt and Wölfle self-consistent theory [25, 26]

$$\nu = \begin{cases} 1/(d-2), & 2 < d < 4 \\ 1/2, & d > 4, \end{cases} \qquad (1)$$

$$s = 1, \quad 2 < d < \infty,$$

where ν and s are critical exponents of the correlation length and conductivity and d is dimensionality of space. Indeed, the result in (1)

(a) distinguishes values $d_{c1} = 2$ and $d_{c2} = 4$ as the lower and the upper critical dimensions;[1]

(b) agrees with the result[2] for $d = 2 + \epsilon$ [33]

$$\nu = \frac{1}{\epsilon} + 0 \cdot \epsilon^0 + 0 \cdot \epsilon^1 + O(\epsilon^2); \qquad (2)$$

(c) agrees with the results $\nu = 1/2$ [35, 36] and $s = 1$ [37] for $d = \infty$;

(d) satisfies the scaling relation $s = (d - 2)\nu$ for $d < d_{c2}$ [1];

(e) gives critical exponents independent of d for $d > d_{c2}$, as is usual for mean field theory;

¶ The article was translated by the author.

[1] The first is a consequence of one-parameter scaling [1], and the second can be seen from different points [27, 28], the main of which is renormalizability. The theory of disordered systems is mathematically equivalent to the φ^4 field theory with a "wrong" sign of interaction [29–31]. The latter is renormalizable for $d \le 4$ and nonrenormalizable for $d > 4$ [32]. For $d \le 4$, the entire physics is determined by small momenta or large distances, in accordance with the expected scale invariance. For $d > 4$, the atomic scale cannot be excluded from the results and no scale invariance is possible.

[2] According to Wegner [34], the term of order ϵ^2 in (2) is finite, large, and negative. However, this result was derived for the zero-component σ-model, whose correspondence with the initial disordered system is approximate and valid for small ϵ; therefore a difference can arise in a definite order in ϵ.

(f) agrees with experimental results for $d = 3$, $s \approx 1$, $\nu \approx 1$ [38, 39].[3] As for numerical results, they can be summarized by the empirical formula $\nu \approx 0.8/(d-2) + 0.5$ [17], which has evident fundamental defects [24].

The finite-sized scaling approach is based on the philosophy that any dimensionless quantity A related to a system spatially restricted on a scale L is a function of a ratio L/ξ,

$$A = F(L/\xi), \tag{3}$$

where ξ is the correlation length. To justify Eq. (3), let us assume that the dependence of A on the parameters can be expressed as its dependence on characteristic length scales L, ξ, l_1, l_2, …. Taking ξ as a unit scale, we can write

$$A = F(L/\xi, l_1/\xi, l_2/\xi, \ldots). \tag{4}$$

Near the critical point, the correlation length ξ is large in comparison with microscopic scales l_1, l_2, … and substitution $l_1/\xi = l_2/\xi = \ldots = 0$ reduces (4) to (3). This derivation is based on assumption that limiting transition $l_i/\xi \longrightarrow 0$ is not singular and the right-hand side of Eq. (4) does not become zero or infinity. Unfortunately, there is no simple way to establish when such an assumption is true.[4] When Eq. (3) is valid, it makes it possible to investigate the dependence of ξ on parameters. If there is anything wrong with Eq. (3), it leads to erroneous conclusions.

Below we present an analytical realization of the commonly used variant of finite-sized scaling based on the concept of the minimal Lyapunov exponent. Our approach is based on an investigation of the second moments for a solution of the Cauchy problem for the Schrödinger equation (Section 3), and in this respect it is close to [42, 43]. Nevertheless, justification of the approach (Section 2) and interpretation of the results (Section 3) are significantly different, and in fact we disagree with most of the statements made in [42, 43].

Briefly, our results consist in the following. If the concept of the minimal Lyapunov exponent is taken seriously, it leads to unambiguous prediction of the 2D phase transition (Section 3). The transition occurs between exponential and power law localization and, consequently, it is of the Kosterlitz–Thouless type [7]. This conclusion does not contradict the numerical results [8–13] if the raw data are considered (Section 4). Interpretation of these data in terms of one-parameter scaling is inadmissible: the minimal Lyapunov exponent does not obey any scaling. We argue that a scaling relation is valid not for minimal, but for some effective Lyapunov exponent whose dependence on parameters is determined by scaling itself (Section 5). After such modification, existence of the 2D transition becomes indefinite, but still rather probable (Section 6). Interpretation of results in terms of the Gell-Mann–Low equation [1] is given in Section 7.

2. BASIC CONCEPTS

2.1. The concept of finite-sized scaling is taken from the theory of phase transitions [44–46] and can be discussed using a ferromagnet as an example. Instead of an infinite 3D system, let us consider a system of size $L \times L \times L_z$ with $L_z \longrightarrow \infty$. Such a system is topologically one-dimensional and does not exhibit phase transition. The correlations in it are always paramagnetic and there is a finite correlation length ξ_{1D}. Relation of ξ_{1D} to the ferromagnetic phase transition in the 3D system is expressed by the following statements. If $T > T_c$ and the 3D system is paramagnetic, then ξ_{1D} obviously coincides with the correlation length ξ of the 3D system when L is sufficiently large:

$$\xi_{1D} \longrightarrow \xi \quad \text{for} \quad L \longrightarrow \infty. \tag{5}$$

If $T < T_c$ and the 3D system is ferromagnetic, then the following statement is valid:

$$\frac{\xi_{1D}}{L} \longrightarrow \infty \quad \text{for} \quad L \longrightarrow \infty, \tag{6}$$

which can be proved by contradiction. Indeed, let the ratio $c = \xi_{1D}/L$ be finite for all L. Let us assume $n \gg c$ and consider a system of size $L \times L \times nL$. The correlations in the length direction are paramagnetic and the average (along the cross-section) magnetic moment changes its sign many times. This situation holds for all L and, in particular, for $L \longrightarrow \infty$; however, such a thermodynamic limit is topologically three-dimensional and a system should become ferromagnetic. This contradiction proves (6).

If $T = T_c$, then any behavior

$$\xi_{1D} \propto L^{\alpha} \quad (0 < \alpha \leq 1) \quad \text{for} \quad L \longrightarrow \infty \tag{7}$$

is possible. Indeed, the ratio $c = \xi_{1D}/L$ is finite or tends to zero, and the above-considered system of size $L \times L \times nL$ possesses paramagnetic correlations. Nevertheless, it is not a true paramagnet, because its correlation

[3] These remarkable properties of result (1) arouse suspicion to the fact that it is exact [40]. In reality, it can be obtained without model approximations on the basis of symmetry considerations [41].

[4] Such a possibility exists in the field-theoretical formulation of the problem. When the maximum microscopic scale l_1 tends to zero, the theory becomes divergent. In nonrenormalizable theories, such divergences are unavoidable and relation (3) never holds. If a theory is renormalizable, all divergencies can be absorbed in a finite number of parameters (such as mass, coupling constant, etc.) and renormalized Green functions (and quantities that can be expressed via them) do not depend on l_i and exhibit scale invariance. If quantity A has no clear field-theoretical interpretation, it is difficult to establish its independence on the "bare mass," "bare coupling," etc. The latter quantities essentially depend on l_i and are observable in condensed matter applications.

length $\xi \sim \xi_{1D}$ is divergent, as it should be at the critical point.

Usually, relation (7) is suggested with $\alpha = 1$, because it is the only possibility compatible with scale invariance. Indeed, if the quantities ξ_{1D}, ξ, and L are related by some functional relation which does not contain any other scales, this relation assumes the form $F(\xi_{1D}/L, \xi/L) = 0$ if L is taken as the unit length. Solving this relation for ξ_{1D}/L we have

$$\frac{\xi_{1D}}{L} = F\left(\frac{L}{\xi}\right), \tag{8}$$

and $\xi_{1D} = F(0)L$ at the critical point in accordance with (7) for $\alpha = 1$.

As a result, the quantity

$$g(L) = \frac{\xi_{1D}}{L} \tag{9}$$

can be taken as a scaling variable whose dependence on L is shown in Fig. 1a. It should be stressed, however, that ξ_{1D} is sensible to the 3D transition independently of the existence of scale invariance. The latter is absent for space dimensions $d > 4$ in the case of a ferromagnet.

2.2. Application of these considerations to the localization theory is based on identification of ξ_{1D} with the inverse of the minimal Lyapunov exponent $\gamma_{\min}$,

$$\xi_{1D} \sim \frac{1}{\gamma_{\min}}. \tag{10}$$

The Lyapunov exponents occur in the solution of the Cauchy problem for the quasi-1D Schrödinger equation with the initial conditions on the left edge of the system. For example, the 1D Anderson model

$$\psi_{n+1} + \psi_{n-1} + V_n\psi_n = E\psi_n \tag{11}$$

can be rewritten in the form of the recurrence relation

$$\begin{vmatrix} \psi_{n+1} \\ \psi_n \end{vmatrix} = \begin{vmatrix} E - V_n & -1 \\ 1 & 0 \end{vmatrix} \begin{vmatrix} \psi_n \\ \psi_{n-1} \end{vmatrix} \equiv T_n \begin{vmatrix} \psi_n \\ \psi_{n-1} \end{vmatrix}, \tag{12}$$

where T_n is a transfer matrix. Then the initial condition problem can be formally solved as

$$\begin{vmatrix} \psi_{n+1} \\ \psi_n \end{vmatrix} = T_nT_{n-1}\ldots T_2T_1 \begin{vmatrix} \psi_1 \\ \psi_0 \end{vmatrix}. \tag{13}$$

An analogous relation occurs for an arbitrary quasi-1D system if the quantity $\psi_n(r_\perp)$, depending on the transverse coordinate $r_\perp$, is considered as a vector ψ_n.

One can try to represent a matrix product P_n in Eq. (13) as the nth power of a constant matrix T. Such a thing is possible, but only for the "Hermitian part" of P_n. As any matrix, P_n can be represented as a product of the unitary matrix U_n and the Hermitian matrix H_n

$$\begin{aligned} P_n &= T_nT_{n-1}\ldots T_2T_1 \equiv U_nH_n, \\ H_n^2 &= P_n^+P_n, \end{aligned} \tag{14}$$

where H_n has real eigenvalues and describes a systematic growth or decrease ψ_n, while U_n has eigenvalues with the unit modulus and describes an oscillatory behavior. Representation $H_n = T^n$ is constructive, because the geometric mean of matrices

$$\begin{aligned} T &= (P_n^+P_n)^{1/2n} \\ &= (T_1^+T_2^+\ldots T_n^+T_n\ldots T_2T_1)^{1/2n} \end{aligned} \tag{15}$$

tends to a nonrandom limit for $n \longrightarrow \infty$ according to the Oseledec theorem [47]. If a vector of initial conditions in (13) is expanded in eigenvectors of T, while its eigenvalues λ_s are written as $\exp(\gamma_s)$, then the following decomposition is valid for $\psi_n(r_\perp)$:

$$\begin{aligned} \psi_n(r_\perp) &= A_1h_n^{(1)}(r_\perp)e^{\gamma_1 n} \\ &+ A_2h_n^{(2)}(r_\perp)e^{\gamma_2 n} + \ldots + A_mh_n^{(m)}(r_\perp)e^{\gamma_m n}. \end{aligned} \tag{16}$$

The quantities $h_n^{(s)}(r_\perp)$ have no systematic growth in n, while the Lyapunov exponents γ_s tend to constant val-

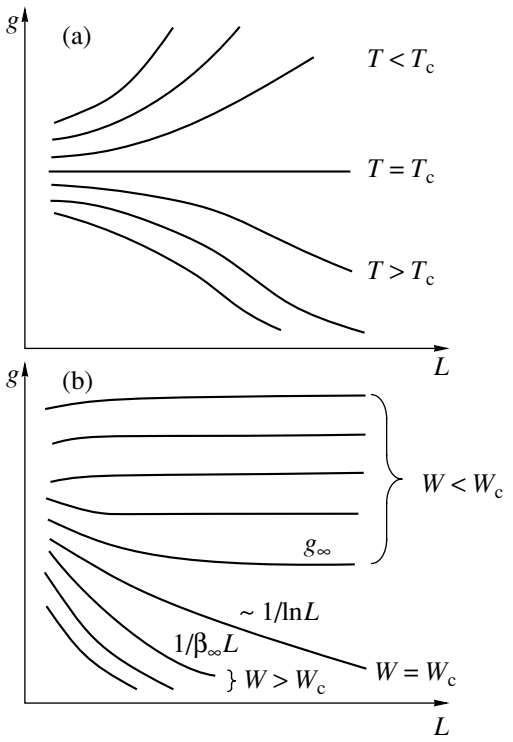

Fig. 1. (a) Typical dependences $g(L)$ in the case of one-parameter scaling; (b) dependences $g(L)$ according to Eq. (50).

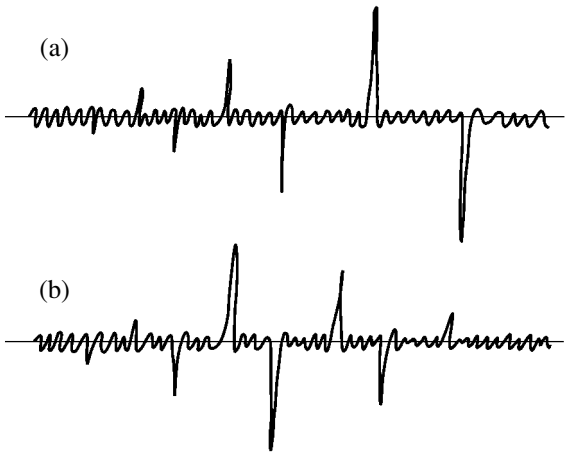

Fig. 2. Solution of the Cauchy problem (a) and a 1D eigenfunction constructed according to Mott (b) in the situation $a = 0$, $b > 0$.

ues in a large n limit. Only terms with positive γ_s are kept in Eq. (16) and they are numerated in the order of decreasing γ_s.

Following to Mott [48], we can construct eigenfunctions of a quasi-1D system by matching two solutions of the type (16) increasing from two opposite edges of the system. The tails of the eigenfunction will be determined by the minimal Lyapunov exponent $\gamma_{\min} \equiv \gamma_m$ and these are grounds for relation (10).

2.3. Decomposition (16) is valid for nonaveraged quantity $\psi_n(r_\perp)$ and its meaning consists in distinguishing the self-averaging exponents γ_s. It will be shown in Section 3 that the mean value of $\psi_n(r_\perp)$ does not obey systematic growth,

$$\langle \psi_n(r_\perp)\rangle \sim 1, \tag{17}$$

while decomposition of type (16) is valid for its second moment

$$\begin{aligned}\langle \psi_n^2(r_\perp)\rangle &= B_1(r_\perp)e^{\beta_1 n}\\ &+ B_2(r_\perp)e^{\beta_2 n} + \ldots + B_m(r_\perp)e^{\beta_m n}\end{aligned} \tag{18}$$

with the same number of positive exponents β_s. Squaring (16) gives m^2 terms that increase as $\exp(\gamma_i n + \gamma_j n)$, and the only possibility to have m terms in (18) suggests averaging to zero for all terms with $i \neq j$. The terms with $i = j$ are positive and cannot vanish in the course of averaging:

$$\begin{aligned}\langle \psi_n^2(r_\perp)\rangle &= \left\langle [A_1 h_n^{(1)}(r_\perp)]^2 e^{2\gamma_1 n}\right\rangle\\ &+ \left\langle [A_2 h_n^{(2)}(r_\perp)]^2 e^{2\gamma_2 n}\right\rangle + \ldots\\ &+ \langle [A_m h_n^{(m)}(r_\perp)]^2 e^{2\gamma_m n}\rangle.\end{aligned} \tag{19}$$

The terms in (18) and (19) are in one-to-one correspondence and relation between γ_s and β_s can be discussed for a pure 1D system when (16) and (18) have only one term in the right-hand side:

$$\psi_n \sim e^{\gamma n}, \quad \langle \psi_n\rangle \sim 1, \quad \langle \psi_n^2\rangle \sim e^{\beta n}. \tag{20}$$

Finiteness of $\langle \psi_n\rangle$ is insignificant in comparison with the exponential growth, and we accept $\langle \psi_n\rangle = 0$. In fact, we should discuss the usual relation between a typical value of a random quantity x and its root mean square value. If $\langle x\rangle = 0$ and $\langle x^2\rangle = \sigma^2$, then the typical value of x should not be necessarily of order σ: one can state only that $|x| \lesssim \sigma$. Indeed, according to the Chebyshev inequality [49], the probability for $|x|$ to be greater than x_0 is less then σ^2/x_0^2. Values of x substantially greater than σ are improbable and σ gives the upper estimate of the distribution width. The lower estimate does not exist in any form. Indeed, if distribution $P(x)$ changes on a scale of $x \sim 1$ and has a tail of $|x|^{-\alpha}$ with $1 < \alpha < 3$, then typical $x \sim 1$, while $\langle x^2\rangle = \sigma^2 = \infty$. It is clear from these considerations that the following relation holds for the exponents in Eq. (20),

$$\beta \geq 2\gamma, \tag{21}$$

and there are no grounds for equality.

In fact, the relation between β and γ can be discussed more constructively, because ψ_n has a log-normal distribution [50]: i.e., the quantity $\tau = \ln|\psi_n|$ has a Gaussian distribution

$$P(\tau) \sim \exp\left\{-\frac{(\tau - an)^2}{2bn}\right\}, \tag{22}$$

where the first and the second moments grow linearly in n. It is easy to see that

$$\psi_n \sim e^{an}, \quad \langle \psi_n^2\rangle \sim e^{(2a+2b)n}, \tag{23}$$

and (21) obviously holds. In the 1D Anderson model we have for $E = 0$

$$a = b = \frac{1}{8}\langle V^2\rangle, \quad \beta = \frac{1}{2}\langle V^2\rangle \tag{24}$$

for weak disorder, and

$$\gamma = a = \langle \ln|V|\rangle, \quad \beta = \ln\langle V^2\rangle \tag{25}$$

for strong disorder. For a typical distribution, Eq. (25) suggests that $b \ll a$. Analogous results are valid for many models, and situation $b \lesssim a$ should be considered typical. In this case, $\beta \sim \gamma$ and $1/\beta$ gives the correct estimate of the correlation length ξ_{1D}.

The situation $b \gg a$ can be discussed for an extremal case when $a = 0$, $b > 0$. Then ψ_n has no systematic growth but has rare peaks with increasing amplitude

(Fig. 2a). Then Mott's construction of an 1D eigenfunction gives the typical "hybrid" state, which is a linear combination of localized and extended states (Fig. 2b). The length of the localized component is evidently on the order of $1/\beta$. Consequently, an exponent β provides essential information which is not present in the mean value of γ. This information can have a practical meaning: parameter b determines the growth of all low even moments ($\langle\psi_n^{2m}\rangle \sim \exp(2ma + 2m^2b)n$), while the fourth moments enter the Kubo–Greenwood formula for conductivity.

According to numerical studies [11], an arbitrary (sth) term in Eq. (16) has a distribution of type (22) with parameters a_s and b_s. Therefore, relations $\gamma_s = a_s$, $\beta_s = 2a_s + 2b_s$ hold for arbitrary s. We see that the second moments of $\psi_n(r_\perp)$ give valuable information: (a) exponents β_s provide a rigorous upper bound for γ_s, $\beta_s \geq 2\gamma_s$; (b) estimates $\beta_s \sim \gamma_s$ are valid in the typical case $a_s \gtrsim b_s$; (c) β_s are related to fluctuations of γ_s in the case $a_s \ll b_s$. As for the heuristic relation with the Anderson transition, the use of the minimal exponents $\gamma_{\min}$ and $\beta_{\min}$ is on the same grounds. For example, scaling relations

$$\frac{1}{\gamma_{\min}L} = F\left(\frac{L}{\xi}\right) \text{ and } \frac{1}{\beta_{\min}L} = F\left(\frac{L}{\xi}\right) \tag{26}$$

can be postulated on the same level of rigorousness. In [11], empirical scaling is stated for $\gamma_{\min}L$ and b/a simultaneously. If this statement is taken seriously, it justifies (26) for $\beta_{\min}L$; in fact, scaling is absent for all these quantities (Sections 3–5).

3. SECOND MOMENTS FOR A SOLUTION OF THE CAUCHY PROBLEM

The idea of the present approach can be found in [51]. Let us rewrite the Schrödinger equation (11) for the 1D Anderson model as a recurrence relation, expressing ψ_{n+1} in terms of ψ_n, ψ_{n-1} and consider the Cauchy problem with the fixed initial conditions for ψ_1 and ψ_0. It is easy to see that ψ_2 is a function of V_1, ψ_3 is a function of V_2, V_1, etc. So ψ_n and V_n are statistically independent and can be averaged separately:

$$\langle\psi_{n+1}\rangle = E\langle\psi_n\rangle - \langle\psi_{n-1}\rangle, \tag{27}$$

$$\begin{aligned}\langle\psi_{n+1}^2\rangle &= (W^2 + E^2)\langle\psi_n^2\rangle \\ &- 2E\langle\psi_n\psi_{n-1}\rangle + \langle\psi_{n-1}^2\rangle \text{ etc.}\end{aligned} \tag{28}$$

We have accepted that V_n are statistically independent and

$$\langle V_n\rangle = 0, \quad \langle V_nV_{n'}\rangle = W^2\delta_{nn'}. \tag{29}$$

Equation (27) has the form (11) with $V_n \equiv 0$ and its solutions are

$$\langle\psi_n\rangle \sim \exp(ipn) \tag{30}$$

with $2\cos p = E$. Inside the allowed band, they have no systematic growth and $\langle\psi_n\rangle \sim 1$. Equation (28) for $E = 0$ is a difference equation for $x_n = \langle\psi_n^2\rangle$,

$$x_{n+1} = W^2x_n + x_{n-1} \tag{31}$$

with exponential solution

$$x_n = \langle\psi_n^2\rangle \sim e^{\beta n}, \quad 2\sinh\beta = W^2. \tag{32}$$

In the case $E \neq 0$, Eq. (28) is not closed and should be completed by the equation

$$\langle\psi_{n+1}\psi_n\rangle = E\langle\psi_n^2\rangle - \langle\psi_n\psi_{n-1}\rangle. \tag{33}$$

As a result, a set of difference equations arises for $x_n = \langle\psi_n^2\rangle$ and $\psi_n = \langle\psi_n\psi_{n-1}\rangle$

$$\begin{aligned}x_{n+1} &= (W^2 + E^2)x_n + x_{n-1} - 2Ey_n, \\ y_{n+1} &= Ex_n - y_n,\end{aligned} \tag{34}$$

with exponential growth of solution.

This approach is easily generalized for an arbitrary quasi-1D system. Consider the 2D Anderson model

$$\begin{aligned}\psi_{n+1,m} + \psi_{n-1,m} + \psi_{n,m+1} + \psi_{n,m-1} + V_{n,m}\psi_{n,m} \\ = E\psi_{n,m}\end{aligned} \tag{35}$$

and interpret it as a recurrence relation in n. Solving (35) for the quantity $\psi_{n+1,m}$ averaging its square, we can express it via the pair correlators of $\psi_{n,m}$ containing lower values of n. Constructing analogous equations for other correlators, we end with the close system of difference equations for the quantities

$$\begin{aligned}x_{m,m'}(n) &\equiv \langle\psi_{n,m}\psi_{n,m'}\rangle, \\ y_{m,m'}(n) &\equiv \langle\psi_{n,m}\psi_{n-1,m'}\rangle, \\ z_{m,m'}(n) &\equiv \langle\psi_{n-1,m}\psi_{n,m'}\rangle,\end{aligned} \tag{36}$$

which for $E = 0$ has the form

$$\begin{aligned}x_{m,m'}(n+1) &= W^2\delta_{m,m'}x_{m,m'}(n) + x_{m+1,m'+1}(n) \\ &+ x_{m-1,m'+1}(n) + x_{m+1,m'-1}(n) + x_{m-1,m'-1}(n) \\ &+ x_{m,m'}(n-1) + y_{m+1,m'}(n) + y_{m-1,m'}(n) \\ &+ z_{m,m'+1}(n) + z_{m,m'-1}(n),\end{aligned} \tag{37}$$

$$\begin{aligned}y_{m,m'}(n+1) &= -x_{m+1,m'}(n) - x_{m-1,m'}(n) - z_{m,m'}(n), \\ z_{m,m'}(n+1) &= -x_{m,m'+1}(n) - x_{m,m'-1}(n) - y_{m,m'}(n).\end{aligned}$$

This is a set of linear equations with coefficients independent of n, and its solution is exponential in n [52]:

$$x_{m,m'}(n) = x_{m,m'}e^{\beta n}, \quad y_{m,m'}(n) = y_{m,m'}e^{\beta n}, \quad z_{m,m'}(n) = z_{m,m'}e^{\beta n}. \tag{38}$$

The formal change of variable is useful

$$x_{m,m'} \equiv \tilde{x}_{m,m'-1} \equiv \tilde{x}_{m,l} \quad \text{etc.}, \tag{39}$$

where $l = m' - m$. Then, we have (with tildes omitted)

$$\begin{aligned}(e^{\beta} - e^{-\beta})x_{m,l} &= W^2\delta_{l,0}x_{m,l} + x_{m+1,l} \\ &+ x_{m-1,l} + x_{m+1,l-2} + x_{m-1,l+2} \\ &+ y_{m+1,l-1} + y_{m-1,l+1} + z_{m,l+1} + z_{m,l-1}, \\ e^{\beta}y_{m,l} &= -x_{m+1,l-1} - x_{m-1,l+1} - z_{m,l}, \\ e^{\beta}z_{m,l} &= -x_{m,l+1} - x_{m,l-1} - y_{m,l}.\end{aligned} \tag{40}$$

The coefficients contain no m dependence, and solution is exponential in m:

$$x_{m,l} = x_l e^{ipm} \quad \text{etc.}, \tag{41}$$

where allowed values for p, $p_s = 2\pi s/L$, $s = 0, 1, \ldots, L-1$ are determined by the periodical boundary conditions in the transverse direction:

$$\psi_{n,m+L} = \psi_{n,m}. \tag{42}$$

Excluding $y_{m,l}$ and $z_{m,l}$ from the first equation in (40), we end with the equation

$$\begin{aligned}x_{l+2}e^{-ip} + x_{l-2}e^{ip} + V\delta_{l,0}x_l &= \epsilon x_l, \quad x_{l+L} = x_l, \\ \epsilon = 2\cosh\beta, \quad V &= \frac{W^2\sinh\beta}{\cosh\beta - \cos p},\end{aligned} \tag{43}$$

describing a single impurity in a periodic chain. For $L \longrightarrow \infty$ its solution has the form $x_l \sim \exp(ipl/2 - \beta|l|/2)$ and the initial correlator

$$\langle \psi_{n,m}\psi_{n,m'}\rangle \sim \exp\left\{ip\frac{m+m'}{2} - \beta\frac{|m-m'|}{2} + \beta n\right\} \tag{44}$$

is localized in the transverse direction on the same scale $1/\beta$, as the scale of its growth in n. As a result, the localization length for the 2D system coincides with ξ_{1D}.

The positive exponents β_s for finite odd L are determined by the equation

$$2(\cosh\beta_s - \cos p_s) = W^2\coth(\beta_s L/2), \quad p_s = 2\pi s/L, \quad s = 0, 1, \ldots, L-1. \tag{45}$$

Their number is equal to L and coincides with a number of positive Lyapunov exponents γ_s for the same problem.[5] Allowed values of p_s and β_s become dense in the large L limit, and the quantities β and p can be considered as continuous:

$$2(\cosh\beta - \cos p) = W^2\coth(\beta L/2). \tag{46}$$

The minimal value of β is realized for $p = \pi$ and can be easily found in the large L limit:

$$\beta_{\min} = \begin{cases}\operatorname{arccosh}(W^2/2 - 1), & W^2 > 4 \\ \dfrac{2}{L}\operatorname{arctanh}(W^2/4), & W^2 < 4 \\ \dfrac{2\ln L - 2\ln\ln L + \ldots}{L}, & W^2 = 4.\end{cases} \tag{47}$$

The character of the solution is qualitatively changed at the critical value $W_c = 2$. If $W > W_c$, Eq. (46) is solved for $\beta \sim 1$, $\beta L \longrightarrow \infty$ and $\beta_{\min}$ tends to a constant in the large L limit. If $W < W_c$, Eq. (46) has solution for $\beta L = \text{const}$, $\beta \longrightarrow 0$ and provides for the behavior[6] $\beta_{\min} \propto 1/L$ for $L \longrightarrow \infty$. If $W = W_c$, solution is sought at conditions $\beta L \gg 1$, $\beta \ll 1$, when Eq. (46) reduces to $\beta^2 = 8\exp(-\beta L)$ and can be solved iteratively.

If the correlation length ξ_{1D} is estimated as $1/\beta_{\min}$, comparison with Section 2 leads to the conclusion that a state with the long-range order (i.e., the metallic phase) is absent. Exponential localization takes place for $W > W_c$, while the critical behavior $\xi_{1D} \sim L$ is realized in the entire range of $W < W_c$. The latter situation corresponds to localization with the divergent correlation length $\xi_{\text{loc}} \sim L$ and should probably be interpreted as power law localization. The transition at $W = W_c$ is of the Kosterlitz–Thouless type and should not be confused with the usual Anderson transition.

[5] The matrix T in Eq. (15) has dimensions $2L \times 2L$, but its eigenvalues occur in pairs of e^{γ_s} and $e^{-\gamma_s}$, so the number of positive γ_s is equal to L. In the case of even L, the number of positive β_s does not coincide with L and there are difficulties in comparing (16) and (18).

[6] Vanishing of $\beta_{\min}$ for $L = \infty$ was obtained in [42].

Calculating the first corrections to (47) related with finiteness of L, we have for $W > W_c$

$$\beta_{\min} = \beta_\infty + \frac{W^2}{\sinh\beta_\infty} e^{\beta_\infty L}, \qquad \beta_\infty = \operatorname{arccosh}\left(\frac{W^2-2}{2}\right) \tag{48}$$

and for $W < W_c$,

$$g = \frac{1}{\beta_{\min} L} = g_\infty + \frac{2(\sinh 1/2g_\infty)^2}{W^2 L^2}, \qquad g_\infty = \frac{1}{2\operatorname{arctanh}(W^2/4)}. \tag{49}$$

Defining the correlation length ξ as a scale, where dependences (48), (49) reach their asymptotics (i.e., where the additional terms become comparable to the main terms), we have (Fig. 3)

$$\xi \sim \begin{cases} 1/\ln W^2, & W^2 \longrightarrow \infty \\ \dfrac{\ln(1/\tau)}{\sqrt{\tau}}, & \tau = |W - W_c| \longrightarrow 0 \\ W^2, & W^2 \longrightarrow 0. \end{cases} \tag{50}$$

If $W > W_c$, the correlational length ξ coincides with the localization length $\xi_{loc} \sim \xi_{1D}$ apart from the logarithmic corrections. If $W < W_c$, the scales ξ and ξ_{loc} are substantially different, as is typical for the metallic phase (Fig. 3).

The scaling parameter $g(L)$ can be defined as $1/\beta_{\min} L$. Its dependence on L is determined by the equation

$$2\cosh\frac{1}{gL} - 2\cos p = W^2 \cot\frac{1}{2g} \tag{51}$$

with $p = \pi$ and presented in Fig. 1b. One can see the significant difference from the typical scaling situation (Fig. 1a). Absence of one-parameter scaling in Fig. 1b is clear from the fact that $g(L)$ is not constant for $W = W_c$, as it should be according (8), (9). It is still more evident for $W < W_c$, when different curves have different constant limits for $L \longrightarrow \infty$ and certainly cannot be matched by a scale transformation.

In the above considerations, we have estimated ξ_{1D} as $1/\beta_{\min}$. This can arouse doubts, because in the absence of scaling the quantities $\beta_{\min}$ and $\gamma_{\min}$ can be very different. In fact, substitution $\beta_{\min}$ by $\gamma_{\min}$ does not lead to qualitative changes in the presented picture. Indeed, $\beta_{\min}$ provides a rigorous upper bound for $\gamma_{\min}$ and (47) leads to

$$\gamma_{\min} \longrightarrow 0 \text{ for } L \longrightarrow \infty, \text{ if } W < W_c. \tag{52}$$

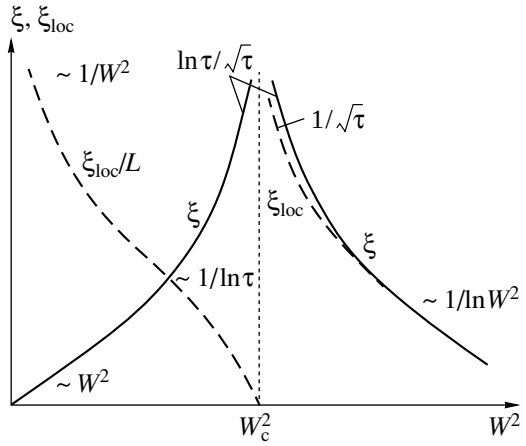

Fig. 3. Characteristic scales ξ and ξ_{loc} obtained under the assumption $\xi_{1D} \sim 1/\beta_{\min}$.

This is sufficient for the existence of the 2D transition, because in the large W region, the existence of exponential localization is beyond any doubt and finiteness of $\gamma_{\min}$ has been reliably established by numerical investigations [8–11]. Of course, the upper bound for $\gamma_{\min}$ does not forbid it to decrease more rapidly than $1/L$, as it should be for a true metallic state. However, such a possibility is reliably excluded by numerical studies (Section 4). Nevertheless, substitution $\gamma_{\min}$ by $\beta_{\min}$ can change the position of the critical point and the character of the critical behavior. Thus, the presented quantitative results should be considered as illustrative.

The influence of the phase transition on conductivity can be seen from the following arguments. Conductance G of a quasi-1D system of length l is roughly given by the exponential $\exp\{-2\gamma_{\min} l\}$ (see [11] and references therein). Extrapolation to $l \sim L$ suggests that $G \sim \exp\{-\text{const} L\}$ for $W > W_c$, while for $W < W_c$ the exponential reduces to a constant (in view of $\gamma_{\min} \sim 1/L$) and dependence $G(L)$ is determined by a preexponential factor.

4. COMPARISON WITH NUMERICAL RESULTS

The idea of power law localization was put forward by Last and Thouless [53] and discussed in a number of papers [54]. The statements, literally coinciding with those of Section 3, were made by Pichard and Sarma in 1981 [7] as the result of a numerical study of the 2D Anderson model. Their dependences of ξ_{1D} on L are presented in Fig. 4a, where values of disorder correspond to the quantity

$$\tilde{W} = W\sqrt{12} \tag{53}$$

(so $\tilde{W}_c = \sqrt{48} = 6.928\ldots$), because a rectangular distribution of width $\tilde{W}$ was used for V_n with $\langle V^2 \rangle =$

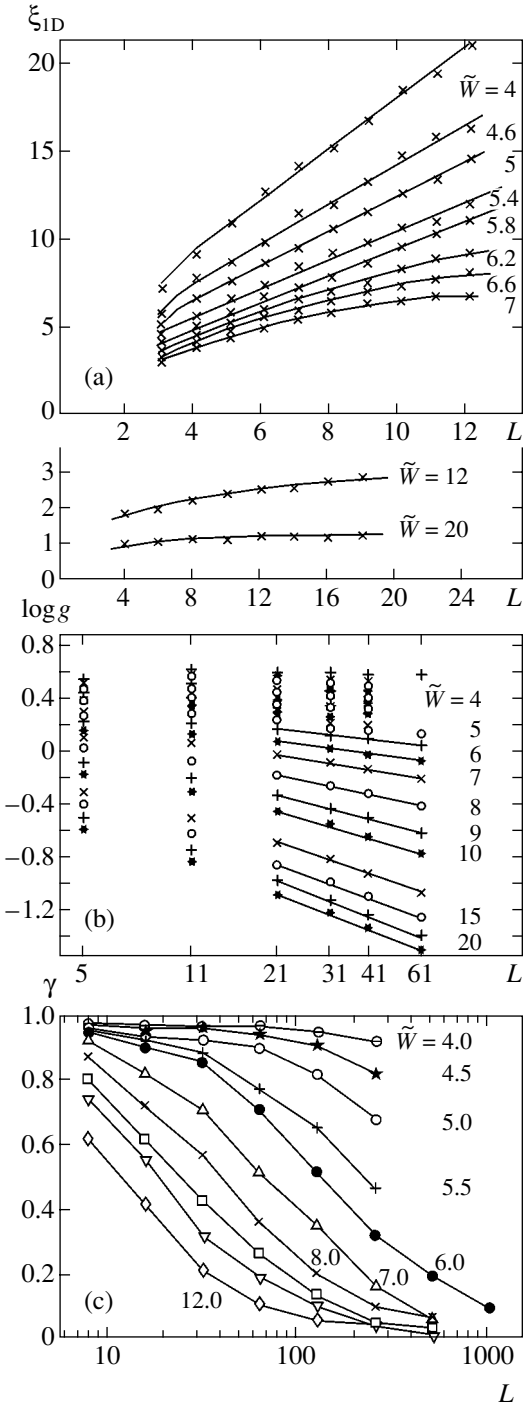

Fig. 4. Numerical results for ξ_{1D} [7], $g = 1/\gamma_{min}L$ [10] and parameter $\gamma(L)$ related to the energy level statistics [13].

$\tilde{W}^2/12 \equiv W^2$. The dependences are clearly linear for $\tilde{W} < 6$, while a tendency to saturation arises for $\tilde{W} > 6$ with a clear saturation for large $\tilde{W}$.

The results of [7] are considered out of date [8–11], and it is instructive to analyze the raw data of [10], which are cited as the best in the context of the transfer

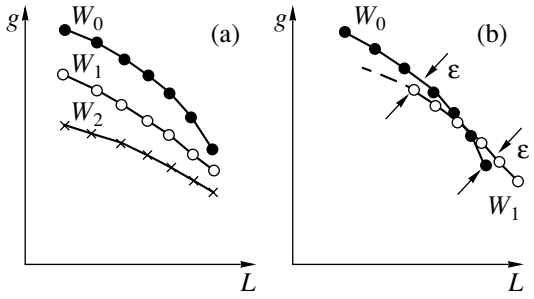

Fig. 5. Construction of scaling curves in a situation with no scaling.

matrix method (Fig. 4b). One can see that the scaling parameter $g = 1/\gamma_{min}L$ decrease convincingly only for large $\tilde{W}$. In the range of intermediate disorder ($\tilde{W}$ = 4–7), one cannot say definitely whether is there a tendency to unbounded decrease or to saturation. The data for weak disorder ($\tilde{W} < 4$) are absent altogether.

Thus, the raw numerical data (Fig. 4b) do not demonstrate absence of the 2D phase transition as stated by the authors of [10]. The latter conclusion is based on interpretation of these data in terms of one-parameter scaling. However, such interpretation is surely invalid. Absence of scaling for β_{min} suggests absence of scaling for γ_{min}, and this is confirmed by the similarity of Figs. 1b and 4b. The use of β_{min} as the upper bound for γ_{min} leads to the conclusion that the curves for $W < W_c$ in Fig. 4b cannot decrease to zero and should tend to finite limits. The scaling ansatz (8) can be formally valid only in the case if these finite limits are the same for all curves with $W < W_c$. Such a possibility does not appear realistic in Fig. 4b and, in fact, can be excluded: for small disorder, the lower bound given by $1/\beta_{min}L$ lies higher than all the data of Fig. 4b.

It is admitted in [8–11] that scaling relation (26) for γ_{min} is not proved, but it is stated that this relation has been convincingly confirmed empirically. Scaling curves $g = F(L/\xi)$ of impressive quality are presented in [10]. However, one should be very careful with empirical proofs of scaling. It is possible to come up with an algorithm that allows "proof" of empirical scaling in practically any situation.

Let us discuss construction of scaling curves in more detail. The raw numerical data are represented by dependences $g(L)$ for fixed values of disorder W_0, W_1, W_2,… (Fig. 5a). They should be plotted in Fig. 5b as functions of L/ξ, where the value of ξ for each curve should be chosen in such a manner that all curves coincide. If the logarithmic scale is chosen along the L axis, this procedure reduces to simple translation. Let the curve for W_0 be taken as a reference and a corresponding value ξ_0 be accepted as unity. Then this curve is carried over to Fig. 5b without changes. Now the curve for W_1 is translated to match the curve for W_0, a corre-

sponding value ξ_1 is determined, and so on. In the logarithmic plot, the dependences $g(L)$ have a simple form (see Fig. 4b) and can be approximated by something like parabolas. If the values W_0 and W_1 are close, the corresponding curves are parabolas with slightly different coefficients and they fit sufficiently well after translation.

Let us take ϵ as the permissible error of fitting and superimpose the curve for W_1 in a crosswise manner (Fig. 5b) on the curve for W_0. If some part of the former curve does not fit sufficiently well (dotted line in Fig. 5b), the corresponding points can be debated on reasonable grounds: scaling is a large-scale property and the raw data for small L are not reliable. The curve for W_2 is superimposed analogously, etc. If there is sufficient scattering of points, such a procedure will look natural. If the scattering of points is small, one can take a small step increment in W: then numerous curves will densely fill a band of width ϵ and the resulting scaling curve will appear accurate.

One can see that it is rather difficult to recognize a situation with no scaling from a situation when scaling holds but there are significant corrections to it. In the case under consideration, the situation is close to scaling in the sense that scaling relation (26) is trivially valid for $L \gtrsim \xi$ in the localized phase, when $\beta_{\min} \approx 1/\xi$ and $g \approx \xi/L$ in correspondence with Eq. (26) for $F(x) \approx 1/x$.

Certain comments should be made on the variant of finite-sized scaling based on the level statistics [12]. In this case, rather large systems are used, up to 1024^2 [13], and localization of all states in 2D systems appear convincing on the level of raw data (Fig. 4c), without interpreting them in terms of one-parameter scaling. However, this approach deals with crossover between the metallic behavior at small L and localized behavior at large L, and no attempt has been made to distinguish between exponential and power law localization.

5. IS ONE-PARAMETER SCALING POSSIBLE?

In Section 3 we have shown violation of one-parameter scaling for the quantity $\beta_{\min}$. If $\beta_{\min} \sim \gamma_{\min}$, then scaling is absent also for $\gamma_{\min}$. If $\beta_{\min}$ and $\gamma_{\min}$ are essentially different, a quasi-1D eigenfunction has a structure corresponding to both these parameters (see Fig. 2) and scaling is impossible on physical grounds. Analysis of numerical data (Section 4) confirms these conclusions. Two possible conclusions can be derived:

(i) the one-parameter scaling hypothesis [1] is fundamentally wrong;

(ii) the minimal Lyapunov exponent is an incorrect scaling variable.

Possibility (i) is not as absurd as it seems. Justifications for scaling in the σ-model approach [33] in fact failed due to a high-gradient catastrophe [55, 56], and absence of scaling on the level of distribution functions [57] set a problem of the correct choice of scaling variables. As for experiment, it confirms the "theory of quantum corrections" rather than the "theory of weak localization." Nevertheless, we consider the one-parameter scaling hypothesis as physically convincing. Its validity is confirmed (a) by analytical scaling in quasi-random systems [58–60]; (b) by validity of scaling relation $s = \nu(d-2)$ in the Vollhardt and Wölfle type theories [25, 26, 41]; (c) by renormalizability for $d < 4$ in the exact field theoretical formulation of the problem [29–31] (see footnote 1).

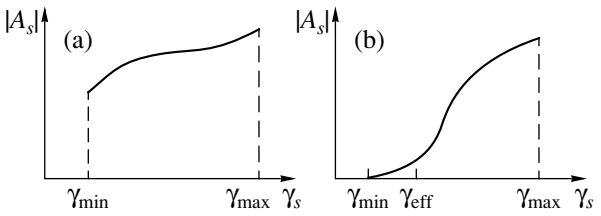

Fig. 6. Coefficients A_s in Eq. (13), appearing in Mott's construction, as function of γ_s.

Let us consider possibility (ii). It is clear from Section 2 that the existence of scaling for the correlation length ξ_{1D} looks convincing, and this is confirmed by the experience of the phase transitions theory [44–46]. As for relation (10) between ξ_{1D} and $\gamma_{\min}$, this is not as evident as it seems: for example, situations with $\gamma_{\min} > 0$ and $\xi_{1D} = \infty$ are known in quasi-random systems [58, 59, 61].[7] Relation (10) is based on Mott's construction of eigenfunctions by matching two solutions of type (16) that increase from two opposite edges of the system. Exact matching needs all terms in Eq. (16), and consequently, the coefficient A_m is finite, providing a length scale related to $1/\gamma_{\min}$. These considerations are valid for a sufficiently small number of terms in Eq. (16). In the large L limit, a spectrum of the Lyapunov exponents becomes quasi-continuous and a number of terms in Eq. (16) tend to infinity. In such a situation, no particular term in Eq. (16) is essential: it is an integral effect from all terms corresponding to some interval of the spectrum γ_s that matters.

Let us consider the coefficients A_s in Eq. (16), appearing in Mott's construction, as a function of γ_s (Fig. 6). Two qualitatively different situations are possible. In the first of them (Fig. 6a), all A_s are of the same order of magnitude; then the vicinity of $\gamma_{\min}$ makes a significant contribution and the length scale $1/\gamma_{\min}$ indeed corresponds to the localization length ξ_{1D}. In the other situation (Fig. 6b), the contribution of the vicinity of $\gamma_{\min}$ is strongly suppressed and the length

[7] In the 1D model (11) with $V_n = V\cos(2\pi\beta n)$ and irrational β, the Anderson transition holds for $V = 2$ [58, 59, 61]. The Lyapunov exponent γ is positive for all irrational β in the $V > 2$ region [61]. Nevertheless, localization length diverges for certain values of β, which are anomalously close to rational numbers [59].

scale $1/\gamma_{\min}$ has no physical meaning. The localization length ξ_{1D} is determined by some effective exponent γ_{eff} that provides a suitable cutoff[8] in the small γ_s region (Fig. 6b)

$$\xi_{1D} \sim \frac{1}{\gamma_{\text{eff}}}. \tag{54}$$

According to (8), scaling relation (26) should be postulated not for $\gamma_{\min}$ but for γ_{eff}.[9] After that, the dependence of γ_{eff} on parameters is determined by scaling itself.

The latter statement can be easily demonstrated in the framework of the numerical algorithm. Let us return to Fig. 5 but now accept that the curves for W_0, W_1, … are related not to $g = 1/\gamma_{\min}L$ but to $g = 1/\gamma_{n_0}L$ where γ_{n_0} is the Lyapunov exponent with the fixed number n_0. In general, the curves for W_0 and W_1 cannot be fit well by a scale transformation. One can improve the situation in the following manner. Taking a step from W_0 to W_1, let us replace γ_{n_0} by γ_{n_1}, i.e., change the number of the Lyapunov exponent. The curve for W_1 will change its form and we can choose $\Delta n = n_1 - n_0$ from the condition of the best fit with the curve for W_0. Analogously, for W_2 we take γ_{n_2}, adjust n_2, and so on. As a result, the scaling construction will determine not only dependence $\xi(W)$ but also dependence $n(W)$. Of course, these dependences are not determined completely: the general scale for ξ and initial number n_0 remain arbitrary.

Thus we came to the constructive modification of the commonly accepted numerical algorithm. This modification makes it possible to improve the quality of scaling and will probably resolve the contradictions discussed in Section 1.

6. ANALYTICAL SCALING

The suggested algorithm can be realized analytically if the raw data are given in the form defining $g = 1/\gamma_p L$ as a function of p, W, L:

$$g = Q(p, W, \tau), \quad \tau = \ln L, \tag{55}$$

where p is a continuous number of the Lyapunov exponent analogous to that in Eq. (51). Linearization of (55) near some value τ_0 gives

$$\begin{aligned} g &= Q(p, Q, \tau_0) + Q'_\tau(p, W, \tau_0)(\tau - \tau_0) \\ &\equiv g_0 + A(\tau - \tau_0). \end{aligned} \tag{56}$$

Analogous linearization for W_1 near the value τ_1 chosen from the condition $Q(p, W_1, \tau_1) = Q(p, W, \tau_0)$

$$\begin{aligned} g &= Q(p, W_1, \tau_1) + Q'_\tau(p, W_1, \tau_1)(\tau - \tau_1) \\ &\equiv g_0 + B(\tau - \tau_1) \end{aligned} \tag{57}$$

gives a slope B different from A, and the linear portions of dependences (56), (57) cannot be matched by a scale transformation. Let us change p in Eq. (57) in such way that equality $A = B$ holds:

$$\begin{aligned} g &= Q(p_1, W_1, \tau_1) + Q'_\tau(p_1, W_1, \tau_1)(\tau - \tau_1) \\ &\equiv g_0 + A(\tau - \tau_1). \end{aligned} \tag{58}$$

If p_1, W_1, τ_1 are close to p, W, τ_0, then correspondence of (56) to (58) gives

$$\begin{aligned} &Q'_p(p, W, \tau_0)\Delta p + Q'_W(p, W, \tau_0)\Delta W \\ &\quad + Q'_\tau(p, W, \tau_0)\Delta\tau = 0, \\ &Q''_{\tau p}(p, W, \tau_0)\Delta p + Q''_{\tau W}(p, W, \tau_0)\Delta W \\ &\quad + Q''_{\tau\tau}(p, W, \tau_0)\Delta\tau = 0, \end{aligned} \tag{59}$$

or solving for Δp and $\Delta\tau$,

$$\begin{aligned} \Delta p &= \frac{Q'_\tau Q''_{\tau W} - Q'_W Q''_{\tau\tau}}{Q'_p Q''_{\tau\tau} - Q'_\tau Q''_{\tau p}}\Delta W, \\ \Delta\tau &= \frac{Q'_W Q''_{\tau p} - Q'_p Q''_{\tau W}}{Q'_p Q''_{\tau\tau} - Q'_\tau Q''_{\tau p}}\Delta W. \end{aligned} \tag{60}$$

If an increment of τ is interpreted as an increment of $\ln\xi$,

$$\Delta\tau = \Delta\ln\xi, \tag{61}$$

then Eq. (58) takes the form

$$\Delta g = Q'_\tau(p, W, \tau_0)\Delta\ln(L/\xi). \tag{62}$$

For infinitesimal increments, Eqs. (60)–(62) turn into a set of the differential equations

[8] It is evident from Eq. (44) that the sth term of Eq. (18) is localized in the transverse direction on the same scale $1/\beta_s$ as the scale of its growth in n. An analogous property is expected for Eq. (16) and provides the equality of the transverse and longitudinal correlation lengths. The latter fundamental property is not spoiled when the lower edge of spectrum $\gamma_{\min}$ is replaced by the effective cutoff γ_{eff}.

[9] A quasi-1D eigenfunction contains a lot of scales $1/\gamma_1$, $1/\gamma_2$, …, $1/\gamma_m$ and all these scales are essential near its center. Small scales succeedingly "die out" when one moves from the maximum of the eigenfunction to its tails. Only scale $1/\gamma_m$ remains in the end, but for the situation of Fig. 6b it occurs at such distances where the eigenfunction is zero for all practical purposes. A single parameter ξ_{1D} cannot adequately describe all scales $1/\gamma_s$. In the best case, it can account for the most significant of them, those which determine the general form of the eigenfunction and correspond to the effective cutoff γ_{eff}.

$$\frac{dp}{dW} = -\frac{Q'_W(p, W, \tau_0)Q''_{\tau\tau}(p, W, \tau_0) - Q'_\tau(p, W, \tau_0)Q''_{\tau W}(p, W, \tau_0)}{Q'_p(p, W, \tau_0)Q''_{\tau\tau}(p, W, \tau_0) - Q'_\tau(p, W, \tau_0)Q''_{\tau p}(p, W, \tau_0)},$$
$$\frac{d\ln\xi}{dW} = -\frac{Q'_p(p, W, \tau_0)Q''_{\tau W}(p, W, \tau_0) - Q'_W(p, W, \tau_0)Q''_{\tau p}(p, W, \tau_0)}{Q'_p(p, W, \tau_0)Q''_{\tau\tau}(p, W, \tau_0) - Q'_\tau(p, W, \tau_0)Q''_{\tau p}(p, W, \tau_0)}, \quad (63)$$
$$\frac{dg}{d\ln(L/\xi)} = Q'_\tau(p, W, \tau_0),$$

defining the dependences $p(W)$, $\xi(W)$ and $g = F(L/\xi)$. Equations (63) correspond to the usual scaling construction (Sections 4 and 5) for the maximal system size $L_0 = \exp(\tau_0)$, where dependences $g(\ln L)$ are linearized near $\ln L_0$ and only linear portions (marked in Fig. 4b) are matched in the course of scale transformations. The τ_0 dependence should vanish in the limit $\tau_0 \longrightarrow \infty$ for the approach to be self-consistent.

If the dependence (55) is given in the implicit form

$$G(g, p, W, \tau) = 0, \quad (64)$$

then Eqs. (63) can be expressed in terms of G:

$$\frac{dp}{dW} = -\frac{G'_W(G''_{g\tau}G'_\tau - G''_{\tau\tau}G'_g) - G'_\tau(G''_{gW}G'_\tau - G''_{\tau W}G'_g)}{G'_p(G''_{g\tau}G'_\tau - G''_{\tau\tau}G'_g) - G'_\tau(G''_{gp}G'_\tau - G''_{\tau p}G'_g)},$$
$$\frac{d\ln\xi}{dW} = -\frac{G'_p(G''_{gW}G'_\tau - G''_{\tau W}G'_g) - G'_W(G''_{gp}G'_\tau - G''_{\tau p}G'_g)}{G'_p(G''_{g\tau}G'_\tau - G''_{\tau\tau}G'_g) - G'_\tau(G''_{gp}G'_\tau - G''_{\tau p}G'_g)}, \quad (65)$$
$$\frac{dg}{d\ln(L/\xi)} = -\frac{G'_\tau}{G'_g}.$$

All quantities in the right-hand side are functions of g_0, p, W, τ_0, where τ_0 is a constant parameter and g_0 is expressed in terms of p, W using the relation $G(g_0, p, W, \tau_0) = 0$.

Unfortunately, relation (64) for the conventional Lyapunov exponents γ_s is not available; therefore, we present here illustrative calculations for the exponents β_s when Eq. (64) has the form (51). The latter equation can be simplified by expansion of $\cosh(1/gL)$ without significant physical consequences.[10] Thus, Eq. (64) can be taken in the form

$$G(g, p, W, \tau) = \frac{\exp(-2\tau_0)}{g^2} + \varphi(p) - W^2 f(g) = 0, \quad (66)$$

where

$$\varphi(p) = 2(1 - \cos p), \quad f(g) = \coth(1/2g).$$

Then Eqs. (65) reduce to

$$\frac{d\varphi(p)}{dW^2} = -\frac{g_0^2 f(g_0)W^2 - \exp(-2\tau_0)}{g_0^2 W^2} = \frac{\varphi(p)}{W^2}, \quad (67)$$

$$\frac{d\ln\xi}{d\ln W} = -1, \quad (68)$$

$$\frac{dg}{d\ln\xi} = \frac{2g_0\exp(-2\tau_0)}{2\exp(-2\tau_0) + W^2 g_0^3 f'(g_0)}, \quad (69)$$

where g_0 is a function of p, W determined by equation $G(g_0, p, W, \tau_0) = 0$. It is easy to solve (67), (68)

$$\varphi(p) = 2(1 - \cos p) = c_0 W^2, \quad \xi = \frac{c_1}{W} \quad (70)$$

and obtain the relations

$$W^2 = \frac{\exp(-2\tau_0)}{g_0^2[f(g_0) - c_0]}, \quad \frac{dg}{dg_0} = 1, \quad (71)$$

which make it impossible to find the dependence $g = F(L/\xi)$ in the implicit form

$$c_1^2 g^2[f(g) - c_0] = (\xi/L)^2. \quad (72)$$

Here c_0 and c_1 are arbitrary constants. The quantity $\varphi(p)$ is restricted, $0 \le \varphi(p) \le 4$ and scaling is possible only for

$$W^2 < \frac{4}{c_0} \equiv W_{c1}^2. \quad (73)$$

[10] It gives only restriction for L from below in the small g region.

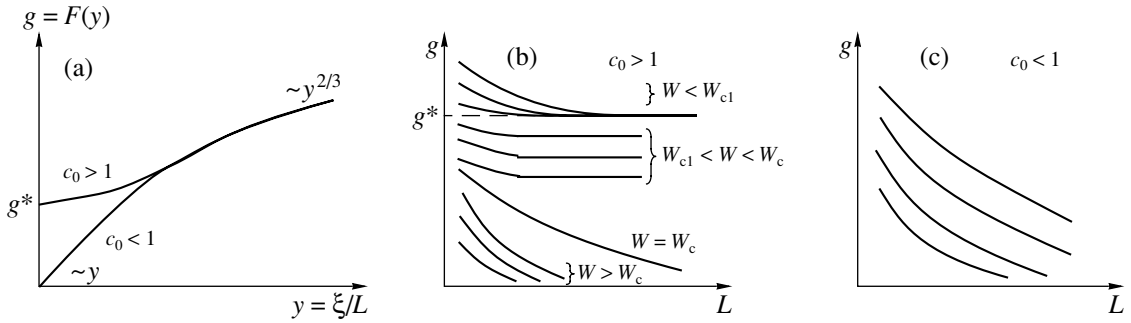

Fig. 7. (a) Scaling function $g = F(\xi/L)$ given by Eq. (72), (b) and (c) dependences $g(L)$ for $c_0 > 1$ and $c_0 < 1$.

If $W > W_{c1}$, the quantity $\varphi(p)$ takes its maximum value at $p = \pi$ and the concept of the minimal Lyapunov exponent is restored; therefore, scaling is absent and the results of Section 3 hold.

The situation is qualitatively different for $c_0 < 1$ and $c_0 > 1$, when $W_{c1} > W_c$ and $W_{c1} < W_c$, respectively. A scaling function $g = F(\xi/L)$ given by Eq. (77) is shown in Fig. 7a: for $c_0 < 1$ it is close to the one empirically found in [10], while for $c_0 >$ I, a finite limit $g^* = 1/2\text{arctanh}(1/c_0)$ is reached for $\xi/L \longrightarrow 0$. The dependences $g(L)$ for $W < W_{c1}$ can be found from Eq. (66) after substitution of $\varphi(p)$ from Eq. (70), while for $W > W_{c1}$ they remain the same as in Section 3 (Figs. 7b and 7c). The behavior of the characteristic scales for $c_0 > 1$ and $c_0 < 1$ is shown in Figs. 8a and 8b, respectively.

It is clear from Figs. 7 and 8 that exponential localization of all states takes place for $c_0 < 1$ in correspondence with the commonly accepted viewpoint, while the phase with power law localization remains for $c_0 > 1$, though the behavior of characteristic scales changes in comparison with Section 3. In fact, singularity at the point W_{c1} is false. It is related to our postulation of exact scaling for $W < W_{c1}$, which is in fact approximate. The correlation length ξ is finite near W_{c1}, and corrections to scaling related to l_i/ξ (see Eq. (4)) cannot be considered vanishingly small. With corrections to scaling taken into account, the qualitative difference between regions $W < W_{c1}$ and $W > W_{c1}$ disappears. There is good scaling for $W \lesssim W_{c1}$ and absence of scaling for $W \gtrsim W_{c1}$, but destruction of scaling occurs gradually due to the increase of corrections to it.

Let us discuss the physical sense of an arbitrary parameter c_0. Formally, it occurs due to the absence of initial conditions to Eqs. (63), while in the specific Anderson model the value of c_0 is definite. However, we have not fixed the distribution function $P(V)$ and used only its first and second moments (see Eq. (27)). Therefore, the initial equation (66) describes not one, but a variety of Anderson models with different forms of $P(V)$. The values of c_0 are different in these models, and we can expect them to cover both $c_0 < 1$ and $c_0 > 1$ regions.[11] As a result, 2D systems can be divided into two classes. The first class is characterized by exponential localization of all states, while in the second class there is a phase transition between exponential and power law localization. Division into two classes was proposed by Zavaritskaya in the middle of 1980s on experimental grounds (see [62] and references therein).

We should note that the above consideration has an illustrative character. The initial Eq. (66) has another form for the conventional Lyapunov exponents, and substantial modification of the quantitative results is possible. In particularly, instead of (70), one expects the exponential dependence $\xi \sim \exp(\text{const}/W^2)$ for the correlation length, as follows from one-parameter scaling [1] or from the Vollhardt and Wölfle theory [25].

7. INTERPRETATION IN TERMS OF THE GELL-MANN–LOW EQUATION

In one-parameter scaling theory [1], a scaling variable $g(L)$ is defined as a conductance G_L of a finite block of size L^d in units of e^2/h. The Gell-Mann–Low equation is valid for it:

$$\frac{d\ln g}{d\ln L} = \beta(g), \tag{74}$$

where $\beta(g)$ has asymptotical behavior,

$$\beta(g) = \begin{cases} (d-2) + \dfrac{A}{g} + \ldots \quad (A < 0), \quad g \gg 1 \\ \ln g, \quad g \ll 1. \end{cases} \tag{75}$$

The zero term of the first asymptotics is related to the existence of finite conductivity σ in the metallic state (so $G_L \sim \sigma L^{d-2}$) and the additional term A/g is obtained by a diagrammatical analysis [63]. The second asymp-

[11] Of course, there may be principal restrictions that make realization of the case $c_0 > 1$ impossible. At present, we know of any such restrictions.

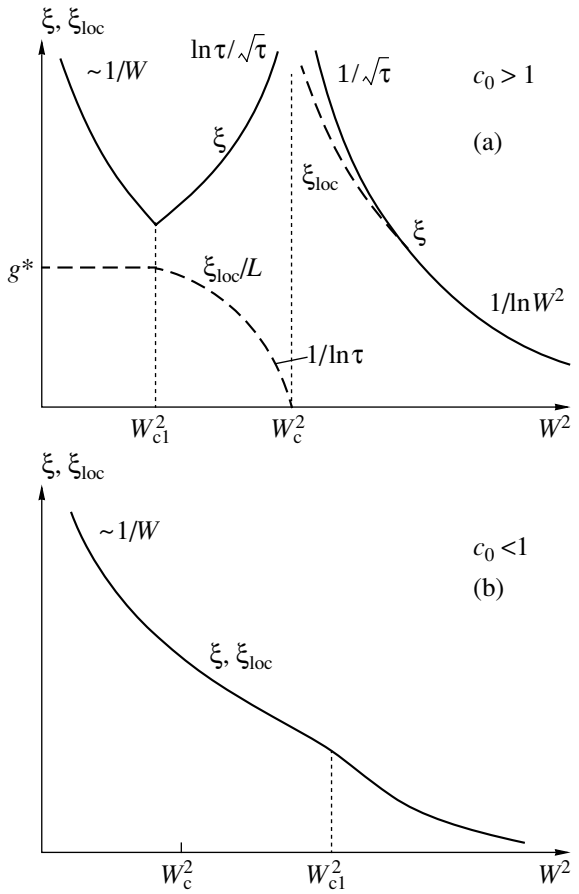

Fig. 8. Behavior of characteristic scales for (a) $c_0 > 1$ and (b) $c_0 < 1$.

totics is related to assumption of exponential localization ($G_L \sim \exp(-\text{const}L)$).

The latter assumption is not valid in the general case. If power law localization takes place, then $G_L \sim L^{-\alpha}$ and

$$\beta(g) = -\alpha, \quad g \ll 1. \tag{76}$$

It is clear from the above considerations that the β-function in the 2D case is not universal for small g and can have a different behavior for different cases (Fig. 9). This conclusion is quite natural from the viewpoint of the general theory of phase transitions [29]. Indeed, scaling is a large-scale property and Eq. (74) has a real sense only for $|\beta(g)| \ll 1$ (that is, in the narrow region near the horizontal axis in Fig. 9), when $g(L)$ slowly changes. In the other case, $g(L)$ changes on an atomic scale and there are no grounds for either scale invariance or universality. From the general viewpoint, existence of universal results (75) is rather random and the assumption on universality of $\beta(g)$ for all g [1] is an obvious idealization (see [62] for experimental aspects).

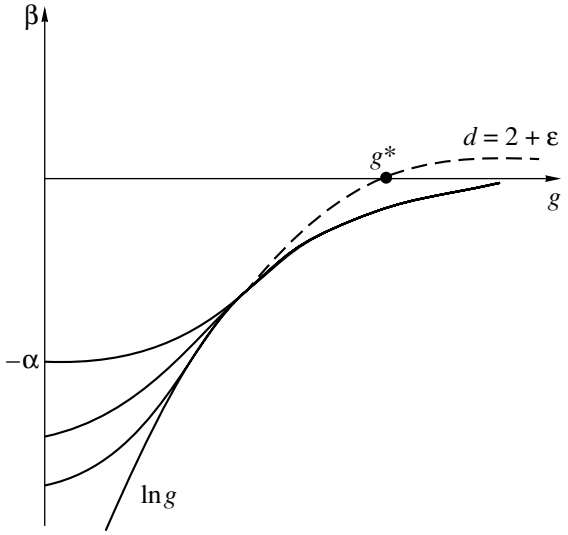

Fig. 9. Gell-Mann–Low function $\beta(g)$ is not universal in the small g region.

For $d > 2$, Eq. (74) has a fixed point g^* that determines the existence of the Anderson transition. For $d = 2 + \epsilon$, g^* is arranged in the large g region and disappears in the limit $\epsilon \longrightarrow 0$: i.e., the Anderson transition is absent in the 2D case. This conclusion should not be revised, because the true metallic state is indeed absent (Section 3). The transition we have discussed is situated deep in the localized phase and corresponds to switching from one β-function to another during a change in the external parameters. Consequently, no substantial revision of the weak localization region is necessary.

8. CONCLUSIONS

We have shown that the commonly accepted numerical algorithm based on the transfer matrix method is deficient, because the minimal Lyapunov exponent does not obey any scaling. To restore scaling, a modification of the algorithm is necessary which constructively reduces to a change in the number of the Lyapunov exponent in the course of scaling constructions. This modification does not require a significant increase in numerical work, because the higher Lyapunov exponents in any case are determined in the course of evaluating $\gamma_{\min}$ [22]. In fact, one can take the old raw data [8–11] and reinterpret them. This will probably resolve the contradictions discussed in Section 1.

Already at this stage one can interpret a strange drift of results for $d = 3$ with increasing system size: $\nu = 0.66$ [7], $\nu = 1.2 \pm 0.3$ [8], $\nu = 1.35 \pm 0.15$ [15], $\nu = 1.54 \pm 0.08$ [16], $\nu = 1.58 \pm 0.02$ [21]. For small L, the number of terms in Eq. (16) is not very large and the maximal scale $1/\gamma_{\min}$ is indeed related to the correlation length; description of the Anderson transition is rough, but the

results are correct in their roughness. For large L, the difference between the minimal and effective Lyapunov exponents becomes significant and the results, being formally accurate, become in fact incorrect.

If the concept of the minimal Lyapunov exponent is taken literally, it leads to unambiguous prediction of the 2D phase transition. This transition is of the Kosterlitz–Thouless type and occurs between exponential and power law localization. Modification of the algorithm leads to division of 2D systems into two classes, the first of which is characterized by exponential localization of all states, while in the second class there is a phase transition between exponential and power law localization.

ACKNOWLEDGMENTS

This work was supported by the Russian Foundation for Basic Research, project 03-02-17519.

REFERENCES

1. E. Abrahams, P. W. Anderson, D. C. Licciardello, and T. V. Ramakrishman, Phys. Rev. Lett. **42**, 673 (1979).
2. B. L. Al'tshuler, A. G. Aronov, D. E. Khmel'nitskii, and A. I. Larkin, in *Quantum Theory of Solids*, Ed. by I. M. Lifshitz (Mir, Moscow, 1982).
3. S. V. Kravchenko, G. V. Kravchenko, J. E. Furneaux, *et al.*, Phys. Rev. B **50**, 8039 (1994).
4. S. V. Kravchenko, W. E. Mason, G. E. Bowker, *et al.*, Phys. Rev. B **51**, 7038 (1995).
5. S. V. Kravchenko, D. Simonian, M. P. Sarachik, *et al.*, Phys. Rev. Lett. **77**, 4938 (1996).
6. E. Abrahams, S. V. Kravchenko, and M. P. Sarachik, Rev. Mod. Phys. **73**, 251 (2001).
7. J. L. Pichard and G. Sarma, J. Phys. C: Solid State Phys. **14**, L127 (1981); J. Phys. C: Solid State Phys. **14**, L617 (1981).
8. A. MacKinnon and B. Kramer, Phys. Rev. Lett. **47**, 1546 (1981).
9. A. MacKinnon and B. Kramer, Z. Phys. **53**, 1 (1983).
10. M. Schreiber and M. Ottomeier, J. Phys.: Condens. Matter **4**, 1959 (1992).
11. K. Slevin, Y. Asada, and L. I. Deych, cond-mat/0404530.
12. B. I. Shklovskii, B. Shapiro, B. R. Sears, *et al.*, Phys. Rev. B **47**, 11487 (1993).
13. I. Kh. Zharekeshev and B. Kramer, Phys. Rev. B **51**, 17 239 (1995).
14. B. Kramer, K. Broderix, A. MacKinnon, and M. Schreiber, Physica A (Amsterdam) **167**, 163 (1990).
15. E. Hofstetter and M. Schreiber, Europhys. Lett. **21**, 933 (1993).
16. A. MacKinnon, J. Phys.: Condens. Matter **6**, 2511 (1994).
17. M. Schreiber and H. Grussbach, Phys. Rev. Lett. **76**, 1687 (1996).
18. I. Kh. Zharekeshev and B. Kramer, Phys. Rev. B **51**, 17239 (1995).
19. I. Kh. Zharekeshev and B. Kramer, Phys. Rev. Lett. **79**, 717 (1997).
20. I. Kh. Zharekeshev and B. Kramer, Ann. Phys. (Leipzig) **7**, 442 (1998).
21. K. Slevin and T. Ohtsuki, Phys. Rev. Lett. **82**, 382 (1999).
22. P. Markos, J. Phys. A: Math. Gen. **33**, L393 (2000).
23. P. Markos and M. Henneke, J. Phys.: Condens. Matter **6**, L765 (1994).
24. I. M. Suslov, cond-mat/0105325; cond-mat/0106357.
25. D. Vollhardt and P. Wölfle, Phys. Rev. B **22**, 4666 (1980); Phys. Rev. Lett. **48**, 699 (1982); in *Modern Problems in Condensed Matter Sciences*, Ed. by V. M. Agranovich and A. A. Maradudin (North-Holland, Amsterdam, 1992), Vol. 32.
26. A. Kawabata, Solid State Commun. **38**, 823 (1981); B. Shapiro, Phys. Rev. B **25**, 4266 (1982); A. V. Myasnikov and M. V. Sadovskiĭ, Fiz. Tverd. Tela (Leningrad) **24**, 3569 (1982) [Sov. Phys. Solid State **24**, 2033 (1982)].
27. I. M. Suslov, Zh. Éksp. Teor. Fiz. **102**, 1951 (1992) [Sov. Phys. JETP **75**, 1049 (1992)].
28. I. M. Suslov, Usp. Fiz. Nauk **168**, 503 (1998) [Phys. Usp. **41**, 441 (1998)].
29. S. Ma, *Modern Theory of Critical Phenomena* (Benjamin, Reading, Mass., 1976; Mir, Moscow, 1980).
30. A. Nitzan, K. F. Freed, and M. N. Cohen, Phys. Rev. B **15**, 4476 (1977).
31. M. V. Sadovskiĭ, Usp. Fiz. Nauk **133**, 223 (1981) [Sov. Phys. Usp. **24**, 96 (1981)].
32. N. N. Bogolyubov and D. V. Shirkov, *Introduction to the Theory of Quantized Fields*, 3rd ed. (Nauka, Moscow, 1976; Wiley, New York, 1980).
33. F. Wegner, Z. Phys. B **35**, 207 (1979); L. Schäfer and F. Wegner, Z. Phys. B **38**, 113 (1980); S. Hikami, Phys. Rev. B **24**, 2671 (1981); K. B. Efetov, A. I. Larkin, and D. E. Khmel'nitskiĭ, Zh. Éksp. Teor. Fiz. **79**, 1120 (1980) [Sov. Phys. JETP **52**, 568 (1980)]; K. B. Efetov, Adv. Phys. **32**, 53 (1983).
34. F. Wegner, Nucl. Phys. B **316**, 663 (1989).
35. H. Kunz and R. Souillard, J. Phys. Lett. **44**, L411 (1983).
36. K. B. Efetov, Zh. Éksp. Teor. Fiz. **93**, 1125 (1987) [Sov. Phys. JETP **66**, 634 (1987)]; Zh. Éksp. Teor. Fiz. **94** (1), 357 (1988) [Sov. Phys. JETP **67**, 199 (1988)].
37. B. Shapiro, Phys. Rev. Lett. **50**, 747 (1983).
38. D. Belitz and T. R. Kirkpatrick, Rev. Mod. Phys. **66**, 261 (1994).
39. N. G. Zhdanova, M. S. Kagan, and E. G. Landsberg, Zh. Éksp. Teor. Fiz. **117**, 761 (2000) [JETP **90**, 662 (2000)].
40. H. Kunz and R. Souillard, J. Phys. Lett. **44**, L506 (1983).
41. I. M. Suslov, Zh. Éksp. Teor. Fiz. **108**, 1686 (1995) [JETP **81**, 925 (1995)].
42. V. N. Kuzovkov, W. von Niessen, V. Kashcheyevs, and O. Hein, J. Phys.: Condens. Matter **14**, 13777 (2002).

43. V. N. Kuzovkov and W. von Niessen, Eur. Phys. J. B **42**, 529 (2004).
44. M. P. Nightingale, Physica A (Amsterdam) **83**, 561 (1976).
45. B. Derrida and J. Vannimenus, J. Phys. Lett. **41**, L473 (1980).
46. B. Derrida, J. Phys. A: Math. Gen. **14**, L5 (1981).
47. V. I. Oseledets, Tr. Mosk. Mat. O-va **19**, 197 (1968).
48. N. F. Mott and E. A. Davis, *Electronic Processes in Non-Crystalline Materials*, 2nd ed. (Clarendon, Oxford, 1979; Mir, Moscow, 1982).
49. G. A. Korn and T. M. Korn, *Mathematical Handbook for Scientists and Engineers*, 2nd ed. (McGraw-Hill, New York, 1968; Nauka, Moscow, 1977).
50. I. M. Lifshits, S. A. Gredeskul, and L. A. Pastur, *Introduction to the Theory of Disordered Systems* (Nauka, Moscow, 1982; Wiley, New York, 1988).
51. D. J. Thouless, Phys. Rep. **93**, 92 (1974).
52. A. O. Gel'fond, *Calculation of Finite Differences* (Nauka, Moscow, 1967) [in Russian].
53. B. J. Last and D. J. Thouless, J. Phys. C: Solid State Phys. **7**, 699 (1974).
54. R. Haydock, Philos. Mag. B **43**, 203 (1981); N. F. Mott and M. Kaveh, Adv. Phys. **34**, 329 (1985).
55. V. E. Kravtsov, I. V. Lerner, and V. I. Yudson, Zh. Éksp. Teor. Fiz. **94** (7), 255 (1988) [Sov. Phys. JETP **67**, 1441 (1988)].
56. F. Wegner, Z. Phys. B **78**, 33 (1990).
57. B. L. Al'tshuler, V. E. Kravtsov, and I. V. Lerner, Zh. Éksp. Teor. Fiz. **91**, 2276 (1986) [Sov. Phys. JETP **64**, 1352 (1986)].
58. I. M. Suslov, Zh. Éksp. Teor. Fiz. **83**, 1079 (1982) [Sov. Phys. JETP **56**, 612 (1982)].
59. I. M. Suslov, Zh. Éksp. Teor. Fiz. **84**, 1792 (1983) [Sov. Phys. JETP **57**, 1044 (1983)].
60. I. M. Suslov, Zh. Éksp. Teor. Fiz. **92**, 1433 (1987) [Sov. Phys. JETP **65**, 806 (1987)].
61. S. Aubry and G. Andre, Ann. Izr. Phys. Soc. **3**, 133 (1980).
62. É. I. Zavaritskaya, Zh. Éksp. Teor. Fiz. **93**, 952 (1987) [Sov. Phys. JETP **66**, 536 (1987)].
63. L. P. Gor'kov, A. I. Larkin, and D. E. Khmel'nitskiĭ, Pis'ma Zh. Éksp. Teor. Fiz. **30**, 248 (1979) [JETP Lett. **30**, 228 (1979)].

Journal of Experimental and Theoretical Physics, Vol. 101, No. 4, 2005, pp. 676–679.
Translated from Zhurnal Éksperimental'noĭ i Teoreticheskoĭ Fiziki, Vol. 128, No. 4, 2005, pp. 785–788.

ORDER, DISORDER, AND PHASE TRANSITIONS IN CONDENSED SYSTEMS

Features of Interatomic Force Interaction in an *i*-AlCuFe Quasicrystal

P. P. Parshin[a], M. G. Zemlyanov[a], and R. A. Brand[b]

[a] *Russian Research Center Kurchatov Institute, Moscow, 123182 Russia*
[b] *Duisburg University, Duisburg, D-47048 Germany*
e-mail: zeml@isssph.kiae.ru

Received May 23, 2005

Abstract—Earlier experimental results on partial thermal vibrational spectra and on the atomic and electronic structure of icosahedral *i*-AlCuFe quasicrystals are used for analyzing the role of Al, Cu, and Fe atoms in interatomic interactions in these quasicrystals. A physical model proposed for the structure of *i*-AlCuFe quasicrystals matches with the available experimental data and provides a qualitative description of the features of the interatomic interaction. © *2005 Pleiades Publishing, Inc.*

1. INTRODUCTION

The interest in quasicrystals is due to the unique properties of these compounds. As a rule, stable quasicrystalline phases are synthesized in ternary systems of metallic elements with the participation of transition metals. In particular, the alloy $Al_{0.62}Cu_{0.255}Fe_{0.125}$ is a typical representative of icosahedral quasicrystals (with a fivefold symmetry axis). It has been established experimentally (see [1] and the literature therein) that the resistivity of quasicrystals is much (sometimes three orders of magnitude) higher than the resistivity of the constituent metals. The thermal conductivity and the thermal expansion coefficient of quasicrystals are substantially lower than the relevant characteristics typical of metals. Optical properties of quasicrystals are also unique (these compounds exhibit selective absorption in various regions of the electromagnetic radiation spectrum. It has been established that the adhesion coefficient of polar liquids at the quasicrystal surface is considerably lower than at the surface of metals or oxides. In addition, the quasicrystal surface exhibits a much smaller friction coefficient and a high corrosion resistance.

In the most general form, the atomic structure of quasicrystals can be visualized as a network of mutually penetrating and quasi-periodically packed clusters whose diameter is equal to several interatomic spacings. In the case of icosahedral quasicrystals, these atomic clusters are constructed from icosahedral or dodecahedral shells with a fivefold symmetry axis [2]. The presence of narrow diffraction peaks in the electron [3], X-ray [4], and neutron [5] diffraction patterns for quasicrystals indicates the existence of the long-range order in the atomic arrangement of these alloys. At the same time, no spatial periodicity is observed since it is incompatible with the existence of the fivefold and tenfold symmetry axes.

The above-mentioned peculiar properties of quasicrystalline phases make these materials candidates for various technical applications, on the one hand, and stimulate experimenters and theorists in their quest for the physical origin of these properties and for the microscopic factors responsible for the stability of these compounds, on the other hand. One of the possible trends in this direction is associated with analysis of specific features in the atomic dynamics of quasicrystalline alloys. A direct method for obtaining such information is the inelastic scattering of slow neutrons using the isotopic contrast technique. In an earlier study [6], we investigated experimentally the inelastic scattering of cold neutrons from icosahedral quasicrystals having a composition of $Al_{0.62}Cu_{0.255}Fe_{0.125}$ and differing in the isotopic composition of copper and iron. We managed for the first time to reconstruct the partial spectra of thermal vibrations of copper, iron, and aluminum ions in this compound directly from experimental data without using any model representation. Here, we carry out a detailed analysis of the results obtained in [6], as well as the results of independent studies, to clarify specific features of the interatomic force interaction in an *i*-AlCuFe icosahedral crystal.

2. DISCUSSION

Let us recall the main results obtained in [6]. Partial vibrational spectra of copper, iron, and aluminum ions display a number of peaks. It was found that Cu and Fe atoms vibrate mainly in a relatively narrow energy range in the vicinity of 16 and 30 meV, respectively, while aluminum atoms vibrate in the entire energy range up to 60 meV. It was found that the vibrational spectrum of Cu atoms is much softer than the vibrational spectrum of Fe atoms. This difference in the spectra cannot be explained by the difference in atomic

masses alone since the atomic masses differ approximately by 10%, while the vibrational energies averaged over the spectrum differ approximately by 40%. It means that copper atoms in the quasicrystal studied here are bound less strongly than iron atoms. In addition, although the density of vibrational states of copper is mainly concentrated in the vicinity of 16 meV, it also spreads to the range of high energies up to 60 meV. The principal bandwidth in the vibrational spectrum of iron atoms is quite large and considerably exceeds the principal bandwidth in the vibrational spectrum of copper atoms. It should be noted that the partial vibrational spectra of Cu, Fe, and Al atoms in the quasicrystal studied here substantially differ from the vibrational spectra in the corresponding pure metals [7–9]. In particular, the mean vibrational energies of Cu and Fe atoms in the quasicrystal are noticeably lower than in the corresponding metals. At the same time, the cutoff energy in the vibrational spectrum of Al atoms in the quasicrystal ($E_{\max} \approx 60$ meV) is noticeably higher than the cutoff energy in the case of metallic aluminum ($E_{\max} =$ 40 meV). These results indicate that force bonds are tighter for Al atoms and weaker for Cu and Fe atoms in the quasicrystal than in the crystals of these metals.

To explain these results, we can use the information on the atomic and electronic structure of *i*-AlCuFe quasicrystals. The extended X-ray absorption fine structure (EXAFS) spectroscopy data available for *i*-AlCuFe quasicrystal [10] and the 1/1 crystal phase of Al(Si)-Cu-Fe approximating the quasicrystal [11] indicate that the average coordination numbers of Cu and Fe atoms in *i*-AlCuFe differ considerably. In particular, it was shown in [10] that the nearest neighborhood of an iron atom is characterized by a single coordination sphere filled with Al and Cu atoms, while two such spheres exist for copper atoms (the nearest sphere is filled with Fe atoms and the next sphere is filled with Al and Cu atoms). In addition, in accordance with the model of the atomic structure based on neutron diffraction data obtained for a monocrystalline sample of an *i*-AlCuFe quasicrystal [12], the atomic structure of the alloy has the form of a network of mutually penetrating atomic clusters. In each cluster of this type, a copper atom is surrounded by twelve Al atoms arranged at the vertices of an icosahedron of radius $R_i = 2.75$ Å and by twenty atoms (approximately 10.5 Al atoms, 8.5 Cu atoms, and one Fe atom) arranged at the vertices of a dodecahedron of radius $R_d = 4.07$ Å. Approximately half the vertices of the external dodecahedron are common for two neighboring clusters. The network of these atomic clusters contains about 80% of all possible atomic positions. The remaining positions belong to clusters of a different type, in which an Fe atom is surrounded by seven atoms distributed among the vertices of a dodecahedron of radius $R_d = 2.51$ Å, which is embedded in a completely filled icosahedron with $R_i =$ 4.65 Å. In accordance with this structural model, three types of positions for Cu atoms, 11 positions for Al atoms, and 20 positions for Fe atoms are available in the structure of an *i*-AlCuFe quasicrystal.

Positions of peaks in the partial vibrational spectra of Al, Cu, and Fe atoms in *i*-AlCuFe quasicrystals

Atom	E_1, meV	E_2, meV	E_3, meV	E_4, meV
Al	7.8 ± 0.6	14.5 ± 0.3	25.3 ± 0.5	40.2 ± 0.8
Cu	7.2 ± 0.4	14.2 ± 0.1	22.1 ± 0.3	38.0 ± 1.8
Fe	9.8 ± 0.4	28.8 ± 0.4	–	–

In view of the above arguments, the difference in the vibrational spectra of Cu and Fe atoms is naturally explained since a substantial number of copper atoms are in different surroundings as compared to iron and, hence, are characterized by a different set of force bonds. In addition, the appreciable width of the principal band in the vibrational spectrum of iron atoms can also be explained by the many ways these atoms are arranged upon a change in the nearest neighborhood and, accordingly, by the difference in the interatomic force interaction of Fe atoms in different possible positions.

It was noted above that the partial spectra of thermal vibrations of Cu, Fe, and Al atoms obtained in [6] exhibit peaks located in a wide energy range. Each such spectrum was approximated by a superposition of the minimal possible number of the Gaussian functions

$$A\exp\left[-\left(\frac{E-E_c}{W}\right)^2\right], \qquad (1)$$

where A, E_c, and W are fitting parameters. Fitting of the parameters of the Gaussian function (1) was carried out by the method of least squares using the χ^2 criterion, which was close to unity in all cases.

The results of such a division of experimentally measured spectra into spectral bands are shown in the figure; it can be seen that the vibrational spectra of copper and aluminum consist of four bands, while the vibrational spectrum of iron has two bands. It should be noted that the positions of the spectral bands on the energy scale in partial vibrational spectra of Cu and Al atoms coincide to a high degree of accuracy (see table). At the same time, the ratio of the energy values corresponding to the vibrational bands of Fe ($E_1 = 9.8$ meV and $E_2 = 28.8$ meV) and Al atoms ($E_2 = 14.5$ meV and $E_4 = 40.2$ meV) is close to the square root of the reciprocal mass ratio:

$$\frac{E_{\mathrm{Fe}}}{E_{\mathrm{Al}}} \approx \sqrt{\frac{M_{\mathrm{Al}}}{M_{\mathrm{Fe}}}} \approx 0.7.$$

Thus, we can conclude that the force coupling existing between the Al and Fe atoms is stronger than the cou-

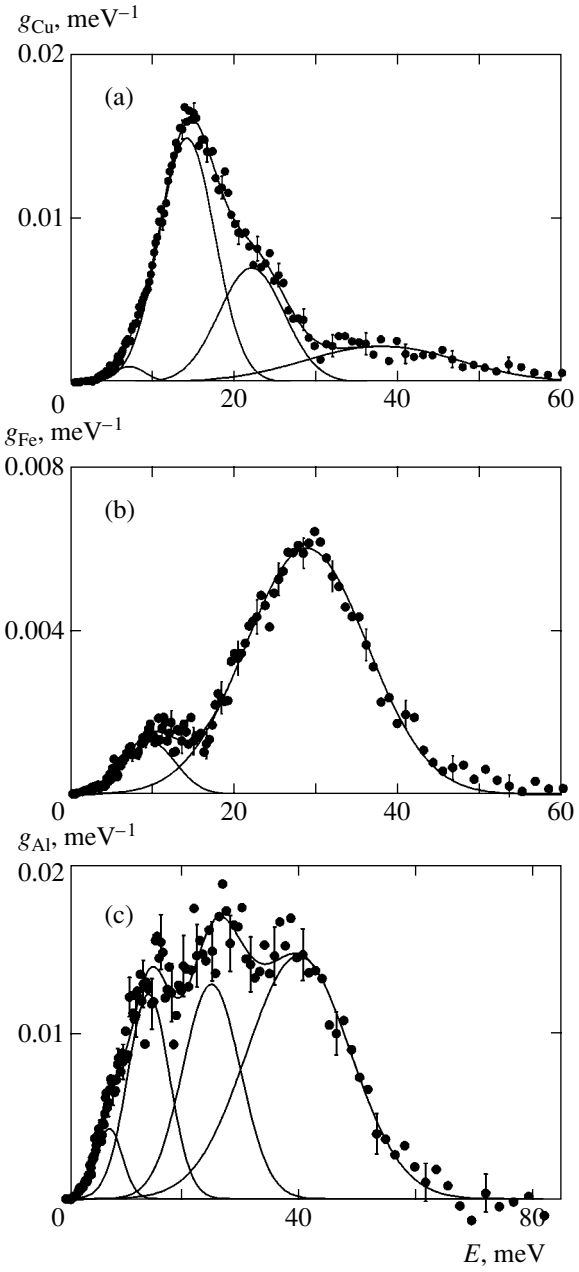

Fig. 1. Partial thermal vibration spectrum of (a) copper, (b) iron, and (c) aluminum atoms in an *i*-AlCuFe quasicrystal. Solid curves describe the division into spectral bands.

pling observed in fcc aluminum and can be correctly described using the simplest model of interaction between the nearest neighbors. The intensity of this force coupling varies depending on the local surroundings of iron in 20 possible positions and, apparently, is almost independent of the presence of copper atoms in the system. In turn, the vibrations of copper atoms can be treated as quasi-local modes in a strongly modified aluminum matrix.

The electronic structure of the icosahedral alloy AlCuFe was studied in detail in [13], where the data on the partial densities of electron states of Al, Cu, and Fe in the valence band were obtained using photoelectron spectroscopy. These data show that the main density of states in the *d* band of copper lies in the bulk of the valence band at a depth much lower than the Fermi level. At the same time, strong overlapping of the *s* and *p* states of aluminum with the *d* states of iron is observed in the vicinity of the Fermi level. This leads to *s*, *p*–*d* hybridization, which is well known for quasicrystals as well as approximating phases and is confirmed in experiments [14]. A part of the valence electrons in aluminum are engaged for filling the *d* band of iron. In this case, iron plays the role of an element with an effective negative valence and forms a rigid covalent bond with aluminum [15]. In view of these arguments, the fact that the vibrational spectrum of iron atoms is harder than that of copper atoms can be naturally explained, as well as the substantial increase in the cutoff energy of the vibrational spectrum of aluminum atoms as compared to that in crystalline fcc aluminum.

As regards copper, it can occupy a limited number of positions and participates in the chemical bond with its only one valence electron, minimizing the electron energy of the system [16, 17]. Copper atoms perform vibrations in the entire spectral band, but the probability of these vibrations strongly depends on energy. The maximal contribution from copper atoms to the spectral distribution of thermal vibrations of the quasicrystal corresponds to an energy of approximately 16 meV, while the contribution from the vibrations of heavy copper atoms for energies exceeding 30 meV is small. In fact, this means that copper can be treated as a heavy impurity in the light Al–Fe matrix, which is tuned, to a considerable extent, to the force interaction in the Al–Fe matrix.

3. CONCLUSIONS

Thus, the available experimental data on the partial vibrational spectra of copper, iron, and aluminum atoms in an icosahedral *i*-AlCuFe crystal are in good agreement with the following model of its structure. A skeleton of clusters formed mainly by aluminum atoms is considerably modified and enforced by rigid covalent bonds with iron. The stability of this system according to the Hume–Rosary rule [17] is ensured by the addition of copper atoms with a single valence electron; to exert the minimal effect on the Al–Fe skeleton, copper occupies a very limited number of positions and is tuned to the force interaction existing in the Al–Fe matrix.

ACKNOWLEDGMENTS

The authors are pleased to express their gratitude to V.G. Vaks for his participation in discussing the results of this study.

The study was supported by the Russian Foundation for Basic Research (project no. 04-02-16448), the Pro-

gram for Supporting Scientific Schools of the Russian Federation (grant no. NSh-2037.2003.2) and the National Science and Engineering Program "Topical Trends in the Physics of Condensed Matter" (Neutron Studies of Condensed Matter, state contract no. 40.012.1.1.1148).

REFERENCES

1. J.-M. Dubois, J. Phys.: Condens. Matter **13**, 7753 (2001).
2. D. Gratias, F. Puyraimond, M. Quiquandon, and A. Katz, Phys. Rev. B **63**, 024 202 (2001).
3. D. Shechtman, I. Blech, D. Gratias, and J. W. Cahn, Phys. Rev. Lett. **53**, 20 (1984); Phys. Rev. Lett. **53**, 1951 (1984).
4. P. A. Bancel, P. A. Heiney, P. W. Stephens, *et al.*, Phys. Rev. Lett. **54**, 2422 (1985).
5. M. Quiquandon, R. Bellissent, Y. Calvayrac, *et al.*, J. Non-Cryst. Solids **153**/**154**, 10 (1993).
6. P. P. Parshin, M. G. Zemlyanov, A. V. Mashkov, *et al.*, Fiz. Tverd. Tela (St. Petersburg) **46**, 510 (2004) [Phys. Solid State **46**, 526 (2004)].
7. E. C. Svensson, B. N. Brockhouse, and J. M. Rowe, Phys. Rev. **155**, 619 (1967).
8. V. J. Minkiewicz, G. Shirane, and R. Nathans, Phys. Rev. **162**, 528 (1967).
9. G. Gilat and R. M. Nicklow, Phys. Rev. **143**, 487 (1966).
10. A. P. Menushenkov, Ya. V. Rakshun, D. S. Shaĭtura, *et al.*, Poverkhnost, No. 11, 66 (2003).
11. V. Simonet, F. Hippert, R. Brand, *et al.*, Phys. Rev. B **72**, 024214 (2005).
12. M. Quiquandon, A. Quivy, S. Lefebre, *et al.*, Phys. Rev. B **44**, 2071 (1991).
13. E. Belin and Z. Danhkazi, J. Non-Cryst. Solids **153**/**154**, 298 (1993).
14. G. Trambly de Laissardière, D. Nguen Manh, L. Magaud, *et al.*, Phys. Rev. B **52**, 7920 (1995).
15. M. Krajčі and J. Hafner, J. Non-Cryst. Solids **334**/**335**, 342 (2004).
16. V. G. Vaks, V. V. Kamyshenko, and G. D. Samolyuk, Phys. Lett. A **132**, 131 (1988).
17. A.-P. Tsai, J. Non-Cryst. Solids **334**/**335**, 317 (2004).

Translated by N. Wadhwa

Journal of Experimental and Theoretical Physics, Vol. 101, No. 4, 2005, pp. 680–685.
Translated from Zhurnal Éksperimental'noĭ i Teoreticheskoĭ Fiziki, Vol. 128, No. 4, 2005, pp. 789–795.

ORDER, DISORDER, AND PHASE TRANSITIONS IN CONDENSED SYSTEMS

Anomalous Magnetoresistivity of the Superconducting $Zr_{80}Pt_{20}$ System in Quasicrystalline and Amorphous States

G. Kh. Panova, N. A. Chernoplekov, and A. A. Shikov

Russian Research Center Kurchatov Institute, pl. Kurchatova 1, Moscow, 123182 Russia
e-mail: shikov@isssph.kiae.ru

Received June 8, 2005

Abstract—The binary icosahedral $Zr_{80}Pt_{20}$ system has been synthesized during the crystallization of an initially amorphous alloy fabricated by melt quenching on the surface of a rotating copper wheel. The temperature and field dependences of the electrical resistivity and magnetoresistivity of the icosahedral and amorphous phases are studied and compared in a temperature range of 1.5–300 K and magnetic fields up to 8 T. Superconductivity has been detected for the first time in the icosahedral and amorphous phases of the $Zr_{80}Pt_{20}$ system. For both phases, the magnetoresistivity is positive and depends anomalously on the magnetic field. The anomalous behavior of magnetoresistivity is satisfactorily described by the theory of weak localization and electron–electron interaction in three-dimensional disordered systems, which takes into account electron scattering by superconducting fluctuations. The absolute values and temperature dependences of the electron–electron interaction constant and the times of inelastic scattering of conduction electrons are estimated for the icosahedral and amorphous phases of this binary system. © *2005 Pleiades Publishing, Inc.*

1. INTRODUCTION

The electronic transport properties of quasicrystals, including their electrical resistivity and the effect of quantum effects on the magnetokinetic properties of amorphous and quasicrystalline systems [1–6], were comprehensively studied in many works. Electron–electron interaction in quasicrystalline and amorphous systems results in qualitative and quantitative changes in the properties of their electronic system, which can be elucidated by studying quantum corrections to their magnetoresistivity. The theory of anomalous magnetoresistivity (AMR) [7] predicts two effects: "weak" localization of conduction electrons and an increase in the electron–electron interaction in the presence of impurity scattering. These effects lead to the appearance of corrections to classic conductivity, which anomalously depend on temperature, magnetic field, and some other factors.

It should be noted that quantum effects in superconducting quasicrystalline metal–metal systems have not been studied in the published experimental works dealing with the AMR phenomenon.

To obtain such information, in this work we comparatively study the structural, electronic, and superconducting properties of icosahedral quasicrystal $Zr_{80}Pt_{20}$ and its amorphous analog by measuring the temperature and field dependences of the resistivity.

Since a number of zirconium quasicrystalline compounds ($Zr_{70}Pd_{30}$, $Zr_{41.5}Ni_{41.5}Ti_{17}$) are superconductors [4, 8], the icosahedral quasicrystal $Zr_{80}Pt_{20}$ was assumed to have superconducting properties. The presence of superconductivity in these amorphous and quasicrystalline states was experimentally supported in this work.

We chose the $Zr_{80}Pt_{20}$ system to study magnetokinetic properties, since its structure has been comprehensively studied and it has been shown that an icosahedral local atomic structure forms around both Zr and Pt atoms [9].

The fact that this system can be in both the amorphous and quasicrystalline states is an important factor for choosing this system: this allows one to study the effect of a change in the short-range order without changing component concentrations during the transition from the amorphous into the quasicrystalline state.

2. EXPERIMENTAL

The metastable binary icosahedral $Zr_{80}Pt_{20}$ system was synthesized during the crystallization of an amorphous $Zr_{80}Pt_{20}$ alloy prepared by melt quenching (at a rate of 10^6 K/s) on the outer surface of a rotating copper wheel in an inert atmosphere. The starting electrolytically pure materials were placed in an ampule of boron nitride, which has the maximum chemical resistance to the melts of transition metals. They were induction-heated with a VChG-440 high-frequency generator. The melt was squeezed due to an excess argon pressure through a hole 1 mm in diameter onto the wheel surface rotating at a linear velocity of 40 m/s. The amorphous

samples thus fabricated were ribbons 1.5–2.0 mm wide and about 0.03 mm thick. After measurements, these amorphous samples were annealed in a flow of gaseous helium in a quartz tube located in a muffle furnace. To find conditions for preparing the most perfect icosahedral sample, the samples were annealed at several temperatures and were then rapidly quenched. Under the optimum conditions for the production of the icosahedral phase, a $Zr_{80}Pt_{20}$ sample was annealed at 873 K for 12 min and was then quenched at a rate of 10^3–10^4 K/s.

The structure of the samples before and after annealing was studied by X-ray diffraction on a diffractometer. The X-ray diffraction pattern of the melt-quenched, amorphous $Zr_{80}Pt_{20}$ sample is shown in Fig. 1a. The shape of this pattern is typical of an amorphous metal and demonstrates the absence of a long-range order. The first broad maximum is localized near $2\theta = 37°$, and the second is localized at $2\theta = 63°$. The X-ray diffraction pattern of the icosahedral phase (Fig. 1b) shows diffraction peaks that correspond to an icosahedral structure; they were indexed according to the scheme proposed in [10].

The temperature dependences of the resistivity and magnetoresistivity were measured on 12-mm-long ribbon samples in a temperature range of 1.5–300 K in an 8-T magnetic field generating by a superconducting solenoid. The magnetic field was oriented normal to the current passing through a sample. The resistivities of the samples were measured by the four-probe method. The geometric factor of a sample s/l introduced a 10% uncertainty in the absolute value of resistivity ρ. The temperature was measured with a TSU carbon thermometer. The temperature-measurement accuracy in the range 1.5–30 K was ±0.01 K. At temperatures $T > 30$ K, the temperature-measurement error was at most 0.1%. The values of T_c were determined from the resistivity data, at the center of the superconducting transition.

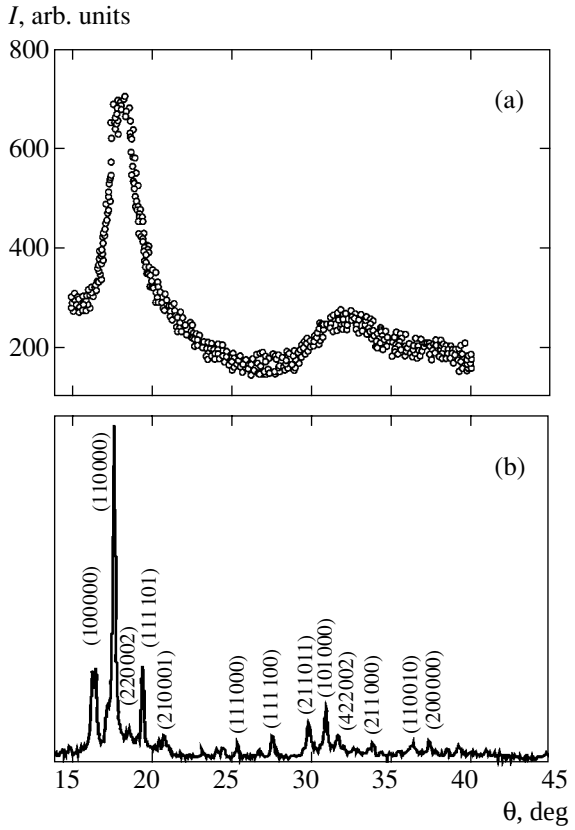

Fig. 1. X-ray diffraction patterns of (a) amorphous and (b) icosahedral $Zr_{80}Pt_{20}$ phases. The Bragg peaks corresponding to icosahedral structure are indexed according to the scheme proposed in [10].

3. BASIC RESULTS OF THE AMR THEORY FOR THE THREE-DIMENSIONAL CASE

In the general case, the contribution of an applied magnetic field to conductivity can be represented as

$$\Delta\sigma_{exp}(H) = \Delta\sigma^{cl}(H) + \Delta\sigma^{q}(H), \quad (1)$$

where the first term is the classic contribution to the magnetoconductivity (MC) and the second term has a quantum origin and is described in the framework of the AMR theory. The condition for the applicability of this theory is given by the inequality

$$k_F l > 1, \quad (2)$$

where l is the electron mean free path and k_F is the electron wavevector. An important feature of $\Delta\sigma^q(H)$ consists in the fact that he effect of a magnetic field is substantial even in the range of classically weak fields, where $\omega_c\tau \ll 1$ and the contribution of $\Delta\sigma^{cl}(H)$ is negligibly small. In terms of the AMR theory, $\Delta\sigma^q(H)$ is represented as a sum of different quantum corrections [7]:

$$\Delta\sigma^{q}(H) = c_3\Delta\sigma^{L}(H) - c_3^{int}\Delta\sigma^{MT}(H) + c_3^{int}\Delta\sigma^{int}(H). \quad (3)$$

The first quantum correction $\Delta\sigma^L(H)$ to the MC (see Eq. (3)) is related to the localization of noninteracting electrons, and the second correction is related to electron scattering by superconducting fluctuations (Maki–Thomson correction). The first correction to the MR, $\Delta\sigma^L(H)$, is suppressed in magnetic fields $H > H_\varphi$. The second and third corrections, $\Delta\sigma^{MT}(H)$ and $\Delta\sigma^{int}(H)$, take into account electron–electron interaction, and they are suppressed at $H > H_{int}$. The coefficients c_3 and c_3^{int} are given in [7]. Analytical relations for the quantum corrections $\Delta\sigma^L(H)$, $\Delta\sigma^{MT}(H)$, and $\Delta\sigma^{int}(H)$ were published in [7], and they were used in [3] to analyze the experimental data on the MR of superconducting amorphous systems.

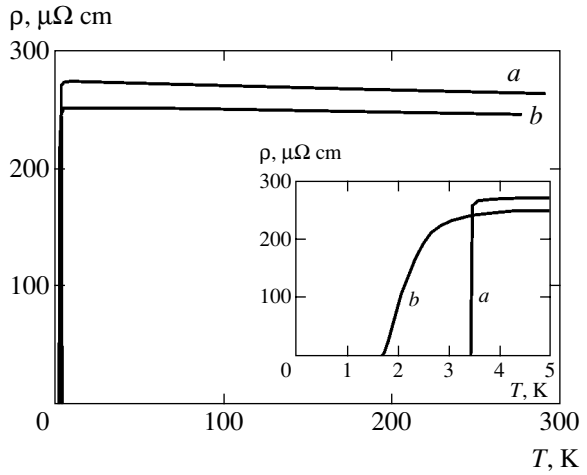

Fig. 2. Temperature dependence of the electrical resistivity of $Zr_{80}Pt_{20}$ in (*a*) amorphous and (*b*) icosahedral states in the temperature range of 1.5 to 300 K. The inset shows the superconducting transition range (1.5–4 K).

The scale of each contribution is specified by the relation between the characteristic magnetic fields (H_φ, H_{int}) and the applied magnetic field in which magnetoresistivity is measured. The characteristic scales of H_φ and H_{int} are $H_\varphi = \hbar c/4eD\tau_\varphi$ and $H_{int} = \pi ck_BT/2eD$, which separate the regions of weak and strong magnetic fields, where MC has the quadratic or square-root dependence on the magnetic field, respectively.[1]

In the magnetic-field range $H \le H_\varphi$, where $\Delta\sigma_{exp}(H) \sim H^2$, AMR is mainly contributed by the quantum effects related to the breakdown of the coherence of electron wavefunctions because of inelastic electron collisions. The characteristic electron phase-breaking time is determined from theoretical relations in this magnetic-field range.

In the magnetic-field range $H_\varphi \ll H \ll H_{int}$, where $\Delta\sigma_{exp}(H) \sim H^{1/2}$, the theory predicts that AMR is mainly contributed by the quantum effects related to electron–electron interaction in the Cooper channel, by the so-called Maki–Thomson corrections [7], which become small at $H \gg H_{int}$. In this magnetic-field range, the Maki–Thomson corrections are expressed as $\Delta\sigma^{MT}(H) = -\beta(T)\Delta\sigma^{L}(H)$, where the dimensionless quantity $\beta(T)$ is experimentally determined and depends only on the electron–electron interaction constant $g(T)$ [7].

Thus, an analysis of the experimental dependence of the MC on the magnetic field within the framework of the AMR theory can find the characteristic time τ_φ of electron phase relaxation caused by inelastic collisions and to determine the $\beta(T)$ parameter related to the electron–electron interaction constant $g(T)$.

4. EXPERIMENTAL RESULTS AND DISCUSSION

Figure 2 and the table give the measured temperature dependences of the electrical resistivity of the $Zr_{80}Pt_{20}$ system in its amorphous and icosahedral states in the temperature range 1.5–300 K.

The resistivity is seen to be high, and the icosahedral and amorphous phases have a weak negative temperature coefficient of resistivity. The resistivity of the icosahedral phase is slightly lower than that of the amorphous phase.

Electron localization plays an important role in low-temperature electron transport in amorphous alloys, and it results from disorder in a system (Anderson localization). Localization in a quasicrystal is caused by the interference (phase coherence) of electron states, and hence it is related to the system symmetry and structure: the more perfect the material, the higher the electron localization [12]. This behavior was also observed in $Zr_{70}Pd_{30}$ quasicrystalline samples in [4]. A comparison of the resistivities of $Zr_{80}Pt_{20}$ in the amorphous and icosahedral states over a wide temperature range indicates electron localization in both phases. The experimental values of ρ for both amorphous and icosahedral systems can be used as the measure of structural and electron disordering.

The inset to Fig. 2 shows the superconducting transition temperatures measured from the resistivities. The samples are found to be superconductors with a transition temperature $T_c = 3.48$ K for the $Zr_{80}Pt_{20}$ amorphous phase and $T_c = 2.50$ K for the icosahedral phase. Thus, the transition from the amorphous into icosahedral state in the system under study results in a decrease in T_c.

The conductivity of quasicrystals depends mainly on two factors: electronic structure and electron-scattering effects. It should be noted that it is difficult to methodically separate these contributions in order to find physical parameters that control certain electron-scattering mechanisms. However, this procedure can be made easier if some interaction mechanisms are suppressed by choosing appropriate temperature and magnetic-field ranges. In this case, theoretical predictions can correctly be compared with experimental results.

The measured MRs of the amorphous and icosahedral $Zr_{80}Pt_{20}$ phases in magnetic fields up to 8 T in the temperature range 1.5–5 K are given in the $\Delta\sigma(H)$ coordinates (see Figs. 3 and 4); here, MC is expressed in terms of MR as

$$\Delta\sigma(H) = \sigma(0) - \sigma(H) = \frac{\rho(H) - \rho(0)}{\rho(H)\rho(0)} \approx \frac{\Delta\rho(H)}{\rho^2(0)}.$$

As follows from $\rho(H)$, the MR is positive and depends anomalously on the magnetic field. A specific

[1] The diffusion coefficient was estimated by the relations $k_Fl = 3Dm^*\hbar = 3/2k_F\sigma/G_0$, where $G_0 = e^2/2\pi^2 \approx 1.23 \times 10^{-5}$ $(\Omega\ m)^{-1}$ and m^* is the effective electron mass. m^* was estimated from the data of [11].

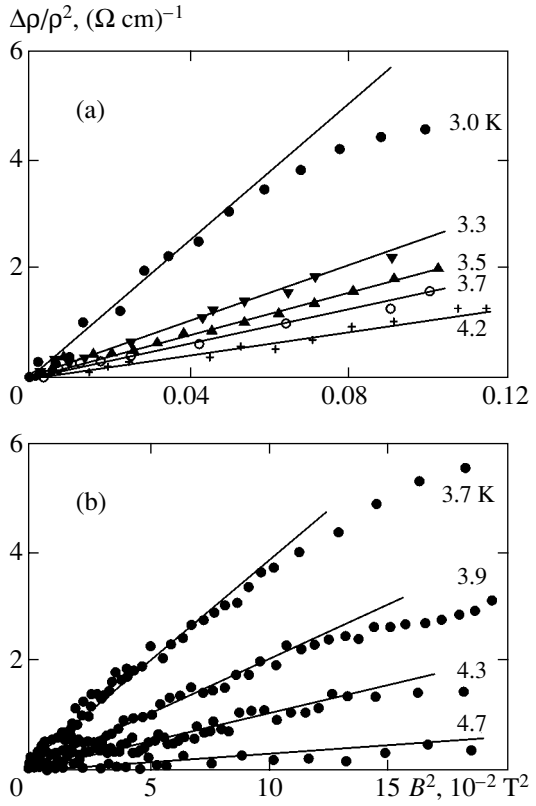

Fig. 3. Field dependence of magnetoresistivity $\Delta\rho(H)/\rho^2(0)$ in the low-field region for (a) icosahedral and (b) amorphous phases.

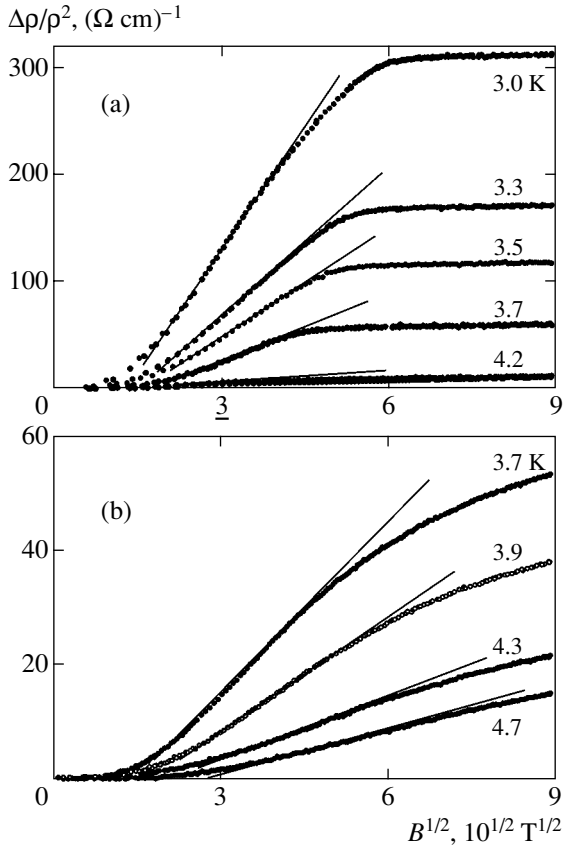

Fig. 4. Field dependence of magnetoresistivity $\Delta\rho(H)/\rho^2(0)$ in the high-field region for (a) icosahedral and (b) amorphous phases.

feature of the $Zr_{80}Pt_{20}$ system is the fact the $\Delta\rho(H)/\rho^2(0)$ dependence has clearly pronounced sections that vary as H^2 in weak fields and as $H^{1/2}$ in strong fields, which are inherent in the $\Delta\sigma(H)$ behavior in three-dimensional disordered systems.

Using the relations that determine the contributions $\Delta\sigma^L(H)$ and $\Delta\sigma^{MT}(H)$ [7] to the MC for weak spin-orbit interaction and the slopes of the dependences of $\Delta\rho(H)/\rho^2(0)$ on H^2 (Fig. 3) and of $\Delta\rho(H)/\rho^2(0)$ on $H^{1/2}$ (Fig. 4), we determined the values of the parameters $\beta(T)$, which is related to the electron–electron interaction constant $g(T)$, and $\tau_\varphi(T)$, which specifies the phase-breaking time for a conduction electron due to inelastic scattering. The characteristic feature of the MR is its sharp decrease with increasing temperature, which specifies a sharp decrease in the slopes for the quadratic (H^2) and square-root ($H^{1/2}$) $\Delta\sigma(H)$ dependences. At T = 5 K, the magnetoresistivity becomes virtually comparable with the experimental error.

The deviations of $\Delta\rho(H)/\rho^2(0)$ from the H^2 and $H^{1/2}$ dependences are caused by the joint effect of two fac-

Parameters of the systems under study in the weak spin-orbit coupling approximation (T = 3.7 K)

Sample	ρ, μΩ cm, T = 6 K	ρ, μΩ cm, T = 300 K	$\beta(T)$	$g(T)$	T_c^*, K	T_c, K	τ_φ, 10^{-11} s	H_φ, T	H_{int}, T	D_{calc}, $cm^2\ s^{-1}$
$Zr_{80}Pt_{20}$ quasicrystalline phase	251.5	245.5	23	~2.0	~2.5	2.48	23.8	~0.03	~12	~0.4
$Zr_{80}Pt_{20}$ amorphous phase	274.0	263.2	12	~5.0	~3.5	3.50	3.0	~0.4	~10	~0.2

Note: ρ is resistivity; the parameter $\beta(T)$ is related to the electron–electron interaction constant $g(T)$; T_c^* is the calculated superconducting transition temperature; T_c is the experimental superconducting transition temperature; τ_φ is the relaxation time of the phase of electron wavefunction due to inelastic collisions; H_φ and H_{int} are the characteristic magnetic fields separating the low- and high-field regions, respectively; and D_{calc} is the electron diffusion coefficient.

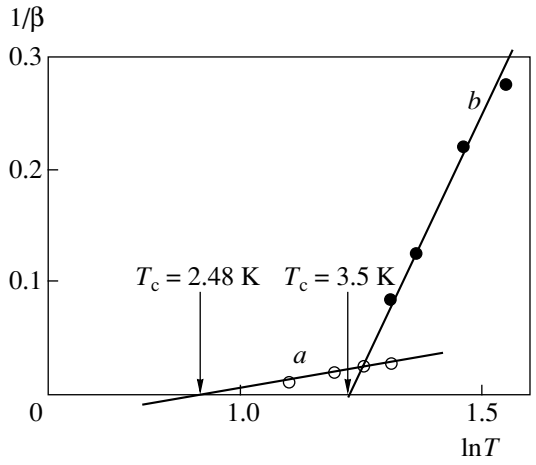

Fig. 5. Temperature dependences of β for the $Zr_{80}Pt_{20}$ system in (*a*) icosahedral and (*b*) amorphous states. Arrows indicate the calculated values of T_c^* averaged over several temperature points.

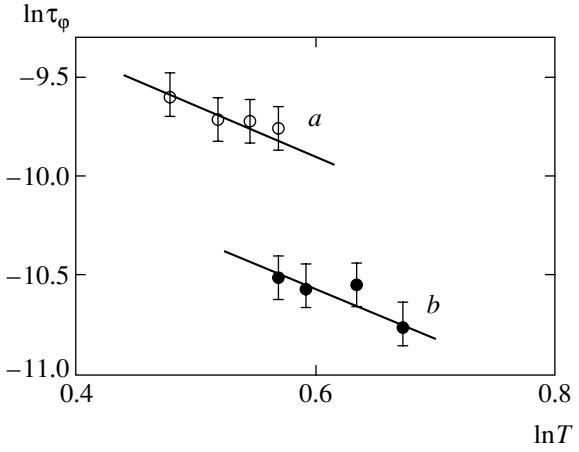

Fig. 6. Temperature dependence of τ_φ for the $Zr_{80}Pt_{20}$ system in (*a*) icosahedral and (*b*) amorphous states.

tors, namely, by the suppression of the $\Delta\sigma^L(H)$ contribution, which is caused by the localization of noninteracting electrons, with increasing magnetic field and by an increase in the $\Delta\sigma^{int}(H)$ contribution, which is related to electron–electron interaction.

The experimental data in Fig. 3 show that the magnetic-field range in which the H^2 dependence is obeyed for the amorphous phase is more than an order of magnitude longer than the analogous H range for the quasicrystalline phase. The magnetic-field ranges where the H^2 dependence is obeyed agree well with the estimates of H_φ (see table) made for both phases in the system under study.

Figure 4 shows the $H^{1/2}$ dependence of $\Delta\rho(H)/\rho^2(0)$ in magnetic fields $H \gg H_\varphi$; as is seen, the magnetic-field ranges where the $H^{1/2}$ law is obeyed are comparable for both phases. The scales of MR at the same temperatures are of the same order of magnitude for both phases. According to the conclusions of the AMR theory [7], an increase in the magnetic field should result in an increase in the role of electron–electron interaction; in the case of superconducting disordered systems, this means the suppression of the $\Delta\sigma^L(H)$ contribution, which is related to the localization of noninteracting electrons, and an increase in the $\Delta\sigma^{MT}(H)$ contribution, which is caused by electron scattering by superconducting fluctuations. The effect of the $\Delta\sigma^{int}(H)$ contribution, which corresponds to electron–electron interaction, depends on the ratio of H, at which the MR is measured, and H_{int}, which is involved in the AMR theory.

H_{int} was estimated to be less than 10–12 T in our case. This means that the $\Delta\sigma^{int}(H)$ contribution to the experimental MC in the magnetic-field range under study is insignificant. This circumstance is also supported by the fact that, in this magnetic-field range, the experimental MC can satisfactorily be described by two contributions to the MC, namely, by $\Delta\sigma^L(H)$ and $\Delta\sigma^{MT}(H)$.

By studying the H dependence of $\Delta\rho(H)/\rho^2(0)$ at $H \ll H_{int}$ and different temperatures, we can determine the temperature dependences of the $\beta(T)$ parameter, which is related to the electron–electron interaction constant $g(T)$, and the characteristic electron phase-breaking time $\tau_\varphi(T)$. The determined $\tau_\varphi(T)$ temperature dependence makes it possible to reveal the dominating phase-breaking mechanism for conduction electrons in disordered and irregular superconductors.

Therefore, we studied the H dependences of $\Delta\rho(H)/\rho^2(0)$ for the $Zr_{80}Pt_{20}$ system in the temperature range $T_c < T < 5$ K and magnetic fields up to 8 T. Figure 5 shows the temperature dependences of the β^{-1} coefficient on ln T. These dependences in the quasicrystalline and amorphous states of the $Zr_{80}Pt_{20}$ system are linear within the limits of experimental error. Their extrapolations to the intersection with the ln T axis gives the calculated values of T^* averaged over several temperature points; these values coincide with the experimental values.

This agreement between the values of T_c calculated from the MR data (from the electron–electron interaction constants $g(T)$) and the values of T_c determined experimentally indicates that the relations of the AMR theory for the case of weak spin-orbit interaction satisfactorily describe the behavior of MR in superconducting quasicrystalline and amorphous systems.

For such systems, Fig. 6 shows the temperature dependence of the electron phase-breaking time ($\tau_\varphi(T)$) in logarithmic coordinates. In each state, the experimental points are seen to fall on one straight line within the limits of experimental error, thus demonstrating the $\tau_\varphi \propto T^{-2}$ dependence. A comparison of the electron

phase-breaking times τ_φ for the quasicrystalline and amorphous phases (see table) indicates a significant increase in τ_φ in the quasicrystalline phase. The presence of the temperature dependence of τ_φ demonstrates that, in the temperature range under study, the electron phase relaxation time coincides with the time of electron inelastic scattering in an order of magnitude. This means that, in the temperature range under study, the main phase-breaking mechanism for conduction electrons is their inelastic scattering by ion vibrations.

The main features of the experimental low-temperature behavior of MR are seen to be satisfactorily described by the existing theory of weak electron localization and electron–electron interaction in three-dimensional disordered systems. Both effects are observed in the AMR, and they can be separated in a magnetic field. The contribution related to electron–electron interaction and caused by electron scattering by superconducting fluctuations dominates, since $|g(T)| > 1$ at $T > T_c$.

5. CONCLUSIONS

The electronic and superconducting properties of icosahedral crystal $Zr_{80}Pt_{20}$ and its amorphous analog were studied and compared by measuring their electrical resistivity and magnetoresistivity, and a number of important parameters were determined.

The icosahedral and amorphous phases are characterized by a high resistivity and a weak negative temperature coefficient of resistivity, and the resistivity of the icosahedral phase is slightly lower than that of the amorphous phase.

We were the first to detect superconductivity in the icosahedral and amorphous $Zr_{80}Pt_{20}$ phases, and the superconducting transition temperature is lower in the icosahedral phase.

The electron phase relaxation times τ_φ were determined in both phases. The phase relaxation time in quasicrystalline $Zr_{80}Pt_{20}$ was found to be much higher than that of the amorphous analog, and this sharp increase is explained by electron localization in the quasicrystal that is related to a sample structure.

The detected decrease in the electron–electron interaction constant $g(T)$ in the quasicrystal, which results in a decrease in T_c, indicates weakening of the electron–electron interaction in the quasicrystal as compared to its amorphous analog.

ACKNOWLEDGMENTS

We thank G.F. Syrykh for preparation of amorphous $Zr_{80}Pt_{20}$ samples.

This work was supported by the Russian Foundation for Basic Research, project no. 04-02-16017-a.

REFERENCES

1. O. Rapp, Mater. Sci. Eng. **294**–**296**, 458 (2000).
2. M. Ahlgren, M. Rodmar, Th. Klein, and O. Rapp, Phys. Rev. B **51**, 7287 (1995).
3. S. G. Gumbatov, G. Kh. Panova, and A. A. Shikov, Zh. Éksp. Teor. Fiz. **89**, 134 (1985) [Sov. Phys. JETP **62**, 76 (1985)].
4. G. Kh. Panova, N. A. Chernoplekov, and A. A. Shikov, Fiz. Tverd. Tela (St. Petersburg) **47**, 1165 (2005) [Phys. Solid State **47**, 1205 (2005)].
5. R. Tamura, H. Sawada, K. Kimura, and H. Ino, in *Proceedings of 6th International Conference on Quasicrystals, Yamada Conference XLVII, Tokyo*, Ed. by S. Takeuchi and T. Fujiwara (World Sci., Singapore, 1997), p. 631.
6. M. Ahlgren, C. Gignoux, M. Rodmar, *et al.*, in *Proceedings of 6th International Conference on Quasicrystals, Yamada Conference XLVII, Tokyo*, Ed. by S. Takeuchi and T. Fujiwara (World Sci., Singapore, 1997), p. 615.
7. B. L. Al'tshuler, A. G. Aronov, A. I. Larkin, and D. E. Khmel'nitskiĭ, Zh. Éksp. Teor. Fiz. **81**, 768 (1981) [Sov. Phys. JETP **54**, 411 (1981)].
8. V. Azhazha, A. Grib, G. Khadzhay, *et al.*, Phys. Lett. A **303**, 87 (2002); V. Azhazha, G. Khadzhay, S. Malikhin, *et al.*, Phys. Lett. A **349**, 539 (2003).
9. M. Kitada, M. Imafuku, I. Saida, and A. Inoue, J. Non-Cryst. Solids **312**–**314**, 594 (2002).
10. P. A. Bancel, P. A. Heiney, P. W. Stephens, *et al.*, Phys. Rev. Lett. **54**, 2422 (1985).
11. G. Kh. Panova, N. A. Chernoplekov, A. A. Shikov, and B. I. Savel'ev, Zh. Éksp. Teor. Fiz. **82**, 548 (1982) [Sov. Phys. JETP **55**, 319 (1982)].
12. Yu. Kh. Vekilov, Usp. Fiz. Nauk **172**, 233 (2002) [Phys. Usp. **45**, 225 (2002)].

Translated by K. Shakhlevich

Journal of Experimental and Theoretical Physics, Vol. 101, No. 4, 2005, pp. 686–692.
Translated from Zhurnal Éksperimental'noĭ i Teoreticheskoĭ Fiziki, Vol. 128, No. 4, 2005, pp. 796–802.

ELECTRONIC PROPERTIES OF SOLIDS

Magnetopolaron State of Particles in Quantum Rings of Finite Width

V. M. Kovalev and A. V. Chaplik

Institute of Semiconductor Physics, Siberian Division, Russian Academy of Sciences, pr. Akademika Lavrent'eva 13, Novosibirsk, 630090 Russia

e-mail: vadimkovalev@isp.nsc.ru

Received February 28, 2005

Abstract—The energies of the electron and hole weak-coupling polarons are determined in quantum rings of finite width in a uniform magnetic field. It is shown that polaron corrections exhibit oscillatory behavior as a function of a magnetic field. The effect of polaron corrections on the absorption and emission spectra of light by excitons in a quantum ring is considered. © *2005 Pleiades Publishing, Inc.*

1. INTRODUCTION

The electron–phonon interaction in reduced-dimension systems has been discussed in the literature since the very beginning of the physics of low-dimensional systems as an independent branch of solid-state physics. The effect of acoustic phonons on the mobility of electrons in an inversion channel was considered as early as 1982 by Ando *et al.* [1] by example of a two-dimensional electron system in silicon. In low-dimensional A_3B_5 systems (just as in bulk samples), polaron phenomena due to optical phonons attract considerable interest. These phenomena have been discussed in [2] (quantum wires) and in [3, 4] (quantum dots) with regard to the effect of a strong (in the sense that the magnetic length is of the same order of magnitude or less than the size of the domain where the charge carriers move) magnetic field. By example of a quantum dot, it was demonstrated in [4] that polaron phenomena become more prominent as the size of a quantum dot is reduced: a shift in the electron energy due to the coupling to polar optical phonons is inversely proportional to the radius of a quantum dot.

Quantum rings occupy a special position among nanoobjects. The main topological feature of these rings is that the domain where an electron moves is not simply connected. This fact leads to Aharonov–Bohm oscillations in a magnetic field. It is well known that Aharonov–Bohm oscillations arise even if an electron is not subject to a Lorentz force (a thin solenoid inside a ring). However, from the experimental point of view, a typical situation is when a uniform magnetic field is applied to the system and the ring has a finite width. In this case, the magnetic field may significantly affect the radial motion of particles.

The manufacturing technology of quantum rings with a characteristic radius of 10 to 100 nm was first described in [5]. In an ensemble of self-organized InAs quantum dots on the surface of GaAs, under certain conditions, InAs diffuses toward the boundaries of the quantum dots. This gives rise to objects that look like the crater of a volcano. At the center of the crater, a region with a typical diameter of 20 nm is formed that is free of InAs. The outer diameter of the crater is estimated to range from 60 to 120 nm [5]. Thus, an ensemble of rings is formed whose radii are comparable to the effective Bohr radius of an electron in InAs.

Polaron phenomena in quantum rings of finite width in a magnetic field must be characterized by distinctive features. The main feature is the nonmonochromaticity of the Aharonov–Bohm oscillations of a polaron shift, which is attributed to the difference in the magnetic fluxes that are enclosed by different electron trajectories. Moreover, when an exciton is generated, the contributions of the electron and the hole to the polarization of the medium have opposite signs, and it is important that the finiteness of the ring should be taken into account when calculating the net effect determined by the wavefunctions of the particles. The present paper is devoted to the theoretical study of the formation of magnetopolarons in a quantum ring with regard to the radial motion of particles and the effect of polaron phenomena on optical interband transitions.

2. ENERGY SPECTRUM AND WAVEFUNCTIONS OF PARTICLES IN A QUANTUM RING

Several models of a potential have been proposed in the current literature to take into account the finiteness of the width of a quantum ring: a rigid-wall potential [6], a parabolic potential [7], and (see [8]) potential energy of the form

$$V(r) = \frac{a_1}{r^2} + a_2 r^2, \tag{1}$$

which will be used in the subsequent calculations.

Here, r is the radius vector of a particle in a polar system of coordinates and a_1 and a_2 are certain parameters. Potential (1) admits an analytic solution of the Schrödinger equation in a magnetic field and, on the other hand, allows one to simulate a ring of finite width.

The expansion of (1) near the minimum $V(r_0) = \min(V(r))$ yields

$$V(r) = \text{const} + \frac{m^*\omega_0^2}{2}(r - r_0)^2, \tag{2}$$

whence one can obtain a relation between a_1 and a_2 and the experimentally determined parameters r_0 and ω_0 [5]:

$$\omega_0 = \sqrt{8a_2/m^*}, \quad r_0 = (a_1/a_2)^{1/4}, \tag{3}$$

where m^* is the effective mass of a particle. Then, the Hamiltonian of an electron in potential (1) in a uniform magnetic field $\mathbf{B} = (0, 0, B)$ (the z axis is perpendicular to the plane of the ring) is given by [8]

$$\begin{aligned}\hat{H}_e &= -\frac{\hbar}{2m_e^*}\left[\frac{1}{r}\frac{\partial}{\partial r}r\frac{\partial}{\partial r} + \frac{1}{r^2}\frac{\partial^2}{\partial\varphi^2}\right] \\ &- i\frac{\hbar\omega_B}{2}\frac{\partial}{\partial\varphi} + \frac{m_e^*\omega_B^2 r^2}{8} + \frac{a_1}{r^2} + \frac{m_e^*\omega_0^2 r^2}{8},\end{aligned} \tag{4}$$

where $\omega_B = eB/m_e^*c$ is the cyclotron frequency of an electron and m_e^* is the effective mass of an electron. The solution to the Schrödinger equation $\hat{H}_e\psi(r, \varphi) = E_e\psi(r, \varphi)$ for a lateral motion of an electron is expressed as (hereupon, we consider states with the radial quantum number $n_r = 0$) [8]

$$\begin{aligned}\psi_M &= C_M r^M \exp\left(-\frac{r^2}{4a_e^2}\right)e^{il_e\varphi}, \\ C_M &= \frac{1}{a_e^{M+1}}\sqrt{\frac{1}{2^M\Gamma(M+1)}}\frac{1}{\sqrt{2\pi}}, \\ M^2 &= l_e^2 + \frac{2m_e^*a_1}{\hbar^2}, \\ E_e &= \hbar\Omega_e\left(\frac{M+1}{2}\right) + \frac{l_e}{2}\hbar\omega_{Be} + E_g;\end{aligned} \tag{5}$$

here, l_e is the eigenvalue of the projection operator of the angular momentum of an electron, $E_g = 0.354$ eV is the bandgap energy of InAs, $\Omega_e = \sqrt{\omega_{Be}^2 + \omega_0^2}$ is the combined frequency, and $a_e = \sqrt{\hbar/m_e^*\Omega_e}$ is the oscillatory length of an electron at the combined frequency Ω_e. The wavefunctions and the spectrum of holes can be determined similarly. For further references, we write out these parameters:

$$\begin{aligned}\psi_N &= C_N r^N \exp\left(-\frac{r^2}{4a_h^2}\right)e^{il_h\varphi}, \\ C_N &= \frac{1}{a_h^{N+1}}\sqrt{\frac{1}{2^N\Gamma(N+1)}}\frac{1}{\sqrt{2\pi}}, \\ N^2 &= l_h^2 + \frac{2m_h^*a_1}{\hbar^2}, \\ E_h &= -\hbar\Omega_h\left(\frac{N+1}{2}\right) - \frac{l_h}{2}\hbar\omega_{Bh}.\end{aligned} \tag{6}$$

Here, the notations are analogous to those used in formulas (5). In (5) and (6), the energy is measured from the top of the valence band. In further calculations, we assume, for simplicity, that the parameters r_0 and ω_0 are the same for electrons and holes (unless otherwise stated) and that the difference between electrons and holes is attributed to the difference between their effective masses and the signs of their charges. This approximation has a small effect on the results.

3. ELECTRON AND HOLE POLARONS

As pointed out above, the strong localization of particles in quantum rings may enhance their interaction with longitudinal optical phonons and thereby significantly change the quantization energies of the particles (a polaron shift). To calculate the coupling energy of a polaron, one should add the Hamiltonian (4) of free phonons and electron–phonon interaction

$$\begin{aligned}H &= T_e + \sum_{\mathbf{q}}\hbar\omega_{\mathbf{q}}b_{\mathbf{q}}^+b_{\mathbf{q}} + \sum_{\mathbf{q}}F_{\mathbf{q}}(\mathbf{r})(b_{\mathbf{q}} + b_{-\mathbf{q}}^+), \\ F_{\mathbf{q}}(\mathbf{r}) &= D_{\mathbf{q}}e^{i\mathbf{q}\cdot\mathbf{r}} = \frac{e}{q}\sqrt{\frac{2\pi\hbar\omega_{\mathbf{q}}}{\varepsilon^*}}e^{i\mathbf{q}\cdot\mathbf{r}},\end{aligned} \tag{7}$$

to Hamiltonian (4), which describes the motion of an electron in a quantum ring. Here, $b_{\mathbf{q}}(b_{\mathbf{q}}^+)$ are the creation (annihilation) operators of phonons with the wavevector $\mathbf{q}$, e is the electron charge, $\varepsilon^{*-1} = \varepsilon_\infty^{-1} - \varepsilon_0^{-1}$ is the effective optical permittivity, and $\omega_{\mathbf{q}}$ is the phonon frequency. In the case of a weak-coupling

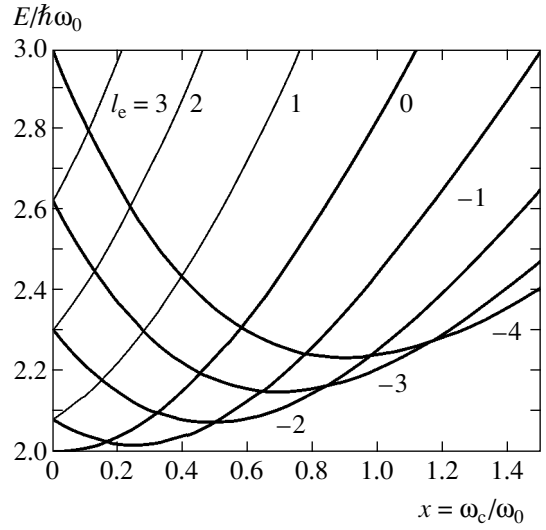

Fig. 1. Energy spectrum of a wide quantum ring.

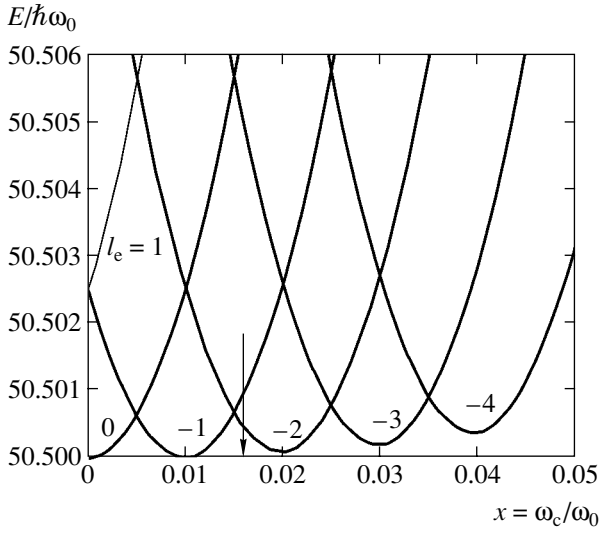

Fig. 2. Energy spectrum of a narrow quantum ring.

polaron, the polaron correction can be calculated by perturbation theory:

$$\Delta E_l = -\sum_{q,\,l'} \frac{|P_{ll'}(q)|^2}{E_{l'} - E_l + \hbar\omega_q - \Delta}, \qquad (8)$$
$$\Delta = \Delta E_l - \Delta E_G,$$

where $P_{ll'}(q)$ is the matrix element of the electron–phonon interaction. The quantity Δ depends on the type of perturbation theory. It is well known (see, for example, [9]) that the Rayleigh–Schrödinger perturbation theory ($\Delta = 0$) well describes only a correction to the ground state of the system. For excited states, one should apply the Wigner–Brillouin perturbation theory with $\Delta = \Delta E_l - \Delta E_G$. Here, ΔE_G is a polaron correction to the ground state calculated for $\Delta = 0$. In the case of dispersion-free optical phonons, ($\omega_q = \omega_{opt} = \text{const}$), the polaron correction to the electron states is given by (see the Appendix)

$$\Delta E(l_e) = -\frac{e^2\hbar\omega_{pot}}{\varepsilon^* a_e}\sum_{l_e'} \frac{A(l_e \longrightarrow l_e')}{E_{l_e'} - E_{l_e} + \hbar\omega_q - \Delta},$$

$$A(l_e \longrightarrow l_e') = \frac{\Gamma^2(\Delta l_e/2 + M'/2 + M/2 + 1)}{\Gamma^2(\Delta l_e + 1)\Gamma(M+1)\Gamma(M'+1)} \qquad (9)$$

$$\times \int_0^\infty \frac{dt}{2\pi} t^{\Delta l_e} F^2\left(\frac{\Delta l_e}{2} + \frac{M'}{2} + \frac{M}{2} + 1;\ \Delta l_e + 1;\ -t^2\right),$$

where F is a degenerate hypergeometric function and Γ is the gamma function. The result for a hole polaron has the same form, except the change $a_e \longrightarrow a_h$. Figure 1 shows the energy spectrum of an electron in a quantum ring for $\hbar\omega_0 = 12\hbar^2/2m^* r_0^2$. One can see that, when the finiteness of the ring width is taken into account, the spectrum significantly differs from the spectrum of the one-dimensional model,

$$E_l = \frac{\hbar^2}{2m^* r_0^2}\left(l + \frac{\Phi}{\Phi_0}\right)^2,$$

where $\Phi_0 = hc/e$ is the quantum of a magnetic flux. Naturally, one should expect that, as the ratio of the radial quantum to the rotational one increases, the spectrum of the system ever more closely approaches the spectrum E_l of the one-dimensional system. This fact is illustrated in Fig. 2, where $\hbar\omega_0 = 400\hbar^2/2m^* r_0^2$. The arrow in this figure indicates the value of the magnetic field equal to 1 T. The values of the quantum number l_e are shown in the figure. In Figs. 1 and 2, energy is normalized by the radial quantum $\hbar\omega_0$. The polaron corrections to the states with different values of l_e calculated by formula (9) are shown in Fig. 3. One can see that, in addition to the oscillatory component, there exists a smooth envelope that comes from the magnetic-field dependence of the radial wavefunctions of an electron. Fig. 4a represents the magnetic-field dependence of the ground state of an electron in a quantum ring, and Fig. 4b shows the polaron correction (ΔE_G) to this dependence calculated by formula (9). One can see that this dependence is also oscillatory. Similar to Fig. 3, the graph has an envelope; however, this envelope much more weakly depends on magnetic field than that for excited states. All the calculations shown in Figs. 2–4 are performed for the ratio of parameters given by $\hbar\omega_0 = 400\hbar^2/2m^* r_0^2$.

4. AN EXCITON POLARON AND INTERBAND OPTICAL TRANSITIONS

The absorption of a quantum of light with energy greater than the bandgap energy of a material gives rise to an electron–hole pair in a quantum ring. Each particle polarizes the medium, the polarization having opposite signs for the electron and the hole. As a result, these polarization wells partially compensate each other. As is shown in [4], in spherical quantum dots, the compensation is not exact when only the degeneracy of the valence band of the material is taken into account. In the case under consideration, due to the strong quantization in the vertical direction, the degeneracy is removed; however, the polarizations are not fully compensated because of the strong difference between the effective masses of an electron and a heavy hole. Now, we consider interband transitions. Before the absorption of a photon, a quantum ring has no charged particles and, hence, the medium is nonpolarized. After the absorption (in the final state of the system), there is an electron in the conduction band and a hole in the valence band; this leads to the polarization of the material. This means that the wavefunctions of the oscillators of the medium before (Φ^i) and after (Φ^f) the absorption are not orthogonal: $\langle\Phi^i|\Phi^f\rangle \neq 0$, because the functions Φ^f have a displaced equilibrium state due to the polarization [4]. Taking into account this circumstance, we can represent the absorption probability of a quantum $\hbar\omega$ of light in the dipole approximation as

$$W_{\text{abs}} = \frac{2\pi}{\hbar}|p_{CV}|^2|I(l_\text{e}, l_\text{h})|^2 \times \sum_K W_K \delta(E_{\text{eh}} - E_K - \hbar\omega), \tag{10}$$

where E_{eh} is the transition energy, $E_K = K\hbar\omega_{\text{opt}}$ (K is an integer) is the total energy of phonons that are involved in the interband transition, W_K is the emission probability of K phonons during the transition, $I(l_\text{e}, l_\text{h})$ is the overlap integral of the envelopes of the electron and the hole, and p_{CV} is the Bloch amplitudes matrix element of the interband transition. The emission probability W_K of phonons is determined by the scalar product of the oscillation functions of the medium, $\langle\Phi^i|\Phi^f\rangle$. In the case of dispersion-free optical phonons $\hbar\omega_q = \hbar\omega_{\text{opt}}$, this probability is determined by (see [4] for the details of calculation)

$$W_K = \frac{S_0^K}{2^K K!}\exp\left(-\frac{S_0^2}{2}\right), \quad S_0 = \frac{\delta K_{\text{ex}}}{\hbar\omega_{\text{opt}}}, \tag{11}$$

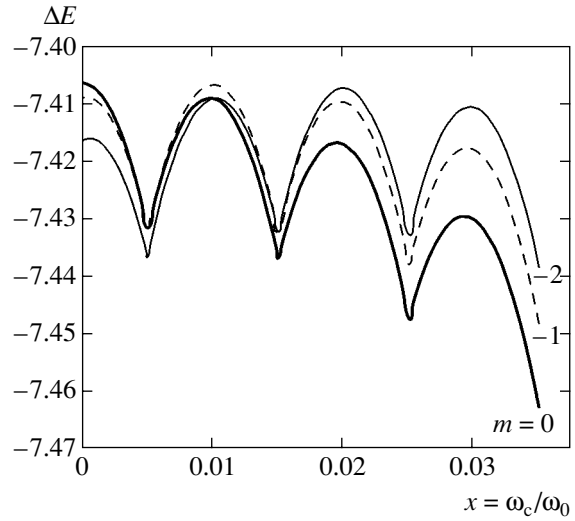

Fig. 3. Polaron corrections to the electron energy as a function of a magnetic field for states with different l_e in a quantum ring.

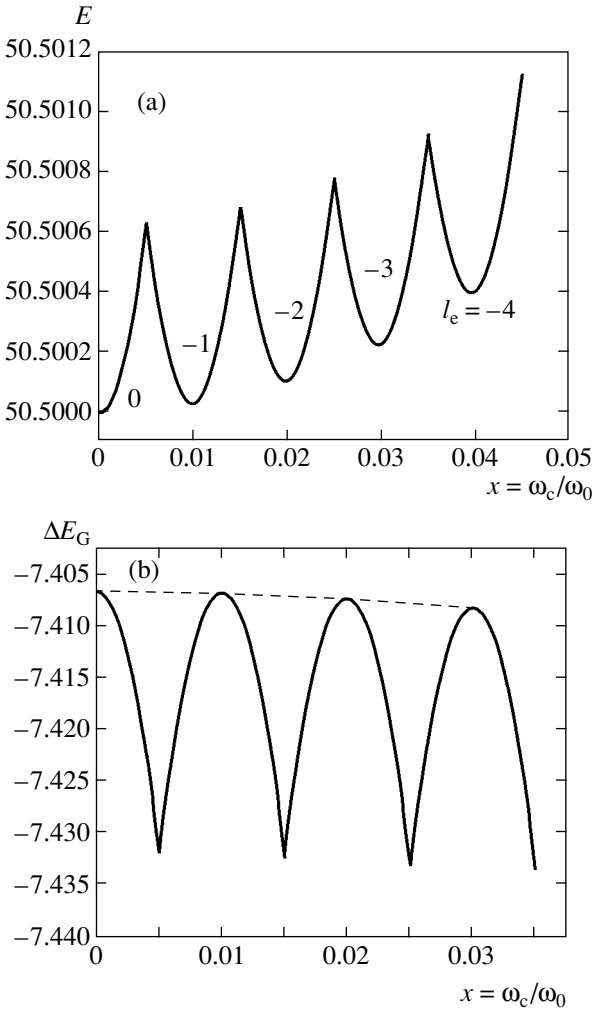

Fig. 4. (a) The ground state of an electron in a quantum ring and (b) a polaron correction to it as functions of a magnetic field.

where δE_{ex} is the total polaron shift of the exciton, which is defined below (see (16) and (17)). The expression for the emission probability of a quantum of light

$$W_{em} = \frac{2\pi}{\hbar}|p_{CV}|^2|I(l_e, l_h)|^2 \times \sum_K W_K \delta(E_{eh} - E_K - \Delta E_S - \hbar\omega) \quad (12)$$

differs from the absorption probability (10) by the Stokes shift ΔE_S, which is given by (see [4])

$$\Delta E_S = 2\delta E_{ex}. \quad (13)$$

Formulas (11) and (13) show that both the intensity of phonon repetitions and the Stokes shift of the spectrum are determined by the quantity δE_{ex}, which represents the renormalization of the exciton spectrum due to the formation of a polaron state. Below, we will show that this quantity is an oscillating function of a magnetic field (similar to the electron spectrum considered in the previous section); this leads to the oscillations of the Stokes shift and of the intensities of phonon repetitions. Note that the oscillations of the intensity of exciton luminescence in quantum rings have been predicted in [10].

To determine δE_{ex}, we write out an expression for the Hamiltonian of two particles, an electron and a hole, in a quantum ring that interact with longitudinal phonons:

$$H = T_e + T_h + V_C(|\mathbf{r}_e - \mathbf{r}_h|) + \sum_{\mathbf{q}} \hbar\omega_{\mathbf{q}} b_{\mathbf{q}}^+ b_{\mathbf{q}} + \sum_{\mathbf{q}} (F_{\mathbf{q}}(r_e) - F_{\mathbf{q}}(\mathbf{r}_h))(b_{\mathbf{q}} + b_{-\mathbf{q}}^+). \quad (14)$$

Since the radius r_0 may vary within rather wide limits during the formation of quantum rings, one should consider two possible situations. For sufficiently small radii ($r_0 \ll a_B^*$, where a_B^* is the effective Bohr radius of an exciton in the ring material), the Coulomb interaction can be neglected. In this case, the dynamics of the electron and the hole are independent, and the Schrödinger equation is decomposed into two equations, for the electron and the hole; the solution to these equations is presented in the Section 2 (formulas (5) and (6)). The polaron corrections to the spectrum of the electron–hole pair are calculated by a formula similar to (8), in which the matrix element $P_{ll'}(q)$ should be replaced by a sum of the matrix elements of the electron–phonon and hole–phonon interactions (the third term in (14)). The calculations yield

$$\delta E_{ex} = \Delta E_e + \Delta E_h + \Delta E_{mix}. \quad (15)$$

Here, ΔE_e and ΔE_h are the polarization shifts of an electron and a hole, respectively, and ΔE_{mix} is a combined shift. Each of these contributions is calculated by a procedure analogous to that described in the Appendix. The one-particle energy shifts ΔE_e and ΔE_h are calculated by formula (9); for ΔE_{mix}, we obtain

$$\Delta E_{mix} = -\frac{e^2\hbar\omega_{opt}}{\varepsilon^*}\sum_{\alpha'}\frac{B_{\alpha\to\alpha'}}{E_{\alpha'} - E_\alpha + \hbar\omega_q - \Delta},$$

$$B_{\alpha\to\alpha'} = [\Gamma(\Delta l_e + 1)\Gamma(\Delta l_h + 1) \times \sqrt{\Gamma(M+1)\Gamma(M'+1)\Gamma(N+1)\Gamma(N'+1)}\,]^{-1} \times \Gamma\left(\frac{\Delta l_e}{2} + \frac{M'}{2} + \frac{M}{2} + 1\right) \quad (16)$$

$$\times \Gamma\left(\frac{\Delta l_e}{2} + \frac{N'}{2} + \frac{N}{2} + 1\right)\frac{a_e^{\Delta l_e} a_h^{\Delta l_h}}{2^{\Delta l_e + \Delta l_h}}\int_0^\infty \frac{dq_x}{2\pi} q_x^{\Delta l_e + \Delta l_h}$$

$$\times F\left(\frac{\Delta l_e + M' + M + 2}{2};\ \Delta l_e + 1;\ -\frac{(q_\parallel a_e)^2}{2}\right)$$

$$\times F\left(\frac{\Delta l_h + N' + N + 2}{2};\ \Delta l_h + 1;\ -\frac{(q_\parallel a_h)^2}{2}\right),$$

where α is the set of quantum numbers (l_e, l_h). Thus, since the particles move independently for $r_0 \ll a_B^*$ and each term in (15) is an oscillating function of a magnetic field, we should expect that the Stokes shift ΔE_S and the intensity W_K will oscillate according to (11) and (13).

In the opposite case, when $r_0 \gg a_B^*$, we should take into account the effect of the Coulomb potential on the dynamics of particles; therefore, we fail to obtain an exact analytic result. Let us carry out a qualitative analysis. By analogy with [11], we assume that the motion is adiabatic in the radial direction. Following the calculation procedure described in [11], we obtain the following relations for the exciton spectrum:

$$E_J = E_{rad} + \langle B\rangle J^2 + \langle E_{rel}(\Phi)\rangle, \qquad B = \frac{\hbar^2}{2(m_e^* r_e^2 + m_h^* r_h^2)}. \quad (17)$$

Here, $J = l_e + l_h$ is the total momentum of the exciton. The first term in the first equation is the energy of the radial motion of particles, the second term is the energy of motion of an exciton as a whole, and the last term represents the energy of the bound state of the particles. The angular brackets denote averaging with respect to the radial coordinates r_e and r_h of the particles. Note that $\langle B\rangle$ depends on the magnetic field only via the

effective oscillation length $a_e = \sqrt{\hbar/m_e^*\sqrt{\omega_{Be}^2 + \omega_0^2}}$. However, Fig. 2 shows that, for sufficiently narrow rings, the variation limits of the magnetic field are such that $\omega_{Be}/\omega_0 \ll 1$, and the quantity $\langle B\rangle$ very weakly depends on the magnetic field. As regards the last term in (17), according to [10], it is proportional to

$$\langle E_{rel}(\Phi)\rangle \propto e^{-2\pi r_0/a_B^*}. \quad (18)$$

In the limit of $r_0 \gg a_B^*$, this expression is exponentially small, and the effect of a magnetic field on the polaron corrections to the spectrum (17) is negligible. It was implicitly assumed in (17) that an electron and a hole in the ring move along circles of identical radii. According to [12], if we take into account that the radius of a circle for an electron, r_0^e, is different from the radius of a circle for a hole r_0^h, we obtain

$$E_J = E_{rad} + \left\langle B\left(J + \frac{\Delta\Phi}{\Phi_0}\right)^2\right\rangle + \langle E_{rel}(\Phi)\rangle, \quad (19)$$

instead of (17); here, $\Delta\Phi$ is proportional to $-e(r_h - r_e)B$, i.e., to the product of the dipole moment of an exciton multiplied by the magnetic field. This correction leads to a considerable reconstruction of the exciton spectrum [12].

Thus, in both situations, the spectra of an electron–hole complex (formulas (5) and (6)) for $r_0 \ll a_B^*$ and of an exciton (19) for r_0^e, $r_0^h \gg a_B^*$, considered as functions of a magnetic field, have intersecting branches. In particular, the ground state oscillates with a magnetic field [12]. This leads to oscillations of ΔE_G in expression (8) for the polaron correction and, hence, to the oscillations of the polaron correction δE_{ex} to the optically active state $J = l_e + l_h = 0$ of the exciton. As pointed out above, the Stokes shift in the absorption and emission spectra of light, as well as the intensity of phonon repetitions, are determined by the quantity δE_{ex} and, hence, oscillate with a magnetic field. However, when r_0^e, $r_0^h \gg a_B^*$, the polaron shift may exhibit appreciable oscillatory phenomena only for a radially polarized exciton $r_0^e \neq r_0^h$.

ACKNOWLEDGMENTS

This work was supported by the Russian Foundation for Basic Research (project no. 05-02-16939), by the program for supporting leading scientific schools of the Russian Federation (project no. NSh-593.2003.2), and by the Ministry of Education and Science of the Russian Federation. One of the authors (V.K.) acknowledges the support of INTAS, project no. 2212.

APPENDIX

Consider a procedure for calculating the matrix element $P_{l\to l'}(\mathbf{q})$ of the electron–phonon interaction:

$$P_{l_e\to l_e'}(\mathbf{q}) = \langle\psi_{M'}|D_{\mathbf{q}}e^{i\mathbf{q}\cdot\mathbf{r}}|\psi_M\rangle. \quad (A.1)$$

Here, ψ_M are electron wavefunctions (5), and the indices M and M' are defined as $M = \sqrt{l_e^2 + 2m_e^*a_1/\hbar^2}$ and $M' = \sqrt{l_e'^2 + 2m_e^*a_1/\hbar^2}$. Let us orient the polar axis along q_x and represent the exponential function in (A.1) as

$$e^{i\mathbf{q}\cdot\mathbf{r}} = e^{iq_sz}\sum_k i^k J(q_sr)e^{ik\varphi}. \quad (A.2)$$

Calculating the integrals in (A.1), we obtain

$$P_{l_e\to l_e'}(\mathbf{q}) = D_{\mathbf{q}}C_MC_{M'}(iq_x)^{l_e'-l_e} \times \frac{\Gamma\left(\frac{l_e'-l_e}{2} + \frac{M'+M+2}{2}\right)}{\Gamma(l_e'-l_e+1)2^{l_e'-l_e+1}}(2a_e^2)^{\frac{l_e'-l_e}{2}+\frac{M'+M+2}{2}} \times F\left(\frac{l_e'-l_e}{2} + \frac{M'+M+2}{2}; l_e'-l_e+1; -\frac{q_x^2a_e^2}{2}\right). \quad (A.3)$$

Substituting C_M and $D_{\mathbf{q}}$ from (5) and (7), respectively, into the expression obtained and squaring the modulus, after simple calculations we arrive at

$$|P_{l_e\to l_e'}(\mathbf{q})|^2 = \frac{e^2\hbar\omega_{opt}}{\varepsilon^*|\mathbf{q}|} \times 2\pi\frac{\Gamma^2\left(\frac{\Delta l_e + M' + M + 2}{2}\right)}{\Gamma^2(\Delta l_e+1)\Gamma(M+1)\Gamma(M'+1)}\left(\frac{q_\parallel^2a_e^2}{2}\right)^{\Delta l_e} \times F^2\left(\frac{\Delta l_e}{2} + \frac{M'+M+2}{2}; \Delta l_e+1; -\frac{q_x^2a_e^2}{2}\right). \quad (A.4)$$

Now, we must sum this expression over the wavevectors of all phonons. Replacing the sum over wavevectors by the integral, for

$$\int\frac{d\mathbf{q}}{(2\pi)^3}|P_{l_e\to l_e'}(\mathbf{q})|^2 = \frac{e^2\hbar\omega_{opt}}{\varepsilon^*a_e}A_{l_e\to l_e'},$$

we finally obtain the following expression ($t^2 = q_x^2 a_e^2/2$):

$$A_{l_e \to l'_e} = \frac{\Gamma^2\left(\frac{\Delta l_e + M' + M + 2}{2}\right)}{\Gamma^2(\Delta l_e + 1)\Gamma(M+1)\Gamma(M'+1)} \times \int_0^\infty \frac{dx}{2\pi} t^{\Delta l_e} F^2\left(\frac{\Delta l_e + M' + M + 2}{2}; \Delta l_e + 1; -t^2\right). \quad \text{(A.5)}$$

REFERENCES

1. T. Ando, A. B. Fowler, and F. Stern, Rev. Mod. Phys. **54**, 437 (1982).
2. L. Wendler, A. V. Chaplik, R. Haupt, and O. Hipolito, J. Phys.: Condens. Matter **5**, 4817 (1993); I. P. Ipatova, A. Yu. Maslov, and O. V. Proshina, Fiz. Tverd. Tela (St. Petersburg) **37**, 1819 (1995) [Phys. Solid State **37**, 991 (1995)]; Phys. Low-Dimens. Semicond. Struct., Nos. 4–5 (1996).
3. L. Wendler, A. V. Chaplik, R. Haupt, and O. Hipolito, J. Phys.: Condens. Matter **5**, 8031 (1993).
4. I. P. Ipatova, A. Yu. Maslov, and O. V. Proshina, Fiz. Tekh. Poluprovodn. (St. Petersburg) **33**, 832 (1999) [Semiconductors **33**, 765 (1999)].
5. J. M. Garsia, G. Medeiros-Ribeiro, K. Schmit, *et al.*, Appl. Phys. Lett. **71**, 2014 (1997); A. Lorke and R. J. Luyken, Physica B (Amsterdam) **256**, 424 (1998); A. Lorke, R. J. Luyken, A. O. Govorov, *et al.*, Phys. Rev. Lett. **84**, 2223 (2000).
6. L. Wendler, V. M. Fomin, A. V. Chaplik, and A. O. Govorov, Phys. Rev. B **54**, 4794 (1996).
7. T. Chakraborty and L. Pietilaihen, Phys. Rev. B **50**, 8460 (1994).
8. W. C. Tan and J. C. Inkson, Phys. Rev. B **53**, 6947 (1996).
9. G. Lindemann, R. Lassing, W. Seidenbusch, and E. Gornik, Phys. Rev. B **28**, 4693 (1983).
10. A. V. Chaplik, Pis'ma Zh. Éksp. Teor. Fiz. **75**, 343 (2002) [JETP Lett. **75**, 292 (2002)].
11. A. V. Chaplik, Zh. Éksp. Teor. Fiz. **119**, 193 (2001) [JETP **92**, 169 (2001)].
12. A. O. Govorov, S. E. Ulloa, K. Karrai, and R. J. Warburton, Phys. Rev. B **66**, 081309(R) (2002).

Translated by I. Nikitin

Journal of Experimental and Theoretical Physics, Vol. 101, No. 4, 2005, pp. 693–698.
Translated from Zhurnal Éksperimental'noĭ i Teoreticheskoĭ Fiziki, Vol. 128, No. 4, 2005, pp. 803–810.

ELECTRONIC PROPERTIES OF SOLIDS

Temperature Dependence of Luminescence Intensity under Bose Condensation of Interwell Excitons

A. V. Gorbunov, V. E. Bisti, and V. B. Timofeev

Institute of Solid-State Physics, Russian Academy of Sciences, Chernogolovka, Moscow oblast, 142432 Russia
e-mail: bisti@issp.ac.ru

Received December 2, 2004; in final form, April 4, 2005

Abstract—Photoluminescence of interwell excitons in GaAs/AlGaAs double quantum wells (*n–i–n* heterostructure) containing large-scale random potential fluctuations in the planes of heteroboundaries is studied. The properties of excitons, in which a photoexcited electron and a hole are spatially separated in neighboring quantum wells, were investigated upon variation of the power density of off-resonance laser excitation and temperature (1.5–4.2 K), both under lateral (in the heteroboundary plane) confinement of the excitation region to a few micrometers and without such a limitation (directly from the region of laser-induced photoexcitation focused to a spot not exceeding 30 μm. Under low pumping (with a power smaller than a microwatt), interwell excitons are strongly localized due to small-scale random potential fluctuations and the corresponding photoluminescence line is nonhomogeneously broadened to 2.5–3.0 meV. With increasing pumping power, the narrow line of delocalized excitons with a width of approximately 1 meV emerges in a threshold manner (the intensity of this line increases superlinearly near the threshold with increasing pumping). For a fixed pumping, the intensity of this line decreases linearly upon heating until it completely vanishes from the spectrum. The observed effect is attributed to Bose condensation in a quasi-two-dimensional system of interwell excitons. Within the proposed model, we show that the linear mode in the behavior of the luminescence intensity until its disappearance in the continuum of the photoluminescence spectrum upon a change in temperature is observed only for the condensed part of interwell excitons. At the same time, the luminescence of the above-the-condensate part of excitons is almost insensitive to temperature variations in the temperature range studied. *© 2005 Pleiades Publishing, Inc.*

1. INTRODUCTION

Tunnel-coupled quantum systems, superlattices, and double quantum wells (DQWs) have been objects of intense studies for a long time [1–16]. The interest in such 2D systems is due, in particular, to the fact that photoexcited electron and hole charge carriers can in principle be separated in space. Excitons in which the electron and the hole are in different quantum wells (QWs) separated by a tunnel-transparent barrier can be generated in DQWs with an electric bias voltage that is applied perpendicularly to the layers and shifts energy bands [2]. Such excitons are referred to as spatially indirect (I), or interwell, excitons in contrast to direct (D) intrawell excitons, in which the electron and the hole are in the same QWs. In contrast to intrawell excitons, interwell excitons are long-lived (the radiation lifetime may attain tens of nanoseconds or more) due to partial overlapping of the electron and hole wavefunctions through a tunnel-transparent barrier in the direction of the applied electric field. Consequently, such excitons can be accumulated and the gas of interwell excitons can be cooled to low temperatures close to the lattice temperature. In view of the broken inverse symmetry, interwell excitons exhibit peculiar properties (possess a dipole moment even in the ground state). In the case of a large dipole moment, such excitons cannot combine to form molecules or other many-particle exciton complexes due to a strong dipole–dipole repulsion.

Excitons are composite bosons since they contain two Fermi quasiparticles (band hole and band electron). For this reason, their collective properties must obey the Bose–Einstein statistics. Precisely this circumstance forms the basis of the assumption formulated in a number of theoretical publications at the beginning of the 1960s [17] and concerning the possibility of Bose–Einstein condensation in a weakly nonideal diluted exciton gas in semiconductors at low temperatures, when $na_{\mathrm{ex}}^{d} \ll 1$ (n is the exciton concentration, a_{ex} is the Bohr radius of an exciton, and d is the dimension of the system). A convenient model object for investigating this effect in semiconducting heterostructures was quasi-two-dimensional interwell excitons [2–5]. It should be borne in mind, however, that Bose–Einstein condensation at finite temperatures cannot occur in principle in an ideal and unlimited 2D system with a constant density of single-particle states. This is associated with divergence of the number of the filled states in the case when the chemical potential μ tends to zero and when fluctuations violate the order parameter [18]. Nevertheless, Bose–Einstein condensation may occur at finite temperatures in quasi-two-dimensional systems with a spatial (lateral) confinement. If a 2D system

is confined in a plane and has a characteristic lateral domain length L, the minimal energy E_0 in the energy spectrum of such a system can be on the order of $E_0 = \hbar^2\pi^2/ML^2$ (M is the lateral mass of an interwell exciton). At temperatures below the critical temperature, macrofilling of the lower energy state must take place (this phenomenon is completely analogous to Bose condensation in the 3D case). The relation between the critical temperature T_c and the threshold concentration n_0 starting from which (i.e., for $n > n_0$) the particles begin to accumulate in the lower energy state is described by the equation

$$n_0(T_c) = \int_{E_0}^{\infty} f(E, \mu = 0)D(E)dE = D(E)T_c \ln\frac{T_c}{E_0}, \quad (1)$$

where $D(E)$ is the density of states and $E_0 \ll T_c$. The critical temperature in the laterally confined 2D system with a finite number of states is given by

$$T_c \approx \frac{2\pi\hbar^2 n}{g_{ex}k_B M \ln(nS)}; \quad (2)$$

i.e., it decreases logarithmically with increasing area $S \propto L^2$ occupied by the 2D gas of Bose particles. g_{ex} is the spin degeneracy factor, k_B is the Boltzmann constant, and L is the characteristic linear domain size.

Spatial limitations can be imposed on the free motion of excitons in the planes of quantum wells due to large-scale random potential fluctuations associated with variations of QW widths $w(r)$ at heteroboundaries. Changes in the effective lateral potential $U(r) = U(w(r))$ can be attributed to these variations. Under quasi-equilibrium conditions, the exciton density distribution is determined by the equality $\mu(n(r)) + U(r) = \mu$, where the chemical potential μ of interwell excitons is associated with their mean density and $\mu(n(r))$ is the chemical potential of the homogeneous exciton phase in the spatial confinement region (domain). Obviously, $\mu(n(r)) < \mu$ since $\mu(n) = -E_{ex} + \delta U$ (E_{ex} is the exciton binding energy) Consequently, it is easier to accumulate excitons in the lateral localization region and the exciton density in such regions, which actually play the role of exciton traps, may substantially exceed their average density in the QW planes [11]. The critical conditions corresponding to Bose condensation of interwell excitons can more easily be realized precisely in lateral domains (traps).

It was shown by us earlier [19, 20] that the collective state of interwell excitons emerges in DQWs in the presence of large-scale random potential fluctuations associated with fluctuations of the AlAs barrier width in GaAs DQWs. Namely, the exciton condensation took place when photoexcited interwell excitons accumulated in macroscopically extended regions with lateral confinement over a few micrometers [19]. To ensure the operation under lateral confinement, we coated the surface of the structure with an opaque metallic mask, in which windows with a size from 0.5 to 10 μm were prepared by electron-beam lithography; photoluminescence was excited and subsequently detected through these windows. It was found that interwell excitons are strongly localized for low densities of excitation and low temperatures and the corresponding photoluminescence band is broadened nonhomogeneously (the photoluminescence bandwidth amounts approximately to 2.5 meV). With increasing pumping, a very narrow line of delocalized interwell excitons (with a width smaller than 1 meV) emerges in a threshold manner. For a fixed pumping, this line vanishes from the spectrum upon heating, its intensity decreases not activationally, but in accordance with a power law. The observed phenomenon was attributed to Bose condensation in a quasi-two-dimensional system of interwell excitons under the spatial limitation determined by the sizes of lateral domains (traps) with a width of a few micrometers.

A strong argument in favor of such an interpretation is the strongly critical dependence of the observed properties on the temperature and pumping intensity. Since the temperature behavior of the exciton luminescence intensity under Bose condensation is not of the activation type and exhibits general features typical of this phenomenon, we study here this effect in greater detail using a structure with a slightly different lateral confinement for interwell excitons as compared to [19]. We will try to answer the important question on the difference in the temperature dependences of the luminescence intensity of condensed interwell excitons and the above-the-condensate part in the temperature range studied here.

2. SAMPLES AND EXPERIMENTAL TECHNIQUE

We studied GaAs/AlGaAs *n–i–n* heterostructure with a GaAs/AlAs/GaAs DQW (the widths of GaAs wells and the AlAs barrier are 120 and 11 Å, respectively). The structure was grown by molecular-beam epitaxy on an *n*-type doped GaAs substrate (the doping impurity (Si) concentration was 10^{18} cm^{-3}) with the (001) crystallographic orientation. First, a 0.5-μm-thick Si-doped GaAs buffer layer was grown on the substrate, followed by a 0.15-μm-thick AlGaAs insulating layer ($x = 0.33$). Then GaAs/AlAs/GaAs DQWs were grown, above which a 0.15-μm-thick AlGaAs insulating layer was deposited. Further, a 0.1-μm-thick Si-doped GaAs layer (with a Si concentration of 10^{18} cm^{-3}) was grown. The entire structure was coated by a 100-Å-thick GaAs layer. Four-monolayer AlAs barriers were grown at the boundaries of DQWs with AlGaAs layers. Growth-interruption technique was used for epitaxial growth of AlAs. The application of this technique resulted in the emergence of long-period lateral random potential fluctuations associated with fluctuations of the widths of AlAs barriers [21]. Then

1×1-mm^2 contact area elements were prepared lithographically on the structure. Metallic contacts prepared from an Au + Ge + Pt alloy were deposited on the buffer and doped layers at the top part of the area elements. The sample resistance between built-in electrodes was about 100 Ω at room temperature and was an order of magnitude higher in liquid helium.

In a metallic mask (120-nm-thick Al film) deposited on the surface of the *n–i–n* structure with the above structure, apertures (windows) with a diameter from 0.5 to 10 μm were etched by explosive electron-beam epitaxy. Experiments were made in such a way that photoluminescence signal excitation and detection was carried out via single windows. The Al film was insulated from the n^+-junction region of the heterostructure.

The luminescence spectra were excited by a cw He–Ne laser whose beam was focused to a spot with a diameter of approximately 30 μm. We analyzed the photoluminescence spectra directly from the photoexcitation region since no appreciable exciton drift from the region of their excitation was observed in this structure. At the exit from a wide-aperture double monochromator (Ramanor U1000), the spectra were recorded with the help of a multichannel optical detector (Si-based CCD camera) cooled with liquid nitrogen. The sample was placed in a helium cryostat. The sample temperature in a range of 1.5–4.2 K was controlled by pumping out ^{4}He vapor and monitored by a resistance thermometer. For a laser power below 10 μW, the sample temperature virtually coincides with the bath temperature.

3. EXPERIMENTAL

Figure 1 shows the behavior of the luminescence spectra of interwell (I_{ex} line) and intrawell (*D* line that cannot be seen for such a representation of the spectra and the *T* line) excitons upon variation of a bias voltage shifting the size quantization levels in DQWs. The *D* and *T* lines correspond to delocalized and localized intrawell excitons. It can be seen that luminescence of interwell excitons (I_{ex} line) emerges in the spectra for voltages $U < -0.2$ V. This happens when the resultant Stark shift eFd (d is the distance between the electron and hole in adjacent QWs and F is the electric field) exceeds the difference between the binding energies of intrawell and interwell excitons (i.e., $eFd \geq E_D - E_I$). With increasing applied voltage, the interwell exciton line in the spectrum is shifted in accordance with a linear law ($\Delta E_I \propto eFd$). On the contrary, the shift of the intrawell exciton is insignificant (see the inset to Fig. 1). The intensity of the interwell exciton line changes insignificantly upon variation of the voltage. This indicates the high quality of the structure. The increase in the *T* line intensity of a localized exciton with voltage is the result of an increase in the current passing through the structure.

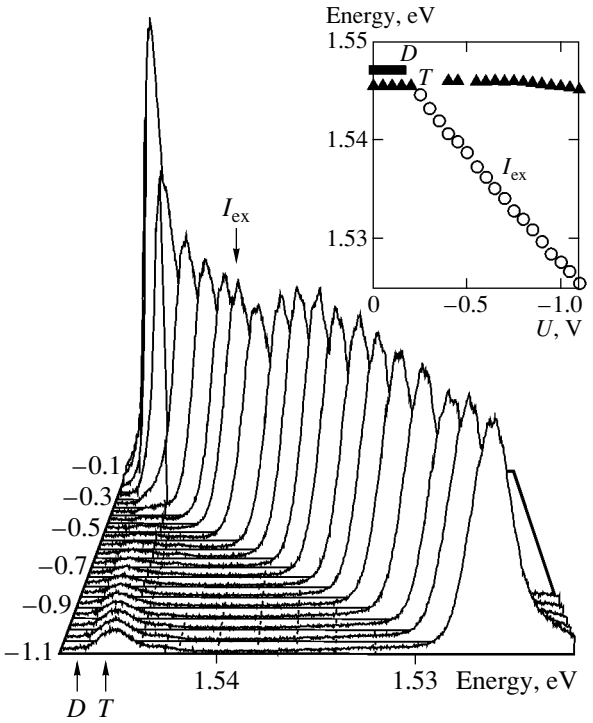

Fig. 1. Photoluminescence spectra for various bias voltages applied to the built-in gate. The inset shows the positions of the direct exciton line (*D*), indirect exciton line (*I*), and the line of a charged complex (*T*) as a function of voltage across the gate. The temperature $T = 2$ K and the He–Ne laser power $P = 10$ μW.

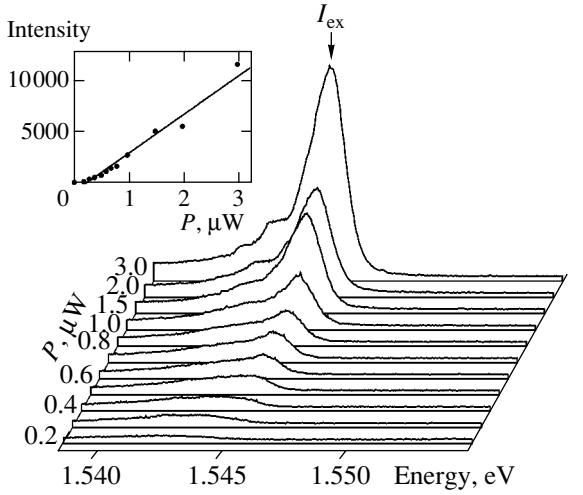

Fig. 2. Photoluminescence spectra for various values of the He–Ne laser power. Temperature is $T = 2$ K and the bias voltage across the gate is $U = -0.149$ V. The inset shows the intensity of the indirect exciton line as a function of the photoexcitation power: experiment (circles) and theory (solid curve).

Let us consider the behavior of luminescence of interwell excitons upon a variation of pumping intensity. For low densities of excitation (less than 1 μW), the luminescence spectra exhibit a relatively broad

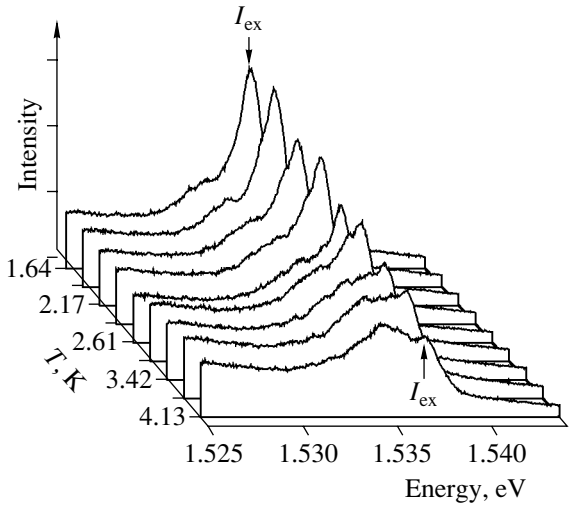

Fig. 3. Photoluminescence spectra for various temperatures. The He–Ne laser power is P = 1 μW and the voltage across the gate is U = –0.330 V.

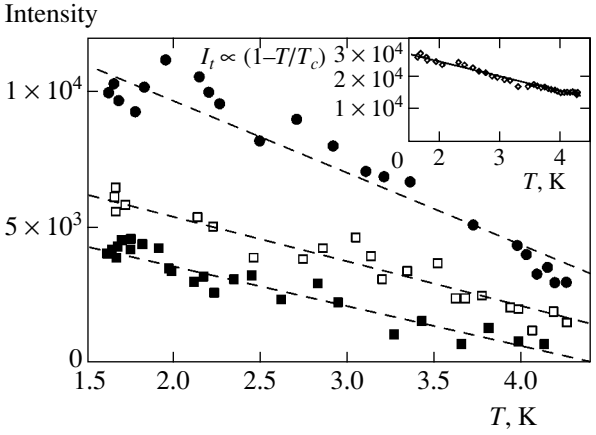

Fig. 4. Temperature dependence of the photoluminescence intensity for an indirect exciton. The symbols correspond to experimental results and the dashed straight lines are the results of fitting by the formula $I \propto (1 - T/T_c)$. Dark squares correspond to the He–Ne laser power P = 1 μW at T_c = 4.4 K, light squares correspond to P = 2 μW and T_c = 5.18 K, and dark circles correspond to P = 5 μW and T_c = 5.54 K. The inset shows the temperature dependence of the indirect exciton line intensity for a 50-μm window (P = 1 μW and T_c = 7.43 K).

asymmetric band corresponding to interwell excitons (the bandwidth is approximately 2.5 meV, Fig. 2). This band is nonhomogeneously broadened and is due to strong localization of interwell excitons at small-scale fluctuations of the random potential associated with residual charged impurities. With increasing pumping (above 0.5 μW), a narrow line emerges in a threshold manner in the violet edge of the broad band. The intensity of this line increases superlinearly with pumping (see the inset to Fig. 2) and the line is slightly shifted (by approximately 0.5 meV) towards low energies. Upon a further increase in pumping (to above 5 μW), broadening of the narrow line of interwell excitons begins and the monotonically broadened line is shifted towards higher energies.

We studied in detail the behavior of the narrow line of interwell excitons as a function of temperature and found that this line vanishes from the spectrum at temperatures $T \geq 5$ K. Figure 3 illustrates the typical behavior of the I line upon variation of temperature for a fixed pumping. It can be seen that this line clearly dominates over the structureless luminescence band of localized excitons and has a higher intensity at T = 1.64 K and a pumping power of 1 μW. With increasing temperature, the intensity of the I line decreases, while its width remains virtually unchanged, and at T = 4.2 K this line practically vanishes against the background of the structureless spectrum of localized excitons, which preserves its shape. Essentially, the decrease in the I line intensity with temperature is not of activation type.

Having measured the temperature dependence of the I line intensity under various pumping intensities, we established the following regularity in its temperature behavior (Fig. 4):

$$I_T \propto (1 - T/T_c); \tag{3}$$

here, I_T is the line intensity at temperature T and T_c is the critical temperature corresponding to vanishing of this line from the spectrum for a given fixed pumping.

We believe that the experimental results described above indicate Bose condensation of interwell excitons in micrometer-scale lateral domains; its origin is associated with large-scale random potential fluctuations. For low-intensity pumping and low temperatures, photoexcited interwell excitons are strongly localized due to small defects (e.g., residual charged impurities). This situation corresponds to a broad, nonhomogeneously broadened luminescence band of interwell excitons for low excitation densities. Not more than one exciton can be localized at a defect due to the strong dipole–dipole repulsion; consequently, this luminescence channel is rapidly saturated. According to our estimates, this is observed in the investigated structures at concentrations not exceeding 5×10^9 cm^{-2}. Upon a further increase in the pumping intensity above the percolation threshold, interwell excitons become delocalized in a domain. When the critical density is attained, excitons are condensed to the lowest delocalized state. This is manifested experimentally in the threshold emergence of the narrow luminescence line, its superlinear growth, and its shift towards lower energies upon filling of the lower state in the domain by excitons obeying the Bose–Einstein statistics. The strongest argument in favor of exciton condensation is the critical temperature dependence of the observed properties.

4. DISCUSSION

Let us now consider the anticipated temperature dependence of the luminescence intensity of quasi-two-dimensional interwell excitons in the Bose condensate in comparison with the luminescence intensity of the part of excitons above the condensate. For this purpose, let us analyze the following model system of interwell quasi-two-dimensional excitons excited by cw laser pumping. According to our estimates, the luminescence quantum yield in the structure studied here is about 0.1; consequently, a substantial part of excitons perish nonradiatively with time τ_n. Radiative annihilation of excitons accompanied by the emission of a photon occurs over a time τ_r. We assume that the exciton gas temperature in the region of interest coincides with the lattice temperature since all characteristic times of exciton departure from the system are much longer than their relaxation time along the energy axis (τ_n, $\tau_r \gg \tau_T$). All these times may in principle be functions of temperature, but we assume that this dependence can be ignored in the temperature range under investigation. The quasi-equilibrium energy distribution of excitons is of the classical (Boltzmann) or Bose type depending on exciton concentration n and temperature T. It should be borne in mind that excitons suffer direct radiative annihilation and contribute to luminescence only within the "light cone" determined by the momentum conservation law (in our case, excitons whose momentum component in the plane is $k \le 3 \times 10^5$ cm^{-1} emit photons; this corresponds to an energy uncertainty δE of about 0.3 meV). To determine the luminescence intensity, we must take into account the contribution of particles from this energy interval. If the observed narrow luminescence line of interwell excitons has a width $\Delta > \delta E$, this can be a consequence of nonhomogeneous broadening. If we assume that the luminescence probability is independent of energy, the temperature dependence of luminescence intensity I can be established by determining the number of particles in the energy interval δE,

$$I \propto \int_0^{\delta E} f(E)D(E)dE, \tag{4}$$

where $f(E)$ is the distribution function. For the Boltzmann distribution, we have

$$I \propto 1 - \exp(-\delta E/T). \tag{5}$$

It was mentioned above that macrofilling of the lowest energy state takes place at a temperature below the critical value (2). In accordance with formula (1), $N_0 = n_0(T)L^2$ is the number of above-the-condensate particles in the domain in question after the beginning of condensation. The critical temperature is defined by two variable parameters, viz., the exciton concentration determined by the pumping power and the domain size, as well as the lateral mass M of an interwell exciton. In other words, it is determined by the minimal energy E_0 of the system and by the number N_0 of above-the-condensate particles in a domain. If we use the value of $M = 0.16m_0$, the observed value of $T_c = 3$ K corresponds to $n \sim 10^{10}$ cm^{-2} and $L \sim 1 - 3\mu$ ($N_0 \sim 100$–300 and $E_0 \sim 0.1$ K), which corresponds to experimental conditions.

The particles in a macroscopically filled state must be coherent (i.e., described by the same wavefunction); consequently, it is natural to assume that the radiative probability of annihilation of interwell excitons in the condensate must be proportional to their number N_c; accordingly, the luminescence intensity is proportional to N_c^2 (N_c is the number of particles in the condensate). For incoherent above-the-condensate particles, the luminescence intensity is proportional just to number N_0. The above considerations are in (at least qualitative) agreement with the experimental observations. Direct measurements of the luminescence kinetics under pulsed laser pumping demonstrated [15] that the luminescence decay time of the narrow line corresponding to the "condensate" part of excitons amounts to approximately 10 ns at 2 K and is almost an order of magnitude shorter than the luminescence decay time for excitons outside the condensate (this time exceeds 100 ns). The dependence of luminescence on temperature or pumping power can be determined from the balance equations taking into account the above-mentioned factors. If w is the exciton generation rate per unit time at a unit area element (which is determined by the pumping power density), we have

$$w = \frac{n}{\tau_0}, \quad \frac{1}{\tau_0} = \frac{1}{\tau_r} + \frac{1}{\tau_n} \tag{6}$$

in the absence of macrofilling. In this case, the luminescence intensity $I \propto n/\tau_r = w\tau_0/\tau_r$. Under the experimental conditions, the quantum yield τ_0/τ_r does not exceed 0.1.

After the beginning of condensation, the balance equation acquires the form

$$wL^2 = \frac{N_c^2}{\tau_r} + \frac{N_c}{\tau_n} + \frac{N_0}{\tau_0}. \tag{7}$$

The threshold value $w_0 = n_0/\tau_0$ corresponds to the beginning of condensation ($N_c = 0$). The luminescence intensity of coherent excitons in the condensate is $I_c \sim N_c^2/\tau_r$. At a fixed temperature at the beginning of condensation, $I_c \propto (w - w_0)^2 L^4 \tau_0^2/\tau_r$; upon a further increase in pumping, we have $I_c \propto (w - w_0)L^2$. The dependence of luminescence intensity changes when $(w - w_0)/w_0 \propto \tau_r/2\tau_0 N_0$.

Figure 2 illustrates the dependence of the luminescence dependence of the condensed part of interwell excitons on pumping intensity. The luminescence

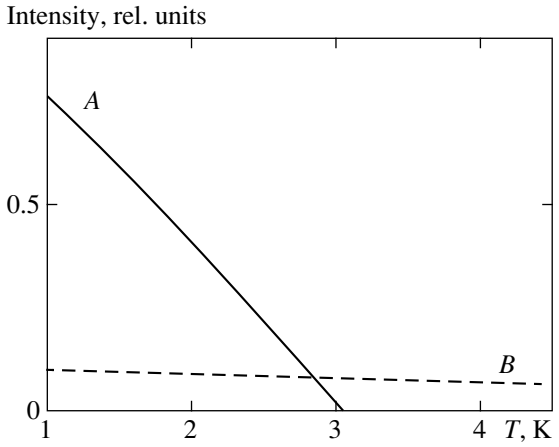

Fig. 5. Temperature dependence of luminescence intensity for a system with coherent macrofilled state (*A*) for E_0 = 8 μeV = 0.09 K, $N_0(T_c) = nL^2 = 100$, and $\tau_r/\tau_0 = 10$ and for a system with the Boltzmann distribution (*B*) with δE = 0.3 meV.

threshold of the exciton line and its superlinear increase followed by a linear increase of the luminescence intensity as a function of pumping intensity can be clearly seen in the figure (see inset). The dynamic range of the superlinear behavior of the intensity is determined by the size of the domain (trap): the smaller the domain area, the larger the range of the nonlinear behavior. The theoretical curve in Fig. 2 is plotted for the following values of parameters: $\tau_r/\tau_0 = 10$ and $N_0 = 100$.

Figure 5 shows the calculated temperature dependence of the luminescence intensity for a system with macroscopic filling of the lowest coherent state of interwell excitons (Bose condensate) and for a system with the Boltzmann distribution for the same values of parameters as in the inset to Fig. 2. It can be seen that the temperature dependence of the luminescence intensity for the Boltzmann distribution is very weak, while the macrofilled state below critical temperature T_c exhibits a sharp increase in the intensity upon cooling and the dependence is close to linear. This is in good (at least qualitative) agreement with experiment. The intensity ratio is $I_c/I_0 \sim \tau_r/\tau_0$ at $T \ll T_c$. It should be emphasized that the experimentally observed strong temperature dependence of the luminescence intensity of the exciton condensate under steady-state pumping is possible only provided that the radiative annihilation probability for excitons in the condensate is considerably higher than the radiative decay probability for above-the-condensate excitons, and the luminescence quantum yield of above-the-condensate excitons is much smaller than unity. On the whole, these observations indicate that the collective state of excitons in the condensate is coherent. The coherence scales have not been measured as yet by a direct method (e.g., by measuring the intensity correlator); however, in all probability these scales are close to the sizes of domain traps.

ACKNOWLEDGMENTS

This study was supported financially by the Russian Foundation for Basic Research.

REFERENCES

1. Yu. E. Lozovik and V. I. Yudson, Zh. Éksp. Teor. Fiz. **71**, 738 (1976) [Sov. Phys. JETP **44**, 389 (1976)].
2. T. Fukuzawa, E. E. Mendez, and J. M. Hong, Phys. Rev. Lett. **64**, 3066 (1990).
3. J. E. Golub, E. E. Mendez, J. P. Harbison, and L. T. Flores, Phys. Rev. B **41**, 8564 (1990).
4. J. A. Kash, M. Zachau, E. E. Mendez, *et al.*, Phys. Rev. Lett. **66**, 2247 (1991).
5. L. V. Butov, A. Zrenner, G. A. Abstreiter, *et al.*, Phys. Rev. Lett. **73**, 304 (1994); L. V. Butov, in *Proceedings of the 23rd International Conference on the Physics of Semiconductors* (Berlin, 1996).
6. V. B. Timofeev, A. I. Filin, A. V. Larionov, *et al.*, Europhys. Lett. **41**, 535 (1998).
7. V. B. Timofeev, A. V. Larionov, A. S. Ioselevich, *et al.*, Pis'ma Zh. Éksp. Teor. Fiz. **67**, 580 (1998) [JETP Lett. **67**, 613 (1998)].
8. V. V. Krivolapchuk, E. S. Moskalenko, A. L. Zhmodikov, *et al.*, Solid State Commun. **111**, 49 (1999).
9. D. Yoshioka and A. H. MacDonald, J. Phys. Soc. Jpn. **59**, 4211 (1990).
10. X. M. Chen and J. J. Quinn, Phys. Rev. B **67**, 895 (1991).
11. Xuejun Zhu, P. B. Littlewood, M. S. Hybersen, and T. Rice, Phys. Rev. Lett. **74**, 1633 (1995).
12. J. Fernandes-Rossier and C. Tejedor, Phys. Rev. Lett. **78**, 4809 (1997).
13. Lerwen Liu, L. Swierkowski, and D. Nelson, Physica B (Amsterdam) **249–251**, 594 (1998).
14. Yu. E. Lozovik and O. L. Berman, Zh. Éksp. Teor. Fiz. **111**, 1879 (1997) [JETP **84**, 1027 (1997)].
15. A. V. Larionov, V. B. Timofeev, J. M. Hvam, and C. Soerensen, Zh. Éksp. Teor. Fiz. **117**, 1255 (2000) [JETP **90**, 1093 (2000)].
16. A. V. Larionov and V. B. Timofeev, Pis'ma Zh. Éksp. Teor. Fiz. **73**, 342 (2001) [JETP Lett. **73**, 301 (2001)].
17. S. A. Moskalenko, Fiz. Tverd. Tela (Leningrad) **4**, 276 (1962) [Sov. Phys. Solid State **4**, 199 (1962)]; I. M. Blatt, K. W. Boer, and W. Brandt, Phys. Rev. **126**, 1691 (1962); R. S. Casella, J. Appl. Phys. **34**, 1703 (1963).
18. P. C. Hoenberg, Phys. Rev. **158**, 383 (1967).
19. A. V. Larionov, V. B. Timofeev, P. A. Ni, *et al.*, Pis'ma Zh. Éksp. Teor. Fiz. **75**, 689 (2002) [JETP Lett. **75**, 570 (2002)].
20. A. A. Dremin, V. B. Timofeev, A. V. Larionov, *et al.*, Pis'ma Zh. Éksp. Teor. Fiz. **76**, 526 (2002) [JETP Lett. **76**, 450 (2002)].
21. D. Gammon, E. S. Snow, B. V. Shanabrook, *et al.*, Phys. Rev. Lett. **76**, 3005 (1996).

Translated by N. Wadhwa

Journal of Experimental and Theoretical Physics, Vol. 101, No. 4, 2005, pp. 699–707.
Translated from Zhurnal Éksperimental'noĭ i Teoreticheskoĭ Fiziki, Vol. 128, No. 4, 2005, pp. 811–821.

ELECTRONIC PROPERTIES OF SOLIDS

Anomalous Magnetoresistance of Two-Dimensional Systems in the Presence of Spin-Orbit Scattering

K. S. Romanov* and N. S. Averkiev

Ioffe Physicotechnical Institute, Russian Academy of Sciences, St. Petersburg, 194021 Russia
**e-mail: const@stella.ioffe.ru*

Received January 13, 2005

Abstract—A theory of weak localization in two-dimensional semiconductor structures and metal films is developed for spin relaxation by the Elliott–Yafet mechanism. The theory is valid in the entire range of classically weak magnetic fields. It is shown that effects due to spin-orbit interaction substantially modify magnetoresistance in both diffusive and ballistic regimes. *© 2005 Pleiades Publishing, Inc.*

1. INTRODUCTION

Weak localization is caused by interference of two electron waves that are scattered by various impurity configurations and propagate in opposite directions along the same closed trajectory [1]. The most pronounced weak localization is observed when phase coherence is destroyed in classically weak magnetic fields. Moreover, dephasing may be caused by spin relaxation, phase relaxation, intersubband transitions, and other factors. The corresponding carrier relaxation times can be determined experimentally.

In the absence of magnetic field, when the dephasing time is much longer than the momentum relaxation time, the negative contribution to conductivity is due to all possible closed trajectories. In nonzero magnetic field, interference is effectively destroyed in the diffusive regime when magnetic length is much larger than mean free path and electron motion along a closed trajectory involves many scattering events. Since dephasing may also be due to spin relaxation, correct description of weak localization in real structures requires characterization of effects due to spin relaxation. To date, the role played by these effects has been well studied for all mechanisms of spin relaxation in semiconductors and metals.

As magnetic length becomes comparable to the mean free path with increasing magnetic field strength, interference tends to break down even for trajectories with relatively few scatterers, and the corresponding carrier motion cannot be treated in diffusion approximation. In a number of studies, spin relaxation effects in the ballistic (nondiffusive) regime were described in phenomenological models without taking into account microscopic mechanisms [2, 3]. The key mechanisms responsible for spin relaxation in semiconductors and metals are the Elliott–Yafet and Dyakonov–Perel mechanisms. The former is associated with spin-flip transitions due to electron scattering by impurities and phonons. The latter is observed only in crystals without inversion symmetry and is associated with odd terms in the Hamiltonian that determines the spectrum of electrons or holes in a semiconductor. The analysis of spin relaxation dominated by the Dyakonov–Perel mechanism presented in [4] exposed the contribution of spin-orbit interaction to the quantum correction to conductivity. The experimental studies presented in [5–7] were focused on anomalous magnetoresistance in classically weak magnetic fields, when magnetic length is comparable to mean free path and spin relaxation is due to elastic scattering by impurities. It was shown in those studies that spin-flip scattering plays a dominant role in InSb-based structures at low temperatures (see also [8]). However, its contribution to magnetoresistance in the ballistic regime has never been analyzed theoretically.

When spin-orbit interaction is weak, the contribution of the Elliott–Yafet spin relaxation mechanism to dephasing must decrease with trajectory length or concentration of scatterers. Accordingly, the effects due to the Elliott–Yafet spin relaxation mechanism are weaker in the ballistic regime of weak localization as compared to the diffusive regime. However, it was found that the contribution of spin relaxation is significant even beyond the scope of diffusion approximation [9].

In this paper, we develop a theory of weak localization in two-dimensional semiconductor-based structures and metal films. The theory is valid in the entire range of classically weak magnetic fields when the Elliott–Yafet mechanism plays a dominant role in spin relaxation.

2. WEAK LOCALIZATION IN ZERO MAGNETIC FIELD

We consider the effect of weak localization on the static conductivity of a two-dimensional system in both zero and nonzero transverse magnetic fields. We assume that the characteristics of the electron gas are

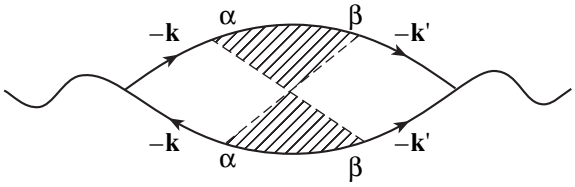

Fig. 1. Diagram representing the dominant contribution to anomalous conductivity $\Delta\sigma_a$ in the diffusive regime. The Cooperon is represented by the hatched area. Greek letters denote spin indices.

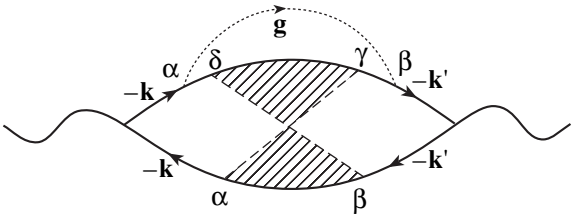

Fig. 2. Diagram representing the weak-localization correction to conductivity in the ballistic regime: **g** is the transferred momentum in correlator (5); **k** and **k'** are the momenta in the propagators meeting at the diagram's vertices.

such that the system behaves as a good conductor: $\varepsilon_F\tau_0 \gg 1$ (ε_F is the Fermi energy, τ_0 is the quantum relaxation time), both phase relaxation time τ_ϕ and spin relaxation time τ_s are much larger than τ_0, and scattering is due to short-range interaction.

Our calculations are performed by using a zero-temperature diagrammatic technique. In this approach, the "normal" (Drude) conductivity corresponds to the sum of loop diagrams with nonintersecting internal lines. It was shown in [10] that only impurity-averaged diagrams of the two types illustrated by Figs. 1 and 2 substantially contribute to anomalous conductivity. The inner part of these diagrams is called the Cooperon propagator. Accordingly, the conductivity is determined by calculating the Cooperon and using the result in summing the diagrams of both types.

To express the conductivity in terms of impurity-averaged Green functions, we must calculate the correlator of the matrix elements for electron scattering by impurities. In [11], expressions for the matrix elements $V_{\alpha\beta}$ of an impurity quantum-well potential were obtained in the case when only one size-quantized subband is occupied and carriers are described by the Kane model (the Fermi energy of two-dimensional electron gas is much smaller than the bandgap width). For a short-range potential, we have

$$V_{\alpha\beta}(\mathbf{k} \longrightarrow \mathbf{k}', \mathbf{a}) = \left\{\delta_{\alpha\beta}\left[\sin^2\frac{\pi a_z}{\lambda} + (A^2 + 2B^2)\times\left(\frac{\pi^2}{\lambda^2} + (\mathbf{k}\cdot\mathbf{k}')\sin^2\frac{\pi a_z}{\lambda}\right)\right]\right.$$
$$\left. + (2B + B^2)\frac{\pi}{2\lambda}[\boldsymbol{\sigma}_{\alpha\beta}\times(\mathbf{k}+\mathbf{k}')]_z\sin^2\frac{2\pi a_z}{\lambda}\right\} \quad (1)$$
$$\times\frac{2}{\lambda}V_0\exp[-i(\mathbf{k}-\mathbf{k}')\mathbf{a}_\rho],$$

where **k** and **k'** denote, respectively, the two-dimensional wavevectors of the incident and scattered particles in the quantum-well plane *xy*; *A* and *B* are Kane's coefficients (assumed to be small in the case of weak spin-orbit interaction); **a** is the three-dimensional position vector of the scattering impurity; V_0 is the intensity of a δ potential; and λ is the quantum-well width.

The expression for the required correlator obtained by averaging over impurity position vectors is [12]

$$W_{\alpha\beta\gamma\kappa}(\mathbf{k} \longrightarrow \mathbf{k}', \mathbf{q} \longrightarrow \mathbf{q}')$$
$$= W\{\delta_{\alpha\beta}\delta_{\gamma\kappa}[1 + c(\mathbf{k}\cdot\mathbf{k}' + \mathbf{q}\cdot\mathbf{q}')] \quad (2)$$
$$+ c_x[\boldsymbol{\sigma}_{\alpha\beta}\times(\mathbf{k}+\mathbf{k}')]_z[\boldsymbol{\sigma}_{\gamma\kappa}\times(\mathbf{q}+\mathbf{q}')]_z\}$$
$$\times\delta^2(\mathbf{k}' + \mathbf{q}' - \mathbf{k} - \mathbf{q}),$$

where

$$W = (2\pi)^2 n\left(\frac{2V_0}{\lambda}\right)^2\left\{\frac{3}{8}\lambda + \lambda^2(A^2 + 2B^2)\frac{\pi^2}{\lambda^2}\right.$$
$$\left. + \lambda\left[(A^2 + 2B^2)\frac{\pi^2}{\lambda^2}\right]^2\right\}^{-1},$$

$$c = A^2 + 2B^2, \quad c_x = \frac{\pi^2}{3\lambda^2}(2AB + B^2)^2,$$

k, **q** and **k'**, **q'** correspond to initial and final momenta, respectively; *n* is the two-dimensional carrier concentration. When spin-orbit interaction is weak, both ck_F^2 and $c_xk_F^2$ are small (k_F is the Fermi momentum). Accordingly, further calculations are performed up to first-order terms in ck_F^2 and $c_xk_F^2$. It is clear from the expression for the correlator that the constants c_x and c correspond to scattering with and without spin flip, respectively.

In the diffusion approximation [1, 12], the calculation of the term proportional to c in the expression for the correlator reduces to the replacement of τ_0 with transport time. Since the contribution corresponding to c can also be taken into account by replacing τ_0 with transport time when the ballistic regime is considered

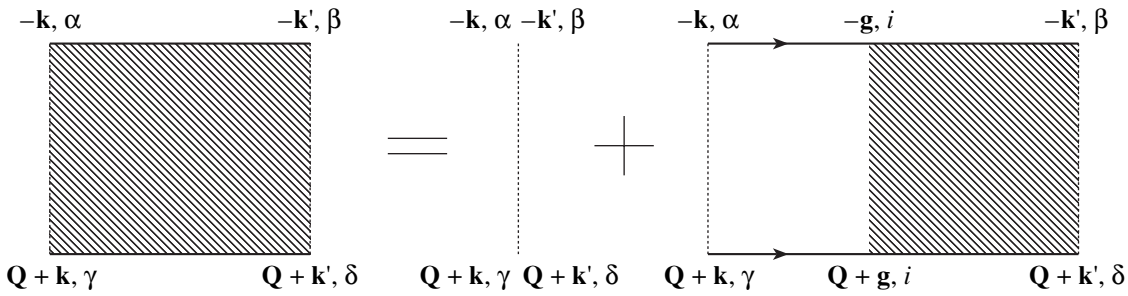

Fig. 3. Cooperon equation in momentum representation.

for small $c_x k_F^2$ and $c k_F^2$, the constant c is omitted here to simplify calculations.

The Dyson equation for the impurity-averaged Green function $G_{\alpha\beta}(p, \omega)$ is

$$\begin{aligned} G_{\alpha\beta}(p,\omega) &= G^0_{\alpha\beta}(p,\omega) \\ &+ \int G^0_{\alpha\gamma}(p,\omega) G_{\kappa\eta}(q,\omega) G_{\xi\beta}(p,\omega) \\ &\times \frac{W}{(2\pi)^4}\{\delta_{\gamma\kappa}\delta_{\eta\xi}(1 + 2c\mathbf{p}\cdot\mathbf{q}) \\ &+ c_x[\boldsymbol{\sigma}_{\gamma\kappa}\times(\mathbf{p}+\mathbf{q})]_z[\boldsymbol{\sigma}_{\eta\xi}\times(\mathbf{p}+\mathbf{q})]_z\} d\mathbf{q}, \end{aligned} \tag{3}$$

where $G^0_{\alpha\beta}(p, \omega)$ is the single-particle Green function in the absence of impurities (summation over repeated spin indices is performed).

Since the correlator is symmetric with respect to spin indices, it can be shown that the solution to Eq. (3) in the Born approximation is proportional to the identity matrix:

$$\begin{aligned} G_{\alpha\beta}(\mathbf{p},\omega) &= G(p,\omega)\delta_{\alpha\beta}, \\ G(p,\omega) &= \left[\omega - \xi(p) + \frac{i\,\mathrm{sgn}(\omega)}{2\tau}\right]^{-1}. \end{aligned} \tag{4}$$

The total dephasing time τ contained in (4) is determined by parameters of the correlator:

$$\frac{1}{\tau} = \frac{1}{\tau_0} + \frac{1}{\tau_s},$$

where $\tau_0 = (2\pi)^2/mW$ is the momentum relaxation time and $\tau_s = \tau_0/2c_x p_F^2$ is the relaxation time for the z-projection of spin in the Elliott–Yafet mechanism (m is the particle mass).

Henceforth, we denote the contributions to anomalous conductivity represented by the diagrams in Figs. 1 and 2 by $\Delta\sigma_a$ and by $\Delta\sigma_b$, respectively. It can be shown that all diagrams similar in order to these, but having different form, cancel out when the spin-orbit effects are described by correlator (2), as they do in the absence of spin-orbit interaction according to [10].

The corresponding expressions are

$$\begin{aligned} \Delta\sigma_a &= \frac{e^2\hbar}{2\pi m^2}\int (\mathbf{k}\cdot\mathbf{k}') G^A(\mathbf{k}) G^R(\mathbf{k}) G^A(\mathbf{k}') \\ &\times G^R(\mathbf{k}')\Gamma_{\alpha\beta\beta\alpha}(-\mathbf{k}, -\mathbf{k}', \mathbf{k}+\mathbf{k}') d\mathbf{k} d\mathbf{k}', \\ \Delta\sigma_b &= \frac{e^2\hbar}{2\pi m^2}\int (\mathbf{k}\cdot\mathbf{k}') G^A(\mathbf{k}) G^R(\mathbf{k}) G^A(\mathbf{k}') \\ &\times G^R(\mathbf{k}') G^A(\mathbf{k}-\mathbf{g}) G^A(\mathbf{k}'-\mathbf{g}) \\ &\times W_{\alpha\iota\sigma\beta}(\mathbf{k} \longrightarrow \mathbf{k}-\mathbf{g}, \mathbf{k}'-\mathbf{g} \longrightarrow \mathbf{k}') \\ &\times \Gamma_{\iota\sigma\beta\alpha}(\mathbf{k}-\mathbf{g}, \mathbf{k}'-\mathbf{g}, \mathbf{k}+\mathbf{k}'-\mathbf{g}) d\mathbf{k} d\mathbf{k}' d\mathbf{g}, \end{aligned} \tag{5}$$

where $G^A(p) \equiv G(p, \omega = -0)$ and $G^R(p) \equiv G(p, \omega = +0)$ denote advanced and retarded Green functions, respectively, and $\Gamma_{\alpha\beta\gamma\kappa}(\mathbf{k}, \mathbf{k}', \mathbf{Q})$ represents the Cooperon. Since photon momenta are assumed to be small, the contributions of vertices reduce to products of $\mathbf{k}$ with $\mathbf{k}'$.

The diagram shown in Fig. 3 represents the Cooperon equation

$$\begin{aligned} &\Gamma_{\alpha\beta\gamma\kappa}(\mathbf{k}, \mathbf{k}', \mathbf{Q}) \\ &= W_{\alpha\beta\gamma\kappa}(-\mathbf{k} \longrightarrow \mathbf{Q}+\mathbf{k}, -\mathbf{k}' \longrightarrow \mathbf{Q}+\mathbf{k}') \\ &+ \int W_{\alpha\iota\gamma\sigma}(\mathbf{k} \longrightarrow \mathbf{Q}+\mathbf{k}, \mathbf{g} \longrightarrow \mathbf{Q}+\mathbf{g}) \\ &\times G^A(-\mathbf{g}) G^R(\mathbf{Q}+\mathbf{g}) \Gamma_{\iota\beta\sigma\kappa}(\mathbf{g}, \mathbf{k}', \mathbf{Q}) d\mathbf{g}. \end{aligned} \tag{6}$$

Since Eq. (6) contains the product $G^A(-\mathbf{g})G^R(\mathbf{Q} + \mathbf{g})$, the dominant contribution to the integral corresponds to the neighborhood of the Fermi surface. Since the loop diagrams in Figs. 1 and 2 contain propagators meeting at the vertices, the dominant contribution to conductivity corresponds to momenta $\mathbf{k}$ and $\mathbf{k}'$ of the Cooperon $\Gamma_{\alpha\beta\gamma\kappa}(\mathbf{k}, \mathbf{k}', \mathbf{Q})$ lying on the Fermi surface and $|\mathbf{Q}|$ is small as compared to the Fermi momentum k_F. There-

fore, Eq. (6) can be solved by assuming that $|\mathbf{k}| \approx |\mathbf{k}'| \approx |\mathbf{g}| \approx k_F$ and dropping $\mathbf{Q}$ in the arguments of the correlator.

Equation (6) is equivalent to 16 independent scalar equations. Their number is reduced by using the relation

$$[W_{\alpha\beta\gamma\kappa}(\mathbf{k} \longrightarrow \mathbf{q}', \mathbf{k}' \longrightarrow \mathbf{q}')]^* = W_{\bar{\alpha}\bar{\beta}\bar{\gamma}\bar{\kappa}}(\mathbf{k} \longrightarrow \mathbf{q}, \mathbf{k}' \longrightarrow \mathbf{q}'),$$

where $\bar{\alpha}$ and α correspond to opposite spin orientations. Since

$$[G^A(-\mathbf{g})G^R(\mathbf{Q}+\mathbf{g})]^* \approx G^A(-\mathbf{g})G^R(\mathbf{g}-\mathbf{Q}),$$

the complex conjugate of Eq. (6) has a similar form with $\Gamma_{\alpha\beta\gamma\kappa}(\mathbf{k}, \mathbf{k}', \mathbf{Q})$ replaced by $\Gamma_{\bar{\alpha}\bar{\beta}\bar{\gamma}\bar{\kappa}}(\mathbf{k}, \mathbf{k}', \mathbf{Q})^*$. Therefore,

$$\Gamma_{\alpha\beta\gamma\kappa}(\mathbf{k}, \mathbf{k}', -\mathbf{Q})^* = \Gamma_{\bar{\alpha}\bar{\beta}\bar{\gamma}\bar{\kappa}}(\mathbf{k}, \mathbf{k}', \mathbf{Q}). \quad (7)$$

Conductivity can be evaluated without calculating all components of $\hat{\Gamma}$. Since the vertices of the diagram shown in Fig. 1 are not associated with spin-flip transitions, the diagram contains only the Cooperon components having the form $\Gamma_{\alpha\beta\beta\alpha}$. The expression for the correlator can be used to show that the following components are also required to calculate the diagram shown in Fig. 2:

$$\Gamma_{-+-+}, \Gamma_{+-+-}, \Gamma_{++--}, \Gamma_{--++}.$$

Thus, in view of relation (7), only four components are required to calculate conductivity:

$$\Gamma_{++++}, \Gamma_{-++-}, \Gamma_{--++}, \Gamma_{+-+-}.$$

To solve Eq. (6), we introduce the angle coordinates ϕ, ϕ', and ψ corresponding to the vectors $\mathbf{k}$, $\mathbf{k}'$, and $\mathbf{Q}$, respectively. The integral of Eq. (6) over the magnitude of $\mathbf{g}$ yields equations for the Cooperon components enumerated above:

$$\Gamma_{++++}(\phi, \phi', \psi, Q) = W + \frac{\tau}{2\pi\tau_0}\int_0^{2\pi}\frac{1}{1 - i(Qk_F\tau/m)\cos\theta} \times \Gamma_{++++}(\psi+\theta, \phi', \psi, Q)d\theta + \frac{\tau}{4\pi\tau_s}\int_0^{2\pi}\frac{[\exp(-i\phi) + \exp(-i(\theta+\psi))]^2}{1 - i(Qk_F\tau/m)\cos\theta} \times \Gamma_{-+-+}(\psi+\theta, \phi', \psi, Q)d\theta,$$

$$\Gamma_{-+-+}(\phi, \phi', \psi, Q) = Wc_x k_F^2[\exp(i\phi) + \exp(i\phi')]^2 + \frac{\tau}{2\pi\tau_0}\int_0^{2\pi}\frac{1}{1 - i(Qk_F\tau/m)\cos\theta}\Gamma_{-+-+}(\psi+\theta, \phi', \psi, Q)d\theta + \frac{\tau}{4\pi\tau_s}\int_0^{2\pi}\frac{[\exp(i\phi) + \exp(i(\theta+\psi))]^2}{1 - i(Qk_F\tau/m)\cos\theta} \times \Gamma_{++++}(\psi+\theta, \phi', \psi, Q)d\theta, \quad (8)$$

$$\Gamma_{++--}(\phi, \phi', \psi, Q) = W + \frac{\tau}{2\pi\tau_0}\int_0^{2\pi}\frac{1}{1 - i(Qk_F\tau/m)\cos\theta} \times \Gamma_{++--}(\psi+\theta, \phi', \psi, Q)d\theta - \frac{\tau}{4\pi\tau_s}\int_0^{2\pi}\frac{2 + 2\cos(\phi - \psi - \theta)}{1 - i(Qk_F\tau/m)\cos\theta}\Gamma_{-++-}(\psi+\theta, \phi', \psi, Q)d\theta, \quad (9)$$

$$\Gamma_{-++-}(\phi, \phi', \psi, Q) = -2Wc_x k_F^2[1 + \cos(\phi - \phi')] + \frac{\tau}{2\pi\tau_0}\int_0^{2\pi}\frac{1}{1 - i(Qk_F\tau/m)\cos\theta}\Gamma_{-++-}(\psi+\theta, \phi', \psi, Q)d\theta - \frac{\tau}{4\pi\tau_s}\int_0^{2\pi}\frac{2 + 2\cos(\phi - \psi - \theta)}{1 - i(Qk_F\tau/m)\cos\theta}\Gamma_{++--}(\psi+\theta, \phi', \psi, Q)d\theta.$$

Thus, we have independent systems (8) and (9) for Γ_{++++}, Γ_{-+-+} and Γ_{-++-}, Γ_{++--}, respectively, where θ is the angle between $\mathbf{g}$ and $\mathbf{Q}$.

In the absence of spin-orbit interaction ($c_x = 0$), the latter equations in systems (8) and (9) reduce to homogeneous equations, Γ_{-+-+} and Γ_{-++-} vanish, and the remaining equations for Γ_{++++} and Γ_{++--} determine the Cooperon propagator [10]. The present analysis is complicated by the dependence of the Cooperon propagator on ϕ, ϕ', and θ.

To solve systems (8) and (9), we represent the Cooperon as an expansion in the harmonics of ϕ:

$$\Gamma_{\alpha\beta\gamma\kappa}(\phi, \phi', \mathbf{Q}) = \sum_n \exp(in\phi)\Gamma^n_{\alpha\beta\gamma\kappa}(\phi', \mathbf{Q}), \quad (10)$$

where n is the harmonic number.

It is clear from the right-hand sides in (8) that only the harmonics $\exp(-2i\phi)$, $\exp(-i\phi)$, and 1 are contained in $\Gamma_{++++}(\phi, \phi', \psi, Q)$, while only $\exp(2i\phi)$, $\exp(i\phi)$, and 1 are contained in Γ_{-+-+}. Thus, the series in (10) are finite sums, and (8) and (9) reduce to exactly solvable systems of eight linear algebraic equations. Moreover, since expressions (1) and (2) are valid only to the lowest order in spin-orbit coupling, systems (8) and (9) can be solved in the first approximation with respect to τ/τ_s and τ/τ_ϕ.

It follows from Eq. (8) that Γ_{-+-+} is on the order of $(\tau/\tau_s)\Gamma_{++++}$. Therefore, Γ_{++++} can be found by dropping the term containing Γ_{-+-+} in the former equation in (8).

Analogously, the term containing Γ_{-++-} is dropped in the former equation in (9), and the resulting equation for Γ_{++--} is similar to the simplified former equation for Γ_{++++} in (8). This equation is independent of angles; i.e., it is analogous to the Cooperon equation for the ballistic regime in the absence of spin-orbit interaction. The final solution is

$$\Gamma_{++++}(\mathbf{k}, \mathbf{k}', \mathbf{Q}) = \Gamma_{++--}(\mathbf{k}, \mathbf{k}', \mathbf{Q}) = \frac{W}{1 - Z_0\tau/\tau_0},$$

where the functions Z_n depend on $|\mathbf{Q}|$:

$$Z_n = \frac{1}{2\pi}\int_0^{2\pi} \frac{\cos^n\theta}{1 + \tau/\tau_\phi - (iQk_F\tau/m)\cos\theta} d\theta.$$

To find Γ_{-++-}, we substitute the expression for Γ_{++--} into the latter equation in (9) and use expansion (10). As a result, we obtain a rank 3 system of linear equations for harmonic coefficients.

The final expression for Γ_{-++-} calculated up to terms of order τ/τ_s is

$$\begin{aligned}\Gamma_{-++-}(\mathbf{k}, \mathbf{k}', \mathbf{Q}) = \frac{W}{2}\Bigg\{ &\frac{1}{1 - Z_0\tau/\tau_0 + Z_0\tau/\tau_s} \\ &\times\Bigg[1 - \frac{2Z_1^2\tau/\tau_s}{1 - Z_0\tau/\tau_0 + Z_0\tau/\tau_s} \\ &- \frac{\tau}{\tau_s} - 2\frac{(\mathbf{k} + \mathbf{k}')\cdot\mathbf{e}}{k_F} Z_1 \frac{\tau}{2\tau_s}\Bigg] \\ &- \frac{1}{1 - Z_0\tau/\tau_0 - Z_0\tau/\tau_s} \\ &\times\Bigg[1 + \frac{2Z_1^2\tau/\tau_s}{1 - Z_0\tau/\tau_0 - Z_0\tau/\tau_s} + \frac{\tau}{\tau_s} \\ &+ 2\frac{(\mathbf{k} + \mathbf{k}')\cdot\mathbf{e}}{k_F} Z_1 \frac{\tau}{2\tau_s}\Bigg] + 2\frac{\tau}{\tau_s}\Bigg\},\end{aligned} \tag{11}$$

where $\mathbf{e}$ is the unit vector parallel to $\mathbf{Q}$. Since $Z_0 \sim 1$ and $Z_1(Q) \sim Q$ in the diffusive regime, the terms in (11) that contain Z_1 can be neglected and an expression similar to that found in [13] is obtained.

The remaining component Γ_{-+-+} can be neglected, because it is on the order of $(\tau/\tau_s)\Gamma_{++++}$ and its contribution to (2) is multiplied by τ/τ_s.

When the magnitude of $\mathbf{Q}$ is small, the expressions for Γ_{++++} and Γ_{-++-} reduce to those found in [13]. When it is large, we obtain

$$\begin{aligned}\Gamma_{++++}(\mathbf{k}, \mathbf{k}', \mathbf{Q}) &= W\Bigg[1 + \frac{1}{\sqrt{D\tau}Q}\left(1 - \frac{\tau}{\tau_s}\right)\Bigg], \\ \Gamma_{-++-}(\mathbf{k}, \mathbf{k}', \mathbf{Q}) &= -2\frac{W}{\sqrt{D\tau}Q}\frac{\tau}{\tau_s}.\end{aligned} \tag{12}$$

The final expression for the anomalous contribution calculated by taking into account the contributions of spin-orbit interaction to the vertices of the diagrams in Figs. 1 and 2 is the sum of $\Delta\sigma_a$ and $\Delta\sigma_b$:

$$\begin{aligned}\Delta\sigma = -\frac{e^2}{2\pi^2\hbar}\Bigg\{ &\ln\left(\frac{1 + \tau_\phi/\tau}{1 + \tau_\phi/\tau_s}\right)\left[1 + \frac{\tau}{2\tau_\phi} + \frac{11}{2}\frac{\tau}{\tau_s}\right] \\ &- \frac{1}{2}\ln\left(1 + \frac{2\tau_\phi}{\tau_s}\right) - \ln 2\Bigg\}.\end{aligned} \tag{13}$$

Since this result is obtained by performing calculations up to τ/τ_s. As $\tau_s \longrightarrow \infty$, it reduces to the expression for the conductivity of a two-dimensional structure obtained in [10] without using the diffusion approximation up to a factor of order τ/τ_ϕ.

In the limit of $\tau/\tau_\phi \gg 1$, expression (13) yields the result obtained in [13] with

$$1/\tau_s^x = 1/\tau_s^z = 1/\tau_{so}^z = 0,$$
$$\tau/\tau_{so}^x = c_x k_F^2 = \tau/2\tau_s.$$

3. MAGNETORESISTANCE

The impurity-averaged Green function corresponding to classically weak magnetic fields can be represented as follows [14]:

$$\begin{aligned}G_H^{R,A}(\mathbf{r}, \mathbf{r}') &= \exp\left[\frac{i}{2l_B^2}(x - x')(y + y')\right] G^{R,A}(\mathbf{r}, \mathbf{r}') \\ &= \exp[i\Phi(\mathbf{r}, \mathbf{r}')] G^{R,A}(\mathbf{r} - \mathbf{r}'),\end{aligned} \tag{14}$$

where $G^{R,A}(\mathbf{r})$ is the impurity-averaged Green function for zero magnetic field. The phase factor is expressed as

$$\Phi(\mathbf{r}, \mathbf{r}') = \frac{(x - x')(y + y')}{2l_B^2},$$

where $l_B = \sqrt{mc/eH}$ is magnetic length. It is assumed here that $\mathbf{H}$ is parallel to the z axis and $\mathbf{A} = \mathbf{e}_y H_z x$.

The change from momentum to coordinate representation is performed by replacing $\mathbf{k}$ with the corresponding gradients. As a result, we have to deal with a

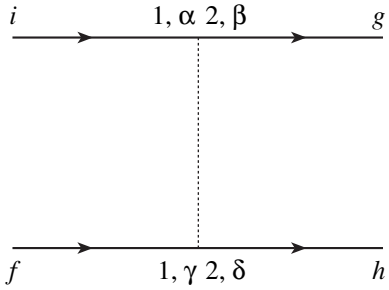

Fig. 4. The simplest diagram representing the correlator in coordinate representation.

much more complicated problem as compared to the case when spin-orbit interaction is absent and the correlator is a function of coordinates only. However, since the angle dependence of the correlator is insignificant in the diffusion approximation (see above), the Cooperon can be calculated by using the correlator averaged over the angles associated with its arguments. The averaged correlator matrix is independent of momenta, and its coordinate representation is a function, not an operator.

Accordingly, the correlator allowing for spin-orbit effects beyond the scope of the diffusion approximation is written in coordinate representation as an operator containing spatial derivatives. For this reason, we use the diagram shown in Fig. 4 instead of the correlator. The corresponding expression (obtained as the inverse Fourier transform of its momentum representation) has the form

$$D = \int \delta(\mathbf{r}_1 - \mathbf{r}_1')\delta(\mathbf{r}_2 - \mathbf{r}_2')\delta(\mathbf{r}_1 - \mathbf{r}_2)$$
$$\times W_0\{\delta_{\alpha\beta}\delta_{\gamma\delta}[1 + c(i\nabla_{\mathbf{r}_1}(-i)\nabla_{\mathbf{r}_2} + i\nabla_{\mathbf{r}_1'}(-i)\nabla_{\mathbf{r}_2'})]$$
$$+ c_x[\boldsymbol{\sigma}_{\alpha\beta}\times(i\nabla_{\mathbf{r}_1} - i\nabla_{\mathbf{r}_2})]_z[\boldsymbol{\sigma}_{\gamma\delta}\times(i\nabla_{\mathbf{r}_1'} - i\nabla_{\mathbf{r}_2'})]_z\} \quad (15)$$
$$\times G_H^{\mathrm{A}}(\mathbf{r}_i, \mathbf{r}_1)G_H^{\mathrm{A}}(\mathbf{r}_2, \mathbf{r}_g)G_H^{\mathrm{R}}(\mathbf{r}_2', \mathbf{r}_h)$$
$$\times G_H^{\mathrm{R}}(\mathbf{r}_f, \mathbf{r}_1')d\mathbf{r}_1 d\mathbf{r}_1' d\mathbf{r}_2 d\mathbf{r}_2'.$$

Since k_{F} is much larger than $1/l_B$ in classically weak magnetic fields, the gradients of Green functions (14) can be calculated by treating the phase $\Phi(\mathbf{r}, \mathbf{r}')$ as independent of the coordinates. Then,

$$\nabla_{\mathbf{r}_1} G_H^{\mathrm{R,A}}(\mathbf{r}_1, \mathbf{r}_2)$$
$$= \nabla_{\mathbf{r}_1}[\exp(i\Phi(\mathbf{r}_1, \mathbf{r}_2))G^{\mathrm{R,A}}(\mathbf{r}_1 - \mathbf{r}_2)]$$
$$\approx \exp[i\Phi(\mathbf{r}_1, \mathbf{r}_2)\nabla_{\mathbf{r}_1} G^{\mathrm{R,A}}(\mathbf{r}_1 - \mathbf{r}_2)] \quad (16)$$
$$= \pm ik_{\mathrm{F}}\mathbf{e}_{12}G_H^{\mathrm{R,A}}(\mathbf{r}_1, \mathbf{r}_2),$$
$$\nabla_{\mathbf{r}_2} G_H^{\mathrm{R,A}}(\mathbf{r}_1, \mathbf{r}_2) \approx \pm ik_{\mathrm{F}}\mathbf{e}_{21}G_H^{\mathrm{R,A}}(\mathbf{r}_1, \mathbf{r}_2),$$

where $\mathbf{e}_{ij} \equiv (\mathbf{r}_i - \mathbf{r}_j)/|\mathbf{r}_i - \mathbf{r}_j|$.

As a result, the diagram in Fig. 4 is expressed as

$$D = \int \delta(\mathbf{r}_1 - \mathbf{r}_2)$$
$$\times W_0\{\delta_{\alpha\beta}\delta_{\gamma\delta}(1 - ck_{\mathrm{F}}^2[\mathbf{e}_{i1}\mathbf{e}_{g1} + \mathbf{e}_{f1}\mathbf{e}_{h1}])$$
$$- c_x k_{\mathrm{F}}^2[\boldsymbol{\sigma}_{\alpha\beta}\times(\mathbf{e}_{i1} - \mathbf{e}_{g1})]_z[\boldsymbol{\sigma}_{\gamma\delta}\times(\mathbf{e}_{f1} - \mathbf{e}_{h1})]_z\} \quad (17)$$
$$\times G_H^{\mathrm{A}}(\mathbf{r}_i, \mathbf{r}_1)G_H^{\mathrm{A}}(\mathbf{r}_2, \mathbf{r}_g)G_H^{\mathrm{R}}(\mathbf{r}_2', \mathbf{r}_h)$$
$$\times G_H^{\mathrm{R}}(\mathbf{r}_f, \mathbf{r}_1')d\mathbf{r}_1 d\mathbf{r}_2.$$

It is clear now that the coordinate representation of the correlator depends on the directions from points 1 and 2 to points *i*, *f*, *g*, and *h* and does not contain any derivatives.

The coordinate representation corresponding to the momentum representation in Fig. 3 must contain tadpole diagrams, since the differentiation operators in both correlator and Cooperon must be replaced with unit vectors of the directions (see Fig. 5). After replacing the differentiation operators in the Cooperon with unit vectors, we can remove these propagators. The

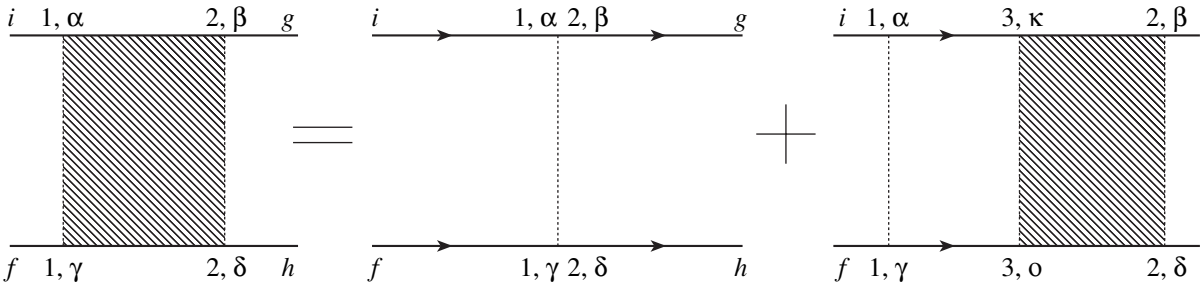

Fig. 5. Coordinate representation of the Cooperon equation in the presence of spin-orbit interaction.

resulting equation for Γ is

$$\begin{aligned}
&\Gamma^{ifgh}_{\alpha\beta\gamma\delta}(\mathbf{r}_1, \mathbf{r}_2)\\
&= W_0\{\delta_{\alpha\beta}\delta_{\gamma\delta} - c_x k_F^2[\boldsymbol{\sigma}_{\alpha\beta}\times(\mathbf{e}_{i1}+\mathbf{e}_{2g})]_z\\
&\times[\boldsymbol{\sigma}_{\gamma\delta}\times(\mathbf{e}_{f1}+\mathbf{e}_{2h})]_z\}\delta(\mathbf{r}_1-\mathbf{r}_2)\\
&+\int W_0\{\delta_{\alpha\kappa}\delta_{\gamma o} - c_x k_F^2[\boldsymbol{\sigma}_{\alpha\kappa}\times(\mathbf{e}_{i1}+\mathbf{e}_{13})]_z\\
&\times[\boldsymbol{\sigma}_{\gamma o}\times(\mathbf{e}_{f1}+\mathbf{e}_{13})]_z\}\\
&\times G_H^{\mathrm{A}}(\mathbf{r}_3, \mathbf{r}_1)G_H^{\mathrm{R}}(\mathbf{r}_3, \mathbf{r}_1)\Gamma^{33gh}_{\kappa\beta o\delta}(\mathbf{r}_3, \mathbf{r}_2)d\mathbf{r}_3,
\end{aligned} \tag{18}$$

where $\Gamma^{ifgh}_{\alpha\beta\gamma\delta}(\mathbf{r}_1, \mathbf{r}_2)$ corresponds to the extreme left diagram in Fig. 5 (Cooperon) with tadpoles removed from points *i*, *f*, *g*, and *h*; $\Gamma^{33gh}_{\kappa\beta o\delta}(\mathbf{r}_3, \mathbf{r}_2)$ is its analog corresponding to the extreme right diagram in Fig. 5. Here, the superscripts correspond to the legs of the removed propagators, and the subscripts are spin indices. Thus, the Cooperon $\Gamma^{ifgh}_{\alpha\beta\gamma\delta}(\mathbf{r}_1, \mathbf{r}_2)$ is a coordinate representation analogous to the Cooperon $\Gamma_{\alpha\beta\gamma\delta}(\mathbf{k}, \mathbf{k}')$ in the momentum representation, and Eq. (18) is similar to Eq. (6).

It is obvious that the solution $\Gamma^{ifgh}_{\alpha\beta\gamma\delta}(\mathbf{r}_1, \mathbf{r}_2)$ to Eq. (18) must depend on the unit vectors $\mathbf{e}_{i1}$, $\mathbf{e}_{f1}$, $\mathbf{e}_{2g}$,, and $\mathbf{e}_{2h}$ rather than on the exact locations of points *i*, *f*, *g*, and *h*, respectively.

By analogy with the calculation of conductivity in momentum representation discussed above, both loop diagrams can be calculated by using only the Cooperon components with an even number of positive (or negative) spin indices:

$$\begin{gathered}
\Gamma^{ifgh}_{----}(\mathbf{r}_1, \mathbf{r}_2), \Gamma^{ifgh}_{++++}(\mathbf{r}_1, \mathbf{r}_2), \Gamma^{ifgh}_{-++-}(\mathbf{r}_1, \mathbf{r}_2),\\
\Gamma^{ifgh}_{+--+}(\mathbf{r}_1, \mathbf{r}_2), \Gamma^{ifgh}_{-+-+}(\mathbf{r}_1, \mathbf{r}_2), \Gamma^{ifgh}_{+-+-}(\mathbf{r}_1, \mathbf{r}_2),\\
\Gamma^{ifgh}_{++--}(\mathbf{r}_1, \mathbf{r}_2), \Gamma^{ifgh}_{--++}(\mathbf{r}_1, \mathbf{r}_2).
\end{gathered}$$

As in calculating the Cooperon in the momentum representation, its complex conjugate can be combined with the relation

$$[G_H^{\mathrm{A}}(\mathbf{r}_1, \mathbf{r}_2)G_H^{\mathrm{R}}(\mathbf{r}_1, \mathbf{r}_2)]^* = G_H^{\mathrm{A}}(\mathbf{r}_2, \mathbf{r}_1)G_H^{\mathrm{R}}(\mathbf{r}_2, \mathbf{r}_1),$$

to show that

$$[\Gamma^{ifgh}_{\bar\alpha\bar\beta\bar\gamma\bar\delta}(\mathbf{r}_1, \mathbf{r}_2)]^* = \Gamma^{ifgh}_{\alpha\beta\gamma\delta}(\mathbf{r}_2, \mathbf{r}_1).$$

Therefore, conductivity can be found by calculating only

$$\begin{gathered}
\Gamma^{ifgh}_{++++}(\mathbf{r}_1, \mathbf{r}_2), \Gamma^{ifgh}_{-++-}(\mathbf{r}_1, \mathbf{r}_2),\\
\Gamma^{ifgh}_{+-+-}(\mathbf{r}_1, \mathbf{r}_2), \Gamma^{ifgh}_{--++}(\mathbf{r}_1, \mathbf{r}_2).
\end{gathered}$$

Changing from the unit vectors $\mathbf{e}_{i1}$, $\mathbf{e}_{f1}$, $\mathbf{e}_{2g}$, $\mathbf{e}_{2h}$, and $\mathbf{e}_{13}$ to the corresponding angles ϕ, ϕ', ψ, ψ', and θ, we rewrite Eq. (18) as

$$\begin{aligned}
&\Gamma_{\alpha\beta\gamma\delta}(\mathbf{r}_1, \mathbf{r}_2, \phi, \phi', \psi, \psi')\\
&= W_{\alpha\beta\gamma\delta}(\mathbf{r}_1, \phi, \phi', \psi, \psi')\delta(\mathbf{r}_1-\mathbf{r}_2)\\
&+\int W_{\alpha o\kappa\delta}(\mathbf{r}_1, \phi, \phi', \theta, \theta)G_H^{\mathrm{A}}(\mathbf{r}_3, \mathbf{r}_1)G_H^{\mathrm{R}}(\mathbf{r}_3, \mathbf{r}_1)\\
&\times\Gamma_{\kappa\beta o\delta}(\mathbf{r}_3, \mathbf{r}_2, \theta, \theta, \psi, \psi')d\mathbf{r}_3,
\end{aligned} \tag{19}$$

where

$$\Gamma_{\alpha\beta\gamma\delta}(\mathbf{r}_1, \mathbf{r}_2, \phi, \phi', \psi, \psi') = \Gamma^{ifgh}_{\alpha\beta\gamma\delta}(\mathbf{r}_1, \mathbf{r}_2),$$

and $W_{\alpha\beta\gamma\delta}(\mathbf{r}_1, \phi, \phi', \psi, \psi')$ is expressed as

$$\begin{aligned}
&W_{\alpha\beta\gamma\delta}(\mathbf{r}_1, \phi, \phi', \psi, \psi') = W_0\{\delta_{\alpha\beta}\delta_{\gamma\delta}\\
&- c_x k_F^2[\sigma^x_{\alpha\beta}(\sin\phi+\sin\psi) - \sigma^y_{\alpha\beta}(\cos\phi+\cos\psi)]\\
&\times[\sigma^x_{\gamma\delta}(\sin\phi'+\sin\psi') - \sigma^y_{\gamma\delta}(\cos\phi'+\cos\psi')]\},
\end{aligned}$$

with σ^i denoting the *i*th Pauli matrix.

Equation (19) can be solved by the method applied to systems (8) and (9) if the solution is represented as the series expansion of the Cooperon in harmonics of the third and fourth arguments. However, we note that the arguments of $\Gamma_{\alpha\beta\gamma\delta}$ on its right-hand side span only the subspace $(\mathbf{r}_1, \mathbf{r}_2, \phi, \phi', \psi, \psi')$ of the space $(\mathbf{r}_1, \mathbf{r}_2, \phi, \phi' \equiv \phi, \psi, \psi')$. Therefore, we can calculate only $\Gamma_{\alpha\beta\gamma\delta}(\mathbf{r}_1, \mathbf{r}_2, \phi, \phi' \equiv \phi, \psi, \psi')$, which is much easier to do because we can use the expansion of the Cooperon in the harmonics of one argument only. Once $\Gamma_{\alpha\beta\gamma\delta}$ is found in the subspace of arguments, $\Gamma_{\alpha\beta\gamma\delta}$ is easily determined in the entire space by substituting the calculated $\Gamma_{\alpha\beta\gamma\delta}(\mathbf{r}_1, \mathbf{r}_2, \phi, \phi, \psi, \psi')$ into the right-hand side of Eq. (19). Accordingly, we begin with solving the equation for $\Gamma_{\alpha\beta\gamma\delta}(\mathbf{r}_1, \mathbf{r}_2, \phi, \phi', \psi, \psi')$.

By analogy with Eq. (6) for the Cooperon in the momentum representation, this equation is equivalent to several independent systems of rank 2 equations. Conductivity can be calculated by solving only two: the system for Γ_{++++} and Γ_{+-+-} and the system for Γ_{++--} and Γ_{-++-}.

Applying the method used to solve systems (8) and (9), we represent $\Gamma_{\alpha\beta\gamma\delta}(\mathbf{r}_1, \mathbf{r}_2, \phi, \phi, \psi, \psi')$ as a series expansion in the harmonics of ϕ. As in the momentum representation, the Cooperon contains a limited number of harmonics. As a result of this substitution, we obtain equations for individual harmonics whose kernels consist of terms of the form

$$\exp(i\theta)G_H^{\mathrm{A}}(\mathbf{r}_3, \mathbf{r}_1)G_H^{\mathrm{R}}(\mathbf{r}_3, \mathbf{r}_1)f(\psi, \psi'),$$

with different $f(\psi, \psi')$.

In the method for solving Eq. (19) in the case of $c_x = 0$ proposed in [14], both the kernel of the integral

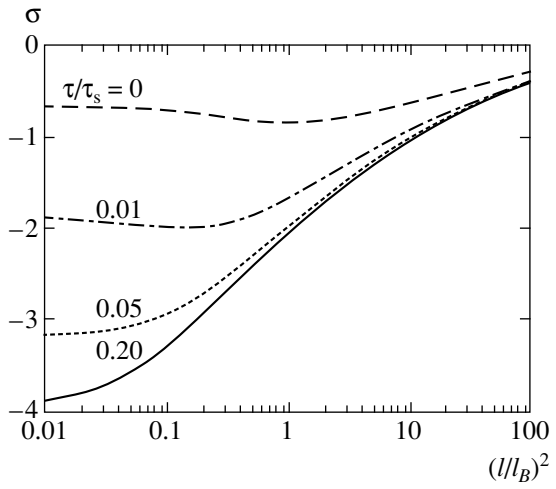

Fig. 6. Anomalous conductivity as a function of the normalized magnetic field strength $H/H_D = l^2/l_B^2$ (H_D is the magnetic field strength corresponding to magnetic length equal to l) for several values of τ/τ_s and $\tau/\tau_\phi = 0.02$.

Cooperon equation and its solution were represented as series expansions in products of wavefunctions of a particle with charge $2e$ moving in uniform magnetic field. Since angle dependence vanishes in the absence of spin-orbit interaction, the kernel of the integral equation for $\Gamma_{\alpha\beta\gamma\delta}(\mathbf{r}_1, \mathbf{r}_2, \phi, \phi, \psi, \psi')$ can be represented as

$$G_H^{\mathrm{A}}(\mathbf{r}_3, \mathbf{r}_1)G_H^{\mathrm{R}}(\mathbf{r}_3, \mathbf{r}_1) = \sum_{N,\chi} G^N \Psi_{N,\chi}(\mathbf{r}_3)\Psi^*_{N,\chi}(\mathbf{r}_1),$$

where G^N are coefficients and $\Psi_{N,\chi}(\mathbf{r})$ is the wavefunction of a particle with charge $-2|e|$ and electron mass m in magnetic field parallel to the z axis. Since the absolute term can also be represented as

$$W_0\delta_{\alpha\beta}\delta_{\gamma\delta}\delta(\mathbf{r}_1 - \mathbf{r}_2) = W_0\delta_{\alpha\beta}\delta_{\gamma\delta}\sum_{N,\chi}\Psi_{N,\chi}(\mathbf{r}_2)\Psi^*_{N,\chi}(\mathbf{r}_1),$$

the solution to the equation in the absence of spin-orbit coupling has a simple form in the basis of functions $\Psi_{M,\chi}(\mathbf{r}_2)\Psi^*_{N,\chi}(\mathbf{r}_1)$:

$$\Gamma_{\alpha\beta\gamma\delta}(\mathbf{r}_1, \mathbf{r}_2) = W_0\delta_{\alpha\beta}\delta_{\gamma\delta}\sum_{N,\chi}\frac{1}{1 - W_0 G^N}\Psi_{N,\chi}(\mathbf{r}_2)\Psi^*_{N,\chi}(\mathbf{r}_1).$$

However, the kernel of the equation for $\Gamma_{\alpha\beta\gamma\delta}(\mathbf{r}_1, \mathbf{r}_2, \phi, \phi', \psi, \psi')$ taking into account spin-orbit interaction contains harmonics of the angle coordinate θ of the vector $\mathbf{r}_1 - \mathbf{r}_3$. Accordingly, the expansion of the kernel in terms of $\Psi_{M,\chi}(\mathbf{r}_2)\Psi^*_{N,\chi}(\mathbf{r}_1)$ involves minor diagonals, because

$$\exp(i\theta)G_H^{\mathrm{A}}(\mathbf{r}_3, \mathbf{r}_1)G_H^{\mathrm{R}}(\mathbf{r}_3, \mathbf{r}_1) = \sum_{N,\chi}(-1)^{(|n|+n)/2}R^{|n|}_{N+(n+|n|)/2}\Psi_{N+n,\chi}(\mathbf{r}_2)\Psi^*_{N,\chi}(\mathbf{r}_1),$$

where

$$R_N^n = \frac{m^2}{k_{\mathrm{F}}\sqrt{N!/(N-n)!}} \times \int_0^\infty \exp\left(-\frac{r^2}{2l_B^2} - \frac{r}{l}\right)L^n_{N-n}\left(\frac{r^2}{l_B^2}\right)\left(\frac{r}{l_B}\right)^n dr.$$

Nevertheless, since the correlator contains only a finite number of harmonics of ϕ and ϕ', the ensuing systems of linear equations for the coefficients in the expansions of the Cooperon components Γ_{++++}, Γ_{+-+-}, Γ_{-++-}, and Γ_{++--} in terms of the first angle argument and $\Psi_{M,\chi}(\mathbf{r}_2)\Psi^*_{N,\chi}(\mathbf{r}_1)$,

$$\Gamma_{\alpha\beta\gamma\delta}(\mathbf{r}_1, \mathbf{r}_2, \phi, \phi, \psi, \psi') = \sum_{M,N,L,\chi}\Gamma_{\alpha\beta\gamma\delta}(M, N, L, \psi, \psi') \times \exp(iL\phi)\Psi_{M,\chi}(\mathbf{r}_2)\Psi^*_{N,\chi}(\mathbf{r}_1),$$

split into an infinite number of rank 6 systems, which can be solved by a standard method. In particular, the system of equations for Γ_{++++} and Γ_{+-+-} s splits into systems relating the components $\Gamma_{++++}(M, N, L, \psi, \psi')$ and $\Gamma_{+-+-}(M, N, L, \psi, \psi')$ with $L = -1$, 0, and 1. Analogous systems are obtained for Γ_{-++-} and Γ_{++--}.

The resulting $\Gamma_{\alpha\beta\gamma\delta}(\mathbf{r}_1, \mathbf{r}_2, \phi, \phi, \psi, \psi')$ is substituted into the right-hand side of Eq. (19) to find $\Gamma_{\alpha\beta\gamma\delta}(\mathbf{r}_1, \mathbf{r}_2, \phi, \phi, \psi, \psi')$. The corresponding components Γ^{ifgh}_{++++}, Γ^{ifgh}_{-++-}, Γ^{ifgh}_{+-+-}, and Γ^{ifgh}_{--++} can be found by using the analogous components $\Gamma_{\alpha\beta\gamma\delta}(\mathbf{r}_1, \mathbf{r}_2, \phi, \phi, \psi, \psi')$.

The resulting expressions in terms of R_N^n for the diagrams shown in Figs. 1 and 2 are simple series expansions, but their terms have a very complicated form. For this reason, we present here only the conductivity calculated by numerical summation of these series.

4. RESULTS AND DISCUSSION

Figure 6 shows the quantum correction to conductivity calculated as a function of magnetic field strength for $\tau/\tau_\phi = 0.02$ and several values of τ/τ_s. The figure demonstrates that spin-orbit interaction reduces the absolute value of the anomalous contribution to magne-

toresistance and plays a significant role in both weak and strong magnetic fields (when $l_B > l$ and $l_B < l$, respectively). When $\tau_s < \tau_\phi$, the correction to conductivity is a nonmonotonic function of magnetic field strength having a shallow minimum. When $\tau_s > \tau_\phi$, it is a monotonic function qualitatively similar to that obtained in the absence of spin-orbit interaction.

The model developed here can be used to determine behavior of the anomalous contribution to magnetoresistance both in weak and relatively strong magnetic fields (when diffusion approximation is inapplicable). Qualitative understanding of behavior in strong fields (when $l_B \ll l$) can be gained by calculating $\Delta\sigma_a$ and $\Delta\sigma_b$ as given by expressions (5) with integrals taken only over the regions where the third argument of the Cooperon exceeds $1/l_B$. The resulting asymptotic formulas can be used to evaluate the spin-orbit correction to conductivity in relatively strong fields:

$$\sigma_a, \sigma_b \propto \left(1 - \frac{3\tau}{\tau_s}\right)\frac{1}{l_B}. \quad (20)$$

We see that the leading-order weak-localization contribution to conductivity is on the order of $1/\sqrt{H}$, and the contribution due to spin-orbit interaction is on the order of $\tau/(\tau_s\sqrt{H})$, i.e., the latter effect is weaker as compared to that predicted for weak fields [13]. Thus, an increase in trajectory length and impurity concentration does reduce the effects due to the Elliott–Yafet spin relaxation mechanism. However, the results of accurate calculations presented in Fig. 6 demonstrate that the effect of spin-orbit interaction due to scattering by impurities is still significant in fields for which $l_B \approx l$ and must manifest itself in experiments.

CONCLUSIONS

We have analyzed weak localization in the entire range of classically weak magnetic fields for spin relaxation by the Elliott–Yafet mechanism. The anisotropic correlator used in the present analysis reflects the effects of both spin-orbit interaction and spin relaxation in two-dimensional structures. The theory developed here describes the variation of the contribution to anomalous magnetoresistance due to the Elliott–Yafet spin relaxation mechanism with increasing magnetic field strength.

The dependence of spin relaxation time on both Fermi momentum and band structure predicted by the proposed model can be used to determine the effect of the mean occupation on the quantum correction to magnetoresistance. Calculations of anomalous magnetoresistance demonstrate that spin-relaxation effects are significant in both strong and weak fields.

ACKNOWLEDGMENTS

This work was supported, in part, by INTAS, Russian Foundation for Basic Research, Ministry of Science and Education of the Russian Federation, and under programs sponsored by the Presidium and Division of Physical Sciences of the Russian Academy of Sciences. One of us (K.S.R.) gratefully acknowledges the support provided by the Dynasty Foundation.

REFERENCES

1. G. Bergmann, Phys. Rep. **107**, 1 (1984).
2. A. Kawabata, J. Phys. Soc. Jpn. **53**, 3540 (1984).
3. A. Zduniak, M. I. Dyakonov, and W. Knap, Phys. Rev. B **56**, 1996 (1997).
4. Y. Lyanda-Geller, Phys. Rev. Lett. **80**, 4273 (1998).
5. W. Knap, C. Skierbiszewski, A. Zduniak, *et al.*, Phys. Rev. B **53**, 3912 (1996).
6. A. M. Kreshchuk, S. V. Novikov, T. A. Polyanskaya, and I. G. Savel'ev, Fiz. Tekh. Poluprovodn. (St. Petersburg) **31**, 459 (1997) [Semiconductors **31**, 391 (1997)].
7. D. D. Bykanov, A. M. Kreshchuk, S. V. Novikov, *et al.*, Fiz. Tekh. Poluprovodn. (St. Petersburg) **32**, 1100 (1998) [Semiconductors **32**, 985 (1998)].
8. I. Zutic, J. Fabian, and S. Das Sarma, Rev. Mod. Phys. **76**, 323 (2004).
9. S. Pedersen, C. B. Sorensen, A. Kristensen, *et al.*, Phys. Rev. B **60**, 4880 (1999).
10. A. P. Dmitriev, V. Yu. Kachorovskii, and I. V. Gornyi, Phys. Rev. B **56**, 9910 (1997).
11. N. S. Averkiev, L. E. Golub, and M. Willander, J. Phys.: Condens. Matter **14**, 271 (2002).
12. A. A. Abrikosov, L. P. Gor'kov, and I. E. Dzyaloshinskiĭ, *Methods of Quantum Field Theory in Statistical Physics* (Fizmatgiz, Moscow, 1962; Prentice-Hall, Englewood Cliffs, N.J., 1963).
13. S. Hikami, A. I. Larkin, and Y. Nagaoka, Prog. Theor. Phys. **63**, 707 (1980).
14. A. Kawabata, J. Phys. Soc. Jpn. **49**, 628 (1980).

Translated by A. Betev

Journal of Experimental and Theoretical Physics, Vol. 101, No. 4, 2005, pp. 708–716.
Translated from Zhurnal Éksperimental'noĭ i Teoreticheskoĭ Fiziki, Vol. 128, No. 4, 2005, pp. 822–830.

ELECTRONIC PROPERTIES OF SOLIDS

Fano Resonances in the Impurity Photoexcitation Spectra of Semiconductors Doped with Shallow Donors

V. Ya. Aleshkin*, A. V. Antonov, L. V. Gavrilenko, and V. I. Gavrilenko

Institute of Physics of Microstructures, Russian Academy of Sciences, Nizhni Novgorod, 603950 Russia

**e-mail: aleshkin@ipm.sci-nnov.ru*

Received June 1, 2005

Abstract—A theory describing the photoexcited current peaks in the spectral region corresponding to the energies of longitudinal optical phonons in semiconductors doped with shallow donors is developed. The experimental data available for *n*-GaAs are in good agreement with the results obtained using the proposed theory.

I. INTRODUCTION

Let us consider the absorption of light by electrons in a semiconductor doped with shallow donors in the case of photon energies in the vicinity of the longitudinal optical (LO) phonon energy. The sample temperature will be assumed sufficiently low to provide that all impurity electrons are in the ground state of the donor centers. In this case, the light quantum can be absorbed in two ways (Fig. 1): first, with a direct electron transition from the donor ground state to the continuum, and second, with the transition into any intermediate state followed by LO phonon emission. It should be noted that the initial and final electron states in the second case are the same and are localized at the donor atoms. The total energy of the final state of the electron–phonon system is equal to the energy of the electron state in the continuum upon a transition of the first type. Therefore, the situation in the second case corresponds to the Fano resonance [1]. Indeed, an electron can absorb a light quantum and pass to a new state either in the continuum or in the discrete spectrum with the same energy. The interference of these transitions can lead to the appearance of asymmetric peaks in the optical absorption spectrum. In what follows, these absorption peaks will be referred to as Fano resonances. Spectral features, which were later called Fano resonances, had been originally observed in silicon doped with acceptors [2] and reported three years before the paper by Fano [1] was published.

The nature of Fano resonances was qualitatively explained in [3–5], but no quantitative theory was proposed at that time because approaches to the description of the states of shallow acceptors in silicon had not yet been developed. Later, Fano resonances in the absorption and photoexcited current (photocurrent) spectra were observed for deep donor centers in silicon [6], and more recently, these resonances were also reported for the photoconductive response in GaAs and InP doped with shallow donors [7]. However, to our knowledge, no quantitative theory of Fano resonances in semiconductors doped with shallow donors has been created until now. Moreover, the observed spectral features have been frequently described either in terms of formulas obtained by Fano [1], which refer to a particular case of the coinciding phases of matrix elements of the operator of transitions to the continuum and to a discrete level [5], or in terms of the approximate formulas obtained in [8] (see, e.g., [7]).

The aim of this study was to develop a quantitative theory of Fano resonances in the photocurrent spectrum of a semiconductor doped with shallow hydrogen-like donors. We have obtained a general expression for cal-

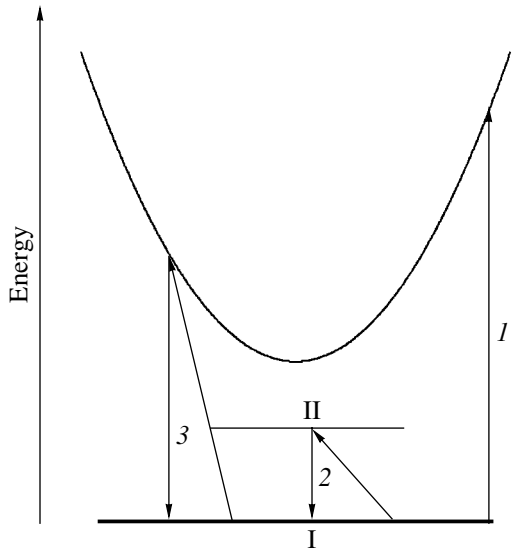

Fig. 1. Schematic diagram of the optical transitions for an electron occurring in the donor ground state I and absorbing a photon with the energy $\hbar\omega_0$: (*1*) a transition to the continuum; (*2*, *3*) transitions to the resonance state $|\varphi_q\rangle$ via intermediate states in the discrete spectrum and in the continuum, respectively (II is the excited state).

culating Fano resonances in the absorption and photocurrent spectra, which is applicable to semiconductors doped both with donors and with acceptors. According to the proposed theory, formulas presented in [1] and [8] do not provide adequate description in the general case of the phenomenon under consideration. This circumstance is related to the fact that the phase difference for the matrix elements of the electron transitions to the continuum and to a localized state is generally nonzero. The proposed theory is in good agreement with experimental data available for GaAs and (with somewhat less perfect coincidence) for InP.

2. CALCULATION OF THE PROBABILITY OF ABSORPTION OF A LIGHT QUANTUM

Let us consider the probability of electron transitions per unit time from the donor ground state to the $|\varphi_q\rangle$ state under the action of light (Fig. 1). In the $|\varphi_q\rangle$ state, the electron again occurs in the donor ground state, but an LO phonon with wavevector q also appears. Obviously, a description of this process must take into account the electron–photon and electron–phonon interactions to within the second order of perturbation theory. Accordingly, the transition from initial to final state can be subdivided into two stages (see, e.g., [9]). In the first stage, the electron absorbs a photon and passes to an intermediate state; in the second stage, the electron emits an optical phonon and passes to the donor ground state. Note that the law of energy conservation is obeyed for the entire process, but not for each stage separately.

The Hamiltonian of this system can be written as

$$H = H_0 + \bar{V}^{\rm ph} + \bar{V}^{\rm LO}, \qquad (1)$$

where the terms $\bar{V}^{\rm ph}$ and $\bar{V}^{\rm LO}$ describe the electron–photon and electron–phonon interactions, respectively;

$$H_0 = \frac{p^2}{2\mu} - \frac{e^2}{r\kappa_0} \qquad (2)$$

is the Hamiltonian of the electron moving in the field of a donor atom; p is the operator of electron quasimomentum; μ is the effective electron mass in the conduction band; r is the radius vector of the electron; κ_0 is the low-frequency permittivity of the semiconductor; and e is the electron charge.

In the dipole approximation, the operator of interaction between the electron and a circularly polarized electromagnetic wave propagating along the z axis can be written as

$$\bar{V}^{\rm ph} = \frac{eA(y-ix)}{\sqrt{2}}e^{-i\omega t} + \text{c.c.}, \qquad (3)$$

where A is the amplitude of the electric field vector in the wave. In expression (3), the first term describes the photon absorption and the second (complex conjugate) term describes the emission. Since we are interested only in the first process, the second term in expression (3) will be not taken into consideration.

The operator of the interaction between the electron and LO phonon has the following form [10]:

$$\bar{V}^{\rm LO} = e\sqrt{\frac{2\pi\hbar\omega_0}{V\bar{\kappa}}}\sum_q \frac{i}{q}\exp(-iqr + i\omega_0 t)b_q^\dagger + \text{h.c.}, \qquad (4)$$

where V is the crystal volume, q is the wavevector, ω_0 is the circular frequency, $1/\bar{\kappa} = 1/\kappa_\infty - 1/\kappa_0$, κ_∞ is the high-frequency permittivity, and $b_q^\dagger$ is the operator of phonon creation. In expression (4), the first term describes the phonon absorption and the second (Hermitian conjugate) term describes the phonon emission. Since we are interested only in the first process, the second term will be omitted.

Then, taking into account only the processes of interest, we can write Hamiltonian (1) in a simpler form

$$H = H_0 + V^{\rm ph}\exp(-i\omega t) + V^{\rm LO}\exp(i\omega_0 t), \qquad (5)$$

where $V^{\rm ph}$ and $V^{\rm LO}$ are the first terms in Eqs. (3) and (4), respectively, without time-dependent exponential terms.

Using the assumption of adiabatic switching of the interaction [9] and relations of perturbation theory, we obtain the following expression for the probability of electron transition from the donor ground state denoted $|i\rangle$ to the $|\varphi_q\rangle$ state:

$$W_{\varphi i} = \frac{2\pi}{\hbar}|S|^2\delta(\hbar\omega - \hbar\omega_0), \qquad (6)$$

where S is the transition matrix with elements

$$S_{\varphi i} = \sum_m \frac{\langle\varphi_q|V^{\rm LO}|m\rangle\langle m|V^{\rm ph}|i\rangle}{\hbar\omega_0 + E_i - E_m + i\lambda}, \quad \lambda \longrightarrow 0, \qquad (7)$$

E_i is the energy of the donor ground state, and m is the set of quantum numbers of an intermediate state. All the intermediate states can be subdivided into two groups as belonging to the discrete spectrum and the continuum. We will take into account the fact that the electron–photon interaction operator is proportional to the spherical function $Y_{1,1}$,

$$V^{\rm ph} = eAr\sqrt{\frac{4\pi}{3}}Y_{1,1}(\theta, \varphi), \qquad (8)$$

and that the wavefunction of the donor ground state is isotropic. Therefore, the intermediate state has a unit angular moment and a unit projection of the moment

onto the *z* axis and, hence, is a *p*-type state. For this reason, all intermediate states in the continuum can be characterized only by the energy, and states in the discrete spectrum, only by the principal quantum number *n*. Below, we will assume that the energy of the optical phonon is greater than the energy of ionization of a shallow donor. Then, expression (7) can be rewritten as

$$S_{\varphi i} = \sum_{n=2}^{\infty} \frac{\langle \varphi_q | V^{\mathrm{LO}} | n \rangle \langle n | V^{\mathrm{ph}} | i \rangle}{\hbar\omega_0 + E_i - E_n} + \mathrm{P}\int dE \frac{\langle \varphi_q | V^{\mathrm{LO}} | \psi(E) \rangle \langle \psi(E) | V^{\mathrm{ph}} | i \rangle}{\hbar\omega_0 + E_i - E} + i\pi \langle \varphi_q | V^{\mathrm{LO}} | \psi(E) \rangle \langle \psi(E_\varphi) | V^{\mathrm{ph}} | i \rangle, \quad (9)$$

where $|n\rangle$ is the wavefunction (normalized to unity) of the intermediate state in the discrete spectrum and $|\psi(\varepsilon)\rangle$ is the wavefunction in the continuum, which is normalized as

$$\int d^3 r \langle \psi(E) | \psi(E') \rangle = \delta(E - E').$$

In these expressions, $E_\varphi = \hbar\omega_0 + E_i$ and "P" in front of the integral denotes the principal value.

Passing from $|n\rangle$ to the new wavefunctions

$$|\psi(E)\rangle = \sqrt{\delta(E - E_n)}|n\rangle,$$

which also belong to the discrete spectrum but are normalized differently, we can rewrite Eq. (9) so that the sum and integral will be replaced by a single term having a form analogous to the integral in this expression. However, the integration domain has to be expanded so as to include the energies of the discrete spectrum. The new wavefunctions $\psi(E)$ belonging to the discrete spectrum obey the normalization condition for the functions of the continuum. In what follows, we use this compact form in writing and assume that the electron energy in the continuum is positive, while the electron energies in the discrete spectrum vary from E_i to zero. Using this substitution, we can readily take into account the influence of states in the discrete spectrum on the interaction between resonance states and states in the continuum within the framework of the Fano theory [1].

The state $|\varphi_q\rangle$ is a resonance state because its energy belongs to the continuum and it interacts with states $\psi(\varepsilon)$ of the continuum by means of the electron–phonon interaction. Thus, the system under consideration is exactly the same as the system considered by Fano [1, Section 5] for an analysis of the interaction of several resonance states with states in the continuum. Accordingly, the exact wavefunction corresponding to the energy *E* can be written as (see [1, Eq. (46)])

$$|\Psi(E)\rangle = \sum_q a_q(E)|\varphi_q\rangle + \int dE' b(E, E')|\psi(E')\rangle, \quad (10)$$

where

$$a_q(E) = -\frac{V_q^*(E)}{E - E_\varphi}\cos[\Delta(E)], \quad (11)$$

$$b(E, E') = -\left[\sum_q \frac{V_q(E')V_q^*(E)}{(E - E')(E - E_\varphi)} + \delta(E - E')\right] \times \cos[\Delta(E)], \quad (12)$$

$$\tan[\Delta(E)] = -\pi\sum_q \frac{|V_q(E)|^2}{E - E_\varphi}, \qquad V_q^*(E) = \langle \varphi_q | V^{\mathrm{LO}} | \psi(E) \rangle. \quad (13)$$

In deriving relations (11)–(13), we set

$$F_{q,q'} \equiv \mathrm{P}\int dE' \frac{V_q^*(E')V_{q'}(E')}{E - E'} = 0,$$

because the off-diagonal elements of the $F_{q,q'}$ matrix vanish on averaging over the ensemble due to an arbitrary phase difference between $V_{q'}$ and V_q^*, while the diagonal elements are inversely proportional to the system volume. For this reason, the sum $\sum_{q'} F_{q,q'}(E)a_{q'}$ in [1, Eq. (49)] can be ignored.

The matrix elements of the operator of optical transition to the $\Psi(E)$ state can be written as follows:

$$\langle \Psi(E) | V^{\mathrm{ph}} | i \rangle = \sum_q a_q^*(E) S_{\varphi i} + \int dE' b^*(E, E') \langle \Psi(E') | V^{\mathrm{ph}} | i \rangle. \quad (14)$$

Taking into account relations (9), (11), and (12), this expression can be rewritten as

$$\langle \Psi(E) | V^{\mathrm{ph}} | i \rangle = -\frac{\cos[\Delta(E)]}{E - E_\varphi} \times \sum_q \left\{ \mathrm{P}\int_{E_i}^{\infty} dE' V_q(E) V_q^*(E') \langle \psi(E') | V^{\mathrm{ph}} | i \rangle \times \left(\frac{1}{E_\varphi - E'} + \frac{1}{E - E'} \right) + i\pi V_q(E) V_q^*(E_\varphi) \langle \psi(E_\varphi) | V^{\mathrm{ph}} | i \rangle \right\} - \cos[\Delta(E)] \langle \psi(E) | V^{\mathrm{ph}} | i \rangle. \quad (15)$$

Using the explicit expression

$$\cos[\Delta(E)] = -\frac{E - E_\varphi}{\sqrt{(E - E_\varphi)^2 + \Gamma^2(E)/4}}, \quad (16)$$

where

$$\Gamma(E) = 2\pi\sum_q |V_q(E)|^2,$$

and $\Gamma(E_\varphi)/\hbar$ is the probability of electron transition from a state in the continuum to the $|i\rangle$ state upon spontaneous emission of an optical phonon, we eventually obtain the matrix element (15) in the following form:

$$\langle\Psi(E)|V^{\rm ph}|i\rangle = \frac{\gamma(E, E_\varphi)\langle\psi(E)|V^{\rm ph}|i\rangle}{\sqrt{(E-E_\varphi)^2 + \Gamma^2(E)/4}} \times\left[\alpha(E) + i\beta(E) + \frac{E-E_\varphi}{\gamma(E, E_\varphi)}\right], \quad (17)$$

where

$$\alpha(E) = \sum_q {\rm P}\int_{E_i}^{\infty} dE' V_q(E) V_q^*(E')\langle\psi(E')|V^{\rm ph}|i\rangle \times\left(\frac{1}{E_\varphi - E'} + \frac{1}{E - E'}\right) \times(\gamma(E, E_\varphi)\langle\psi(E)|V^{\rm ph}|i\rangle)^{-1},$$

$$\beta(E) = \frac{\langle\psi(E_\varphi)|V^{\rm ph}|i\rangle}{\langle\psi(E)|V^{\rm ph}|i\rangle},$$

$$\gamma(E, E_\varphi) = \pi\sum_q V_q(E) V_q^*(E_\varphi).$$

Expression (17) is the main result of this investigation. It should be noted that this formula was obtained without using an explicit form of the Hamiltonian H_0. Therefore, Eq. (17) is also valid for semiconductors doped with acceptors and for the semiconductors with an anisotropic law of dispersion in the conduction band.

For an analysis of the behavior of the square of matrix element (17) in the vicinity of E_φ, we can put

$$\alpha \approx 4\sum_q {\rm P}\int_{E_i}^{\infty} dE' V_q(E) V_q^*(E')\langle\psi(E')|V^{\rm ph}|i\rangle \times(E_\varphi - E')^{-1}(\Gamma\langle\psi(E_\varphi)|V^{\rm ph}|i\rangle^{-1}), \quad (18)$$

$$\beta(E) = 1, \quad \gamma(E, E_\varphi) \approx \frac{\Gamma(E_\varphi)}{2} = \frac{\Gamma}{2}.$$

Then, the square modulus of matrix element (17) can be written as

$$|\langle\Psi(E)|V^{\rm ph}|i\rangle|^2 \approx \frac{|\langle\psi(E)|V^{\rm ph}|i\rangle|^2}{1+x^2}|\alpha + i + x|^2 = \frac{|\langle\psi(E)|V^{\rm ph}|i\rangle|^2}{1+x^2}[(\alpha + x)^2 + 1], \quad (19)$$

where $x = 2(E - E_\varphi)/\Gamma$ is the dimensionless energy.

Expression (19) is analogous to the formula obtained by Fano (see [1, Eq. (21)]) for a single resonance level, which is frequently used for the description of photocurrent peaks in the vicinity of the optical phonon energy [5, 6]. Setting in [1, Eq. (21)] the parameter q (which is not related to the phonon wavevector) equal to $\alpha + i$, one can readily obtain expression (19).

Thus, the probability of absorption of a light quantum is

$$W(\omega) = \frac{2\pi}{\hbar}\int dE|\langle\Psi(E)|V^{\rm ph}|i\rangle|^2\delta(\hbar\omega + E_i - E) = \frac{2\pi}{\hbar}|\langle\Psi(\hbar\omega + E_i)|V^{\rm ph}|i\rangle|^2. \quad (20)$$

3. CALCULATION OF FANO RESONANCES IN THE PHOTOCURRENT SPECTRUM FOR A HYDROGEN-LIKE DONOR

Let us calculate the matrix elements $\langle\psi(E)|V^{\rm ph}|i\rangle$ and $V_q(E)$ for a hydrogen-like donor described by Hamiltonian (2). Using an expression for the wavefunctions of a hydrogen atom and passing to the new variables of length (measured in units of the Bohr radius $a_{\rm B} = \hbar^2\kappa_0/\mu e^2$) and energy (measured in units of $\varepsilon_0 = \mu e^4/\hbar^2\kappa_0^2$) we can write the wavefunction of the donor ground state as [9]

$$|i\rangle = R_{10}(r)Y_{0,0} = 2e^{-r}/\sqrt{4\pi}. \quad (21)$$

The wavefunctions of intermediate states in the discrete spectrum can be expressed as [9]

$$|n\rangle = R_{n1}(r)Y_{11}(\theta, \varphi) = -\frac{2}{n^2}\sqrt{\frac{(n-2)!}{[(n+1)!]^3}}e^{-r/n} \times\frac{2r}{n}L_{n+1}^3\left(\frac{2r}{n}\right)Y_{11}(\theta, \varphi), \quad (22)$$

and those in the continuum as

$$|\psi(E)\rangle = \frac{2}{2\pi(2kr)^2}\sqrt{\frac{1 + 1/k^2}{1 - e^{-2\pi/k}}}\oint dt \times e^{2ikrt}\left(t + \frac{1}{2}\right)^{i/k-2}\left(t - \frac{1}{2}\right)^{-i/k-2}Y_{11}(\theta, \varphi), \quad (23)$$

where $L_{n+1}^3(2r/n)$ are the generalized Laguerre polynomials and the integration contour contains the branching points $t = \pm 1/2$.

The matrix elements of the operator of interaction with electromagnetic radiation can be determined using the formula for the transitions to states in the discrete

spectrum given in [11, Eq. (63.4)]. The matrix elements of transitions to the continuum can be determined using the method described in the same monograph [11, Paragraph 71]. The resulting expressions for the matrix elements of transitions to the discrete spectrum and continuum are as follows:

$$\frac{\langle n|V^{\rm ph}|i\rangle}{eA} = \frac{1}{\sqrt{3}}\sqrt{\frac{2^8 n^7 (n-1)^{2n-5}}{(n+1)^{2n+5}}}, \tag{24}$$

$$\frac{\langle \psi(E)|V^{\rm ph}|i\rangle}{eA} = \sqrt{\frac{1}{1-e^{-2\pi/k}}} \times \frac{16}{\sqrt{3}(1+k^2)^{5/2}}\exp\left(-\frac{2}{k}\arctan k\right), \tag{25}$$

where k is the electron wavenumber (expressed in units of the inverse Bohr radius) corresponding to the energy E. For passing to the dimensional units, Eq. (24) has to be multiplied by $a_{\rm B}$, and expression (25), by $a_{\rm B}/\sqrt{\varepsilon_0}$.

In order to calculate $V_q(E)$ via relations (4) and (5), we have to determine the matrix element of the operator $\exp(-i\mathbf{q}\cdot\mathbf{r})$. This can be done using expansion of the exponent in terms of spherical harmonics [9]:

$$e^{-i\mathbf{q}\cdot\mathbf{r}} = 4\pi\sum_{l=0}^{\infty}\sum_{m=-l}^{l}(-i)^l j_l(qr)Y_{lm}^*\left(\frac{\mathbf{q}}{q}\right)Y_{lm}\left(\frac{\mathbf{r}}{r}\right), \tag{26}$$

where $j_l(x) = \sqrt{\pi/2x}\,J_{l+1/2}(x)$ and $J_{l+1/2}(x)$ is the Bessel function with a half-integer index. In particular, below we will use the function

$$j_1(qr) = \frac{\sin^2(qr)}{(qr)^2} - \frac{\cos(qr)}{qr}.$$

According to Eq. (13), the matrix element can be represented as $V_q = \langle\psi(E)|V^{\rm LO}|\varphi_q\rangle$. The angular dependence of the wavefunction $|\psi(E)\rangle$ (as a function of the electron coordinates) is described by $Y_{1,1}$, while the electron wavefunction in the $|\varphi_q\rangle$ state is spherically symmetric (because the electron is in the donor ground state). As is shown in the Appendix, the wavefunctions of the continuum can be written as

$$\langle\psi(E)|e^{-i\mathbf{q}\cdot\mathbf{r}}|i\rangle = \frac{i}{k^2\sqrt{\pi}}\sqrt{\frac{1+1/k^2}{1-e^{-2\pi/k}}}I(k,q)Y_{1,1}^*\left(\frac{\mathbf{q}}{q}\right), \tag{27}$$

where

$$I(k,q) = -16\pi k^3\int_0^1 dx x \times {\rm Im}\left\{\left(\frac{qx+k-i}{qx-k-i}\right)^{i/k}[(qx-i)^2-k^2]^{-2}\right\},$$

while the wavefunctions in the discrete spectrum can be written as

$$\langle n|e^{-iqr}|i\rangle = -i\sqrt{4\pi}I_2(n,q)Y_{11}^*(\mathbf{q}/q), \tag{28}$$

where

$$I_2(n,q) = \int_0^\infty dr r^2 R_{n1}(r)R_{1,0}(r)\left[\frac{\sin(qr)}{q^2r^2} - \frac{\cos(qr)}{qr}\right].$$

According to the law of angular moment conservation, the angular moment of the emitted phonon is equal to that of the absorbed photon (because the electron wavefunctions in the ground and resonance states are the same) and $V_q \sim Y_{11}^*(\mathbf{q}/q)$. Using expressions (27) and (28) and taking into account relation (4), we eventually obtain

$$\alpha(E) = \frac{2{\rm P}\int_0^\infty dk' \frac{\exp\left(-\frac{2}{k'}\arctan k'\right)}{k'^2(1+k'^2)^2(1-e^{-2\pi/k'})}\left(\frac{1}{k_\varphi^2-k'^2}+\frac{1}{k^2-k'^2}\right)\int_0^\infty dq I(k,q)I(k',q)}{\frac{\pi}{k_\varphi^3}\sqrt{\frac{1+k_\varphi^2}{(1-e^{-2\pi/k_\varphi})(1-e^{-2\pi/k})}}\frac{\exp\left(-\frac{2}{k}\arctan k\right)}{(1+k^2)^{5/2}}\int_0^\infty dq I(k,q)I(k_\varphi,q)}$$
$$+\frac{\frac{1}{4}\sum_{n=2}^\infty\sqrt{\frac{2^8n^7(n-1)^{2n-5}}{(n+1)^{2n+5}}}\left(\frac{1}{k_\varphi^2+1/n^2}+\frac{1}{k^2+1/n^2}\right)\int_0^\infty dq I_2(n,q)I(k,q)}{\frac{1}{k_\varphi^3}\sqrt{\frac{1+k_\varphi^2}{(1-e^{-2\pi/k_\varphi})(1-e^{-2\pi/k})}}\frac{\exp\left(-\frac{2}{k}\arctan k\right)}{(1+k^2)^{5/2}}\int_0^\infty dq I(k,q)I(k_\varphi,q)}, \tag{29}$$

$$\beta(E) = \sqrt{\frac{1-e^{-2\pi/k}}{1-e^{-2\pi/k_\varphi}}}\left(\frac{1+k_\varphi^2}{1+k^2}\right)^{5/2} \times \exp\left(\frac{2}{k_\varphi}\arctan k_\varphi - \frac{2}{k}\arctan k\right), \quad (30)$$

$$\gamma(E, E_\varphi) = \frac{\hbar\omega_0\kappa_0}{(2\pi)^2\bar{\kappa}}\frac{1}{(kk_\varphi)^2}\sqrt{\frac{1+1/k^2}{1-e^{-2\pi/k}}} \times \sqrt{\frac{1+1/k_\varphi^2}{1-e^{-2\pi/k_\varphi}}}\int_0^\infty I(k, q)I(k_\varphi, q)dq. \quad (31)$$

4. COMPARISON OF THEORY TO EXPERIMENT FOR GaAs AND InP

Contributions to the photocurrent are due to electrons occurring in delocalized states upon the absorption of light quanta. For this reason, it might seem that the photocurrent spectrum could be determined as a product of Eq. (20) and the probability of an electron occurring in such a delocalized state. However, using relation (10) and taking into account the behavior of the wavefunction $\psi(E)$ at large r (where $\psi(E) \propto \sin(kr + \delta)$), one can readily check that the wavefunctions $\Psi(E)$ and $\psi(E)$ at large r differ only by their phases, while their amplitudes are the same (see calculations following [1, Eq. (4)]). This situation implies that an electron in the $\Psi(E)$ state is fully delocalized and its interaction with the resonance states does not lead to partial localization of the wavefunction.

In the vicinity of a Fano resonance, the spectrum of the photocurrent is significantly influenced by the frequency dependences of the coefficients of light reflection and absorption. These coefficients rapidly vary in this region as a result of the light absorption by transverse optical (TO) phonons. Taking into account these factors, the photocurrent can be expressed as

$$J(\omega) = BI(\omega)\frac{W(\omega)}{|A|^2}[1-R(\omega)]\int_0^d e^{-\eta(\omega)x}dx, \quad (32)$$

where B is a frequency-independent constant, $I(\omega)$ is the incident light intensity, $\eta(\omega)$ is the optical absorption coefficient, and d is the thickness of a doped region. The absorption and reflection of light in this spectral interval are determined primarily by optical oscillations of the lattice and can be described in terms of the permittivity as [12]

$$\kappa(\omega) = \kappa_\infty + \frac{\kappa_0 - \kappa_\infty}{1 - \frac{\omega^2}{\omega_{TO}^2} - i\frac{\omega\gamma}{\omega_{TO}^2}}, \quad (33)$$

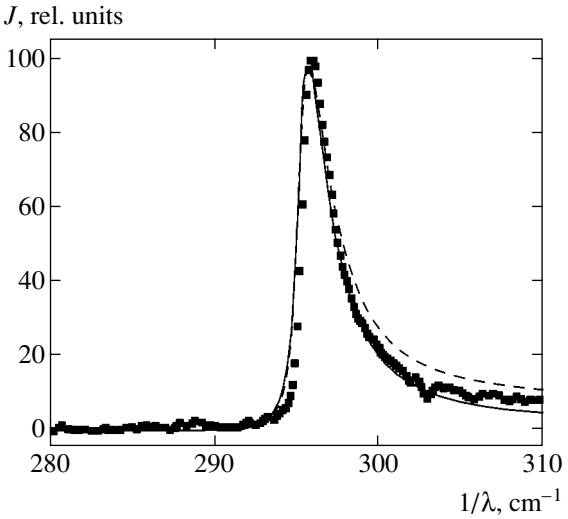

Fig. 2. The photocurrent spectra of *n*-GaAs at $T = 4.2$ K: points represent the experimental data; solid and dashed curves show the theoretical spectra calculated for $\eta d \ll 1$ and $\eta d \gg 1$, respectively (the spectra are normalized to 100).

where ω_{TO} and γ are the frequency and the decay constant of the TO phonon, respectively. Then, the reflection $R(\omega)$ and absorption $\eta(\omega)$ coefficients can be expressed as

$$R(\omega) = \frac{[\mathrm{Re}(\sqrt{\kappa(\omega)}) - 1]^2 + \mathrm{Im}^2(\sqrt{\kappa(\omega)})}{[\mathrm{Re}(\sqrt{\kappa(\omega)}) + 1]^2 + \mathrm{Im}^2(\sqrt{\kappa(\omega)})}, \quad \eta(\omega) = \frac{2\omega}{c}\mathrm{Im}(\sqrt{\eta(\omega)}), \quad (34)$$

where c is the velocity of light.

Figure 2 shows the calculated and measured spectra of the photocurrent in the region of the Fano resonance in *n*-GaAs. The calculation was performed using the following values of parameters for GaAs:

$$\mu = 0.0665m_0, \quad \kappa_0 = 12.46, \quad \kappa_\infty = 10.58,$$

$$\hbar\omega_0 = 36.588 \text{ meV [13]}, \quad \gamma = 0.001\omega_{TO},$$

$$\omega_{TO} = \omega_0\sqrt{\kappa_\infty/\kappa_0},$$

where m_0 is the free electron mass. One spectrum (Fig. 2, solid curve) was calculated for a particular case where the thickness d of a layer producing the main contribution to the photocurrent is much smaller than $1/\eta(\omega)$. In this case, the photocurrent was calculated using expression (32), where the integration over x gave d. Another spectrum (Fig. 2, dashed curve) was calculated assuming that the photoelectron yield depth is much greater than $1/\eta(\omega)$. In this case, the integral in Eq. (32) is equal to $1/\eta(\omega)$. Apparently, the spectrum for an arbitrary d value must fall between the two limiting curves in Fig. 2.

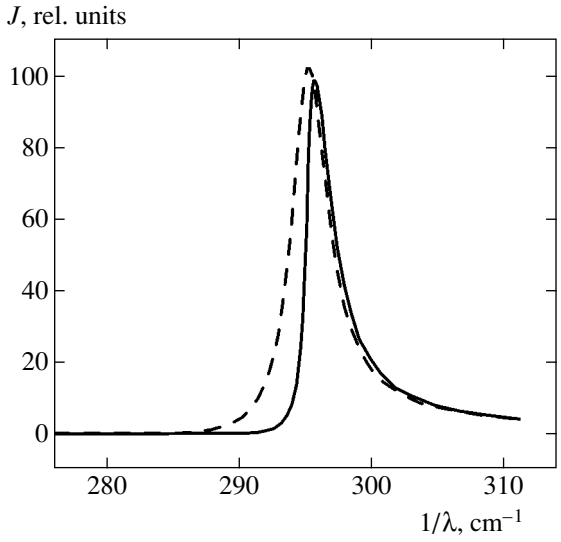

Fig. 3. Theoretical photocurrent spectra of *n*-GaAs calculated with (solid curve) and without (dashed curve) allowance for the reflection.

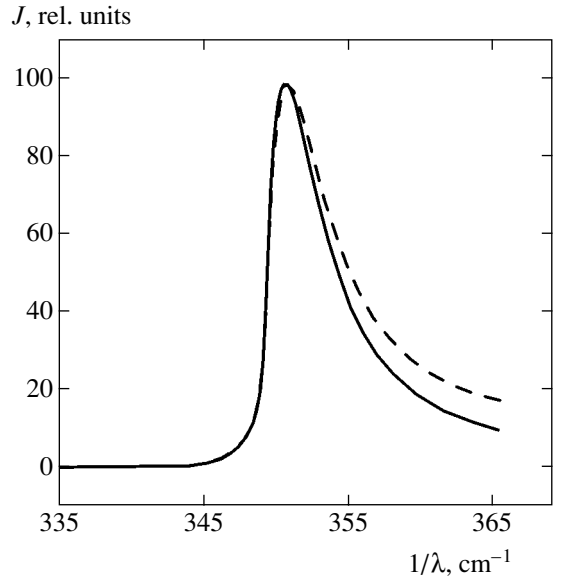

Fig. 4. Theoretical photocurrent spectra of InP calculated for $\eta d \ll 1$ (solid curve) and $\eta d \gg 1$ (dashed curve) (the spectra are normalized to 100).

Experimental photocurrent spectra were obtained for an epitaxial *n*-GaAs layer grown by liquid phase epitaxy on a semi-insulating GaAs substrate. The epilayer was doped with silicon at a concentration of 8.3×10^{14} cm^{-3} and had a thickness of 70 μm. The electron mobility at 77 K was 5.9×10^4 cm^2/(V s). The measurements were performed at $T = 4.2$ K using a BOMEM Fourier-transform spectrometer.

As can be seen from Fig. 2, the experimental curve agrees well with the spectrum calculated for a thin semiconductor layer. In the spectral interval studied, the characteristic η value is on the order of 10^3 cm^{-1} and $\eta d \gg 1$. It should be noted that the photocurrent spectrum for GaAs reported in [7] is more asymmetric than our spectrum and shows a much worse agreement with the results of calculations.

The calculation of $\alpha(E)$ showed that the contribution to this value due to states of the discrete spectrum of GaAs is about 28%. It should be also noted that the spectrum of the photocurrent in *n*-GaAs calculated using formula (19) is practically the same as that obtained using the exact expression (17). The values of α and Γ calculated using formulas (18) are as follows:

$$\alpha_{GaAs} = 7.962, \quad \Gamma_{GaAs} = 0.413 \text{ eV}.$$

Figure 3 presents the results of photoresponse calculations for *n*-GaAs, which illustrate the influence of the reflection coefficient on the shape of the Fano resonance in the photocurrent spectrum. As can be seen, allowance for the reflection makes the resonance peak more asymmetric and narrow.

Figure 4 shows the theoretical spectra of the photocurrent in the vicinity of the Fano resonance for InP, which were calculated for the following parameters:

$$\mu = 0.081 m_0, \quad \kappa_0 = 12.2, \quad \kappa_\infty = 9.487,$$

$$\hbar\omega_0 = 43.33 \text{ meV [13]},$$

$$\gamma = 0.001\omega_{TO}, \quad \hbar\omega_{TO} = 38.21 \text{ meV}.$$

The position of the calculated resonance peak is in good agreement with that in the experimental spectrum reported in [7]. However, the halfwidth of the measured spectrum [7] is only about half the calculated value. In addition, the experimental photocurrent peak for InP (as well as that for GaAs) is more asymmetric than the theoretical curve. The reason for the discrepancy between calculations and the results of measurements reported in [7] for both GaAs and InP remains unclear. It should also be noted that the calculated halfwidth of the photocurrent peak for GaAs is about half that for InP (because $\Gamma_{InP} = 0.852$ meV), whereas the halfwidths of the experimental resonance peaks for the two semiconductors are approximately equal [7].

5. CONCLUSIONS

Let us consider the question why Fano resonances in the photocurrent spectra of *n*-GaAs and *n*-InP are manifested as peaks, whereas the same resonances in the spectra of photocurrent and absorption in *p*-Si are manifested as narrow dips. It should be noted that the energies of ionization for shallow donors in both materials, GaAs and InP, are five to six times lower than the LO phonon energy. For this reason, the electron upon absorption of a light quantum with an energy equal to that of the optical phonon passes to a high level in the

continuum. The probability of such transitions is not high because the matrix elements of the dipole moment rapidly decreases with increasing light quantum energy in this region (i.e., the transition is almost prohibited). Therefore, the probabilities of photon absorption via resonance states (which are of the second order of smallness) become greater than the probabilities of direct transitions. Owing to the interaction between resonance states and states in the continuum, the wavefunction $\Psi(E)$ of the continuum near the resonance energy contains the wavefunctions φ_q of the resonance states and the wavefunctions $\psi(E')$. As a result, the probability of absorption of a photon with an energy close to that of the optical phonon sharply increases.

The situation in boron-doped *p*-Si is substantially different. Here, the optical phonon energy is about 64 meV and the ionization energy for boron is on the same order of magnitude (about 45 meV). In this case, the Fano resonance is close to the position of the maximum probability of acceptor ionization and, hence, the probability of a direct transition to the continuum in this spectral region significantly exceeds the probabilities of transitions both to a resonance state and to states with different energies in the continuum. For this reason, an "admixture" of the resonance state leads to a decrease in the absorption, which is manifested by narrow dips both in the photocurrent and in the absorption spectrum.

ACKNOWLEDGMENTS

The authors are grateful to B.A. Andreev for fruitful discussions, which stimulated the appearance of this paper.

This work was supported in part by the Russian Foundation for Basic Research (project no. 04-02-17178) and the International Scientific-Technological Center (grant no. 2293).

APPENDIX

Consider the matrix element $\langle\psi(E)|\exp(-i\mathbf{q}\cdot\mathbf{r})|i\rangle$. Using the expressions for wavefunctions (21) and (23), expansion (26), and the condition of orthonormalization for the Y_{lm} functions, one can obtain the following expression for this matrix element:

$$\begin{aligned}&\langle\psi(E)|\exp(-i\mathbf{q}\cdot\mathbf{r})|i\rangle\\ &= -\frac{i}{k^2}\sqrt{\frac{1+1/k^2}{\pi(1-e^{-2\pi/k})}}Y^*_{1,1}\left(\frac{\mathbf{q}}{q}\right)\\ &\times\int_0^\infty dre^{-r}\left[\frac{\sin^2(qr)}{q^2r^2}-\frac{\cos(qr)}{qr}\right]\\ &\times\oint e^{2ikrt}\left(t+\frac{1}{2}\right)^{i/k-2}\left(t-\frac{1}{2}\right)^{-i/k-2}dt.\end{aligned} \tag{A.1}$$

The integral with respect to r is readily calculated to yield

$$\begin{aligned}&\int_0^\infty dre^{-r+2ikrt}\left[\frac{\sin(qr)}{q^2r^2}-\frac{\cos(qr)}{qr}\right]\\ &= \frac{1}{q}\left\{1+\frac{1-2ikt}{q}\left[\arctan\left(\frac{1-2ikt}{q}\right)-\frac{\pi}{2}\right]\right\}.\end{aligned} \tag{A.2}$$

The contour integral obtained using expression (A.2) can be calculated only by numerical methods. However, sharp spikes of the integrand function make this expression inconvenient for numerical calculations. In order to reduce it to a more convenient form, expression (A.2) can be represented in an integral form, which reduces the calculation to integration along a contour:

$$\begin{aligned}&\frac{1}{q}\left\{1+\frac{1-2ikt}{q}\left[\arctan\left(\frac{1-2ikt}{q}\right)-\frac{\pi}{2}\right]\right\}\\ &= \frac{1}{q}\left[1-\left(\frac{1-2ikt}{q}\right)^2\int_0^1\frac{dx}{x^2+(1-2ikt)^2/q^2}\right].\end{aligned} \tag{A.3}$$

The contour integral involving the right-hand side of expression (A.3) can be calculated using the theory of residues. For this purpose, the integration contour is selected in the form of a circle of infinite radius and the residues are calculated in the two poles where the sum $x^2 + (1 - 2ikt)^2/q^2$ vanishes. The contour integral from the first term in square brackets in the right-hand side of Eq. (A.3) is zero. Consider the following function:

$$\begin{aligned}I(k,q) &= \frac{1}{q}\oint dt\left(t+\frac{1}{2}\right)^{i/k-2}\left(t-\frac{1}{2}\right)^{-i/k-2}\\ &\times\left[1+\left(\frac{1-2ikt}{q}\right)^2\int_0^1\frac{dx}{x^2+(1-2ikt)^2/q^2}\right]\\ &= -16\pi k^3\int_0^1 dxx\\ &\times\mathrm{Im}\left\{\left(\frac{qx+k-i}{qx-k-i}\right)^{i/k}[(qx-i)^2-k^2]^{-2}\right\}.\end{aligned} \tag{A.4}$$

As can be seen, the integral in the right-hand side of expression (A.4) is readily calculated by numerical methods. Using relation (A.4), we obtain the required expression (27).

REFERENCES

1. U. Fano, Phys. Rev. **124**, 1866 (1961).
2. H. J. Hrostowski and R. H. Kaiser, J. Phys. Chem. Solids **4**, 148 (1958).
3. A. Onton, P. Fisher, and A. K. Ramdas, Phys. Rev. **163**, 686 (1967).
4. H. R. Chandrasekhar, A. K. Ramdas, and S. Rodriguez, Phys. Rev. B **14**, 2417 (1976).
5. G. D. Watkins and W. B. Fowler, Phys. Rev. B **16**, 4524 (1977).
6. E. Janzen, G. Grossmann, R. Stedman, and H. G. Grimmeiss, Phys. Rev. B **31**, 8000 (1985).
7. K. Jin, J. Zhang, Z. Chen, *et al.*, Phys. Rev. B **64**, 205203 (2001).
8. M. W. Klein, in *Light Scattering in Solids*, Ed. by M. Cardona (Springer, Berlin, 1975).
9. L. D. Landau and E. M. Lifshitz, *Course of Theoretical Physics*, Vol. 3: *Quantum Mechanics: Non-Relativistic Theory*, 4th ed. (Nauka, Moscow, 1989; Pergamon, Oxford, 1980).
10. V. F. Gantmakher and I. B. Levinson, *Scattering of Carriers in Metals and Semiconductors* (Nauka, Moscow, 1984) [in Russian].
11. H. A. Bethe and E. E. Salpeter, *Quantum Mechanics of One- and Two-Electron Atoms* (Academic, New York, 1957).
12. P. Y. Yu and M. Cardona, *Fundamentals of Semiconductors* (Springer, Berlin, 1996).
13. W. J. Moore and R. T. Holm, J. Appl. Phys. **80**, 6939 (1996).
14. A. Dargys and J. Kundrotas, *Handbook on Physical Properties of Ge, Si, GaAs, and InP* (Science and Encyclopedia, Vilnius, 1994).

Translated by P. Pozdeev

Journal of Experimental and Theoretical Physics, Vol. 101, No. 4, 2005, pp. 717–727.
Translated from Zhurnal Éksperimental'noĭ i Teoreticheskoĭ Fiziki, Vol. 128, No. 4, 2005, pp. 831–843.

ELECTRONIC PROPERTIES OF SOLIDS

Intersubband Excitations in Single- and Double-Layer Electron Systems in a Parallel Magnetic Field

L. V. Kulik, I. V. Kukushkin, V. E. Kirpichev, S. V. Tovstonog, and V. E. Bisti

Institute of Solid State Physics, Russian Academy of Sciences, Chernogolovka, Moscow oblast, 142432 Russia
e-mail: kulik@issp.ac.ru

Received June 13, 2005

Abstract—The spectrum of neutral intersubband excitations in single and double quantum wells has been studied by the inelastic light scattering method. It is shown that excitation energies in an external magnetic field have an anisotropic component proportional to the dipole moment of excitations along the growth axis of the quantum wells. Consequently, the measurement of excitation energy in a magnetic field makes it possible to experimentally estimate the quantitative measure of asymmetry of the quantum wells (dipole moment of the intersubband transition). In addition, a parallel magnetic field makes it possible to considerably extend the range of momenta studied since it shifts the dispersion curves in the momentum space by the value of the anisotropic component. A new method is proposed for determining the symmetry of double quantum wells. In asymmetric wells, intersubband excitations appear between the layers and have a large dipole moment along the growth axis. In symmetric wells, the magnetic field itself induces the dipole moment of intersubband excitations so that the excitation spectrum does not change upon magnetic field inversion. Analysis of energy anisotropy in intersubband excitations in double quantum wells makes it possible to determine the symmetry of double wells to a high degree of accuracy. *© 2005 Pleiades Publishing, Inc.*

1. INTRODUCTION

It is well known that the Hamiltonian of a system of positive and negative charges with a total charge equal to zero in a constant uniform magnetic field exhibits translational invariance. The corresponding integral of motion is the generalized momentum all of whose components commute with one another. For a system of two particles, the generalized momentum can be represented in the form

$$\mathbf{k} = -i(\nabla_1 + \nabla_2) + \frac{e}{c}(\mathbf{A}_1 - \mathbf{A}_2) - \frac{e}{c}(\mathbf{r}_2 - \mathbf{r}_1) \times \mathbf{B}, \quad (1)$$

where $\hbar = 1$, subscripts "1" and "2" denote negatively and positively charged particles, **A** is the vector potential, and **B** is the magnetic field strength [1, 2]. The generalized momentum in a magnetic field plays the same role as the momentum in zero field (absorption or emission of electromagnetic waves by a neutral system may serve as an example). The interaction with radiation preserves the sum of the photon momentum and the generalized momentum of the system [3].

In a two-dimensional (2D) space, a neutral system has an analogous integral of motion [4]. Examples of such systems are the 2D hydrogen atom and the Mott exciton with a narrow semiconducting quantum well in a magnetic field. Magnetoexcitons or magnetoplasma modes, viz., bound states of a hole at the filled level and an electron at one of the empty Landau levels, are less obvious examples which, nevertheless, are important for physical applications [5].

In view of the finite width of the electron wavefunctions in the direction of quantum well growth, quasiparticles in wells are not two-dimensional, but quasi-two-dimensional. However, this is immaterial as long as an electron and a hole move in the same plane and the energy gaps between size-quantized subbands in quantum wells are larger than the energy of interaction between the electron and the hole. If, however, the electron and the hole move in two spatially separated planes, the system can be described in terms of a 2D dipole (i.e., a neutral 2D quasiparticle having a nonzero dipole moment **d** along the axis perpendicular to the planes),

$$\mathbf{d} = -e|z_0 - z_1|\mathbf{n}, \quad (2)$$

where **n** is the normal to the plane of the quantum well,

$$z_0 - z_1 = \int dz \psi_0^*(z) z \psi_0(z) - \int dz \psi_1^*(z) z \psi_1(z)$$

is the mean distance between the electron and hole, and $\psi_{0(1)}(z)$ is the component of the electron (hole) wavefunction in the direction of growth of the quantum well. In an external magnetic field oriented in the plane, vector [6, 7]

$$\mathbf{P} = \mathbf{\Pi} + \frac{1}{c}\mathbf{d} \times \mathbf{B} \quad (3)$$

plays the role of the generalized momentum of the 2D dipole and is preserved in scattering processes (here, **Π** is the kinematic momentum of the electron and hole in

the plane of the well) [8]. The kinetic energy of a 2D dipole in an external magnetic field is a function of kinematic momentum,

$$E(\mathbf{\Pi}) = E\left(\mathbf{P} - \frac{1}{c}\mathbf{d}\times\mathbf{B}\right); \quad (4)$$

i.e., in addition to the generalized momentum, the energy depends on the gauge contribution $c^{-1}\mathbf{d}\times\mathbf{B}$, which is due to the impossibility of simultaneous vanishing of the vector potential in two spatially separated layers. Thus, we can analyze dispersion of 2D dipoles by applying an appropriately oriented magnetic field. If the resonance condition

$$\mathbf{P} = \frac{1}{c}\mathbf{d}\times\mathbf{B} \quad (5)$$

is satisfied, the kinematic momentum and, hence, the kinetic energy of the dipole vanish. In spite of the fact that the momentum transferred to a 2D dipole via scattering processes is finite, it is "frozen" (stationary in the plane).

Examples of 2D dipoles are Mott excitons in asymmetric single and double quantum wells and (intersubband) electron excitations between charge quantization subbands in asymmetrically doped single and double quantum wells. Mott excitons in physically feasible systems possess a large effective mass and nonparabolic (usually unknown) dispersion relation, which is a consequence of a complex valence band in semiconducting materials of quantum wells. To observe the effects associated with the presence of the gauge term in the generalized momentum of excitons, strong magnetic fields are required, which noticeably affect the quantizing potential of the wells and, accordingly, perturb the hole and electron states [9]. Conversely, the energies of subband excitations in quantum wells vary significantly even in the long-wave limit. Consequently the experimental conditions required for fulfillment of expressions (3)–(5) are created in weak magnetic fields on the order of 1 T, which corresponds to a magnetic quantization energy much lower than the characteristic energy of intersubband quantization. Excitations in double quantum wells, where the intersubband quantization energy can be infinitely small, constitute a special case.

In addition to analysis of dispersion of 2D dipoles, relations (3)–(5) can be used for experimental determination of physical characteristics of the confining potential in single and double quantum wells. Experimental methods for determining the potential asymmetry in double quantum wells, which are interesting from the standpoint of ferromagnetism and, probably, the superfluidity discovered in quasicrystals, are of special importance [10, 11]. The key parameter determining the possible ground state of the electron system in double quantum wells is the degree of spatial asymmetry. Here, we propose an experimental method for determining the degree of asymmetry and provide the most complete contemporary analysis of the spectrum and dispersion of intersubband excitations in single and double quantum wells in a parallel magnetic field, which generalizes our earlier results [12–15].

The article has the following structure. In Section 2, the original experimental technique developed by the authors for measuring the spectra of inelastic scattering of light in an external parallel magnetic field (the field and the momenta of the photons being excited and scattered could be varied simultaneously). The intersubband excitation spectrum in a magnetic field is considered in Section 3, where the correctness of relations (3)–(5) is confirmed experimentally for the energies of intersubband collective excitations [12]. The effect of the transverse magnetic field component on relations (3)–(5) [13] is analyzed in Section 4. In Section 5, the influence of a parallel magnetic field on the one-particle excitation energies is studied and a method for determining spatial asymmetry of the electron system in double quantum wells is demonstrated [14, 15].

2. EXPERIMENTAL TECHNIQUE

Experiments were made on a batch of high-quality heterostructures grown using molecular-beam epitaxy. The heterostructures were in the form of asymmetric selectively doped $Al_xGa_{1-x}As/GaAs$ single quantum wells of width 120–450 Å and double symmetric quantum wells of width 200 Å, separated by a 25-Å-wide insulating barrier. The electron densities n_s in the samples were $(1–6.8)\times10^{11}$ cm^{-2} and the mobilities were at a level of $(1–2)\times10^6$ cm^2/V s. The electron concentrations in the samples studied could be varied over a wide range. For this purpose, the photodepletion technique was used: under continuous photoexcitation by laser radiation with a photon energy exceeding the energy gap of the barriers in the quantum wells, ionized donors in the barrier were neutralized and the electron concentration decreased. The mechanism of this phenomenon was considered in detail in [16]. Balancing of double quantum wells was performed analogously. Since the barrier absorption coefficient in the energy range of photodepleting radiation is large and doping impurities for each well are on different sides of the wells in the barrier, the well located closer to the heterostructure surface is depleted to a much higher extent than the well lying at a larger distance from the surface. Thus, selecting the power density of photodepleting radiation, one can smoothly vary the asymmetry of double quantum wells [14].

In our experiment, an original two-fiber technique was employed. The first fiber was used for exciting the electron system, while the other fiber served for detecting the inelastic light scattering signal (Fig. 1). The component of the momentum **q** in the plane of a quantum well, which was transferred to the electron system

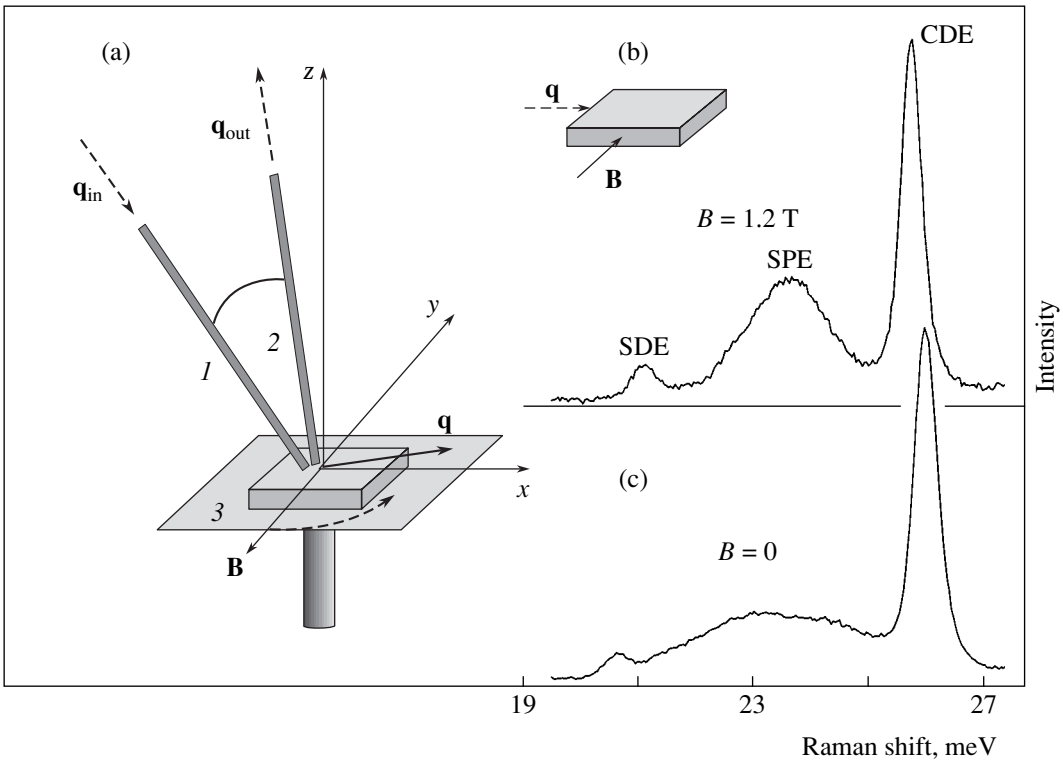

Fig. 1. (a) Schematic diagram of resonant inelastic scattering of light: *1*—fiber for supplying a laser beam to the sample; *2*—fiber collecting the scattered light; *3*—holder with the sample. The holder and the fibers can be rotated about the *z* axis in a constant magnetic field. (b, c) Spectra of inelastic scattering of light for a sample with a 250-Å-wide quantum well for $n_s = 3.5 \times 10^{11}$ cm^{-2}, measured at $B = 1.2$ T (b) and for $B = 0$ (c), $q = 1 \times 10^5$ cm^{-1}. Mutual orientation of vectors **q** and **B** is shown in the inset to (b).

during inelastic scattering of light was determined by the arrangement of the fiber ends relative to the sample surface. The maximal transferred momentum attained a value of 1.2×10^5 cm^{-1}. The fibers and the sample were rigidly fixed to a rotating holder so that the sample was either in the vertical or in the horizontal position. The holder was placed in a cryostat containing a superconducting solenoid, in which the field was horizontal. The angle between the directions of the magnetic field and the momentum transferred to the electron system during inelastic scattering of light could be varied by rotating the holder. In the horizontal orientation of the sample, the magnetic field was directed along the quantum well plane (parallel magnetic field). For the vertical orientation, a nonzero magnetic field component emerged along the quantum well growth axis (transverse magnetic field). Measurements were made at a temperature of 1.5 K. The electron system was excited by a tunable titanium–sapphire laser with a photon energy higher than the forbidden gap of the quantum well material (GaAs), but smaller than the forbidden gap of the barrier material (AlGaAs). The characteristic power density of excitation was 0.1–1 W/cm^2. The signal from inelastic scattering of light was fed to a triple Raman spectrometer and was detected by a CCD camera. The spectral resolution of the detecting system was 0.04 meV and the line widths of inelastic scattering of light ranged from 0.1 to 0.5 meV. Simultaneous measurement of the inelastic scattering signal and the luminescence signal made it possible to monitor the electron density under quasi-continuous excitation by light [14].

3. SINGLE QUANTUM WELL IN A PARALLEL MAGNETIC FIELD

Intersubband excitation in a single asymmetrically doped quantum well consists of an electron in the empty excited subband, which interacts with a hole under the Fermi level for electrons in the principal size-quantized subband. In view of asymmetry of the confining potential, the electron and the hole are spatially separated in the quantum well growth direction. The energy of interaction of the electron and hole is usually much lower than the intersubband energy; consequently, intersubband excitations can be treated as well-defined 2D dipoles. The intersubband excitation spectrum consists of two collective excitations, viz., the charge density excitations (CDEs) and the spin density excitations (SDEs) and the continuum of single-particle excitations (SPEs) [17, 18]. Principal charge and spin density excitations can be treated as the singlet and triplet states of excitons. Energy E_{SDE} is lower than the single-particle intersubband energy due to the Coulomb interaction between the electron and hole (exciton

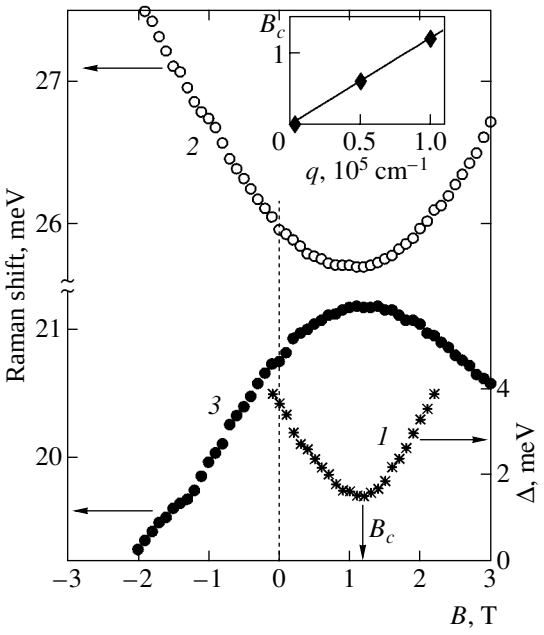

Fig. 2. Magnetic-field-dependence of the SPE band (*1*) and energies E_{CDE} (*2*) and E_{SDE} (*3*). The inset shows the measured (symbols) and calculated by formula (5) (straight line) values of B_c as a function of q. In calculations, we used the value of dipole moment $d = e \times 54$ Å obtained from theoretical calculations.

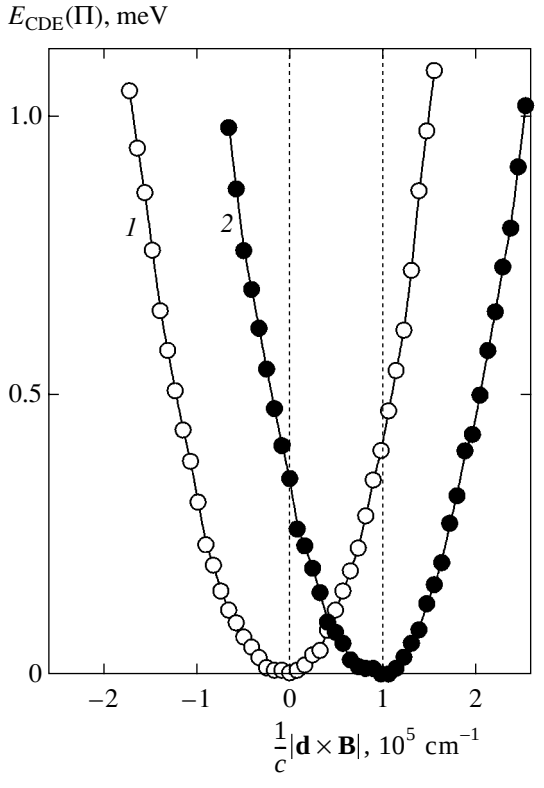

Fig. 3. Kinetic energy E_{CDE} as a function of $c^{-1}|\mathbf{d}\times\mathbf{B}|$. Vector $c^{-1}\mathbf{d}\times\mathbf{B}$ for two values of $P = 0$ (*1*) and 2×10^5 cm^{-1} (*2*) is directed along momentum **P**. Kinetic energy $E_{CDE} = 0$ for $\mathbf{P} = c^{-1}\mathbf{d}\times\mathbf{B} = 0$.

shift), while energy E_{CDE} may be higher or lower than the intersubband energy [19]. In addition to the exciton shift, E_{CDE} contains the macroscopic polarization energy of the electron system (depolarization shift). Consequently, in contrast to a Wannier–Mott exciton, principal excitations of charge and spin density excitations are nondegenerate.

Figure 1 shows examples of inelastic light scattering spectra in zero field and in a parallel magnetic field of 1.2 T. A momentum of 1×10^5 cm^{-1} transferred to the electron system in the plane of the well is directed at right angles to the magnetic field vector. The spectra consist of three main components, viz., a broad band with an energy of 23.5 meV, which is connected with intersubband SPEs, and two narrow lines corresponding to two intersubband collective modes (SDE and CDE) [17]. In a magnetic field, the SPE band is narrowed. The width Δ of the SPE band attains its minimal value for $B_c = 1.2$ T and increases with increasing field. In the same magnetic field, the energies of both collective modes have extrema (E_{CDE} has a minimum and E_{SDE} has a maximum) (Fig. 2). Energies E_{CDE}, E_{SDE}, as well as Δ, are anisotropic; if we rotate the holder with the sample (i.e., change the direction of the momentum relative to the direction of the magnetic field), the values of these quantities vary. Rotational anisotropy decreases with the value of momentum q.

It can be proved that the anisotropy in the intersubband excitation energies is associated with the gauge term in Eq. (4). For this purpose, we consider, for example, quantity E_{CDE}. When $q = 0$, the value of E_{CDE} is a quadratic function of the magnetic field (Fig. 3). Applying a finite momentum $q = 1 \times 10^5$ cm^{-1} so that vector **q** is parallel to vector $\mathbf{d}\times\mathbf{B}$, we observe the magnetic field shift by $|c^{-1}\mathbf{d}\times\mathbf{B}| = 1 \times 10^5$ cm^{-1}. Thus, the dependence $E_{CDE}(c^{-1}\mathbf{d}\times\mathbf{B})$ can be identified with the dispersion relation and the quantity B_c can be identified with the critical magnetic field for which equality (5) is satisfied. Subsequently, the momentum of inelastic light scattering in the quantum well plane and the generalized momentum of excitations will be identified ($\mathbf{q} \equiv \mathbf{P}$).

To verify the dependence of the excitation energy on **P** and $c^{-1}\mathbf{d}\times\mathbf{B}$, the relative orientation of vectors **P** and $\mathbf{d}\times\mathbf{B}$ for $c^{-1}|\mathbf{d}\times\mathbf{B}| = |\mathbf{P}| = 1\times10^5$ cm^{-1} was varied continuously and the kinetic energy of excitations was measured as a function of angle α between the directions of vectors **P** and $\mathbf{d}\times\mathbf{B}$ (Fig. 4). The observed angular dependence can be described to a high degree of accuracy by the expression

$$E(\mathbf{\Pi}) = \frac{1}{2m^*}\left(\mathbf{P} - \frac{1}{c}\mathbf{d}\times\mathbf{B}\right)^2, \qquad (6)$$

where m^* is the effective mass of principal excitation, obtained from the dispersion dependence depicted in Fig. 3. We verified relations (3)–(5) for the remaining

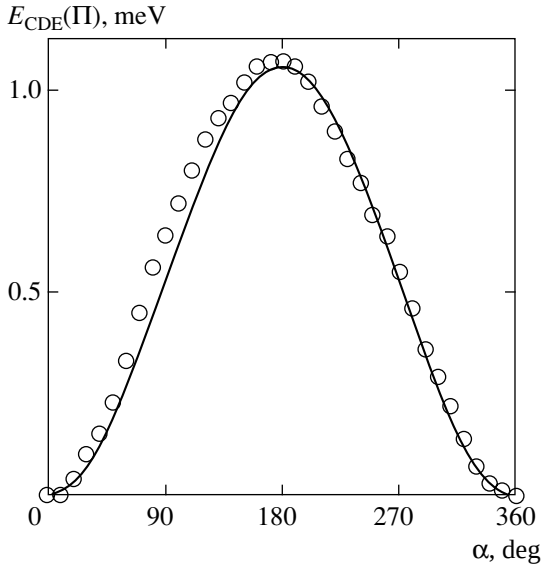

Fig. 4. Kinetic energy E_{CDE} as a function of the angle between the directions of vectors **P** and **d** × **B** for $P = |\mathbf{d} \times \mathbf{B}| = 1 \times 10^5$ cm^{-1}.

intersubband excitations. In spite of the fact that the excitations under investigation differ in the quantum numbers of intrinsic and spin degrees of freedom, they possess the same dipole moments and their dispersion dependences behave analogously. Singe-particle excitations constitute a special case since they are not coupled complexes with natural dispersion. The dispersion relation for single-particle excitations can be obtained from the difference in the dispersion relations of the excited electron and hole and, hence, exhibits a dependence on α different from that for collective excitations. Measurements in the parallel magnetic field essentially make it possible to distinguish collective excitations from single-particle ones, which is a serious experimental problem in the physics of excitations of low-dimensional systems. Single-particle excitations will be investigated in greater detail in Section 6.

4. A SINGLE QUANTUM WELL IN A TILTED MAGNETIC FIELD

Let us now consider dispersion of intersubband excitations in an external magnetic field oriented at an arbitrary angle to the quantum well plane. In this case, the expression for the 2D generalized momentum is analogous to Eq. (1), while the dispersion relations for intersubband excitations are modified. Figures 5 and 6 show spectra of inelastic light scattering from intersubband excitations in a magnetic field with a nonzero component along the quantum well growth axis. Quantities E_{CDE} and E_{SDE} exhibit a weak dependence on the magnetic field, which can be easily understood on account of the fact that the main charge and spin density excitations in a magnetic field are connected with inter-

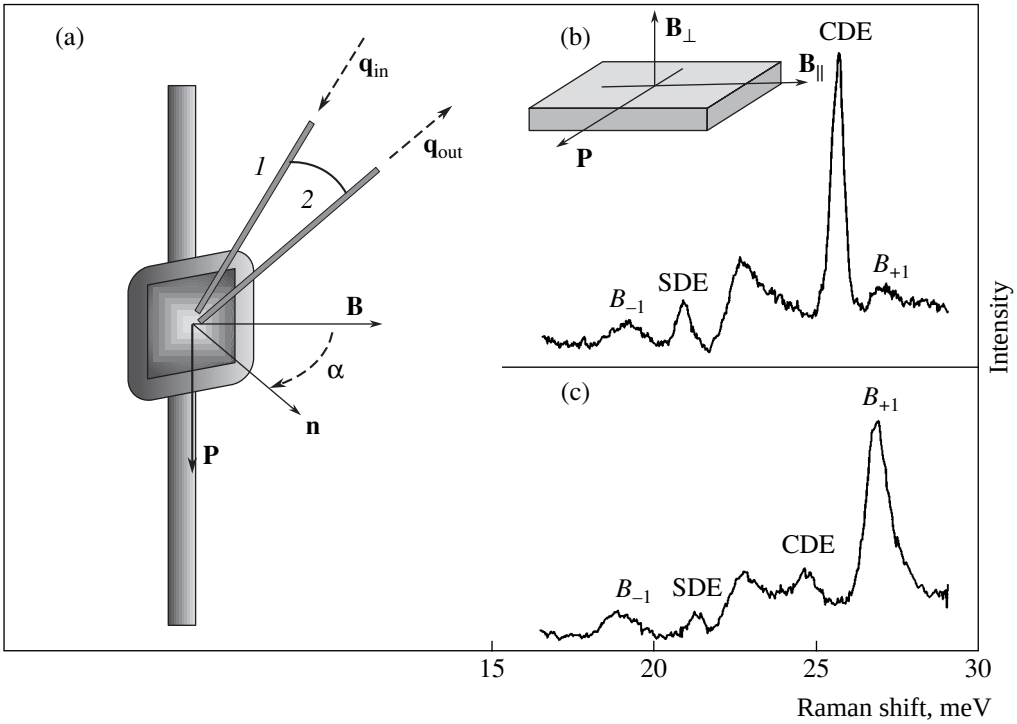

Fig. 5. (a) Schematic diagram of resonant inelastic scattering of light in a tilted magnetic field. The holder and the fibers can be rotated about the vertical axis. (b, c) Spectra of inelastic scattering of light for a sample with a 250-Å-wide quantum well for $n_s = 3.5 \times 10^{11}$ cm^{-2}, measured at $P = c^{-1}dB$, vectors **P** and **d** × **B** are (b) parallel and (c) antiparallel. Mutual orientation of vectors **q** and **B** is shown in the inset to (b).

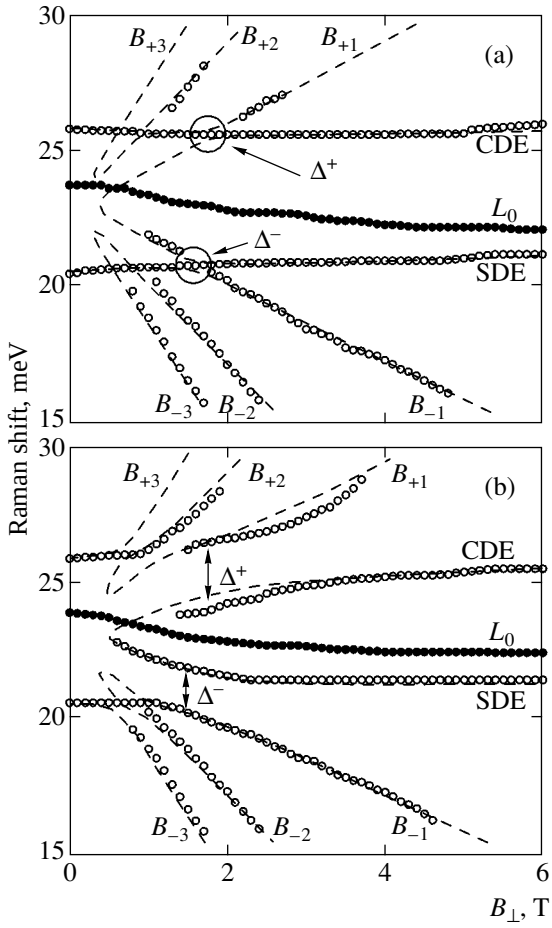

Fig. 6. Spectra of inelastic scattering of light for a sample with a 250-Å-wide quantum well for $n_s = 3.5 \times 10^{11}$ cm^{-2} measured at $P = c^{-1}dB$; vectors **P** and $\mathbf{d} \times \mathbf{B}$ are (a) parallel and (b) antiparallel. The dashed curves describe the results of theoretical calculations of excitation energies in the local density approximation [20] under the assumption that the parallel magnetic field component makes a contribution to the excitation energy only via the gauge term $c^{-1}\mathbf{d} \times \mathbf{B}$; i.e., $P = 0$ (a) and $P = 2 \times 10^5$ cm^{-1} (b). Line L_0 is discussed in [20].

subband transitions conserving the Landau level number. If we disregard the nonparabolicity of the electron effective mass in the subband splitting energy, the energies of all such transitions are equal and independent of the magnetic field. In addition to such excitations lines, the spectrum displays the $B_{\pm n}$ lines that form the negative and positive "fans" of the Landau levels emerging from the intersubband quantization energy. These lines are associated with intersubband Bernstein modes, viz., excitations with simultaneous variation of the size-quantized subband index and the Landau level number. For $q \longrightarrow 0$, their energies can be expressed as

$$E_{B\pm n} = |\Omega \pm n\omega_c|, \quad n \neq 0, \tag{7}$$

where Ω and ω_c are the electron intersubband and cyclotron frequencies [20]. With increasing quasi-momentum, the energies of the B_{+1} (B_{-1}) and CDE (SDE) lines deviate from straight lines in the energy resonance region so that formula (7) becomes inapplicable. It was shown in [20] that the dispersion relations in the resonance regions are linear and determined by the many-particle Coulomb interaction. For this reason, we chose the magnetic field component along the quantum well growth axis (1.5 T) for which the dispersion dependence has the largest slope. As in the case of a parallel magnetic field, dispersion of collective excitations is anisotropic upon a change in the mutual orientations of vectors **P** and $\mathbf{d} \times \mathbf{B}$.

Let us prove that the parallel magnetic field affects the excitation energy only via the gauge term $c^{-1}\mathbf{d} \times \mathbf{B}$. In a magnetic field oriented so that the magnetic field component in the quantum well plane vanishes, we measured the total dispersion $\Delta^\pm$ of intersubband excitations in the resonance region (Fig. 6). If, however, we fix momentum $P = 1 \times 10^5$ cm^{-1} and vary the magnetic field component so that vector $\mathbf{d} \times \mathbf{B}$ is directed along vector **P**, quantity $\Delta^+(|\mathbf{P} - c^{-1}\mathbf{d} \times \mathbf{B}|)$ exhibits the same linear dependence on $c^{-1}\mathbf{d} \times \mathbf{B}$ as that of $\Delta^+(\mathbf{P})$ in the case of zero parallel magnetic field,

$$\Delta^\pm \propto \left|\mathbf{P} - \frac{1}{c}\mathbf{d} \times \mathbf{B}\right|; \tag{8}$$

the dispersion dependence is shifted along the abscissa axis by the momentum of inelastic scattering of light (Fig. 7) and $\Delta^\pm = 0$ for $\mathbf{P} = c^{-1}\mathbf{d} \times \mathbf{B}$, although quantities q and $|\mathbf{d} \times \mathbf{B}|$ differ from zero separately.

Thus, we can conclude that dispersion of intersubband dipole excitations for an arbitrary magnetic field orientation relative to the quantum well plane is determined by the transverse magnetic field component. On the other hand, the parallel component appears only in the generalized momentum of excitations and shifts the dispersion of excitations by $c^{-1}\mathbf{d} \times \mathbf{B}$ in the momentum space. By applying a parallel magnetic field, one can measure the dispersion of intersubband magnetic excitations in the range of momenta unattainable in standard experiments on inelastic scattering of light.

5. A DOUBLE QUANTUM WELL IN A PARALLEL MAGNETIC FIELD

Intersubband excitations in single quantum wells have much in common with interlayer excitations in double quantum wells. However, when the layer index is not a good quantum number any longer (symmetric double wells), the effect of a parallel field on excitations in double and single quantum wells is quite different. We will consider double quantum wells with a weak tunnel coupling between the layers (the Fermi energy of electrons is much higher than the tunnel energy). Figure 8 shows typical light scattering spectra for low-energy neutral excitations in double-layer electron systems (both symmetric and asymmetric). We

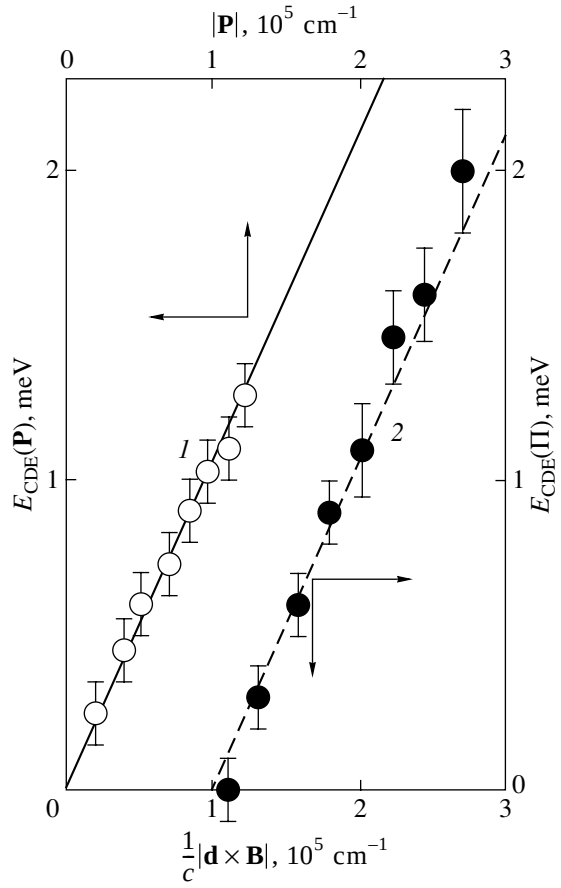

Fig. 7. Energy E_{CDE} for $B_\perp = 1.5$ T as a function of P for $|c^{-1}\mathbf{d}\times\mathbf{B}| = 0$ (*1*) and as a function of $c^{-1}|\mathbf{d}\times\mathbf{B}|$ (vector $\mathbf{d}\times\mathbf{B}$ is parallel to vector $\mathbf{P}$) for $P = 1\times10^5$ cm^{-1} (*2*). The solid line is a linear approximation of experimental points. The dashed line is the same approximation shifted by 1×10^5 cm^{-1}.

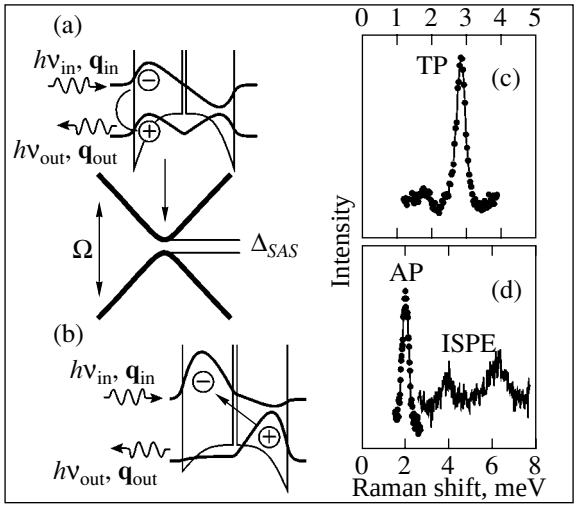

Fig. 8. Schematic of inelastic scattering of light in a double quantum well in the (a) symmetric and (b) asymmetric states. The solid curves describe the electron wavefunctions for two lower size-quantized subbands. The dependence of the intersubband gap Ω on the disbalance of quantum wells is shown schematically by bold curves. Examples of the spectra of inelastic scattering of light in (c) symmetric and (d) asymmetric states of double quantum wells (TP, AP, and ISPE stand for the tunnel plasmon, acoustic plasmon, and interlayer single-particle excitations, respectively).

will call symmetric the state in which the electron system Hamiltonian is specularly symmetric relative to the center of the barrier in a double quantum well. In turn, the state of the electron system is considered asymmetric if the electron wavefunctions of the lowest quantum subbands are concentrated in individual layers; i.e., the indices of the layers and of size-quantized subbands are identical quantum numbers. Strictly speaking, the asymmetric state is correctly defined only in the absence of tunnel coupling between the layers. However, in the case of weak tunneling, there exists a state of asymmetric double quantum well, such that its further asymmetrization does not lead to a change in the wavefunctions (see the diagram in Fig. 9). In this case, the layer indices can be regarded as "good" quantum numbers.

The observed lines of inelastic scattering of light correspond to interlayer (intersubband) single-particle excitations and antisymmetric collective modes, an acoustic plasmon in an asymmetric state, and a tunnel plasmon in a symmetric state. We will not discus collective modes [21] since their energies weakly depend on the parallel field [22], and we will focus our attention on interlayer single-particle excitations. In accordance with the energy and momentum conservation laws, single-particle excitations are in the energy interval $[\Omega - qv_{F_1}, \Omega + qv_{F_1}]$; the inelastic scattering probability is maximal at the boundaries of the interval $\Omega \pm qv_{F_1}$ due to filling of the phase space of the excited subband [23]. Here and below, $v_{F_{1(2)}}$ is the Fermi velocity in the layer with a higher (lower) electron density.

Figure 9 shows the spectra of inelastic light scattering for a sample in a double quantum well in the asymmetric state for two magnetic field orientations in the plane of the wells (along and across the momentum $\mathbf{q}$ of inelastic scattering of light). As in the case of single quantum wells, the energies of interlayer excitations are anisotropic due to the fact that interlayer excitations in the asymmetric states possess a very large dipole moment along the axis of separation between the layers. In accordance with formulas (3)–(5), the energies of one-particle excitations at the boundaries of the continuum are linear functions of the magnetic field and are given by

$$\Omega \pm qv_{F_1} + \frac{1}{c}dBv_{F_1}, \quad \mathbf{q}\parallel\mathbf{B},$$

$$\Omega \pm \left|\mathbf{q} - \frac{1}{c}\mathbf{d}\times\mathbf{B}\right| v_{F_1}, \quad \mathbf{q}\perp\mathbf{B}.$$

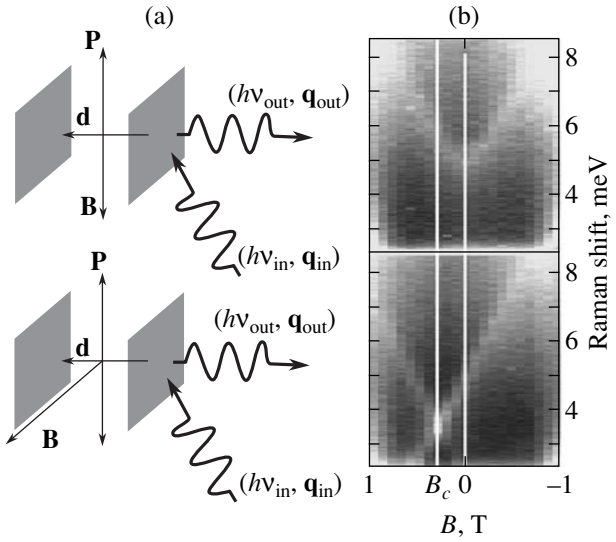

Fig. 9. (a) Schematic diagram of inelastic light scattering in an asymmetric double quantum well in two experimental geometries with a momentum of light parallel (top) and perpendicular (bottom) to the magnetic field vector. (b) Corresponding experimental spectra. Solid curves show the critical and zero magnetic fields.

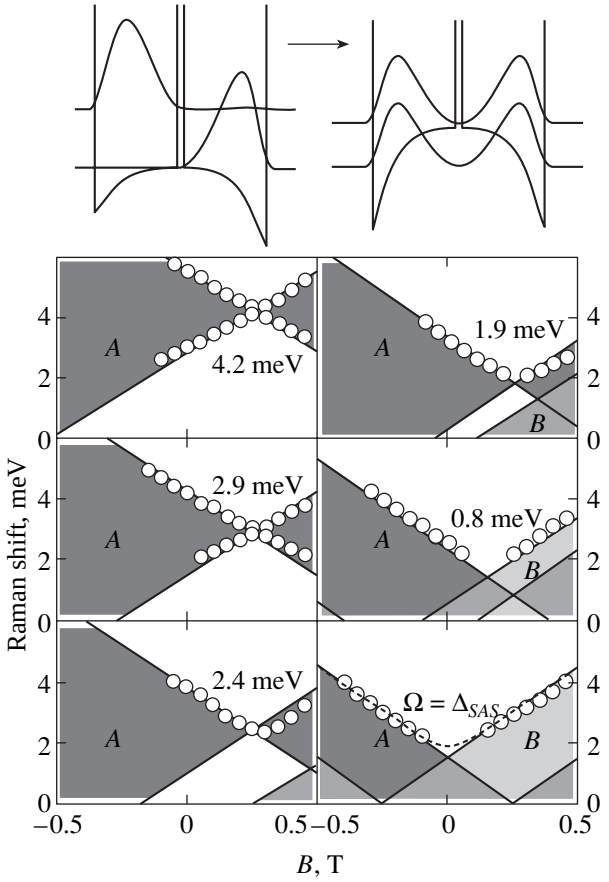

Fig. 10. Variation of the intersubband excitation spectrum in a double quantum well upon a transition from the asymmetric to the symmetric state. The double quantum well confining potential profile and the squares of the electron wavefunctions in the asymmetric (left) and symmetric (right) cases are shown on the top. Dark regions correspond to excitations from the first to the second quantum subband (branch *A*), while light regions denote excitations from the second to the first subband (branch *B*) disregarding tunneling. The regions in which the energies of the two branches coincide are gray. Experimental points are shown by light circles. Intersubband gap Ω for each state is indicated. In the symmetric case ($\Omega = \Delta_{SAS}$), the dashed curve shows the upper boundary of excitations obtained in the tunnel Hamiltonian approximation.

For $\mathbf{q} \perp \mathbf{B}$, the kinetic energies of single-particle excitations are zero in a critical magnetic field of 0.25 T, for which neither $\mathbf{q}$ nor $c^{-1}\mathbf{d} \times \mathbf{B}$ are equal to zero separately. Using the value of the critical magnetic field, the dipole moment of interlayer excitations can be assessed from formula (5) as $e \times 240$ Å, which matches with the distance of 225 Å between the geometrical centers of the quantum wells.

The change in the excitation spectrum upon a transition of a two-layer system to a symmetric state can be grasped qualitatively by considering a nonrealistic model of virtual interlayer excitations between two isolated quantum wells (Fig. 10). The energies of intersubband excitations decrease in proportion to the decrease in intersubband gap Ω. The critical magnetic field (0.25 T) does not change since the dipole moment is constant. A nontrivial situation arises when the term $|\mathbf{q} - c^{-1}\mathbf{d} \times \mathbf{B}|v_{F_2}$ exceeds the intersubband gap Ω. In this case, the spectrum acquires two branches of single-particle excitations corresponding to direct electron transitions from the first to the second subband (branch *A*),

$$\left[\Omega - \left|\mathbf{q} - \frac{1}{c}\mathbf{d} \times \mathbf{B}\right| v_{F_1},\ \Omega + \left|\mathbf{q} - c^{-1}\mathbf{d} \times \mathbf{B}\right| v_{F_1}\right],$$

and reverse transitions from the second to the first subband (branch *B*),

$$\left[0, -\Omega + \left|\mathbf{q} - \frac{1}{c}\mathbf{d} \times \mathbf{B}\right| v_{F_2}\right].$$

The dipole moments corresponding to excitations of both branches are modulo equal but opposite in direction; consequently, an increase in the energy of one branch in a magnetic field is accompanied by a decrease in the energy in the other branch, and vice versa. For a certain value of the system parameters,

$$\Omega < \frac{1}{2}\left(\left|\mathbf{q} - \frac{1}{c}\mathbf{d} \times \mathbf{B}\right| v_{F_2} - \left|\mathbf{q} - \frac{1}{c}\mathbf{d} \times \mathbf{B}\right] v_{F_1}\right),$$

the upper boundary of branch *B* exceeds that for branch *A*, which leads to symmetrization of the excitation spectrum (see Fig. 10).

This model describes virtual interlayer excitations, which have the same dipole moment in any state. In real double quantum wells, the dipole moment of excita-

tions decreases upon symmetrization. Nevertheless, excitation energies experience a shift in magnetic field as if the dipole moment of excitations remained unchanged (see Fig. 10). Such a behavior of the energies of intersubband excitations is associated with the fact that, in contrast to single quantum wells, splitting between the symmetric and antisymmetric subbands in symmetric double quantum wells is smaller than or comparable in magnitude to the magnetic quantization energy in the range of magnetic fields under investigation. Consequently, the magnetic field changes single-particle electron states in quantum wells. We will take into account this change in the framework of the tunnel Hamiltonian approximation [22, 24].

For two tunnel-coupled (generally different) quantum wells a and b, the Hamiltonian of the electron system can be written in the form

$$\begin{aligned} H &= \sum_{\mathbf{k}}\left(E^1_{\mathbf{k}}a^+_{\mathbf{k}}a_{\mathbf{k}} + E^2_{\mathbf{k}}b^+_{\mathbf{k}}b_{\mathbf{k}} - \frac{\Delta_{SAS}}{2}(a^+_{\mathbf{k}}b_{\mathbf{k}} + b^+_{\mathbf{k}}a_{\mathbf{k}})\right) \\ &= \sum_{\mathbf{k}}(\tilde{E}^1_{\mathbf{k}}A^+_{\mathbf{k}}A_{\mathbf{k}} + \tilde{E}^2_{\mathbf{k}}B^+_{\mathbf{k}}B_{\mathbf{k}}), \end{aligned} \tag{9}$$

where

$$E^{1,2}_{\mathbf{k}} = E_0 \pm \frac{\Delta E}{2} + \frac{k^2}{2m} \tag{10}$$

are the energies of electrons in quantum wells without tunneling; E_0 is the electron energy in the lowest quantum subband of a single well; ΔE is the asymmetry parameter; Δ_{SAS} is the tunnel gap; $a^+_{\mathbf{k}}$, $a_{\mathbf{k}}$, $b^+_{\mathbf{k}}$, and $b_{\mathbf{k}}$ are the electron creation and annihilation operators in two layers; and $\mathbf{k}$ is the electron momentum in the plane of the well. This approximation is applicable for $E_0 \gg \Delta_{SAS}$ and $E_0 \gg \Delta E$; i.e., the electron wavefunctions ψ_a and ψ_b in each well vary only slightly as functions of these parameters.

The electron energies in the subbands are given by

$$\tilde{E}^{1,2}_{\mathbf{k}} = E_0 + \frac{k^2}{2m} \pm \frac{1}{2}\sqrt{\Delta E^2 + \Delta^2_{SAS}}. \tag{11}$$

The electron wavefunctions in the subbands in the z direction are given by

$$\begin{aligned} \Psi_i &= C^i_a\psi_a(z) + C^i_b\psi_b(z), \quad i = 1, 2, \\ C^i_a &= \frac{\Delta_{SAS}}{\sqrt{\Delta^2_{SAS} + 4(E^1_{\mathbf{k}} - \tilde{E}^i_{\mathbf{k}})^2}}, \\ C^i_b &= \frac{2(E^1_{\mathbf{k}} - \tilde{E}^i_{\mathbf{k}})}{\sqrt{\Delta^2_{SAS} + 4(E^1_{\mathbf{k}} - \tilde{E}^i_{\mathbf{k}})^2}}, \end{aligned} \tag{12}$$

and are independent of momentum $\mathbf{k}$. In the symmetric case, we have

$$\begin{aligned} \Psi_1 &= \frac{1}{\sqrt{2}}[\psi_a(z) - \psi_b(z)], \\ \Psi_2 &= \frac{1}{\sqrt{2}}[\psi_a(z) + \psi_b(z)]. \end{aligned} \tag{13}$$

For $\Delta_{SAS} \ll \Delta E$, we obtain

$$\Psi_1 = \psi_a(z), \quad \Psi_2 = \psi_b(z). \tag{14}$$

In a parallel magnetic field $\mathbf{B} = (0, B, 0)$, the tunnel Hamiltonian for $\Delta E_c \ll E_0$ has the form

$$\begin{aligned} H &= \sum_{\mathbf{k}}\left[E^1_{\mathbf{k}}(B)a^+_{\mathbf{k}}a_{\mathbf{k}} + E^2_{\mathbf{k}}(B)b^+_{\mathbf{k}}b_{\mathbf{k}}\right. \\ &\quad \left. - \frac{\Delta_{SAS}}{2}(a^+_{\mathbf{k}}b_{\mathbf{k}} + b^+_{\mathbf{k}}a_{\mathbf{k}})\right] \\ &= \sum_{\mathbf{k}}[\tilde{E}^1_{\mathbf{k}}(B)A^+_{\mathbf{k}}A_{\mathbf{k}} + \tilde{E}^2_{\mathbf{k}}(B)B^+_{\mathbf{k}}B_{\mathbf{k}}], \end{aligned} \tag{15}$$

where

$$E^{1,2}_{\mathbf{k}}(B) = E_0 \pm \frac{\Delta E}{2} + \frac{(k_x \mp k_B)^2 + k_y^2}{2m}, \tag{16}$$

$k_B = eaB/c$, $2a = z_a - z_b$ is the distance between the centers of the layers. The electron energies assume the form

$$\begin{aligned} \tilde{E}^{1,2}_{\mathbf{k}}(B) &= E_0 + \frac{k^2 + k_B^2}{2m} \\ &\pm \frac{1}{2}\sqrt{\left(\Delta E - \frac{2k_xk_B}{m}\right)^2 + \Delta^2_{SAS}}. \end{aligned} \tag{17}$$

The electron wavefunctions are transformed analogously with the substitution $E^{1,2}_{\mathbf{k}} \longrightarrow E^{1,2}_{\mathbf{k}}(B)$ and $\tilde{E}^{1,2}_{\mathbf{k}} \longrightarrow \tilde{E}^{1,2}_{\mathbf{k}}(B)$, thus acquiring a dependence on $\mathbf{k}$. Depending on the direction of the electron momentum, the wavefunctions may be independent of magnetic field (for $k_x = 0$) or may vary with the field (for $k_x \neq 0$). For example, for $\Delta E = 0$, when the wavefunctions in the subbands in zero field are symmetric and antisymmetric combinations, the magnetic field under weak tunneling ($2k_xk_B/m \gg \Delta_{SAS}$) leads to almost complete localization of electrons in individual wells.

Let us now consider single-particle intersubband excitations with small excitation momenta $\mathbf{q}$ in a weak magnetic field ($q \ll k_F$, $k_B \ll k_F$). The energy of excita-

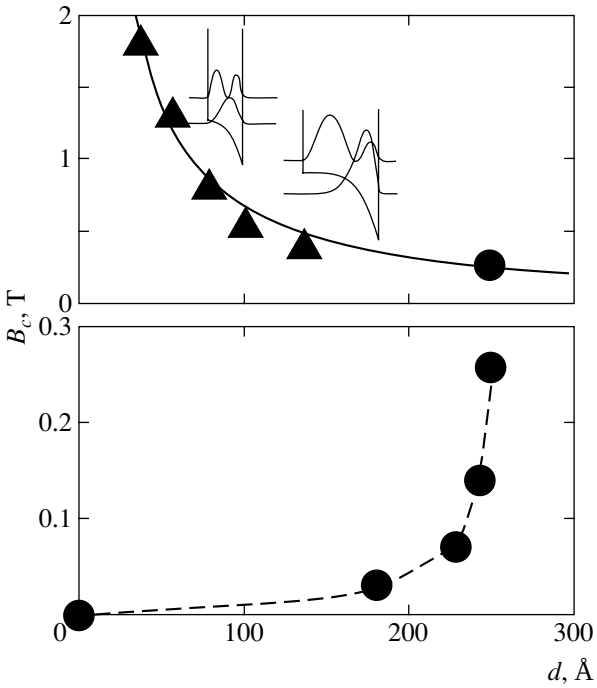

Fig. 11. Critical magnetic field as a function of the dipole moment for a single (triangles) and double (circles) quantum wells. The profile of the confining potential and the squares of the electron wavefunctions in the two lowest size-quantized subbands of single quantum wells, corresponding to the widest and narrowest wells, are shown schematically.

tions corresponding to transitions from the lower to the upper subband (or back) has the form

$$E_{\mathrm{ISPE}} = \left|\frac{\mathbf{k}_F\cdot\mathbf{q}}{m} + \sqrt{\left(\Delta E - \frac{2k_{Fx}k_H}{m}\right)^2 + \Delta_{SAS}^2}\right|. \quad (18)$$

Single-particle excitations form a continuum with a density of states peak at $\cos(\widehat{\mathbf{k}_F, \mathbf{q}}) = \pm 1$. Consequently, two excitation branches corresponding to angles $(\widehat{\mathbf{k}_F, \mathbf{q}}) = 0, \pi$. For $\Delta_{SAS} \gg |\Delta E|$ and $\Delta_{SAS} \gg |2k_Fk_B/m|$, the energies of both excitation branches can be represented in the form

$$E_{\mathrm{ISPE}}^{\pm} = \Delta_{SAS} \pm \frac{k_F q}{2m} + \frac{1}{2\Delta_{SAS}}\left(\Delta E \mp \frac{2k_Fk_B}{m}\right)^2. \quad (19)$$

For $\Delta_{SAS} \longrightarrow 0$ and $\Delta E \neq 0$, we have interlayer excitations with dipole moments $\pm\mathbf{d}$, $\mathbf{d} = (0, 0, 2ea)$. Specific expressions for transition energies are determined by the relations between the quantities ΔE, qv_F, and $c^{-1}dBv_F$. For example, for $\Delta E > c^{-1}dBv_F$, we have

$$E_{\mathrm{ISPE}}^{+} = \left|\Delta E \pm \left(q - \frac{1}{c}dB\right)v_F\right|. \quad (20)$$

In the symmetric case with weak tunneling, due to rearrangement of wavefunctions, intersubband excitations can be treated as interlayer excitations with a dipole moment (acquired in the given case in a parallel magnetic field) everywhere except a small range of magnetic fields, in which $\Delta_{SAS} \sim 2k_Fk_B/m$:

$$E_{\mathrm{ISPE}}^{\pm} = \left|q \pm \frac{1}{c}dB\right|v_F. \quad (21)$$

In this case, excitations corresponding to two interlayer transitions are combined into two branches so that they correspond to intersubband excitations in zero magnetic field. The critical magnetic field for the common branches is not defined by formula (5), but is zero (see Fig. 10).

It is expedient to compare the critical magnetic fields for double-layer and single-layer systems as functions of the dipole moment in zero magnetic field (Fig. 11). The dipole moment can be determined by using the electron wavefunctions obtained self-consistently from one-dimensional Poisson and Schrödinger equations by varying the asymmetry so that the calculated intersubband energy Ω becomes equal to the experimental energy. From the known wavefunctions, we can find the dipole moment

$$\mathbf{d} = -e|z_{00} - z_{11}|\mathbf{n}, \quad (22)$$

where $\mathbf{n}$ is the normal to the quantum well plane,

$$z_{00} - z_{11} = \int dz\psi_0^*(z)z\psi_0(z) - \int dz\psi_1^*(z)z\psi_1(z)$$

is the mean distance between electrons in two subbands, and $\psi_n(z)$ is the z component of the electron wavefunction in the nth subband. In a single-layer system, the dipole moment decreases with the well width (see Fig. 11). In a double-layer system, the dipole moment decreases upon symmetrization of the system (see Fig. 10). The two systems (single- and double-layer) differ in the effect of a parallel magnetic field on the electron states in the size-quantized subbands. The magnetic field completely transforms the wavefunctions in the double-layer system, while the magnetic field in the single layer system hardly affects the wavefunctions. As a result, the critical magnetic field is inversely proportional to the dipole moment for a single layer system, which is in accordance with expression (5), while the critical field tends to zero upon symmetrization of a double-layer system (see Fig. 11).

Inelastic scattering of light from single-particle excitations in a parallel magnetic field can be used for determining the asymmetry of a double-layer electron system. For example, electron density disbalance of two layers by just 3% transforms a symmetric electron system into an asymmetric one [21]. In view of such a small balancing range, a symmetric state can hardly be established with the help of the standard magnetotransport balancing procedure [25, 26]. On the other hand, the dipole moment associated with the system asymme-

try can be easily measured using inelastic light scattering. To transform a double-layer system into a symmetric state, we must transfer a finite momentum to electron excitations and balance the system until the excitation energies become symmetric to magnetic field inversion. The accuracy of this method is determined by the relation between the inelastic light scattering linewidth and the tunnel energy. According to experimental estimates, the electron system can be balanced in double quantum wells with a tunnel energy of up to 0.1 meV.

6. CONCLUSIONS

It has been shown that dispersion of intersubband excitations in a quantum well placed in a parallel magnetic field is anisotropic. The anisotropic contribution to energy is a linear function of the magnetic field and the momentum of excitations. The method for determining the dipole moment of excitations, which characterizes the asymmetry of the confining potential, has been demonstrated. The symmetry between the magnetic-field-induced shift in the momentum space and excitation momentum opens a unique possibility for studying the dispersion of intersubband excitations; the experimentally accessible range of momenta can be doubled thereby. In addition, this makes it possible to eliminate a serious experimental problem associated with a change in the excitation momentum by using an experimental configuration similar to that used in this article, in which the momentum is fixed while the parallel field varies. It has been shown that interlayer (intersubband) excitations in double quantum wells in an asymmetric state possess a large dipole moment and their behavior in a parallel magnetic field is analogous to the behavior of intersubband excitations in single quantum wells. In the symmetric case, on the contrary, the magnetic field transforms the electron wavefunctions so that excitation energies acquire an anisotropic component, and excitations themselves become effectively interlayer excitations. A new method has been proposed for measuring the asymmetry of double layers.

ACKNOWLEDGMENTS

This study was financed by the Russian Foundation for Basic Research (project no. 04-02-17393).

REFERENCES

1. W. Lamb, Phys. Rev. **85**, 259 (1952); L. P. Gor'kov and I. E. Dzyaloshinskiĭ, Zh. Éksp. Teor. Fiz. **53**, 717 (1967) [Sov. Phys. JETP **26**, 449 (1968)].
2. B. R. Johnson, J. O. Hirschfelder, and K.-H. Yang, Rev. Mod. Phys. **55**, 109 (1983).
3. J. E. Avron, I. W. Herbst, and B. Simon, Ann. Phys. (New York) **114**, 431 (1978).
4. I. V. Lerner and Yu. E. Lozovik, Zh. Éksp. Teor. Fiz. **78**, 1167 (1980) [Sov. Phys. JETP **51**, 588 (1980)].
5. C. Kallin and B. I. Halperin, Phys. Rev. B **30**, 5655 (1984).
6. I. Dzyaloshinskii, Phys. Lett. A **165**, 69 (1992).
7. X. G. He and B. H. J. McKellar, Phys. Rev. A **47**, 3424 (1993); M. Wilkens, Phys. Rev. Lett. **72**, 5 (1994); J. P. Dowling, C. P. Williams, and J. D. Franson, Phys. Rev. Lett. **83**, 2486 (1999).
8. A. B. Dzyubenko and A. Yu. Sivachenko, Phys. Rev. Lett. **84**, 4429 (2000).
9. A. Parlangeli, P. C. M. Christianen, J. C. Maan, *et al.*, Phys. Rev. B **62**, 15323 (2000); L. V. Butov, C. W. Lai, D. S. Chemla, *et al.*, Phys. Rev. Lett. **87**, 216804 (2001).
10. K. Muraki, T. Saku, and Y. Hirayama, Phys. Rev. Lett. **87**, 196801 (2001).
11. I. B. Spielman, J. P. Eisenstein, L. N. Pfeiffer, and K. W. West, Phys. Rev. Lett. **87**, 036803 (2001); M. Kellogg, J. P. Eisenstein, L. N. Pfeiffer, and K. W. West, Phys. Rev. Lett. **93**, 036801 (2004).
12. L. V. Kulik, I. V. Kukushkin, V. E. Kirpichev, *et al.*, Phys. Rev. B **61**, 1712 (2000).
13. L. V. Kulik, I. V. Kukushkin, V. E. Kirpichev, *et al.*, Phys. Rev. B **66**, 073306 (2002).
14. S. V. Tovstonog, L. V. Kulik, V. E. Kirpichev, *et al.*, Pis'ma Zh. Éksp. Teor. Fiz. **78**, 1151 (2003) [JETP Lett. **78**, 654 (2003)].
15. L. V. Kulik, I. V. Kukushkin, S. V. Tovstonog, *et al.*, Phys. Rev. B **71**, 165303 (2005).
16. I. V. Kukushkin and V. B. Timofeev, Adv. Phys. **45**, 147 (1996).
17. A. Pinczuk, S. Schmitt-Rink, G. Danan, *et al.*, Phys. Rev. Lett. **63**, 1633 (1989).
18. D. Gammon, B. V. Shanabrook, J. C. Ryan, *et al.*, Phys. Rev. Lett. **68**, 1884 (1992).
19. S. Ernst, A. R. Goni, K. Syassen, and K. Eberl, Phys. Rev. Lett. **72**, 4029 (1994).
20. V. E. Kirpichev, L. V. Kulik, I. V. Kukushkin, *et al.*, Phys. Rev. B **59**, R12751 (1999).
21. L. V. Kulik, S. V. Tovstonog, V. E. Kirpichev, *et al.*, Phys. Rev. B **70**, 033304 (2004).
22. G. Gumbs and G. R. Aĭzin, Phys. Rev. B **51**, 7074 (1995); G. R. Aĭzin and G. Gumbs, Phys. Rev. B **54**, 2049 (1996).
23. J. K. Jain and S. Das Sarma, Phys. Rev. B **36**, 5949 (1987).
24. A. A. Gorbatsevich and I. V. Tokatly, Semicond. Sci. Technol. **13**, 288 (1998).
25. J. A. Simmons, S. K. Lyo, J. F. Klem, *et al.*, Phys. Rev. B **47**, 15741 (1993); J. A. Simmons, S. K. Lyo, N. E. Harff, and J. F. Klem, Phys. Rev. Lett. **73**, 2256 (1994).
26. N. E. Harff, J. A. Simmons, S. K. Lyo, *et al.*, Phys. Rev. B **55**, R13 405 (1997).

Translated by N. Wadhwa

Journal of Experimental and Theoretical Physics, Vol. 101, No. 4, 2005, pp. 728–740.
Translated from Zhurnal Éksperimental'noĭ i Teoreticheskoĭ Fiziki, Vol. 128, No. 4, 2005, pp. 844–858.

STATISTICAL, NONLINEAR, AND SOFT MATTER PHYSICS

Self-Action of Laser Radiation in Cluster Plasma

N. A. Zharova*, A. G. Litvak, and V. A. Mironov

Institute of Applied Physics, Russian Academy of Sciences, ul. Ul'yanova 46, Nizhni Novgorod, 603950 Russia
**e-mail: zhani@appl.sci-nnov.ru*

Received June 17, 2004

Abstract—We have analytically and numerically studied the self-action dynamics of laser radiation in a plasma with ionized gas clusters. Based on the simplified model of a cluster in the form of a superposition of two charged (electron and ion) bunches, we analyze the nonlinearity mechanisms. We refine the electrodynamic cluster model by the molecular dynamics method. The polarization behavior of the plasma bunch in the main part of the laser pulse is shown to be the same as that in the simplified model. We investigate the self-action dynamics of laser radiation under conditions when the nonlinearity of the stratified medium is determined by the anharmonicity of the electron motion in the cluster, while the group velocity dispersion is determined by both the background plasma and the ionized clusters. Since the characteristic field for the electron nonlinearity depends strongly on the cluster size, the peculiarities of the self-action dynamics result from plasma bunch expansion. The spatiotemporal evolution of the wave field is shown to be accompanied by pulse self-compression near the trailing edge. © *2005 Pleiades Publishing, Inc.*

1. INTRODUCTION

Experimental studies of the interaction between laser radiation and cluster targets have become particularly topical in recent years in connection with prospects for solving such important application problems as the initiation of nuclear reactions, the acceleration of charged particles, and the production of an intense X-ray source for biomedical applications (see, e.g., [1–5]). Cluster targets are materials composed of a random set of atomic and molecular clusters. The great variety of structural features of cluster targets is determined by the properties of chemical elements and by the Van der Waals interaction between molecules. A broad class of atoms forms a condensed phase with free electrons, i.e., a system with "metallic" nanoirregularities [6]. For a number of chemical elements, a cluster is a stable structure with a definite number of atoms and their mutual spatial arrangement [7]. Since the interaction between atoms has anisotropic properties, fractal (porous) clusters can be formed [8]. Gas cluster targets are mainly used in laser radiation–material interaction experiments. Clusters are formed in them during the expansion of a dense jet of rare gases into a vacuum. Such a cluster target composed of condensed rare-gas atoms had the practical advantages of gas targets, while making it possible to realize the processes characteristic of a medium with a density close to the solid density. Such effects as the formation of multiply charged ions with completely vacant inner shells (hollow ions) [5], the generation of high harmonics [9], and the generation of ions with energies above 1 MeV [3] at radiation intensities lower than those in a homogeneous gas were observed using cluster targets. The interaction of laser radiation with a cluster plasma is usually interpreted based on the model of an isolated cluster in a strong electric field. However, the observation of wave-field self-focusing in a cluster plasma [5, 10] indicates that the radiation–medium interaction is self-consistent in nature. This problem is discussed in [10, 11].

In this paper, we investigate the self-action of an ultrashort laser pulse in a nanodispersed cluster plasma. After the formulation of the problem (Section 2), in Section 3, we consider the polarization dynamics of a plasma bunch in an electric field. The nonlinearity mechanisms of a nanodispersed medium are discussed in Section 4. The final section presents the results of our numerical simulations of the self-consistent evolution of an ultrashort laser pulse in a stratified medium. In the Conclusions, we discuss the relationship between the theory and the experimentally observed peculiarities of the laser self-focusing in a cluster plasma.

2. FORMULATION OF THE PROBLEM

The electrodynamic model of the interaction between ultrashort laser pulses and clusters is based on the following assumptions. Almost all of the electrons at the pulse leading edge are removed from their atoms, remaining inside the cluster. This inner ionization produces a fine-dispersed medium composed of plasma bunches and a background plasma. Subsequently, the ionized clusters expand and lose some of their electrons into the surrounding space; i.e., outer ionization takes place. Experimental studies show that the characteristic lifetime of a plasma bunch is ~100–300 fs [3, 10] and that the main part of a femtosecond laser pulse propagates in a rare plasma with ionized clusters in which the electron density exceeds its critical value. In the linear regime of interaction, the electrodynamic properties of a cluster plasma for laser wavelengths that appreciably

exceed the characteristic separation between the clusters, $\lambda \gg L_c$, can be analyzed in the approximation of an effective refractive index of the medium n_{eff} [12]. For spherical clusters with a uniform plasma distribution, the refractive index is

$$n_{\text{eff}}^2 = n_{\text{bg}}^2 + \mathcal{V}\frac{\varepsilon_c - 1}{\varepsilon_c + 2}. \quad (1)$$

Here,

$$n_{\text{bg}}^2 = 1 - \omega_{\text{bg}}^2/\omega^2$$

is the background plasma permittivity, ω is the wave frequency,

$$\omega_{\text{bg}}^2 = 4\pi e^2 N_{\text{bg}}/m,$$

N_{bg} is the background plasma electron density, $\mathcal{V}$ is the relative volume occupied by the clusters,

$$\varepsilon_c = 1 - \omega_{\text{p}}^2/\omega^2$$

is the cluster plasma permittivity,

$$\omega_{\text{p}}^2 = 4\pi e^2 N/m,$$

and N is the cluster electron density.

To investigate the self-action of laser radiation in a cluster plasma, we will primarily use the parameters of the medium and the laser pulse in a self-focusing experiment [10]. This experiment was carried out using laser radiation with a wavelength of 800 nm, an intensity of 5×10^{15} W cm^{-2}, and a pulse duration of 100 fs in a medium with clusters 30 nm in diameter.

Figure 1 shows a plot of the effective refractive index squared (1) against the field frequency. We see from this figure that the presence of ionized clusters leads to a noticeable modification of the eigenmode spectrum near the geometrical resonance of the plasma bunch. For waves with frequencies

$$\omega \le \omega_c = \omega_{\text{p}}/\sqrt{3},$$

the refractive index of a nanodispersed medium is larger than unity ($n_{\text{eff}} > 1$); hence, the resonant interaction of electromagnetic radiation with plasma particles becomes possible [13] The dispersion of the pulse group velocity v_g is normal ($\partial v_g/\partial\omega < 0$) in this frequency range and anomalous ($\partial v_g/\partial\omega > 0$) at higher frequencies, as in a homogeneous plasma.

We use an approach that is popular in electrodynamics of continuous media to construct the self-consistent picture of the interaction between laser radiation and a cluster plasma. Initially, based on a model of the medium, we determine the (linear and nonlinear) responses of the macrosystem to the presence of a field. Subsequently, we find the nonlinear field modification

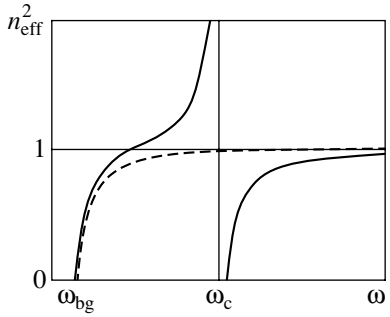

Fig. 1. Effective refractive index squared n_{eff}^2 versus frequency of the incident radiation ω. The dashed line indicates the corresponding dependence in the absence of clusters.

using the Maxwell equations in a medium whose permittivity depends on the radiation intensity. Since the constitutive equations are complex, we use simplified models that reflect the structural features of the medium at the initial stage of our study of the characteristic features of the radiation–material interaction. This description of the macrosystem is successful, because the effective permittivity of the medium (e.g., (1)) is averaged over a volume containing quite a few microirregularities and, hence, depends weakly on the fine structural features of the material. To derive the constitutive equations (2) in a cluster plasma, we use and substantiate the model of a nonlinear oscillator in Section 3. Clearly, in the linear approximation, Eq. (1) for the effective permittivity can be easily derived by using this model and by taking into account the contribution of the background plasma to the polarization of the medium. Subsequently, in Section 4, we consider the nonlinearity mechanisms that lead to radiation self-action and determine the characteristic fields for these effects and relaxation times. Finally, in Section 5, we consider the self-consistent picture of the spatiotemporal evolution of an ultrashort laser pulse in a nanodispersed medium under typical conditions of cluster nonlinearity and group velocity dispersion of the medium determined by both the ionized clusters and the background plasma.

3. CLUSTER POLARIZATION DYNAMICS

When the interaction of laser pulses with a cluster plasma is investigated, two stages of the process that differ greatly in pattern should be distinguished. At the first stage, which is strongly nonstationary and takes a time of the order of several field oscillation periods, inner ionization of clusters takes place and plasma bunches are formed. The subsequent (main) part of the pulse propagates in a strongly inhomogeneous medium composed of expanding plasma bunches.

Let us next consider the dynamical processes in the model of an isolated cluster in an external variable electric field. First, we will analyze the polarization behav-

ior of the medium using the simplified model of a spherical cluster and then consider a more rigorous model that includes both the cluster ionization and its structural changes. In both cases, we will assume that the cluster size is much smaller than the wavelength. This condition is satisfied in experiments on the interaction of laser radiation with cluster targets and allows the processes in an isolated cluster to be considered under the assumption that the external electric field is uniform.

3.1. Polarization Dynamics of a Spherical Cluster

To find the nonlinear response of the medium at the laser frequency, let us first consider the simplified model of a cluster[1] in the form of a superposition of two uniformly charged spheres of radius a: positively charged "heavy" and negatively charged "light" spheres. In the presence of an external electric field $E(t)$, the charged-particle density n increases and the cluster is polarized. The displacement x of the center of mass of the electron subsystem along the field is described by the equation[2]

$$\frac{d}{dt}\left(a^3 n\frac{dx}{dt}\right) + \omega_c^2\frac{a^6 nx}{(x^2+a^2)^{3/2}} = \frac{ena^3}{m}E(t), \qquad (2)$$

where the oscillation eigenfrequency $\omega_c = \omega_p/\sqrt{3}$ of the electron subsystem (the dipole resonance frequency of the sphere) was introduced. The change in plasma density inside a cluster during the ionization of atoms is a rather complex process. The various (tunneling, above-barrier, thermal, etc.) ionization mechanisms are discussed in detail in [14]. However, for our purposes, determining the (linear and nonlinear) dipole moment that emerges during field cluster ionization proves to be sufficient for the ionization to be fast near the pulse leading edge. We will describe the actual cluster ionization process by a model field dependence of ionization,

$$\frac{\partial n}{\partial t} = 4\omega_a(n_a - n)\frac{E_a}{|E|}\exp\left(-\frac{2E_a}{3|E|}\right), \qquad (3)$$

where ω_a is the atomic frequency, n_a is the atomic density in the cluster, and E_a is the atomic field ($E_a = e/r_a^2$, r_a is the atomic size). Here, it is important that the plasma density at electric fields of the order of the atomic fields reaches a stationary value, $n = n_a$, on time scales shorter than the duration of the pulse leading edge. Below, we will compare the results obtained using this simple model with our numerical simulations of the ionization kinetics by the molecular dynamics method (see Section 3.2). It is convenient to represent the system of equations (2) and (3) in dimensionless form:

$$\frac{d}{dt}\left(a^3 n\frac{dx}{dt}\right) + \frac{a^3 nx}{(x^2/a^2+1)^{3/2}} = \delta\frac{na^3}{q}E(t), \qquad (4)$$

$$\frac{\partial n}{\partial t} = \alpha(1-n)\frac{1}{|E|}\exp(-2/3|E|), \qquad (5)$$

where we normalized the displacement x and the cluster size a to the initial cluster size a_0 ($x/a_0 \longrightarrow x$, $a/a_0 \longrightarrow a$), the density n to the maximum charged-particle density equal to the atomic density n_a in the cluster ($n/n_a \longrightarrow n$), and the electric field E to the atomic field; the variable t is related to the dimensional time as $t \longrightarrow \omega_c t$; and the parameters α, δ, and q are defined by the relations

$$\alpha = 4\omega_a/\omega_c, \quad \delta = r_a/a_0, \quad q = 4\pi n_0 r_a^3/3$$

(q is the total number of ionized particles in the volume of the atom).

Let us consider the behavior of a cluster in an external harmonic electric field

$$E(t) = E_0(t)\cos\omega t.$$

For a stationary ionized cluster ($a = 1$, $n \approx 1$) in the linear regime ($x \ll a = 1$), Eq. (4) describes the forced oscillations with the frequency of the external field ω and the free oscillations with the frequency $\omega_c = 1$ excited during cluster ionization. Under the experimental conditions, the external electric field is a low-frequency one, $\omega \approx 0.1\omega_c \ll \omega_c$. At electric fields of the order of the atomic fields, the inner cluster ionization occurs on time scales much shorter than the period of free oscillations. This implies that the interaction of the incident radiation with the plasma is nonadiabatic. Since the plasma density in the cluster increases much faster than the field amplitude, let us estimate the amplitude of the free oscillations in the approximation of instantaneous ionization. Assuming that $a = 1$ and

[1] The simplified cluster model was used previously in [15] to study the harmonic generation effects in a cluster plasma.

[2] Equation (2) describes the dynamics of a plasma bunch with a variable number of particles and, in fact, implies that the particles at the time of their production (or loss) have a velocity equal to the mean velocity of the distribution. This approximation is adequate to allow for the particle losses through outer ionization. The appearance of new particles via ionization will be taken into account more accurately if the density n in the first term on the left-hand side of Eq. (2) is placed under the sign of the time derivative. This corresponds to the production of electrons with a zero velocity at the point with $x = 0$. Note, however, that this inaccuracy has virtually no effect on the results at the high ionization rate that takes place for intense ultrashort laser pulses.

$n = \theta(t - t_0)$ ($\theta(t)$ is the Heaviside unit step function) in Eq. (3), we find the amplitude of the free oscillations

$$A_0 = \frac{\delta E(t_0)}{q(\omega_c^2 - \omega^2)} \approx \frac{dE(t_0)}{q}$$

and the amplitude of the forced oscillations

$$A = \frac{\delta E_0(t)}{q}.$$

Thus, the dipole moment of the free cluster oscillations is of the same order of magnitude as that at the frequency of the external field.

The radiative damping time scale ($\tau_r \approx ((ka)^3\omega_c)^{-1}$, where k is the wave number) of the free oscillations even for large clusters is

$$\tau_r = 10^2(2\pi/\omega_c) \sim 10^3(2\pi/\omega); \quad (6)$$

i.e., it exceeds the duration of the femtosecond laser pulses used. However, the amplitude of the free oscillations can change as the ionized cluster expands. At a fixed total number of particles inside the cluster, the frequency of the free oscillations decreases proportionally to $a^{-3/2}$. In accordance with the adiabatic invariant, their amplitude increases rather slowly (proportionally to $a^{3/4}$). At the same time, the amplitude of the forced oscillations increases much faster:

$$A \approx \delta\frac{a^3}{q}E_0(t), \quad (7)$$

i.e., proportionally to a^3. As a result, the free oscillations become invisible against the background of the forced oscillations in a certain time, and their contribution to the polarization can be disregarded.

Our numerical analysis of the system of equations (4) and (5) in an external periodic electric field

$$E(t) = E_0(1 - \exp(-\gamma t))\cos\omega t \quad (8)$$

with a relaxation time scale of $1/\gamma$ confirms the results of the above qualitative analysis of the cluster polarization dynamics. The initial conditions were chosen to be the following:

$$x(t) = 0, \quad \frac{dx}{dt}(t = 0) = 0, \quad n(t = 0) = 0. \quad (9)$$

The calculations were performed for $\omega = 0.1$, $E_0 = 0.3$, and $\alpha = 10$. Figure 2 shows the time evolution of velocity for a cluster expanding as

$$a = 1 + 0.003t.$$

The expansion coefficient, $\beta = 0.003$, was chosen in such a way that the electron plasma frequency in the ionized cluster decreased to the frequency of the external field at a time equal to 2/3 of the laser pulse duration. We see (inset to Fig. 2) the excitation of intense free oscillations at the leading edge.

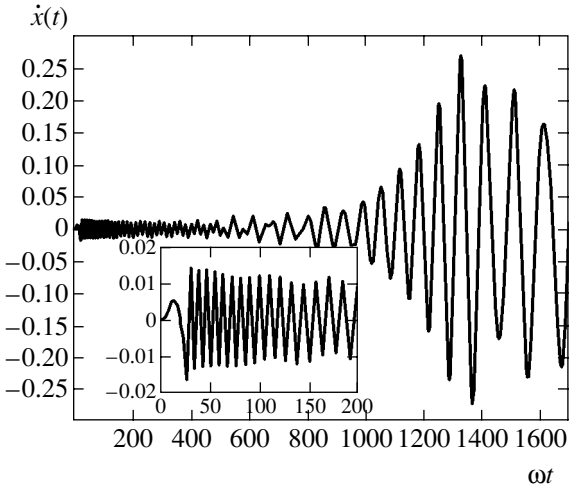

Fig. 2. The oscillation dynamics of an expanding cluster exposed to an external quasi-harmonic electric field. At $\omega t > 1350$, the linear oscillatory regime becomes nonlinear, which is accompanied by the stabilization of the oscillation amplitude. The inset illustrates the evolution of the cluster at the initial stage immediately after its ionization.

As the cluster expands, the amplitude of the forced oscillations increases as (7) to values at which the electron nonlinearity begins to play a stabilizing role. The transition between the linear ($x \propto a^3$) and nonlinear ($x \propto a$) regimes is clearly seen in Fig. 2 and occurs (for the parameters used in our numerical calculations) at $\omega t > 1350$. On these time scales, the oscillator frequency decreases to the frequency of the external field, but the free oscillations are excited weakly, since the process is nonstationary. An increase in external field E_0 leads to an increase in oscillation amplitude to values on the order of the plasma bunch size a and to the subsequent detachment of the electron component from the ion component, i.e., to the cluster decay. In what follows, we will consider the interaction of ultrashort laser pulses of moderate intensity at which the nonlinearity is weak with clusters.

3.2. A Kinetic Model of the Cluster Dynamics

Simulations of the processes by the molecular dynamics method are increasingly used to study the kinetic effects in a cluster [16]. Despite its well-known shortcomings, we investigated the polarization dynamics of a cluster in an external electric field by this method. Our numerical calculations show the following. During its evolution, the cluster loses its electrons (outer ionization takes place) and expands (predominantly in the direction of the external field); these processes prove to be mutually stimulating. The electron cloud oscillates at the frequency of the external field

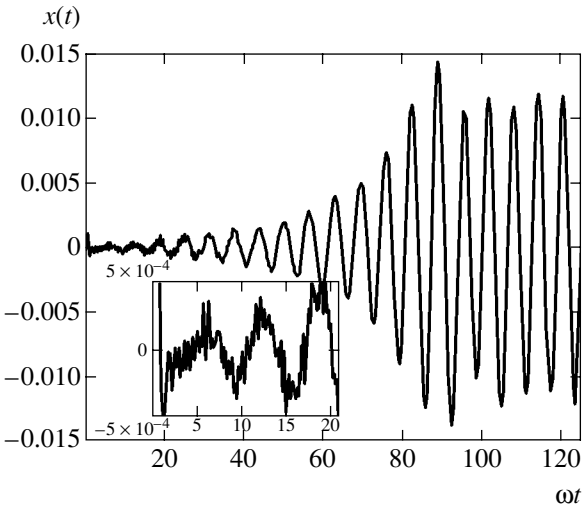

Fig. 3. The time dependence of the mean electron velocity qualitatively resembles the results obtained in the simplified model for the motion of an electron sphere against the background of an expanding ion sphere.

against a background of the expansion of the ion subsystem. These oscillations are accompanied by electrons periodically "splashing out" into the surrounding space at times corresponding to the maximum acceleration. As a result, the near-boundary region of the cluster is depleted in electrons. The fraction of the electron losses in the outer ionization process reaches half of the total number. However, despite the new details in the picture of cluster dynamics (a self-consistent expansion of the plasma bunch, a deviation of the shape from a sphere, a nonuniform electron density distribution inside the ionized cluster, etc.), the qualitative behavior of the dipole moment (an integrated characteristic) of the cluster (Fig. 3) is the same as that in the simplified model (Fig. 2). We clearly see an increase in the amplitude of the forced oscillations attributable to cluster expansion followed by the stabilization determined by nonuniformity saturation. The electrodynamic response of a cluster to an external field at the initial stage of its evolution is shown separately on an enlarged scale, in the inset to Fig. 3. We see that the high-frequency component of the process, as in the simplified model, decreases appreciably in a time of the order of several oscillation periods of the external field. Apart from the cluster expansion, the internal dissipative relaxation of high-frequency irregularities also contributes to the damping; this eventually leads to the rise in the temperature of the electron subsystem observed in numerical experiments.

At $\omega t = 90$, the frequency of the external field is equal to the "current" frequency of the free oscillations of the cluster, and one might expect the object's resonant properties to manifest themselves. However, since the process is nonstationary, the resonant amplification of the oscillations manifests itself weakly.

Thus, a comparative analysis indicates that the simple model in which the expansion rate is fixed (Section 3.1) satisfactorily describes the polarization dynamics of a cluster in the main part of an electromagnetic pulse.

4. ANALYSIS OF SELF-ACTION MECHANISMS

Before we turn to a self-consistent description of the self-action effects, let us consider in more detail the self-action mechanisms in a cluster plasma and estimate the characteristic fields for the nonlinear effects and the relaxation time scales.

The amount of material in the gaseous state (outside clusters) is variously estimated to reach 90%. The Kerr nonlinearity of the atoms of the background medium can play a certain (focusing) role near the leading edge of a laser pulse. As the gas is ionized, its contribution becomes appreciably weaker. For ultrashort laser pulses, the relativistic nonlinearity related to the dependence of the electron mass on the oscillation velocity in the wave field is commonly considered as the main nonlinearity mechanism. However, the characteristic field for this nonlinearity exceeds appreciably the threshold value for the cluster decay (10). Below, we consider other possibilities.

4.1. Electron Nonlinearity

In the model of uniformly charged spheres in a field with a frequency ω much lower than the eigenfrequency of the ionized cluster, we can estimate the maximum amplitude of the external field from Eq. (2),

$$\frac{e}{m}\frac{E_{\max}}{\omega_c^2} \approx 0.4a, \tag{10}$$

at which the oscillations of the plasma bunch remain localized near the ion core. If the amplitude of the forced oscillations is on the order of the cluster size a, the oscillatory system decays (the electron cloud is detached from the ion cloud).

To determine the characteristic field for the electron nonlinearity of the cluster, let us find the nonlinear correction to x from (2) using the perturbation method ($x \ll a$). Averaging over the field period yields

$$x = \frac{e}{m\omega_c^2}E(t)\left(1 + \frac{3}{4}\frac{e^2|E|^2}{m^2\omega_c^4 a^2}\right). \tag{11}$$

Thus, the nonlinearity is a focusing one; the characteristic field is

$$E_e = \frac{m\omega_c^2 a}{e}; \tag{12}$$

i.e., it is virtually identical to field (10) at which the cluster decays. When the total number of particles

inside the plasma bunch is conserved ($\omega_c^2 a^3 = \text{const}$), this implies that the characteristic field for the electron nonlinearity decreases with cluster expansion as

$$E_e \propto a^{-2}(t). \tag{13}$$

The cluster dipole moment

$$p = \omega_c^2 a^3 x m/e$$

in this approximation is

$$p = a^3 E(t)(1 + |E|^2/E_e^2). \tag{14}$$

Given relation (13), it can be seen that the nonlinear part of the polarization increases with cluster expansion as the seventh power of the plasma bunch size,

$$p^{NL} \propto a^7. \tag{15}$$

4.2. Ionization Nonlinearity

Our numerical analysis of the processes inside a cluster by the molecular dynamics method shows that some of the electrons are lost even at fields weaker than the plasma bunch decay field (10).[3] To estimate this effect, we proceed as follows. Let us consider a test electron located near the cluster boundary. The force of inertia acting on it in an oscillating electric field is

$$F_i = eE\omega^2/\omega_c^2. \tag{16}$$

This electron will not return to the cluster during the oscillations if the centrifugal force (16) exceeds the force of attraction to the uncompensated ion charge of the cluster

$$F_a = eq/a^2. \tag{17}$$

Comparing (16) and (17), let us estimate the charge q that the cluster will lose in an oscillating external electric field:

$$q \le E\omega^2 a^2/\omega_c^2. \tag{18}$$

Thus, the outer cluster ionization causes the dipole moment of the plasma bunch to decrease,

$$\Delta p^{NL} = -\frac{e|E|\omega^2}{m\omega_c^4 a} p.$$

The characteristic field for the ionization nonlinearity

$$E_i = \frac{\omega_c^2}{\omega^2} E_e \tag{19}$$

appreciably exceeds the corresponding field for the electron nonlinearity (15).

The inverse process, the settling of electrons on the cluster surface, is possible in the presence of a background plasma. Estimates indicate that the effect of this recombination is appreciably weaker than the contribution from the outer ionization and that the characteristic field for the recombination nonlinearity is considerably larger than (15).

A similar conclusion can also be reached for the thermoionic emission of electrons from the cluster. Assuming the temperature of the plasma bunch to be equal to (larger than) the electron oscillation energy, the cluster charge can be easily estimated using the expression for the number of thermal electrons emitted by a heated surface [14]. It differs little in magnitude from that obtained above from the balance of forces (18). Consequently, the striction nonlinearity also dominates over the thermal-ionization nonlinearity in this case.

4.3. Striction Nonlinearity

In view of the structural peculiarities of the cluster plasma, the possibilities of the ponderomotive action of the field on the medium are enhanced significantly. On the one hand, the background plasma density is redistributed in the nonuniform field of the wave beam, as in a homogeneous medium. In our case, however, the relaxation time scale of the ordinary striction nonlinearity, $\tau_s = L_\perp/v_s$ ($L_\perp$ is the transverse scale of the wave beam, and v_s is the speed of ion sound), appreciably exceeds the laser pulse duration, $\tau_s \gg \tau$, which significantly weakens its role. Another possibility is associated with the deformation of an ionized cluster in a wave field. The time scale of this process for a cluster is $\tau_c \approx a/v_s$, i.e., considerably (by a factor of $a/L_\perp$) shorter than the plasma redistribution time on the transverse scale of the beam. Let us determine the nonlinear polarization of a plasma bunch as it is deformed in a wave field. Following [12], we assume that the deformation consists in uniform contraction or extension of the object and that its shape remains unchanged. The expression for the total thermodynamic potential of a spherical body in an external uniform electric field is [12]

$$\Phi = \Phi_0(P, T) - \frac{V}{16\pi}\frac{3(\varepsilon - 1)}{\varepsilon + 2}\bar{E}^2, \tag{20}$$

where Φ_0 pertains to the body in the absence of a field at fixed pressure P and temperature T; ε and V are the permittivity and volume of the body, respectively, considered as functions of P and T. Hence, the change in volume $\Delta V = V - V_0$ (V_0 is the initial volume of the body) can be found by differentiating ε with respect to the pressure (at constant T and $\bar{E}^2$). For an ionized cluster (a medium in which the permittivity depends on the

[3] In what follows, we will call this process outer ionization.

density, $\varepsilon - 1 \sim 1/V$, and the equation of state is $PV = RT$), we get

$$\frac{\Delta V}{V} = \frac{3(\varepsilon_c - 1)^2}{(\varepsilon_c + 1)^2}\frac{\bar{E}^2}{16\pi P}. \quad (21)$$

As a result, we obtain the same expression for the dipole moment

$$p = a^3 E(t)(1 + \Delta V/V)$$

of a plasma bunch as that for the electron nonlinearity (14). The characteristic field for the (focusing) striction nonlinearity under the conditions in question ($|\varepsilon_c| \gg 1$) is

$$E_s = 4(\pi P)^{1/2}/\sqrt{3}. \quad (22)$$

Comparing the characteristic fields of the electron (12) and striction (22) nonlinearities,

$$\frac{E_e}{E_s} = \frac{a}{2r_D}, \quad (23)$$

we note that the electrostriction effect is dominant for clusters with a size a much larder than the Debye length r_D. However, the relaxation time scale of the electrostriction nonlinearity

$$\tau_c \approx (M/m)^{1/2} a/r_D\omega_p \quad (24)$$

is comparable to the duration of the laser pulses used in our experiments even for the initial cluster size. The expansion of plasma bunches is accompanied by a further weakening of the contribution from the striction nonlinearity.

The following conclusions can be drawn from our analysis of the nonlinearity mechanisms that lead to the self-action of electromagnetic radiation. Since the ionized-cluster size exceeds the Debye length ($a > r_D$), the striction nonlinearity of a plasma bunch in an electric field (Section 4.3) has the lowest threshold. However, the time scale of the electrostriction nonlinearity is longer than (on the order of) the duration of the laser pulses under consideration. In addition, the characteristic field for the inertia-free electron nonlinearity (12) decreases with cluster expansion at an appreciably higher rate than the corresponding field for the electrostriction nonlinearity (22). As regards the ionization and recombination nonlinearities, they not only are determined by higher characteristic fields, but also weaken one another. Thus, we have every reason to believe that the self-action dynamics in the main part of the laser pulse is determined by the electron nonlinearity of plasma bunches in a fine-dispersed medium.

5. SELF-ACTION DYNAMICS OF LASER RADIATION IN A CLUSTER PLASMA

The above analysis of the electrodynamic processes in a cluster plasma leads to the following formulation of the problem. Let us next consider the spatiotemporal evolution of an ultrashort laser pulse in a nanodispersed medium in which the nonlinearity is determined by the system of plasma bunches, while the group velocity dispersion is determined by the ionized clusters and the background plasma. We assume that the spherical clusters expand according to a given law and that the nonlinearity mechanism is associated with the anharmonicity of the electron motion (Section. 4.1).

5.1. Equation of Nonlinear Optics

To describe the self-action dynamics of radiation at a frequency ω much shorter than the eigenfrequency of the ionized cluster $\omega_c = \omega_p/\sqrt{3}$, but higher than the background plasma frequency ω_{bg} (see Fig. 1), we use the following equation for a wavepacket propagating along the z axis:

$$\frac{\partial^2 E}{\partial t^2} - c^2\frac{\partial^2 E}{\partial z^2} - c^2\Delta_\perp E + 4\pi\frac{\partial^2 P_c}{\partial t^2} + \omega_{bg}^2 E = 0. \quad (25)$$

The last term in Eq. (25) describes the background plasma effect. We define the cluster-related polarization as

$$P_c = n_c p,$$

where n_c is the cluster density. We find the dipole moment of a single cluster p by solving Eq. (2) by the perturbation method. In the approximation under consideration, it differs from (14) in that it includes the dynamical part of Eq. (2). As a result, we obtain the following expression for the polarization of the cluster subsystem:

$$P_c = n_c a^3 E\left(1 + \frac{E^2}{E_{cr}^2}\frac{a^4}{a_0^4}\right) - n_c a^3\frac{\partial^2}{\partial t^2}\left(\frac{Ea^3}{\omega_c^2 a_0^3}\right), \quad (26)$$

where ω_c is the frequency of the free oscillations of a cluster with the initial size a_0. In Eq. (26), we took into account the fact that the total number of particles in the volume is conserved as the cluster expands ($na^3 = \text{const}$). Substituting (26) into (25) yields an equation for the electric field of the wave beam,

$$\frac{\partial^2 E}{\partial t^2} - \alpha\frac{\partial^2 (bE)}{\partial t^2} - \frac{\alpha}{\omega_c^2}\frac{\partial^2}{\partial t^2}\left(b\frac{\partial^2 (bE)}{\partial t^2}\right) + \alpha\frac{\partial^2}{\partial t^2}\left(b^{7/3}\frac{E^3}{E_{cr}^3}\right) - c^2\frac{\partial^2 E}{\partial z^2} - c^2\Delta_\perp E + \omega_{bg}^2 E = 0, \quad (27)$$

where

$$\alpha = 4\pi n_c a_0^3, \quad b = a^3/a_0^3.$$

The linear dispersion relation for a field

$$E \sim \exp(ik_z z - i\omega t)$$

in a medium with fixed parameters is

$$k_z = \frac{(\omega^2(1+\alpha b) - \omega_{bg}^2 + \alpha b^2\omega^4/\omega_c^2)^{1/2}}{c}. \quad (28)$$

It describes the waves in the approximation of weak dispersion of the cluster subsystem (see Fig. 1). For quasi-monochromatic radiation, expanding the right-hand side near the central frequency ω_0 yields

$$k_z = k_z^0 + \left.\frac{\partial k_z}{\partial\omega}\right|_{\omega=\omega_0}(\omega-\omega_0) + \frac{1}{2}\left.\frac{\partial^2 k_z}{\partial\omega^2}\right|_{\omega=\omega_0}(\omega-\omega_0)^2. \quad (29)$$

Hence, we obtain

$$v_g = c(1 - \omega_{bg}^2/2\omega^2 - \alpha b/2 - 3\alpha b^2\omega^2/2\omega_c^2 \quad (30)$$

for the group velocity of the wavepacket $v_g = \partial\omega/\partial k_z$ and

$$k_2 = \frac{\partial^2 k_z}{\partial\omega^2} \approx \frac{-\omega_{bg}^2 + 3\alpha b^2\omega^4/\omega_c^2}{\omega^3 c} \quad (31)$$

for the group velocity dispersion parameter. Thus, in a cluster plasma with a low background density,

$$\omega_{bg}^2 < 3\alpha b^2\omega^4/\omega_c^2, \quad (32)$$

the group velocity dispersion is normal ($k_2 > 0$). Moreover, as the cluster expands, inequality (32) is satisfied better and better; i.e., the dispersion of the medium remains normal. If, however, the background plasma density is fairly high and the plasma (anomalous) dispersion dominates at the leading edge of the wavepacket,

$$\omega_{bg}^2 > 3\alpha b^2\omega^4/\omega_c^2, \quad (33)$$

the plasma cluster expansion can lead to a change of the dispersion from anomalous to normal inside the pulse. In this more complex regime of wave field propagation, expansion (29) is not enough, and the third-order dispersion should be taken into account. Our calculations show that the coefficient $\partial^3 k/\partial\omega^3$ is positive and equal to

$$\frac{\partial^3 k}{\partial\omega^3} = \frac{3}{\omega c^2}\left(\frac{\omega_{bg}^2}{\omega^2} + \alpha b^2\frac{\omega^2}{\omega_c^2}\right). \quad (34)$$

To describe the self-action dynamics of wavepackets, we can pass from Eq. (29) to the equation for the complex amplitude of the field envelope. In our case, the cluster is a nonstationary object. To use the standard procedure for shortening (27), we assume that the cluster expansion rate is the same in the beam cross section ($b = b(t, z)$ depends only on the time and the longitudinal coordinate inside the pulse). As a result, for the complex amplitude of the envelope

$$E(z, t, \mathbf{r}_\perp) = A(z, \xi = z - z_c(t), \mathbf{r}_\perp)\exp(i\phi(z, \xi) - i\omega t),$$

we obtain an equation in the frame of reference moving with the local group velocity (30) in the adiabatic approximation:

$$2ik_z\frac{\partial A}{\partial z} + 2i\omega\frac{\alpha}{c}b^{7/4}\frac{|A|^2}{E_{cr}^2}\frac{\partial(b^{7/12}A)}{\partial\xi} - \omega c\frac{\partial}{\partial\xi}k_2\frac{\partial A}{\partial\xi} + \Delta_\perp A + \alpha b^{7/3}\frac{\omega^2}{c^2}\frac{|A|^2}{E_{cr}^2}A = 0, \quad (35)$$

where $k_z = \partial\phi/\partial z$, z_c is the coordinate of the center of mass of the wavepacket, and $dv_g/dt = V_g$. At a fixed frequency k_z, V_g, and b are generally functions of ξ. Equation (35) does not include the correction for the nonstationarity of the medium. It is well known [17] that in a nonstationary medium, the expression for the permittivity $\varepsilon(\omega, t)$ in the wave equation should be substituted with

$$\varepsilon(\omega, t) + \frac{i}{2}\frac{\partial^2\varepsilon}{\partial\omega\partial t}.$$

The correction to the quasi-stationary value of $\varepsilon(\omega, t)$ proves to be significant near the geometrical resonance $\omega = \omega_c/\sqrt{3}$. Since we are interested in the processes in the range of parameters

$$\omega_{bg} \ll \omega \ll \omega_c/\sqrt{3},$$

in which the permittivity $\varepsilon(\omega, t)$ is close to unity, this correction can be ignored. This equation differs from the equations that are usually obtained in this case by the term containing the dependence of the group velocity on the wavepacket amplitude.

To investigate the self-action dynamics in a cluster plasma, it is convenient to pass from Eq. (35) to an equation in dimensionless variables:

$$i\frac{\partial\Psi}{\partial z} + id^{7/4}|\Psi|^2\frac{\partial}{\partial\tau}(d^{7/12}\Psi) - \frac{\partial}{\partial\tau}\chi\frac{\partial\Psi}{\partial\tau} + \Delta_\perp\Psi + d^{7/3}|\Psi|^2\Psi = 0, \quad (36)$$

where

$$\Psi = A/A_{cr}, \quad A_{cr} = \frac{\sqrt{5}\omega E_{cr}}{\omega_c a_{max}^{1/2}}, \quad z_{new} = \frac{10\alpha a_{max}^6 \omega^3 z}{\omega_c^2 c},$$

$$\tau = \frac{2\omega\xi}{c}, \quad \mathbf{r}_{new} = \frac{\omega^2 a_{max}^6 (20\alpha)^{1/2}\mathbf{r}}{c\omega_c},$$

$$d = \frac{a^3}{a_{max}^3}, \quad \chi = d^2 - \frac{\omega_{bg}^2\omega_c^2}{3\alpha\omega^4 a_{max}^6},$$

a_{max} is the maximum cluster size reached at the pulse trailing edge. Since these coefficients depend strongly on the cluster size (e.g., the coefficient of the nonlinearity is proportional to a^7), we assume, for simplicity, that $d = d_{min} = 0$ at the leading edge. Depending on the background plasma density, the cluster expansion rate, and the pulse duration, the parameter χ can be positive or negative and change sign inside the pulse.

Let us next consider the self-action of laser radiation in a cluster plasma separately for normal ($\chi > 0$), anomalous ($\chi < 0$), and combined dispersions. Since the coefficients in (36) depend on τ, Eq. (36) is not a Hamiltonian equation. Therefore, the only integral relation that holds here is the total pulse energy integral related to the absence of dissipation in the system:

$$\int |\Psi|^2 d\tau dr_\perp = W. \tag{37}$$

We can find from the corresponding continuity equation,

$$\frac{\partial|\Psi|^2}{\partial z} + \frac{\partial}{\partial\tau} d^{7/2}|\Psi|^4 + i\frac{\partial}{\partial\tau}\chi(\Psi^*\Psi_\tau - \Psi\Psi_\tau^*) + i\,\mathrm{div}_\perp(\Psi^*\nabla_\perp\Psi - \Psi\nabla_\perp\Psi^*) = 0, \tag{38}$$

that the center of mass of an axisymmetric wavepacket moves with the velocity

$$u = \frac{d}{d\tau}\int \tau|\Psi|^2 d\tau dr_\perp = -\int (d^{7/2}|\Psi|^4/2 + i\chi(\Psi^*\Psi_\tau - \Psi\Psi_\tau^*) d\tau dr_\perp, \tag{39}$$

i.e., generally nonuniformly. This leads to a change in the laser pulse shape, which also takes place in a homogeneous medium where it is determined by the dependence of the group velocity on the wavepacket amplitude. In our case of an expanding cluster, the sharp increase in d and χ when passing from the leading edge of the pulse to its trailing edge makes the deformation of the envelope near the trailing edge the dominant process.

To investigate the self-action in a cluster plasma, let us turn to numerical simulations of the evolution of the system.

5.2. Self-Action in a Normally Dispersive Medium

The self-action of a laser pulse in a homogeneous medium with normal group velocity dispersion ($\chi > 0$) is determined by the competition between the transverse self-focusing compression and the longitudinal spreading. For three-dimensional wavepackets with a power P exceeding its critical value, the self-compression process is predominant (see, e.g., [18–23]) and is accompanied by a significant field strengthening near the system's axis. Estimation of the critical self-focusing power in a cluster plasma yields

$$P_c = \left(\frac{a_0}{a}\right)^7 \frac{c^2}{4\alpha\omega^2} E_{cr}^2 c P_{cr}, \tag{40}$$

where $P_{cr} = 11.7$ is a quantity well known from the theory (the dimensionless critical power of an axisymmetric homogeneous wave beam). Considering (40) as a local relation, we conclude that the part of the pulse (the τ region) in which self-focusing is possible is determined by the condition $P/P_c > 1$ and that optimal conditions for self-focusing are created in the τ_{opt} section where the ratio $P/P_c \sim Pa^7$ reaches its maximum. Thus, the increase in cluster size on the pulse length displaces the τ_{opt} section to the trailing edge. Apart from the deformation of the envelope profile of a three-dimensional wavepacket, the nonlinear dispersion in a homogeneous medium [24] also affects the self-focusing rate by enhancing it at low values of α and weakening or even preventing self-focusing at high values of this coefficient.

The results of our numerical analysis of the self-action dynamics of a Gaussian wavepacket for normal dispersion are presented in Figs. 4 and 5.

The initial distribution was specified in the form

$$\psi(z = 0, r, \tau) = A_0 \exp(-0.5(r/a_r)^2 - 0.5(\tau/a_\tau)^2) \tag{41}$$

with the parameters $a_r = 4$, $a_\tau = 20$, and $A_0 = 1$. In numerically solving Eq. (39), we approximated the dependence $d(\tau)$ by a piecewise linear function of the longitudinal coordinate,

$$d = 0, \quad \tau > 0, \quad d = -\tau/a_\tau, \quad \tau < 0,$$

which models a power-law increase in cluster size on the laser pulse length. According to qualitative models, the field maximum shifts rapidly to the pulse trailing edge. The position of the maximum is determined primarily by the optimal conditions for self-focusing and, thus, depends on the pulse intensity profile and the critical power profile. Since the group velocity depends on the amplitude, strengthening of the self-focusing field gives rise to a paraxial energy flux toward the pulse leading edge. Accordingly, the field peak shifts to the region where the characteristic field for the nonlinearity

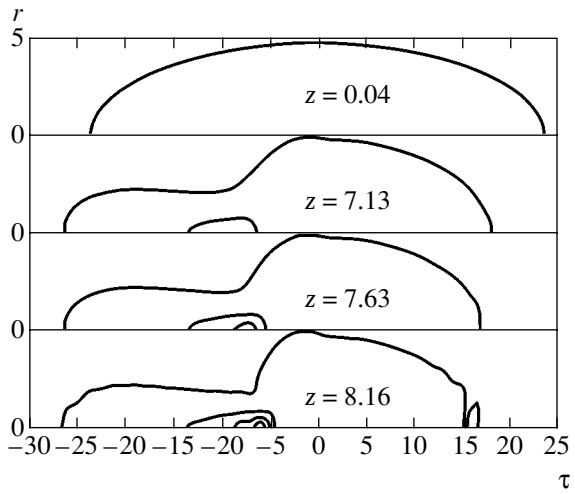

Fig. 4. The pattern of isolines of a field with the initial distribution $\psi(z = 0, r, \tau) = \exp(-0.5(r/4)^2 - 0.5(\tau/20)^2)$ for consecutive pulse positions in the case of normal dispersion. The splitting of the field peak into two secondary peaks is typical of a homogeneous medium without nonlinear dispersion.

increases, and the self-focusing process weakens. As the maximum shifts, it fragments, as in a homogeneous nonlinear medium with normal dispersion.

We see from Fig. 5a how strongly the wavepacket dynamics depends on the initial conditions. For a pulse with an initial amplitude of $A_0 = 1$, we have a relatively small maximum strengthening, $A_{max}/A_0 \approx 5.5$, at a distance of $z \approx 8.5$ from the entrance to a nonlinear medium. An increase in the initial amplitude to $A_0 = 1.25$ causes a sharp increase in the field strengthening at half the distance. The computational accuracy in the numerical scheme used is determined by the longitudinal cell size; when longitudinal field scales of the order of the cell size appear, the accuracy becomes insufficient and the computation is interrupted. The computation of the case with $A_0 = 1.25$ was interrupted because the accuracy was violated at $A_{max}/A_0 \approx 40$. However, we believe that there is no real singularity in the solution, but the same processes as those in the case with a smaller amplitude A_0 take place; these processes also lead to the limitation of the singularity, but at much higher intensities in the peak. Figure 5b illustrates the behavior of the characteristic scales of the field peak in the case with $A_0 = 1$. The characteristic scales a_r and a_τ were defined here as the (respectively, radial and longitudinal) distances at which the field decreased by a factor of e compared to its maximum value. The dotted curve in Fig. 5b shows that the field distribution is not isotropized during the evolution (the ratio a_τ/a_r of the longitudinal and transverse scales does not tend to unity), which is also typical of self-action in a homogeneous medium [18–23].

5.3. Self-Action in an Anomalously Dispersive Medium

At a fairly high background plasma density ($\omega_{bg}^2/\omega^2 > \alpha a_{max}^3/a_0^3$), the group velocity dispersion in the medium is anomalous. In this case, a self-action regime is realized in which the dispersion is determined by the background plasma, while the nonlinearity is determined by the ionized clusters. A peculiar feature

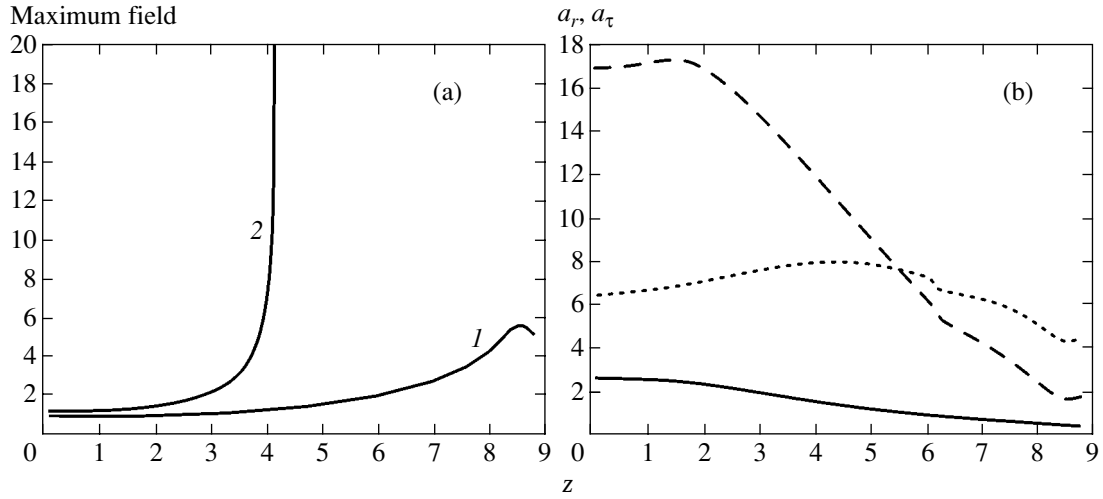

Fig. 5. Dynamical picture of the parameters that characterize the field structure. Panel (a) shows the dynamics of the field maximum. For the case with an initial amplitude of $A_0 = 1$ (curve *1*), the maximum field strengthening, $A_{max}/A_0 \approx 5.5$, is reached at a distance $z \approx 8.5$ from the entrance into a nonlinear medium. Increasing the initial amplitude to $A_0 = 1.25$ (curve *2*) leads to a sharp increase in maximum field strengthening (in fact, to the formation of a field singularity) at half the distance, $z \approx 4.14$. Panel (b) shows the behavior of the transverse, a_r (solid line), and longitudinal, a_τ (dashed line), characteristic scales of the field peak. The dotted line indicates a ratio of a_τ/a_r.

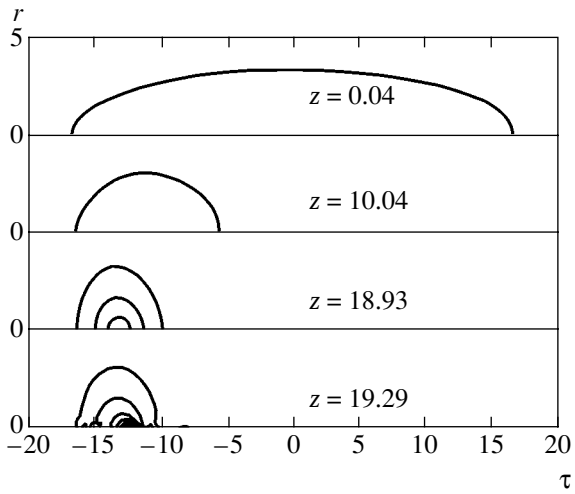

Fig. 6. The pattern of isolines of a field $\psi(z = 0, r, \tau) = 0.71\exp(-0.5(r/4)^2 - 0.5(\tau/20)^2)$ for consecutive pulse positions in the case of anomalous dispersion ($\omega_{bg}^2/\omega^2 = 2\alpha$). There is a clear tendency for the maximum in the field peak to shift to the pulse leading edge at the final evolutionary stage.

of this self-action regime in a homogeneous medium is the possibility of distributed (three-dimensional) collapse. As a result, one might expect the highest rate of spatiotemporal self-focusing. Clearly, the decrease in the characteristic field for the electron nonlinearity as the ionized clusters expand will also contribute to this process.

Our numerical simulations of the self-action dynamics of laser radiation for anomalous dispersion confirm the features noted above. The self-focusing of a wavepacket proves to be possible when much milder conditions than those in a normally dispersive medium are satisfied (the field strength in the case with field collapse shown in Fig. 6 is half that for the case without any singularity in Fig. 4). A characteristic feature in the system's evolution is the tendency for the wave field structure to be symmetrized (see Fig. 7b). The corresponding singular solutions of the nonlinear Schrödinger equation with a finite energy flux into the singularity in the regime of spherically symmetric collapse were constructed in [25, 26].

Just as in a normally dispersive medium, the initial evolutionary stage is characterized by a shift of the field maximum to the pulse trailing edge, to the region of optimal self-focusing conditions. As the amplitude increases, the nonlinear dispersion also increases in importance: as the velocity increases, the field maximum begins to shift toward the pulse leading edge, where the role of nonlinear effects weakens. The pattern of field isolines corresponding to the last computed evolution times clearly shows a tendency for the field maximum to escape from the peak. Clearly, the time it takes for the field maximum to traverse the characteristic longitudinal scale of the peak serves as a criterion in this case. If this occurred earlier than the formation of a singularity in the solution, then this would imply escape from the regime of collapse.

Based on the well-known behavior of the singularity of the solution in the homogeneous case ($|\psi| \propto \zeta^{-1/2}$, $\zeta = 0$ is the singularity formation time) [25, 26], we conclude that the nonlinear dispersion has time to prevent the collapse, since the distance that the field peak

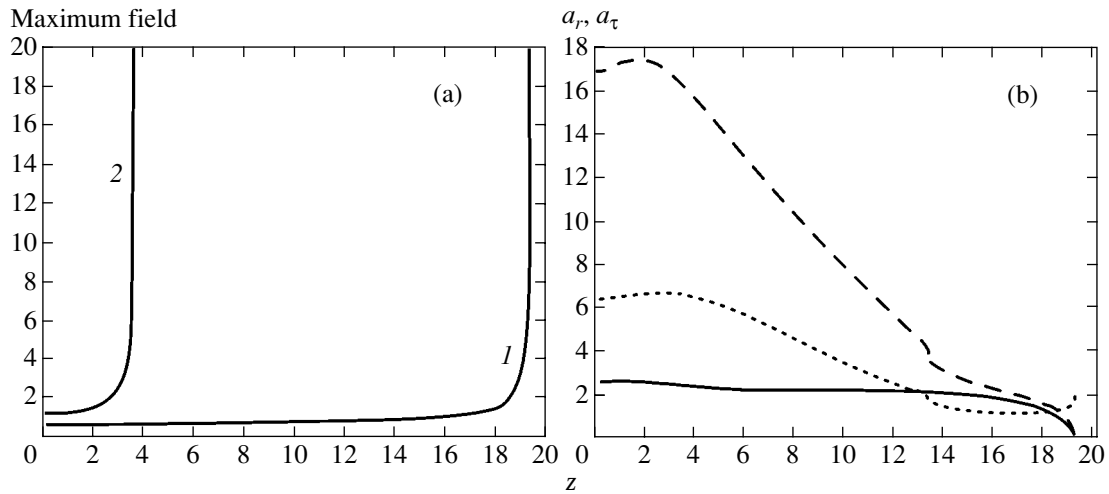

Fig. 7. The dynamical picture of the parameters that characterize the field structure. Panel (a) shows the dynamics of the field maximum. The solution with an initial amplitude of $A_0 = 0.71$ (curve *1*) approaches the singularity at a distance $z \approx 19.3$ from the entrance into a nonlinear medium. When the amplitude is increased to $A_0 = 1.25$, the singularity is formed earlier (curve *2*), at $z \approx 3.6$. Panel (b) shows the behavior of the transverse, a_r (solid line), and longitudinal, a_τ (dashed line), characteristic scales of the pulse. The dotted line indicates a_τ/a_r ratio, which is close to unity at the final evolutionary stage. Such symmetrization of a contracting structure is typical of spherically symmetric collapse.

traverses in the "time" ζ_0 is logarithmically large in this case:

$$\int_{\zeta_0}^{\zeta} |\psi|^2 d\zeta \propto \ln(\zeta/\zeta_0) \xrightarrow{\zeta \to 0} \infty.$$

However, the field amplitudes reached by this time are so large and the characteristic scales are so small that, in fact, collapse can be said to take place.

Thus, the presence of a background plasma significantly affects the self-action dynamics, and this effect is particularly strong for pulses in which the characteristic dispersion and diffraction scales are of the same order of magnitude: the pulse shortening in an anomalously dispersive medium has virtually no effect on the singularity formation conditions and time, while a significant increase in radiation intensity is required for self-focusing to take place in a normally dispersive medium (a cluster plasma without any background).

At a lower background plasma density,

$$\omega_{bg}^2/\omega^2 < \alpha a_{max}^3/a_0^3,$$

the medium has a combined dispersion: the group velocity dispersion is anomalous at the leading edge of the pulse and normal at its trailing edge. Since the cluster and plasma dispersions have opposite signs, they compensate each other to some degree; in the section where

$$\omega_{bg}^2/\omega^2 = \alpha a^3/a_0^3,$$

the compensation is full. Since the region of effective self-action shifts to the pulse trailing edge and back, which is typical of both types of dispersion of the medium, the behavior of the solution is intermediate between the two behaviors considered above.

6. CONCLUSIONS

We considered the self-action dynamics of laser radiation in a cluster plasma. Based on the model of an isolated cluster in the form of a plasma bunch in a background plasma, we substantiated the constitutive equation for a nanodispersed ionized medium. A comparative analysis of the nonlinearity mechanisms showed that the electron nonlinearity of an ionized cluster related to the anharmonicity of the electron oscillations in the laser field has the lowest threshold in the field of an ultrashort laser pulse. The response of the medium to the field action and particularly its nonlinear part were found to depend strongly on the ionized-cluster size. Therefore, in constructing the self-consistent picture of the interaction between laser radiation and a cluster plasma, we made the necessary allowance for the plasma bunch expansion corresponding to experimental data.

We investigated the self-action dynamics of an ultrashort laser pulse. The evolution of the envelope of a wavepacket is determined by the electron nonlinearity of an ionized cluster and by the dispersion of a highly inhomogeneous medium. The evolution of the system was shown to be similar for all types of group velocity dispersion (normal, combined, and anomalous). For a rare background plasma at a laser power exceeding the critical self-focusing power, the self-action dynamics of a wavepacket develops as in a homogeneous medium with normal dispersion. The new features related to the sharp dependence of the critical self-focusing power on the cluster size manifest themselves in an appreciable increase in the compression rate of the wave beam, the attainment of higher fields, and the shift of the field maximum to the pulse trailing edge. Since the self-compression of the wave field takes place mainly in the trailing part of the pulse, the pattern of self-action for combined dispersion (anomalous dispersion at the leading edge changes to normal dispersion at the trailing edge) is virtually identical to that for normal dispersion. In a fairly dense background plasma, in which the dispersion is anomalous, the formation of an almost spherically symmetric region of a strong field should be noted among the new features in the self-action dynamics.

In application to an experimental study of the interaction between laser radiation and a cluster plasma, a strong dependence of the processes under consideration on the ionized-cluster size should be noted. It turns out that the self-action of laser radiation is similar in pattern over a wide range of parameters of the medium if the power exceeds the critical self-focusing power. Here, one might expect both an appreciable shortening of the pulse duration and a decrease in the transverse size of the wave beam passed through the medium.

The critical power for the electron nonlinearity,

$$P_{cr} \approx \left(\frac{a_0}{a}\right)^7 \left(\frac{\omega_c^2}{\omega^2}\frac{\omega}{c}a_0\right)^2 \times 10^{12}\ \text{W}, \qquad (42)$$

decreases greatly with increasing relative size of the expanding ionized cluster. The possibility of experimental observation of the self-action effects in a cluster plasma is thus seen to depend significantly on the cluster expansion rate. The critical power is fairly large near the pulse leading edge. However, in the dynamical regime, a twofold increase in size compared to the initial size decreases the critical power by one and a half orders of magnitude. For example, for the parameters of the experiment [10] (λ = 800 nm, $a_0 \approx$ 300 Å, $n_a \approx 10^{24}$ cm^{-3}), the critical self-focusing power is

$$P_{cr} \approx 10^{13}(a_0/a)^7\ \text{W}. \qquad (43)$$

Thus, for peak powers in these experiments of $P \sim 10^{10}$ W, the threshold conditions for the observation of self-focusing will be satisfied if the cluster size near the

field maximum increases by a factor of $a/a_0 = 3$. Hence, we conclude that the self-focusing experiments in [10] can be interpreted in terms of the suggested mechanism. It should be noted that the absorbability of self-focusing inferred from the critical power parameter should be considered as an overestimate, as suggested by our numerical simulations of the self-focusing dynamics in a medium with normal group velocity dispersion. An even larger decrease in threshold characteristics might be expected at a higher background plasma density and for anomalous dispersion.

ACKNOWLEDGMENTS

This work was supported by the Russian Foundation for Basic Research (project nos. 05-02-17509 and 04-02-16684).

REFERENCES

1. A. McPherson, T. S. Luk, D. D. Thompson, *et al.*, Phys. Rev. Lett. **72**, 1810 (1994).
2. Y. L. Shao, T. Ditmire, T. W. G. Tisch, *et al.*, Phys. Rev. Lett. **77**, 3343 (1996).
3. T. Ditmire, T. W. G. Tisch, E. Springate, *et al.*, Phys. Rev. Lett. **78**, 2732 (1997); M. Lezius, S. Dobosz, D. Normand, *et al.*, Phys. Rev. Lett. **80**, 261 (1998).
4. Y. Kumarappan, M. Krishnamurthy, and J. Mathuv, Phys. Rev. Lett. **87**, 085 005 (2001).
5. A. B. Borisov, J. W. Longworth, A. McPherson, *et al.*, J. Phys. B **29**, 247 (1996); J. Phys. B **29**, 113 (1996).
6. É. L. Nagaev, Usp. Fiz. Nauk **162** (9), 47 (1992) [Sov. Phys. Usp. **35**, 747 (1992)]; A. A. Likal'ter, Usp. Fiz. Nauk **162** (7), 119 (1992) [Sov. Phys. Usp. **35**, 591 (1992)].
7. A. V. Eletskiĭ and B. M. Smirnov, Usp. Fiz. Nauk **163** (3), 33 (1993) [Phys. Usp. **36**, 202 (1993)]; B. M. Smirnov, Usp. Fiz. Nauk **170**, 495 (2000) [Phys. Usp. **43**, 453 (2000)].
8. B. M. Smirnov, *Physics of the Fractal Clusters* (Nauka, Moscow, 1991) [in Russian].
9. T. Donnelly, T. Ditmire, N. Neuman, *et al.*, Phys. Rev. Lett. **76**, 2472 (1996).
10. I. Alexeev, T. M. Antonsen, K. Y. Kim, and H. M. Milchberg, Phys. Rev. Lett. **90**, 103402 (2003); K. Y. Kim, I. Alexeev, E. Parra, and H. M. Milchberg, Phys. Rev. Lett. **90**, 023401 (2003); K. Y. Kim, I. Alexeev, V. Kumarappan, *et al.*, Phys. Plasmas **11**, 2882 (2004).
11. N. A. Zharova, A. G. Litvak, and V. A. Mironov, Pis'ma Zh. Éksp. Teor. Fiz. **78**, 1112 (2003) [JETP Lett. **78**, 619 (2003)].
12. L. D. Landau and E. M. Lifshitz, *Course of Theoretical Physics*, Vol. 8: *Electrodynamics of Continuous Media*, 2nd ed. (Nauka, Moscow, 1982; Pergamon, New York, 1984).
13. T. Tajima, Y. Kishimoto, and M. G. Downer, Phys. Plasmas **10**, 3759 (1999); J. W. G. Tisch, Phys. Rev. A **62**, 041802 (2000).
14. V. P. Kraĭnov and M. B. Smirnov, Usp. Fiz. Nauk **170**, 969 (2000) [Phys. Usp. **43**, 901 (2000)]; V. P. Krainov and M. B. Smirnov, Phys. Rep. **370**, 237 (2002).
15. P. B. Parks, T. E. Cowan, R. B. Stephens, and E. M. Campbell, Phys. Rev. A **63**, 063203 (2001); S. V. Fomichev, S. V. Popruzhenko, D. F. Zaretsky, and W. Becker, J. Phys. B **36**, 3817 (2003).
16. C. Jungreuthmayer, M. Geissler, J. Zanghellini, and T. Brabec, Phys. Rev. Lett. **92**, 133401 (2004).
17. L. P. Pitaevskiĭ, Zh. Éksp. Teor. Fiz. **39**, 1450 (1960) [Sov. Phys. JETP **12**, 1008 (1961)]; Yu. A. Kravtsov and Yu. I. Orlov, *Geometrical Optics of Inhomogeneous Media* (Nauka, Moscow, 1980) [in Russian].
18. N. A. Zharova, A. G. Litvak, T. A. Petrova, *et al.*, Pis'ma Zh. Éksp. Teor. Fiz. **44**, 12 (1986) [JETP Lett. **44**, 13 (1986)]; Izv. Vyssh. Uchebn. Zaved., Radiofiz. **29**, 1137 (1986).
19. J. E. Rothenberg, Opt. Lett. **17**, 583 (1992); P. Chernev and V. Petrov, Opt. Lett. **17**, 172 (1992); Opt. Commun. **87**, 28 (1992).
20. G. G. Luther, A. C. Newell, and J. V. Moloney, Physica A (Amsterdam) **49**, 4085 (1994); G. G. Luther, A. C. Newell, J. V. Moloney, *et al.*, Opt. Lett. **19**, 789 (1994); Opt. Lett. **19**, 862 (1994).
21. L. Berge and J. J. Rasmussen, Phys. Plasmas **3**, 824 (1996); L. Berge, J. J. Rasmussen, E. A. Kuznetsov, *et al.*, J. Opt. Soc. Am. B **13**, 1879 (1996); L. Berge, E. A. Kuznetsov, and J. J. Rasmussen, Phys. Rev. E **53**, R1340 (1996); G. Fibich, V. M. Malkin, and G. C. Papanicolaou, Phys. Rev. A **52**, 4218 (1995).
22. N. A. Zharova, A. G. Litvak, and V. A. Mironov, Pis'ma Zh. Éksp. Teor. Fiz. **75**, 655 (2002) [JETP Lett. **75**, 539 (2002)]; Zh. Éksp. Teor. Fiz. **123**, 726 (2003) [JETP **96**, 643 (2003)].
23. L. Berge, K. Germaschewski, R. Grauer, and J. J. Rasmussen, Phys. Rev. Lett. **89**, 153902 (2002).
24. N. A. Zharova, A. G. Litvak, and V. A. Mironov, Izv. Vyssh. Uchebn. Zaved., Radiofiz. **46**, 331 (2003).
25. S. N. Vlasov, L. V. Piskunova, and V. I. Talanov, Zh. Éksp. Teor. Fiz. **95**, 1945 (1989) [Sov. Phys. JETP **68**, 1125 (1989)]; S. N. Vlasov, Izv. Vyssh. Uchebn. Zaved., Radiofiz. **42**, 468 (1999).
26. V. E. Zakharov, N. E. Kosmatov, and V. F. Shvets, Pis'ma Zh. Éksp. Teor. Fiz. **49**, 431 (1989) [JETP Lett. **49**, 492 (1989)]; V. M. Malkin, Pis'ma Zh. Éksp. Teor. Fiz. **48**, 603 (1988) [JETP Lett. **48**, 653 (1988)].

Translated by V. Astakhov

Journal of Experimental and Theoretical Physics, Vol. 101, No. 4, 2005, pp. 741–759.
Translated from Zhurnal Éksperimental'noĭ i Teoreticheskoĭ Fiziki, Vol. 128, No. 4, 2005, pp. 859–878.

STATISTICAL, NONLINEAR, AND SOFT MATTER PHYSICS

Turbulent Boundary Layer over a Flat Plate with Uniform Wall Suction

I. I. Vigdorovich
Baranov Central Institute of Aviation Motors, Moscow, 111116 Russia
e-mail: ivigdorovich@ciam.ru
Received May 24, 2005

Abstract—A complete theory of turbulent boundary layer flow over a flat plate with uniform wall suction is proposed. The theory relies on an asymptotic analysis of the Reynolds equations and dimensional considerations and does not involve any special closure hypotheses. Characteristics of the turbulent boundary layer with suction are calculated for the entire range of flow parameters by using the known characteristics of a reference flow (turbulent boundary layer over an impermeable flat plate). The velocity and shear stress profiles, the distribution of skin friction along the plate, and integral flow characteristics are obtained by using only the known velocity profile in the reference flow. The normal Reynolds stresses are calculated by using analogous characteristics of the reference flow. Results are presented in terms of scaling variables. © *2005 Pleiades Publishing, Inc.*

1. INTRODUCTION

Turbulent boundary layer flow is generally modeled by using various semiempirical hypotheses about turbulent transport, turbulence model equations, and other approximations. The relatively few results that can be obtained without invoking any hypotheses (for zero-pressure-gradient flows) include Prandtl's law of the wall, von Kármán's velocity defect law, the logarithmic velocity profile, the von Kármán skin-friction law, and certain scaling relations for Reynolds stress components.

These results can be called "exact" to the extent that they were derived by dimensional analysis under very general assumptions [1–3] (see also [4]).

It was shown in [5–9] that the variety of "exact" solutions can be substantially increased by using the fact that the flow in a turbulent boundary layer with transpiration is determined by a finite number of known parameters [5–7]. Accordingly, there exists a universal relation between turbulent shear stress and mean-velocity gradient. For the dynamic problem, this fact can be used to reduce the momentum equation to a first-order ordinary differential equation. Its analysis yields a scaling law for the mean velocity profile extending the logarithmic law for velocity to flows with transpiration.

This approach makes use of dimensional analysis and the physical assumptions underlying the classical results [1–3], but essentially relies on equations of motion.

The approach developed in [5–7] can be extended to other boundary layer problems depending on a finite number of parameters. In particular, it was shown in [8, 9] that the Reynolds stress components in a zero-pressure-gradient boundary layer flow over a flat plate with uniform transpiration are universal functions of the streamwise-velocity gradient. For boundary layers with suction [9], these functions can be completely determined by using known characteristics of a reference flow, namely, the well-studied turbulent boundary layer flow over an impermeable flat plate. In particular, only the profile of streamwise velocity in the reference flow is required to find the relation between shear stress and velocity gradient.

In the present analysis, a closure condition derived by this method is used to solve the problem for an arbitrary suction velocity by the asymptotic method developed in [10, 11] for boundary-layer equations at high Reynolds numbers.

The resulting "exact" profiles of mean velocity, Reynolds stress components, skin friction coefficient, and integral flow characteristics are expressed in terms of scaling variables and compared with DNS results and experimental data. This comparison can be used to evaluate the experimental accuracy.

2. STATEMENT OF THE PROBLEM

Consider the incompressible turbulent boundary layer flow over a smooth flat plate with a constant free-stream velocity U_e and a constant wall suction velocity v_w parallel to the normal vector. The turbulent flow is assumed to develop from an origin located at the leading edge of the plate. The effect of free-stream fluctuations on the boundary layer flow is neglected.

2.1. Closure Condition

The mean flow characteristics (streamwise-velocity gradient, turbulent shear stress, and boundary-layer

thickness Δ) are universal functions of Cartesian coordinates x and y and flow parameters:

$$\frac{\partial u}{\partial y} = F_1(x, y, \nu, v_w, U_e),$$
$$\langle u'v'\rangle = F_2(x, y, \nu, v_w, U_e), \quad (1)$$
$$\Delta = F_3(x, \nu, v_w, U_e),$$

where ν is kinematic viscosity and the origin of the Cartesian coordinate system is set at the leading edge of the plate. The definition of Δ is given in the context of the analysis presented below. Before this is done, this quantity is tentatively treated as the transverse length scale of turbulent boundary layer flow.

The first and third equations in (1) are solved for x and U_e, and the results are substituted into the second equation in (1) to obtain

$$\langle u'v'\rangle = F_4\left(y, \nu, v_w, \Delta, \frac{\partial u}{\partial y}\right).$$

By applying Buckingham's Π-theorem, this relation is rewritten as

$$\langle u'v'\rangle = -\left(y\frac{\partial u}{\partial y}\right)^2 S(R_l, \beta, \eta), \quad R_l = \frac{y^2}{\nu}\frac{\partial u}{\partial y},$$
$$\beta = \frac{v_w}{R_l y\partial u/\partial y}, \quad \eta = \frac{y}{\Delta}, \quad (2)$$

where S is a universal function for the class of flows considered here, which are parameterized by ν, v_w, and U_e. It is assumed that this function is continuous at

$$0 \le R_l \le \infty, \quad -\infty \le \beta \le 0, \quad 0 \le \eta < \infty,$$

and differentiable inside these intervals. Moreover, it is assumed that

$$S(\infty, 0, 0) \neq 0.$$

It was shown in [7] that this condition must be satisfied if the reference flow over an impermeable flat plate has a logarithmic velocity distribution.

Expression (2) relates shear stress to the mean-velocity gradient. Since the dependence of this relation on the suction velocity must weaken with increasing distance from the wall, the parameter β is defined so that the denominator contains the local Reynolds number R_l.

Analogously, the normal Reynolds stress components are expressed as

$$\langle u'^2\rangle = \left(y\frac{\partial u}{\partial y}\right)^2 S_1(R_l, \beta, \eta),$$
$$\langle v'^2\rangle = \left(y\frac{\partial u}{\partial y}\right)^2 S_2(R_l, \beta, \eta), \quad (3)$$
$$\langle w'^2\rangle = \left(y\frac{\partial u}{\partial y}\right)^2 S_3(R_l, \beta, \eta),$$

where S_1, S_2, and S_3 are universal functions. However, the continuity condition holds only for S_2, which describes the behavior of the Reynolds stress component associated with transverse velocity fluctuations. According to theoretical results presented in [12, 13] and supported by measurements, its behavior near the wall is similar to that of shear stress. Therefore, there exists a nonzero quantity

$$S_2(\infty, 0, 0) = (\kappa/\sigma_2)^2, \quad (4)$$

where $\kappa = 0.41$ is von Kármán's constant and $\sigma_2 = 0.95$ according to experimental data [4].

The behavior of the stress components $\langle u'^2\rangle$ and $\langle w'^2\rangle$, which are associated with velocity fluctuations parallel to the wall, is more complicated:

$$S_1(\infty, 0, \eta) = -A_1\kappa^2\ln\eta + O(1),$$
$$S_3(\infty, 0, \eta) = -A_3\kappa^2\ln\eta + O(1), \quad \eta \longrightarrow 0, \quad (5)$$

where A_1 and A_3 are universal constants. According to the results of the direct numerical simulations of turbulent boundary layer flow performed in [14] for Reynolds numbers R_{δ^*} (based on the displacement thickness) not higher than 2000,[1]

$$A_1 = 1.1, \quad A_3 = 0.36. \quad (6)$$

The conditions formulated here for S, S_1, S_2, and S_3 are based on the following physical assumptions [12, 13]: viscosity is essential only within a thin viscous sublayer, and the behavior of $\langle u'v'\rangle$ and $\langle v'^2\rangle$ near the wall is independent of the outer length scale (boundary-layer thickness), whereas the stress components $\langle u'^2\rangle$ and $\langle w'^2\rangle$ must depend on this scale because of the substantial anisotropy of near-wall turbulence.

[1] The numerical value $A_3 = 0.66$ given in [14] must be a misprint, because the value in (6) is obtained by processing the data presented therein.

2.2. Change of Variables

The streamfunction $\psi(x, y)$ of the mean flow satisfies the boundary-layer equation for zero-pressure-gradient flow:

$$\begin{aligned} &\psi_y\psi_{xy} - \psi_x\psi_{yy} = (\nu\psi_{yy} - \langle u'v'\rangle)_y, \\ &x > 0, \quad y = 0: \ \psi_y = 0, \quad \psi_x = -v_w, \\ &y \longrightarrow \infty: \ \psi_y \longrightarrow U_e, \quad \langle u'v'\rangle \longrightarrow 0. \end{aligned} \tag{7}$$

The following change of variables is performed in (7) [10]:

$$\begin{aligned} &\psi = U_e\Delta\Psi(\xi, \eta), \quad \Lambda(\xi) = \frac{dR_\Delta}{dR_x}, \quad \xi = \ln R_\Delta, \\ &R_x = \frac{U_e x}{\nu}, \quad R_\Delta = \frac{U_e\Delta}{\nu}. \end{aligned} \tag{8}$$

The independent variables ξ and η are defined as the logarithm of the Reynolds number based on the boundary-layer thickness and the normalized distance from the wall, respectively. In addition to the dimensionless streamfunction $\Psi(\xi, \eta)$, the unknown function $\Lambda(\xi)$ is introduced here. It is defined as the slope of Δ as a function of the streamwise coordinate. By virtue of (2), $\Psi(\xi, \eta)$ and $\Lambda(\xi)$ satisfy the following equation [10]:

$$\begin{aligned} &\Lambda[\Psi_\eta\Psi_{\xi\eta} - \Psi_{\eta\eta}(\Psi + \Psi_\xi)] \\ &= [(\eta\Psi_{\eta\eta})^2 S(R_1, \beta, \eta) + e^{-\xi}\Psi_{\eta\eta}]_\eta, \\ &R_1 = e^\xi\eta^2\Psi_{\eta\eta}, \quad \beta = B(\eta R_1\Psi_{\eta\eta})^{-1}. \end{aligned} \tag{9}$$

$$\begin{aligned} &\xi > -\infty, \quad \eta = 0: \\ &\Psi_\eta = 0, \quad \Lambda(\Psi + \Psi_\xi) = -B, \end{aligned} \tag{10}$$

$$\eta \longrightarrow \infty: \ \Psi_\eta \longrightarrow 1, \quad \eta\Psi_{\eta\eta}\sqrt{S(R_1, \beta, \eta)} \longrightarrow 0, \tag{11}$$

where $B = v_w/U_e$ is the normalized wall suction velocity. Boundary conditions (10) and (11) are set on the plate and in the free stream, respectively. In accordance with the order of the differential equation, two conditions (for velocity and shear stress) are set at the outer boundary.

To find an asymptotic solution to problem (9)–(11) at $\xi \longrightarrow \infty$, a small parameter ε and a new independent variable are introduced:

$$\zeta = \varepsilon\xi, \quad 1/\zeta = O(1).$$

Thus, the small parameter used in the present analysis is inversely proportional to the logarithm of the Reynolds number based on the transverse length scale of the flow.

The normalized wall suction velocity is expressed as

$$B = \varepsilon^2 b, \quad b = O(1); \tag{12}$$

i.e., the transverse velocity component at the wall is assumed to be a small quantity of second order in ε.

The solution is represented by different asymptotic expansions in ε for different flow regions. In the transverse direction, two regions develop: an outer region and a near-wall region. In the former, molecular viscosity can be neglected in the boundary-layer equations and the characteristic length scale is the boundary-layer thickness. In the latter, the characteristic length scale is determined by the condition that turbulent and viscous stresses are similar in order of magnitude.

3. NEAR-WALL REGION

The variables used in the near-wall region are

$$\begin{aligned} &y_+ = \frac{yU_e\sqrt{c_f/2}}{\nu}, \quad u_+ = \frac{\psi_y}{U_e\sqrt{c_f/2}}, \\ &v_+ = \frac{v_w}{U_e\sqrt{c_f/2}}, \end{aligned} \tag{13}$$

where c_f is the skin friction coefficient.

According to [7], since v_+ is a small quantity (estimated as $v_+ = O(\varepsilon)$ below), the near-wall velocity and shear-stress profiles can be related to the velocity profile $u_+^0(y_+)$ in the turbulent boundary layer flow over an impermeable plate:

$$E \equiv \frac{2}{v_+}(\sqrt{1 + v_+u_+} - 1) = u_+^0(y_+) + O(v_+), \tag{14}$$

$$\begin{aligned} &\frac{2}{v_+}\left(\sqrt{\frac{du_+}{dy_+} - \langle u'v'\rangle_+} - 1\right) = u_+^0(y_+) + O(v_+), \\ &y_+ \geq 0. \end{aligned} \tag{15}$$

The profile of rms transverse-velocity fluctuation can also be expressed in terms of known functions:

$$\begin{aligned} &\sqrt{\langle v'^2\rangle_+} = \sqrt{\langle v'^2\rangle_+^0(y_+)} + \frac{v_+}{2\sigma_2}u_+^0(y_+) + O(v_+), \\ &y_+ \geq 0. \end{aligned} \tag{16}$$

The first term on the right-hand side in (16) is the corresponding profile in the reference flow, and the constant σ_2 is defined by (4). The estimate $O(v_+)$ for the remainder term in (14)–(16) is uniformly valid for all $y_+ \geq 0$.

Outside the viscous sublayer, the function u_+^0 exhibits its logarithmic asymptotic behavior:

$$u_+^0(y_+) = \frac{1}{\kappa}(\ln y_+ + C_0) + w_+(y_+),$$
$$w_+(y_+) = O(y_+^{-\alpha}), \quad y_+ \longrightarrow \infty, \quad \alpha > 0. \tag{17}$$

The role of von Kármán's constant κ is played by $\sqrt{S(\infty, 0, 0)}$. According to experimental data, $C_0 = 2.05$ [4].

4. OUTER REGION

Generally, two regions develop in a boundary layer with suction along the streamwise direction [11, 15]. In the upstream (moderate-suction) region, the shear stress at the wall is similar in order of magnitude to that in the outer region. While the wall suction velocity remains constant, a strong-suction region develops as the Reynolds number increases downstream of the moderate-suction region, where the shear stress at the wall is much stronger than that in the outer region. The Reynolds stress components in the outer region are comparable to $\Lambda^2(\xi)$ in order of magnitude. The moderate-suction solution obtained in [11] has a singularity at

$$\zeta = 2\kappa(-b)^{-1/2},$$

which corresponds to a vanishing leading-order term in the expansion of $\Lambda(\xi)$.

To analyze the strong-suction flow in the neighborhood of this singular point (or line if the flow variable in question depends on the transverse coordinate), a new variable $s = O(1)$ is introduced by the following formula [15]:

$$s = \xi - 2\kappa(-B)^{-1/2} - k\ln(-B)$$
$$= \varepsilon^{-1}[\xi - 2\kappa(-b)^{-1/2}] - 2k\ln\varepsilon - k\ln(-b), \tag{18}$$

where k is a constant parameter to be determined.

The function $\Lambda(\xi)$ is a quantity on the order of ε in the moderate-suction region. Since its leading-order part vanishes at the singular point [11], the strong-suction solution is sought in the following form (see [15]):

$$\Lambda(\xi) = -\varepsilon^2 b\lambda(s) + O(\varepsilon^3), \tag{19}$$

$$\Psi(\xi, \eta) = \Psi_w(\xi) + \eta - \varepsilon^2 b g(s, \eta) + O(\varepsilon^3). \tag{20}$$

Here, $\Psi_w(\xi)$ is the streamfunction value on the wall, and $g(s, 0) = 0$ accordingly. By virtue of the second wall boundary condition in (10) combined with (12) and (19), it holds that

$$\Psi_w(\xi) + \frac{d\Psi_w(\xi)}{d\xi} = \frac{1}{\lambda(s)} + O(\varepsilon). \tag{21}$$

Substituting (19)–(21) into Eq. (9), using (18), and taking the limit for $s = O(1)$ and $1/\eta = O(1)$ as $\varepsilon \longrightarrow 0$, one obtains a partial differential equation for $g(s, \eta)$ and $\lambda(s)$:

$$[(\eta g_{\eta\eta})^2 S]_\eta + (1 + \eta\lambda) g_{\eta\eta} = \lambda g_{s\eta},$$
$$g(s, 0) = g_\eta(s, \infty) = 0, \quad \lim_{\eta\to\infty} \eta g_{\eta\eta}\sqrt{S} = 0. \tag{22}$$

Hereinafter, S is used to denote $S(\infty, 0, \eta)$ for brevity.

The moderate-suction solution corresponds to the limit of Eq. (22) as

$$s \longrightarrow -\infty, \ \lambda(s) \longrightarrow \infty, \ g(s, \eta) \longrightarrow \lambda(s) f(\eta). \tag{23}$$

The function $f(\eta)$ satisfies the following boundary value problem for an ordinary differential equation:

$$[(\eta f'')^2 S]' + \eta f'' = 0,$$
$$f(0) = f'(\infty) = 0, \quad \lim_{\eta\to\infty} \eta f''\sqrt{S} = 0. \tag{24}$$

The solution to problem (24) is

$$f'(\eta) = -\int_\eta^\infty \frac{\Phi d\eta}{2\eta\sqrt{S}}, \quad \Phi(\eta) = \int_\eta^\infty \frac{d\eta}{\sqrt{S}}. \tag{25}$$

The function $f'(\eta)$ describes the velocity profile in turbulent boundary layer flow over an impermeable flat plate [10]. It follows from (25) that its asymptotic form at the wall is

$$f'(\eta) = \frac{F_1}{\kappa}(\ln\eta + A_0 - \ln F_1) + O(\eta^\alpha),$$
$$\eta \longrightarrow 0, \quad \alpha > 0, \quad F_1 \equiv \sqrt{-f(\infty)} = \frac{\Phi(0)}{2}, \tag{26}$$

where A_0 is a constant. Expression (26) is obtained by evaluating the integral in (25) by parts.

The opposite limit, $\lambda = 0$, corresponds to the asymptotic suction boundary layer (one-dimensional flow in which all averaged flow variables depend only on the distance from the wall [9]). This region develops far downstream from the plate's leading edge. Setting $\lambda = 0$ in Eq. (22) yields the following boundary value problem for an ordinary differential equation in g:

$$[(\eta g'')^2 S]' + g'' = 0,$$
$$g(0) = g'(\infty) = 0, \quad \lim_{\eta\to\infty} \eta g''\sqrt{S} = 0. \tag{27}$$

Hence,

$$g' = -\frac{h^2}{4}, \quad h(\eta) = \int_\eta^\infty \frac{d\eta}{\eta\sqrt{S}}. \tag{28}$$

The formula for $h(\eta)$ in (28) is used to obtain the following logarithmic asymptotic expression at the wall:

$$h(\eta) = -\frac{1}{\kappa}(\ln\eta + A_\infty - \ln F_1) + O(\eta^\alpha), \quad \eta \longrightarrow 0, \quad \alpha > 0, \tag{29}$$

where A_∞ is a constant.

Thus, solutions to Eq. (22) describe the entire family of velocity profiles in turbulent boundary layers with suction, including the limit cases of flow over an impermeable plate and asymptotic boundary layer flow.

Equation (22) has the first integral

$$(\eta g_{\eta\eta})^2 S + (1 + \lambda\eta) g_\eta - \lambda(g + g_s) = G, \tag{30}$$

$$G(s) = -\lambda(s)\left[g(s, \infty) + \frac{d}{ds} g(s, \infty)\right]. \tag{31}$$

The analysis presented below makes use of the function $\gamma(s, \eta)$ related to $g(s, \eta)$ as follows:

$$g_\eta = -\gamma^2/4 - \gamma\sqrt{G}. \tag{32}$$

Substituting (32) into (30) yields

$$(\eta\gamma_\eta)^2 S = 1 + O(\eta), \quad \eta \longrightarrow 0.$$

Hence, the asymptotic form of $\gamma(s, \eta)$ at the wall is

$$\gamma(s, \eta) = -\frac{1}{\kappa}[\ln\eta + A(s) - \ln F_1] - w(s, \eta), \quad w(s, \eta) = O(\eta^\alpha), \quad \eta \longrightarrow 0, \quad \alpha > 0, \tag{33}$$

where $A(s)$ is some function.

5. MATCHING OF SOLUTIONS

The skin friction coefficient is sought in the following form [15]:

$$\frac{c_f}{2} = -\varepsilon^2 b + \varepsilon^4 b^2 t(s) + O(\varepsilon^5). \tag{34}$$

The solutions for the outer and near-wall regions of the boundary layer flow are matched with the use of (14), (17), (32), and (33) as follows. The wall variables y_+ and u_+ are related to the outer variables η and Ψ_η by expressions (13), where the first one can be rewritten by using (18) as

$$y_+ = \varepsilon^{2k}(-b)^k \sqrt{\frac{c_f}{2}} \exp\left(\frac{2\kappa}{\varepsilon\sqrt{-b}} + s\right)\eta. \tag{35}$$

It follows from (12) and (34) that

$$v_+ = -\varepsilon\sqrt{-b} + O(\varepsilon^2). \tag{36}$$

According to (20) and (32),

$$\Psi_\eta = 1 + \varepsilon^2 b\left[\frac{\gamma^2(s, \eta)}{4} + \gamma(s, \eta)\sqrt{G(s)}\right] + O(\varepsilon^3). \tag{37}$$

Rewrite (14) in terms of the outer variables by using (13) and (35), taking into account (34), (36), and (37). For $s = O(1)$ and $1/\eta = O(1)$, consider the expansion of (14) in ε to terms of order unity. The expansion of the left-hand side of (14) is

$$\frac{2}{\varepsilon\sqrt{-b}} - \sqrt{\gamma^2 + 4\gamma\sqrt{G} + 4t} + O(\varepsilon). \tag{38}$$

By virtue of asymptotic formula (17), the expansion of the right-hand side is

$$\frac{2}{\varepsilon\sqrt{-b}} + \frac{2k+1}{\kappa}\ln\varepsilon + \frac{1}{\kappa} + \left[\ln\eta + s + \left(k + \frac{1}{2}\right)\ln(-b) + C_0\right] + O(\varepsilon). \tag{39}$$

Equating like terms in (38) and (39), one obtains $k = -1/2$ and

$$\sqrt{\gamma^2 + 4\gamma\sqrt{G} + 4t} = -\frac{1}{\kappa}(\ln\eta + s + C_0).$$

According to the asymptotic matching principle [16], this equality is compared to asymptotic formula (33) to obtain

$$t(s) = G(s), \tag{40}$$

$$A(s) - \ln F_1 = s + C_0 - 2\kappa\sqrt{G(s)}. \tag{41}$$

The latter relation here is used as a closure condition to solve boundary value problem (22) for $g(s, \eta)$ and $\lambda(s)$. The former combined with (31) relates the skin friction coefficient to the resulting solution. Relation (40) can also be derived from the integral momentum equation for turbulent boundary layer flow.

To solve boundary value problem (22) under additional condition (41), only the function $S(\infty, 0, \eta)$ is required. By virtue of Eq. (24), it can be expressed in quadratures by using its relation to $f'(\eta)$:

$$S = \frac{f - f(\infty) - \eta f'}{(\eta f'')^2}. \tag{42}$$

Since $f'(\eta)$ describes the velocity profile in turbulent boundary layer flow over an impermeable plate, it is well known from experimental data. In this study, it is calculated by using an empirical formula proposed in [17]:

$$\frac{f'(\eta)}{F_1} = \frac{1}{\kappa}[\ln\eta - 0.55(1 + \cos(\pi\eta))], \quad 0 < \eta \le 1, \quad F_1 = \frac{1.55}{\kappa}, \quad \eta = \frac{y}{\Delta}. \tag{43}$$

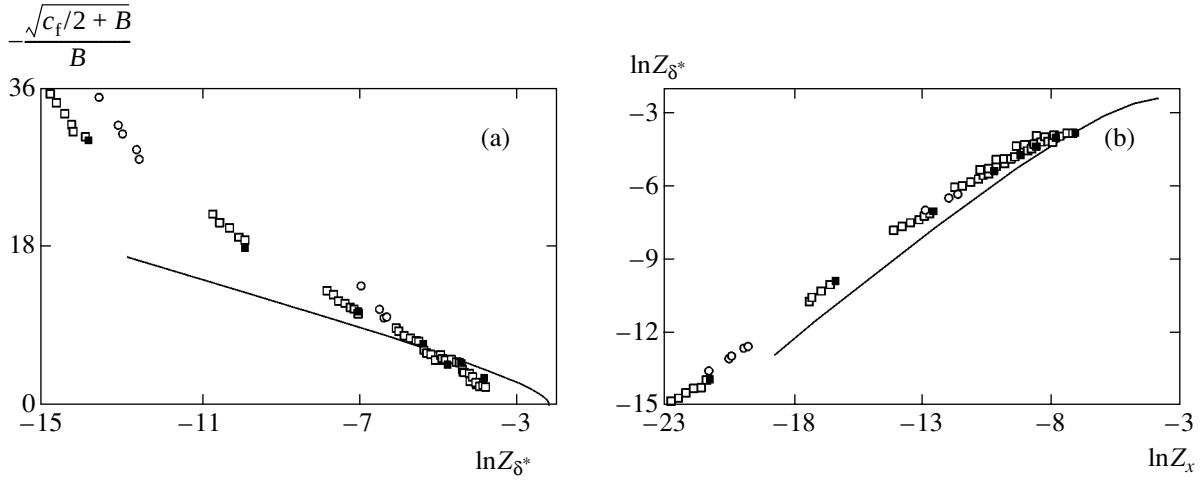

Fig. 1. Experimental results from [18, 19] (symbols) and computed curves of (a) skin friction coefficient and (b) displacement thickness plotted in terms of scaling variables for the strong-suction flow: ○—[18]; □—[19] (indirect measurements); ■—[19] (measured with floating elements).

The boundary-layer thickness Δ is defined here as the distance from the wall to the point where the streamwise mean-velocity component differs from U_e by 0.5%. This definition of boundary-layer thickness related to a specific velocity profile in the reference flow is used in what follows.

6. SCALING LAWS

6.1. Skin Friction and Displacement Thickness

Define the scaling variables

$$Z_{\left\{\begin{smallmatrix}\delta^*\\ x\end{smallmatrix}\right\}} \equiv (-B)^{1/2\mp 1}\exp\left(\frac{-2\kappa}{\sqrt{-B}}\right)R_{\left\{\begin{smallmatrix}\delta^*\\ x\end{smallmatrix}\right\}}. \tag{44}$$

By virtue of (20), the displacement thickness is

$$\delta^* = -\varepsilon^2 b e^{\xi}[g(s,\infty)+O(\varepsilon)]. \tag{45}$$

By the definition of $\Lambda(\xi)$ in (8), it holds that

$$R_x = \int_{-\infty}^{\xi}\frac{de^{\xi}}{\Lambda(\xi)}.$$

For the strong-suction region, these expressions are combined with (18) and (19) to obtain

$$Z_{\delta^*} = -g(s,\infty)e^s + O(\varepsilon), \tag{46}$$

$$Z_x = \int_{-\infty}^{s}\frac{e^s}{\lambda(s)}ds + O(\varepsilon). \tag{47}$$

Representations (46) and (47), boundary value problem (22) for $g(s,\eta)$ and $\lambda(s)$, the ensuing relations (31) and (41), and expression (40) for $t(s)$ suggest that the distributions of skin friction and displacement thickness along the plate obey the following scaling laws in the strong-suction region:

$$\ln Z_{\left\{\begin{smallmatrix}\delta^*\\ x\end{smallmatrix}\right\}} = \Phi_{\left\{\begin{smallmatrix}1\\ 2\end{smallmatrix}\right\}}(t) + O(\sqrt{-B}),$$
$$t = \frac{c_f/2+B}{B^2} + O(\sqrt{-B}), \tag{48}$$

where Φ_1 and Φ_2 are universal functions.

Figure 1a shows the distribution of skin friction coefficients along the plate plotted by representing experimental results from [18, 19] in terms of scaling variables (44) and using (48). Here, the intervals of the Reynolds number and normalized suction velocity correspond to well-developed turbulent boundary layer flow: $4 \le R_x \times 10^{-5} \le 20$ and $1.2 \le -B \times 10^3 \le 2.4$ in [18], and $3.8 \le R_x \times 10^{-5} \le 35$ and $1 \le -B \times 10^3 \le 3.6$ in [19]. In [18], the skin friction coefficient was determined indirectly from measured velocity profiles. In [19], it was determined both indirectly by three different methods and directly by using "floating elements" on the wall surface.

Small values of Z_{δ^*} correspond to the moderate-suction region. In agreement with the scaling law formulated above, the data points shown in Fig. 1a tend to follow a unique curve with increasing Z_{δ^*}, approaching the solution obtained by computing boundary value problem (22), (41) (see Section 10).

Figure 1b shows the distribution of displacement thickness along the plate measured in [18, 19]. It is clear that the measured results plotted in terms of variables (44) can be approximated by a single curve. How-

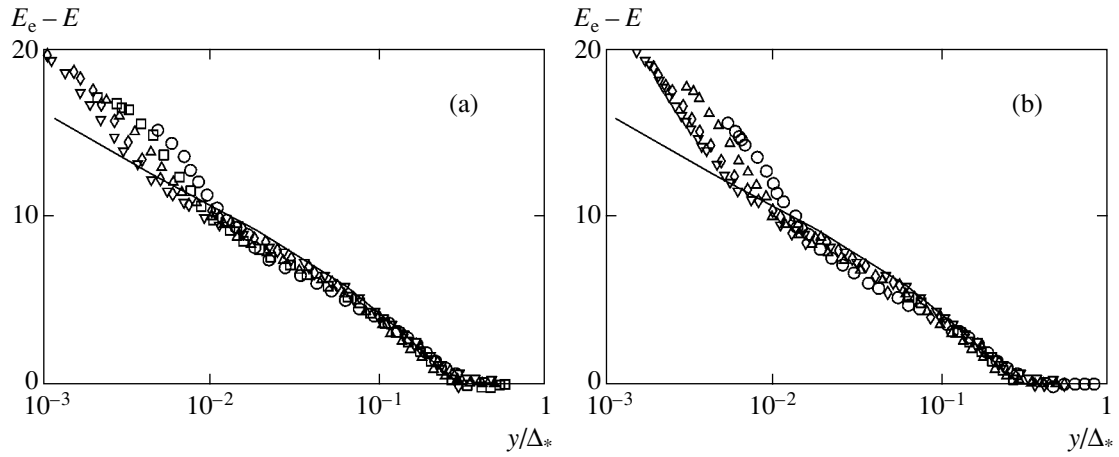

Fig. 2. Experimental velocity profiles from [21] plotted in terms of scaling variables for $R_x \times 10^{-5} = 4.0$ (○), 6.8 (□), 9.3 (△), 12 (▷), 15 (◇), and 20 (▽): (a) $B = -0.0012$, $-0.036 \le q \le -0.029$; (b) $B = -0.0024$, $-0.1 \le q \le -0.072$.

ever, this curve approaches the computed solution only within a small interval corresponding to the strong-suction region.

6.2. Velocity and Reynolds Stress Components

Solution of (37) as a quadratic equation for γ, combined with (40) and (14), yields

$$E_e - E = \frac{2(U_e - u)}{U_e(\sqrt{c_f/2 + B} + \sqrt{c_f/2 + Bu/U_e})} = \gamma(q, \eta) + O(\sqrt{c_f}), \quad (49)$$

$$q \equiv \frac{B}{\sqrt{c_f/2 + B}} = -\frac{1}{\sqrt{t}} + O(\sqrt{-B}), \quad -\infty \le q \le 0.$$

Here, E_e denotes the value of E in the free stream. Relation (49) demonstrates that velocity profiles outside the viscous sublayers of boundary layers with suction depend on a single variable q. When $q = 0$, scaling law (49) reduces to the well-known velocity defect law for the flow over an impermeable flat plate. By virtue of (23), (31), and (40),

$$\gamma(0, \eta) = -\frac{f'(\eta)}{F_1}. \quad (50)$$

The other limit case, $q = -\infty$, corresponds to the asymptotic boundary layer, where

$$\gamma(-\infty, \eta) = h(\eta).$$

A convenient representation of results makes use of the transverse length scale defined as

$$\Delta_* = \int_0^\infty (E_e - E)dy. \quad (51)$$

For the flow over an impermeable plate, it reduces to the boundary-layer thickness $\delta^*/\sqrt{c_f/2}$ introduced in [20]. By virtue of (49), it holds that

$$\frac{\Delta_*}{\Delta} = \int_0^\infty \gamma(q, \eta)d\eta + O(\sqrt{c_f}). \quad (52)$$

For $q = 0$, this expression combined with (50) yields

$$\frac{\Delta_*}{\Delta} = F_1 + O(\sqrt{c_f}).$$

In Fig. 2, the velocity profiles measured in [21] for turbulent boundary layer over a flat plate with suction are represented in terms of scaling variables (49) for several Reynolds numbers and two values of B. The corresponding intervals of q are specified in the figure caption to Fig. 2. Solid curves represent velocity profiles in the turbulent boundary layer flow over an impermeable flat plate. Since the experimental conditions correspond to small values of q, all data points lie close to the curves, except for the points representing the viscous sublayer.

The Reynolds stress components also obey one-parameter scaling laws. Substituting (37) into (2) and (3) yields

$$\frac{\sqrt{\nu \partial u/\partial y - \langle u'v' \rangle}}{U_e(\sqrt{c_f/2 + B} - B)} = Q(q, \eta)\sqrt{S(\infty, 0, \eta)} + O(\sqrt{c_f}), \quad (53)$$

$$\frac{\sqrt{\langle v'^2 \rangle}}{U_e(\sqrt{c_f/2 + B} - B)} = Q(q, \eta)\sqrt{S_2(\infty, 0, \eta)} + O(\sqrt{c_f}), \quad (54)$$

$$Q(q, \eta) = \frac{\eta \gamma_\eta(q, \eta)}{1 - q}\left(\frac{q\gamma(q, \eta)}{2} - 1\right), \quad -\infty \le q \le 0.$$

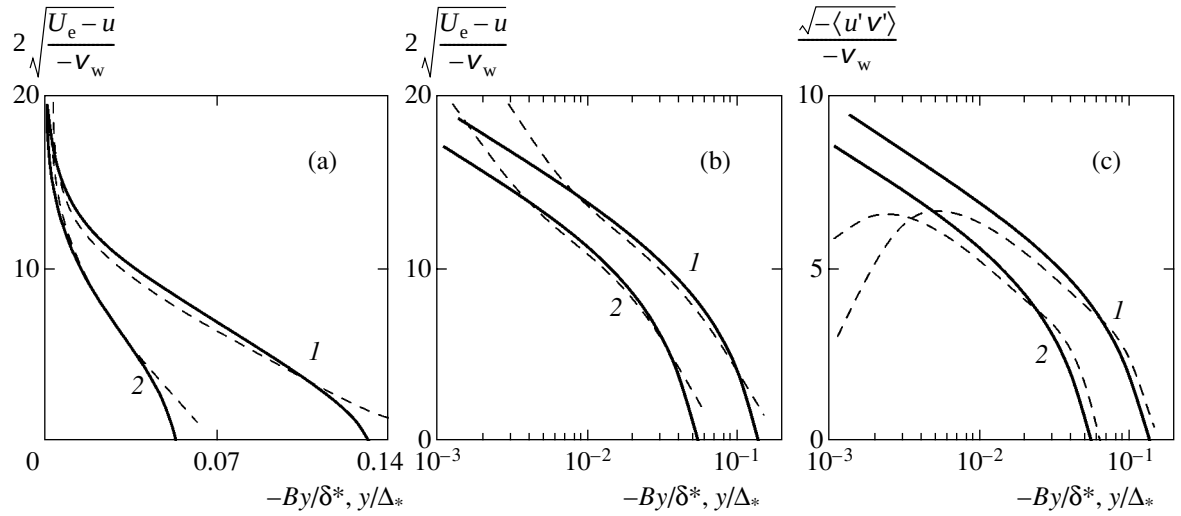

Fig. 3. Velocity (a, b) and turbulent shear stress (c) profiles in asymptotic boundary layer calculated by using (28) (solid curves) and predicted in DNS studies [22, 23] (dashed curves). Curves *1* and *2* are plotted with Δ_* and $-\delta^*/B$ (*2*) used as a transverse length scale, respectively.

The formulas for the components $\langle u'^2\rangle$ and $\langle w'^2\rangle$ are analogous to (54). The expressions for shear stress and rms transverse velocity fluctuation must hold everywhere outside the viscous sublayer. The scaling laws for the streamwise and spanwise velocity fluctuations are valid in the narrower region where asymptotic representations (5) hold.

By virtue of Eqs. (24) and (27), formula (53) reduces to

$$\frac{\nu\partial u/\partial y - \langle u'v'\rangle}{c_f U_e^2/2} = 1 + \frac{\eta f'(\eta) - f(\eta)}{f(\infty)} + O(\sqrt{c_f}),$$
$$\frac{\sqrt{\nu\partial u/\partial y - \langle u'v'\rangle}}{-v_w} = \frac{h(\eta)}{2} + O(\sqrt{c_f}), \tag{55}$$

in the limit cases of $q = 0$ and $q = -\infty$, respectively.

By using (4), (5), and (33), the following expansions are obtained for the Reynolds stress components:

$$\sqrt{\nu\frac{\partial u}{\partial y} - \langle u'v'\rangle} = \frac{v_w}{2\kappa}\ln\eta + O(1),$$
$$\sqrt[3]{\langle u'^2\rangle} = -\sqrt[3]{\frac{A_1 v_w^2}{4\kappa^2}}\ln\eta + O(1),$$
$$\sqrt{\langle v'^2\rangle} = \frac{v_w}{2\kappa\sigma_2}\ln\eta + O(1), \tag{56}$$
$$\sqrt[3]{\langle w'^2\rangle} = -\sqrt[3]{\frac{A_3 v_w^2}{4\kappa^2}}\ln\eta + O(1), \quad \eta \longrightarrow 0.$$

These results show that there exists a near-wall region where both square root of shear stress and rms transverse velocity fluctuation are proportional to the logarithm of distance from the wall, while the rms streamwise and spanwise velocity fluctuations behave as the logarithm to the power 3/2. All constants in (56) are known from experimental data for the turbulent boundary layer flow over an impermeable flat plate.

6.3. Asymptotic Boundary Layer

As applied to the asymptotic boundary layer, formulas (49) and (51) reduce to

$$2\sqrt{\frac{U_e-u}{-v_w}} = h(\eta) + O(\sqrt{c_f}),$$
$$\Delta_* = 2\int_0^\infty \sqrt{\frac{U_e-u}{-v_w}}\,dy. \tag{57}$$

Taking the integral in (28) by parts yields

$$\int_0^\infty h\,d\eta = 2F_1.$$

Hence,

$$\frac{\Delta_*}{\Delta} = 2F_1 + O(\sqrt{c_f}).$$

Thus, the values of the integral in (52) corresponding to $q = 0$ and $-\infty$ differ by a factor of two.

By squaring both sides of (57) and integrating the result across the boundary layer, the following relation is obtained:

$$-\frac{\delta^*}{B\Delta} = \int_0^\infty \frac{h^2}{4}d\eta + O(\sqrt{c_f}).$$

It holds that

$$\int_0^\infty \frac{h^2}{4} d\eta = \frac{F_1 D}{\kappa}, \quad D = A_0 - A_\infty. \tag{58}$$

This relation is derived by rewriting (25) with the use of (28) as

$$f' = \int_\eta^\infty \frac{\Phi h' d\eta}{2} = -\frac{h\Phi}{2} + \frac{\eta h^2}{4} + \int_\eta^\infty \frac{h^2}{4} d\eta, \tag{59}$$

setting $\eta = 0$, and taking into account asymptotic laws (26) and (29).

Figures 3a, 3b, and 3c show, respectively, linear and semilogarithmic plots of velocity and turbulent shear-stress profiles. Solid and dashed curves represent the results of calculations based on (28) and the DNS results obtained for $B = -0.00361$ and $R_{\delta^*} = 1000$ in [22, 23]. Even though the simulations were performed for a relatively low Reynolds number, the solid and dashed curves shown in Figs. 3a and 3b demonstrate very good agreement outside the viscous sublayer, while those in Fig. 3c are in fair agreement. The dashed curves shown in Figs. 3b and 3c contain intervals of logarithmic behavior, which are relatively narrow because of the low Reynolds number, in agreement with theoretical predictions.

Figures 2 and 3 demonstrate that the profiles of velocity and shear stress in the outer region measured and computed in [21] and [22, 23], respectively, are in good agreement with theory when represented in terms of the outer scaling variables. When plotted in terms of the near-wall scaling variables, the same set of data points does not follow scaling laws (14) and (15). In particular, the velocity profiles have logarithmic portions with slopes close to $1/\kappa$, but they are shifted relative to the velocity profile predicted for the turbulent boundary layer flow over an impermeable plate. This discrepancy between computed and measured results can be attributed, respectively, to the low Reynolds number used in [22, 23] and the error of near-wall velocity measurements with a Prandtl–Pitot tube in flows with transpiration in [21] (see [24]).

Figure 4 shows the rms velocity fluctuations in the asymptotic boundary layer with suction plotted by using the results reported in [22, 23]. For comparison, the figure also shows line segments corresponding to scaling laws (56) with constants known for the turbulent boundary layer flow over an impermeable plate. Figure 4 demonstrates that at least curves *2* and *3* (which represent the *y* and *z* components of velocity fluctuations, respectively) have distinct logarithmic portions.

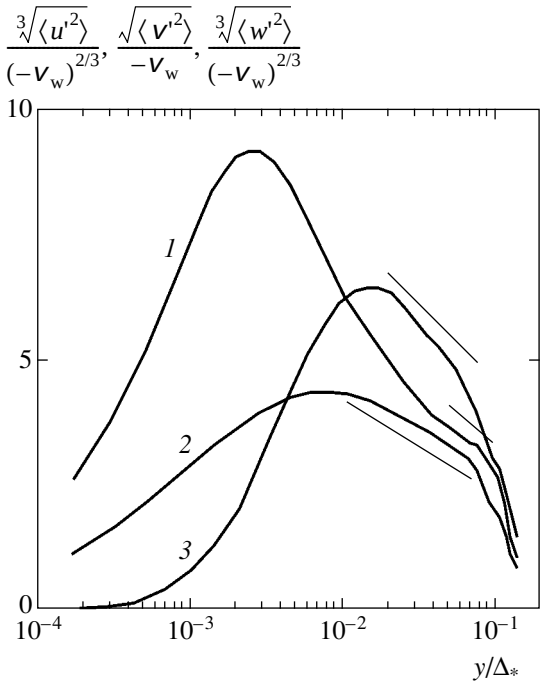

Fig. 4. Rms velocity fluctuations in asymptotic boundary layer based on results reported in [22, 23]: (*1*) $\langle u'^2\rangle$; (*2*) $\langle v'^2\rangle$; (*3*) $\langle w'^2\rangle$.

6.4. Boundary-Layer Shape Factors

By virtue of (20), the velocity profile in the outer region can be represented as

$$\frac{U_e - u}{v_w} = g_\eta(s, \eta) + \varepsilon g_1(s, \eta, \varepsilon),$$

$$g_1(s, \eta, \varepsilon) = O(1), \quad \varepsilon \longrightarrow 0.$$

Hence, the following expressions are obtained for integral characteristics of boundary layer flow:

$$\frac{\delta^*}{B\Delta} = g(s, \infty) + \varepsilon I_1(s),$$

$$\frac{\theta}{B\Delta} = g(s, \infty) + \varepsilon I_1(s) + Bg(s, \infty) I(s) + O(\varepsilon^3), \tag{60}$$

$$\frac{\delta^{**}}{2B\Delta} = g(s, \infty) + \varepsilon I_1(s) + \frac{3B}{2} g(s, \infty) I(s) + O(\varepsilon^3),$$

$$I_1(s) = \int_0^\infty g_1(s, \eta, \varepsilon) d\eta,$$

$$I(s) = -\int_0^\infty \frac{[g_\eta(s, \eta)^2] d\eta}{g(s, \infty)},$$

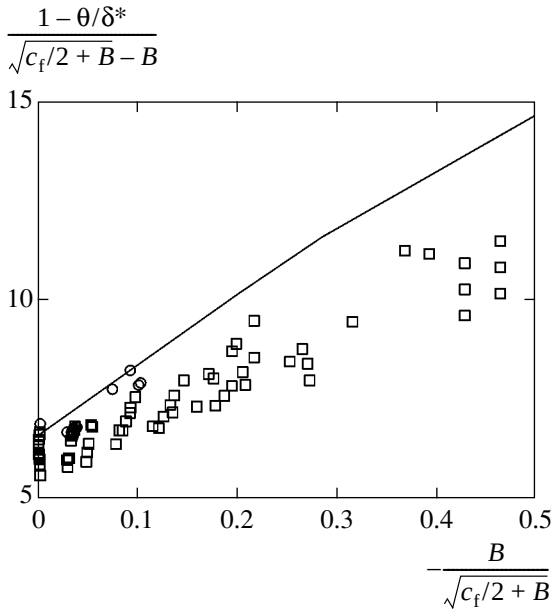

Fig. 5. Boundary-layer shape factor: experimental results from [18, 19] (symbols) and computed curve. Symbol notation is the same as in Fig. 1.

where θ and δ^{**} are the momentum and energy thicknesses, respectively. Formulas (60) entail the relations

$$\frac{1}{B}\left(1-\frac{\theta}{\delta^*}\right) = I(s) + O(\varepsilon),$$

$$\frac{1}{B}\left(\frac{2}{3}-\frac{\delta^{**}}{\delta^*}\right) = I(s) + O(\varepsilon).$$

Combined with (40), they determine relations between the boundary-layer shape factors, suction velocity, and skin friction coefficient:

$$\begin{aligned}\frac{1-\theta/\delta^*}{\sqrt{c_f/2+B}-B} &= \Phi(q) + O(\sqrt{c_f}),\\ \frac{2/3-\delta^{**}/\delta^*}{\sqrt{c_f/2+B}-B} &= \Phi(q) + O(\sqrt{c_f}),\end{aligned} \qquad (61)$$

$$\Phi(q) = \frac{qI(s)}{q-1}.$$

By virtue of (32) and (50), it follows that

$$\Phi(0) = \int_0^\infty \frac{f'^2 d\eta}{F_1^3}$$

in the limit case of the flow over an impermeable flat plate. This integral is known as Clauser's shape factor [20]. Calculations based on (43) yield

$$\Phi(0) = 6.61. \qquad (62)$$

In the opposite limit case of asymptotic boundary layer, it is expressed as

$$\Phi(-\infty) = \frac{\kappa\int_0^\infty h^4 d\eta}{16F_1 D}.$$

The numerical value $\Phi(-\infty) = 39.3$ combined with (61) and $B = -0.00361$ can be used to find the shape factor for the asymptotic boundary layer flow: $\delta^*/\theta = 1.17$. Its value calculated by using DNS results reported in [22, 23] is 1.29.

Figure 5 compares the values of the boundary-layer shape factors measured in [18, 19] with a curve computed as described in Section 10. According to measurements reported in [18] and [19], Clauser's shape factor varies from 6.4 to 6.9 and from 5.6 to 6.4, respectively. The latter result is considerably lower than both 6.8 (recommended in [20]) and the value in (62) calculated in this study. The results obtained for the flow with suction by using data from [19] also lie below the calculated curve.

7. NEAR-MODERATE-SUCTION REGIME

The sum of the two expressions for g_η in the limit cases,

$$\lambda f' - h^2/4,$$

solves Eq. (22) with right-hand side set to zero. Substituting

$$g_\eta = \lambda f' - h^2/4 + \varphi_\eta \qquad (63)$$

into (22) and changing from s to the independent variable $\tau = 1/\lambda$, one finds that the functions $\varphi(\tau, \eta)$ and

$$\Omega(\tau) = -\frac{d\lambda}{ds} = \frac{d\tau}{\tau^2 ds} \qquad (64)$$

solve the boundary value problem

$$\begin{aligned}(\Phi + \tau h)(\eta\sqrt{S}\varphi_{\eta\eta})_\eta + \tau[(\eta\sqrt{S}\varphi_{\eta\eta})^2]_\eta\\ = \Omega(\tau^2\varphi_{\tau\eta} - f'),\end{aligned} \qquad (65)$$

$$\varphi(\tau, 0) = \varphi_\eta(\tau, \infty) = 0, \quad \lim_{\eta\to\infty}\eta\sqrt{S}\varphi_{\eta\eta} = 0, \qquad (66)$$

$$s(\tau) = A(\tau) - \ln F_1 - C_0 - 2\kappa\sqrt{t(\tau)}, \qquad (67)$$

$$\begin{aligned}t(\tau) = \frac{F_1^2}{\tau^2} + \frac{F_1 D}{\kappa\tau} - \frac{F_1^2\Omega(\tau)}{\tau} - \frac{\varphi(\tau,\infty)}{\tau}\\ - \tau\Omega(\tau)\frac{d\varphi(\tau,\infty)}{d\tau},\\ 0 \le \tau < \infty.\end{aligned} \qquad (68)$$

Expression (68) is equivalent to (31) rewritten by using (58) and taking into account (63).

7.1. Asymptotic Solution to Boundary Value Problem

As $\tau \longrightarrow 0$, the asymptotic solution to boundary value problem (65)–(67) is sought as a regular expansion in terms of τ:

$$\varphi(\tau, \eta) = \varphi_0(\eta) + \tau\varphi_1(\eta) + O(\tau^2), \tag{69}$$

$$s(\tau) = \sigma_1\tau^{-1} + \sigma_2 + O(\tau). \tag{70}$$

The derivative of (70) is combined with the definition of $\Omega(\tau)$ in (64) to obtain

$$\Omega(\tau) = \Omega(0) + O(\tau^2). \tag{71}$$

It follows from (68), (69), and (71) that

$$\sqrt{t} = F_1\tau^{-1} + O(1), \quad \tau \longrightarrow 0. \tag{72}$$

Taking the limit of (32) as $\tau \longrightarrow 0$ and using (40) and (72) yields

$$\gamma = -f'/F_1 + O(\tau).$$

Therefore, $A(\tau) = A_0 + O(\tau)$, and differentiation of (67) combined with (72) and (64) yields

$$\Omega(0) = 1/2\kappa F_1.$$

Substituting (69) and (71) into (65), one obtains linear ordinary differential equations for φ_0 and φ_1:

$$\Phi(\eta\sqrt{S}\varphi_0'')' + \frac{f'}{2\kappa F_1} = 0, \tag{73}$$

$$\Phi(\eta\sqrt{S}\varphi_1'')' + [(\eta\varphi_0'')^2 S]' + h(\eta\sqrt{S}\varphi_0'')' = 0. \tag{74}$$

The solution to Eq. (73) satisfying free-stream boundary condition in (66) is

$$\varphi_0' = \int_\eta^\infty \frac{N_1 d\eta}{2\kappa\eta\sqrt{S}} = \frac{hN_1 - N_2}{2\kappa},$$
$$N_1 = -\int_\eta^\infty \frac{f' d\eta}{F_1\Phi}, \quad N_2 = -\int_\eta^\infty \frac{hf' d\eta}{F_1\Phi}. \tag{75}$$

In view of (75), the solution to Eq. (74) satisfying the conditions set on the outer boundary has the form

$$\varphi_1' = -\int_\eta^\infty \frac{N_3 d\eta}{2\kappa F_1\eta\sqrt{S}} = \frac{N_4 - hN_3}{2\kappa F_1},$$
$$N_3 = \int_\eta^\infty \left(\frac{N_1}{\kappa} - h\right)\frac{f' d\eta}{\Phi^2}, \tag{76}$$
$$N_4 = \int_\eta^\infty \left(\frac{N_1}{\kappa} - h\right)\frac{hf' d\eta}{\Phi^2}.$$

Since the function S is given by (42), the latter integral in (25) can be calculated in explicit form:

$$\Phi = 2\sqrt{f - f(\infty) - \eta f'}.$$

Substituting (69) and (71) into the first integral of Eq. (65),

$$\eta\sqrt{S}(\Phi + \tau h)\varphi_{\eta\eta} + \tau(\eta\sqrt{S}\varphi_{\eta\eta})^2$$
$$+ (\tau + \eta)\varphi_\eta - \varphi + \Omega(f - \tau^2\varphi_\eta) \tag{77}$$
$$= \Omega\left[f(\infty) - \tau^2\frac{d\varphi(\tau, \infty)}{d\tau}\right] - \varphi(\tau, \infty)$$

using (75) and (76); and taking the left-hand side of Eq. (77) yields the following expressions required for further analysis:

$$\varphi_0(\infty) = \frac{F_1}{\kappa}\left(N_1(0) - \frac{1}{2}\right),$$
$$\varphi_1(\infty) = \frac{N_2(0) - 2N_3(0)}{2\kappa} - \frac{N_1^2(0)}{4\kappa^2}. \tag{78}$$

Analogous calculations are performed to find an asymptotic expansion of t as given by (68), which yields

$$\sqrt{t} = \frac{F_1}{\tau} + a_0 + \frac{a_1\tau}{F_1} + O(\tau^2), \quad \tau \longrightarrow 0,$$
$$a_0 = \frac{D - N_1(0)}{2\kappa}, \tag{79}$$
$$a_1 = \frac{2N_3(0) - N_2(0)}{4\kappa} - \frac{D^2 - 2DN_1(0)}{8\kappa^2}.$$

7.2. Asymptotic Forms of Universal Functions

The expansion of γ for a near-moderate-suction regime is sought in the following form:

$$\gamma(q, \eta) = -\frac{f'(\eta)}{F_1} + \frac{\gamma_1(\eta)}{\sqrt{t}} + \frac{\gamma_2(\eta)}{t} + O(t^{-3/2}),$$
$$t \longrightarrow \infty. \tag{80}$$

Substituting (80) into (32), using (79), equating the result to (63) combined with (69), and taking into account (75) and (76), one obtains

$$\gamma_1 = \frac{h^2}{4} - \frac{f'^2}{4F_1^2} + \frac{a_0 f'}{F_1} - \frac{hN_1 - N_2}{2\kappa},$$
$$\gamma_2 = \frac{(\gamma_1 + 2a_1)f'}{2F_1} + \frac{hN_3 - N_4}{2\kappa}. \tag{81}$$

Combined with the expressions for a_0 and a_1 and

asymptotic representations (26) and (29), this yields

$$\gamma_1(0) = \frac{D^2 - 2DN_1(0)}{4\kappa^2} + \frac{N_2(0)}{2\kappa},$$
$$\gamma_2(0) = \frac{DN_3(0)}{2\kappa^2} - \frac{N_4(0)}{2\kappa}. \quad (82)$$

Thus, while the first term in expansion (80) has a logarithmic asymptotic form, the functions γ_1 and γ_2 have no singularities on the wall. Calculations performed with the use of (43) yield the following values of the constant parameters in (82):

$$A_0 = 0.230, \quad A_\infty = -1.809, \quad N_1(0) = 0.601,$$
$$N_2(0) = 6.233, \quad N_3(0) = 3.354, \quad N_4(0) = 38.35.$$

The asymptotic expansion of the function A in (33) can now be written as

$$A = A_0 - \kappa\gamma_1(0)t^{-1/2} - \kappa\gamma_2(0)t^{-1} + O(t^{-3/2}), \quad t \longrightarrow \infty. \quad (83)$$

The functions Φ_1 and Φ_2 defined by (46), (47) are calculated by integrating (63) and using (58) and (69):

$$g(\tau, \infty) = -F_1^2\tau^{-1} - F_1D/\kappa + \varphi_0(\infty) + \varphi_1(\infty)\tau + O(\tau^2), \quad \tau \longrightarrow 0.$$

By using (79) to change to the variable t in this expansion and taking into account (67), (78), and (83), the following asymptotic expression for Φ_1 is obtained:

$$\Phi_1(t) = \Phi_1^\infty(t) + b_1t^{-1/2} + b_2t^{-1} + O(t^{-3/2}), \quad t \longrightarrow \infty, \quad (84)$$
$$\Phi_1^\infty(t) = -2\kappa\sqrt{t} + \ln\sqrt{t} + A_0 - C_0,$$
$$b_1 = \frac{D - N_1(0) + 1}{2\kappa} - \kappa\gamma_1(0),$$
$$b_2 = \frac{2N_3(0) - N_2(0)}{4\kappa} + \frac{N_1^2(0) - 2D + 2N_1(0) - 1}{8\kappa^2} - \kappa\gamma_2(0).$$

Evaluating the integral in (47) by parts yields

$$\Phi_2 = s + \ln\tau - \Omega(0)\tau + \frac{3}{2}\Omega^2(0)\tau^2 + O(\tau^3), \quad \tau \longrightarrow 0.$$

By using (79) to change to the variable t in this expansion and taking into account (67) and (83), this expansion is rewritten as

$$\Phi_2(t) = \Phi_2^\infty(t) + \left(b_1 - \frac{1}{\kappa}\right)t^{-1/2} + \left(b_2 + \frac{1}{2\kappa^2}\right)t^{-1} + O(t^{-3/2}), \quad t \longrightarrow \infty, \quad (85)$$
$$\Phi_2^\infty(t) = -2\kappa\sqrt{t} - \ln\sqrt{t} + A_0 - C_0.$$

8. NEAR-ASYMPTOTIC BOUNDARY-LAYER FLOW REGIME

To analyze the opposite limit of $\lambda \longrightarrow 0$, i.e., a near-asymptotic boundary-layer flow regime, the expression

$$g_\eta = -h^2/4 + \lambda\psi_\eta \quad (86)$$

is substituted into Eq. (22), and λ is treated as an independent variable instead of s. The functions $\psi(\lambda, \eta)$ and

$$\Omega_1(\lambda) = -\frac{d\lambda}{ds} = \Omega(\lambda^{-1}) \quad (87)$$

solve the boundary value problem

$$h(\eta\sqrt{S}\psi_{\eta\eta})_\eta + \lambda[(\eta\sqrt{S}\psi_{\eta\eta})^2]_\eta + \lambda\eta\psi_{\eta\eta} + \Omega_1(\lambda\psi_{\lambda\eta} + \psi_\eta) + \frac{h}{2\sqrt{S}} = 0, \quad (88)$$

$$\psi(\lambda, 0) = \psi_\eta(\lambda, \infty) = 0, \quad \lim_{\eta\to\infty}\eta\sqrt{S}\psi_{\eta\eta} = 0, \quad (89)$$

$$s(\lambda) = A(\lambda) - \ln F_1 - C_0 - 2\kappa\sqrt{t(\lambda)}, \quad (90)$$

$$t(\lambda) = \frac{F_1D}{\kappa}\lambda + \lambda\psi(\lambda, \infty)[\Omega_1(\lambda) - \lambda] + \lambda^2\Omega_1(\lambda)\frac{d\psi(\lambda, \infty)}{d\lambda}, \quad 0 \le \lambda < \infty. \quad (91)$$

8.1. Eigenvalue Problem

It follows from (88) that the function $\psi_0(\eta) \equiv \psi(0, \eta)$ is the solution to the ordinary differential equation

$$h(\eta\sqrt{S}\psi_0'')' + \frac{\omega\psi_0'}{F_1} + \frac{h}{2\sqrt{S}} = 0,$$
$$\omega = F_1\Omega_1(0), \quad (92)$$
$$\psi_0(0) = \psi_0'(\infty) = 0, \quad \lim_{\eta\to\infty}\eta\sqrt{S}\psi_0'' = 0.$$

If h is treated as an independent variable in (92), then the following equation is obtained for the function $z(h) = \psi_0'$:

$$\frac{d^2z}{dh^2} + \frac{\omega\eta\sqrt{S}z}{F_1 h} + \frac{\eta}{2} = 0,$$

$$z(0) = \frac{dz(0)}{dh} = 0, \quad 0 \le h < \infty.$$

Its solution can be represented near the wall as

$$z = F_1[Z_1(\omega)h + Z_2(\omega)] + O(e^{-\kappa h}), \quad h \longrightarrow \infty, \quad (93)$$

where the estimate for the remainder term is derived from (29). Consequently, the near-wall asymptotic behavior of ψ_0' follows a logarithmic law.

By solving (32) as a quadratic equation for γ and using (86), the function γ is expressed as

$$\gamma = \sqrt{h^2 - 4\lambda\psi_\eta + 4t} - 2\sqrt{t}.$$

Hence, in view of asymptotics (29), (33), and (93), it follows that

$$A = A_\infty + 2\kappa F_1 \lambda Z_1(\omega) + 2\kappa\sqrt{t} + O(\lambda^2), \quad \lambda \longrightarrow 0. \quad (94)$$

This expression is substituted into closure condition (90) and the result is differentiated with respect to λ. By virtue of (87), this yields an equation for ω:

$$2\kappa\omega Z_1(\omega) + 1 = 0. \quad (95)$$

Thus, the leading terms of asymptotics of the desired functions can be found by solving eigenvalue problem (92), (95).

The last two terms on the left-hand side of Eq. (92) are moved to the right, and the result is treated as a second-order equation with known right-hand side and solved by using the free-stream boundary conditions. Thus, an equation subject to initial conditions is replaced with an equivalent integral equation:

$$\psi_0'(\eta) = \omega\int_\eta^\infty \left[1 - \frac{h(\eta)}{h(\eta_1)}\right]\frac{\psi_0'(\eta_1)}{F_1}d\eta_1 + f'(\eta). \quad (96)$$

Then, the solution can be represented as a series expansion in ω:

$$\psi_0'(\eta) = f'(\eta) + \omega F_1\left[h(\eta)M(\eta) - 1 - \frac{f(\eta)}{F_1^2}\right] + O(\omega^2),$$

$$\omega \longrightarrow 0, \; M = -\int_\eta^\infty \frac{f'd\eta}{F_1^2 h},$$

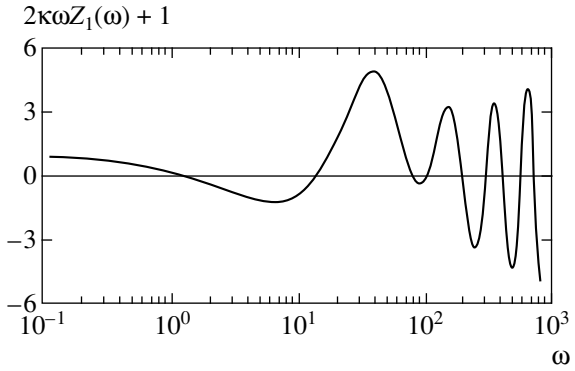

Fig. 6. Right-hand side of Eq. (95).

which is combined with (26) and (29) to obtain

$$Z_1(\omega) = -1 + M(0)\omega + O(\omega^2), \quad \omega \longrightarrow 0,$$

$$M(0) = 0.40.$$

A numerical analysis of (96) shows that Eq. (95) has an infinite number of positive roots (see the graph of its right-hand side in Fig. 6) and no negative roots. The smallest root is $\omega = 1.423$.

Thus, the desired asymptotic solution cannot be uniquely determined by analyzing boundary value problem (88)–(90) for a parabolic equation in the neighborhood of $\lambda = 0$. The value of ω is found numerically in Section 10 by taking into account the initial conditions at $\lambda = \infty$.

8.2. Asymptotic Behavior of the Universal Functions

Expression (91) can be rewritten as

$$t = \left[\frac{F_1 D}{\kappa} + \frac{\omega\psi_0(\infty)}{F_1}\right]\lambda + O(\lambda^2), \quad \lambda \longrightarrow 0. \quad (97)$$

By virtue of (86), (90), and (94), the function Φ_1 in (48) is represented as

$$\Phi_1 = D_1 + \ln\frac{D}{\kappa} - \left[\frac{F_1}{\omega} + \frac{\kappa\psi_0(\infty)}{F_1 D}\right]\lambda + O(\lambda^2),$$

$$\lambda \longrightarrow 0, \quad D_1 = A_\infty - C_0.$$

Combined with (97), this expression becomes

$$\Phi_1 = D_1 + \ln\frac{D}{\kappa} - \frac{\kappa t}{\omega D} + O(t^2), \quad t \longrightarrow 0. \quad (98)$$

By virtue of (47), (90), and (94), the function Φ_2 sat-

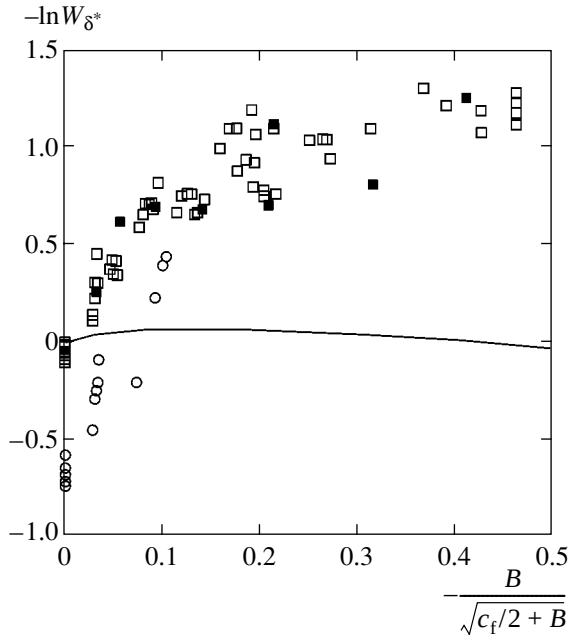

Fig. 7. Skin friction coefficients in flows over impermeable plates and plates with suction: experimental results from [18, 19] (symbols) and computed curve. Symbol notation is the same as in Fig. 1.

isfies the relation

$$\exp\Phi_2 = -\frac{\exp D_1}{\omega}\ln\lambda + O(1), \quad \lambda \longrightarrow 0.$$

In view of (97), it is equivalent to

$$\exp\Phi_2 = -\frac{\exp D_1}{\omega}\ln t + O(1), \quad t \longrightarrow 0. \qquad (99)$$

By eliminating t from (98) and (99), the displacement thickness is determined as a function of the streamwise coordinate:

$$Z_{\delta^*} = \frac{D}{\kappa}\exp D_1 - \frac{1}{\omega}\exp(D_1 - Z_x\omega\exp D_1) + \ldots,$$
$$Z_x \longrightarrow \infty.$$

These relations demonstrate that the asymptotic suction boundary layer develops only as $R_x \longrightarrow \infty$. In this limit, both $c_f/2 + B$ and the difference of the current and asymptotic values of displacement thickness vanish exponentially.

9. SKIN-FRICTION LAW AND VELOCITY AND REYNOLDS-STRESS PROFILES

9.1. Universal Skin-Friction Law

The expressions for skin friction in flow over a flat plate obtained in [11] for moderate and zero suction velocity can be written as

$$W_{\left\{\begin{smallmatrix}\delta^*\\ x\end{smallmatrix}\right\}} \equiv \frac{(c_f/2)^{1/2}}{(c_f/2+B)^{\pm 1/2}}$$
$$\times \exp\left[\frac{2\kappa}{B}(\sqrt{c_f/2} - \sqrt{c_f/2+B}) - A_0 + C_0\right] \qquad (100)$$
$$\times R_{\left\{\begin{smallmatrix}\delta^*\\ x\end{smallmatrix}\right\}} = O(\sqrt{c_f}).$$

To unify (100) and (48) into a universal skin-friction law, expression (34) for skin friction coefficient is substituted into (100) and the limit is taken for $t = O(1)$ as $B \longrightarrow -0$. The result is

$$\ln W_{\left\{\begin{smallmatrix}\delta^*\\ x\end{smallmatrix}\right\}} = \ln Z_{\left\{\begin{smallmatrix}\delta^*\\ x\end{smallmatrix}\right\}} - \Phi^{\infty}_{\left\{\begin{smallmatrix}1\\ 2\end{smallmatrix}\right\}}(t) + O(\sqrt{-B}) \qquad (101)$$

with Φ_1^{∞} and Φ_2^{∞} given by (84) and (85), respectively. The universal skin-friction law valid in the entire range of suction velocity has the form

$$\ln W_{\left\{\begin{smallmatrix}\delta^*\\ x\end{smallmatrix}\right\}} = \Gamma_{\left\{\begin{smallmatrix}1\\ 2\end{smallmatrix}\right\}}(t) + O(\sqrt{c_f}),$$
$$\Gamma_i(t) \equiv \Phi_i(t) - \Phi_i^{\infty}(t), \quad i = 1, 2. \qquad (102)$$

In the case of moderate suction, when $1/t = O(B)$, skin-friction law (102) is equivalent to (100) by virtue of (84) and (85). In the case of strong suction, when $t = O(1)$, it follows from (101) that (102) is equivalent to (48).

For the near-moderate-suction regime, asymptotic expansions (84) and (85) yield

$$\Gamma_1(t) = b_1 t^{-1/2} + b_2 t^{-1} + O(t^{-3/2}),$$
$$\Gamma_2(t) = \left(b_1 - \frac{1}{\kappa}\right)t^{-1/2} + \left(b_2 + \frac{1}{2\kappa^2}\right)t^{-1} + O(t^{-3/2}), \qquad (103)$$
$$t \longrightarrow \infty.$$

For the near-asymptotic boundary-layer flow regime, (98) and (99) yield

$$\Gamma_1(t) = -\ln\sqrt{t} - D + \ln\frac{D}{\kappa} + 2\kappa\sqrt{t} - \frac{\kappa t}{\omega D} + O(t^2),$$
$$\Gamma_2(t) = \ln\sqrt{t} + \ln(-\ln t) - D$$
$$- \ln\omega + 2\kappa\sqrt{t} + O\left(\frac{1}{\ln t}\right), \qquad (104)$$
$$t \longrightarrow 0.$$

Figure 7 shows experimental results from [18, 19] represented in the variables used in universal skin-fric-

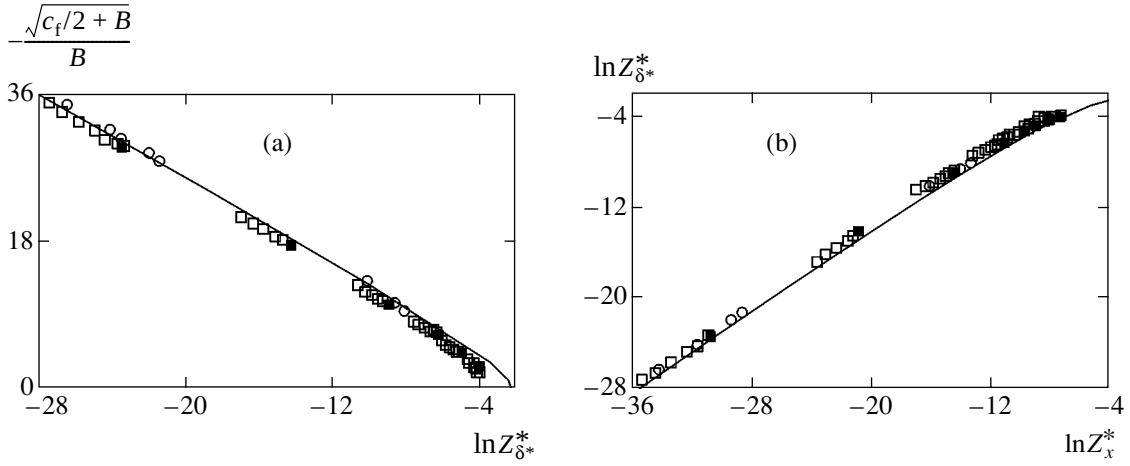

Fig. 8. Experimental results from [18, 19] (symbols) and computed curves of (a) skin friction coefficient and (b) displacement thickness plotted in terms of universal variables. Symbol notation is the same as in Fig. 1.

tion law (102) and the curve of $-\Gamma_1$ versus $t^{-1/2} = -q$ computed by solving the boundary value problem. In agreement with asymptotic expansions (103), the computed curve has the slope $-b_1 = 1.19$ at the origin, reaches a maximum at $-q = 0.15$, and tends to $-\infty$ as $-q \longrightarrow \infty$, as predicted by (104).

The experimental results reported in [18] substantially differ from the corresponding numerical predictions even for the flow over an impermeable plate. The experimental data points taken from [19] lie fairly close to the origin at $q = 0$, but widely deviate from the computed curve with increasing suction velocity.

The use of the variable $W_{\delta*}$ makes it possible to find the leading-order part of the relation between Reynolds number, suction velocity, and skin friction coefficient. Accordingly, Γ_1 plays the role of a relatively small correction to a known leading-order term at $q = O(1)$, which is determined from experimental data as the difference of large quantities. Therefore, the discrepancy between the values of $\sqrt{c_f/2}$ derived from the results reported in [19] and those predicted by using skin-friction law (102) does not exceed 7%. The discrepancy can be explained by the aforementioned inaccuracy of velocity measurements, which were performed in [19] by using a Prandtl–Pitot tube.

Moving Φ_1^∞ and Φ_2^∞ to the left-hand sides in (102), using the expression for t in (48), and collecting like terms, one obtains an alternative form of the universal skin-friction law:

$$\ln Z^*_{\left\{\begin{smallmatrix}\delta*\\ x\end{smallmatrix}\right\}} = \Phi_{\left\{\begin{smallmatrix}1\\ 2\end{smallmatrix}\right\}}(t) + O(\sqrt{c_f}),$$
$$Z^*_{\left\{\begin{smallmatrix}\delta*\\ x\end{smallmatrix}\right\}} \equiv \sqrt{\frac{c_f}{2}}(-B)^{\mp 1}\exp\left(\frac{2\kappa\sqrt{c_f/2}}{B}\right)R_{\left\{\begin{smallmatrix}\delta*\\ x\end{smallmatrix}\right\}}. \quad (105)$$

By virtue of (101), the variables Z_x, $Z_{\delta*}$, Z_x^*, and $Z_{\delta*}^*$ have similar values up to $O(\sqrt{-B})$. However, whereas scaling law (48) is valid only for strong-suction flows, universal law (105) is consistent with experimental results in the entire range of suction velocity. This is illustrated by Fig. 8a, where the data presented in Fig. 1a are plotted in terms of the variables used in (105). Here, the experimental data points follow a unique curve and are close to the computed curve. Even though the disagreement between the experimental results of [18, 19] and the predicted curve is less pronounced in terms of the variables used in (105) as compared to those in (102), the largest discrepancy is also observed at high suction velocities.

Since the distribution of displacement thickness shown in Fig. 8b is plotted in terms of the modified variables used in (105), the scatter of experimental data points is also reduced as compared to Fig. 1b and good agreement with computed results is achieved in the entire range of parameters.

The universal skin-friction law formulated above can be derived by a different method as follows. Adding (14) and (49) term by term, using asymptotics (17) and (33), substituting

$$y_+ = \sqrt{\frac{c_f}{2}}R_\Delta\eta, \quad (106)$$

and taking the double limit as $y_+ \longrightarrow \infty$ and $\eta \longrightarrow 0$, one obtains

$$\ln R_\Delta = \frac{2\kappa}{B}\left(\sqrt{\frac{c_f}{2}+B} - \sqrt{\frac{c_f}{2}}\right)$$
$$- \ln\sqrt{\frac{c_f}{2}} + A(q) - C_0 - \ln F_1 + O(\sqrt{c_f}). \quad (107)$$

In view of expression (45) for displacement thickness and relations (41) and (46), it is clear that scaling law (107) is equivalent to (105).

9.2. Velocity and Reynolds Stress Profiles

Scaling law (49) describes the velocity distribution across the boundary layer outside the viscous sublayer, while scaling law (14) is valid in the near-wall region and the part of the outer region where E has a logarithmic profile. A composite expansion that unifies (49) and (14) can be written in two forms:

$$\begin{aligned} E &= u_+^0(y_+) + w(q,\eta) + O(\sqrt{c_f}),\\ E_e - E &= \gamma(q,\eta) - w_+(y_+) + O(\sqrt{c_f}),\\ 0 &\le \eta < \infty. \end{aligned} \tag{108}$$

The functions $u_+^0(y_+)$ and $\gamma(q,\eta)$ describe the velocity distributions in the near-wall and outer regions, respectively, whereas $w_+(y_+)$ and $w(q,\eta)$ represent their deviations from logarithmic laws in the viscous sublayer and free stream, respectively. When $y_+ = O(1)$ and $R_\Delta \longrightarrow \infty$, the former expression in (108) reduces to (14) by virtue of (106) and the asymptotic form of $w(q,\eta)$ given by (33). When $1/\eta = O(1)$ and $R_\Delta \longrightarrow \infty$, substituting asymptotic expression (17) yields

$$\begin{aligned} E &= \frac{1}{\kappa}\left(\ln\eta + \ln R_\Delta + \ln\sqrt{\frac{c_f}{2}} + C_0\right)\\ &\quad + w(q,\eta) + O(\sqrt{c_f}). \end{aligned}$$

By virtue of (49) and (107), this expression is equivalent to (33). The uniform validity of the latter expression in (108) is demonstrated analogously.

It follows from (107) that the scaling factor $R_\Delta\sqrt{c_f/2}$ relating the transverse coordinates used in the outer and near-wall regions is a function of two arguments, v_+ and q. Therefore, unified velocity profile (108) is also a function of two variables, v_+ and q.

To derive composite expansions of the unified profiles of shear stress and rms transverse velocity fluctuation, asymptotic expression (33) is used to represent the right-hand sides of (53) and (54) as follows:

$$\begin{aligned} Q(q,\eta)\sqrt{S(\infty,0,\eta)} &= P(q,\eta) + \Pi(q,\eta),\\ Q(q,\eta)\sqrt{S_2(\infty,0,\eta)} &= \frac{P(q,\eta)}{\sigma_2} + \Pi_2(q,\eta),\\ P(q,\eta) &= \frac{q}{2\kappa(1-q)}[\ln\eta + A(q) - \ln F_1] + \frac{1}{1-q},\\ \Pi(q,\eta) &= O(\eta^\alpha),\quad \Pi_2(q,\eta) = O(\eta^\alpha),\quad \eta \longrightarrow 0. \end{aligned}$$

Combining (15) with (53) and (16) with (54), one obtains scaling laws for shear stress,

$$\begin{aligned} &\frac{\sqrt{\nu\partial u/\partial y - \langle u'v'\rangle}}{U_e(\sqrt{c_f/2+B}-B)} = Q(q,\eta)\sqrt{S(\infty,0,\eta)}\\ &\quad + \frac{qw_+(y_+)}{2(1-q)} + O(\sqrt{c_f}),\\ &\frac{2}{v_+}\left(\sqrt{\frac{du_+}{dy_+} - \langle u'v'\rangle_+} - 1\right)\\ &= u_+^0(y_+) + \frac{2(1-q)\Pi(q,\eta)}{q} + O(\sqrt{c_f}), \end{aligned}$$

and rms transverse velocity fluctuation,

$$\begin{aligned} &\frac{\sqrt{\langle v'^2\rangle}}{U_e(\sqrt{c_f/2+B}-B)}\\ &= Q(q,\eta)\sqrt{S_2(\infty,0,\eta)} + \frac{qw_+(y_+)}{2\sigma_2(1-q)}\\ &\quad + \frac{q}{v_+(1-q)}\left(\sqrt{\langle v'^2\rangle_+^0(y_+)} - \frac{1}{\sigma_2}\right) + O(\sqrt{c_f}),\\ &\sqrt{\langle v'^2\rangle_+} = \sqrt{\langle v'^2\rangle_+^0(y_+)} + \frac{v_+}{2\sigma_2}u_+^0(y_+)\\ &\quad + \frac{v_+(1-q)}{q}\Pi_2(q,\eta) + O(\sqrt{c_f}),\\ &0 \le \eta < \infty, \end{aligned}$$

which are uniformly valid across the boundary layer.

10. NUMERICAL ANALYSIS

In computations, problem (65)–(67) is solved for $0 \le \tau \le a$ ($0.8 \le a \le 1.5$), and then problem (88)–(90) was solved for $0 \le \lambda \le 1/a$.

By rewriting (65) as

$$\begin{aligned} (\eta\sqrt{S}\varphi_{\eta\eta})_\eta &= G_1,\\ G_1(\tau,\eta) &= \frac{\Omega(\tau^2\varphi_{\tau\eta} - f')}{\Phi + \tau h + 2\tau\eta\sqrt{S}\varphi_{\eta\eta}}, \end{aligned} \tag{109}$$

solving (109) as a second-order equation with a known right-hand side, and using the free-stream conditions in (66), the following integrodifferential equation is obtained for φ_η:

$$\varphi_\eta(\tau,\eta) = \int_\eta^\infty [h(\eta) - h(\eta_1)]G_1(\tau,\eta_1)d\eta_1.$$

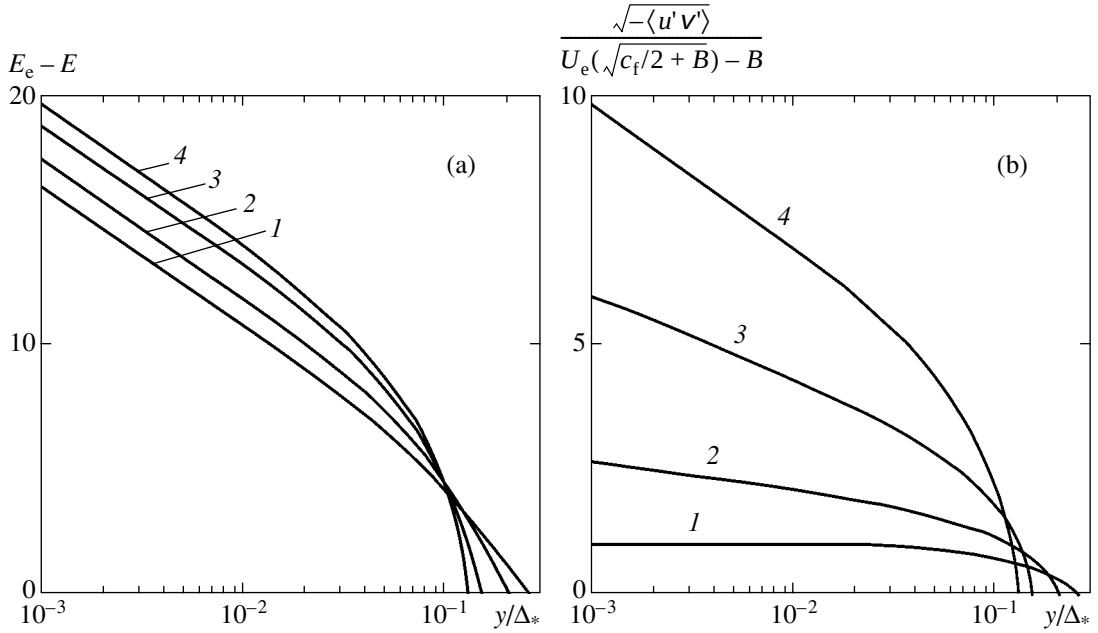

Fig. 9. Velocity (a) and turbulent shear stress (b) profiles in boundary layer flow calculated for $q = 0$ (*1*), –0.25 (*2*), –1.5 (*3*), and $-\infty$ (*4*).

Substituting

$$\varphi_\eta = hy$$

to avoid singularity of the desired function on the wall, one obtains

$$y(\tau, \eta) = \int_\eta^\infty \left[1 - \frac{h(\eta_1)}{h(\eta)}\right] G_2(\tau, \eta_1) d\eta_1,$$
$$G_2(\tau, \eta) = \frac{\Omega(\tau^2 h y_\tau - f')}{\Phi + \tau h + 2\tau\eta\sqrt{S} h y_\eta - 2\tau y}. \quad (110)$$

Relation (67) entails the closure condition

$$\Omega(\tau) = \left[2\kappa F_1 + 2\kappa\tau^2 \frac{dy(\tau, 0)}{d\tau}\right]^{-1}. \quad (111)$$

Equations (110) and (111) for $y(\tau, \eta)$ and $\Omega(\tau)$ are computed by an iterative method on the rectangular domain $\{0 \le \tau \le a, 0 \le \eta \le 1\}$ partitioned into a uniform grid.[2] For a prescribed $\Omega(\tau)$ ($\Omega(\tau) \equiv \Omega(0)$ at the first iteration step), Eq. (110) is solved to determine $y(\tau, \eta)$ on each τ layer, with the integral approximated by Gregory's formula (modified trapezoid rule that is exact for third-degree polynomials). The partial derivative with respect to τ is approximated by using the values of the desired function on the current and previous τ layers; i.e., the scheme is fully implicit in τ. The calculated values of $y(\tau, \eta)$ are substituted into (111) to compute new values of $\Omega(\tau)$ by smoothed numerical differentiation.

Computations has shown that $\Omega(\tau)$ is nearly constant on the interval $0 \le \tau \le a$ and the iterative process can be terminated after performing the third iteration step.

Boundary value problem (88)–(90) is solved by a similar method. Equation (88) is represented as

$$(\eta\sqrt{S}\psi_{\eta\eta})_\eta = -H_1 - \frac{1}{2\sqrt{S}},$$
$$H_1(\lambda, \eta) = \frac{\Omega_1(\lambda\psi_{\lambda\eta} + \psi_\eta)}{h + 2\lambda\eta\sqrt{S}\psi_{\eta\eta}}.$$

The equivalent integrodifferential equation

$$\psi_\eta(\tau, \lambda) = \int_\eta^\infty [h(\eta_1) - h(\eta)] H_1(\lambda, \eta_1) d\eta_1 + f'(\eta),$$

after substituting

$$\psi_\eta = hz$$

is rewritten as

$$z(\lambda, \eta) = \int_\eta^\infty \left[\frac{h(\eta_1)}{h(\eta)} - 1\right] H_2(\lambda, \eta_1) d\eta_1 + \frac{f'(\eta)}{h(\eta)},$$
$$H_2(\lambda, \eta) = \frac{\Omega_1(z_\lambda + z)}{1 + 2\lambda\eta\sqrt{S} z_\eta - 2\lambda z/h}. \quad (112)$$

[2] Since the function $S(\infty, 0, \eta)$ is calculated by using (43), the domain of η is restricted to [0, 1].

The following closure condition is used:

$$\Omega_1(\lambda) = -\left[2\kappa z(\lambda, 0) + 2\kappa\lambda\frac{dz(\lambda, 0)}{d\lambda}\right]^{-1}. \quad (113)$$

The initial values of $z(1/a, \eta)$ are calculated by using the known $y(a, \eta)$ and the constraint that follows from (63) combined with (86), with $\Omega_1(\lambda) \equiv \Omega(1/a)$ at the first iteration step.

As in the former problem, $\Omega_1(\lambda)$ is a slowly varying function on $[0, 1/a]$ and the iterative process can be terminated after performing the third iteration step.

Note that the computed results are stable with respect to the only empirical function used in the analysis, $f'(\eta)$.

The calculated limit value $F_1\Omega_1(0)$ equals the smallest root of Eq. (95). Thus, the function $-F_1 d\lambda/ds$ monotonically increases from $1/2\kappa = 1.220$ at $\lambda = \infty$ to 1.423 at $\lambda = 0$.

Figure 9 shows the distributions of velocity and shear stress computed for several values of q. In Fig. 9b, the curves for $q = 0$ and $-\infty$ are plotted by using formulas (55).

Computed results are also presented in Figs. 1, 5, 7, and 8.

11. CONCLUSIONS

A closure condition is derived for turbulent boundary layer flow over a flat plate with suction in the form of a universal relation between shear stress and mean-velocity gradient. The mean velocity is determined by using only one empirical function: the velocity profile in the turbulent boundary layer flow over an impermeable flat plate. The only characteristic of the profile that is important with regard to computations is the existence of an interval of logarithmic near-wall behavior.

As a result, the distributions of velocity, shear stress, and skin friction are calculated in the entire range of parameters by solving averaged equations under very general physical assumptions without invoking any special closure hypotheses.

The theory developed here can be used to calculate the rms transverse velocity fluctuation in the entire flow and the rms streamwise and spanwise velocity fluctuation in the outer region of the boundary layer. These calculations can be performed by using only the corresponding distributions for the flow over an impermeable plate.

Universal distributions of mean velocity, shear stress, and rms transverse velocity fluctuation are obtained for the near-wall region of the boundary layer. The distributions of these quantities outside the viscous sublayer represented in terms of scaling variables are described by a family of curves depending only on q. Their profiles in the entire boundary-layer flow are functions of two variables, v_+ and q.

The Reynolds stress components associated with streamwise and spanwise velocity fluctuations also obey one-parameter scaling laws in the outer region of the boundary layer.

There exists a near-wall region where both square root of shear stress and rms transverse velocity fluctuation are proportional to the logarithm of the distance from the wall, while the rms streamwise and spanwise velocity fluctuations scale with the logarithm to the power 3/2.

The skin-friction distribution is described by a single scaling curve for flows with arbitrary suction velocities at various Reynolds numbers.

Far downstream, the limit of asymptotic boundary layer is approached as $R_x \longrightarrow \infty$. In this limit, all flow variables depend only on the transverse coordinate. The corresponding values of $c_f/2 + B$ and difference between the current and asymptotic displacement thicknesses vanish exponentially.

ACKNOWLEDGMENTS

This work was supported under the State Program for Support of Leading Science Schools, grant 1635.2003.

REFERENCES

1. A. A. Izakson, Zh. Éksp. Teor. Fiz. **7**, 919 (1937).
2. C. B. Millikan, in *Proceedings of 5th International Congress on Applied Mechanics* (Wiley, New York, 1939), p. 386.
3. R. von Mises, in *Th. von Kármán Anniversary Volume* (Calif. Inst. Tech. Press, Pasadena, 1941), p. 317.
4. B. A. Kader and A. M. Yaglom, Itogi Nauki Tekh., Ser.: Mekh. Zhidk. Gaza **18**, 81 (1980).
5. I. I. Vigdorovich, Dokl. Akad. Nauk **392**, 340 (2003) [Dokl. Phys. **48**, 528 (2003)].
6. I. I. Vigdorovich, in *Advances in Turbulence X: Proceedings of 10th European Turbulence Conference,* Ed. by H. I. Andersson and P.-A. Krogstad (CIMNE, Barcelona, 2004), p. 129.
7. I. I. Vigdorovich, Zh. Éksp. Teor. Fiz. **126**, 1180 (2004) [JETP **99**, 1028 (2004)].
8. I. I. Vigdorovich, in *Proceedings of 4th International Symposium on Turbulence, Heat and Mass Transfer,* Ed. by K. Hanjalic *et al.* (Begell Hous, New York, 2003), p. 147.
9. I. I. Vigdorovich, Dokl. Akad. Nauk **396**, 47 (2004) [Dokl. Phys. **49**, 303 (2004)].
10. I. I. Vigdorovich, Izv. Ross. Akad. Nauk, Mekh. Zhidk. Gaza, No. 4, 106 (1993) [Fluid Dyn. **28**, 514 (1993)].
11. I. I. Vigdorovich, Dokl. Akad. Nauk **331**, 443 (1993) [Phys. Dokl. **38**, 335 (1993)].
12. A. A. Townsend, *The Structure of Turbulent Shear Flow* (Cambridge Univ. Press, Cambridge, 1976).

13. A. E. Perry, S. Henbest, and M. S. Chong, J. Fluid Mech. **165**, 163 (1986).
14. P. R. Spalart, J. Fluid Mech. **187**, 61 (1988).
15. I. I. Vigdorovich, Dokl. Akad. Nauk **356**, 42 (1997) [Phys. Dokl. **42**, 506 (1997)].
16. M. Van Dyke, *Perturbation Methods in Fluid Mechanics* (Academic, New York, 1964; Mir, Moscow, 1967).
17. D. Coles, J. Fluid Mech. **1** (Part 2), 191 (1956).
18. R. L. Simpson, R. J. Moffat, and W. M. Kays, Int. J. Heat Mass Transf. **12**, 771 (1969).
19. K. Depooter, PhD Thesis (Univ. Waterloo, Canada, 1973).
20. F. H. Clauser, Adv. Appl. Mech. **4**, 1 (1956).
21. R. L. Simpson, R. J. Moffat, and W. M. Kays, Rep. HMT-2 (Stanford Univ., 1967).
22. P. Mariani, P. Spalart, and W. Kollmann, in *Proceedings of International Conference on Near-Wall Turbulent Flows*, Ed. by R. M. C. So *et al.* (Elsevier, Amsterdam, 1993).
23. R. A. Antonia, P. R. Spalart, and P. Mariani, Phys. Fluids **6**, 430 (1994).
24. P. S. Andersen, W. M. Kays, and R. J. Moffat, J. Fluid Mech. **69** (Part 2), 353 (1975).

Translated by A. Betev